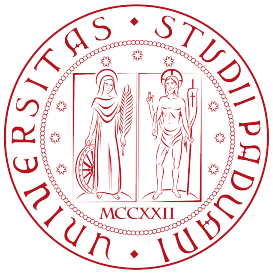

UNIVERSITÀ DEGLI STUDI DI PADOVA

DIPARTIMENTO DI FISICA E ASTRONOMIA
"GALILEO GALILEI"

DOCTORAL THESIS IN PHYSICS

Measurement of heavy-flavour decay electrons and heavy-flavour baryon production with ALICE experiment at LHC

Candidate:
Mattia FAGGIN

P.h.D. School Coordinator:
Prof. Franco SIMONETTO

Supervisor:
Prof. Marcello LUNARDON

Co-supervisor:
Dr. Andrea ROSSI

PhD school in Physics - XXXIV Cycle

Declaration of Authorship

I, Mattia FAGGIN, declare that this thesis titled, "Measurement of heavy-flavour decay electrons and heavy-flavour baryon production with ALICE experiment at LHC" and the work presented in it are my own. I confirm that:

- This work was done wholly or mainly while in candidature for a research degree at this University.
- Where any part of this thesis has previously been submitted for a degree or any other qualification at this University or any other institution, this has been clearly stated.
- Where I have consulted the published work of others, this is always clearly attributed.
- Where I have quoted from the work of others, the source is always given. With the exception of such quotations, this thesis is entirely my own work.
- I have acknowledged all main sources of help.
- Where the thesis is based on work done by myself jointly with others, I have made clear exactly what was done by others and what I have contributed myself.

Signed: _____

Date: _____

Abstract

The ALICE experiment at the LHC at CERN is devoted to the study of collisions of heavy nuclei accelerated at ultra-relativistic energies. These collisions are employed to reproduce in laboratory the quark-gluon plasma (QGP), a deconfined state of the strongly-interacting matter. The existence of this state is predicted by the QCD theory under extreme conditions of energy-density and temperature. The QGP is supposed to constitute the early universe in the first $\sim$ 10 μs after the Big Bang. Charm and beauty quarks are unique probes for investigating the QGP. Given a mass of the GeV order, they are produced in the hard-scattering processes in the early stages of the nucleus-nucleus collision, experiencing the full evolution of the system. Charm and beauty quarks lose energy by interacting with the plasma constituents. These phenomena can be studied by measuring the heavy-flavour hadron production and exploited to infer properties of the system. In this thesis, the production of electrons from charm and beauty hadron decays in central (0–10%), semicentral (30–50%) and peripheral (60–80%) Pb–Pb collisions at $\sqrt{s_{\rm NN}} = 5.02$ TeV measured with the ALICE experiment is presented. These results are compared with those in pp collisions by means of the nuclear modification factor ($R_{\rm AA}$) and a significant suppression with respect to what expected in absence of a deconfined medium is observed in central and semicentral events. This behaviour indicates that charm and beauty quarks are subject to in-medium energy loss. The observed effect decreases in more peripheral events. The measurement is pushed down to $p_{\rm T}^{\rm e^-} = 500$ MeV/c, where the heavy quark production is sensitive to the shadowing effects. The $R_{\rm AA}$ does not overcome unity, signalling that the production of heavy-flavour hadrons is suppressed. The QGP formation in heavy-ion collisions is expected to induce a modification of the heavy quark hadronisation mechanisms. In order to disentangle the effects of the medium produced in Pb–Pb collisions, a deep comprehension of the mechanisms that govern the hadronisation in pp collisions is required. Recent results on baryon-to-meson production ratios in pp collisions at the LHC showed an enhancement with respect to $\rm e^+e^-$ and $\rm e^-p$ collisions. In this thesis, the measurement of the $\Lambda_{\rm c}^+$ and $\Sigma_{\rm c}^{0,++}$ baryon production cross section in pp collisions at $\sqrt{s} = 13$ TeV with the ALICE experiment is described. The ratio to the $\rm D^0$ meson production of both baryons is significantly higher than what measured in $\rm e^+e^-$ and $\rm e^-p$ collisions. The measurements are described by several model calculations assuming different mechanisms for the charm quark hadronisation. Moreover, the first measurement of the prompt $\Lambda_{\rm c}^+$ feed-down from $\Sigma_{\rm c}^{0,+,++}$ decays in pp collisions is presented and observed to be $\sim$ 2 times larger than $\rm e^+e^-$ collisions in the interval $2 < p_{\rm T} < 12$ GeV/c. The investigation of the charm quark hadronisation mechanisms in hadronic collisions can significantly benefit from production measurements of more charm baryons. In the last Chapter, a few studies on the capabilities to perform such measurements in the future with the ALICE experiment are discussed. New frontiers in the heavy-flavour hadron production measurements will be allowed by the significantly higher statistics that the experiment will collect in the upcoming years, as well as the improved pointing resolution provided by the upgraded ITS detector.

Keywords: heavy-flavour, charm, beauty, electrons, baryons, hadronisation, quark-gluon plasma, QCD

Contents

For my parents.

Introduction

Quantum Chromo-Dynamics (QCD) is the gauge theory describing the strong interaction between quarks and gluons, the latter being the gauge vector bosons mediating the interaction. Gluons carry colour charge so they can interact as described by the non-Abelian structure of the theory. The gluon self-coupling is directly related to the asymptotic freedom and the confinement, which are peculiar properties of the strong interaction. According to asymptotic freedom, quarks and gluons can be considered as free particles in processes with a high momentum transfer, where the coupling is small. On the other hand, in processes with lower exchange of momentum the interaction coupling increases. Moreover, the confining potential increases linearly with the distance among partons, so that quarks and gluons are confined within hadrons. According to Lattice QCD (lQCD) calculations, under extreme conditions of high temperature and energy-density strongly interacting matter can undergo a phase transition from the hadronic phase to a deconfined one, called quark-gluon plasma (QGP). Such a state is described in terms of quark and gluon degrees of freedom, since they are no more confined within hadrons. The QGP characterised the early universe in the first $\sim$ 10 µs after the Big Bang and only after such a time it underwent the phase transition to the hadronic phase. The QGP state can be reproduced in the laboratory with ultra-relativistic heavy-ion collisions, which allow to reach the necessary energy-density and temperature conditions. The two main facilities nowadays engaged in the exploration of this exotic state of matter are the Relativistic Heavy Ion Collider (RHIC) at Brookhaven National Laboratory (BNL) and the Large Hadron Collider (LHC) at CERN. The experiment mainly devoted to the study of heavy-ion collisions at ultra-relativistic energies at CERN is A Large Ion Collider Experiment (ALICE).

Charm and beauty quarks are a unique probe for the study of the QGP. Given their mass of the GeV scale, they are mainly produced in the hard scattering processes in the early stages of the collision, before the formation of the QGP. Therefore, they experience the full space-time evolution of the QGP. Heavy quarks are expected to lose energy due to the interactions with the medium via both radiative and collisional processes. Moreover, heavy quark production in heavy-ion collisions is sensitive to the "cold nuclear matter" effects, not related to the presence of QGP but to that of heavy ions in the initial state of the collision. A complete comprehension of the heavy-flavour physics in nucleus-nucleus collisions requires a deep understanding of the phenomenology in pp collisions.

The goal of this thesis is to contribute to the investigation of the charm and beauty quark production and dynamics in hadronic collisions at the LHC. The two measurements described here regard the production of electrons from semileptonic decays of charm and beauty hadrons in Pb–Pb collisions at $\sqrt{s_{\rm NN}} = 5.02$ TeV and the production of Λ_c^+ and $\Sigma_c^{0,++}(2455)$ baryons in pp collisions at $\sqrt{s} = 13$ TeV.

In Chapter 1 the basic concepts of the strong interaction and the deconfinement phase transition are described. Moreover, the main signatures of the QGP production and its space-time evolution are introduced. Some concepts about the charm and beauty quark production and dynamics in hadronic collisions at the LHC are

treated in detail in Chapter 2, with a particular emphasis on the heavy-quark hadronisation mechanisms in the second half of the Chapter. In Chapter 3 the structure of the ALICE experiment and of the main subsystems used in the analyses reported in this thesis are described. The event characterisation in terms of trigger requirements and centrality determination is treated later in the Chapter, together with the description of vertex and track reconstruction procedures, as well as the particle identification techniques employed in the analyses described in this thesis. Dedicated studies on the comparison between data and Monte Carlo (MC) simulations of the matching efficiency to the ITS detector for the TPC-reconstructed tracks are discussed in Section 3.6.4. Moreover, the data-driven smearing procedure on the impact parameter values of reconstructed tracks in MC simulations is described in Section 3.6.5.[1]

In Chapter 4 the measurement of electrons from semi-leptonic decays of heavy-flavour hadrons in central (0–10%), semicentral (30–50%) and peripheral (60–80%) Pb–Pb collisions at $\sqrt{s_{\rm NN}} = 5.02$ TeV in the transverse momentum range $p_{\rm T} < 6$ GeV/c is described. A pure sample of electrons is isolated by exploiting the excellent PID capabilities of the ALICE apparatus in the central barrel. In particular, the electron identification is performed by means of the $\mathrm{d}E/\mathrm{d}x$ signals released in ITS and TPC as well as the time of flight measured with the TOF detector. The electrons from heavy hadron decays are then obtained from the inclusive electron sample by subtracting the signal from background components, among which the contributions of photon conversions in the material and of Dalitz decays of pseudo-scalar mesons are dominant. A measurement of the nuclear modification factor ($R_{\rm AA}$) is obtained and provides insights in the charm and beauty energy loss in the QGP. Moreover, this measurement is pushed down to $p_{\rm T}^{\rm e^-} = 500$ MeV/c in order to study the shadowing effect, which influences the charm and beauty quark production at low Bjorken-x.

The modifications on the heavy-flavour hadron production in heavy-ion collisions induced by the formation of a deconfined medium can be studied by comparing with results obtained in pp collisions. Despite an energy density reached probably insufficient to produce a hot and high-density deconfined medium, a complete understanding of the hadronisation processes involving heavy quarks in pp collisions at the LHC is still an open point. Recent results of the $\Lambda_{\rm c}^+/{\rm D}^0$ ratio show a significant enhancement with respect to the results in $\mathrm{e^+e^-}$ and $\mathrm{e^-p}$ collisions, pointing to a non-universality of fragmentation functions among the collision systems. A crucial contribution in this context is provided by the measurement of prompt $\Lambda_{\rm c}^+$ (udc) and $\Sigma_{\rm c}^{0,+,++}(2455)$ (ddc, udc, uuc) baryon production in pp collisions at $\sqrt{s} = 13$ TeV. In this thesis, such measurements are performed in the $\Lambda_{\rm c}^+ \rightarrow \mathrm{pK^-}\pi^+$ and $\Sigma_{\rm c}^{0,++} \rightarrow \Lambda_{\rm c}^+\pi^{-,+}$ decay channels, exploiting the reconstruction of $\Lambda_{\rm c}^+$ decay vertices. In this work, the fraction of prompt $\Lambda_{\rm c}^+$ from $\Sigma_{\rm c}^{0,+,++}(2455)$ decays is measured to be around $\sim 38\%$, quantifying for the first time the fraction of $\Lambda_{\rm c}^+$ deriving from these strong decays in hadronic collisions at the LHC. The $\Sigma_{\rm c}^{0,+,++}(2455)$ covers a crucial role for the understanding of charm hadronisation in pp collisions at the TeV scale. According to conventional fragmentation, the production of $\Sigma_{\rm c}^{0,++}$ baryons should be strongly suppressed by a large penalty factor on the (uu) and (dd) di-quark formation, which is not predicted by several models. All these aspects are discussed in detail in Chapter 5.

[1] These studies were carried on the pp and Pb–Pb collision samples collected by the ALICE experiment in 2018 and on the associated MC productions during the service-task activity.

The optimisation of the selections adopted in the reconstruction of charm baryons can be further improved by the usage of Machine Learning (ML) techniques. In addition, the measurement of charm baryon production in hadronic collisions will significantly benefit from the improvement of the spatial resolution of the tracking system and from a larger integrated luminosity. Considering the major upgrades that several ALICE subsystems are undergoing during the long shutdown 2 (LS2) and 3 (LS3) of the LHC, the ALICE experiment will be able to operate at a peak luminosity of $\mathcal{L} = 6 \times 10^{27}$ cm^{-2}s^{-1} and an interaction rate of about 50 kHz in Pb–Pb collisions at $\sqrt{s_{\rm NN}} = 5.5$ TeV, with the possibility to collect a sample of about $\mathcal{L} = 10$ nb^{-1} in central collisions. According to this scenario, some performance studies on the expected significance for the $\Xi_c^+ \rightarrow {\rm pK}^-\pi^+$ signal measurement are shown in Chapter 6. The production of Ξ_c^+ baryon in Pb–Pb collisions is expected to be largely enhanced in a scenario where charm quarks hadronise via coalescence with light quarks from the medium, given the measured enhancement of strange quark production in the QGP. Moreover, the ${\rm pK}^-\pi^+$ may be a promising channel given the improved spatial resolution provided by the upgraded ITS detector. Finally, some pilot studies for the reconstruction of $\Omega_c^0 \rightarrow \Omega^-\pi^+$ decay signal with the upgraded ITS detector during Run 4 at the LHC (ITS 3) are reported in the last Section. These studies are mainly focused on the separation of primary Ω^- baryons from the products of the Ω_c^0 decays by means of an impact parameter analysis.

Chapter 1

QCD and ultra-relativistic heavy-ion collisions

The strong interaction between quarks and gluons, the elementary constituents of the hadronic matter, is described by Quantum Chromo-Dynamics (QCD), as introduced in Sec. 1.1. This theory predicts the existence of a phase transition for the strongly interacting matter from the hadronic phase to a deconfined one, called quark-gluon plasma (QGP), where quarks and gluons are not confined within hadrons. Such a state characterised the early universe in the first $\sim$ 10 µs after the Big Bang. QCD calculations on lattice provide quantitative predictions of the basic properties of the QGP and the QCD phase transition, as described in Sec. 1.2 where the QCD phase diagram is discussed. Such a transition can occur only under extreme conditions of temperature and energy density, which are reached in laboratory with ultra-relativistic heavy-ion collisions, as described in Sec. 1.3. The Chapter is concluded with Sec. 1.4, where the main signatures of the QGP formation and space-time evolution as well as some measurements from the experiments at the LHC and RHIC colliders are described.

1.1 Quantum Chromo-Dynamics

Strong interaction is one of the fundamental forces present in nature. It regulates nuclear phenomena and describes the interaction among quarks through gluon exchange. The quantum field theory that describes this interaction is *Quantum Chromo-Dynamics* (QCD), non-abelian gauge theory based on the local symmetry under the SU(3) colour group. The lagrangian density can be written as [1, 2]:

$$\mathcal{L}_{QCD} = -\frac{1}{4} G^a_{\mu\nu} G^{\mu\nu}_a + \sum_{f=1}^{n_f} \bar{q}^f_i \left(i\gamma_\mu D^\mu_{ij} - m_f \delta_{ij} \right) q^f_j \,, \tag{1.1}$$

where f indicates the quark flavour (u, d, c, s, t, b), γ^μ corresponds to the Dirac matrices and δ_{ij} is the Dirac delta function. The term:

$$\begin{aligned} G^a_{\mu\nu} &= \partial_\mu A^a_\nu - \partial_\nu A^a_\mu - i g_S [A_\mu, A_\nu] \\ &= F^a_{\mu\nu} + g_S f_{abc} A^\mu_b A^\nu_c \end{aligned} \tag{1.2}$$

represents the *gluon field strength tensor*, where a, b, c are colour indices running over the octet base of the SU(3) adjoint representation. The gauge field associated to the gluon is:

$$A_\mu = \sum_{k=1}^{8} A^a_\mu \lambda^a / 2 \,, \tag{1.3}$$

where A^a_μ, $a = 1, \ldots, 8$ are eight gauge fields, as there are eight conserved charges and λ^a are the Gell-Mann matrices. They satisfy the SU(3) algebra, defined by the commutation rules;

$$\left[\frac{\lambda^a}{2}, \frac{\lambda^b}{2}\right] = i f_{abc} \frac{\lambda^c}{2} \tag{1.4}$$

with f_{abc} the SU(3) *structure constants*. Using Eq. 1.2, the first term of Eq. 1.1 becomes:

$$\begin{aligned} \mathcal{L}_G = & \frac{1}{4} F^a_{\mu\nu} F^{\mu\nu}_a \\ & + g_S f_{abc} A^a_\mu A^b_\nu \partial^\mu A^\nu_c - \frac{1}{4} g_S^2 f_{abc} f_{ade} A^\mu_b A^\nu_c A^d_\mu A^e_\nu \end{aligned} \tag{1.5}$$

The Eq. 1.5 shows the gluonic part of the QCD lagrangian. It contains a kinetic term (first line) and, differently from QED, a gluon self-interaction one (second line). This feature derives from the non-abelian structure of the SU(3) group, that introduces the additional non-null term $-ig_S[A_\mu, A_\nu]$ in the gluon strength tensor. This aspect differentiates QCD, where the gluons carry themselves colour charge and therefore can self-interact, from QED, where the photons are electrically neutral and do not self-interact. The quantity:

$$D^\mu_{ij} = \partial^\mu \delta_{ij} - i g_S \frac{\lambda^a_{ij}}{2} A^\mu_a \tag{1.6}$$

is the *covariant derivative*. Using Eq. 1.6, the second term of the QCD lagrangian Eq. 1.1 associated to quarks can be explicitly written as:

$$\begin{aligned} \mathcal{L}_Q &= \sum_{f=1}^{n_f} \bar{q}^f_i (i\gamma_\mu D^\mu_{ij} - m_f \delta_{ij}) q^f_j \\ &= \sum_{f=1}^{n_f} \bar{q}^f_i \left[i\gamma_\mu \partial^\mu \delta_{ij} - m_f \delta_{ij}\right] q^f_j + g_S \sum_{f=1}^{n_f} \bar{q}^f_i \left[\frac{\lambda^a_{ij}}{2} \gamma_\mu A^\mu_a\right] q^f_j \\ &\equiv \mathcal{L}_0 + \mathcal{L}_I \, . \end{aligned} \tag{1.7}$$

The first part $\mathcal{L}_0$ describes the free quark-field lagrangian density, which is invariant under global SU(3) transformations and includes the kinetic and the mass terms for each quark flavour. The second part $\mathcal{L}_I$ is naturally introduced by retaining the lagrangian invariance when applying local phase SU(3) transformations to $\mathcal{L}_0$. This term automatically generates the interactions between quarks and gluons [2].

The adimentional constant g_S quantifies the intensity of the strong interaction. This quantity is defined as $g_S = \sqrt{4\pi\alpha_S}$, where α_S is the *strong coupling constant*. The value of α_S is not actually constant, but it depends on the energy scale of the considered process. As theorised in 1973 by H. D. Politzer [8], D. Gross & F. Wilczek [9], it evolves with respect to the momentum transfer Q according to the equation:

$$\alpha_S\left(|Q|^2\right) = \frac{\alpha_S(\mu^2)}{1 + \frac{\alpha_S(\mu^2)}{12\pi}(33 - 2n_f)\ln\left(|Q|^2/\mu^2\right)} \, , \tag{1.8}$$

where μ is a renormalization energy scale and n_f is the number of flavours that contribute to 1-loop corrections, namely those which $m_f < |Q|$ [10]. The trend of α_S described in Eq. 1.8 is confirmed by experimental data, as shown in Fig. 1.1. The strong coupling constant tends to zero for short distances, namely when the momentum transfer diverges. It implies that in processes with infinite energy scale

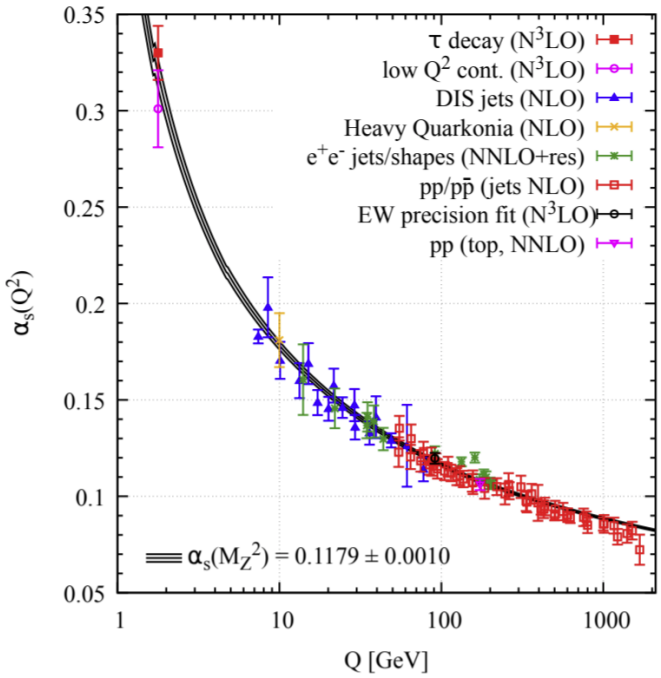

FIGURE 1.1: Summary of measurements of α_S as a function of the momentum transfer Q. The respective degree of QCD perturbation theory used in the extraction of α_S is indicated in brackets (NLO: next-to-leading order; NNLO: next-to-next-to-leading order; NNLO+res.: NNLO matched to a resummed calculation; N3LO: next-to-NNLO). Figure from [3].

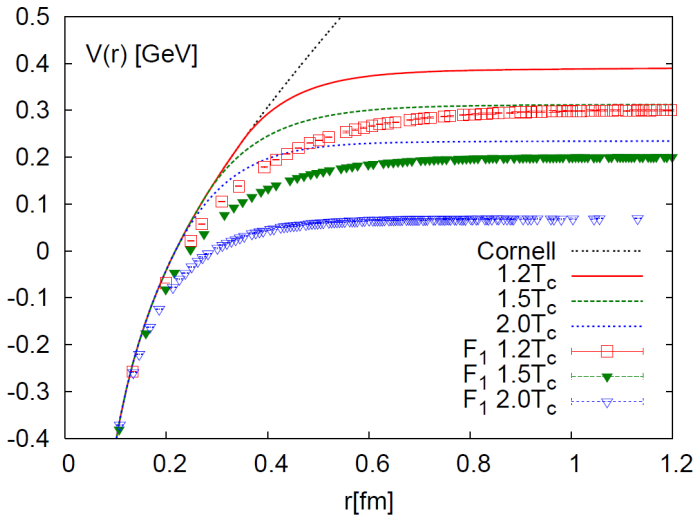

FIGURE 1.2: Cornell potential compared with confining $q\bar{q}$ potential for heavy quarks at finite temperature calculated with potential models combined with perturbative QCD [4] and from lattice data on singlet free energy [5–7]. Figure from [4].

the partons can be considered as unperturbed free particles: this is a property called *asymptotic freedom*. On the contrary, at large distances (low energies, $|Q| \lesssim 1\ \mathrm{GeV}/c$) the value of α_S diverges, meaning that the strong interaction assumes higher and higher intensity.

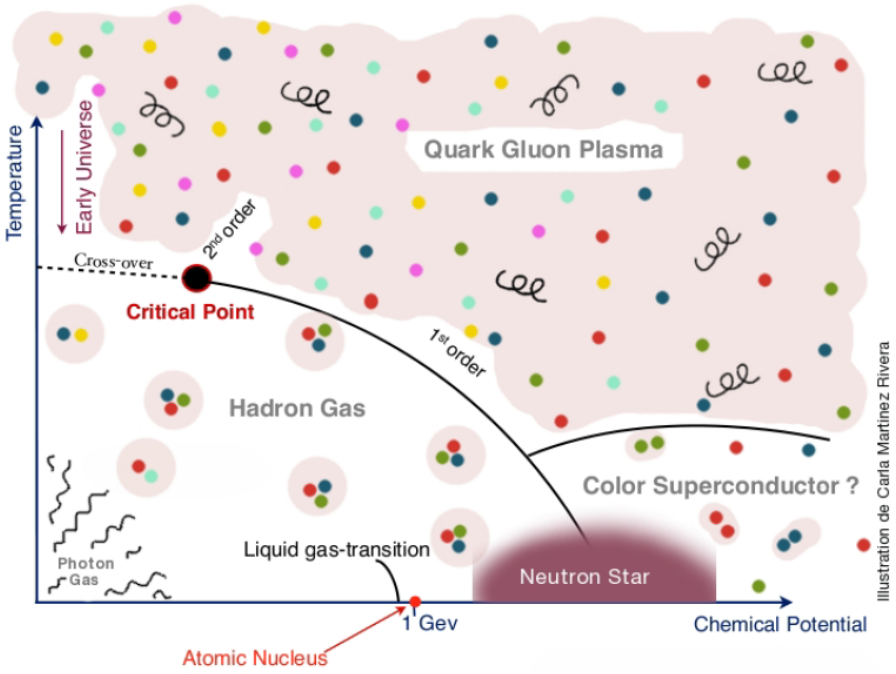

FIGURE 1.3: Layout of the QCD phase diagram. Figure from [12].

The interaction of a $q\bar{q}$ pair can be described by the Cornell potential [11]:

$$V(r) = \sigma r - \frac{\alpha}{r}\,, \tag{1.9}$$

where σ represents the string tension between the two quarks and α is a Coulombian-like constant. For a $c\bar{c}$ system at $T = 0$, typical values for these quantities are $\sigma \simeq 0.16$ GeV^2 and $\alpha \simeq 1/2$ [11]. At high distances, the linear term of the potential increases the system energy until it overcomes the threshold for the formation of a new $q\bar{q}$ pair, therefore a split in two $q\bar{q}$ pairs takes place. This QCD phenomenon is called *confinement*. The potential formulation reported in Eq. 1.9 is valid at $T = 0$. At finite temperature, the linear term of the confining potential gets smaller due to the reducing string tension, with a consequent decrease of the confining potential at large radii. In Fig. 1.2 the Cornell potential is compared with the confining $q\bar{q}$ potential for heavy quarks at finite temperature calculated with potential models combined with perturbative QCD [4] and from lattice data on singlet free energy [5–7]. For distances larger than $0.4 \div 0.6$ fm the confining potential reaches a plateau that decreases with increasing temperature. This behaviour is responsible of the quarkonia suppression in the QGP, as explained in Sec. 1.4.8.

1.2 Lattice QCD and phase diagram

Due to the different scales of the α_S constant depending on the energy regime, the theoretical methods needed to study the physics of strong interaction are different. If in the former case the small value of α_S permits a perturbative approach for the calculation of scattering amplitudes (perturbative QCD, pQCD), for the latter α_S is too large and different techniques must be adopted. One possibility is to evaluate the QCD lagrangian Green's functions on a discrete space-time grid, as done in lattice QCD (lQCD [13]). This theory considers a discrete space-time structure,

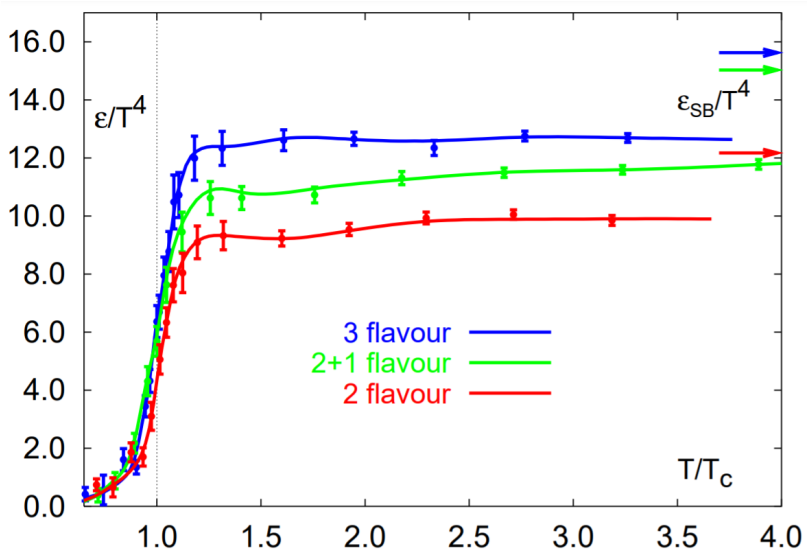

FIGURE 1.4: Energy density dependence as a function of the temperature of strongly interacting matter at $\mu_B = 0$ from lQCD calculations, with the hypothesis of either 2 or 3 light quarks, or with 2 light quarks plus a four times heavier strange quark. The arrows in the right side indicate the ε/T^4 value expected for an ideal gas. Figure from [15].

corresponding to a complex-time hypercubic lattice where the sites are occupied by quarks and linked by gluons. This grid is the environment where the equations of theory are solved. The predictions of physics phenomena are obtained in the limit $a \to 0$, where a is the spacing between two adjacent sites of the grid.

Lattice QCD at finite temperature allows to investigate the $\mu_B \approx 0$ of the phase diagram of the strongly-interacting matter, which is reported in Fig. 1.3. The quantity in abscissa is the *baryon-chemical potential* μ_B, which corresponds to the energy needed to increase by one unity the total baryon number and it is proportional to the net baryon density $n_B - n_{\bar{B}}$. The ordinary matter sits in the region around $T \approx 0$ and $\mu_B \approx 1$ GeV. For higher values of the baryon-chemical potential, corresponding to a system pressure above 10^{32} Pa, the matter can be described as a degenerated gas of neutrons, whose structure is close to that of the atomic nucleus and should compose the core of the neutron stars. If the pressure increases of about 3 orders of magnitude, above 10^{35} Pa, the repulsive force of the degenerated gas cannot compensate this pressure any more and the matter becomes a low-temperature gas of quarks that are no more constrained inside hadrons. Usually, this exotic state of matter is referred in literature as a colour superconductive state [14]. At higher temperatures, above $T \approx 100$ MeV, the nucleon gas converts into a hadron gas and for even higher values it is expected to undergo a transition to the *quark-gluon plasma* (QGP), a deconfined state of matter characterized by partonic degrees of freedom, since quarks and gluons are no more constrained within hadrons. This state of matter is supposed to characterise the early universe during the first ~ 10 µs after the Big Bang. If we consider the low-μ_B regime ($\mu_B \approx 0$) the transition of matter to the QGP occurs as a cross-over at a temperature of $T \approx 154 - 174$ MeV ($\approx 1.8 - 2.0 \times 10^{12}$ K) given the non-null values of the light quark masses $m_{u,d,s}$ [12, 15, 16]. For higher values of the baryon-chemical potential, the matter undergoes a first-order phase transition to QGP, and the coexistence with the cross-over at low μ_B implies the presence of a *critical point*.

The QGP can be considered as an ideal fluid constituted by all elementary particles with a mass lower than the system temperature, according to lQCD calculations at finite temperature ($T > \Lambda_{\mathrm{QCD}} \approx 200$ MeV). As shown in Fig. 1.4, the system energy density follows a $\propto T^4$ trend for values above the critical temperature T_c, in line with the ideal gas picture, where both bosons and fermions are in chemical equilibrium and their energy densities follow a Stefan-Boltzmann law:

$$\varepsilon = 3p = g\frac{k_{\mathrm{B}}^4}{\hbar^3 c^3}\frac{\pi^2}{30}T^4 \text{ , where } g = \begin{cases} n_{\mathrm{d.o.f.}}, \text{ bosons} \\ \frac{7}{8}n_{\mathrm{d.o.f.}}, \text{ fermions} \end{cases} . \tag{1.10}$$

The coefficient g includes the number of degrees of freedom due to spin, flavours and charges ($n_{\mathrm{d.o.f.}}$), modulo a constant factor that refers to the differences between the Bose-Einstein and Fermi-Dirac statistics. A fast increase of ε/T^4 is noticeable in correspondence of the critical temperature T_c that according to Eq. 1.10 can be interpreted as a change in the number of degrees of freedom occurring during the phase transition, while moving from $g = 3$ in the colourless pion gas to the 37 (with two flavours) in the deconfined state [1]. In Fig. 1.4 the scenarios with 2 light quarks, 3 light quarks and 2 light plus 1 heavier (strange) quarks are shown. Presumably, the latter one is likely to be closest to the physically-realised quark mass spectrum and provides a critical value of the energy density of $\varepsilon_c \approx 0.7$ GeV/fm^3.

The nature of the QCD phase transition, such as its order and the behaviour at the critical point, is ruled by the intrinsic symmetries of the QCD lagrangian density. A phase transition is usually classified according to the behaviour of the system free energy. In the case of the QCD phase transition, the free energy is linked to the *Polyakov loop* [17], defined as:

$$L(\vec{x}) = \mathrm{Tr}\left[\mathcal{P}\exp\left(ig\int_0^\beta \mathrm{d}x_0 A_0(x_0,\vec{x})\right)\right], \quad \text{with } \beta = 1/T , \tag{1.11}$$

where A_μ is the gluon field in the fundamental representation. The Polyakov loop is invariant under transformations of the centre group of SU(3) gauge group, satisfying the so-called *centre symmetry* [18], and its expectation value $\langle L\rangle$ serves as order parameter of the confinement-deconfinement phase transition in QCD [19]. The quark confinement realises in the null value for the Polyakov loop expectation value, $\langle L\rangle = 0$. The transition to the deconfined phase is characterised by a non-null value, $\langle L\rangle > 0$. The Polyakov loop expectation value is linked to the system free energy F by the equation:

$$\langle L\rangle = \exp(-F/T) . \tag{1.12}$$

This equation indicates that in the deconfined phase, where $\langle L\rangle > 0$, the cost in free energy to insert a single quark in the system is finite. On the contrary, the cost is infinite in case of the confined phase, where $\langle L\rangle = 0$, according to Eq. 1.12.

The QCD lagrangian density shown in Eq. 1.1 and, in particular, the quark term explicitly reported in Eq. 1.7 exhibits a symmetry under flavour transformation, since the nature of the quark interaction with the gauge bosons does not depend on

[1] The degrees of freedom for the pion gas correspond to the three values of the isospin quantum number, referred to the three mesons π^0, π^+, π^-. For the deconfined state, the bosonic and fermionic degrees of freedom need to be treated separately. Neglecting the contribution of electromagnetic particles, which in a small radius QGP do not thermalize with the medium [12], the bosonic degrees of freedom come from gluons and are $g_{\mathrm{gluon}} = \mathrm{N}_{\mathrm{gluon}}(8) \times \mathrm{N}_{\mathrm{spin}}(2) = 16$, while the fermionic ones, considering the 2 light quark scenario, are $g_{\mathrm{quarks}} = \frac{7}{8} \times \mathrm{N}_{\mathrm{flavour}}(2) \times \mathrm{N}_{\mathrm{spin}}(2) \times \mathrm{N}_{\mathrm{colour}}(3) \times \mathrm{N}_{\mathrm{(anti)particles}}(2) = 21$, for a total number of $g = 37$ degrees of freedom.

the flavour. This property is reflected in the symmetry under isospin transformation, which is observed in the hadron properties. However, this is an exact symmetry only in case of identical quark masses $m_u = m_d = m_s$. In addition, if the quark masses are all null, the lagrangian is invariant under chiral transformations. Considering that the quark fields can be written as the sum of the left-handed and right-handed components:

$$q = q_{\mathrm{L}} + q_{\mathrm{R}} \quad \text{, with} \quad q_{\mathrm{L,R}} = \frac{1}{2}(1 \mp \gamma_5)q \,, \tag{1.13}$$

then the lagrangian remains untouched when the transformations:

$$\begin{matrix} \mathrm{SU(3)_L} \ni \Lambda^{\mathrm{L}} : q_{\mathrm{L}} \to \Lambda^{\mathrm{L}} q_{\mathrm{L}} \\ \mathrm{SU(3)_R} \ni \Lambda^{\mathrm{R}} : q_{\mathrm{R}} \to \Lambda^{\mathrm{R}} q_{\mathrm{R}} \end{matrix} \text{, with} \quad q_{\mathrm{L,R}} = \begin{pmatrix} u_{\mathrm{L,R}} \\ d_{\mathrm{L,R}} \\ s_{\mathrm{L,R}} \end{pmatrix} \tag{1.14}$$

are applied. This means that the QCD lagrangian with massless quarks exhibits an exact symmetry under flavour and chiral transformations, with a null expectation value of the $\mathrm{q\bar{q}}$ operator, called *condensate*, corresponding to the order parameter of the transition: $\langle \mathrm{q\bar{q}} \rangle = 0$. Nevertheless, the nature shows the existence of several $\langle \mathrm{q\bar{q}} \rangle \neq 0$ condensates, for example the π^+ $(u\bar{d})$ and the K^+ $(u\bar{s})$: this is the consequence of the spontaneous breaking of the chiral symmetry at low temperatures, where the non-null condensates correspond to the related Goldstone bosons [1]. This symmetry, which is explicitly broken by the low-energy states, is naturally restored at high energies and this restoration is a sufficient condition for the existence of a phase transition in QCD.

A priori, the chiral symmetry restoration is not granted to be linked to the matter transition from the hadronic to the deconfined state, being in principle a different phase transition. However, lQCD calculations [15] showed a coincident behaviour of the susceptibilities of the deconfinement and chiral transitions (Polyakov susceptibility χ_{L}, chiral susceptibility χ_{m}), showing a strong correlation between their maxima whose locations occur at similar temperatures. This behaviour suggests that these two transitions could be the same one.

1.3 Heavy-ion collisions

Heavy-ion collisions at ultra-relativistic energies are the experimental tool to reproduce the QGP in the laboratory. The main facilities where ultra-relativistic heavy-ion collisions are studied are the *Relativistic Heavy Ion Collider* (RHIC [20]) at the Brookhaven National Laboratory (BNL) since 2000 and at the *Large Hadron Collider* (LHC [21]) at CERN since 2010. The centre-of-mass energies per nucleon-nucleon pair reach the maximum values of $\sqrt{s_{\mathrm{NN}}} = 200$ GeV for gold–gold (Au–Au) collisions at RHIC and $\sqrt{s_{\mathrm{NN}}} = 5.02$ TeV for lead–lead (Pb–Pb) collisions at the LHC. At such high energies the colliding nuclei are not stopped at the collision point, therefore the net baryon density is very small: this allows to explore the $\mu_{\mathrm{B}} \approx 0$ region of the QCD phase diagram. This region is called *Bjorken* or *transparency regime*, different from the *stopping regime* realised when the accelerated ions are stopped in correspondence of the collision point [22]. The latter regime was explored at the *Super Proton Synchrotron* (SPS [23]) at CERN and at the *Alternating Gradient Synchrotron* (AGS [24]) at BNL, as well as many other facilities like during the Beam Energy Scan (BES [25]) multi-experiment program at RHIC and the Nuclotron-based Ion Collider fAcility (NICA [26]) at the Joint Institute for Nuclear REsearch in Dubna, Russia. These facilities were used to perform several fixed-target and collider measurements carried

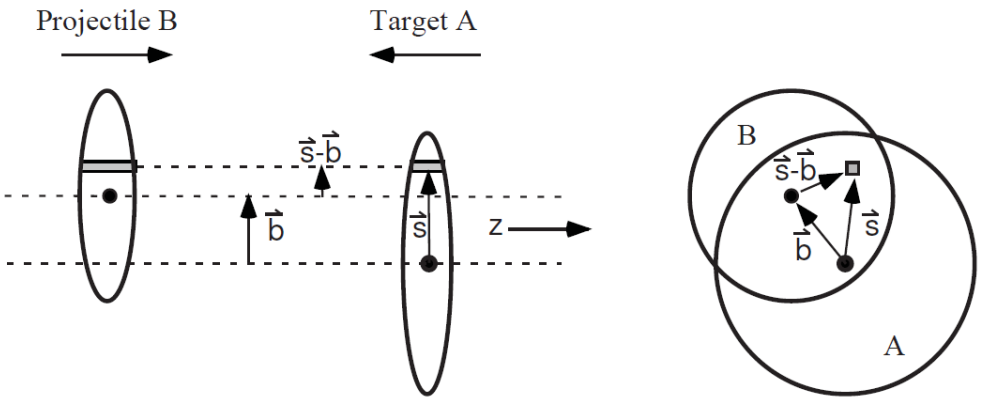

FIGURE 1.5: Schematic representation of a nucleus–nucleus (Å) collision in the optical limit, with transverse (left) and longitudinal (right) views. Figure from [28].

out at centre-of-mass energies per nucleon pairs ranging in $\sqrt{s_{\rm NN}} = 7.7 - 17.3$ GeV, exploring values of the baryon-chemical potential in the range $\mu_{\rm B} = 200 - 500$ MeV.

1.3.1 The geometry of the collision: the Glauber model

Considering that the nuclei are extended objects, a modelling of the collision geometry is needed to determine the average number of nucleon-nucleon collisions ($\langle N_{\rm coll}\rangle$) and of participant nucleons ($\langle N_{\rm part}\rangle$) involved in a particular nucleus-nucleus collision or, more precisely, in a sample of selected collisions. Protons and neutrons are distributed within the nucleus influencing its dimension, since the nuclear radius depends on the mass number according to the relation $R \approx 1.2$ fm $\times A^{1/3}$. The Glauber model [27, 28] provides a semi-classical picture of a nucleus-nucleus collision intended as a incoherent superimposition of the compounding nucleons, considered as undistinguishable. In the so called *optical limit*, the nucleons are considered as moving independently in linear trajectories and to carry a sufficient amount of momentum to be considered undeflected when the two nuclei cross each other. In this way, the collision between two nuclei can be modelled as a sum of nucleon-nucleon events, where protons and neutrons are distributed in the nuclei according to a Woods-Saxon density ρ and their interactions are regulated by the inelastic nucleon-nucleon cross section $\sigma_{\rm NN}^{\rm inel.}$, both provided as input for the model calculations.

In Fig. 1.5 a schematic representation of a nucleus-nucleus collision under the assumptions made above is reported. Focusing on the transverse plane, namely the plane orthogonal to the nuclei direction, the system is centred in the centre of nucleus A, with respect to which the coordinates of a certain nucleon are expressed with the vector $\vec{s}$. The same position with respect to the centre of nucleus B is given by the vector $\vec{b} - \vec{s}$, where $\vec{b}$ is the vector that connects the centres of the two nuclei, called *impact parameter*. Considering $\rho(\vec{s}, z)$ the probability per unit volume to find a nucleon inside the nucleus A located in $\vec{s}$, then the probability expressed in terms of unit transverse area is quantified by the *thickness function*:

$$\hat{T}_{\rm A}(\vec{s}_{\rm A}) = \int \rho_{\rm A}(\vec{s}_{\rm A}, z_{\rm A}) {\rm d}z_{\rm A} \ , \tag{1.15}$$

where $\rho_A(\vec{s}_A, z_A) \equiv \rho(\vec{s}, z)/A$[2]. A similar expression is valid for the nucleus B. The *nuclear overlap function* is then defined as [3]:

$$\hat{T}_{AB}(\vec{b}) = \int \hat{T}_A(\vec{s}) \cdot \hat{T}_B(\vec{s} - \vec{b}) d^2s \, . \tag{1.16}$$

This quantity has the dimension of the inverse of an area and it is related to the probability for a nucleon in A to interact with a nucleon in B. For this reason, the probability of any nucleon in A to collide with any nucleon in B is quantified by:

$$p(\vec{b}) = \sigma_{NN}^{inel.} \hat{T}_{AB}(\vec{b}) \, . \tag{1.17}$$

The expression reported in Eq. 1.17 quantifies the probability of success for a single nucleon-nucleon collision. Considering that the maximum number of possible binary collisions between two nuclei with mass numbers A and B is equal to AB[4], the probability $P_{n,AB}(\vec{b})$ to have n binary collisions out of AB follows the binomial distribution:

$$P_{n,AB}(\vec{b}) = \binom{AB}{n} \cdot \left(\sigma_{NN}^{inel.} \hat{T}_{AB}(\vec{b})\right)^n \cdot \left(1 - \sigma_{NN}^{inel.} \hat{T}_{AB}(\vec{b})\right)^{AB-n} \, , \tag{1.18}$$

where $\binom{AB}{n}$ represents the possible combinations among nucleons in A and B and $1 - \sigma_{NN}^{inel.} \hat{T}_{AB}(\vec{b})$ quantifies the probability of failure for a single binary collision. The average number of binary collisions is naturally defined by the first moment of the binomial distribution of Eq. 1.18, namely:

$$\langle N_{coll} \rangle (\vec{b}) = AB \cdot \sigma_{NN}^{inel.} \hat{T}_{AB}(\vec{b}) \, . \tag{1.19}$$

The Eq. 1.18 allows to quantify the total probability of interaction between the nuclei A and B, which can be estimated as the complementary probability not to have any nucleon-nucleon collision:

$$p_{AB}^{inel.} = 1 - P_{0,AB}(\vec{b}) = 1 - \left[1 - \sigma_{NN}^{inel.} \hat{T}_{AB}(\vec{b})\right]^{AB} \, , \tag{1.20}$$

and the total inelastic nucleus-nucleus cross section can be defined as the surface integral over the full transverse plane of the mentioned probability, namely:

$$\sigma_{AB}^{inel.} = \int_0^{+\infty} 2\pi b db \cdot \left[1 - \left(1 - \sigma_{NN}^{inel.} \hat{T}_{AB}(\vec{b})\right)^{AB}\right] \, . \tag{1.21}$$

[2] The redefinition of the nuclear density per unit nucleon $\rho_A(\vec{s}_A, z_A)$ is driven by the nuclear density normalization, such that its integral over the nuclear volume is equal to the total number of nucleons and the surface integral on the transverse plane of $\hat{T}_A(\vec{s}_A)$ is equal to unity: $\int ds^2 \hat{T}_A(\vec{s}_A) = \int ds^2 dz_A \rho_A(\vec{s}_A, z_A) = 1$. Thus one can define $\langle T_A(\vec{s}_A) \rangle \equiv \hat{T}_A(\vec{s}_A) \cdot A$, which is normalised such that $\int ds^2 \langle T_A(\vec{s}_A) \rangle = A$.

[3] Similarly to what said before, one can define $\langle T_{AB}(\vec{b}) \rangle \equiv \hat{T}_{AB}(\vec{b}) \cdot AB$, which is normalised such that $\int db^2 \langle T_{AB}(\vec{b}) \rangle = AB$.

[4] A single nucleon of A sees B nucleons in the opponent nucleus, then it can have B interactions. This argument must be extended to all the undistinguishable nucleons in A, which are indeed A, therefore the total number of possible binary collisions is AB.

The inelastic nucleus-nucleus cross section in Eq. 1.21 linearly increases with the impact parameter:

$$\frac{\mathrm{d}\sigma_{\mathrm{AB}}^{\mathrm{inel.}}}{\mathrm{d}b} \propto 2\pi b \,. \tag{1.22}$$

This relation is valid for high values of the nuclear overlap function $\hat{T}_{\mathrm{AB}}(\vec{b})$. As soon as this quantity falls down, which happens when the impact parameter is high and tends to the sum of the colliding nuclei radii, this linear dependence is broken due to the absence of nucleon-nucleon collisions given the reducing amount of participants.

Another important quantity related to the collision between two nuclei is the the number of nucleons involved (N_{part}). Fixing a specific test nucleon in nucleus A positioned in $\vec{s}$, its probability to collide with a nucleon in B is equal to $\sigma_{\mathrm{NN}}^{\mathrm{inel.}} \hat{T}_{\mathrm{B}}(\vec{s}-\vec{b})$, where the thickness function is calculated in the position of the test nucleon in A, considered with respect to the centre of nucleus B. According to this, the probability that the test nucleon does not interact with any nucleon in B is $(1-\sigma_{\mathrm{NN}}^{\mathrm{inel.}} \hat{T}_{\mathrm{B}}(\vec{s}-\vec{b}))^{\mathrm{B}}$, namely the product of all failure probabilities. Therefore, we can define the probability for the test nucleon in A to be involved in at least one binary collision with a nucleon in B as $1-(1-\sigma_{\mathrm{NN}}^{\mathrm{inel.}} \hat{T}_{\mathrm{B}}(\vec{s}-\vec{b}))^{\mathrm{B}}$. Analogously to what done in Eq. 1.17, the probability for any test nucleon in A to participate in at least one binary interaction can be defined as:

$$p_{\mathrm{part}}(\vec{b}) = \int \mathrm{d}^2 s \cdot \hat{T}_{\mathrm{A}}(\vec{s}) \cdot \left[1-(1-\sigma_{\mathrm{NN}}^{\mathrm{inel.}} \hat{T}_{\mathrm{B}}(\vec{s}-\vec{b}))^{\mathrm{B}}\right] \,, \tag{1.23}$$

where the integral is done to take into account all the possible positions of the test nucleon in A, whose density per unit area is quantified by the thickness function $\hat{T}_{\mathrm{A}}(\vec{s})$. Also in this case, the probability to have n participant nucleons out of the A available in the first nucleus is given by a binomial distribution with A as number of total cases and $1-(1-\sigma_{\mathrm{NN}}^{\mathrm{inel.}} \hat{T}_{\mathrm{B}}(\vec{s}-\vec{b}))^{\mathrm{B}}$ as probability of a single success. From the calculation of the first moment of this binomial distribution, the average number of participant nucleons for the nucleus A turns out to be A times the probability in Eq. 1.23. Since the same argument can be repeated in a specular way for a test nucleon in B, the total number of participant nucleons in A and B can be estimated by the following expression:

$$\begin{aligned} \langle N_{\mathrm{part}} \rangle (\vec{b}) = \mathrm{A} \cdot \int \mathrm{d}^2 s \cdot \hat{T}_{\mathrm{A}}(\vec{s}) \cdot \left[1-(1-\sigma_{\mathrm{NN}}^{\mathrm{inel.}} \cdot \hat{T}_{\mathrm{B}}(\vec{s}-\vec{b}))^{\mathrm{B}}\right] \\ + \mathrm{B} \cdot \int \mathrm{d}^2 s \cdot \hat{T}_{\mathrm{B}}(\vec{s}-\vec{b}) \cdot \left[1-(1-\sigma_{\mathrm{NN}}^{\mathrm{inel.}} \cdot \hat{T}_{\mathrm{A}}(\vec{s}))^{\mathrm{A}}\right] \end{aligned} \,. \tag{1.24}$$

The results of the Glauber model can be obtained with a Monte Carlo (MC) simulation. The positions of the nucleons inside the colliding nuclei are fixed according to the density functions ρ provided as input, used to determine the nuclear thickness (Eq. 1.15) and a random value for the impact parameter is picked according to the impact parameter distribution, which derives from Eq. 1.22. The interaction between the two nuclei is considered as a superposition of many independent nucleon-nucleon collisions, regulated by the input inelastic cross section $\sigma_{\mathrm{NN}}^{\mathrm{inel.}}$. In particular, two nucleons are assumed to collide if the distance d between them is

$$d < \sqrt{\sigma_{\mathrm{NN}}^{\mathrm{inel.}} / \pi} \,. \tag{1.25}$$

Using this convention, the simulations are repeated several times to reproduce many heavy-ion collisions, in order to estimate the geometrical quantities related to these

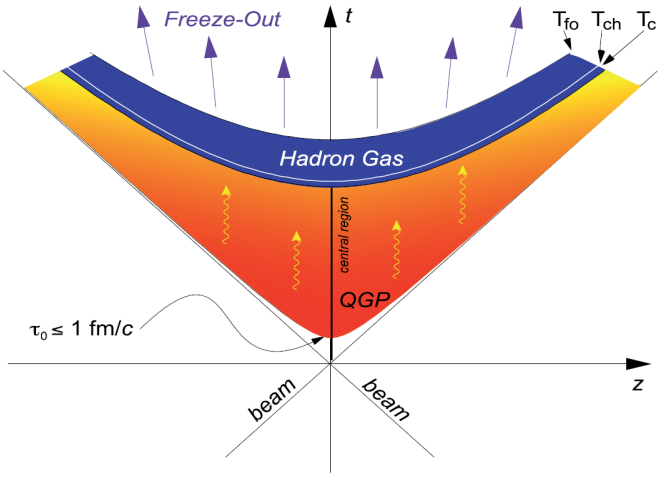

FIGURE 1.6: Space-time diagram of longitudinal QGP evolution. From the collision of heavy ions at ultra-relativistic energies the critical energy density is overcome within a time $\tau_0 \sim 1$ fm/c and the QGP phase is reached. The system expands following the laws of relativistic hydrodynamics and cools down to the critical temperature T_c, when the transition to the hadron gas phase takes place. Due to the further expansion of the system, the particle abundances are determined by the end of inelastic interactions among hadrons at the kinetic freeze-out temperature $T_{\rm ch}$, followed by a kinetic freeze-out at $T_{\rm fo} < T_{\rm ch}$ where the particle energy are definitively established. Image taken from [30].

events, such as $\langle N_{\rm part} \rangle$ and $\langle N_{\rm coll} \rangle$. These results are used to determine the collision centrality starting from experimental quantities, as explained in Section 3.5. The average number of participants and binary collisions for central (0–10%) Pb–Pb collisions at $\sqrt{s_{\rm NN}} = 5.02$ TeV at the LHC are about $\langle N_{\rm part} \rangle \simeq 360$ and $\langle N_{\rm coll} \rangle \simeq 1600$ [29].

1.3.2 Space-time evolution of the collision

The space-time evolution of the system formed in a nucleus-nucleus collision is shown in Figs. 1.6 and 1.7 and it develops as follows [12]:

a) heavy ions are accelerated so that they gain ultra-relativistic energies ($E \geq m$) and collide for a crossing time $\tau_{\rm cross}$, estimated as:

$$\tau_{\rm cross} = 2R/\gamma \,, \tag{1.26}$$

where R is the nucleus radius, while γ is the Lorentz factor that contracts them. The crossing time for Pb–Pb collisions at $\sqrt{s_{\rm NN}} = 5.02$ TeV at LHC is estimated to be about 5.7×10^{-3} fm/c, given a Pb radius of about 7.1 fm and a Lorentz factor $\gamma \simeq 2.5 \times 10^3$. The interval $\tau_{\rm cross}$ is lower than the time-scale of strong interactions $\tau_0 = 1/\Lambda_{\rm QCD} \simeq 1/200$ MeV $\simeq 1$ fm/c;

b) the system reaches a local thermal equilibrium at a time $\tau_{\rm term}$, due to multiple scatterings among constituent particles, characterized by the mean free-path $\lambda \approx 0.1$ fm. The expected temperature for the QGP reproduced at LHC is ≥ 600 MeV and its values decreases as $T \sim \tau^{-1}$ [30]. This stage follows a pre-equilibrium one, where the energy density provided in the collision needs to

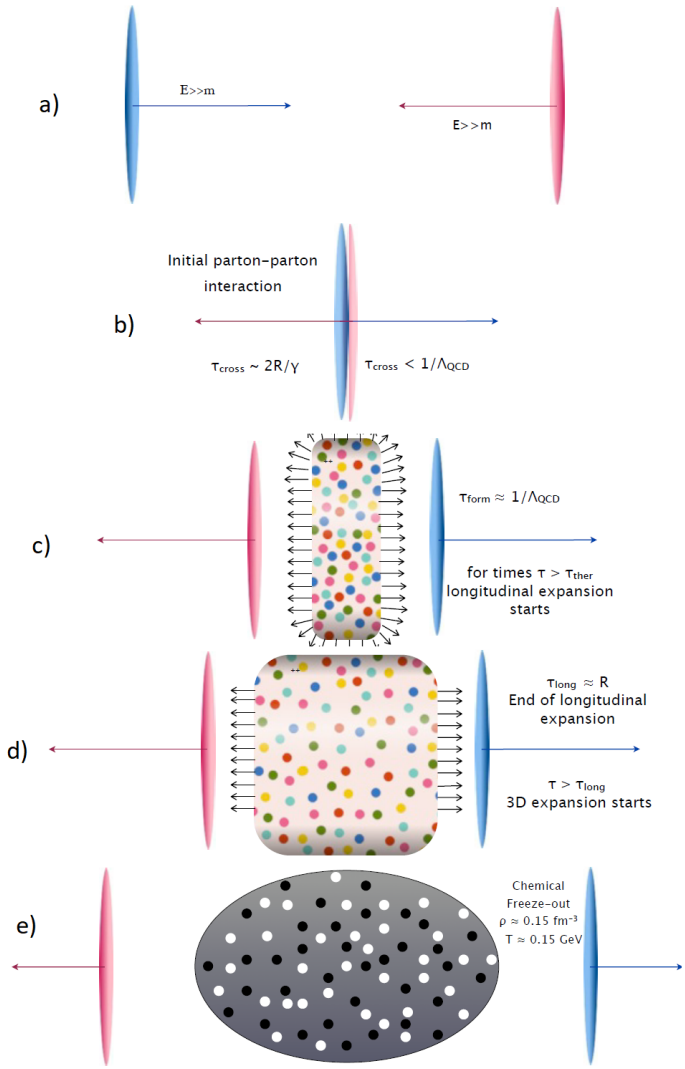

FIGURE 1.7: Space-time evolution on a heavy ion collision. Image taken from [12].

be high enough to produce the QGP. In the mid-rapidity range[5] the net baryon density is close to zero and it is possible to estimate the system energy density in the Bjorken regime as [22, 30]:

$$\varepsilon = \frac{1}{\pi R^2}\frac{1}{\tau_0}\left.\frac{\mathrm{d}E_\mathrm{T}}{\mathrm{d}y}\right|_{y=0}, \tag{1.28}$$

where the initially produced collision volume is considered as a cylinder of length $\mathrm{d}z = \tau_0 \mathrm{d}y$ and transverse area πR^2, with $R \approx 1.2$ fm $\times A^{1/3}$. The

[5]The rapidity of a particle with energy E and longitudinal momentum component p_z is defined as:

$$y := \frac{1}{2}\ln\left(\frac{E+p_z}{E-p_z}\right). \tag{1.27}$$

quantity E_T is the transverse energy [6] . Considering the heavy-ion collisions at RHIC and LHC at their top centre-of-mass energies per nucleon pair and assuming $\tau_0 = 1$ fm/c, the energy densities reached for these colliders range between $\sim$5 GeV/fm^3 and $\sim$12 GeV/fm^3 [31], values significantly higher than the critical value discussed in Sec. 1.2;

c) for times $\tau > \tau_{term}$, the system evolves according to relativistic hydrodynamics laws. First of all, it is subject to a longitudinal expansion, because the pressure gradient along the nuclei direction of motion is stronger than that in the transverse plane. Considering the hydrodynamic law [22]:

$$\frac{d\epsilon}{d\tau} = -\frac{\epsilon + p}{\tau} , \tag{1.31}$$

where p is the system pressure, then the energy density ϵ evolves as $\epsilon \sim 1/\tau^n$, with $1 \leq n \leq 4/3$. For an ideal ultra-relativistic gas, this coefficient is $n = 4/3$ and the equation of state corresponds to $\epsilon = 3p$. This expansion cools down the QGP and lasts until the time $\tau_{long} \sim R/c$;

d) for times $\tau \geq \tau_{long}$, the system stops expanding longitudinally, starting to be subject to a tridimentional expansion until the temperature reaches the critical value $T = T_C$. This is the moment when the phase transition from QGP to hadron gas state takes place;

e) after the phase transition, the system experiences these two subsequent moments:

- *chemical freeze-out*: the inelastic interactions among hadrons stop, fixing the species abundances. It happens immediately after the phase transition, namely at $T_{ch} = 156.5 \pm 1.5$ MeV [32];
- *kinetic freeze-out*: when the system cools down to $T_{fo} < T_{ch}$ also elastic interactions among hadrons stops, then energy and momentum of final particles are definitively established.

1.4 Signatures of the QGP

In this section, an overview of the experimental results and the observables that mainly contribute to the actual understanding of the QGP properties produced in laboratory with heavy-ion collisions at ultra-relativistic energies is reported.

1.4.1 Charged particle multiplicity

The charged particle multiplicity corresponds to the number of charged particles produced in a collision. This quantity is strictly related to the energy-density involved in the pre-equilibrium phase described in Sec. 1.3.2, which determines whether

[6] The transverse energy [30] E_T for a particle with energy E that flies with a polar angle θ with respect to the beam direction is defined as:

$$E_T := E \sin(\theta) . \tag{1.29}$$

Analogously, the transverse mass for the same particle, having a mass m, is defined as:

$$m_T := \sqrt{m^2 + p_T^2} . \tag{1.30}$$

In case of massless particles ($m = 0$) the two quantities are equal to p_T.

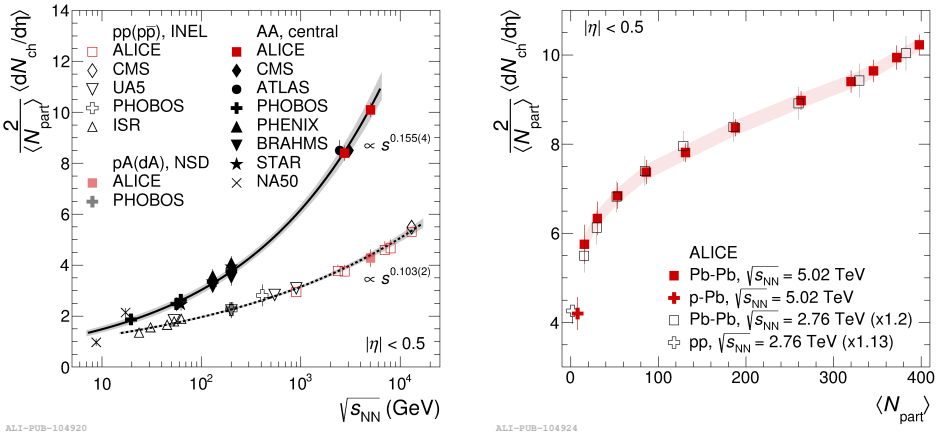

FIGURE 1.8: Charged particle pseudorapidity densities per participant nucleon pair $\frac{2}{\langle N_{\text{part}}\rangle}\langle \mathrm{d}N/\mathrm{d}\eta\rangle$ measured at mid rapidity in different collision systems as a function of centre-of-mass energy per nucleon pair $\sqrt{s_{\text{NN}}}$ (left) and number of participants N_{part} (right). Figures taken from [33].

the matter undergoes a transition to the QGP or not. The energy-density at mid rapidity, reported in Eq. 1.28 can be approximated as $\left.\frac{\mathrm{d}E_{\text{T}}}{\mathrm{d}y}\right|_{y=0} \approx \langle E_{\text{T}}\rangle \cdot \left.\frac{\mathrm{d}N}{\mathrm{d}y}\right|_{y=0}$, where the last factor corresponds to the rapidity distribution of charged particles at midrapidity. Experimentally, the *pseudorapidity*:

$$\eta := -\ln\left(\tan\frac{\theta}{2}\right) , \tag{1.32}$$

where θ is the polar angle, defined in the yz plane (see Sec. 3.2), is used in place of the rapidity[7]. In Fig. 1.8 the charged particle pseudorapidity density at mid rapidity in pp, p–Pb and Pb–Pb collisions measured by ALICE is shown [33]. This quantity is often normalised by the number of participant pairs $\langle N_{\text{part}}\rangle/2$ in order to be comparable among different collision systems. The charged particle pseudorapidity density per participant nucleon pair $\frac{2}{\langle N_{\text{part}}\rangle}\langle \mathrm{d}N/\mathrm{d}\eta\rangle$ measured by ALICE is compared with the results from other experiments at different $\sqrt{s_{\text{NN}}}$ (left). The particle multiplicity shows a monotonic increase as a function of $\sqrt{s_{\text{NN}}}$. The results regarding central nucleus-nucleus collisions (AA) follow a power law function as^b with parameter b equal to 0.155 ± 0.004, while the results for pp collisions constitute a different group following a power law increase regulated by $b = 0.103 \pm 0.002$. It is interesting to notice that the results in nucleon-nucleus (pA, dA) collisions lie on the pp curve, indicating that the behaviour observed in AA collision cannot be attributed only to a larger number of multiple interactions among the participant nucleons, also present in pA and dA collisions. The $\frac{2}{\langle N_{\text{part}}\rangle}\langle \mathrm{d}N/\mathrm{d}\eta\rangle$ shows a significant enhancement as a function of the number of participant nucleons (right). The charged particle multiplicity in Pb–Pb collisions at $\sqrt{s_{\text{NN}}} = 5.02$ TeV increases almost linearly with $\langle N_{\text{part}}\rangle$ and significantly differs from what measured in pp and

[7] Rapidity and pseudorapidity are equivalent in in the high energy limit ($p \gg m$):

$$y = \frac{1}{2}\ln\frac{E+p_{\text{L}}}{E-p_{\text{L}}} \to \frac{1}{2}\ln\frac{1+\cos\theta}{1-\cos\theta} = -\ln\left[\tan\frac{\theta}{2}\right] .$$

For this reason sometimes, talking about rapidity, the η parameter is taken into account.

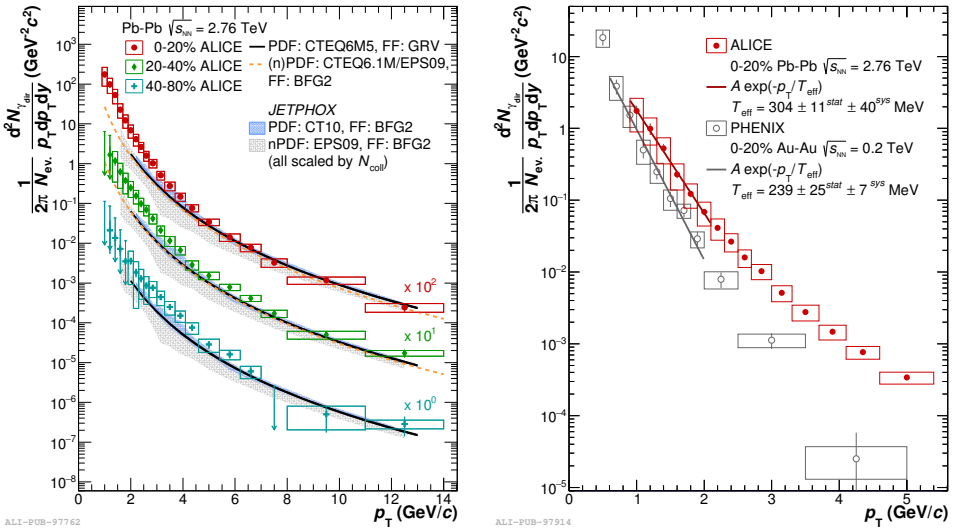

FIGURE 1.9: Left: direct-photon spectra measured by the ALICE experiment in Pb–Pb collisions at $\sqrt{s_{NN}} = 2.76$ TeV for the 0-20% (scaled by a factor 100), the 20-40% (scaled by a factor 10) and 40-80% centrality classes compared to NLO pQCD predictions for the direct photon yield in pp collisions at the same energy, scaled by the number of binary nucleon collisions for each centrality class. Right: direct photon spectra in Pb–Pb collisions at $\sqrt{s_{NN}} = 2.76$ TeV and Au–Au collisions at $\sqrt{s_{NN}} = 200$ GeV measured by the ALICE experiment at the LHC and the PHENIX experiment at RHIC, respectively. For $p_T < 2.1$ GeV/c the exponential function $A \cdot \exp(-p_T/T_{eff})$ is used to estimate the average temperature of the medium produced in the collisions. Figures taken from [34].

p–Pb collisions at the same energy, where the observed multiplicity is significantly lower compared to the most central Pb–Pb collisions. This trend does not depend on the collision energy and is described by models which ascribe the lower multiplicity in smaller systems to the saturation of parton densities, which therefore limits the production of partons and, finally, of particles [33].

1.4.2 Direct-photon p_T-spectrum

Direct photons, defined as photons not produced by the decay of hadrons, are a unique tool to investigate the time evolution of the QGP produced in heavy-ion collisions. Differently from the hadrons, they are produced at all stages of the collision and they traverse the medium almost unaffected, since they do not interact strongly and their mean-free path is much larger than nuclear scales. For this reason, they provide a direct probe of the different stages of the QGP evolution, even of the earliest ones. In particular, the *prompt* direct photons produced in the hard scatterings among partons in the colliding nuclei provide information on the parton densities in nuclei. They dominate the high-p_T distribution of the spectrum ($p_T > 5$ GeV/c). On the other hand, the low-p_T region is dominated by the *thermal* component [34]. The direct-photon p_T spectra in central (0-20%), semicentral (20-40%) and peripheral (40-80%) Pb–Pb collisions at $\sqrt{s_{NN}} = 2.76$ TeV measured by ALICE are shown in Fig. 1.9 (left panel). The direct photon distribution for $p_T > 5$ GeV/c is well described by the pQCD calculations for pp collisions at the same energy scaled by the expected $\langle N_{coll} \rangle$ for each centrality class. In semicentral and more clearly in central collisions the power-law dependence on p_T, expected from the hard process component, is

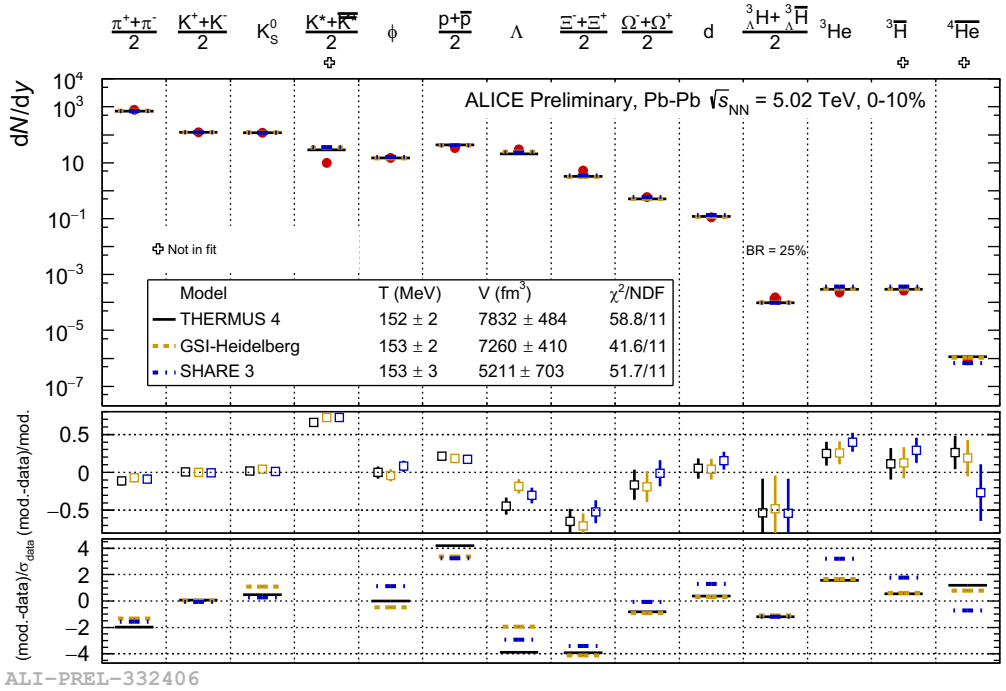

FIGURE 1.10: Simultaneous fit of particle yield measured by ALICE experiment in 0-10% Pb–Pb collisions at $\sqrt{s_{\rm NN}} = 5.02$ TeV. Figure from the ALICE Figure Repository ©.

broken at low $p_{\rm T}$ due to an excess of thermal photons following an exponential law. According to the theoretical models, the inverse slope parameter of the exponential trend reflects an effective temperature of the medium ($T_{\rm eff}$) averaged over its whole evolution. A fit of the ALICE data in the interval $0.9 < p_{\rm T} < 2.1$ GeV/c with the exponential function $A \cdot \exp(-p_{\rm T}/T_{\rm eff})$ provides a value of the effective temperature of the QGP produced in central Pb–Pb collisions, which at $\sqrt{s_{\rm NN}} = 2.76$ TeV corresponds to $T_{\rm eff} = (304 \pm 11({\rm stat.}) \pm 40({\rm syst.}))$ MeV. This is about 1.8 times larger than the critical temperature $T_{\rm c}$ of the phase transition (see Sec. 1.2). The QGP produced in central Pb–Pb collisions at $\sqrt{s_{\rm NN}} = 2.76$ TeV at LHC is about 1.3 times hotter than the QGP produced in Au–Au collisions at $\sqrt{s_{\rm NN}} = 200$ GeV in the same centrality class at RHIC.

1.4.3 Identified hadron abundances: the chemical freeze-out temperature

The evolution of the QGP produced in heavy-ion collisions ends with the hadronization of partons into different hadronic species. The description of the production of soft hadrons is basically impossible from a microscopic point of view, due to the innumerable channels that may contribute in this non-perturbative process and the in-medium rescattering of soft partons that erases the memory about their initial production. For this reason a statistical approach is appealing, in which the hadron production is determined in terms of the macroscopic properties of the system [35]. At the stage of the chemical freeze-out, the system is assumed to be at thermal and chemical equilibrium, corresponding to a hadron-resonance gas formed by strongly interaction hadrons forming an ensemble in which the conservation of energy and quantum numbers is respected. Under these hypotheses, the abundance N_i of a

given particle species i thermally produced by the system with volume V and temperature T_{ch} is obtained with the *grand-canonical ensemble* formalism:

$$N_i(T_{\mathrm{ch}}, V, \mu_i) = \frac{g_i V}{(2\pi)^3} \int \frac{\mathrm{d}^3 p}{\exp\left(\frac{E_i - \mu_i}{T_{\mathrm{ch}}}\right) \pm 1} \,. \tag{1.33}$$

In the above expression, g_i indicates the spin degeneracy, E_i quantifies the energy of the particle and the integral is performed in the entire momentum space. The "$\pm$" symbol accounts for the difference in the Bose-Einstein and Fermi-Dirac statistics. The parameter μ_i is the chemical potential for the given particle species, which is governed by its quantum numbers, $\mu_i = \mu_{\mathrm{B}} B_i + \mu_{\mathrm{S}} S_i$, where B_i is the baryonic number and S_i the strangeness number, each of them multiplied by the corresponding chemical potential. The expression in Eq. 1.33 may not be formally correct in case of a non-perfect thermal and chemical equilibrium, for example, of the strange quark, whose behaviour may deviate from the one expected according to the grand-canonical description. In this case, the thermal abundance in Eq. 1.33 is scaled by $\gamma_S^{S_i}$, where γ_S is called *strangeness suppression factor*. This quantity is expected to be lower than unity in case of non-equilibrium, as expected in peripheral AA collisions and for smaller collision systems. Similar arguments can be moved for the charm quark (γ_{c}), which in particular is mainly produced in the initial hard scatterings among partons. Finally, another parameter γ_{q} is introduced in the SHARE model, which describes a non-equilibrium QGP which undergoes a sudden hadronization without additional re-scatterings.

The particle yields per unit of rapidity measured by the ALICE experiment in 0-10% Pb–Pb collisions at $\sqrt{s_{\mathrm{NN}}} = 5.02$ TeV are shown in Fig. 1.10. The experimental data are compared with the results from SHARE [36], THERMUS [37] and GSI [38] models, which base on different assumptions on the equilibrium condition of the system and/or conservation laws at the chemical freeze-out and perform a simultaneous fit of the different particle yields leaving T_{ch}, V and μ as free parameters. The models describe the particle abundances in a range of about 9 orders of magnitude with a χ^2/NDF between 3.8 and 5.3. In particular, a significant tension is present with the measured yield of excited K mesons, excluded from the fits, and with the proton-antiproton one possibly due to the large baryon-antibaryon annihilation cross section in the hadronic phase [39]. All the models find a value of the chemical freeze-out temperature of about $T_{\mathrm{ch}} = 153$ MeV. This value is close to the expected critical temperature of the phase transition from the hadronic to the deconfined state, suggesting that the chemical freeze-out should happen very soon after it.

1.4.4 Kinetic freeze-out temperature and radial flow

After the chemical freeze-out, the particle abundances produced by the fireball cooling are fixed, but the particle energy can still change due to residual elastic interactions. After the kinetic freeze-out the particle p_{T} spectra are fixed and their study at low transverse momenta gives fundamental insights about the medium properties at this stage of its evolution. Given a static system in thermal equilibrium, the low-p_{T} spectrum of particles follows a Boltzmann-Gibbs law:

$$\frac{1}{p_{\mathrm{T}}} \frac{\mathrm{d}^2 N}{\mathrm{d}p_{\mathrm{T}} \mathrm{d}y} = \frac{1}{m_{\mathrm{T}}} \frac{\mathrm{d}^2 N}{\mathrm{d}m_{\mathrm{T}} \mathrm{d}y} \propto e^{-m_{\mathrm{T}}/T_{\mathrm{kin}}} \,, \tag{1.34}$$

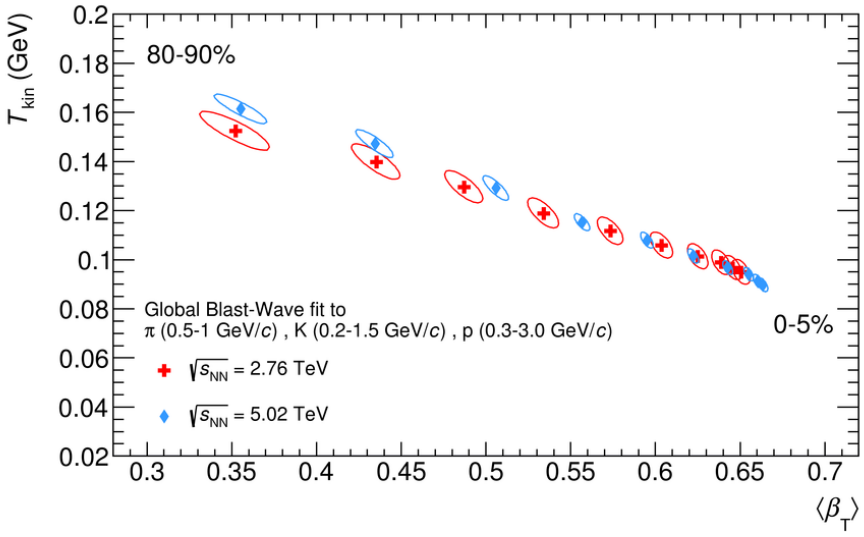

FIGURE 1.11: Average expansion velocity ($\langle\beta_T\rangle$) and kinetic freeze-out temperature (T_{kin}) progression from the simultaneous Boltzmann-Gibbs Blast-Wave fit to $\pi^{\pm}$, $K^{\pm}$ and p($\bar{p}$) spectra measured in Pb–Pb collisions at $\sqrt{s_{NN}}$ = 5.02 and 2.76 TeV. The correlated uncertainties from the global fit are shown as ellipses. The elliptic contours correspond to 1σ uncertainties, with statistical and systematic uncertainties being added in quadrature. Figure from [40].

where m_T is the particle transverse mass (see Eq. 1.30) and T_{kin} is the system temperature at the kinetic freeze-out. According to this expression, all particle species follow the same exponential trend and this behaviour is usually called m_T-*scaling* [41]. It describes reasonably well the spectra of different particle species (e.g. π^-, $\bar{K}^0$, Λ, ρ^0 and ω) produced in hadronic collisions at centre-of-mass energy of 8 and 16 GeV [42,43]). Results from the ALICE experiment in pp collisions at 7 TeV [44] challenge the universal validity of this property. In general, at the LHC energies the hadron p_T spectra deviate from this trend, as also observed in the measurement of identified hadron p_T spectra in Pb–Pb collisions at $\sqrt{s_{NN}}$ = 2.76 TeV [45] and 5.02 TeV [40]. The reason for this evident disagreement has to be found in the internal pressure gradients that are generated by the QGP, which provoke a collective expansion in the transverse plane, called *radial flow* that superimpose to the thermal random motion of particles. For this reason, the slope parameter in Eq. 1.34 is no more constituted only by the kinetic freeze-out temperature T_{kin}, but needs to be changed into

$$\bar{T} = T_{kin} + \frac{m}{2}\langle\beta_T\rangle^2 , \tag{1.35}$$

where the second addendum represents the kinetic energy related to the radial expansion velocity $\langle\beta_T\rangle$, which pushes up to higher values the average transverse momentum of the particles, proportionally to their mass. This quantity is not constant, but changes with a power law of the distance r with respect to the centre of the expanding system:

$$\beta_T(r) = \beta_s \left(\frac{r}{R}\right)^n , \tag{1.36}$$

where β_s is the velocity of the surface of the expanding system and R is the maximum radius of the fireball. The particle production as a function of momentum is described by the Boltzmann-Gibbs Blast-Wave function [46], which contains T_{kin},

$\langle\beta_T\rangle$ and n as free parameters. This approach allows to analyse the measured spectra of the different hadron species, separating the random thermal motion from the possible collective motions. In the Blast-Wave model each infinitesimal volume element of the fireball is assumed at the thermal equilibrium at a certain temperature T and undergoes a radial boost with velocity β_T. The spectrum is finally influenced by a superposition of thermal sources with different radial expansion velocities. The correlation between the average expansion velocity β_T and the kinetic freeze-out temperature T_{kin} measured by the ALICE experiment in Pb–Pb collisions at $\sqrt{s_{NN}} = 2.76$ TeV [45] and 5.02 TeV [40] is reported in Fig. 1.11. The two parameters are estimated with a simultaneous fit of pion, kaon and proton p_T spectra at low transverse momenta measured at different centralities. For Pb–Pb collisions at $\sqrt{s_{NN}} = 5.02$ TeV, the average transverse expansion reaches a maximum value of $\langle\beta_T\rangle = 0.663 \pm 0.003$ in 0–5% centrality class, while the kinetic temperature decreases from peripheral to central collisions, varying between $T_{kin} = (0.161 \pm 0.006)$ GeV and $T_{kin} = (0.090 \pm 0.003)$ GeV. These results indicate a more rapid expansion with increasing centrality, given the larger system size, and they show that the kinetic freeze-out is delayed in more central collisions, since it takes place when the system cools down to lower temperatures. No significant differences are spotted between the results at the two collision energies. The values of T and $\langle\beta_T\rangle$ obtained from the simultaneous fit of the particle spectra gain a physical meaning only if theoretical models based on the dynamical expansion of the system reproduce them. This is done via a relativistic hydrodynamics formalism, which connects the collective expansion of the medium with its equation of state.

1.4.5 Strangeness enhancement

Below the critical temperature T_c, the mass of the strange quark is of order of ~ 0.5 GeV/c^2, implying a production threshold for a $s\bar{s}$ pair larger than 1 GeV. However, due to the chiral symmetry restoration in QGP (see Sec. 1.2), above the critical temperature the effective mass of the strange quark reduces by a factor up to 10, with a consequent increase of the $s\bar{s}$ production. For this reason, the strangeness production is expected to significantly increase in heavy-ion collisions with respect to smaller systems. This was originally proposed as a key signature of the QGP formation in heavy-ion collisions [47]. Strange quarks are expected to be abundantly produced in the QGP via the gluon fusion process $gg \rightarrow s\bar{s}$, thanks to the huge gluon density in the system, leading to an increase of the relative production of hadrons containing strange quarks.

The enhanced production of strangeness in heavy-ion collisions can be explained in a reversed way as a suppression of strangeness production in smaller collision systems [48]. According to the grand-canonical description, the conservation laws for all quantum numbers in the QGP need to be respected inside the volume of the system. Their conservation is not required to take place locally but only on average in the whole volume, regulated by the corresponding chemical potential. This means that the production of a hadron containing a strange quark at a given position in the fireball does not require a formation of another hadron with anti-strange content in the nearby, but this can take place everywhere inside the system volume. On the contrary, in smaller colliding systems, such as pp, the grand-canonical ensemble cannot be used: the reduced dimensions of the phase-space require a description in terms of a canonical ensemble. In this framework, the exact conservation of all the quantum numbers must take place locally, meaning that the production of a strange hadron implies the production of a compensating anti-strange hadron in the same

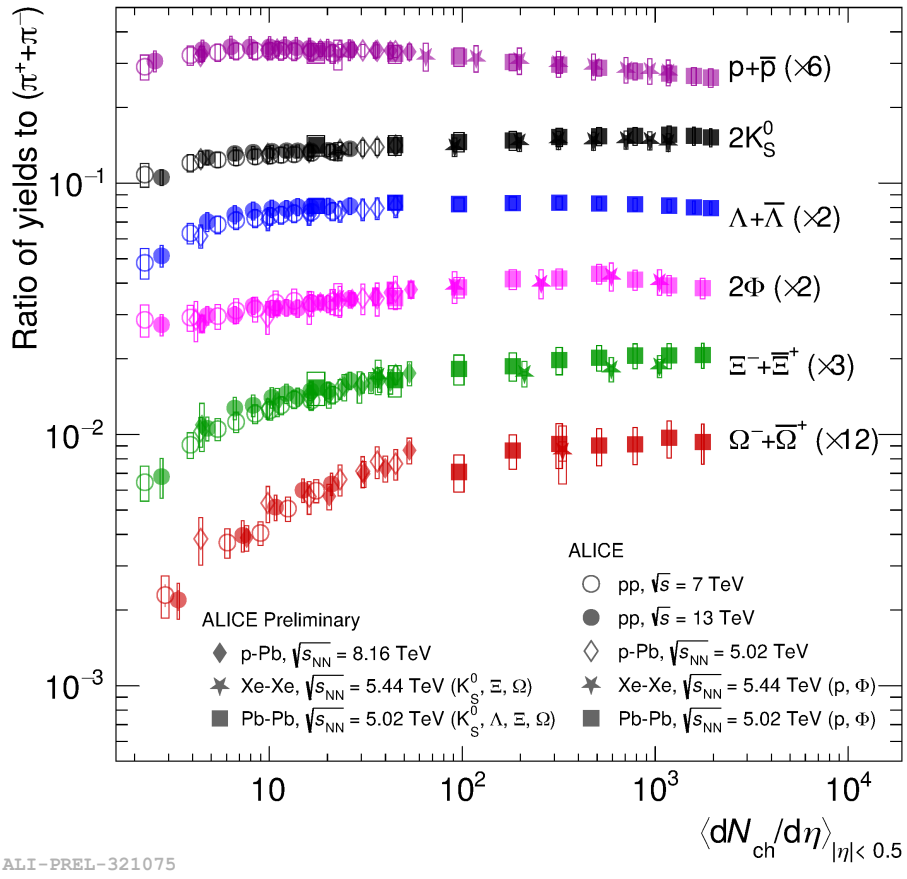

FIGURE 1.12: Relative yields to $(\pi^+ + \pi^-)$ of $(p + \bar{p})$, $2K^0_S$, $(\Lambda + \bar{\Lambda})$, 2Φ, $(\Xi^- + \bar{\Xi}^+)$ and $(\Omega^- + \bar{\Omega}^+)$ as a function of charged particle multiplicity at mid rapidity measured by the ALICE experiment in pp collisions at $\sqrt{s} = 7$ and 13 TeV, in p–Pb collisions at $\sqrt{s_{NN}} = 5.02$ and 8.16 TeV, in Pb–Pb collisions at $\sqrt{s_{NN}} = 5.02$ TeV and in Xe–Xe collisions at $\sqrt{s_{NN}} = 5.44$ TeV. Figure from the ALICE Figure Repository ©.

space-time position. For these reasons, the strangeness enhancement in the QGP is usually interpreted as the removal of the so-called *canonical suppression* in small colliding systems. This is expressed as a γ_S factor lower than unity in pp collisions (see Eq. 1.33), signalling the deviation from the grand-canonical description valid in heavy-ion collisions ($\gamma_S = 1$).

An enhanced production of strange hadrons was observed in heavy-ion collisions at both RHIC [49] and LHC [50]. The production yields normalized to those of $(\pi^+ + \pi^-)$ of $(p + \bar{p})$, $2K^0_S$, $(\Lambda + \bar{\Lambda})$, 2Φ, $(\Xi^- + \bar{\Xi}^+)$ and $(\Omega^- + \bar{\Omega}^+)$ as a function of charged particle multiplicity at mid rapidity $\langle dN/d\eta \rangle|_{|y|<0.5}$ measured by the ALICE experiment in pp collisions at $\sqrt{s} = 7$ and 13 TeV, in p–Pb collisions at $\sqrt{s_{NN}} = 5.02$ and 8.16 TeV, in Pb–Pb collisions at $\sqrt{s_{NN}} = 5.02$ TeV and in Xe–Xe collisions at $\sqrt{s_{NN}} = 5.44$ TeV are shown in Fig. 1.12. The experimental results show an augmented production of strange hadrons in Pb–Pb collisions with respect to the low-multiplicity pp events, registering a larger enhancement for particles with a higher strange-quark content. The relative increase between the two colliding systems is highest for the $\Omega^-(sss)$ baryons, whose production increases by a factor ~ 5 in Pb–Pb with respect to low-multiplicity pp collisions. The experimental data do not show a significant dependence neither on the centre-of-mass energy

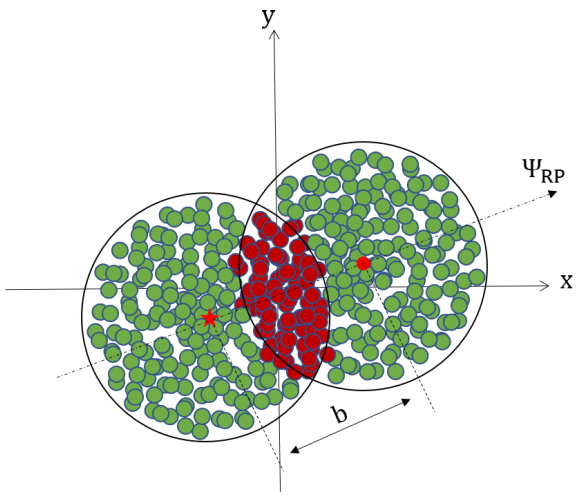

FIGURE 1.13: Left: collision between two lead ions. The direction of motion $\hat{z}$ is perpendicular to the transverse plane xy. The quantity Ψ_{RP} identifies the orientation of the reaction plane. The impact parameter b is defined as the distance in the transverse plane between the ion centres.

per nucleon-nucleon pair nor on the colliding system, showing compatible production yields in collisions producing similar final state multiplicity $\langle dN/d\eta \rangle|_{|y|<0.5}$. In particular, recent results from the ALICE collaboration [51] show that the production yields of strange hadrons in high-multiplicity pp collisions is comparable with those measured in Pb–Pb collisions. According to this affinity, it is not clear whether the strangeness enhancement measured in high-multiplicity pp events is caused by similar underlying mechanisms governing the physics of the different colliding systems, becoming equivalent as soon as a specific multiplicity class of events is taken into account.

1.4.6 Azimuthal anisotropy

As described in Sec 1.3.1, the geometry of a nucleus-nucleus collision depends on the impact parameter between them. When this quantity is close to zero, the event is defined as *central*, since most of the nucleons of the two projectiles are involved in the collision. When the impact parameter is larger, the event is defined as *non-central* and only a fraction of the nucleons participate in the interaction, while the others move forward untouched (*spectators*). As shown in Fig. 1.13, in non-central events the overlapping region identified by the participant nucleons assumes an almond-like shape, whose projection in the transverse plane corresponds to an ellipse with increasing eccentricity as much as the distance between the two colliding nuclei increases. This geometrical anisotropy of the initial state is converted into an anisotropy in momentum space, due to the formation of anisotropic pressure gradients in the transverse plane, causing an azimuthal anisotropy in the collective flow of the constituents partons before their hadronization. The measurement of the anisotropic flow enables the study of the equation of state of the system and the transport coefficients related to the hydrodynamic expansion, such as the shear viscosity to entropy density η/s and the bulk viscosity to entropy density ζ/s.

The azimuthal anisotropy of the system can be evaluated through the measurement of the particle production as a function of the azimuthal angle φ, which can be

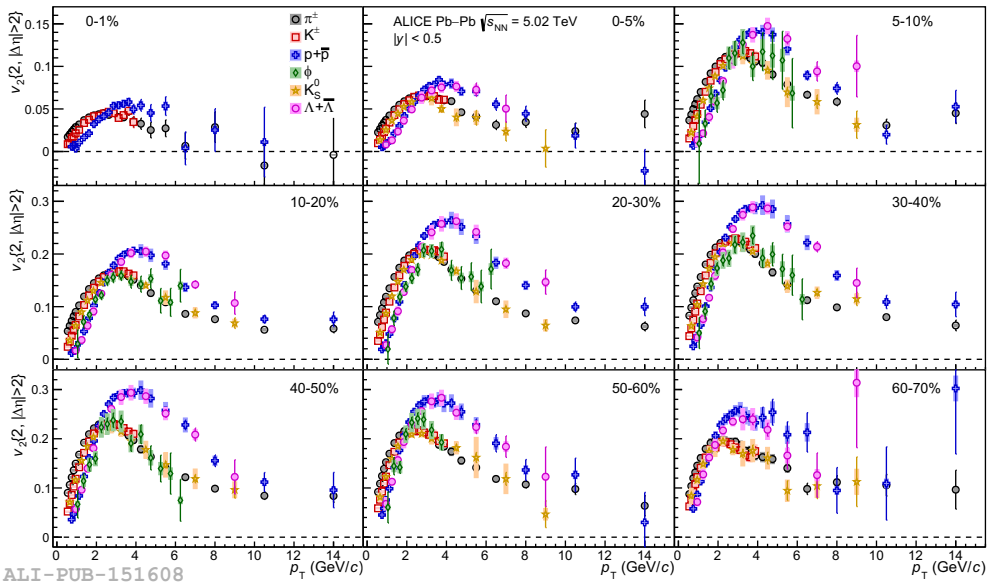

FIGURE 1.14: p_T-differential v_2 of $\pi^{\pm}$, $K^{\pm}$, $p + \bar{p}$, $\Lambda + \bar{\Lambda}$, K^0_S and ϕ-meson in Pb–Pb collisions at $\sqrt{s_{NN}} = 5.02$ TeV at different centrality classes. Figure from [52].

decomposed with a Fourier expansion [53] as:

$$E\frac{d^3N}{dp^3} = \frac{1}{2\pi}\frac{d^2N}{p_T dp_T dy}\left(1 + 2\sum_{n=1}^{\infty} v_n(p_T)\cos[n(\varphi - \Psi_n)]\right) . \tag{1.37}$$

The quantity Ψ_n in Eq. 1.37 is the symmetry plane of the harmonic of n-th order. For n = 2 this quantity identifies the *event plane* of the collision, which in case of no fluctuations in the geometrical distribution of the participants corresponds to the so-called *reaction plane*, defined by the direction of the impact parameter vector and the fly direction of the colliding nuclei. The quantity v_n represents the n-th order flow Fourier coefficient and is calculated as:

$$v_n(p_T) = \langle \cos[n(\varphi - \Psi_n)] \rangle , \tag{1.38}$$

where the brackets denote the average among all the particles with a given p_T present in all the events with a given centrality. The second order flow coefficient v_2 is called *elliptic flow* and constitutes the major contribution to the asymmetry in non-central collision, given the almond-like shape of the overlapping region. The measurement of a large v_2 is a clear signature of the QGP, indicating the presence of a thermalised system that follows the laws of relativistic hydrodynamics already in the partonic phase. The higher order coefficients v_3 and v_4, called respectively *triangular* and *quadrangular flow* coefficients, are generated mainly by fluctuations of the distributions of participants in the nuclei in the initial state and by non-linear hydrodynamic response of the medium [54–59].

The study of the anisotropic flow for identified particles permits to achieve a deeper knowledge of the physics underlying the QGP evolution. In particular, its dependence on the particle p_T allows to investigate different kinematic regions of interest, where different physics phenomena influence the flow. The p_T-differential elliptic flow coefficient of $\pi^{\pm}$, $K^{\pm}$, ϕ, $p + \bar{p}$, $\Lambda + \bar{\Lambda}$ and K^0_S measured by the ALICE

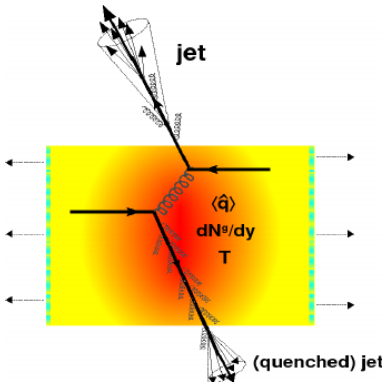

FIGURE 1.15: Sketch of jet quenching in QGP. Figure from [68].

experiment in Pb–Pb collisions at $\sqrt{s_{\rm NN}} = 5.02$ TeV at different centrality classes is shown in Fig. 1.14 [52]. The v_2 coefficient increases from most central collisions (0-1%) to semi-central ones (30-40%) because of the increased spatial anisotropy of the overlapping region between the two colliding nuclei. For more peripheral collisions, the v_2 decreases again due to the lowering of pressure gradients in the produced system. In the low-$p_{\rm T}$ region ($p_{\rm T} \lesssim 3$ GeV/c) the elliptic flow shows a clear mass ordering, namely the v_2 coefficient decreases with the increasing hadron mass. This behaviour is expected due to the interplay with the radial flow (see Sec. 1.4.4) pushing more massive particles to higher $\langle p_{\rm T} \rangle$. At intermediate transverse momenta ($3 \lesssim p_{\rm T} \lesssim 8$ GeV/c) the values of v_2 tend to be higher for baryons with respect to mesons. This property supports the hypothesis of quark hadronization via coalescence, which implies that the v_2 of each single constituent quark contributes to the elliptic flow of the final state hadron. This implies a larger v_2 for baryons with respect to mesons, showing a v_2 dependence on the number of constituent quarks rather than the hadron mass.

The measurement of anisotropic flow at high $p_{\rm T}$, when $p_{\rm T} \gg m$, is therefore sensitive to the in-medium path-length dependent energy loss effects. For transverse momenta $p_{\rm T} \gtrsim 8$ GeV/c the anisotropic flow is generated when hard partons propagate through the QGP loosing energy via multiple scatterings and gluon radiation, leading to a non-zero elliptic flow up to very high $p_{\rm T}$ [60–63]. Finally, the comparison of the measured v_n coefficient with model predictions permits to give important constraints to the hydrodynamical properties of the QGP. In particular, the experimental results support the description of the QGP as a perfect fluid, since they are fairly described by model calculations [64,65] which assume a η/s close to the lower limit of $1/4\pi$. This value is imposed by first principle calculations and confirmed by anti-de Sitter/conformal field theory (AdS/CFT [66]), even if recent theoretical developments seem to challenge this limit [67].

1.4.7 Jet quenching

The production of high energy partons in hadronic collisions is mainly ascribed to the hard-scattering processes, where two partons from the initial state hadrons interact with a large momentum exchange. This process at leading order produces a pair of back-to-back high-energy partons. It manifests macroscopically as a 2, 3 or 4- jets, according to the number of high-energy partons produced in the event. A jet is defined as a spray of hadrons deriving from the parton shower caused by the high-energy parton fragmentation. In nucleus-nucleus collisions, the back-to-back

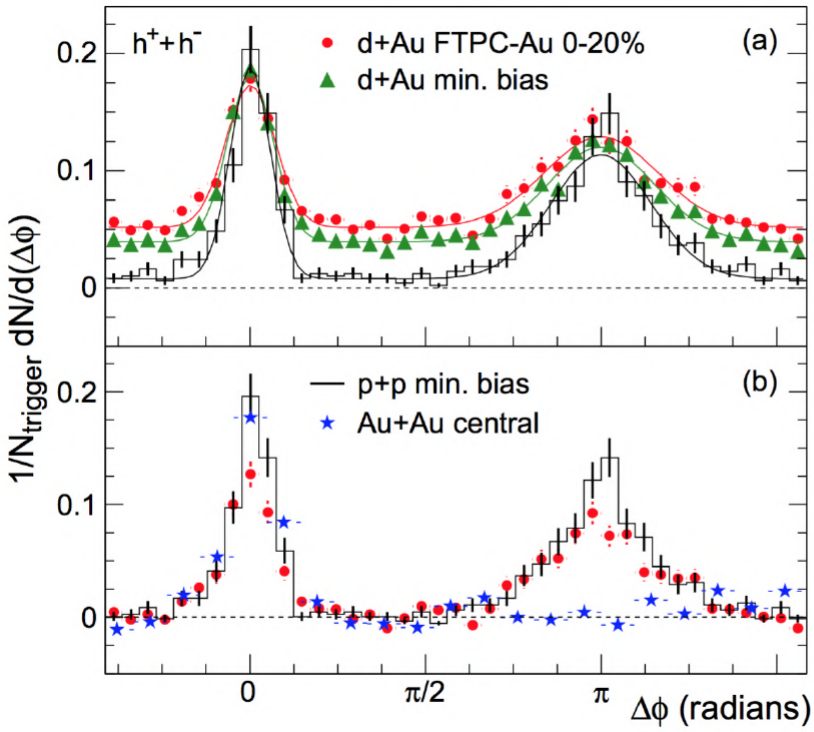

FIGURE 1.16: (a) Azimuthal distributions for minimum bias and central d–Au collisions, and for pp collisions at $\sqrt{s_{\rm NN}} = 200$ GeV measured by the STAR experiment at RHIC. (b) Comparison of pedestal subtracted two-particle azimuthal distributions for central d–Au collisions to those seen in pp and central Au–Au collisions at $\sqrt{s_{\rm NN}} = 200$ GeV measured by the STAR experiment at RHIC. Figure from [69].

topology and the kinematic correlations are broken by the presence of the QGP. As depicted in the sketch in Fig. 1.15, the two partons produced in the hard-scattering process lose energy in the form of gluon radiation ("gluonsstrahlung") while traversing the medium, where the amount of energy loss depends on the path-length. This phenomenon is called *jet quenching* and was observed at RHIC [69], comparing the di-hadron azimuthal correlation in nucleus-nucleus collisions with the results from smaller systems. Quarks that are produced close to the surface of the fireball maintain most of their original energy and are later detectable as high-$p_{\rm T}$ jets. This is usually used as a possible "trigger" particle and the region with $\Delta\varphi = 0$ around it is called *near-side*. The opposite parton ("associated"), expected in the *away-side* region, namely at $\Delta\varphi = \pi$ with respect to the trigger particle, needs to cover a longer path before leaving the QGP, loosing a larger amount of energy. The measurements from the STAR experiment in pp, deuteron–gold (d–Au) and Au–Au collisions at $\sqrt{s_{\rm NN}} = 200$ GeV are reported in Fig. 1.16. While the near-side peak has similar height and shape among different collision systems, the away-side peak in central (0-20%) Au–Au collisions disappears, signalling that the back-scattered parton loses a significant amount of energy which is dissipated at large angles. This behaviour is not observed in d–Au collisions, where no medium formation is expected.

The hadrons possibly produced from the hadronization of the away-side parton are affected by the reduction of the quark energy, causing an overall softening of the measured $p_{\rm T}$-spectrum of final state particles. This effect is studied experimentally

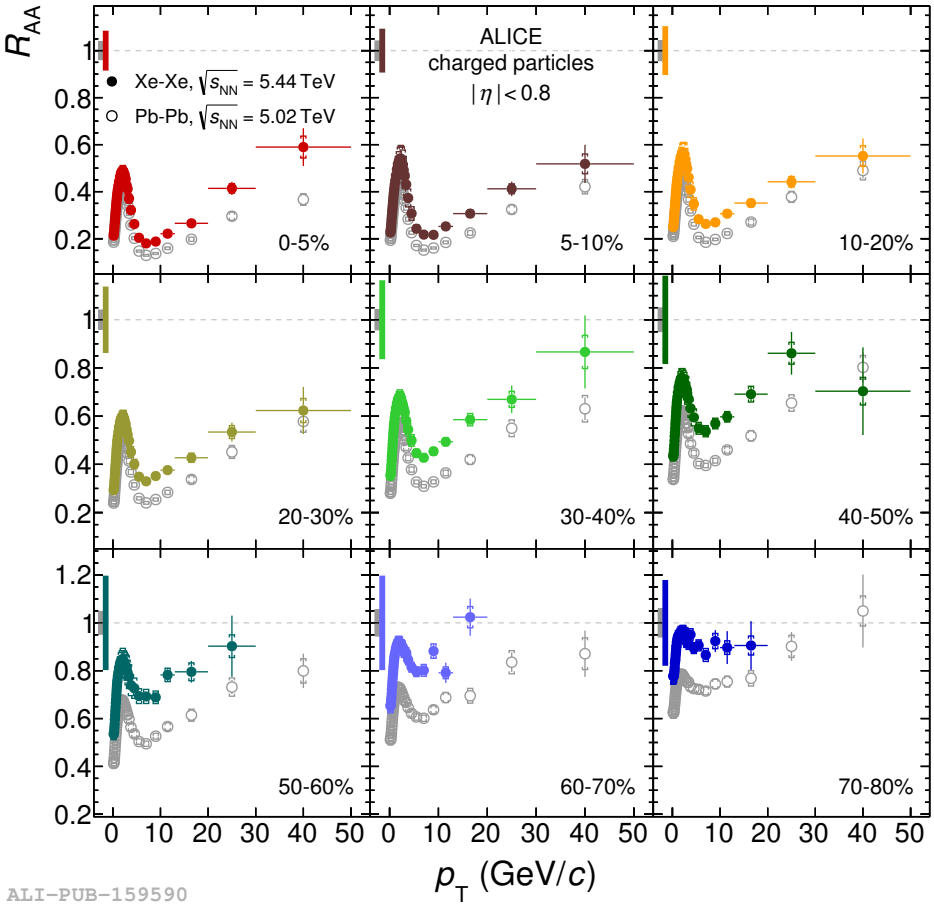

FIGURE 1.17: Nuclear modification factor in Xe–Xe at $\sqrt{s_{NN}}$ = 5.44 TeV and Pb–Pb at $\sqrt{s_{NN}}$ = 5.02 TeV collisions for charged particles measured by the ALICE experiment in nine centrality classes. Figure from [70].

with the measurement of the *nuclear modification factor* (R_{AA}), which is defined as follows:

$$R_{AA}(p_T, y) = \frac{1}{\langle T_{AA} \rangle} \frac{d^2N_{AA}/dp_T dy}{d^2\sigma_{pp}/dp_T dy}, \tag{1.39}$$

where $\langle T_{AA} \rangle = \langle N_{coll} \rangle / \sigma_{pp}^{inel.}$ (see Eq. 1.19). The quantity defined in Eq. 1.39 corresponds to the p_T- and rapidity- differential yield measured in nucleus-nucleus collisions divided by the same quantity in pp collisions scaled by the average number of expected nucleon-nucleon interactions, given by the Glauber model (see Sec. 1.3.1). The nuclear modification factor is expected to be at unity in case a nucleus-nucleus collision can be described as a pure superimposition of nucleon-nucleon interactions, without any further effect emerging from the different nature of the initial state. The scaling with the average number of nucleon-nucleon interactions $\langle N_{coll} \rangle$ is somehow valid for hard processes, for which the cross section $\sigma_{NN}^{hard} \ll \sigma_{NN}^{inel.}$ is small. Considering Eq. 1.21, 1.22 and using σ_{NN}^{hard} instead of σ_{NN}^{inel} and applying a

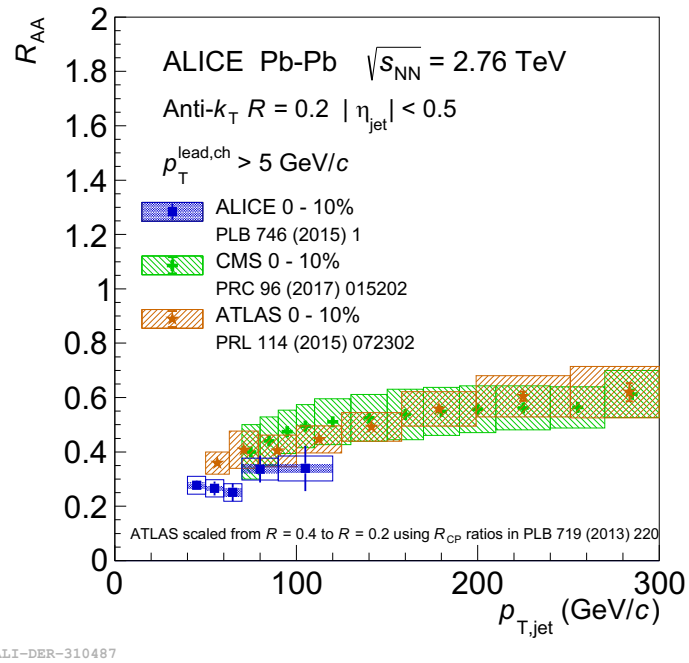

FIGURE 1.18: Nuclear modification factor of charged jets in central (0–10%) Pb–Pb collisions at $\sqrt{s_{NN}} = 2.76$ TeV measured by the ALICE experiment [71] compared with the one of inclusive jets measured by the CMS [72] and ATLAS [73] experiments at the same collision energy and centrality. Figure from the ALICE Figure Repository ©.

Taylor expansion around σ_{NN}^{hard} one obtains:

$$\frac{d\sigma_{AB}^{hard}}{db} \simeq 1 - \left[1 - AB \cdot \sigma_{NN}^{hard} \cdot \hat{T}_{AB}(\vec{b})\right] = AB \cdot \sigma_{NN}^{hard} \cdot \hat{T}_{AB}(\vec{b}) \propto \sigma_{NN}^{hard} \cdot \langle N_{coll}(\vec{b})\rangle \,, \tag{1.40}$$

where Eq. 1.19 is exploited in the last step. Eq. 1.40 shows that the hard processes cross section in nucleus-nucleus collisions scales with $\langle N_{coll}\rangle$. According to this, a $R_{AA} = 1$ would confirm this *bynary scaling* assumption. Deviations from unity of the nuclear modification factor as a function of p_T are expected in case jet quenching for high-p_T partons plays a role, causing $R_{AA} < 1$ for intermediate values of the hadron p_T. This effect was first observed at RHIC in Au–Au collisions at $\sqrt{s_{NN}} = 130$ GeV as a suppression of the particle yields with respect to the reference pp results in the region $3 \lesssim p_T \lesssim 6$ GeV/c [74,75]. The nuclear modification factor for charged particles measured by the ALICE experiment in Xe–Xe collisions at $\sqrt{s_{NN}} = 5.44$ TeV and Pb–Pb collisions at $\sqrt{s_{NN}} = 5.02$ TeV shows a maximum suppression with respect to unity in the interval $5 \lesssim p_T \lesssim 10$ GeV/c in all centrality classes, as visible in Fig. 1.17. The comparison among the different centrality classes clearly shows a systematic reduction of the suppression as the collision becomes more peripheral, indicating that a lower system size implies a lower loss of energy for the traversing partons. Moreover, the clear ordering between Xe–Xe and Pb–Pb collisions is representative of the energy loss dependence on the system size, being more pronounced in the more extended QGP produced in the latter case. A further confirmation of the link between $R_{AA} < 1$ at intermediate-p_T and energy loss in the QGP comes from the observation of a $R_{AA} = 1$ for photons, W and Z bosons in the same transverse momentum interval [34,76–79]. The R_{AA} at unity indicates that the energy loss in QGP originates from the strong interaction with the medium of high-energy quarks

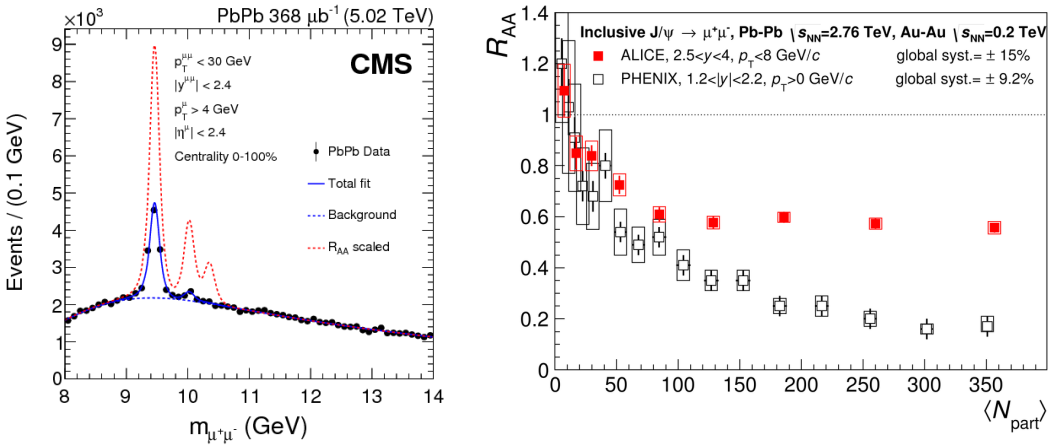

FIGURE 1.19: Left: invariant mass distribution of muon pairs in Pb–Pb collisions at $\sqrt{s_{\rm NN}} = 5.02$ TeV reconstructed by the CMS experiment. The data are reported as black points and their fit with a solid blue line. The dotted red line represents the same distribution scaled by the inverse of the nuclear modification factor. Figure from [80]. Right: nuclear modification factor as a function of $\langle N_{\rm part} \rangle$ of J/ψ reconstructed in the $\mu^+\mu^-$ channel measured by the ALICE and PHENIX experiments in Pb–Pb collisions at $\sqrt{s_{\rm NN}} = 2.76$ TeV and Au–Au collisions at $\sqrt{s_{\rm NN}} = 200$ GeV respectively. Figure from [81].

and gluons, which does not affect electroweak bosons and their decay leptons. The charged particle $R_{\rm AA}$ in all centrality classes grows for $p_{\rm T} \gtrsim 10$ GeV/c towards unity, while a pretty constant $p_{\rm T}$ dependence is observed for charged jets within the same $p_{\rm T}$ interval. This is visible in Fig. 1.18, where the nuclear modification factor of charged jets in central (0–10%) Pb–Pb collisions at $\sqrt{s_{\rm NN}} = 2.76$ TeV measured by the ALICE experiment [71] compared with that of inclusive jets measured by the CMS [72] and ATLAS [73] experiments at the same collision energy and centrality is shown. Such a rise at the level of charged particle $R_{\rm AA}$ is not accompanied by a similar rise of the charged jet $R_{\rm AA}$, which reaches a plateau at around 0.5 for $p_{\rm T,jets} \gtrsim 200$ GeV/c. This comparison suggests that part of the energy is spread out of the jet cone in Pb–Pb collisions, causing a $R_{\rm AA}$ for charged jets lower than unity.

The binary scaling hypothesis would not be violated in case of a $R_{\rm AA} > 1$ for lower transverse momenta, as a consequence of the $p_{\rm T}$ reduction caused by the jet quenching, but the reported results show a $R_{\rm AA} < 1$ for transverse momenta down to zero. This behaviour is not ascribable to the presence of QGP (*hot nuclear matter effects*), but to the involvement of nuclei in the collisions, which modify the conditions of the initial state with respect to a pp collision. A dedicated environment for the study of these *cold nuclear matter effects* (CNM) are the p–Pb collisions, where the QGP formation is not expected and the $R_{\rm pPb}$ is only affected by them. Moreover, the particle production at low transverse momenta ($p_{\rm T} \lesssim 3$ GeV/c) is dominated by soft processes, which scale with $\langle N_{\rm part} \rangle$, therefore the mentioned binary scaling is not expected to be valid even in absence of medium effects. These aspects will be addressed with more details later in this thesis.

State	J/ψ	χ_c	$\psi(2S)$	$\Upsilon(1S)$	$\Upsilon(2S)$	$\Upsilon(3S)$
T_d/T_c	2.10	1.16	1.12	> 4.0	1.60	1.17

TABLE 1.1: Dissociation temperature in units of the critical temperature for different charmonia and bottomonia states. Table from [82].

1.4.8 Quarkonia suppression

The study of $c\bar{c}$ and $b\bar{b}$ bound states, called *quarkonia*, represents an interesting tool to inspect the QGP properties. This was firstly proposed by Matsui and Satz [11], who identified in the suppression of the charmonia production in heavy-ion collisions a powerful probe of the deconfinement, sensitive to the medium temperature [4]. The quarkonium binding energy in the vacuum can be derived from the Cornell potential reported in Eq. 1.9, which allows to define the bound state radius that for the J/ψ ranges in $0.2 \leq r_{J/\psi} \leq 0.5$ fm at $T = 0$, depending on the value of the charm quark mass and of the string tension σ and α at null temperature. At finite T, the string tension coefficient decreases until $\sigma(T_c) = 0$, therefore the linear confining term of the potential vanishes for $T \geq T_c$, when it becomes:

$$V(r)^{QGP} = -\frac{\alpha(T)}{r} \cdot e^{-r/r_D(T)} \,. \tag{1.41}$$

The Cornell potential reduces to a colour-screened coulombic one, where the colour charges are subject to a screening effect similar to that experienced by electric charges inside a plasma of electrons and ions. The quantity $r_D(T)$ is the *Debye radius*, which quantifies the typical extension of the colour screening effect in the deconfined medium. The Debye radius strongly depends on the system temperature and it is expected to decrease as soon as the medium temperature increases. Therefore the bound states which extend to a radius $r > r_D$ cannot survive in the QGP, due to the exponential drop of the potential in Eq. 1.41. Moreover, the temperature dependence of the confining potential coefficients influences the effective radius of the bound state: according to Lattice QCD calculations, at $T/T_c = 1.5$ the coulombian-like coefficient amounts to $\alpha \simeq 0.2$, consequently the J/ψ radius at these temperatures reaches values within $0.5 \leq r_{J/\psi} \leq 1.3$ fm. Considering that the radius is inversely proportional to the binding energy, a decrease of the Debye radius implies a reduction of the formation and the survival probability of quarkonia states in the QGP [83]. Since the binding energy of excited $q\bar{q}$ pairs ($\psi(2S)$, $\Upsilon(2S)$, $\Upsilon(3S)$) is lower than that of the quarkonium ground states (J/ψ, $\Upsilon(1S)$), a sequential depletion of the various quarkonium resonances according to their binding energy is expected and this feature can be in principle used to estimate the temperature of the medium according to the melting of specific bound states. In other words, the quarkonia dissociation, and the consequent decrease of the measured production yields, can be exploited as a thermometer of the QGP [4]. Some indicative values of dissociation temperature for the different quarkonia states are reported in Tab. 1.1.

The J/ψ suppression was firstly observed at SPS in Pb–Pb collisions at $\sqrt{s_{NN}} = 17.4$ GeV [85] and at RHIC in Au–Au collisions at $\sqrt{s_{NN}} = 200$ GeV [86] and the suppression of the quarkonia yields has been confirmed at the LHC in nucleus-nucleus collisions at the TeV scale. In the left panel of Fig. 1.19 the $\mu^+\mu^-$ invariant mass distribution in Pb–Pb collisions at $\sqrt{s_{NN}} = 5.02$ TeV reconstructed by the CMS experiment is reported [80]. The analysed range is $8 < m_{\mu^+\mu^-} < 14$ GeV/c^2, in order to highlight the reconstructed signal for the bottomonia states $\Upsilon(1S)$, $\Upsilon(2S)$ and

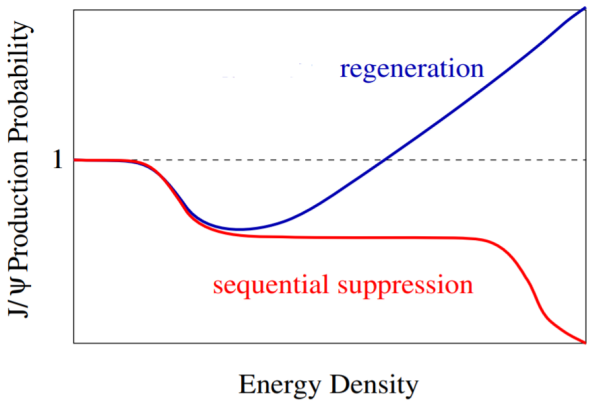

FIGURE 1.20: J/ψ sequential suppression compared with statistical recombination as a function of the system energy density. Figure from [84].

Υ(3S), with a mass of $m(\Upsilon(1S)) = 9.460$ GeV/c^2, $m(\Upsilon(2S)) = 10.023$ GeV/c^2 and $m(\Upsilon(3S)) = 10.355$ GeV/c^2 respectively [3]. From the comparison of the reconstructed distribution (black points and blue line) with the abundances expected in absence of QGP effects (red dotted line), the experimental data show a reduction of the $\Upsilon(1S)$ yield of more than a factor $\times 2$ and the almost complete disappearance for the excited quarkonia states. These results confirm the assumption of a medium-induced colour screening and the consequent sequential melting of quarkonia states. As a consequence, with increasing temperature the quarkonium state production is expected to be more suppressed and this can be studied experimentally with the increase of the centre-of-mass energy until the nuclear modification factor goes to zero. The nucleus-nucleus collisions performed at the LHC are in principle a perfect environment to observe a reduction of the quarkonia production with respect to pp collisions at the same energy as well as nucleus-nucleus collisions performed at a lower energy, like the ones at RHIC which are characterised by a lower $\sqrt{s_{\rm NN}}$ by about an order of magnitude. The comparison of the nuclear modification factor for J/ψ mesons measured in Pb–Pb collisions at $\sqrt{s_{\rm NN}} = 2.76$ TeV by the ALICE experiment at LHC and in Au–Au collisions at $\sqrt{s_{\rm NN}} = 200$ GeV measured by the PHENIX experiment at RHIC is shown in the right panel of Fig. 1.19. Differently from what expected, a larger J/ψ suppression is observed at RHIC, given a $R_{\rm AA} \simeq 0.2$ for most central collisions versus a 3 times larger nuclear modification factor for Pb–Pb events at $\sqrt{s_{\rm NN}} = 2.76$ TeV in correspondence of the same $\langle N_{\rm part} \rangle$. This behaviour suggests the existence of an underlying phenomenon that counterbalances the quarkonium suppression due to the screening. A production increase at LHC can be expected due to a larger *quarkonium regeneration*. According to this mechanism [87–89], part of the charmonia production comes from the statistical recombination of charm and anti-charm quarks coming from unrelated hard-scatterings. This contribution is expected to be more relevant at high centre-of-mass energies due to the higher number of produced $c\bar{c}$ pairs, as shown in Fig. 1.20. The $c\bar{c}$ production at LHC energies is expected to be ~ 10 times higher than RHIC ones, therefore a larger regeneration is expected. Moreover, the experimental measurements of $R_{\rm AA}$ as a function of transverse momentum [81] show a nuclear modification factor about 4 times larger at LHC energies with respect to RHIC ones for $p_{\rm T}(J/\psi) < 1$ GeV/c, suggesting that the recombination mechanism is much more relevant for the charmonia production at low transverse momenta. The charm quark hadronization via recombination in

the QGP is expected to enhance also the production of open-charm hadrons, due to the coalescence of a charm quark with light ones picked up from the medium. This will be discussed in the next Chapter.

Chapter 2

Heavy-flavour production in hadronic collisions

The charm (c) and beauty (b) quarks can be considered as unique probes of the heavy-ion collision dynamics. Due to their high mass ($m_c \simeq 1.3$ GeV/c^2, $m_b \simeq 4.2$ GeV/c^2 [3]), charm and beauty quarks are mainly produced in the hard scatterings among partons of the colliding hadrons. These processes take place with a characteristic timescale $\Delta\tau \sim 1/Q$ of $\Delta\tau_c \sim 0.08$ fm/c and $\Delta\tau_b \sim 0.03$ fm/c[1],which is smaller than the typical QGP formation time $\tau_{QGP} \sim 0.2 \div 1$ fm/c (see Sec. 1.3.2). Therefore, charm and beauty quark production foreruns the QGP and they survive through the medium expansion, interacting with the free partons in the plasma. For these reasons, the measurement of open heavy-flavour hadrons, namely hadrons containing at least one heavy valence quark, are excellent tools for the study of the whole QGP space-time evolution.

To address the heavy quark dynamics in the QGP it is crucial to disentangle the effects induced on charm and beauty quarks by the medium from those caused by the presence of heavy nuclei in the initial state of the collision. These aspects, discussed in detail in Sec. 2.2.1, are experimentally accessible with precise measurements of heavy-flavour hadron production in heavy-ion collisions down to low transverse momenta. In this thesis, such measurement is performed by tagging the electrons from the semi-leptonic decays of charm and beauty hadrons in Pb–Pb collisions at $\sqrt{s_{NN}} = 5.02$ TeV, as discussed in Chapter 4.

The formation of a colour-deconfined state can modify the hadronisation mechanisms involving the heavy quarks, but to completely understand the medium-induced effects a study of the hadronisation processes involving heavy quarks in pp collisions, where the QGP formation is not expected, is mandatory. These aspects are introduced in Sec. 2.1 and rediscussed in more details in Sec. 2.3. The production measurements of charm baryons and the relative abundances with the mesons cover a key role in this puzzle. In Chapter 5 the measurement of prompt Λ_c^+ and $\Sigma_c^{0,++}$ baryons in pp collisions at $\sqrt{s} = 13$ TeV is described and the comparison with the D^0 meson is discussed. An important result obtained in this work is the first measurement of the prompt Λ_c^+ fraction from $\Sigma_c^{0,+,++}$ strong decays in pp collisions at the TeV scale, which is crucial to better understand the baryon production enhancement in hadronic collisions at the LHC.

In this Chapter, a brief description of the open heavy-flavour production in pp collisions is provided in Sec. 2.1, then the production in p–Pb and Pb–Pb collisions is addressed in Sec. 2.2. Finally, in Sec. 2.3 a more detailed dissertation about the heavy quark hadronisation is reported.

[1] A value equal to twice the quark mass ($\sim 2m_q$) is taken into account as an indicative (minimum) value for the momentum transfer Q

2.1 Open heavy-flavour production in pp collisions

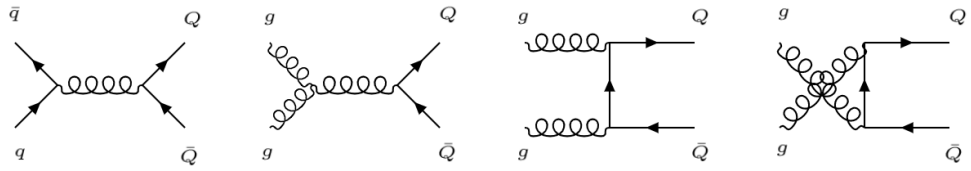

FIGURE 2.1: Feynman diagram of leading order quark-antiquark annihilation and gluon fusion for the production of $c\bar{c}$ and $b\bar{b}$.

The pp collisions provide a good environment where to probe the pQCD predictions, given that the large Q^2 required for the $c\bar{c}$ and $b\bar{b}$ pair production implies a value for α_S which is significantly lower than unity (see Sec. 1.1). Moreover, the measurement of the open heavy-flavour hadron production in pp collisions provides the fundamental baseline for the studies in larger collision systems. In such conditions, perturbative expansions in α_S can be engaged in the calculations of elementary $q\bar{q}$ production cross section. The main contributing processes at leading order ($\mathcal{O}(\alpha_S^2)$) are the quark-antiquark annihilation $\sigma_{q\bar{q}\to Q\bar{Q}}$ and the gluon fusion $\sigma_{gg\to Q\bar{Q}}$ [90], as shown in Fig. 2.1. In pQCD calculations the production cross section of heavy-flavour hadrons (H_Q) $d\sigma_{pp\to H_Q+X}$ is calculated with a factorization approach, as described by the following equation:

$$\begin{aligned} d\sigma_{pp\to H_Q+X}(\sqrt{s}) = &\sum_{i,j=q,\bar{q},g} f_1(x_i,\mu_F^2) f_2(x_j,\mu_F^2) \\ &\otimes d\sigma^{hard}_{ij\to Q\bar{Q}}(\alpha_S(\mu_R^2),\mu_F^2,m_Q),x_i x_j s) \\ &\otimes D_Q^{H_Q}(z,\mu_F^2)\ . \end{aligned} \tag{2.1}$$

The formulation in Eq. 2.1 is justified by the *factorization theorem* [91]. Considering two colliding protons, labelled as "1" and "2", the open heavy-flavour hadron production cross section can be expressed as the convolution of three different terms. The first term is $f_1(x_i,\mu_F^2) f_2(x_2,\mu_F^2)$, where $f_{1,2}$ are the *parton distribution functions* (PDFs) of the two colliding protons. They represent the probability for a given parton to carry a certain fraction of momentum of the original proton $x = p_{parton}/p_p$, called *Bjorken-x*. The second term $\sigma^{hard}_{ij\to Q\bar{Q}}$ corresponds to the cross section of the hard scattering process, where the heavy-$Q\bar{Q}$ pair is produced by the interaction of partons. The third term $D_Q^{H_Q}(z,\mu_F^2)$ corresponds to the *fragmentation function*, which quantifies the probability for a heavy quark Q to fragment into a hadron H_Q carrying a fraction $z = p_{H_Q}/p_Q$ of the original quark momentum. Both the PDF and the fragmentation functions values depend on the virtuality (Q^2) of the process, linked to the *factorization scale* μ_F. PDFs are usually parametrised from measurements of deep-inelastic scattering processes [92–94] and the fragmentation functions from hadron production measurements performed in e^+e^- collisions [95, 96]. This approach is valid under the assumption of universality of the fragmentation functions among the collision systems. These parametrizations are performed at a certain energy scale Q_0^2 and their extrapolation to a different virtuality is done using the Dokshitzer–Gribov–Lipatov–Altarelli–Parisi (DGLAP) equations [97]. The hard scattering cross section is calculated as a perturbative series on α_S. Its value depends on the energy scale, which is indicated by the *renormalization scale* μ_R defined for the

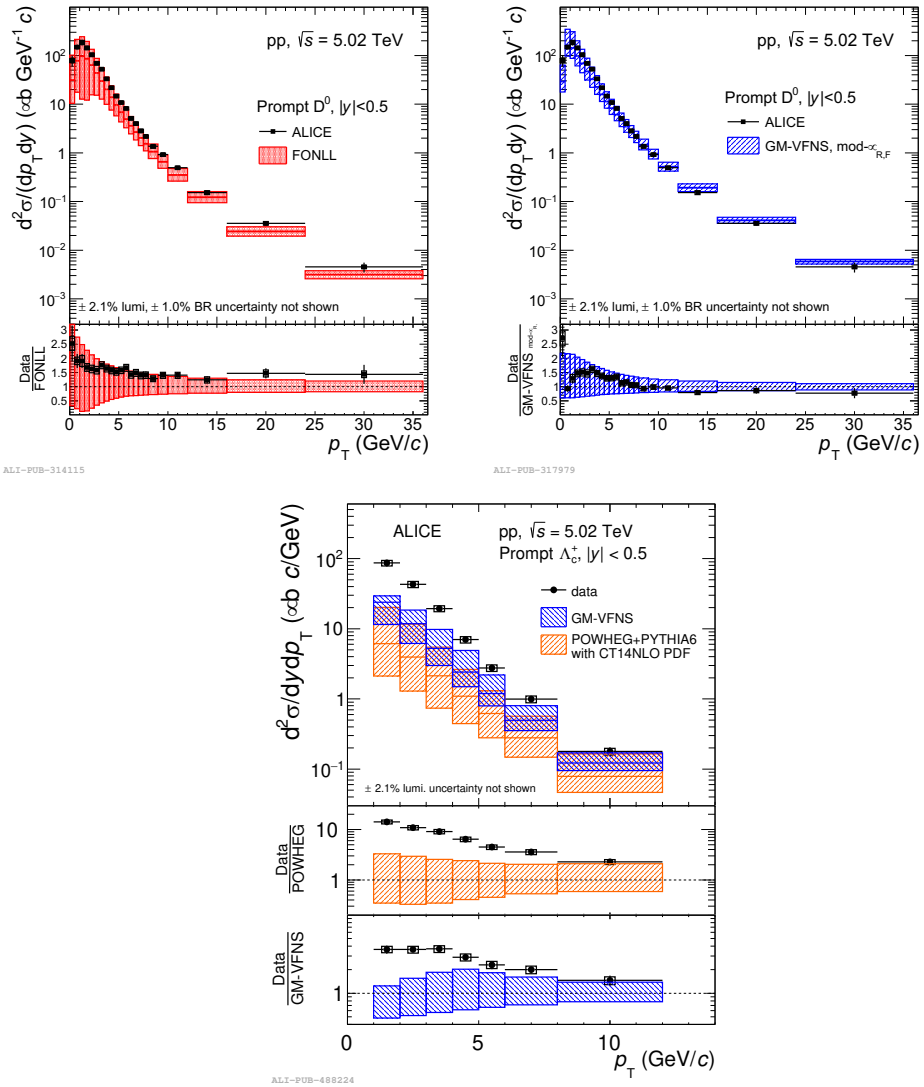

FIGURE 2.2: p_{T}-differential production cross section of D^0 mesons and Λ_{c}^+ baryons in pp collisions at $\sqrt{s} = 5.02$ Tev measured by the ALICE experiment compared with theoretical predictions from different pQCD calculations (details in the text). Figures taken from [107] and [108, 109].

ultraviolet divergences renormalization in loop calculations. Both the factorization and normalization scales are usually set to the same order of the momentum transfer of the hard process $\mu_{\mathrm{F}} \sim \mu_{\mathrm{R}} \sim \mu_0 \equiv \sqrt{m_{\mathrm{Q}}^2 + p_{\mathrm{T,Q}}^2}$. In addition, apart on the factorization scale μ_{F} and the bare value of the heavy mass m_{Q}, the cross section depends also on the pp collision energy square $s = 4E_{\mathrm{p}}^2 \simeq 4p_{\mathrm{p}}^2$, which at the partonic level reflects in $x_i x_j s$. At present, the perturbative calculations are performed up to the next-to-leading order $\mathcal{O}(\alpha_{\mathrm{S}}^3)$ (NLO) and at a fixed order with the next-to-leading-log resummation in GM-VFNS [98, 99] and in FONLL [100, 101]. In particular, the next-to-leading-log corrections are more relevant at high p_{T}, where $p_{\mathrm{T}} \gg m$ given the quark mass m. Recently, predictions for the $\mathrm{c\bar{c}}$ and $\mathrm{b\bar{b}}$ production cross section are provided via next-to-next-to-leading-order (NNLO) calculations with QCD radiative corrections [102–106].

The factorization approach is tested with the comparison between model predictions and measurements of the open heavy-flavour hadron production in pp collisions. The results from the ALICE experiment for the $\mathrm{D}^0(\mathrm{c\bar{u}})$ meson and $\Lambda_\mathrm{c}^+(\mathrm{udc})$ baryon production cross section in pp collisions at $\sqrt{s} = 5.02$ TeV are shown in Fig. 2.2 [107–109]. In the top panels the experimental D^0 cross section is compared with FONLL and GM-VFNS calculations. Different PDFs [92,93] and fragmentation functions are considered in the two approaches. The two calculations assume also a different value for the charm quark mass, that is set to $m_\mathrm{c} = 1.5\,\mathrm{GeV}/c^2$ and $m_\mathrm{c} = 1.3$ GeV/c^2 in FONLL and GM-VFNS, respectively. The error bands around the theoretical points derive from the PDF and fragmentation function uncertainties, as well as on the scale variation on the value of the charm quark mass. The measured D^0 cross section is well described by the two predictions, even if it lies systematically on the upper edge of the FONLL-based calculations. These results indicate that the factorization approach works for the meson sector, as also observed by other LHC experiments [110–112]. However, the results from the charm baryon sector do not support the same conclusion. As visible in the bottom figure in Fig. 2.2, the Λ_c^+ production is not well described by GM-VFNS. In this case an updated fragmentation function for Λ_c^+ is used, deriving from the fit of OPAL data in $\mathrm{e^+e^-}$ collisions at $\sqrt{s} = 10$ GeV [113] and measurements from the Belle experiment at $\sqrt{s} = 10.52$ GeV [114]. The measurement is also compared with different pQCD calculations based on the POWHEG framework [115], where the PYTHIA 6 generator is used to generate the parton shower and hadronisation. The charm quark mass in POWHEG is set to $m_\mathrm{c} = 1.5$ GeV/c^2. In this case, the error bands on the theoretical prediction are estimated by varying the renormalization and factorization scales within $0.5\mu_0 < \mu_{\mathrm{R,F}} < 2\mu_0$. In both cases, the theoretical calculations significantly underestimate the experimental results with a maximum discrepancy up to a factor $\times 9$ for transverse momenta below 2 GeV/c. These results completely differ from the D^0 ones, showing that the factorization approach does not work for the description of open heavy-baryon production even if it does well on the meson sector. A possible explanation for this behaviour is the non-universality among the collision systems of the fragmentation functions, implying that those derived from $\mathrm{e^+e^-}$ collisions cannot be used for pp collisions. This signals that the hadronisation processes differ in the two collision systems [105] and these aspects will be exhaustively developed in Section 2.3.2.

2.2 Open heavy-flavour production in p–Pb and Pb–Pb collisions

2.2.1 Cold nuclear matter (CNM) effects

A fundamental requirement to precisely investigate the properties of the medium and the influence on the quark dynamics is to disentangle the medium effects, usually called *hot nuclear matter* effects, from nuclear effects not caused by the presence of a deconfined state, denoted as *cold nuclear matter* (CNM) effects. These phenomena are usually studied with electroweak bosons in AA collisions and with production measurements in minimum bias p–A and d–A collisions. In these collision systems the effects related to the formation of a hot and dense QCD matter can be neglected. This is confirmed by the charged particle R_AA measured in p–Pb collisions at $\sqrt{s_\mathrm{NN}} = 5.02$ TeV [116], which is compatible with unity for $p_\mathrm{T} \gtrsim 8$ GeV/c.

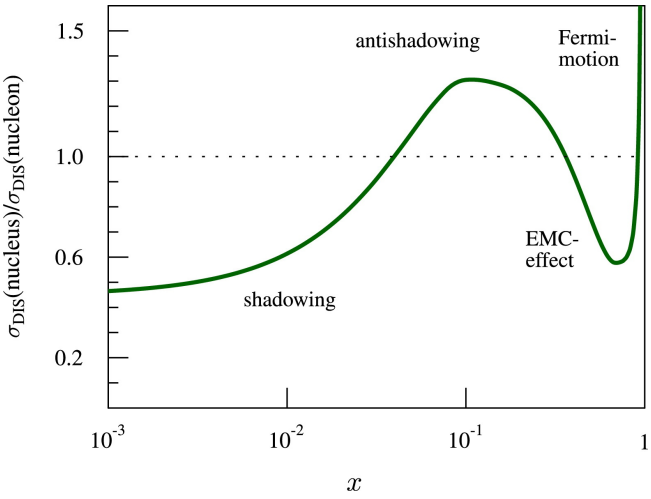

FIGURE 2.3: Sketch of nuclear PDF modification observed in deep inelastic scattering measurements. Figure from [117].

The dominant effect for heavy quarks at the LHC energies is related to the modification of nucleon parton functions [118], in case either the nucleon is free or is a constituent of a nucleus. Due to the quantum Fermi motion, bound nucleons are not at rest inside the nucleus and this modifies the effective nucleon structure function, which corresponds to a convolution of the bare nucleon structure function and their momentum distribution inside the nucleus $f_{\mathrm{N}}(z)$, namely $F_2^{\mathrm{A}}(x) \sim \int \mathrm{d}z f_{\mathrm{N}}(z) F_2^{\mathrm{N}}(x/z)$, where z is the fraction of nucleus momentum carried by the considered nucleon. Due to the Fermi motion the structure functions of bound nucleons are expected to increase with respect to that of free nucleons at large Bjorken-x values, about $x \gtrsim 0.5 \div 0.6$ [119–123]. Different experiments of deep inelastic scatterings observed further PDF modifications, according to the Bjorken-x regime reached in the experiment. The PDFs modification for bound protons in nuclei is usually expressed as [117]:

$$f_i^{\mathrm{p,A}}(x, Q^2) = R_i^{\mathrm{A}}(x, Q^2) f_i^{\mathrm{p}}(x, Q^2) \,, \tag{2.2}$$

where the nuclear modification on the free-proton PDF $f_i^{\mathrm{p}}(x, Q^2)$ is expressed by $R_i^{\mathrm{A}}(x, Q^2)$. The index i refers to the parton species taken into account (e.g. u, d, $\bar{u}$, $\bar{d}$, g, ...). In case of no nuclear effects, the term $R_i^{\mathrm{A}}(x, Q^2)$ is expected to be at unity, meaning that the PDF for a bound proton $f_i^{\mathrm{p,A}}(x, Q^2)$ is equal to that of a free one. However, a nuclear PDF modification depending on the Bjorken-x magnitude is observed, as shown in the sketch of Fig. 2.3. For $x \lesssim 0.05$ a significant suppression with respect to unity is observed and this is usually addressed as *shadowing* effect [124]. This behaviour can be explained by the presence of a spatial overlap among partons from different nucleons, which for very low-x mainly consist in gluons, as measured in e^-p deep-inelastic scatterings experiments at HERA [125]. This phenomenology is formally addressed in the *Colour Glass Condensate* (CGC) model [126], an effective field theory designed for the description of the low-x parton production. In this framework, the gluon density increases with decreasing Bjorken-x until a saturation level is reached, defined by a maximum phase space occupancy of order $\sim 1/\alpha_S$. This is determined by the saturation scale Q_s^2, parametrised by the "pocket" formula:

$$Q_s^2 \sim \mathrm{A}^{1/3} x^{-0.3} \,. \tag{2.3}$$

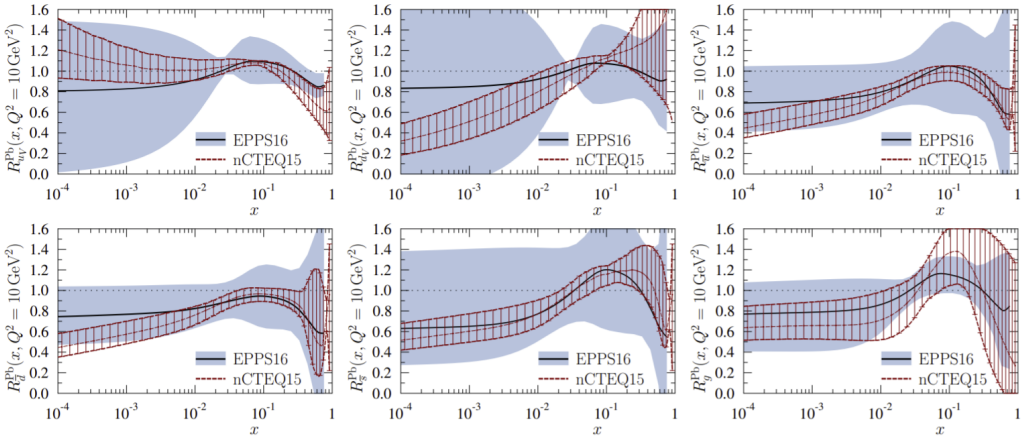

FIGURE 2.4: Comparison between PDF nuclear modification in lead nuclei from EPPS16 with nCTEQ15 ones at $Q^2 = 10$ GeV^2. Figure from [127].

According to Eq. 2.3, the saturation scale grows with decreasing x and the mentioned bound on the gluon occupancy of order $\sim 1/\alpha_S$ is saturated for gluons with transverse momentum lower than Q_s. For this reason, due to the rapid rise of gluon distribution at low x, as described by the Balitsky-Fadin-Kuraev-Lipatov (BFKL) equation [128], the saturation regime is reached and the system can be seen as a colour *condensate*. For Bjorken-x values in the range $0.05 \lesssim x \lesssim 0.3$ an *anti-shadowing* behaviour is present, as a consequence of the shadowing that depletes partons at low-x and requires a slight increase of partons at larger x for momentum conservation. At $0.3 \lesssim x \lesssim 0.8$ the nuclear modification reaches a minimum, which is usually ascribed to the *EMC effect* [129]. Then, for larger Bjorken-x the nuclear modification increases due to the Fermi motion, as mentioned above. Similar arguments can be driven for the neutron PDFs. The full nuclear PDFs $f_i^{\mathrm{A}}(x, Q^2)$ correspond to linear combinations of proton $f_i^{\mathrm{p,A}}$ and neutron $f_i^{\mathrm{n,A}}$ ones, according to proton and neutron abundances Z and N=A-Z respectively: $f_i^{\mathrm{A}}(x, Q^2) = (\mathrm{Z}/\mathrm{A}) f_i^{\mathrm{p,A}}(x, Q^2) + (\mathrm{N}/\mathrm{A}) f_i^{\mathrm{n,A}}(x, Q^2)$. The understanding of nuclear PDFs is mainly driven by the fit to several experimental data from deep-inelastic scattering and Drell-Yan processes. The constraints to nuclear PDF at low x are quite poor, due to the large uncertainty bands on the PDF parametrisations. This is visible in Fig. 2.4, where the nuclear modification for valence and sea quarks as well as for gluons from the global fit models EPPS16 [127] and nCTEQ15 [130] are reported.

According to the involved beams and the collision energy, different Bjorken-x regimes can be investigated. Let's consider a collision between two partons, in the context of a nucleus with atomic and mass numbers Z_1 and A_1 colliding with another nucleus with atomic and mass numbers Z_2 and A_2, as shown in Fig. 2.5. Assuming that the two nuclei are accelerated in the same apparatus with a given rigidity, then calling p the longitudinal ($\hat{z}$) momentum transferred to a free proton accelerated by the collider, the total momentum of the nuclei corresponds to $\mathrm{Z}_1 p$ and $-\mathrm{Z}_2 p$ respectively. The total momentum is shared among all the constituent nucleons. Therefore, each of them owns a momentum equal to $(\mathrm{Z}_1/\mathrm{A}_1)p$ and $-(\mathrm{Z}_2/\mathrm{A}_2)p$ respectively. Calling x_1 and x_2 the Bjorken-x values for the two partons involved in the collision, the carried momenta are then equal to $x_1(\mathrm{Z}_1/\mathrm{A}_1)p$ and $-x_2(\mathrm{Z}_2/\mathrm{A}_2)p$ respectively.

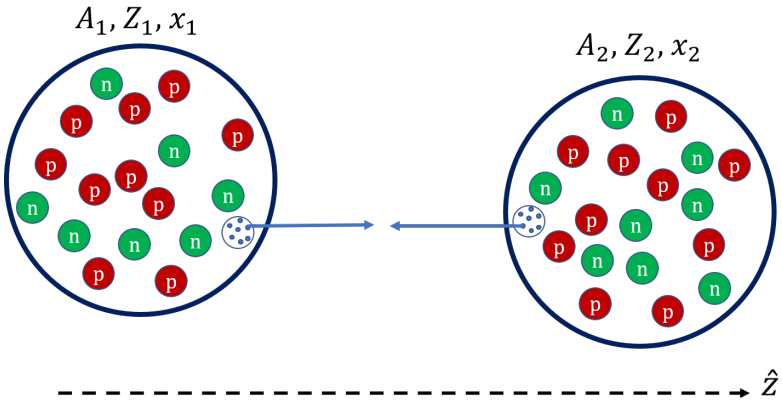

FIGURE 2.5: Sketch of a partonic hard scattering in nucleus-nucleus collisions.

According to this, the centre-of-mass energy of the parton-parton collision $s_{q\bar{q}}$ corresponds to:

$$s_{q\bar{q}} \simeq 4p_1p_2 = 4x_1x_2\frac{Z_1Z_2}{A_1A_2}p^2 = x_1x_2\frac{Z_1Z_2}{A_1A_2}s_{pp} = x_1x_2s_{NN}\,, \tag{2.4}$$

where s_{pp} is the corresponding Mandelstam s variable for a free-proton collision with momentum p and $s_{NN} \equiv s_{pp}(Z_1Z_2)/(A_1A_2)$ the same quantity for a nucleon-nucleon collision. In the same framework, the rapidity of the centre-of-mass frame of the two colliding partons can be calculated. Assuming them to have equal mass, it can be demonstrated that $y_{CM} = (y_1 + y_2)/2$, which brings, after some calculations, to[2]:

$$y^{q\bar{q}}_{CM} \simeq \frac{1}{2}\ln\left(\frac{x_1}{x_2}\frac{Z_1A_2}{A_1Z_2}\right)\,. \tag{2.5}$$

Thanks to Eq. 2.4 and 2.5 one can derive the Bjorken-x values carried by the colliding partons:

$$x_1 = \sqrt{\frac{A_1Z_2}{Z_1A_2}}\cdot\frac{\sqrt{s_{q\bar{q}}}}{\sqrt{s_{NN}}}e^{y^{q\bar{q}}_{CM}}\,,\; x_2 = \sqrt{\frac{A_2Z_1}{Z_2A_1}}\cdot\frac{\sqrt{s_{q\bar{q}}}}{\sqrt{s_{NN}}}e^{-y^{q\bar{q}}_{CM}}\,. \tag{2.6}$$

Considering symmetric colliding systems, the Bjorken-x value for the two partons are equal at central rapidity ($y \simeq 0$) and it is proportional to the centre-of-mass energy of the hard scattering $\sqrt{s_{q\bar{q}}}$. If a $c\bar{c}$ or a $b\bar{b}$ pair is produced in the hard scattering, this imposes an energetic threshold for the process equal to $\sqrt{s_{q\bar{q}}} \approx 2m_c \simeq 2.6$ GeV/c^2 or $\sqrt{s_{q\bar{q}}} \approx 2m_b \simeq 8.4$ GeV/c^2, which influences linearly the lowest Bjorken-x value accessible in the collision. In Tab. 2.1 the minimum Bjorken-x values at mid-rapidity reached in different collision systems and energies for leading order hard scatterings at the $c\bar{c}$ or $b\bar{b}$ thresholds are reported. With the nucleus-nucleus collisions at the TeV scale performed at the LHC it is possible to explore x down to $x \simeq 10^{-4}$ with charm and $x \simeq 10^{-3}$ with beauty the regime where the shadowing effect dominates, causing a depletion of charm and beauty hadron production.

[2]Note that in these calculations the hypothesis of equal momentum p for bound nucleons in the two nuclei is crucial, otherwise an explicit dependence on the nucleon momentum would be present. This result is also obtained requiring $p \gg m$ in the final steps.

Machine	SPS	RHIC	LHC	LHC	LHC
System	Pb–Pb	Au–Au	Pb–Pb	Pb–Pb	Xe–Xe
$\sqrt{s_{\rm NN}}$	17 GeV	200 GeV	2.76 TeV	5.02 TeV	5.44 TeV
$c\bar{c}$	$x \simeq 2 \times 10^{-1}$	$x \simeq 10^{-2}$	$x \simeq 9 \times 10^{-4}$	$x \simeq 5 \times 10^{-4}$	$x \simeq 5 \times 10^{-4}$
$b\bar{b}$	–	–	$x \simeq 3 \times 10^{-3}$	$x \simeq 2 \times 10^{-3}$	$x \simeq 2 \times 10^{-3}$

TABLE 2.1: Bjorken-x values at mid-rapidity reached in nucleus-nucleus collisions at different energies for leading order hard-scattering processes at the threshold energy for the $c\bar{c}$ ($\simeq 2.6$ GeV/c^2) and $b\bar{b}$ ($\simeq 8.4$ GeV/c^2).

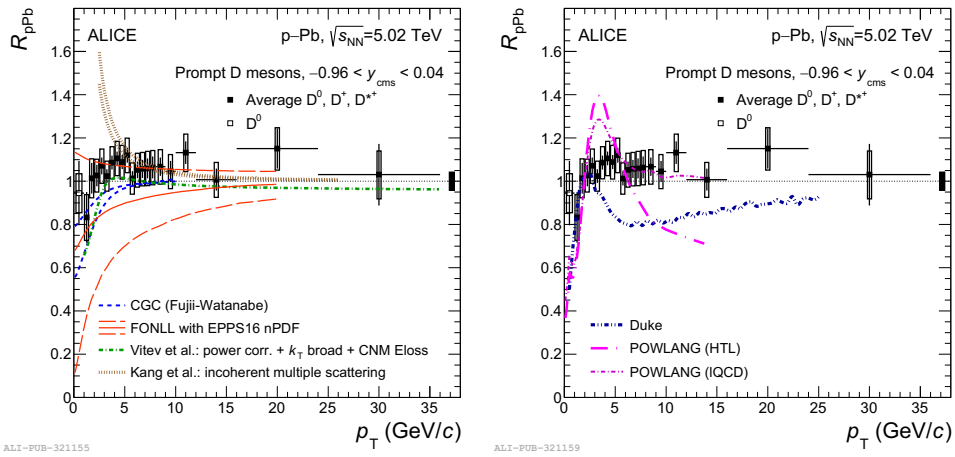

FIGURE 2.6: Nuclear modification factor $R_{\rm pPb}$ of prompt non-strange D mesons in p–Pb collisions at $\sqrt{s_{\rm NN}} = 5.02$ TeV. In the left panel, the data are compared with calculations of theoretical models that include only CNM effects: CGC [100], FONLL [101] with EPPS16 nPDFs [127], a LO pQCD calculation (Vitev et al.) [132], and a calculation based on incoherent multiple scatterings (Kang et al.) [133]. In the right panel, the predictions of the Duke [134] and POWLANG [135] transport models are compared with the measured D-meson $R_{\rm pPb}$. Figure from [136]

Another CNM effect contributing to the modification of heavy-flavour production in p–A collisions with respect to pp is the *Cronin* effect, which was firstly observed at Fermilab [131]. This effect consists in a slight increase of the measured nuclear modification factor above unity in intermediate-$p_{\rm T}$ region. A possible interpretation is a shift towards larger transverse momenta of the parton $p_{\rm T}$ distribution, usually called $k_{\rm T}$ *broadening*. This broadening may result from the multiple elastic scattering among the projectile partons and the target ones before a hard scattering. As explained in Sec. 1.4, a similar shift towards higher $p_{\rm T}$ values in the particle spectra is ascribed to radial flow effects in the presence of QGP. Following the measurement of flow-like effects in p–A collisions which are observed to be larger for protons, some hypothesis of a "small QGP" formation in small systems has been proposed, but at the moment this possibility is still largely debated.

The observable usually adopted experimentally to study the CNM in p–A collisions is the nuclear modification factor $R_{\rm pPb}$. The measured $R_{\rm pPb}$ for non-strange D-mesons in p–Pb collisions at $\sqrt{s_{\rm NN}} = 5.02$ TeV from the ALICE experiment is

shown in Fig. 2.6. The experimental data are compared with several model calculations [100,101,127,132–135], which are able to describe the data within 2σ only when including CNM effects. This is still not enough for the model prediction by Kang et al. [133], where a higher-twist calculation based on incoherent multiple scatterings is implemented without being able to match the data for $p_{\mathrm{T}} < 4$ GeV/c (left panel). In the right panel, the measurement is compared with the calculations of two transport models, Duke [134] and POWLANG [135], both assuming that a small-size QGP is formed in p–Pb collisions. These models are both based on the Langevin approach for the transport of heavy quarks in an expanding deconfined medium described by relativistic viscous hydrodynamics, including both collisional and radiative energy loss in the former case and only collisional processes with two choices for the transport coefficients in the latter one. According to this comparison, the experimental data disfavour the presence of a suppression of high-p_{T} D-mesons spectrum due to the QGP formation in p–Pb collisions.

2.2.2 Parton energy loss in the QGP

As explained in the introduction to this Chapter, the heavy quark production in heavy-ion collisions takes place in hard scatterings ($\Delta\tau_{\mathrm{c,b}} = 0.08, 0.03$ fm/c) within a characteristic timescale that is lower than the typical QGP formation time ($\Delta\tau_{\mathrm{QGP}} = 0.2 \div 1$ fm/c). For this reason, heavy quarks witness the whole evolution of the QGP. The traversing quark undergoes several interactions with the medium constituents. In particular, elastic ("collisional") and inelastic (gluon radiation) processes cause medium-high p_{T} quarks to lose energy, depending on the parton mass m and its initial energy E, on the medium thickness L and the strength of the parton-medium coupling, given by $\alpha_S(Q^2)$ and the colour charge. At low p_{T} the multiple interactions of heavy quarks with the medium constituents cause a push to higher transverse momenta, given the radial flow of the bulk (Sec. 1.4.4). In particular, the typical thermal momentum of low-p_{T} heavy quarks of mass m_{Q} corresponds to $p_{\mathrm{Q}}^{\mathrm{th}} = \sqrt{3m_{\mathrm{Q}}T}$, which is significantly higher than the typical momentum exchange with the medium $Q \sim T$. Therefore, the motion of heavy quarks inside the medium can be described as a Brownian one among the plasma constituents, which work as scattering centres giving several small kicks providing a typical momentum transfer of order T. The transverse momentum distribution of resulting heavy-flavour hadrons is significantly influenced by these interaction processes, making heavy quarks unique probes to investigate the medium properties.

Energy loss in QCD cannot be compared with the QED one, due to the deep differences characterising the strong and the electromagnetic interactions. The coupling constants α_S and α_{em} follow different trends as a function of the process energy scale Q and their values $\alpha_S(Q^2)$ and $\alpha_{\mathrm{em}}(Q^2)$ must be taken into account in theoretical calculations. Moreover, the non-abelian structure of the SU(3) colour group of QCD introduces the possibility for gluons to self-interact and differentiates the coupling strengths for quarks and gluons. These properties derive from the structure of the QCD lagrangian density (Eq. 1.1), where different couplings emerge in case of gluon-gluon or gluon-quark vertices. As a consequence, the probability of gluon radiation for a quark ($q \to qg$) is different from that of a gluon ($g \to gg$) considering that the related cross sections are proportional to the Casimir factors $C_{\mathrm{F,A}}$, defined as [137]:

$$\sigma(q \to qg) \propto C_{\mathrm{F}} = \frac{N_{\mathrm{c}}^2 - 1}{2N_{\mathrm{c}}} = \frac{4}{3}\,, \tag{2.7}$$

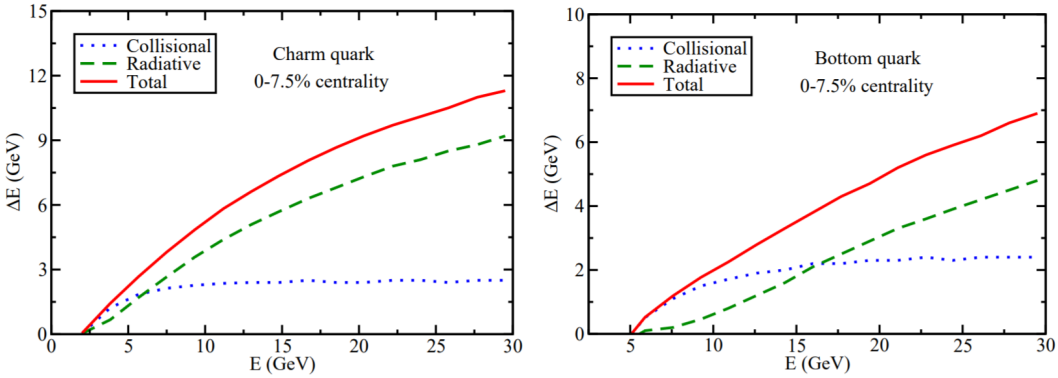

FIGURE 2.7: Interplay between radiative and collisional energy loss for charm (left) and beauty (right) quarks in QGP created in central Pb–Pb collision at $\sqrt{s_{\rm NN}} = 2.76$ TeV at the LHC, as calculated in [138]. The quantity in abscissa corresponds to the quark energy. Figures taken from [138].

$$\sigma(g \to gg) \propto C_{\rm A} = N_{\rm c} = 3\,, \tag{2.8}$$

where $N_{\rm c} = 3$ is the number of colours in the theory. For this reason, the probability for a gluon to irradiate another gluon is 9/4 times larger than for a quark. The gluon radiation at low angles is further suppressed for massive partons by the dead-cone effect, as discussed in the next Sections.

The interplay between radiative and collisional energy loss for charm and beauty quarks in central (0-7.5%) Pb–Pb collisions at $\sqrt{s_{\rm NN}} = 2.76$ TeV as a function of the initial quark energy E is shown in Fig. 2.7 [138]. According to these calculations, high-$p_{\rm T}$ quarks are mostly subject to energy loss via gluon radiation, while the relative importance of collisional processes increases with decreasing $p_{\rm T}$, becoming dominant at low transverse momenta. In the following Sections, more details about collisional and radiative energy loss are provided.

Collisional energy loss

Multiple elastic collisions with the medium constituents is the main source of energy loss affecting low-$p_{\rm T}$ heavy quarks traversing deconfined matter. The average loss of energy caused by elastic collisions between the parton and the plasma constituents can be expressed as [139–141]:

$$\langle \Delta E_{\rm coll} \rangle = \approx \frac{1}{\sigma T} \int t \frac{{\rm d}\sigma}{{\rm d}t} {\rm d}t\,, \tag{2.9}$$

where $t = Q^2$ is the transferred momentum squared, T is the system temperature and σ refers to the parton-parton cross section, where in particular ${\rm d}\sigma/{\rm d}t$ quantifies the parton probability to interact with plasma constituents per unit of momentum transfer. The main contribution to the parton-parton differential cross section is provided by the gluon-quark t-channel processes, bringing to the approximation:

$$\frac{{\rm d}\sigma}{{\rm d}t} \approx \frac{4\pi C_i \alpha_{\rm S}^2}{t^2}\,, \tag{2.10}$$

where the C_i factor depends on the gg, gq and qq vertices involved in the scatterings. In the ultra-relativistic limit $ET \gg m_{\rm q}^2$, one obtains that the collisional energy loss

per unit length ($\frac{\mathrm{d}E_{\mathrm{coll}}}{\mathrm{d}x}$) corresponds to:

$$-\frac{\mathrm{d}E_{\mathrm{coll}}}{\mathrm{d}x}\bigg|_{\mathrm{q,g}} = C_{\mathrm{R}}\pi T^2\left[\left(1+\frac{n_f}{6}\right)\alpha_S(\mu^2)\alpha_S(ET)\ln\left(\frac{ET}{\mu^2}\right)+\mathcal{O}(\alpha_S^2)\right] \tag{2.11}$$

$$-\frac{\mathrm{d}E_{\mathrm{coll}}}{\mathrm{d}x}\bigg|_{\mathrm{Q}} = -\frac{\mathrm{d}E_{\mathrm{coll}}}{\mathrm{d}x}\bigg|_{\mathrm{q}} - C_{\mathrm{F}}\pi T^2\left[\frac{2}{9}\alpha_S(m_{\mathrm{Q}}^2)\alpha_S(ET)\ln\left(\frac{ET}{m_{\mathrm{Q}}^2}\right)+\mathcal{O}(\alpha_S^2)\right] \tag{2.12}$$

where $C_{\mathrm{R}} \equiv C_{\mathrm{F}}$, C_{A} correspond to the colour factors mentioned above and μ is an effective infrared cut-off that can be taken as the Debye screening mass in the QGP, namely $\mu \sim gT$ [139]. Eq. 2.11 represents the in-medium energy loss for light quarks and gluons, while in Eq. 2.12 the same quantity for the heavy quarks is reported, which differs due to the significantly larger mass of the considered quarks. According to these equations, the total collisional energy loss increases linearly with the medium thickness and logarithmically with the initial energy of the parton. The typical energy loss per unit length of a heavy quark traversing the QGP produced at RHIC in Au–Au collisions at $\sqrt{s_{\mathrm{NN}}} = 200$ GeV is of the order of $\mathrm{d}E/\mathrm{d}x \simeq 0.6$ GeV/fm [140].

The multiple elastic collisions with the medium constituents transfer to the heavy quark the radial and anisotropic flow carried by the QGP bulk. A description of the heavy quark dynamics with the transport formalism is mandatory, given that the transport coefficients are related to the matrix elements describing the elastic scattering with the light partons in the QGP, allowing for a direct comparison of microscopic models of the heavy-quark interaction. The heavy quark dynamics in the QGP and its space-time evolution can be formally described by the Boltzmann equation, as usually done in kinetic theory, namely [142]:

$$\left[\frac{\partial}{\partial t}+\frac{\vec{p}}{E_p}\frac{\partial}{\partial \vec{x}}+\vec{F}\frac{\partial}{\partial \vec{p}}\right] f_{\mathrm{Q}}(t,\vec{x},\vec{p}) = C[f_{\mathrm{Q}}]\ , \tag{2.13}$$

where $E_p = \sqrt{m_{\mathrm{Q}}^2+p^2}$ corresponds to the quark energy. The term f_{Q} denotes the heavy-quark phase-space distribution function, whose space-time evolution is governed by the first two terms of the left-hand side of Eq. 2.13. For a static medium in thermal equilibrium the distribution function tends to the Boltzmann distribution $f_{\mathrm{Q}} \sim e^{-\frac{E_p}{T}}$. The third term of the left-hand side describes the total mean-field force that acts on the heavy quark. The right-hand side of the equation corresponds to the collisional term, where the scattering amplitude between the considered heavy quark and the parton in the medium enters. As discussed above, the condition $m_{\mathrm{Q}} \gg T$ holds for charm and beauty quarks, and the typical momentum transfer from the heat bath to the heavy quark should be small with respect to the heavy quark momentum, implying that they undergo multiple incoherent collisions typical of a Brownian motion. The scattering rate in the right-hand side can be expanded in powers of the momentum transfer by neglecting mean-field effects and by assuming a rather uniform medium. The Boltzmann equation is approximated by the Fokker-Planck equation:

$$\frac{\partial}{\partial t}f_{\mathrm{Q}}(t,\vec{p}) = \frac{\partial}{\partial p_i}\left\{A_i(\vec{p})f_{\mathrm{Q}}(t,\vec{p})+\frac{\partial}{\partial p_j}\left[B_{ij}(\vec{p})f_{\mathrm{Q}}(t,\vec{p})\right]\right\}\ , \tag{2.14}$$

where the key ingredients of the equation become the transport parameters A_i and

B_{ij}. The A_i coefficient represents the average momentum change per unit time of the heavy quark, thus describing the friction induced by the medium, while the B_{ij} coefficient describes the average momentum broadening per unit time, namely the diffusion in space-momentum. In the non-relativistic limit, the Fokker-Planck equation further simplifies in the form:

$$\frac{\partial}{\partial t} f_{\mathrm{Q}}(t,p) = \gamma \frac{\partial}{\partial p_i} \left[p_i f_{\mathrm{Q}}(t,p) \right] + D_p \nabla_{\vec{p}} f_{\mathrm{Q}}(t,p) \ . \tag{2.15}$$

The new equation only depends on two coefficients γ and D_p, which correspond respectively to the drag or friction coefficient and to the momentum-diffusion constant related to momentum fluctuations. Since in thermal equilibrium heavy quarks are in equilibrium with the bath, the drag and diffusion coefficients satisfy the Einstein dissipation-fluctuation equation:

$$D = m_{\mathrm{Q}} \gamma T \ , \tag{2.16}$$

where m_{Q} is the heavy quark mass and T is the medium temperature. Moreover, the drag coefficient is related to the spatial diffusion coefficient D_s, which quantifies the broadening of the spatial distribution with time:

$$D_s = \frac{T}{m_{\mathrm{Q}} \gamma} = \frac{T}{m_{\mathrm{Q}}} \tau_{\mathrm{Q}}^{r} \ , \tag{2.17}$$

where the drag coefficient is written as the inverse of the heavy quark thermalization time τ_{Q}^{r}. Typical values for charm and beauty quarks are 5-15 fm/c, which corresponds approximately to the QGP lifetime reproduced in central heavy-ion collisions at RHIC and the LHC [142].

Radiative energy loss

The radiation of gluons is the main source of energy loss for a high-p_{T} parton that traverses the QGP. This phenomenon is similar to the electromagnetic Bremsstrahlung and it is sometimes called *gluonsstrahlung*. The calculation of the emitted gluon energy distribution is performed by several theoretical groups, where different assumptions are made. As an example, in the case of the BDMPS model [143] the average energy loss of a parton traversing the medium can be calculated as:

$$\langle \Delta E_{\mathrm{rad}} \rangle = \int_0^{\omega_c} \omega \frac{\mathrm{d}N}{\mathrm{d}\omega} \mathrm{d}\omega \ , \tag{2.18}$$

where ω is the energy of a single gluon, $\mathrm{d}N/\mathrm{d}\omega$ is the gluon energy distribution and ω_c is the characteristic energy of an emitted gluon, given L the path length travelled by the emitting parton. In this model the deconfined matter is considered as a set of static scattering centres that the traversing parton encounters during its path. The emission of a gluon takes place when the transverse momentum transferred by the kick k_{T} is large enough to decohere the gluon from the wave function of the emitting parton. Given $\langle k_{\mathrm{T}} \rangle$ the average transverse momentum transfer and L the path length covered by the emitting parton, the quantity:

$$\hat{q} = \frac{\langle k_{\mathrm{T}}^2 \rangle}{L} \tag{2.19}$$

is called *transport coefficient*, and it quantifies the average squared transverse momentum transferred by the medium to the projectile per unit path length. The characteristic energy for the emitted gluons corresponds to [144]:

$$\omega_c = \frac{1}{2}\hat{q}L^2 \,. \tag{2.20}$$

The energy distribution of emitted gluons can be expressed as [144]:

$$\frac{\mathrm{d}N}{\mathrm{d}\omega} \simeq \frac{\alpha_S C_R}{\omega\pi}\sqrt{\frac{\omega_c}{\omega}} \,, \tag{2.21}$$

where C_R is the colour factor introduced in previous Section. As explained in Ref. [144], the angular distribution of emitted gluons is concentrated at a characteristic energy- (and medium-) dependent emission angle:

$$\theta \simeq \frac{k_T}{\omega} \sim \left(\frac{\hat{q}}{\omega^3}\right)^{1/4} \,, \tag{2.22}$$

where Eq. 2.19 and Eq. 2.20 are used in the last step to rewrite k_T. Using Eq. 2.21 into Eq. 2.18, the average radiative energy loss can be then written as:

$$\langle \Delta E_{rad} \rangle \simeq \int_0^{\omega_c} \frac{\alpha_S C_R}{\pi}\sqrt{\frac{\omega_c}{\omega}}\mathrm{d}\omega \propto \alpha_S C_R \omega_c \propto \alpha_S C_R \hat{q} L^2 \,, \tag{2.23}$$

where Eq. 2.20 is used in the last step. According to Eq. 2.23, the average energy lost by a parton via gluon radiation inside the QGP only depends on medium properties ($\hat{q}$) and it does not depend on its kinematic properties, such as the initial parton energy E. The radiation energy loss increases quadratically with the path length L covered by the parton and depends linearly on the colour factor described in Eq. 2.8 and Eq. 2.7, therefore the average energy loss for a gluon in 9/4 times larger than for a quark. On top of this, the gluon radiation for different quark flavours does not coincide. As explained in Refs. [144, 145], the gluon emission in vacuum depends on the quark mass, and this dependence becomes more relevant for heavier quarks. In particular, the gluon emission is forbidden for angles $\theta < \theta_0 \equiv m/E$ around the parton direction of motion, defining then a solid angle where the gluon emission is suppressed. This phenomenon is called *dead-cone effect* and the angular coverage of the forbidden region linearly increases with the emitting parton mass. For charm and beauty quarks, this effect implies a harder fragmentation due to the reduction of the radiation phase space already in vacuum and it is also assumed to influence the heavy quark dynamics in QGP [146]. As a matter of fact, being the gluon emission angle in QGP quickly decreasing for increasing emitted energy (Eq. 2.22), the high-momentum part of the radiation spectrum is strongly suppressed by the dead cone effect. Given all these considerations, the radiative energy loss in the QGP is expected to follow a clear hierarchy: $\Delta E(\mathrm{g}) > \Delta E(\mathrm{q}) > \Delta E(\mathrm{c}) > \Delta E(\mathrm{b})$.

As already explained in Sec. 1.4.7, the nuclear modification factor R_{AA} is an observable sensitive to parton energy loss in the QGP. In the left panel of Fig. 2.8 the average R_{AA} of prompt D^0, D^+ and D^{*+} as a function of p_T in central (0–10%), semicentral (30–50%) and peripheral (60–80%) Pb–Pb collisions at $\sqrt{s_{NN}} = 5.02$ TeV are shown [147]. The experimental measurements show a significant suppression with respect to unity, which reaches a minimum of about 0.2, 0.4 and 0.7 in central, semicentral and peripheral collisions, respectively, for D mesons with $5 \lesssim p_T \lesssim 10$ GeV/c, where the hierarchy follows that of the collision centrality. On

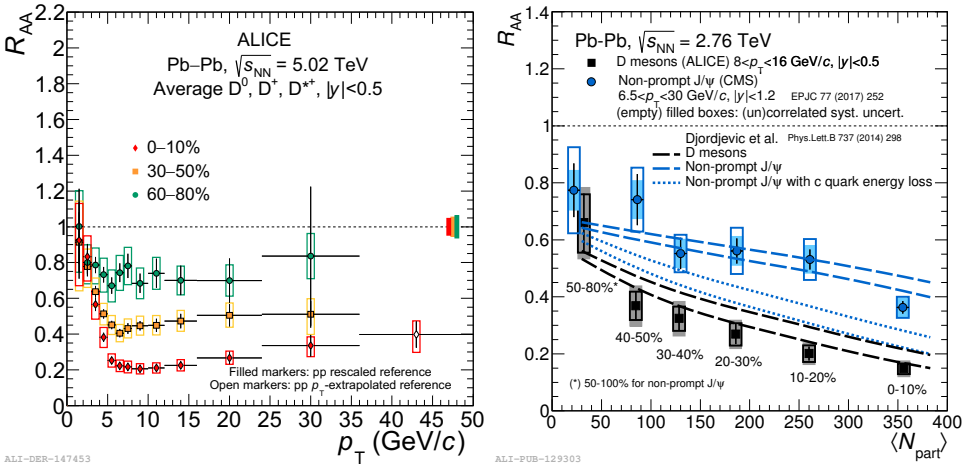

FIGURE 2.8: Left: average R_{AA} of prompt D^0, D^+ and D^{*+} as a function of p_T in central (0–10%), semicentral (30–50%) and peripheral (60–80%) Pb–Pb collisions at $\sqrt{s_{NN}} = 5.02$ TeV. Figure from [147]. Right: average R_{AA} of prompt D^0, D^+ and D^{*+} as a function of collision centrality, expressed in term of N_{part}, in Pb–Pb collisions at $\sqrt{s_{NN}} = 2.76$ TeV from the ALICE Collaboration [148] compared with the non-prompt J/ψ one collision system and energy from the CMS Collaboration [149] compared with model calculations implementing charm and beauty energy loss [150]. Figure from [148].

the right panel, the average R_{AA} of prompt D^0, D^+ and D^{*+} in Pb–Pb collisions at $\sqrt{s_{NN}} = 2.76$ TeV from the ALICE Collaboration [148] is compared with the non-prompt J/ψ one in the same collision system and energy from the CMS Collaboration [149]. These results are obtained via the reconstruction of D mesons in the range $8 < p_T < 16$ GeV/c and of J/ψ with $6.5 < p_T < 30$ GeV/c to match as much as possible the p_T intervals of D and B mesons. The measurements are performed in six different centrality classes, expressed in terms of average number of participant nucleons $\langle N_{part} \rangle$ and the R_{AA} of prompt D mesons shows a higher suppression from unity with respect to non-prompt J/ψ in all centrality classes. This hierarchy is in line with the expected radiative energy loss and with the fact that the dead cone effect suppresses the loss of energy for the beauty quark due to its higher mass. The energy loss processes of the charm and beauty quarks in the deconfined medium are implemented in theoretical calculations [150], which are able to describe the $\langle N_{part} \rangle$ dependence of the nuclear modification factor for both mesons (dashed lines). For the non-prompt J/ψ, an alternative prediction is provided (dotted lines). In this case, where the beauty mass is set to that of the charm quark, the calculations significantly underestimate the experimental data.

2.2.3 Anisotropic flow

The geometry of a semicentral heavy-ion collision induces a spatial anisotropy on the transverse plane that quickly translates into an expansion process. The particles thermalised within the produced QGP are dragged by the expanding medium and the flow processes as described in Sec. 1.4.4 and 1.4.6. The study of the anisotropy for heavy quarks provides fundamental information on the coupling strength of the quarks to the system, namely how effective the elastic and radiative processes described in Sec. 2.2.2 are in bringing the heavy quarks towards equilibrium. Being produced in the initial hard scattering processes that precede the QGP formation,

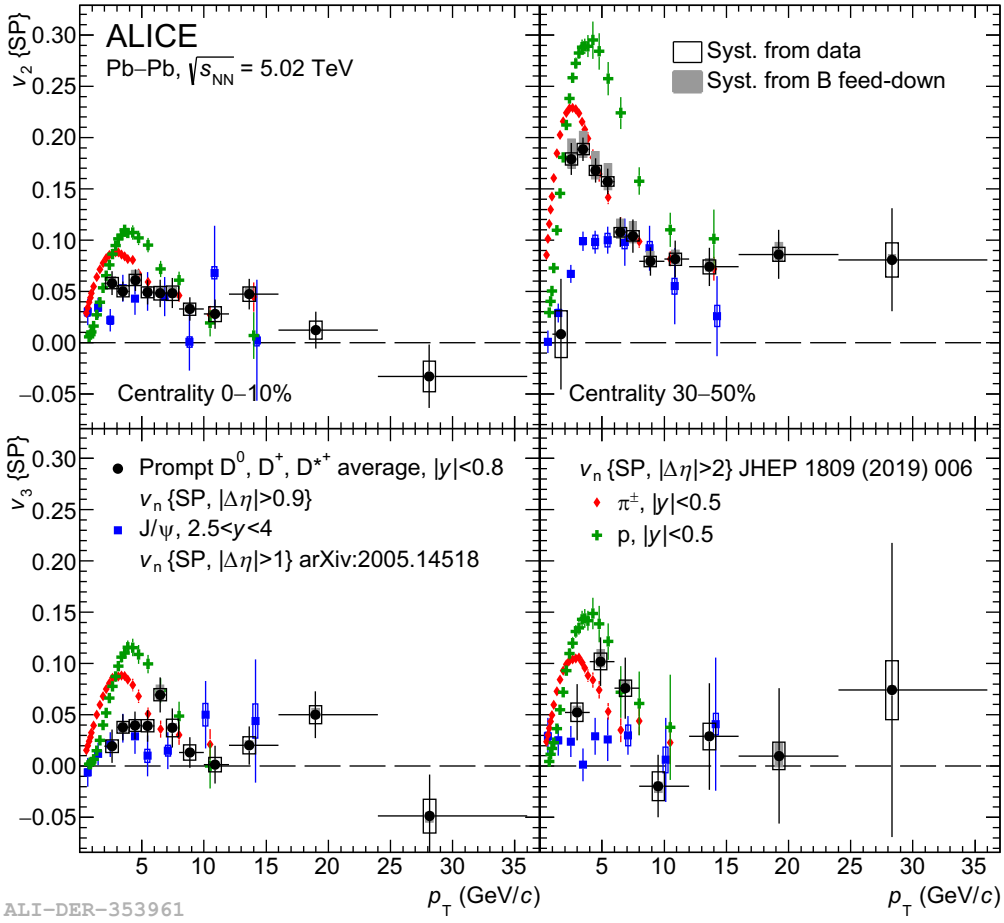

FIGURE 2.9: Average elliptic (top row) and triangular (bottom row) flow coefficiencts v_2 and v_3 of prompt D^0, D^+ and D^{*+} mesons as a function of p_T in central (0–10%) and semicentral (30–50%) central Pb–Pb collisions at $\sqrt{s_{NN}} = 5.02$ TeV. The same quantities for $\pi^{\pm}$, $p + \bar{p}$ and inclusive J/ψ are reported for comparison. Figure from [151].

in principle the heavy quarks are not expected to be in equilibrium with the light partons in the expanding medium. However, heavy quarks receive part of the bulk flow through multiple scatterings with the medium constituents and this may bring to a non-null flow for charm and beauty. The experimental variables sensitive to heavy quark flow are the azimuthal anisotropy coefficients introduced in Eq. 1.38 of charm and beauty hadrons. On top of the partonic interactions, another source of azimuthal anisotropy can be the hadronisation, given that in a scenario where a heavy quark coalesces with a lighter comoving one the elliptic flow can be amplified [156]. The v_2 and v_3 coefficients of heavy hadrons are also sensitive to the flow of the light flavour content and only a close comparison with model calculations including both light and heavy quark flow can help to quantify the contribution of charm and beauty quarks. Moreover, further insights come from the comparison of elliptic flow of identified hadrons, due to the different contents in terms of flavour and number of constituent quarks. Such a comparison is shown in Fig. 2.9, where the elliptic and triangular flow coefficients v_2 and v_3 of prompt D^0, D^+ and D^{*+} mesons [151] as a function of p_T in central (0–10%) and semicentral (30–50%) Pb–Pb

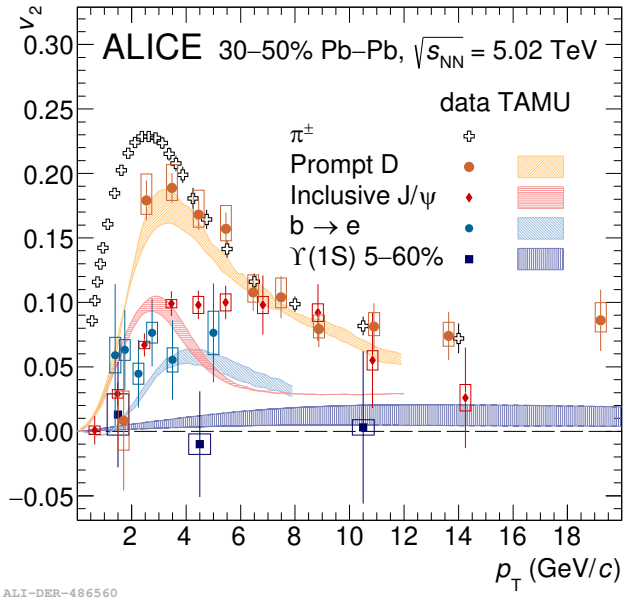

FIGURE 2.10: Elliptic flow of $\pi^{\pm}$ [152], prompt D mesons [151], inclusive J/ψ [153], electons from beauty hadron decays [154] and Υ(1S) [155] in semicentral (30–50%) Pb–Pb collisions at $\sqrt{s_{NN}} = 5.02$ TeV.

collisions at $\sqrt{s_{NN}} = 5.02$ TeV are shown, together with those of $\pi^{\pm}$, p + $\bar{\text{p}}$ and inclusive J/ψ. The magnitude of the v_2 coefficient is significantly larger in semicentral collisions, reflecting the higher initial spatial anisotropy. For $p_T \lesssim 3$ GeV/c a clear ordering among the different species is present, namely $v_2(\text{D}) < v_2(\text{p}) < v_2(\pi^{\pm})$. This behaviour can be explained as an interplay between the anisotropic flow and the isotropic expansion of the medium (radial flow), that imposes an equal velocity boost to all particles, dragging the heavier ones to higher transverse momenta [151]. In the intermediate p_T region the ordering mentioned before is broken, because here the protons have the largest elliptic flow. These results are in agreement with the v_2 scaling with the number of constituent quarks, according to which baryons have a larger v_2 with respect to mesons due to one more constituent quark that undergoes the flow, in agreement with the hypothesis of hadronisation via coalescence [157]. This aspect partially explains the lower v_2 for J/ψ, since the D mesons benefit of the larger flow of the constituent quark lighter than the charm. For higher p_T, namely $p_T \gtrsim 8$ GeV/c, the elliptic flow of all particles tends to the same value. This behaviour might be explained by the fact that in this regime $p \gg m$ for all quarks and the path length for all particles coincides (Eq. 2.19). For this reason, the path-length dependence of the in-medium energy loss at high p_T is similar among light and heavy quarks, as well as gluons. The elliptic flow of D mesons is described reasonably by theoretical calculations that use a spatial diffusion coefficient for the charm quark within $1.5 < 2\pi D_S T < 7$ at the critical temperature, corresponding to a thermalisation time of $\tau_c^r = (m_c/T) \cdot D_s$ =3-14 fm/c (Eq. 2.17) at $T = T_c = 155$ MeV, which is comparable to the QGP lifetime [151].

Further insight on the heavy quark elliptic flow come from the comparison of different open heavy-flavour hadrons and quarkonia. In Fig. 2.10 the elliptic flow of $\pi^{\pm}$ [152], prompt D mesons [151], inclusive J/ψ [153], electrons from beauty hadron decays [154] and Υ(1S) [155] in semicentral (30–50%) Pb–Pb collisions at $\sqrt{s_{NN}} = 5.02$ TeV is reported. This compilation suggests that the beauty quark is less affected by flow effects. The b $\rightarrow$ e elliptic flow is around $\sim$ 0.05 without a

significant dependence on p_{T} and shows a hint of lower v_2 with respect to J/ψ, even if the experimental uncertainties do not permit a quantitative conclusion. The $\Upsilon(1S)$ v_2 reveals a null elliptic flow for $p_{\mathrm{T}} < 12$ GeV/c. This behaviour might be explained by the scaling of the peak flow with the mass of the particle according to the hydrodynamic description of the QGP evolution. For $\Upsilon(1S)$ mesons this should be above $p_{\mathrm{T}} \approx 10$ GeV/c, where the uncertainties on the measurement are actually large [155].

2.3 Heavy quark hadronisation in hadronic collisions

The heavy quarks produced in the initial hard scattering processes generate hadrons in the final state, which are colourless particles accessible to the experiments. In the factorization approach the probability for a given quark to produce a hadron with a fraction z of the original quark momentum is described by the fragmentation functions $D_{\mathrm{Q}}^{\mathrm{H_Q}}(z, \mu_{\mathrm{F}}^2)$. The presence of the QGP can in principle modify the quark hadronisation, providing new mechanisms that involve the free partons in the medium. Anyway, to completely understand the hadronisation in heavy-ion collisions the comprehension of the mechanisms underlying the hadronisation in pp collisions is a prerequisite. In this Section, the current knowledge of hadronisation mechanisms of charm quark in ultra-relativistic hadronic collisions is reported. In Sec. 2.3.1 the charm hadronisation in heavy-ion collisions is treated, while in Sec. 2.3.2 the theoretical models providing an explanation of the charm quark hadronisation in pp collisions at the LHC are discussed.

2.3.1 Charm hadronisation in the QGP

As discussed in Sec. 2.2, the dynamics of a heavy quark is significantly influenced by the QGP. In addition to the energy loss and flow effects, the presence of surrounding free colour charges introduces the possibility for the heavy quark to produce hadrons without fragmenting, but associating with lighter quarks that are picked-up from the deconfined medium. This process is usually called *recombination* or *coalescence*. According to this picture, the production of baryons with a given $p_{\mathrm{T}}(\mathrm{H})$ is favoured with respect to that of mesons with the same transverse momentum or, at least, the baryon-over-meson ratio is enhanced at intermediate p_{T} with respect to a scenario with pure quark fragmentation. Considering that the quark p_{T} distribution is quickly decreasing, low-p_{T} quarks are more abundant. Therefore, it is more probable to create a baryon by mixing three low-p_{T} quarks with respect to creating a meson, because in this case the two quarks need a larger p_{T} to reach the final $p_{\mathrm{T}}(\mathrm{H})$. An enhancement of the relative abundance of baryons with respect to mesons in heavy-ion collisions has been observed at RHIC [159] and the LHC [160] firstly for the light-flavour sector. A similar behaviour has been recently observed also for charm hadrons, as shown in the top panel of Fig. 2.11, where the $\Lambda_{\mathrm{c}}^{+}/\mathrm{D}^0$ ratio is compared with $\mathrm{p}/\pi^{\pm}$ and $\Lambda/\mathrm{K}_{\mathrm{S}}^0$ measured in Au–Au collisions at $\sqrt{s_{\mathrm{NN}}} = 200$ GeV at RHIC by the STAR Collaboration [158]. The result for the charm flavour shows a similar magnitude with the other two measurements, given the experimental uncertainties. In particular, the ratios reach a maximum value around $p_{\mathrm{T}} = 2$ GeV/c, where the contribution of coalescence is significant. In general, the recombination mechanism is expected to contribute significantly to the production of low-p_{T} hadrons, while the fragmentation dominates at high p_{T}. The interplay between these two mechanisms is investigated by comparing the experimental results with model

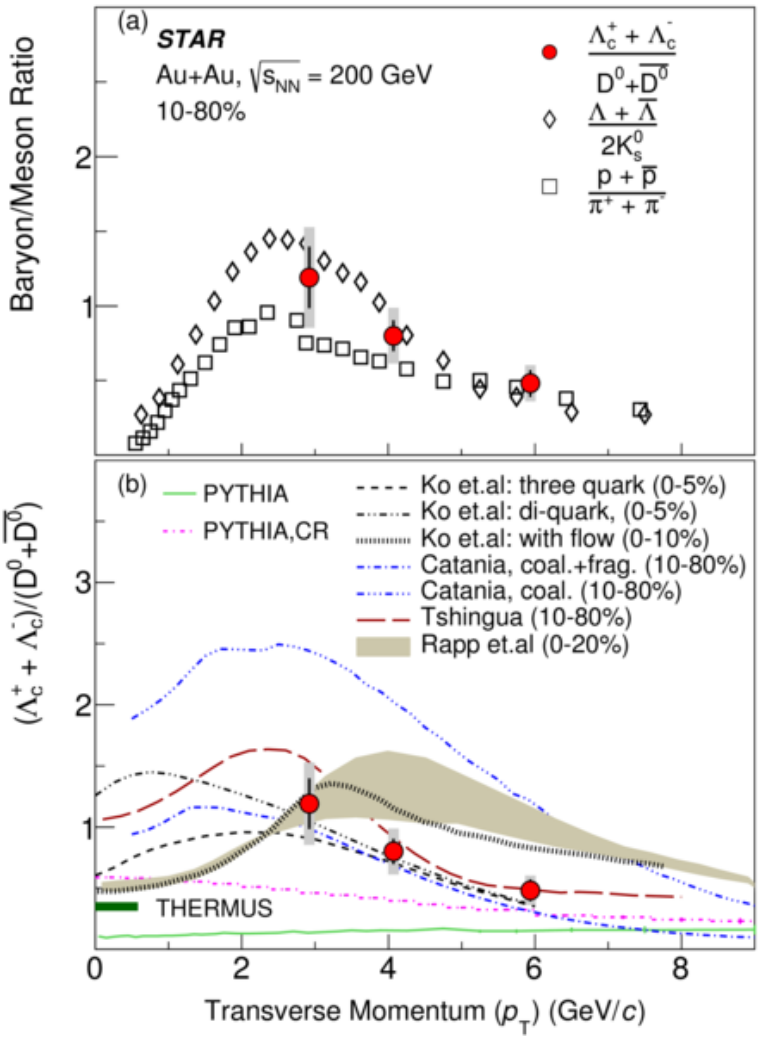

FIGURE 2.11: Measurement of Λ_c^+/D^0 ratio at midrapidity ($|y| < 1$) in Au–Au collisions in the 10-80% centrality class at $\sqrt{s_{NN}} = 200$ GeV from the STAR experiment at RHIC. The measurement is compared (a) with baryon-over-meson ratios from the light-flavour sector and (b) with model calculations implementing the charm hadronisation via coalescence. Figure from [158].

calculations based on different assumptions for the charm hadronisation. In the bottom panel of Fig. 2.11 the Λ_c^+/D^0 ratio is compared with model predictions that implement the charm coalescence with the light quarks in the QGP. On top of fragmentation, in the calculations provided by Ko et. al. [161] the production of heavy baryons can occur via the coalescence of a heavy quark with the free light quarks from the system, as well as with a bound light di-quark pre-existing in the medium. A revised version of the model is provided by the authors in Ref. [162], where the presence of collective flow is taken into account by letting a produced hadron to have the same centre-of-mass velocity of the coalesced quarks. The predictions coming from the latter model tend to overestimate the experimental results at high-p_T, which are instead better described assuming the charm coalescence with light di-quarks from the deconfined medium. Also the predictions from He and Rapp [163] overestimate the measurement at high p_T. In this model a quark recombination with four-momentum conservation for heavy-flavour hadrons is developed, recovering the thermal and chemical equilibrium limits and accounting for space-momentum

correlations of charm and beauty quarks with the partons of the hydrodynamically expanding medium. Furthermore, the ground state baryons are foreseen to be fed by strong decays of an augmented set of excited states with respect to those listed by the PDG. Another model prediction that describes the data within uncertainties is the Tsinghua one [164], where the two-body Dirac equation is solved with a lattice-simulated quark-antiquark potential in order to determine the coalescence temperature for charm mesons. In this model, the coalescence time for different hadrons is obtained from the hydrodynamical equations describing the fireball evolution, during which the charm quantum number is assumed to be conserved. Another prediction that successfully describes the data comes from the Catania theory group [165], where the hadronisation via fragmentation is combined with a coalescence process governed by the Wigner functions, which describe the probability for a hadron to be produced from quarks with given phase-space coordinates. In particular, this model shows the importance of the interplay between fragmentation and recombination, highlighting that a pure coalescence picture overestimates the data by about a factor $\times 2$, as shown in Fig. 2.11. From these comparisons one can conclude that the recombination process covers a key role to understand the hadronisation in the QGP, where the only fragmentation does not justify the observed abundances. This is also suggested by PYTHIA predictions [166, 167] based only on fragmentation, which strongly underestimates the data.

2.3.2 Charm hadronisation in pp collisions

To disentangle and understand the hadronisation processes in the QGP a complete comprehension of the heavy quark hadronisation in pp collisions, where no deconfined medium is expected, is required. The recent results in pp collisions at the LHC clearly show that the conventional picture based on the factorization theorem is not able to correctly quantify the abundances for all particles produced in hadronic collisions. In particular, this approach fails for the baryon production description, which is significantly larger with respect to what is expected assuming universal fragmentation functions constrained by e^+e^- and e^-p data (see Fig. 2.2).

The interest for the internal structure of hadrons arose in the scientific community during the 70's of the twentieth century, when the first models about the hadron formation were proposed. One of them is the *Bag Model* [168, 169], in which the confinement as well as the asymptotic freedom are built with a simple phenomenological description. In this model a hadron is considered as a "bag" of massless valence quarks surrounded by a perturbative QCD vacuum, which differs from the normal QCD vacuum outside the bag. The difference between them is characterized by the *Bag constant* defined as $B = \varepsilon_{\text{pert.}} - \varepsilon_{\text{vac.}}$, which quantifies the energy density difference between the perturbative ($\varepsilon_{\text{pert.}}$) and the normal QCD vacuum ($\varepsilon_{\text{vac.}}$). The value of the bag constant is ~ 200 MeV, obtained by minimizing the total energy of the bag as a function of its radius, and with this approach the critical temperature T_c for the deconfinement is estimated to be ~ 150 MeV.

In the same years, the quark formation and hadronisation started to be treated with different approaches. Among them, those based on colour strings to account for the $u\bar{u}$, $d\bar{d}$ and $s\bar{s}$ pair production became the most used [171, 172]. The most widely used today is the *Lund string model* [173–175], which is implemented in Monash, the default tune of PYTHIA event generator [166].

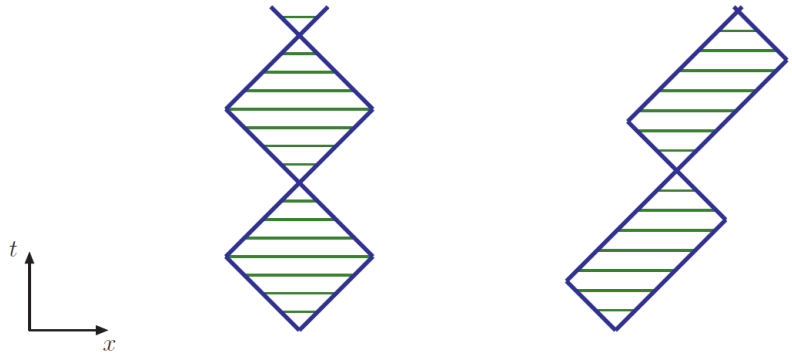

FIGURE 2.12: "yo-yo" modes characterizing a $q\bar{q}$ pair with quark and antiquark moving apart from each other. This is shown in the $q\bar{q}$ rest frame (left) and in a boosted frame (right). Figure from [170].

The Lund model: a dynamical picture of fragmentation

In the Lund model, only the linear component of the Cornell potential (Eq. 1.9) confining a $q\bar{q}$ pair in a meson is considered. As soon as the two involved quarks move one away from the other, the linear part is the dominant one, therefore the Cornell potential is approximated with $V(r) \simeq \kappa r$, where the typical values assumed for the string tension are $\kappa \sim 1$ GeV/fm, implying a constant force $dp/dt = \pm\kappa$. Considering a $q\bar{q}$ massless pair with the quark and antiquark flying apart at the speed of light, a colour string arises between them with a constant tension until the stored potential in the string encodes all their kinetic energy. At that point, the colour string turns the quark and antiquark around, accelerating them towards each other until they meet back and they start to move away again, repeating the sequence. This is the so-called *"yo-yo" motion*, shown in Fig. 2.12 and consisting in the basic ingredient to understand the structure of hadrons coming out from a high-energy e^+e^- collision, where the two leptons annihilate in a $q\bar{q}$ pair [170]. The light cone for the high-energy $q\bar{q}$ pair is shown in Fig. 2.13 in the 1+1 dimension description of the Lund model. In the high-energy limit, the quarks are considered massless: their back-to-back trajectory is represented by the 45 degrees diagonals of the light cone. In principle, the $q\bar{q}$ pair is supposed to undergo the "yo-yo" modes, but the intense colour field causes a different dynamics. The gradual distancing between the original quark and antiquark provokes a stretching of the colour string due to the linear increase of the energy stored in the string. When it exceeds the amount required to produce an additional $q\bar{q}$ pair, the string can break into two $q\bar{q}$ pairs. The new $q\bar{q}$ pair, $q_1\bar{q}_1$, created in the space-time point (x_1, t_1) starts then moving on parallel direction with respect to the original light cone. If another $q_2\bar{q}_2$ is produced in the point (x_2, t_2), then a hadron can be formed by the new available pair $\bar{q}_1 q_2$. Multiple additional string breaks may happen and produce new $q\bar{q}$ pairs, giving then new $q_i\bar{q}_j$ systems which are either hadrons or else that further fragments, until only hadrons remain. In the latter case, the $q\bar{q}$ pairs are subject to "yo-yo" modes within the produced meson, being more elongated due to the Lorentz boost with respect to the original $q\bar{q}$ centre-of-mass frame. No time ordered sequence is supposed to rule the string breaks, which are causally disconnected, but additional breaks happen in specific space-time points to ensure the formation of a meson with a specific mass m. Considering the $q_1\bar{q}_1$ and $q_2\bar{q}_2$ pairs, the energy of the $\bar{q}_1 q_2$ meson is $\kappa(x_2 - x_1)$ and its momentum is $\kappa(t_2 - t_1)$. The invariant mass of the $\bar{q}_1 q_2$ system is $m^2 = \kappa^2 \left[(x_2 - x_1)^2 + (t_2 - t_1)^2\right]$, therefore

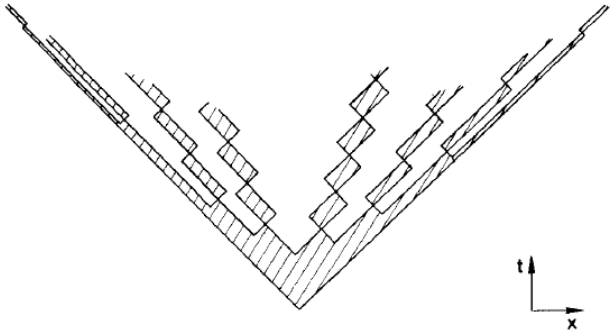

FIGURE 2.13: Picture of string fragmentation in the Lund model for a massless $q\bar{q}$ pair move with large energy in opposite directions. The string colour field is broken in several places by the production of $q\bar{q}$ pairs and the hatched areas indicate where the colour field does not vanish. Figure from [173].

the production point (x_2, t_2) of the $q_2\bar{q}_2$ pair must lie on the hyperbola:

$$(x_2 - x_1)^2 - (t_2 - t_1)^2 = m^2/\kappa^2 \,, \tag{2.24}$$

which can be parametrized to:

$$(x_2 - x_1, t_2 - t_1) = \frac{m}{\kappa}(\cosh y, \sinh y) \,, \tag{2.25}$$

where y is the rapidity of the produced meson in the original frame[3]. According to this parametrization, the produced hadrons are ordered in rapidity, which increases linearly, as soon as the field lengths in the non-vanishing areas decrease. In this treatment, the colour field does not carry any momentum, which is fully carried by the endpoint quark and antiquark [173]. In this framework, the production of a meson with transverse mass m_T originating from a quark with flavour α that combines with an antiquark with flavour β is described by the following fragmentation function:

$$f_{\alpha\beta}(z) = N_{a_\alpha} \frac{1}{z} \cdot z^{a_\alpha} \left(\frac{1-z}{z}\right)^{a_\beta} e^{-bm_T^2/z} \,, \tag{2.26}$$

where z is the fraction of the original energy-momentum carried by the produced meson, $N_{\alpha\beta}$ is a normalization factor, b is a parameter equal for all vertices and $a_{\alpha,\beta}$ are free parameters related to the involved quark flavours, which are usually considered all equal. This relation, which is evidently symmetric with respect to the origin of the spatial coordinates, indicates that the fragmentation into a meson is exponentially suppressed with the square of the meson transverse mass.

A similar discussion can be done for massive quarks, namely for $c\bar{c}$ and $b\bar{b}$ pairs produced in the hard scattering. However, the finite and non-negligible quark mass m_Q forbids the trajectories to stay along the light cone bisectors and the kinematics

[3]Here the energy and the longitudinal momentum are expressed in term of the hadron rapidity y according to the following formulas, which derive from Eq. 1.27 and 1.30:

$$E = m_T \cdot \cosh y \quad , \quad p_L = m_T \cdot \sinh y \,.$$

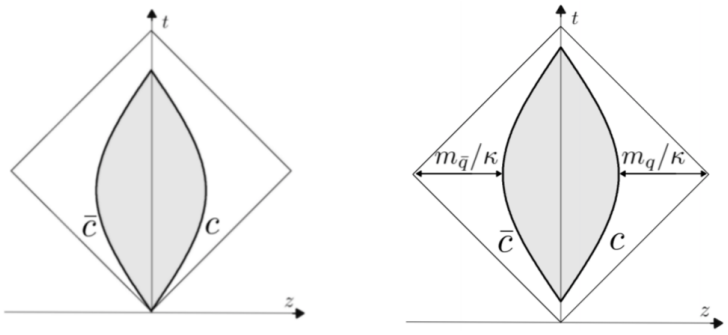

FIGURE 2.14: Light cone of a massive $q\bar{q}$ pair (left), compared with the equivalent system constituted by massless quarks (right). Figure from [175].

of the process forces the motion along the hyperbola:

$$(x - x_1)^2 - (t - t_1)^2 = m_Q^2/\kappa^2 \, . \tag{2.27}$$

In this case, the space-time plane bisectors constitute the asymptotes of the massive systems hyperbolic trajectories and the "yo-yo" modes for a heavy $Q\bar{Q}$ pair are squashed according to m_Q, as shown in Fig. 2.14. Similarly to what concluded for a massless $q\bar{q}$ pair, the produced meson satisfies Eq. 2.24 and 2.25, but now the hadron mass is necessarily $m > 2m_Q$. Up to now, we have assumed that the $q_i\bar{q}_i$ pairs generated from string breaking are massless and do not carry momentum. Both q_i and $\bar{q}_i$ are then created as real particles at a common space–time location, with vanishing energy–momentum. However, if the pair is massive or carries transverse momentum the $q\bar{q}$ pair cannot be produced in the same space-time point. Using a classical picture, they must be produced at a distance $2l$ apart so that the field energy in the middle is able to produce the mass: $2\kappa \cdot l = 2m_{T,q}$. The $q\bar{q}$ pair production is therefore a quantum mechanical process in which each quark of the pair needs to tunnel a distance $l = m_{T,q}/\kappa$ in the colour string in order to acquire enough energy from it to correspond its transverse mass $m_{T,q}$. In other words, the string breaking corresponds to a quantum mechanical tunneling process, whose probability is:

$$P(\text{string breaking}) \propto \exp\left(-\frac{\pi m_{T,q}^2}{\kappa}\right) = \exp\left(-\frac{\pi m_q^2}{\kappa}\right) \exp\left(-\frac{\pi p_{T,q}^2}{\kappa}\right) \, . \tag{2.28}$$

The string breaking probability is subject to a Gaussian suppression factor that increases exponentially with the square of the transverse mass of the quarks that are produced by the string breaking. According to this, the probability for the colour field to produce a $c\bar{c}$ pair is extremely smaller than the one for lighter particles. Using the string tension value $\kappa \simeq 0.2$ GeV^2 introduced before, the following suppression for $s\bar{s}$ and $c\bar{c}$ pairs is estimated with respect to $u\bar{u}$ and $d\bar{d}$ pairs [173, 175]:

$$u : d : s : c \simeq 1 : 1 : 1/3 : 10^{-11} \, . \tag{2.29}$$

The main consequence of this property is that the soft production of heavy-flavour quarks in the string breaking is extremely suppressed, therefore $c\bar{c}$ and $b\bar{b}$ pairs mainly come from the hard scattering between e^+e^- (or partons, in case of hadronic collisions).

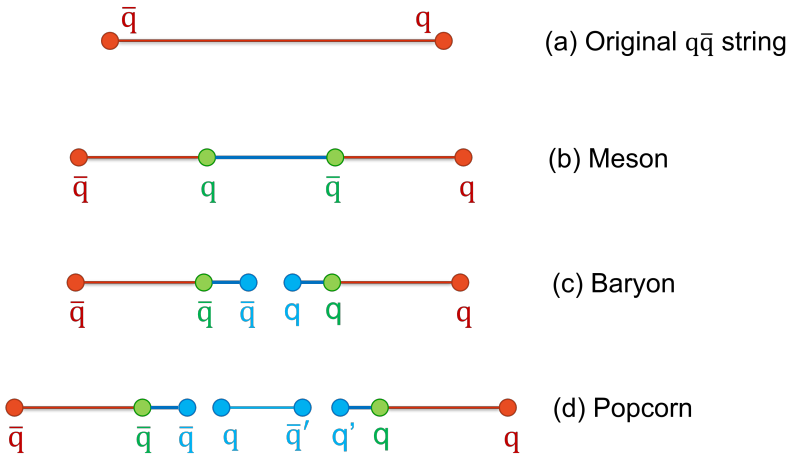

FIGURE 2.15: qq̄ string stretching (a) and consequent (b) meson-antimeson and (c) baryon-antibaryon formation as concept in the Lund model. The popcorn topology is shown in panel (d).

The prescriptions for the baryon formation in the Lund model are pretty similar to those ruling the meson production [173]. According to the SU(3) algebra, the quark is considered as a colour triplet that combines with an antiquark in a colour antitriplet to form a singlet that is identified as the meson of the final state. In a completely similar way, the baryon formation can be described as a quark combining with a diquark, taken to be a colour antitriplet just like a simple antiquark. In this way, a baryon-antibaryon pair is produced by the string breaking, as shown in Fig. 2.15. In this case, the di-quark formation substitutes that of a single antiquark and this process is ruled by different features. In particular, the a exponents in the fragmentation functions (Eq. 2.26) become flavour dependent and the larger formation time of di-quarks is expressed in terms of $a_{qq} > a_q$. Another possibility for the hadron formation is given by the *popcorn* picture [176], as shown in panel (d) of Fig. 2.15. In this case, the production of several mesons and baryons may happen due to multiple string breaks.

Hadronization models in pp collisions

The conventional string fragmentation described in the Lund model had been successfully used for the description of hadron production in e^+e^- and e^-p collisions. However, the results in hadronic collisions at the LHC energies are not in line with the predictions of the model, especially for what concerns the production of charmed baryons. In the upper panel of Fig. 2.16 the Λ_c^+/D^0 ratios in pp collisions at $\sqrt{s_{NN}} = 5.02$ [109] and 7 TeV [178] measured by the ALICE experiment are reported. The experimental results are hugely underestimated by the predictions from Monash, the PYTHIA tune where the conventional fragmentation is implemented. In particular, the data are higher than the models by about a factor 5 at low p_T. In order to understand this behaviour, other theoretical approaches need to be considered and several models different from the Lund one have been proposed.

1. **PYTHIA CR Mode 0, 2, 3** [179]. Traditionally, Monte Carlo generators make use of the *leading-colour (LC)* approximation, which traces the colour flow on an event-by-event basis. This approach assumes that each quark is connected only to another coloured parton in the event, similar to a leading-colour QCD

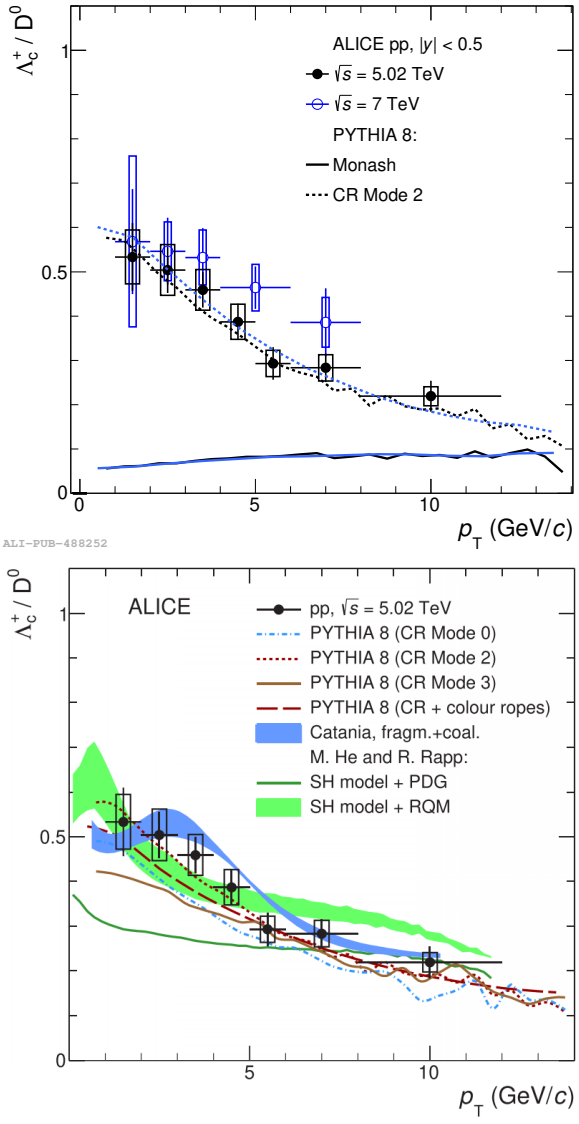

FIGURE 2.16: Λ_c^+/D^0 ratio in pp collisions at $\sqrt{s_{NN}} = 5.02$ and 7 TeV compared with predictions from Pythia predictions with Monash and colour reconnection beyond leading colour approximation (CR) (up). The experimental results in pp collisions at $\sqrt{s} = 5$ TeV are compared also with predictions from Catania model, SHM+RQM model and Herwig [177] (low). Figures from [109].

dipole [181], where the gluons carry a colour and an anticolour charge, being then connected to two other partons. In terms of strings, this can be interpreted as gluons forming transverse "kinks" on strings whose endpoints are a quark and an antiquark, as dictated by the Lund model [174]. This approach, which provides a good approximation to describe the hadronisation in e^+e^- collisions, is challenged when moving to hadronic collisions systems, such as pp. In this case, the initial state is no more insensitive to the strong force, but the partons inside protons carry colour charge and coloured beam remnants remain after the collision. Moreover, in such a collision system multiple parton interactions (MPI) can occur and they are crucial to explain the underlying event and soft-inclusive physics, especially in high-multiplicity events, and the

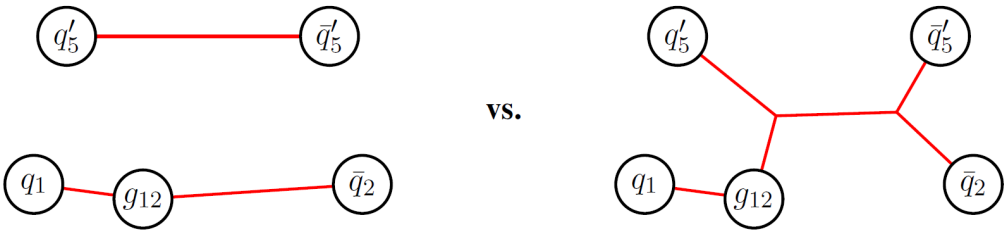

FIGURE 2.17: Illustration of a multi-parton state, with a leading-colour string topology (left) and with a junction-antijunction string topology, allowed by cyclically matching "2" and "5" indices. Figure from [179].

possibility of phase-space overlaps among particles produced in different MPI events is non negligible. Earlier works [182, 183] already considered the possibility for the different MPI systems to be colour-connected within a colour "chain", in order to minimise the total colour charge of the remnant and therefore the number of strings stretched to it. However, the effect of this basic colour reconnection was estimated to be small, without significant changes in the per-particle spectra in high-multiplicity events (many MPI's) with respect to low-multiplicity ones (low MPI's). In particular, the average p_{T} of charged particle for such events is estimated by this approach to be flat as a function of particle multiplicities, but the experimental data [184–186] ruled out this possibility, remarking the need to introduce non-trivial colour reconnection effects. The pure SU(3) group structure of QCD already provides some sub-leading combinations among different partons that, in particular, may create colour singlet before the single parton fragmentation. For example, considering three uncorrelated colour triplets (i.e. quarks) the Lie algebra of the SU(3) group foresees:

$$3 \otimes 3 \otimes 3 = 10 \oplus 8 \oplus 8 \oplus 1 \,. \tag{2.30}$$

In this equation, the decuplet corresponds to the LC topology, where for each MPI initiating parton one or two strings[4] are added to be stretched to the corresponding beam remnant. This is done incoherently, namely no strings are stretched among different MPI systems. The other multiplets describe additional sub-leading topologies that are not affected by fragmentation and, in particular, one of them already produces a colour singlet, corresponding to a baryon. However, these additional combinations are insufficient to describe the measured baryon production in hadronic collision. Therefore, a revisited *colour reconnection beyond leading colour approximation* (CR-BLC) has been implemented. This model [179] assumes a "simplified QCD" framework, in which parton combinations are ruled by 9 colour indices, leading to 9 possible states for quarks and 72 for gluons, which allow recombinations among partons in different MPIs and from beam remnants. In this new framework, all the possible combinations among partons in the whole event are considered and this enriches the string topology that will undergo the hadronisation. The additional combinations introduced in this framework are the so-called *junctions* and are reported in the right panel of Fig. 2.17 and augment the set

[4] A quark carries just a (anti-)colour charge, then this is connected to just a colour string. On the other hand, the gluons carry a colour and an anti-colour charges, therefore it connects with the corresponding beam remnants with two strings, each of them carrying either the colour or the anti-colour charge.

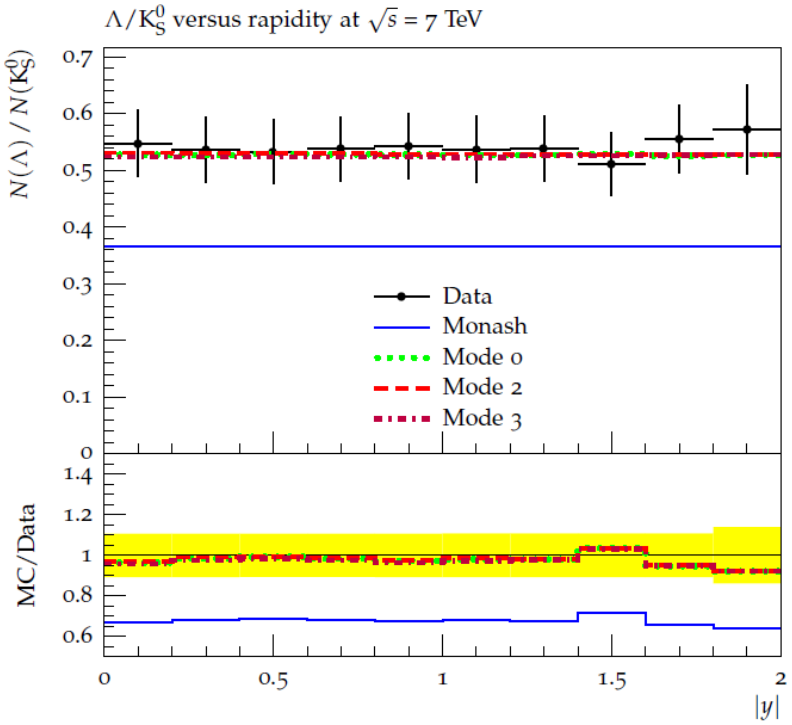

FIGURE 2.18: Λ/K^0_S ratio in pp collisions at $\sqrt{s} = 7$ TeV as a function of rapidity y measured by the CMS collaboration [180] compared with predictions from PYTHIA 8 tunes Monash, Mode 0, Mode 2, Mode 3. Figure from [179].

of possible string topologies that would be available with the LC structure[5]. The possible topologies that can be realised in a specific event are dictated by the minimization of the λ *string-length measure*, which corresponds to the area spanned by the string before the hadronisation, namely the potential energy of the string. A necessary condition for a colour string to be suitable for a reconnection is that its invariant mass must overcome a certain threshold m_0, whose value evidently influences the amount of possible reconnections. The parameter $C_j \equiv m_{0j}/m_0$, where to a high m_{0j} corresponds a low λ and $C_j > 1$ translates in an enhancement of junctions, finally governs the amount of reconnections. Another ingredient that influences the string topology is the *causal connection* among the strings themselves. In particular, if either string has already hadronised before the formation of the other, there is no space-time region available for the reconnection among them to occur. In particular, to make sure that two strings are able to reconnect, they must resolve each other between the string formation and its hadronisation, taking into account the time dilation occurring due to the relative boost. Calling $\tau_{\text{form.}} \sim 1/m_{\text{string}}$ the proper formation time of a string and $\tau_{\text{had.}} = r_{\text{had.}}/c \sim 1/\Lambda_{\text{QCD}}$ its proper hadronisation time, the causal contact between the two strings can be expressed in terms of the

[5] In this CR framework, two *colour* indices can coherently sum to form an *anticolor* index within three separate groups, that are [1, 4, 7], [2, 5, 8] and [3, 6, 9]. Considering the right panel of Fig. 2.17, the combination of the "5" index in q'_5 with the "2" index in g_{12} gives "$\bar{8}$" and equivalently the sum of the "$\bar{5}$" and "$\bar{2}$" in $\bar{q}_5$ and $\bar{q}_2$ respectively gives "8", which finally permits the shown junction.

Particle	New CR model (with junctions)	Old CR model
Λ_c^+ /# events	1.2×10^{-2}	6.6×10^{-3}
Σ_c^{++} /# events	1.3×10^{-2}	5.4×10^{-4}
Σ_c^{+} /# events	1.5×10^{-2}	5.2×10^{-4}
Σ_c^{0} /# events	1.3×10^{-2}	5.1×10^{-4}

TABLE 2.2: Primary particle production in PYTHIA 8, using the old CR model (Monash) or the new CR one (Mode 0, Mode 2, Mode 3). Numbers taken from [179].

following relation for the relative boost parameter γ:

$$\gamma\tau_{\text{form.}} < C_{\text{time}}\tau_{\text{had.}} \;\Rightarrow\; \frac{\gamma c}{m_{\text{string}} r_{\text{had.}}} < C_{\text{time}} \,, \tag{2.31}$$

where C_{time} is a tunable parameter. The different "modes" of this model depend on the requirement and the strength of this causal contact criterion. In the Mode 0 no time-dilation constraint is applied, but the amount of colour reconnection is dictated only by the invariant-mass threshold m_0. In Mode 2 the strictest condition is applied, since the causal contact is required to be valid among all the dipoles involved in a reconnection. In Mode 3, the constraint is relaxed by requiring only the first reconnection between two dipoles to satisfy Eq. 2.31, even if further reconnections take place later. The parameters of the model were tuned using existing experimental results: for example, the C_j parameter that rules the amount of junctions was tuned to reproduce the Λ/K_S^0 data in pp collisions at $\sqrt{s} = 7$ TeV by the CMS experiment [180], as shown in Fig. 2.18. Thanks to these tunings the model then acquires prediction power and the comparison with further experimental results becomes crucial to understand the nature of hadronisation in hadronic collisions. According to this model, the junction topology significantly enhances the production of open charmed baryons in pp collisions at the LHC energies, as reported in Tab. 2.2. For example, an increase of about a factor 20 is expected for the production of the Σ_c^0 baryon with respect to what foreseen according to the ordinary string fragmentation, where a dd-diquark must be produced from the parton shower to have a Σ_c^0. These diquark states must have spin 1 due to symmetry, being then strongly disfavoured with respect to the ud ones that can exist in the lighter states with spin 0. On the contrary, in the junction framework no penalty factor is expected for the dd-diquarks and in addition a charm quark can combine with another d quark as end-point of a junction leg, forming a cd-diquark which then connects to another d quark. This explains the mentioned enhancement for the Σ_c^0 production. Similar arguments are valid for the Σ_c^{++} as well as for the production of the analogous b-baryons, motivating an effort from the experimental side to provide precise measurements of their production rates in pp collisions at the LHC.

2. **Statistical Hadronization Model with Relativistic Quark Model states** [187]. In the statistical hadronisation model (SHM) [38] the complexity of the hadronisation processes is treated with the usage of thermo-statistical weights, only governed by the mass of the producible hadrons at a given hadronisation temperature T_H. This approach has been successfully adopted to describe the light and strange hadron production in heavy-ion collisions and in smaller systems,

$n_i(\times 10^{-4}\mathrm{fm}^{-3})$	D^0	D^+	D^{*+}	D_s^+	Λ_c^+	$\Xi_\mathrm{c}^{0,+}$	Ω_c^0
PDG ($T_\mathrm{H} = 170$ MeV)	1.161	0.5098	0.5010	0.3165	0.3310	0.0874	0.0064
RQM ($T_\mathrm{H} = 170$ MeV)	1.161	0.5098	0.5010	0.3165	0.6613	0.1173	0.0144

TABLE 2.3: Thermal densities estimated by the SHM model for prompt ground state charmed hadrons at the hadronisation temperature $T_\mathrm{H} = 170$ MeV either including only hadrons listed in the PDG or adding also the ones foreseen by the RQM. Numbers taken from [187].

with the introduction in the latter case of a strangeness suppression factor $\gamma_S < 1$ (see Sec. 1.4.3). However, the description of the baryon-to-meson ratio using a statistical approach based only on the charm-hadron states reported in the PDG [3] cannot describe the $\Lambda_\mathrm{c}^+/\mathrm{D}^0$ ratio measured by the ALICE experiment in pp collisions at $\sqrt{s} = 7$ TeV [178], which exhibits larger values with respect to the predicted ones. The model in Ref. [187] provides a revisited framework that includes an augmented set of charm-baryon states foreseen by the Relativistic Quark Model (RQM [188]). They consist in 18 extra Λ_c^+ states, 42 Σ_c's, 62 Ξ_c's and 34 Ω_c's up to a mass of 3.5 GeV/c^2. All the considered hadron states are governed by thermal densities ruled by specific weights that depend on the hadron mass m_i and their spin degeneracy $d_i = 2\mathrm{J} + 1$, namely:

$$n_i = \frac{d_i}{2\pi^2} m_i^2 T_\mathrm{H} K_2 \left(\frac{m_i}{T_\mathrm{H}} \right) , \tag{2.32}$$

where K_2 is the modified Bessel function of second order and T_H is the hadronisation temperature. The upper estimate of T_H is assumed to be 170 MeV, according to the results in Ref. [189]. The thermal densities in Eq. 2.32 are used to assign the proper normalization to the charm-quark fragmentation functions, which are deduced from those assumed in the FONLL framework, employed to compute the charm p_T spectrum produced in pp collisions. All the additional excited charmed baryons mentioned above are forced to decay into a ground state one. This process does not alter the abundances of the ground state D mesons, but it results in a significant enhancement of the ground state charmed baryons, as explicitly reported in Tab. 2.3.

3. **Catania coalescence model** [190]. Recent measurements in pp collisions at the LHC [51, 108, 109, 191], where the centre-of-mass energy is of the TeV order, show a phenomenology similar to that observed in AA collisions, such as strangeness and baryon-over-meson enhancement, especially when particle yields are studied as a function of event multiplicity. Different theoretical studies [192–195] performing hydrodynamical and transport-based calculations are able to provide reasonable description of p_T spectra and two-particle correlations, pointing to a possible formation of a hot QCD matter with a lifetime $\tau \approx 2$ fm/c. Based on this, the Catania model assumes the presence of a thermalized system of gluons and u, d, s quarks and antiquarks already in pp collisions, characterised by a lifetime $\tau = 2.5$ fm/c, a transverse radius $R = 2$ fm and a temperature $T = 165$ MeV, according to what provided by the hydrodynamical simulations in Ref. [192]. The bulk does not contain free charm quarks, since the charm thermalization time is larger (see Sec. 2.2.3) therefore no thermalized charm quarks are expected. The presence of a deconfined medium

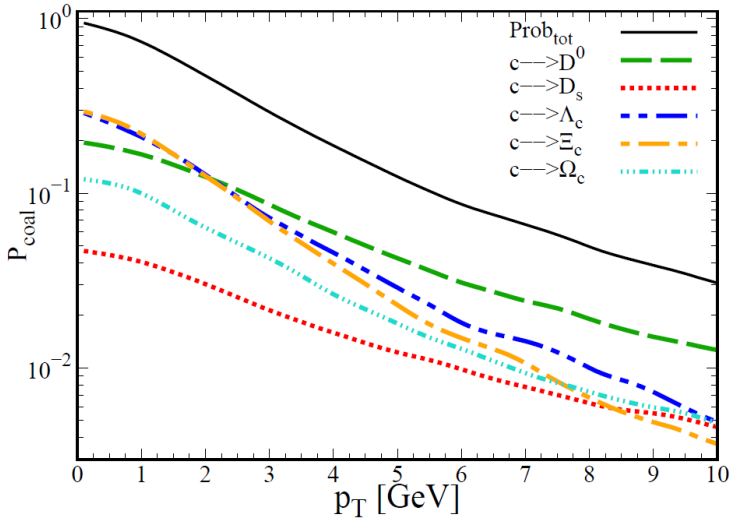

FIGURE 2.19: Charm coalescence probability as a function of the charm p_{T} for pp collisions at the LHC. The coloured lines correspond to the probability of the charm quark to coalesce in a given hadron species, while the black solid line represents the total coalescence probability. Figure from [190].

is crucial for this model, where a hybrid hadronisation via fragmentation and coalescence is assumed for the charm quark. The interplay between these two processes is ruled by requiring that a charm quark can hadronise only with either one of these ways, therefore the probability for a charm quark to coalesce with a light parton of the bulk is complementary to the fragmentation probability, namely $P_{\mathrm{fragm.}} = 1 - P_{\mathrm{coal.}}$. In this model, the coalescence is treated with the Wigner formalism, according to which the momentum spectrum of a hadron produced by the charm coalescence can be described as:

$$\begin{aligned}\frac{\mathrm{d}^3 N_{\mathrm{H}}^{\mathrm{coal.}}}{\mathrm{d}y\mathrm{d}^2 p_{\mathrm{T}}} = g_{\mathrm{H}} \int \prod_{i=1}^{N_{\mathrm{q}}} \frac{\mathrm{d}^3 p_i}{(2\pi)^3 E_i} p_i \cdot \mathrm{d}\sigma_i f_{\mathrm{q}_i}(x_i, p_i) \\ \times f_{\mathrm{H}}(x_1, \ldots, x_{N_{\mathrm{q}}}, p_1, \ldots, p_{N_{\mathrm{q}}}) \delta^{(2)} \left(p_{\mathrm{T}} - \sum_{i=1}^{n} p_{\mathrm{T},i} \right) .\end{aligned} \tag{2.33}$$

In Eq. 2.33, g_{H} indicates the statistical degeneracy factor to form a colourless hadron from quarks and antiquarks with spin 1/2 and corresponds to 1/36 for mesons and 1/108 for baryons. The quantity $\mathrm{d}\sigma_i$ denotes an element of a space-like hypersurface and $f_{\mathrm{q},i}$ corresponds to the (anti)quark phase-space distribution for the i-th (anti)quark. Finally, $f_{\mathrm{H}}(x_1, \ldots, x_{N_{\mathrm{q}}}, p_1, \ldots, p_{N_{\mathrm{q}}})$ corresponds to the *Wigner function*, which describes the probability for a hadron to be produced from quarks with given phase-space coordinates. The Eq. 2.33 describes the production via coalescence of mesons and baryons in case of $N_{\mathrm{q}} = 2$ and 3 respectively. The Wigner function is assumed to follow a Gaussian shape in space and momentum:

$$f_{\mathrm{H}}(x_1, \ldots, x_{N_{\mathrm{q}}}, p_1, \ldots, p_{N_{\mathrm{q}}}) = \prod_{i=1}^{N_{\mathrm{q}}-1} A_W \exp\left(-\frac{x_{r_i}^2}{\sigma_{r_i}^2} - p_{r_i}^2 \sigma_{r_i}^2 \right) , \tag{2.34}$$

where A_W is a normalization factor fixed to assure that for $p \to 0$ a charm quark certainly hadronises via coalescence. This is imposed by requiring that the total coalescence probability satisfies $\lim_{p\to 0} P^{\text{tot.}}_{\text{coal.}} = 1$. The Wigner function depends on x_{r_i} and p_{r_i}, which are the relative phase-space coordinates among the valence quarks in the hadron and σ_{r_i} are covariant widths, related to the root-mean-square charge radius of the hadron: $\langle r^2\rangle_{ch} = \sum_{i=1}^{N} Q_i \langle (x_i - X_{\text{CM}})^2\rangle$, with $N = 2, 3$ for mesons and baryons respectively. The hadron radii considered in this model are taken from the quark model [196, 197]. The momentum spectrum for a hadron produced from the charm fragmentation can be written as:

$$\frac{\mathrm{d}^3 N^{\text{fragm.}}_{\text{H}}}{\mathrm{d}y\mathrm{d}^2 p_{\text{T}}} = \sum \int \mathrm{d}z \frac{\mathrm{d}N_{\text{fragm.}}}{\mathrm{d}^2 p_{\text{T}}\mathrm{d}y} \frac{D_{\text{H}/c}(z, Q^2)}{z^2} \,, \tag{2.35}$$

where $D_{\text{H}/c}(z, Q^2)$ corresponds to the fragmentation function, linked to the probability for the charm quark to produce a hadron H with a fraction z of the original charm momentum, given $Q^2 = (p_{\text{had.}}/2z)^2$ the momentum scale of the fragmentation process. These functions correspond to the Peterson ones [198], taken from Ref. [199] for the charm quark. The interplay between fragmentation and coalescence depends on the charm p_{T}. In Fig. 2.19 the coalescence probability of the charm quark to the different hadron species (coloured lines) is shown as a function of the charm p_{T}. The total probability tends to unity for $p \to 0$ as required in the definition of A_W in Eq. 2.34 and quickly decreases with increasing charm p_{T}, meaning that at low p_{T} the charm quark only coalesces, while at high p_{T} the fragmentation contribution grows with p_{T}. It is important to notice that for $p_{\text{T}} < 2$ GeV/c the coalescence probabilities into Λ_{c}^+ and Ξ_{c} are compatible and higher than the probability to coalesce into a D^0. This implies an enhancement of the $\Lambda_{\text{c}}^+/\text{D}^0$ and $\Xi_{\text{c}}/\text{D}^0$ ratios. In particular, the model foresees $P_{\text{fragm.}} > P_{\text{coal.}}$ for the charm mesons and $P_{\text{fragm.}} < P_{\text{coal.}}$ for baryons given a hadron p_{T} lower than 10 GeV/c. Furthermore, the Catania model predicts a $\Lambda_{\text{c}}^+(\leftarrow \Sigma_{\text{c}}^{0,+,++})/\Lambda_{\text{c}}^+$ ratio in pp collisions at the LHC energies higher by about a factor 2 with respect to the fragmentation in e^+e^- collisions, where the $\Sigma_{\text{c}}^{0,+,++}$ strong decays is observed to contribute only to 10% of the Λ_{c}^+ production.

4. **Quark (re-)Combination Mechanism (QCM)** [200]. In this model, the production of low-p_{T} charm hadrons is conceived as the coalescence of a perturbatively-created charm quark with equal-velocity light flavour ones deriving from fragmentation. The charm mesons and baryons are produced with a characteristic momentum $p_{\text{H}} = p_c + p_{\bar{\text{q}},\text{qq}}$ from a charm quark (p_c) that picks up a co-moving light antiquark ($p_{\bar{\text{q}}}$) or two co-moving light quarks (p_{qq}) respectively. The momentum distribution of a single-charm meson $M_{c\bar{l}}$ and baryon $B_{cll'}$, with l and l' indicating two light-flavour quarks among u, d and s, is written as:

$$f_{M_{c\bar{l}}}(p) = \int \mathrm{d}p_1 \mathrm{d}p_2 f_{c\bar{l}}(p_1, p_2) \mathcal{R}_{M_{c\bar{l}}}(p_1, p_2; p) \,, \tag{2.36}$$

$$f_{B_{cll'}}(p) = \int \mathrm{d}p_1 \mathrm{d}p_2 \mathrm{d}p_3 f_{cll'}(p_1, p_2, p_3) \mathcal{R}_{B_{cll'}}(p_1, p_2, p_3; p) \,. \tag{2.37}$$

The quantity $f_{c\bar{l}}(p_1, p_2)$ is the joint momentum distribution for charm quark and light antiquark and $\mathcal{R}_{M_{c\bar{l}}}(p_1, p_2; p)$ corresponds to the probability density for the c and $\bar{l}$ with momenta p_1 and p_2 respectively to be combined into a

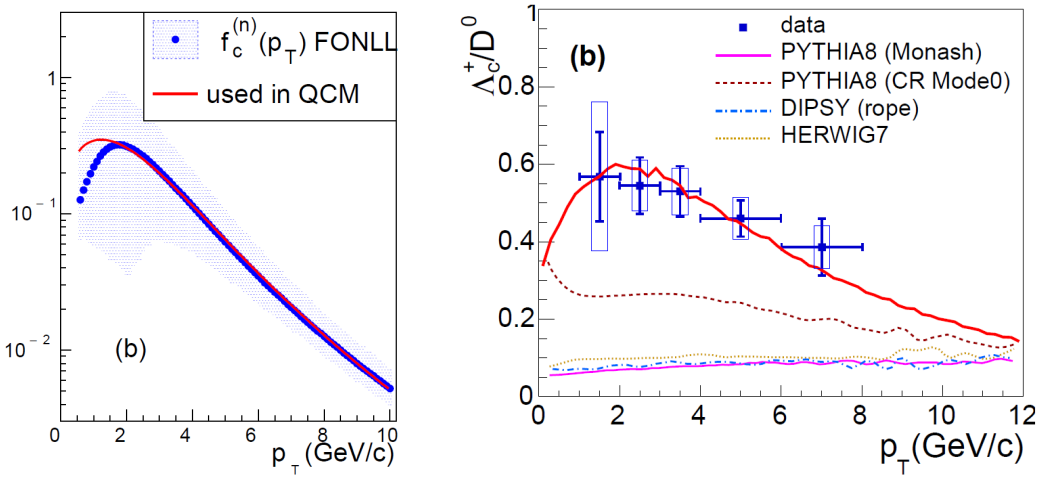

(A) (B)

FIGURE 2.20: Left: normalised p_T distribution of charm quarks from FONLL (blue) compared with the one used in the QCM model (red). Right: Λ_c^+/D^0 ratio in pp collisions at $\sqrt{s} = 7$ TeV measured by the ALICE experiment [178] compared with the prediction of the QCM model. Figures from [200].

meson $M_{c\bar{l}}$ with momentum p. The same description is valid for baryons $B_{cll'}$. The combination functions $\mathcal{R}_{M_{c\bar{l}}}$ and $\mathcal{R}_{B_{cll'}}$ are defined as:

$$\mathcal{R}_{M_{c\bar{l}}}(p_1, p_2; p) = \kappa_{M_{c\bar{l}}} \prod_{i=1}^{2} \delta(p_i - x_i p) \,, \tag{2.38}$$

$$\mathcal{R}_{B_{cll'}}(p_1, p_2, p_3; p) = \kappa_{B_{cll'}} \prod_{i=1}^{3} \delta(p_i - x_i p) \,, \tag{2.39}$$

so that the combination takes place only if the i-th quark carries a given fraction x_i of the final hadron momentum p. The momentum fraction x_i is defined under the co-moving approximation, which assumes that a charm quark combines with a light antiquark moving at the same velocity to form a meson. Considering that under the assumption of equal velocity the momentum is proportional to the mass, namely $p_i = \gamma v m_i \propto m_i$, the momentum fraction x_i is defined as:

$$x_i := m_i / \sum_j m_j \,, \tag{2.40}$$

where the considered values for the quark masses are $m_u = m_d = 0.33\ \mathrm{GeV}/c^2$, $m_s = 0.5\ \mathrm{GeV}/c^2$ and $m_c = 1.5\ \mathrm{GeV}/c^2$. Assuming uncorrelated probability distributions for quarks of different flavours, Eqs. 2.36 and 2.37 can be written as:

$$f_{M_{c\bar{l}}}(p) = \kappa_{M_{c\bar{l}}} f_c(x_1 p) f_{\bar{l}}(x_2 p) \,, \tag{2.41}$$

$$f_{B_{cll'}}(p) = \kappa_{B_{cll'}} f_c(x_1 p) f_l(x_2 p) f_{l'}(x_3 p) \,. \tag{2.42}$$

Rewriting these distributions as:

$$f_{M_{c\bar{l}}}(p) = N_{M_{c\bar{l}}} f^{(n)}_{M_{c\bar{l}}}(p) \,, \tag{2.43}$$

$$f_{B_{cll'}}(p) = N_{B_{cll'}} f^{(n)}_{B_{cll'}}(p) \,, \tag{2.44}$$

where $f^{(n)}_{M_{c\bar{l}}}(p)$ and $f^{(n)}_{B_{cll'}}(p)$ are introduced, corresponding to the normalised distribution functions so that $\int \mathrm{d}p f^{(n)}_{M_{c\bar{l}}}(p) = 1$ and $\int \mathrm{d}p f^{(n)}_{B_{cll'}}(p) = 1$, then the momentum integrated yield for the charm meson $M_{c\bar{l}}$ is:

$$N_{M_{c\bar{l}}} = \kappa_{M_{c\bar{l}}} \int \mathrm{d}p f_c(x_1 p) f_{\bar{l}}(x_2 p) = N_c N_{\bar{l}} \frac{\kappa_{M_{c\bar{l}}}}{A_{M_{c\bar{l}}}} = N_c N_{\bar{l}} \mathcal{R}_{c\bar{l}\to M_{c\bar{l}}} \,, \tag{2.45}$$

where at the second step the same logic of Eq. 2.43 is used to introduce $1/A_{M_{c\bar{l}}} := \int \mathrm{d}p f^{(n)}_c(x_1 p) f^{(n)}_{\bar{l}}(x_2 p)$. The quantity $\mathcal{R}_{c\bar{l}\to M_{c\bar{l}}} := \kappa_{M_{c\bar{l}}/A_{M_{c\bar{l}}}}$ corresponds to the momentum-integrated probability for a c and $\bar{l}$ quarks to produce a meson $M_{c\bar{l}}$. With the same arguments, the momentum-integrated yield for the charm baryon $B_{cll'}$ is:

$$N_{B_{cll'}} = N_c N_l N_{l'} \frac{\kappa_{B_{cll'}}}{A_{B_{cll'}}} = N_c N_l N_{l'} \mathcal{R}_{cll'\to B_{cll'}} \,. \tag{2.46}$$

Introducing the probability $P_{\bar{l}} := N_{\bar{l}}/N_{\bar{\mathrm{q}}}$ of an antiquark $\bar{\mathrm{q}}$ to be of flavour $\bar{l}$ and the total number of single-charm mesons N_{M_c}, the momentum-integrated yield of the charm meson $M_{i,c\bar{l}}$, where the index i denotes a particular $c\bar{l}$ spin state, is:

$$N_{M_{i,c\bar{l}}} = C_{M_{i,c\bar{l}}} P_{\bar{l}} N_{M_c} \,. \tag{2.47}$$

The quantities $C_{M_{i,c\bar{l}}}$ denotes the probability to form the i-th spin state and they are ruled by the thermal weights used in [201–203], representing the ratio between ratio and pseudo-scalar mesons with the same quark flavours. With a similar logic, the momentum-integrated yield of the charm baryon $B_{i,cll'}$ in the i-th spin state is:

$$N_{B_{cll'}} = N_{\mathrm{iter}_{ll'}} C_{B_{i,cll'}} P_l P_{\bar{l}} N_{B_c} \,, \tag{2.48}$$

where $N_{\mathrm{iter}_{ll'}}$ is equal to 1 if $l = l'$ and equal to 2 if $l \neq l'$. The p_{T} distributions of the quarks at hadronisation are inputs of the model. The light-quark spectra are obtained from the light-flavour hadron production in pp collisions at $\sqrt{s} = 7$ TeV, as explained in [204], while the p_{T} distribution of charm is reversely obtained from the D^{*+} production measurements in pp collisions at $\sqrt{s} = 7$ TeV and p–Pb collisions at $\sqrt{s_{\mathrm{NN}}} = 5.02$ TeV [205, 206]. This is shown in the panel (A) of Fig. 2.20, where it is compared with the prediction from FONLL. The two spectra are very similar in the range $p_{\mathrm{T}} \gtrsim 1.5$ GeV/c, while the QCM one is higher for lower transverse momenta with respect to the FONLL one, even if they are compatible within the theoretical uncertainties. Given these inputs, the QCM model provides predictions for the production of pseudo-scalar $J^{\mathrm{P}} = 0^-$ (D^+, D^0 and $\mathrm{D}_{\mathrm{s}}^+$) and vector $J^{\mathrm{P}} = 1^-$ (D^{*+}, D^{*0} and $\mathrm{D_s}^{*+}$) D mesons as well as the triplet ($\Lambda_{\mathrm{c}}^+, \Xi_{\mathrm{c}}^+$ and Ξ_{c}^0) with $J^{\mathrm{P}} = (1/2)^+$, sextet (Σ_{c}^0, Σ_{c}^+, Σ_{c}^{++}, $\Xi_{\mathrm{c}}^{\prime 0}$, $\Xi_{\mathrm{c}}^{\prime +}$ and Ω_{c}^0) with $J^{\mathrm{P}} = (1/2)^+$ and sextet (Σ_{c}^{*0}, Σ_{c}^{*+}, $\Sigma_{\mathrm{c}}^{*++}$, Ξ_{c}^{*0}, Ξ_{c}^{*+} and Ω_{c}^{*0}) with $J^{\mathrm{P}} = (3/2)^+$ charm baryons. In the panel (B) of Fig. 2.20 the $\Lambda_{\mathrm{c}}^+/\mathrm{D}^0$ ratio measured by the ALICE experiment in pp collisions at $\sqrt{s} = 7$ TeV [178] is compared with the prediction from the QCM model, which correctly describes both the magnitude and the p_{T} dependence within the experimental uncertainties, differently from other models not including the charm quark coalescence that significantly underestimate the data.

The theoretical predictions mentioned above are compared to the Λ_c^+/D^0 ratio measured in pp collisions at $\sqrt{s} = 5$ TeV in the lower panel of Fig. 2.16. The PYTHIA 8 predictions including the updated colour reconnection topologies well describe the p_T dependence of the measured ratio and catch its magnitude over the whole range when the Mode 2 is adopted. The SHM also describes the data, but only if the augmented set of charm baryons predicted by the RQM is included, while the Λ_c^+/D^0 ratio is significantly underestimated at low p_T if only the PDG states are taken into account. Finally, also the Catania model describes the measurement within uncertainties. This comparison indicates that different scenarios are plausible for the charm hadronisation in pp collisions and the actual experimental precision does not permit a discrimination among the different models. Moreover, additional baryon-over-meson measurements, like $\Xi_c^{0,+}/D^0$, $\Sigma_c^{0,+,++}/D^0$ and Ω_c^0/D^0, as well as baryon-over-baryon ratios, like $\Xi_c^{0,+}/\Sigma_c^{0,+,++}$, are fundamental to further test the validity of the models. Such results, corresponding to the ratio of the charm fragmentation fraction ratios in different hadron species, cover a crucial role to understand the hadronisation mechanisms of the charm quark in hadronic collisions.

Chapter 3

ALICE: A Large Ion Collider Experiment

3.1 The LHC collider

The Large Hadron Collider (LHC) is placed in the *Conseil Européen pour la Recherche Nucléaire* (CERN), in the vicinity of the borders between France and Switzerland, next to the city of Geneva. The ring is installed at an average of 100 m underground and it has a $\sim$ 27 km long circumference. The tunnel that now hosts LHC was built in 1984 in order to host the *Large Electron Positron collider* (LEP [207]), dismantled in 2001 to leave place to the actual accelerator, where proton-proton (pp), proton-lead (p–Pb) and lead-lead (Pb–Pb) collisions are studied [1]. The LHC collider was designed to accelerate proton beams and provide collisions at the maximum centre-of-mass energy of $\sqrt{s} = 14$ TeV with the luminosity peak of $\mathcal{L} = 10^{34}$ cm^{-2} s^{-1}, as well as lead nuclei beams providing collisions at $\sqrt{s} = 5.02$ TeV/nucleon with a peak luminosity of $\mathcal{L} = 10^{27}$ cm^{-2} s^{-1}[2].

In Fig. 3.1 an LHC overview and the position of the four main experiments connected to the collider are shown. ATLAS (*A Toroidal Lhc ApparatuS* [208]), experiment placed in site 1, and CMS (*Compact Muon Solenoid* [209]), placed in site 5, are optimized for pp collisions measurement with the highest interaction rate and designed for new physics research. Their work brought to the experimental discovery of the Higgs boson in 2012 [210, 211]. The LHCb (*Large Hadron Collider beauty* [212]) experiment, placed in site 8, is specialized in the study of heavy flavour physics, in particular of hadrons with *beauty* quarks. Finally, in site 2 there is ALICE (*A Large Ion Collider Experiment* [213]), specialized in the measurement of events with a high multiplicity of produced particles, obtained through heavy-ion collisions. This experiment is conceived for the study of QGP. In Fig. 3.1 the LHC injection system is shown. This collider is only the last step of a long chain of devices used to accelerate protons and lead ions to higher and higher energy [214,215]. Protons, extracted from hydrogen atoms, are subject to the action of the *LINear ACcelerator 2* (LINAC2 [216]),

[1] In the LHC collider ^{208} Pb^{82+} ions are accelerated.

[2] Proton energy and ^{208} Pb^{82+} ion nucleons energy are different due to the *rigidity* parameter:

$$R = \frac{p}{q} = r_{\mathrm{LHC}} B_{\mathrm{LHC}} \,, \tag{3.1}$$

where p and q are respectively momentum and charge of the particle, while r_{LHC} is the LHC radius and $B_{\mathrm{LHC}} = 8.33$T is the applied magnetic field. Since the product at last member is constant, protons and lead nuclei have the same rigidity, then:

$$p_{\mathrm{proton}} = \frac{p_{\mathrm{tot}}(\mathrm{Pb}^{82+})}{q(\mathrm{Pb}^{82+})} = \frac{A p_{\mathrm{nucleon}}}{Z} \;\Rightarrow\; p_{\mathrm{nucleon}} = \frac{Z}{A} p_{\mathrm{proton}} < p_{\mathrm{proton}} \,.$$

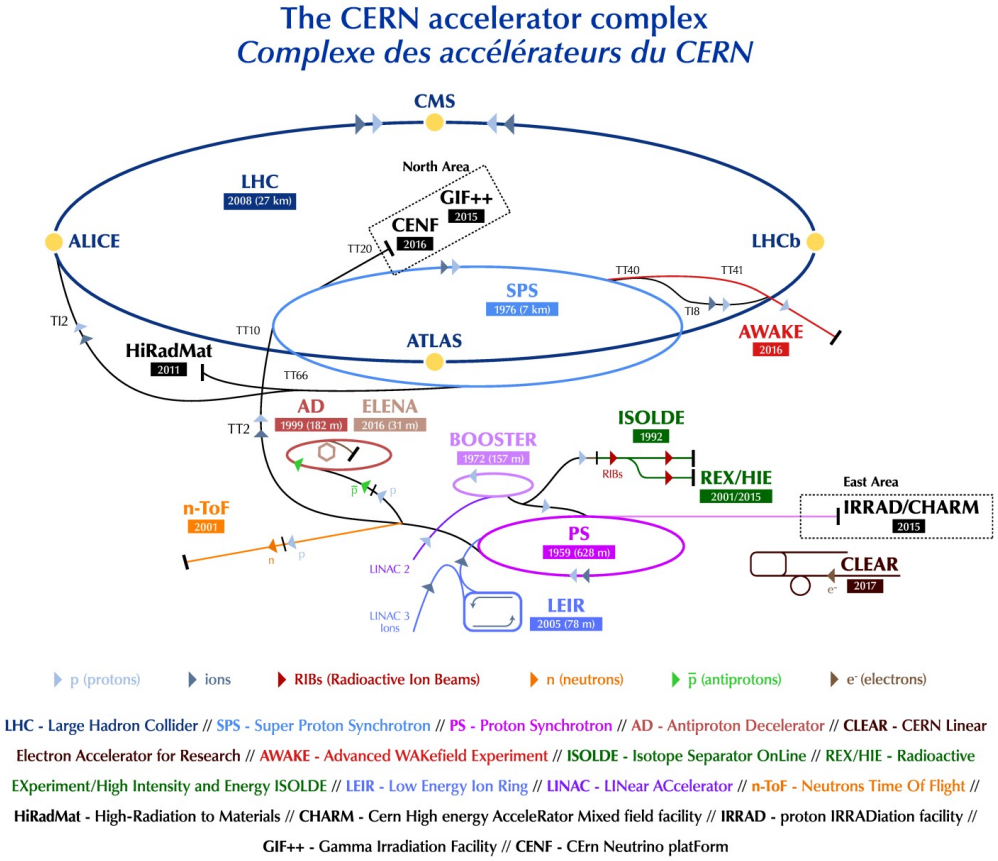

FIGURE 3.1: Injection system of LHC. Image taken from [221].

which brings them to $\sim$ 50 MeV. Then they are injected in the *Proton Synchrotron Booster* (PSB [217]), that accelerates them up to the energy of $\sim$ 1.4 GeV and send them to the *Proton Synchrotron* (PS [218]), where they reach the energy of $\sim$ 25 GeV. Before entering the LHC collider, protons are accelerated in the *Super Proton Synchrotron* (SPS) until the energy of $\sim$ 450 GeV. The led ions follow a different path. They are produced through metallic lead evaporation and following ionization, then they are initially accelerated into the *LINear ACcelerator 3* (LINAC3 [219]) to the energy of $\sim$ 4.2 MeV/nucleon. Later they go into the *Low Energy Ion Ring* (LEIR [220]), which brings them to the energy of $\sim$ 72 MeV/nucleon. Finally, the ions follow the same path of the protons, namely passing through PS ($\sim$ 5.9 GeV/nucleon) and through SPS ($\sim$ 177 GeV/nucleon) before being injected into the LHC.

3.2 The ALICE experiment

ALICE [213] is a general purpose experiment conceived to study heavy-ion collisions at ultra-relativistic centre-of-mass energies. The main goal of this experiment is the characterization of QGP at extreme values of energy and densities, produced with Pb–Pb collisions in order to investigate the QCD phase diagram, and the study of the physics regarding the strongly-interacting matter. To address this kind of physics, the apparatus must succeed in reconstructing charged particles in a wide momentum range (down to $\sim$ 100 MeV/c) in a high-multiplicity environment, given that the charged particle multiplicity at mid rapidity reaches values of several thousands

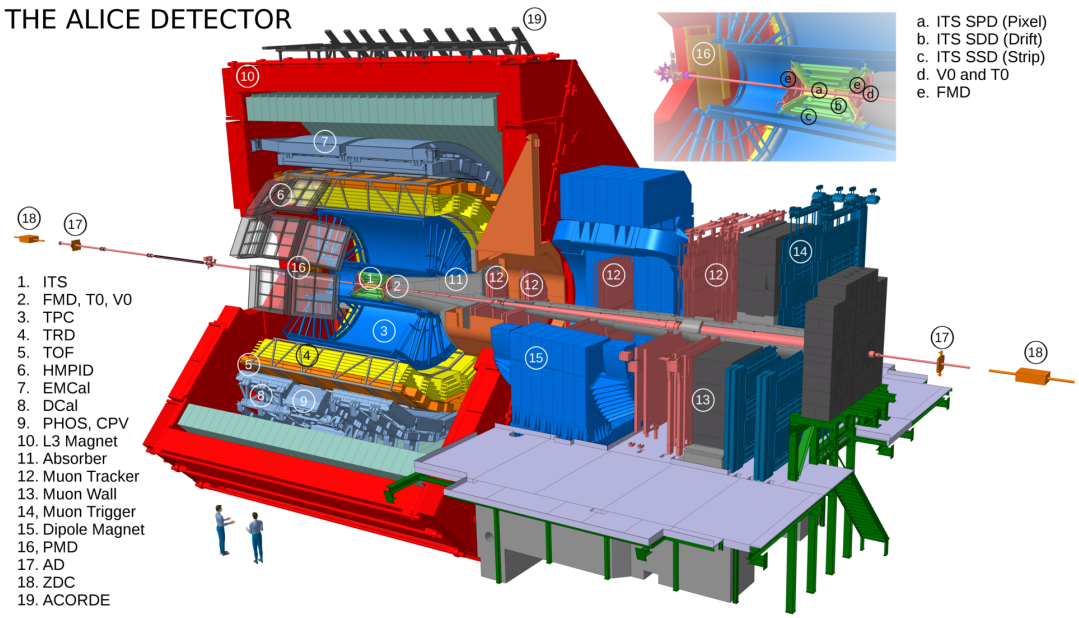

FIGURE 3.2: ALICE experiment. Image taken from the ALICE Figure Repository ©.

per unit of figure in central Pb–Pb collisions. For this reason, in the region surrounding the interaction point only detectors with a high-granularity and with a low material budget to reduce multiple scattering are adopted, like the Inner Tracking System and the Time Projection Chamber, as described below. Moreover, the different subsystems provide excellent PID capabilities, which permit the identification of charged particles in a wide momentum range.

The full apparatus, shown in Fig. 3.2, is 26 m long, 16 m wide and 16 m high, weighting more than 10000 tons. The experiment is divided in two main parts, according to the covered acceptance: a *central barrel*, covering the range $-0.9 < \eta < 0.9$, and a *muon spectrometer*, which covers the acceptance range $-4.0 < \eta < -2.4$. The detectors of the central barrel are designed with a cylindrical geometry and they are embedded inside the L3 solenoid magnet, which is capable of a longitudinal magnetic field of 0.5 T and was previously equipped the L3 experiment at the LEP collider. The nominal interaction point is surrounded by cylindrical systems with increasing radii, namely the Inner Tracking System (ITS), the Time Projection Chamber (TPC), the Transition Radiation Detector (TRD) and the Time Of Flight (TOF). On top of them, additional detectors with a limited azimuthal acceptance are installed, namely a Ring Imaging Cherenkov (HMPID) detector and two electromagnetic calorimeters (PHOS and EMCal). A spectrometer at forward rapidity, specialised for the muon detection, is composed of a dedicated dipole magnet and a heavy absorber apparatus, followed by fourteen layers of Resistive Plate Chambers (RPC) used to trigger on events with muons and to reconstruct them. The experiment is then equipped with several smaller detectors at backward and forward rapidity (V0, T0, FMD, PMD and ZDC), which main purposes are the characterization of the global event properties. Finally, an array of scintillators (ACORDE) is installed outside the L3 solenoid to trigger on then remove cosmic rays, which can also be used for alignment purposes.

ALICE experiment uses a right handed Cartesian coordinate system, centred in the middle of the central barrel. The $\hat{z}$ identifies the beams direction of motion and

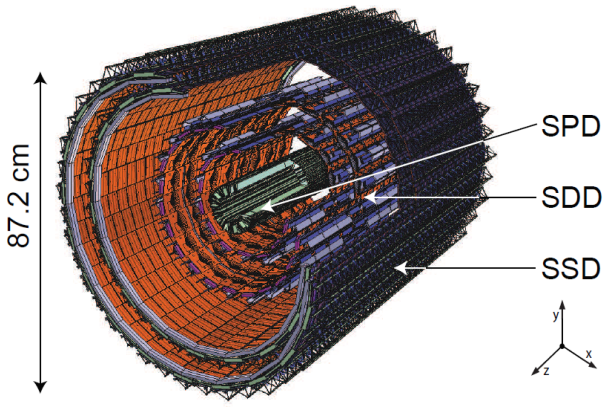

FIGURE 3.3: ITS detector structure. Image taken from [222].

goes towards the opposite way respect to the muon spectrometer, while the transverse plane is defined by $\hat{x}$ and $\hat{y}$ axis, where the $\hat{x}$ axis goes towards the centre of the LHC ring and the $\hat{y}$ axis towards the top (see figure 3.3). In addition, ALICE uses a spherical coordinates system, based on the azimuthal angle φ, defined on the transverse plane xy, and the polar one θ, which is used to define the rapidity and pseudorapidity parameters (see Eq. 1.27, 1.32).

3.2.1 Inner Tracking System (ITS)

The *Inner Tracking System* (ITS) [222] is the most internal tracking detector in ALICE. It is made of six layers of silicon detectors, based on different technologies during Run 1 and 2 at the LHC. The first two layers constitute the *Silicon Pixel Detector* (SPD), based on a five cells bi-dimensional sensors matrix formed by 256 $\times$ 160 pixels, with dimensions 50 μm$(r\varphi)$ $\times$ 425 μm(z). Two matrices are mounted together along the longitudinal direction to form a 141.6 mm long *half-stave*. Two of them, mounted head-to-head along the z direction on a carbon-fibre support sector that also provides the cooling services, form a *stave*. The SPD detector includes ten azimuthal sectors, each of them mounting two staves in the innermost layer and four staves in the outermost one. The two layers are at a distance of about 3.9 cm and 7.6 cm from the beam pipe, with a pseudorapidity acceptance of $|\eta| < 2.0$ and $|\eta| < 1.4$ respectively. Their position is designed so that the whole coverage in the azimuthal angle is ensured. The spatial resolution of the pixel matrix, measured during the preliminary tests, is $\sim$ 12 μm in the radial direction and $\sim$ 100 μm along z. The two intermediate layers constitute the *Silicon Drift Detector* (SDD). The basic module is a silicon volume sized 72.5$\times$75.3 mm divided into two drift regions by a high voltage central cathode, where the electrons move in opposite directions due to the presence of a $\sim$ 500 V/cm electric field. These modules are mounted on linear supports called *ladders*: the inner layer, placed at 15 cm from the beam pipe is made of 14 ladders with six moduli each, while the outer one, 24 cm from the beam pipe, is made of 22 ladders with 8 moduli each. The spatial resolution ensured by the SDD device is $\sim$ 35 μm along the radial drift direction and $\sim$ 25 μm along $\hat{z}$. Both SDD layers have a pseudorapidity acceptance of $|\eta| < 0.9$. The last two layers constitute the *Silicon Strip Detector* (SSD). The basic building block of this detector corresponds to a double-sided module, where each side represents the p- and n-junction side, that are both segmented in 768 parallel strips with a pitch of 95 μm. The stereo angle among the strips in the two halves is 35 mrad, chosen to reduce the ambiguities deriving from a high particle density environment. The detecting modules are mounted on

Layer	r (cm)	$\pm z$ (cm)	Material budget ($\%X_0$)	Active area per module $r\phi \times z$ (mm^2)	Resolution $r\phi \times z$ (μm^2)
SPD	3.9	14.1	1.14	12.8×70.7	12×100
SPD	7.6	14.1	1.14	12.8×70.7	12×100
SDD	15.0	22.2	1.13	70.17×75.26	35×25
SDD	23.9	29.7	1.26	70.17×75.26	35×25
SSD	38.0	43.1	0.83	73×40	20×830
SSD	43.0	48.9	0.86	73×40	20×830

TABLE 3.1: Properties of ITS layers [213].

supports with the same technology of those used for the SDD. In particular, the inner layer, placed at 38 cm from the beam pipe, is made of 34 ladders with 22 moduli along the beam axis, while the last ITS layer, 43 cm from the beam pipe, is made of 38 ladders, each of them with 25 moduli, ensuring a spatial resolution of $\sim$ 20 μm in the radial direction and $\sim$ 830 μm along $\hat{z}$. Both SSD layers have a pseudorapidity acceptance of $|\eta| < 0.9$ Few relevant numbers of the ITS layers are reported in Tab. 3.1.

The ITS detector was designed to ensure a precise track and secondary vertex reconstruction close to the interaction point, in condition of high charged particles multiplicity, typical for heavy-ion collisions at ultra-relativistic energy. In particular, this detector was originally build in order to:

- improve spatial, angular and momentum resolution for tracks reconstructed inside the *Time Projection Chamber* (TPC);
- identify secondary decay vertices for particles with a short lifetime, for example heavy-flavour hadrons ($c\tau(\mathrm{D}^0) = 122.9$ μm, $c\tau(\Lambda_c^+) = 60$ μm), distinguishing them from the primary one [3];
- reconstruct the primary vertex with a resolution better than 100 μm;
- reconstruct and identify charged particles with $p_\mathrm{T} \lesssim 200$ MeV/c;
- enhance the PID capabilities of the apparatus, thanks to the analogical readout equipped on the SDD and SSD layers;
- offer additional trigger opportunities through the SPD detector, the first silicon vertexer able to provide this feature.

3.2.2 Time Projection Chamber (TPC)

The *Time Projection Chamber* (TPC) [223] is the main tracking detector of the ALICE experiment. It is optimized to measure the momentum of charged particles, to identify them and to find the interaction vertex, together with the ITS. The azimuthal acceptance is 360^o, while the covered pseudorapidity range is $|\eta| < 0.9$ for particles able to reach the TOF detector. The pseudorapidity acceptance for slower particles is $|\eta| < 1.5$. The TPC has a cylindrical shape, with an internal radius of $\sim$ 85 cm, an external one of $\sim$ 247 cm and a length of $\sim$ 510 cm, for a total active volume of $\sim$ 88 m^3, being currently the largest TPC mounted on an experimental apparatus. It is divided in two sectors by the presence of a central cathode kept at the high negative

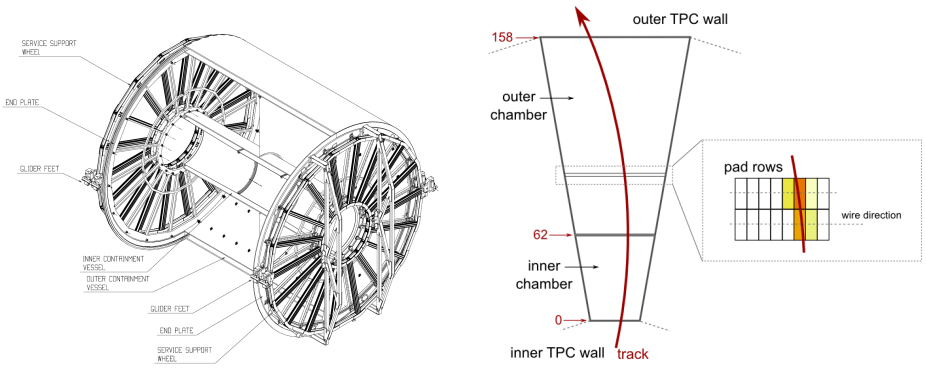

FIGURE 3.4: Left: TPC detector structure. Image taken from [213]. Right: Bases azimuthal sections of TPC detector. Every trapezoidal section is divided in inner region (*Inner ReadOut Chamber*, IROC) and outer region (*Outer ReadOut Chamber*, OROC). Image taken from [224].

potential V ~ -100 kV, which generated a constant electric field of E $\simeq$ 400 V/cm thanks to the action of the external field cage. The internal volume is divided in two sections $\sim$ 2.5 m long, filled with a $Ne/CO_2/N_2$ mixture (90/10/5) which, in these conditions, guarantees a maximum drift time for electrons of $\sim$ 90 µs. The disadvantage of this mixture is the strong velocity dependence on the temperature, consequently the TPC needs a proper thermal stability ($\Delta T \leq 0.1$ K [225]). Electrons produced in the gas ionisation from traversing charged particles are subject to a drift motion towards the cylinder basis, which are azimuthally segmented in 18 trapezoidal sections, divided in an inner and an outer region, each of them equipped with a Multi-Wire Proportional Chamber (MWPC), for a total of 36. (see right panel in Fig. 3.4). The two MWPC together count 159 readout pad rows, the cathodes collecting the avalanche originated by the primary electrons. This signal is used to reconstruct the *x-y* projection of the particle trajectory while the spatial information along the beam direction is provided by the drift time, measured thanks to a buffering of the collected charge with a fixed frequency. In this way, the TPC detector ensures a tridimensional track reconstruction for charged particles and delivers with a magnetic field of 0.5 T a resolution of 1% for low-momentum particles ($p_T \sim 1$ GeV/c) growing up to$\sim$ 3.5% for $p_T \sim 100$ GeV/c. The other fundamental TPC goal is to identify charged particles measuring their energy loss per unit length while passing through the gas using the amplitude of the MWPC signal (see the right panel of Fig. 3.19 and Sec. 3.7 for more details.).

3.2.3 Time Of Flight (TOF)

The *Time Of Flight* (TOF) [226] detector has a cylindrical geometry ensuring an azimuthal acceptance of 360° and a pseudorapidity coverage in the $|\eta| < 0.9$ range, with internal and external radius of $\sim$ 370 cm and $\sim$ 399 cm respectively. The basic constituent of this detector is a strip of Multi-gap Resistive-Plate Chamber (MRPC) in double-stack configuration, with an active area of 120×7.4 cm^2 (see right panel of Fig. 3.5). This device is composed by two cathodes and a central anode and the space among them is filled by a stack of fine glass plates separated by a 250 µm gap. In the full volume a uniform electric field of the order of $\sim$ kV/cm is applied. As a consequence, when a charged particle interacts with the gas in the active volume

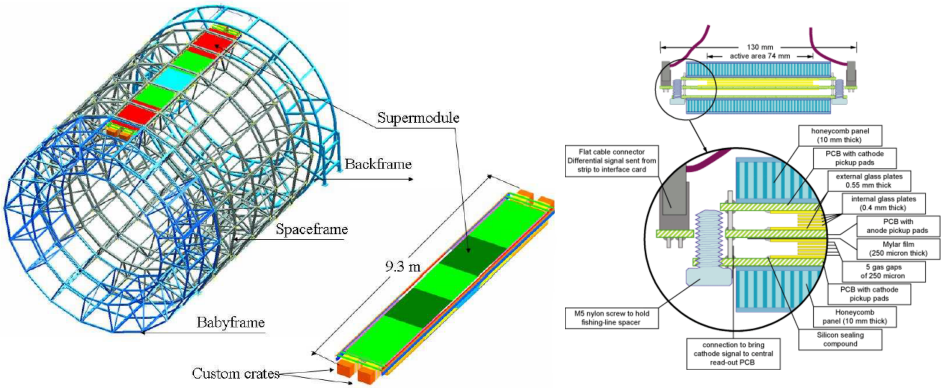

FIGURE 3.5: Left: TOF detector structure. Right: MRPC used in ALICE. Images taken from [213].

producing ionisation charges, an electron avalanche is produced in every vacuum space between two plates. The plates themselves stop the formed avalanches, but they are transparent to the fast signals induced on the electrodes by the ionisation electrons movement. Therefore, the final signal detected on the electrodes is the sum of the signals coming from every vacuum space between two plates. A detecting module is built placing the strips transversally oriented respect to the beam direction and tilted in order to suppress the number of very oblique transversal paths, which can create sharing effects of the signal among adjacent pads. In order to cover the full cylinder along the $\hat{z}$ direction, 5 modules of different lengths are used, in order to superimpose the junction regions with the dead areas of other detectors, so that the interference with external devices is reduced. For this reason, the central module is $\sim$ 117 cm long, the intermediate ones $\sim$ 137 cm and the external ones $\sim$ 177 cm, altogether making up one of the 18 supermodules composing the barrel.

The TOF detector is a PID dedicated system, which identifies charged particles measuring their time of flight on a fixed length L and with a given momentum p measured by the TPC. More details are reported in Sec. 3.7. The time of flight resolution reached by the TOF detector during the LHC Run 2 is about 56 ps [227].

3.2.4 ElectroMagnetic Calorimeter (EMCal)

The *ElectroMagnetic Calorimeter* (EMCal) [228] is positioned approximately opposite in azimuth with respect to the Photon-Spectrometer (PHOS) [229] and covers $|\eta| < 0.7$ and $80^o < \varphi < 187^o$ ($\Delta\varphi = 107^o$). It has a cylindrical geometry and it is located close to the ALICE magnet coil at a radius of $\sim$ 4.5 m from the beam pipe. The chosen technology is a layered lead-scintillator sampling calorimeter with a longitudinal pitch of 1.44 mm lead and 1.76 mm scintillator with longitudinal wavelength-shifting fibre light collection. The detector is segmented into 12288 towers, grouped into 12 Super Modules (Fig. 3.6) of two different types: 10 "full size" super modules (12×24 modules), spanning $\Delta\eta = 0.7$ and $\Delta\varphi = 20^o$, and 2 "one-third size" super modules (4×24 modules), which span $\Delta\eta = 0.7$ and $\Delta\varphi = 7^o$. Each module is made of 2×2 towers.

The EMCal detector is focused on the measurement of high-p_{T} photons, neutral mesons and electrons. It enables the full jet reconstruction in all collision systems from pp to Pb–Pb, by measuring the neutral energy component of jets. The energy

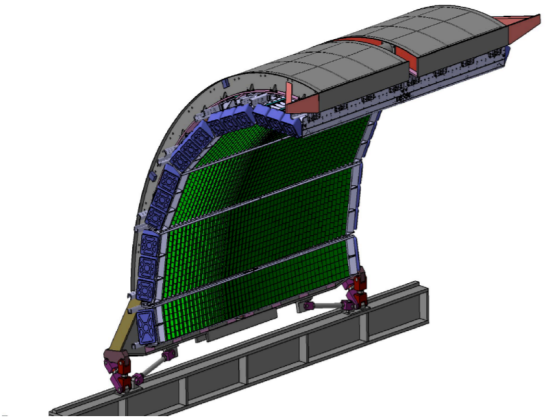

FIGURE 3.6: Array of EMCal Super Modules on the support structure. Figure from [228].

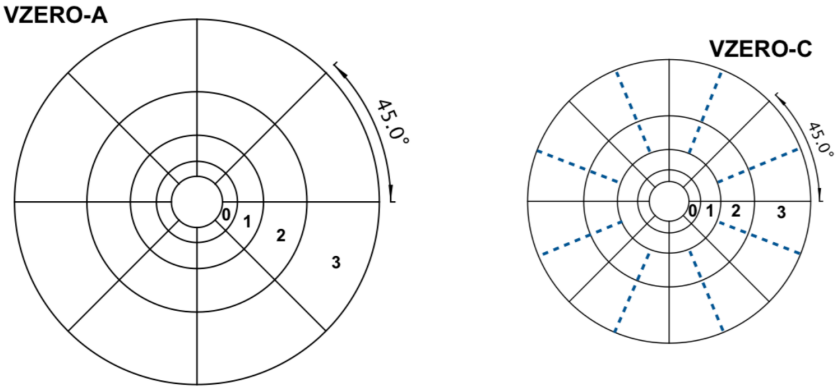

FIGURE 3.7: VZERO detector modules. Image taken from [230].

resolution provided by the EMCal can be parametrised as:

$$\frac{\sigma(E)}{E} = \sqrt{\left(\frac{a}{E}\right)^2 + \frac{b}{E} + c^2}\,, \tag{3.2}$$

where a, b, c are parameters determined from a fit of the energy resolution as a function of the incident energy determined with test beam runs using electrons with known energy. The energy resolution is better than 4% for $p_{\mathrm{T}} > 10$ GeV/c. The EMCal detector also provides a fast trigger (L0, L1 levels) for jets, photons and electrons, allowing the ALICE experiment to exploit the full luminosity of the LHC.

3.2.5 VZERO

The VZERO detector [230] is composed by two modules placed asymmetrically respect to the nominal interaction position ($z = 0$), covering the pseudorapidity ranges $2.8 < \eta < 5.1$ (VZEROA) and $-3.7 < \eta < -1.7$ (VZEROC) respectively (see Tab. 3.2). They are segmented in 4 rings in the radial direction and each of them is divided in 8 sectors 45° wide, for a total of 32 plastic scintillators for each module (see Fig. 3.7). The VZERO detector is used to select collisions between the two beams inside the central barrel and to distinguish them from background events due to the beam

Ring	VZEROA			VZEROC		
	η_{min}/η_{max}	r_{min}/r_{max} (cm)/(cm)	z (cm)	η_{min}/η_{max}	r_{min}/r_{max} (cm)/(cm)	z (cm)
0	5.1/4.5	4.3/7.5	329	-3.7/-3.2	4.5/7.1	-86
1	4.5/3.9	7.7/13.7	329	-3.2/-2.7	7.3/11.7	-87
2	3.9/3.4	13.9/22.6	329	-2.7/-2.2	11.9/19.3	-88
3	3.4/2.8	22.8/41.2	329	-2.2/-1.7	19.5/32.0	-88

TABLE 3.2: Geometric properties of VZEROA and VZEROC. Numbers from [230].

interaction with the gas inside the beam pipe. In addition, this detector measures basic physical quantities, like luminosity, charged-particles multiplicity used to define the centrality, and reaction plane direction in case of nucleus-nucleus collisions.

3.3 The ALICE offline framework

The raw data collected by the ALICE experiment in the last years sum to more than 160 PB. This huge amount of data requires a solid framework, able to process and analyse the stored collision events efficiently and to optimize the available computing resources. The complex of procedures to achieve this goal is referred to as a "computing model". The ALICE computing model is based on the Worldwide LHC Computing Grid (WLCG [231, 232]), a global infrastructure coordinated by CERN that connects 170 computing centres spread in 42 different countries in order to handle, store and process the data collected by the LHC experiments. The WLCG is the largest computing grid in the world, which provides near real-time access to LHC data regardless to the physical location. This is used for the reconstruction and analysis of collected data, as well as the processing of Monte Carlo simulations and it guarantees the storage and backup of LHC stored data, which totally amount to about 1 EB. The WLCG is hierarchically organised according to the MONARC model [233] in three "Tiers", which provide different levels of data collection and processing. The Tier 0 is located at the CERN computing centre and that at the Wigner Research Centre for Physics in Budapest, which keeps one replica and performs the first reconstruction of the raw data. A second replica of the raw and reconstructed data is stored in the Tier 1 centres, which are also involved in the reprocessing of the data and partially in the reconstruction. Finally there are the Tier 2 centres where the Monte Carlo simulations and the data analyses are performed. During a standard data taking year, when about 10^9 pp collisions and 10^8 Pb–Pb collisions are collected respectively, the storage of raw and reconstructed data, as well as the associated simulations and the information for detector calibration require about 12 PB [213]. The access to the ALICE collected and simulated data from everywhere in the WLCG is ensured by Alien (ALICE Environment [234]), a software that provides an interface dedicated for data access, analysis and simulation task execution on the grid and their status monitoring. The ALICE data are converted in the file format used in the ROOT framework [235], an object-oriented C++ coded tool designed for data manipulation and statistical analysis. ROOT is the core of the ALICE offline framework, which is organised in two main parts:

- AliRoot: this software is used for detector alignment and calibrations, Monte Carlo simulations and data reconstruction. It provides an interface to several event generators, such as PYTHIA [236] for pp collisions, used for Monte Carlo simulations. AliRoot includes a detailed description of the detector geometry and material budget, implemented in independent modules dedicated to the different subsystems. The detector response to the passage of charged particles is simulated with the help of different transport codes, such as GEANT3 [237], GEANT4 [238] and FLUKA [239];

- AliPhysics: this software contains all the code dedicated to the physics analysis. This is based on multiple tasks with a predefined structure, which are designed to process the collected and simulated events stored in the grid.

The ALICE offline framework will be completely renewed in view of the data taking campaigns in Run 3 and 4 at the LHC, being fully replaced by the O^2 framework [240] (see Chapter 6). The physical information about the collisions from real data and Monte Carlo simulations are stored in Event Summary Data (ESD) files. This format is mainly used for detector calibrations and performance studies and only the information relevant at the analysis level are kept in the Analysis Object Data (AOD), the data format typically processed by the analysis tasks. The latter format is lighter by about a factor 6 with respect to the ESD one, where the average size is about 400 kB/event and 2.2 MB/event for pp and Pb–Pb collisions respectively.

3.4 The trigger system and data acquisition

The ALICE experiment collects pp, p–Pb and Pb–Pb collision events with several trigger requirements. The trigger decision is produced in the Central Trigger Processor (CTP) [241] according to the signals from detectors and the LHC bunch filling scheme [242]. The CTP manages different trigger classes, which are mainly defined in terms of logical conditions demanded for the inputs and the set of detectors, called "clusters", required in the readout. According to the trigger class, events with different topologies are stored for the offline processing. In particular, the several hardware trigger classes are subdivided in two categories, Level 0 (L0) and Level 1 (L1), which are subsequently called during the events processing. The CTP evaluates the trigger inputs every $\sim$ 25 ns, which corresponds to a LHC clock cycle, and produces a L0 trigger decision $\sim$ 0.9 ns after the beam collide, exploiting the signal from fast detectors, namely SPD, V0, T0, EMCal, PHOS and muon trigger. The event selected by the L0 trigger is further processed by the L1 algorithm in the CTP, whose decision is made $\sim$ 6.5 µs after the L0 one, corresponding to a delay of 260 LHC clock cycles. The latency between L0 and L1 decisions is provoked by the computing time needed by some trigger detectors (for example TRD and EMCal), which generally depends on the events size, therefore on the collision system and background conditions. The L0 and L1 decisions are transmitted to the detectors with a further latency of $\sim$ 300 ns and trigger the event buffering in the detector front-end electronics. After that, the event is processed by the Level 2 decision (L2). This happens with a global delay with respect to the collision time of $\sim$ 100 µs, corresponding to the drift time of electron in the TPC. This time interval also includes the time required by the past-future protection circuits ($\sim$ 88 µs), which are employed in order to avoid the collisions selected for the readout to be spoilt by pile-up events. Finally, the several detector signals for the L2 accepted events are sent to the Data Acquisition System

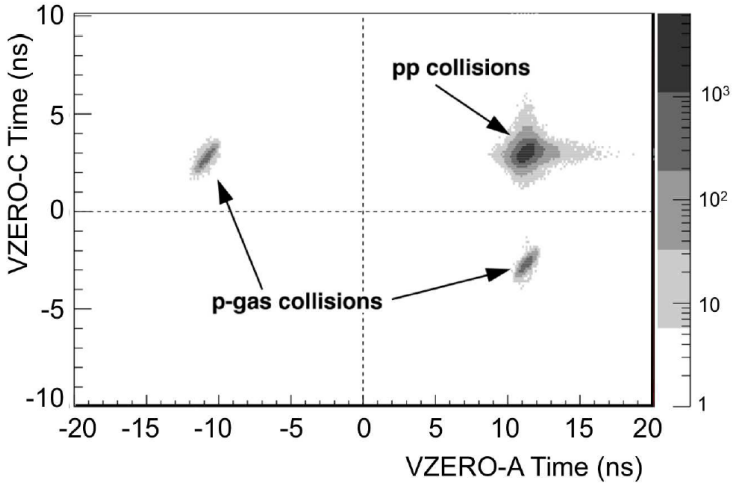

FIGURE 3.8: Time of flight of the particles detected in V0C versus V0A arrays. The dashed line intersection represents the time of the collisions at the nominal interaction point, or the crossing time of the background tracks at the vertical plane $z = 0$. Figure taken from [245].

(DAQ) [243] and the High Level Trigger (HLT) system [244], where the event building and online data compression are performed. The whole busy time is mainly determined by the CTP waiting for all detectors completing the readout. As an example, the busy time necessary for the electron drift and ion collection in the TPC is about ~ 300 μs.

3.4.1 The Minimum Bias trigger

The Minimum bias (MB) trigger, defined by the less biasing conditions for the data acquisition, is driven by the top ALICE physics goals, which mainly involve measurements at low transverse momenta for which demanding trigger selections cannot be applied. During the 2009 and 2010 data taking, a $\mathrm{MB_{OR}}$ trigger was built by requiring a hit in the SPD or in either one of the V0 arrays, ensuring a high event selection efficiency for both pp and Pb–Pb collisions. In the following years, with the increase of LHC luminosity and background amount, the MB trigger definition underwent several adaptations. The high-purity $\mathrm{MB_{AND}}$ trigger requires the coincidence between the V0A and V0C arrays and this is exploited also in the $\mathrm{MB_Z}$ trigger scheme for Pb–Pb events, where a further coincidence with signals in both the ZDC modules is required to suppress the contamination from the electromagnetic interactions between lead ions [230, 242].

In all the hadronic collision systems studied at LHC, a non-negligible background comes from the interaction of the beam with the residual gas inside the beam pipe, as well as the interactions of the beam halo with the several LHC components, such as beam collimators [230]. This beam-induced background is removed exploiting the timing of the V0 signal, reflecting the different arrival time to the V0 arrays of particles produced either by a beam-beam (BB) interaction of a beam-gas (BG) one. Given the instant time t_0 of the bunch crossing at the nominal interaction point, provided to the V0 detector from the LHC clock, three categories of events can be distinguished according to signal timing on the V0 arrays:

1. BB collisions: by definition, these events develop after the start provided by the t_0 instant, therefore particles coming from a physics event arrive at the V0A and V0C arrays approximately after 11.3 ns and 3.0 ns, respectively;

2. BG collisions behind V0C: if a beam-induced background event takes place at $z < -90$ cm with respect to the nominal interaction point, the produced particles arrive at the V0C counter 3.0 ns before the starting instant t_0, while they will be tagged at the opposite counter after 11.3 ns with respect to t_0;

3. BG collisions behind V0A: the symmetrical situation may happen in a spatial point with $z > 340$ cm with respect to the nominal interaction point and in this case the produce particles arrive at the V0A array about 11.3 ns before the t_0 instant, while they reach the V0C counter 3.0 ns after the t_0.

The V0 triggers use these different arrival times to define four interaction windows for each channel. They are called BBA, BBC, BGA and BGC, where BB stands for beam–beam (i.e. pp) and BG for beam–background interactions. The windows are centred at $+11.3$, $+3.0$, -11.3 and -3.0 ns with respect to t_0 for BBA, BBC, BGA and BGC respectively. The trigger is built with logical combinations of the status (hit or empty) of the windows [245]. In Fig. 3.8 the scatter plot between the two V0 array times is shown for particle produced in BB and BG events. Thanks to the time correlation between the two counters, the three categories of events described above can be clearly distinguished, since they lie on different quadrants. In particular, BB collisions are the only ones with a positive time for both the counters. These events can be still contaminated by BG interactions taking place between the two V0 counters, producing entries around the main correlation core, due to the random instant when these beam induced background events can happen.

3.5 Centrality determination in Pb–Pb collisions

The QGP is reproduced in the laboratory using collisions between lead beams accelerated at ultra-relativistic energies. In this way, energy-density values larger than 1 GeV/fm^3 are reached and the conditions for the QGP formation are met [242]. The topology of a single Pb–Pb collision is unknown a priori. Being the Pb nucleus a compound object with a radius $r = r_0 \cdot \mathrm{A}^{1/3} = 1.2$ fm $\cdot 208^{1/3} \approx 7.1$ fm, the event is characterised by the non-null impact parameter b between the colliding nuclei. This is defined as the distance between the centres of the two colliding ions on the transverse plane xy, where the ions move along the longitudinal direction $\hat{z}$. The impact parameter b and the $\hat{z}$ axis define the reaction plane of the collision. As one can see in Fig. 1.13, the amount of nucleons that participate (N_{part}) in the collision, as well as the number of binary interactions among nucleons (N_{coll}), directly depend on the impact parameter. This quantity influences the fraction of nuclear volume and the energy-density involved in the collision, determining the event centrality. The centrality is defined as the fraction of event characterised by an impact parameter up to a certain value b (percentile) and it is expressed as a fraction of the total hadronic cross section σ_{AA}:

$$c(b) = \frac{\int_0^b \frac{\mathrm{d}\sigma}{\mathrm{d}b'}\mathrm{d}b'}{\int_0^{+\infty} \frac{\mathrm{d}\sigma}{\mathrm{d}b'}\mathrm{d}b'} = \frac{1}{\sigma_{\mathrm{AA}}} \int_0^b \frac{\mathrm{d}\sigma}{\mathrm{d}b'}\mathrm{d}b' \,. \tag{3.3}$$

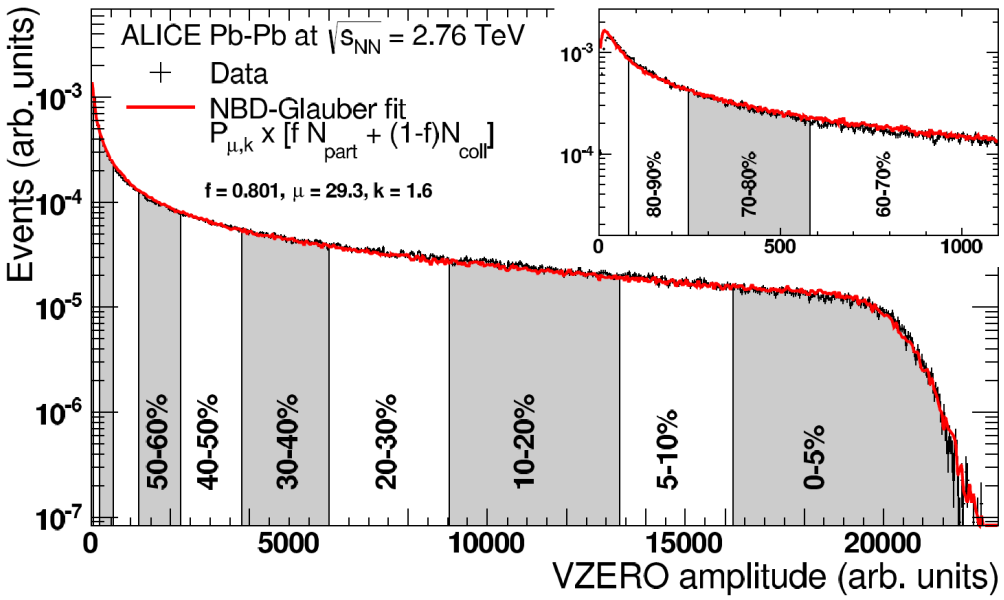

FIGURE 3.9: Distribution of the sum of signals registered by VZERO scintillator of ALICE experiment in Pb–Pb collisions at $\sqrt{s_{\rm NN}} = 2.76$ TeV. See the text for details. Image taken from [246].

The impact parameter cannot be accessed experimentally, therefore the collision centrality is estimated according to the event activity, using the produced particle multiplicity ($N_{\rm ch}$). Under the assumption that the particle multiplicity grows monotonically with the event centrality, this quantity can be experimentally computed as:

$$c \approx \frac{1}{\sigma_{\rm AA}} \int_{N_{\rm ch}}^{+\infty} \frac{{\rm d}\sigma}{{\rm d}N'_{\rm ch}} {\rm d}N'_{\rm ch} = \frac{1}{n_{\rm ev}^{\rm tot}} \int_{N_{\rm ch}}^{+\infty} \frac{{\rm d}n_{\rm ev}}{{\rm d}N'_{\rm ch}} {\rm d}N'_{\rm ch} \,, \tag{3.4}$$

where $n_{\rm ev}^{\rm tot}$ is the total number of collisions and ${\rm d}n_{\rm ev}$ is the number of events within a certain event multiplicity ${\rm d}N'_{\rm ch}$. The event multiplicity used to estimate the event centrality is usually determined with the V0 detectors. The distribution of the sum of signal amplitudes on the two V0 modules is used to determine the percentile of the hadronic cross section for each event, associated to a given value of V0 signal amplitudes. The centrality percentile is determined with respect to a so called "anchor point" that pinpoints the $\sim$ 90% of the total hadronic cross section, which determines the absolute scale of the centrality. This choice is driven by the fact that collisions characterised by an event multiplicity lower than that of the "anchor point" are strongly contaminated by electromagnetic events, which are not connected with the strong interaction between the two colliding beams and therefore they are not used for the centrality determination. Moreover, the low-multiplicity events are characterised by a fast-decreasing trigger efficiency, implying a larger amount of rejected events. In Fig. 3.9 the distributions of the sum of V0 signal amplitudes for Pb–Pb collisions at $\sqrt{s_{\rm NN}} = 2.76$ TeV is reported [246]. The distribution of particle multiplicity produced in Pb–Pb collisions is described by the analytical function:

$$g(n) = P_{\mu,k}(n) \times [f \cdot N_{\rm part} + (1-f) N_{\rm coll}] \,, \tag{3.5}$$

where the particle multiplicity produced in a single nucleon-nucleon interaction is described by the Negative binomial Distribution (NBD):

$$P_{\mu,k}(n) = \frac{\Gamma(n+k)}{\Gamma(n+1)\Gamma(k)} \cdot \frac{(\mu/k)^n}{(\mu/k+1)^{n+k}} \,. \tag{3.6}$$

The Eq. 3.6 defines the probability that a single emitting source (called "ancestor") produces n particles in the final state, with μ the mean multiplicity produced per ancestor and k a parameter governing the distribution width $D := \sqrt{\langle n^2 \rangle - \langle n \rangle} = \sqrt{\mu\,(1+\mu/k)}$. To determine the multiplicity distribution probability produced in a Pb–Pb collision, which is characterized by $N_{\rm part}$ participant nucleons and $N_{\rm coll}$ binary collisions among them, the probability of Eq. 3.6 is multiplied by the number of ancestors, parametrised by the second factor in Eq. 3.5. This linear combination is inspired by two-component models [247, 248] that decompose a nucleus-nucleus collision in soft processes, whose probability is proportional to $N_{\rm part}$, and hard processes, whose probability is proportional to $N_{\rm coll}$. The number of participant nucleons ($N_{\rm part}$) and the number of binary collisions among nucleons ($N_{\rm coll}$) derive from calculations based on the Glauber model [28]. Thanks to this technique, the limits of the centrality classes are defined in terms of percentiles of the total integral of the distribution. The resolution on the determination of the centrality varies from 0.5% in central events to 2% in peripheral Pb–Pb collisions.

3.6 Primary vertex and track reconstruction in the central barrel

The determination of the primary vertex and the track reconstruction in the central barrel follow a predefined workflow [242]. First of all, the signal released in the different detectors by charged particles are converted into "clusters", characterized by position, signal amplitudes, signal times and so on. After this procedure is repeated separately for each detector, a first reconstruction of the primary vertex is performed exploiting only the signal in the SPD, then the track finding and fitting are performed in the TPC and ITS with a Kalman filter- based algorithm [249]. After that, the track matching with the other central barrel detectors takes place and a final fit provides the global reconstructed tracks, which are finally used to definitively determine the primary vertex of the collision.

3.6.1 Preliminary determination of the primary vertex

The first step of the track reconstruction in the central barrel is a preliminary determination of the interaction vertex, which takes place exploiting the SPD "tracklets", namely lines that connect two clusters on the SPD, one cluster per layer. Candidate vertices are searched as the space points where a large number of tracklets converge and by definition the interaction vertex is identified as the one characterized by the maximum number of converging tracklets.

3.6.2 Track reconstruction

The track finding and fitting procedure is characterized by three subsequent steps, following the inward-outward-inward scheme shown in Fig. 3.10.

The first stage consists is a preliminary reconstruction of tracks in the TPC, which are then matched with the ITS detector. The procedure starts at the outermost radius

of the TPC detector, where tracks seeds are firstly defined as the connection among two clusters and the primary vertex, then among three consequent clusters without any vertex constraint. The clusters in the TPC derive from the granularity of the readout chambers, which are subdivided in 159 rows, therefore a track can produce up to 159 clusters in the TPC readout system. The inward propagation of the seeds takes place with a Kalman filter procedure, where at each step the track is updated considering the closest cluster according to specific proximity criteria. In order to avoid the same track to be reconstructed multiple times, due to the possibility for a cluster to be reused in multiple seeds, a special algorithm is used to look for pair of tracks that share a certain amount of clusters (between 25% and 50%), and according to some quality parameters based on cluster number, cluster density and momentum only one candidate track is kept. The track prolongation continues until the inner TPC radius is reached and only the tracks with at least 20 out of 159 possible clusters are accepted. The efficiency for the reconstruction of tracks in the TPC in pp collisions at $\sqrt{s} = 8$ TeV and for central (0-5%) and peripheral (80-90%) in Pb–Pb collisions at $\sqrt{s_{\mathrm{NN}}} = 2.76$ TeV as a function of the reconstructed transverse momentum p_{T} is shown in Fig. 3.11, showing no dependences on the detector occupancy. For low-p_{T} values, the trend of the efficiency is characterised by an evident drop, caused by the multiple scattering and energy loss in the detector material of charged particles that deflect the trajectory from the expected helix given by the magnetic field bending. At larger values, the efficiency assumes a characteristic shape given by the loss of clusters in the dead zones between consequent TPC end plate sectors. The tracks reconstructed in the TPC are then propagated to the outermost radius of the SSD detectors and are used as seeds for the track finding in the ITS. Similarly to what happens in the TPC, the ITS seeds are prolonged inward adding cluters in

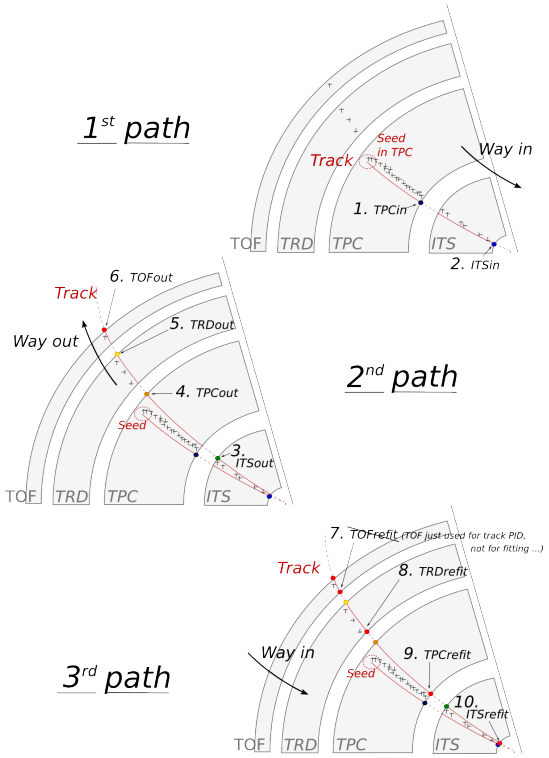

FIGURE 3.10: Principles of track reconstruction in ALICE, showing the three main steps in which this procedure develops. Image taken from [224].

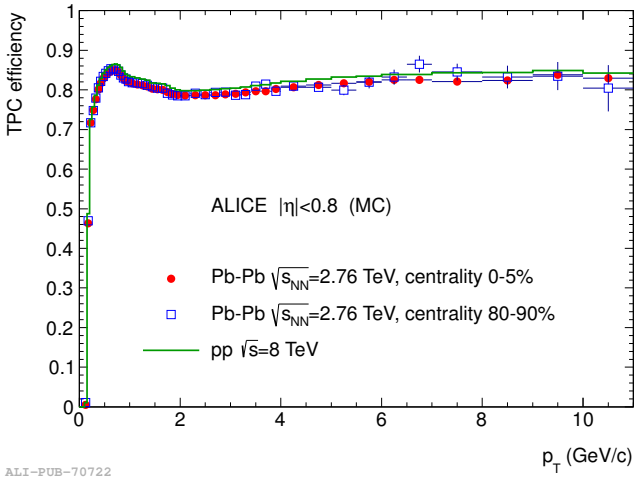

FIGURE 3.11: Reconstruction efficiency of TPC tracks in pp collisions at $\sqrt{s} = 8$ TeV and for central (0-5%) and peripheral (80-90%) in Pb–Pb collisions at $\sqrt{s_{\mathrm{NN}}} = 2.76$ TeV. Image taken from [242].

the following ITS layer according to specific proximity criteria. For each TPC track, all the possible inward propagations are buffered and at each prolongation step the reduced χ^2 from the Kalman-filter procedure is updated. Also in this case the track finding is performed in two consecutive passes, with and without the primary vertex constraint. Once all the candidates associated to a single seed are prolonged towards the innermost ITS layer, they are sorted in according to the reduced χ^2 and only the highest quality track is maintained. At this stage, the chosen track is selected from a bunch of high-quality candidates, which are inspected to look for cluster sharing: if any, an additional attempt is done to find an alternative among the other candidates. At this stage, the efficiency drop for low-p_{T} particles shown in Fig. 3.11 is counterbalanced by an ITS standalone tracking procedure. Helical seeds are built using two clusters from the three innermost ITS layers and the primary vertex, then each seed is propagated to the outer layers according to the proximity criteria cited above. Also in this case, the final track is chosen to be that with the highest reduced χ^2 from the Kalman-filter fitting, and the tracking efficiency is maximised by repeating the procedure several times and enlarging the opening angle adopted for the track prolongation. Only clusters not yet used for the global track reconstruction are used at this stage. In this way, charged particles with transverse momenta down to about 80 MeV/c are reconstructed, removing the efficiency drop mentioned above, which for pions and protons takes place below the cutoff values of $p_{\mathrm{T}} = 200$ MeV/c and $p_{\mathrm{T}} = 400$ MeV/c respectively[3].

When the reconstruction in ITS is complete, the tracks are propagated to the point of closest approach to the preliminary vertex found before using the SPD tracklets only, then an outward refitting of the track starts. This procedure adopts the same clusters of previous stages until the outer radius of the TPC is reached. At this stage, an attempt to match the track with a TRD tracklet takes place, and in case of success this procedure is repeated with the TOF and the outermost detectors, namely EMCal, PHOS and HMPID. The kinematic properties of the tracks are not updated by the detectors more external to the TPC, but their information is kept for particle identification purposes (see 3.7).

[3]The different cutoff values are due to the mass dependence of the multiple scattering of charged particles with the detector material.

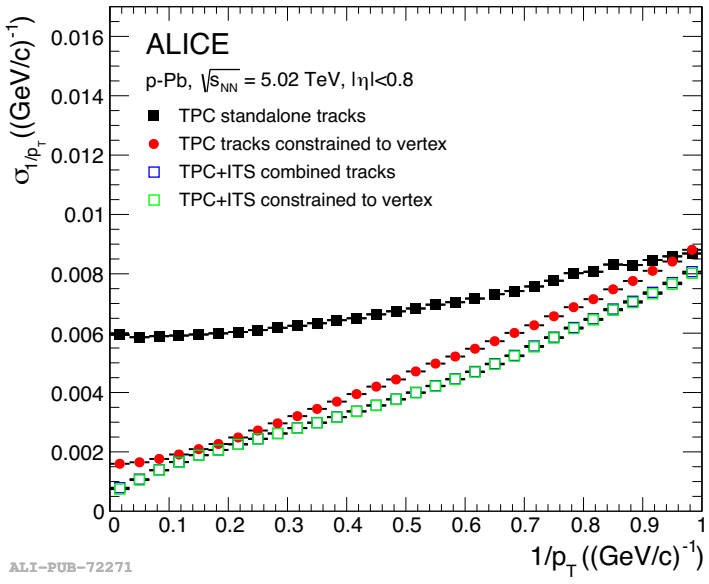

FIGURE 3.12: Resolution of $1/p_{\mathrm{T}}$ track parameter as a function of $1/p_{\mathrm{T}}$ in p–Pb collisions at $\sqrt{s_{\mathrm{NN}}} = 5.02$ TeV. This quantity is reported for tracks fitted either only with the TPC or matching them to the ITS detector. The cases with and without the constraint to vertex are also reported. Figure taken from [242]

Finally, all tracks are re-propagated inwards with the Kalman-filter procedure through the same clusters adopted at the previous stages. The track parameters and the associated covariance matrix are finally determined.

In Fig. 3.12 the $1/p_{\mathrm{T}}$ resolution for reconstructed tracks either only with the TPC or with the matching to the ITS detectors is shown as a function of $1/p_{\mathrm{T}}$. This is one parameter of the six-component vector defining a track in the Kalman filter algorithm and it is proportional to the track curvature, therefore its resolution comes directly from the covariance matrix of the track. This quantity is related to the transverse momentum resolution by the following relation:

$$\sigma_{p_{\mathrm{T}}} = p_{\mathrm{T}}^2 \cdot \sigma_{1/p_{\mathrm{T}}} \quad \Rightarrow \quad \frac{\sigma_{p_{\mathrm{T}}}}{p_{\mathrm{T}}} = \frac{\sigma_{1/p_{\mathrm{T}}}}{1/p_{\mathrm{T}}} \,. \tag{3.7}$$

According to the measured curvature resolutions, the relative precision on the reconstructed p_{T} changes from a value of about 1% at $p_{\mathrm{T}} = 1$ GeV/c to about 10% for tracks with $p_{\mathrm{T}} = 100$ GeV/c. In Fig. 3.12 the effect of the constraint to vertex is shown for tracks reconstructed either with the TPC only or with the prolongation to the ITS detector. In the former case, the curvature precision is strongly improved and its almost comparable to that of the global tracks. This experimental constraint may be helpful in case of significant ITS inefficiencies, which reduces the available statistics due to a decrease of the matching efficiency for TPC tracks with the ITS.

3.6.3 Final determination of the interaction vertex

When the final set of global tracks is established, a new determination of the interaction vertex takes over the one performed with the SPD tracklets, described in Sec. 3.6.1. The global tracks are extrapolated inward to their point of closest approach and a first determination of the interaction vertex takes place. At this stage, the far outliers with respect to the nominal beam line are not taken into account. After

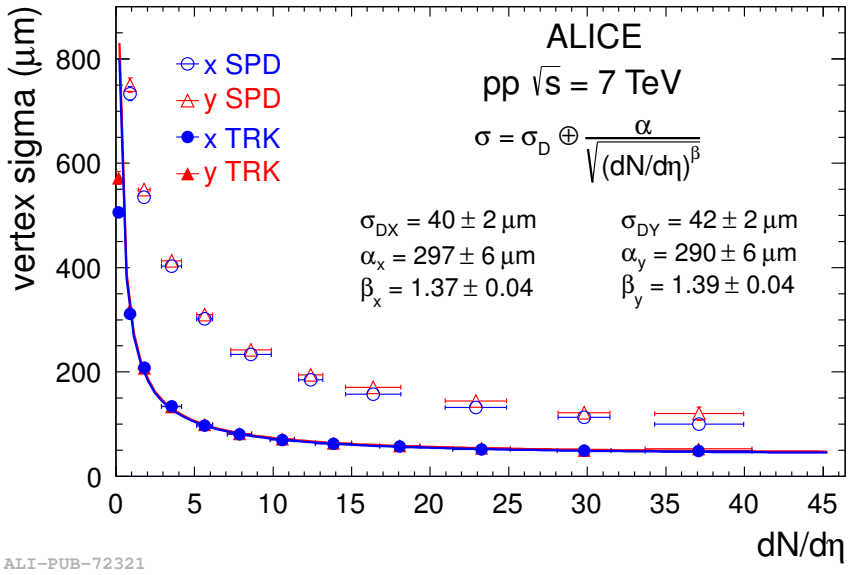

FIGURE 3.13: Resolution of the interaction vertex position as a function of the charge particle multiplicity per unit of pseudorapidity in pp collisions at $\sqrt{s} = 7$ TeV. The trend of the vertex width determined with the global tracks is parametrized with the power law function $\alpha/(\mathrm{d}N/\mathrm{d}\eta)^{\beta/2}$, where α and β are free parameters. This quantity is added in quadrature with the baseline width σ_{D}, corresponding to the size of the luminous region. Figure taken from [242].

that, a more precise vertex fitting is performed using the track-weighting procedure described in Ref. [250], in order to suppress the contribution of the remaining outliers. The precision on the vertex determination increases with the number of tracks involved in the vertex fitting procedure. For this reason, the transverse vertex position in low-multiplicity events is improved by adding in the fit the nominal beam position, considered as an independent measurement with the transverse size of the luminous region as associated uncertainties [4]. A more sophisticated algorithm, based on Tukey bisquare weights [251] is adopted in high-multiplicity events, where a high pileup rate is expected, in order to further suppress outliers.

In Fig. 3.13 the resolution of the interaction vertex position as a function of the charge particle multiplicity per unit of pseudorapidity in pp collisions at $\sqrt{s} = 7$ TeV is shown. As mentioned before, the precision in the interaction vertex determination with the global tracks fast improves as a function of track multiplicity and its trend can be parametrized with the power law function $\alpha/\sqrt{(\mathrm{d}N/\mathrm{d}\eta)^{\beta}}$. The primary vertex determination described in this Section guarantees an improvement of more than a factor 2 in resolution with respect to the SPD tracklet- based technique mentioned in Sec. 3.6.1.

3.6.4 ITS-TPC matching efficiency

The propagation of the TPC reconstructed tracks towards the ITS detector is a crucial step for the definition of global tracks, as described in Sec. 3.6.2. This operation consists in matching a TPC track with clusters of the ITS detector. In case the matching

[4] The interaction region, also called "beam size", is defined as the convolution of the particle distributions of the two colliding bunches. The interaction vertex lies within the luminous region with dimensions $\sigma_i^{\mathrm{lumi}} = \sigma_i^{\mathrm{beam}}/\sqrt{2}$, where $i = x, y, z$.

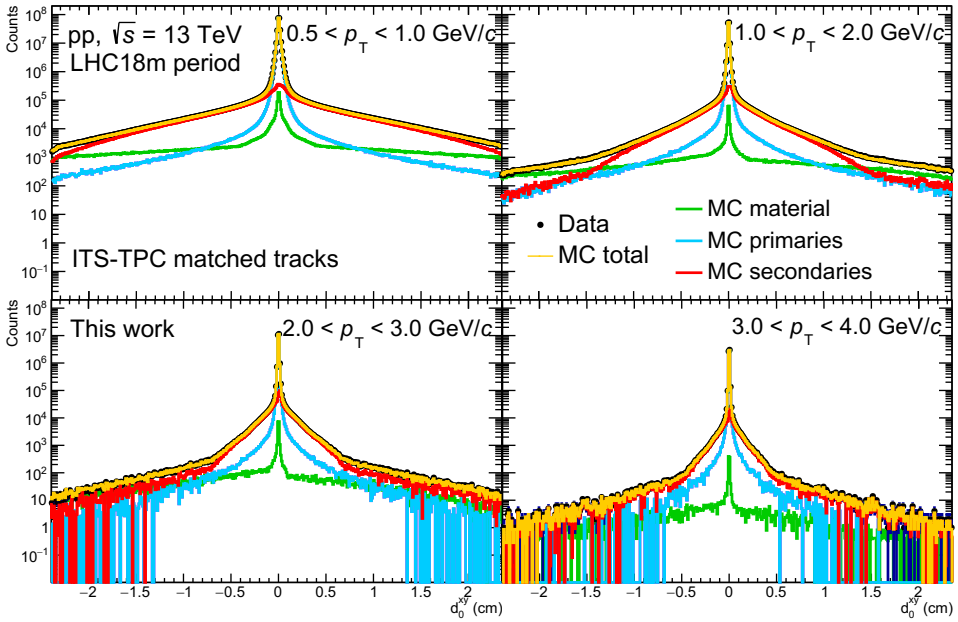

FIGURE 3.14: Single track impact parameter d_0^{xy} distribution in different single-track transverse momentum intervals in a sample of pp collisions at $\sqrt{s} = 13$ TeV collected in 2018 described with a template fit, where the profiles of primary (blue) and secondary (red) particles as well as that for particles produced in the interaction with the material (green) are taken from MC simulations.

efficiency in Monte Carlo simulations is not representative of that in collected data, the MC-based efficiency correction may introduce a bias in the measurement. Such an effect is evaluated by looking at the ITS-TPC matching efficiency as a function of particle p_T separately in data and MC and quantifying a systematic uncertainty according to the possible differences. The ITS-TPC matching efficiency is computed as the number of tracks successfully fitted with the Kalman filter in the TPC and ITS, with at least one hit in the SPD layers ($N_{\mathrm{ITS-TPC}}(p_T)$), divided by the number of reconstructed tracks successfully fitted in the TPC ($N_{\mathrm{TPC}}(p_T)$):

$$\varepsilon^{\mathrm{matching}}_{\mathrm{ITS-TPC}}(p_T) = \frac{N_{\mathrm{ITS-TPC}}(p_T)}{N_{\mathrm{TPC}}(p_T)} , \tag{3.8}$$

where p_T indicates the transverse momentum of the track. This procedure is performed separately on the collected collision samples and the associated MC productions, independently for each data taking period. The discrepancy between data ($\varepsilon^{\mathrm{Data}}$) and the MC simulation ($\varepsilon^{\mathrm{MC}}$) is used to estimate a systematic uncertainty as:

$$\mathrm{syst.}^{\mathrm{matching}}_{\mathrm{ITS-TPC}} = \frac{\varepsilon^{\mathrm{Data}}(p_T) - \varepsilon^{\mathrm{MC}}(p_T)}{\varepsilon^{\mathrm{Data}}(p_T)} . \tag{3.9}$$

The ITS-TPC matching efficiency is expected to be higher for primary particles, namely those produced in the collision or coming from decays of charm and beauty hadrons with a proper decay length of order of tens-hundred of microns, than for secondary particles produced in the interactions with the detector material or in decays of strange hadrons, which have a typical proper decay length of several centimetres. This separation is not doable on data for tracks reconstructed in the TPC,

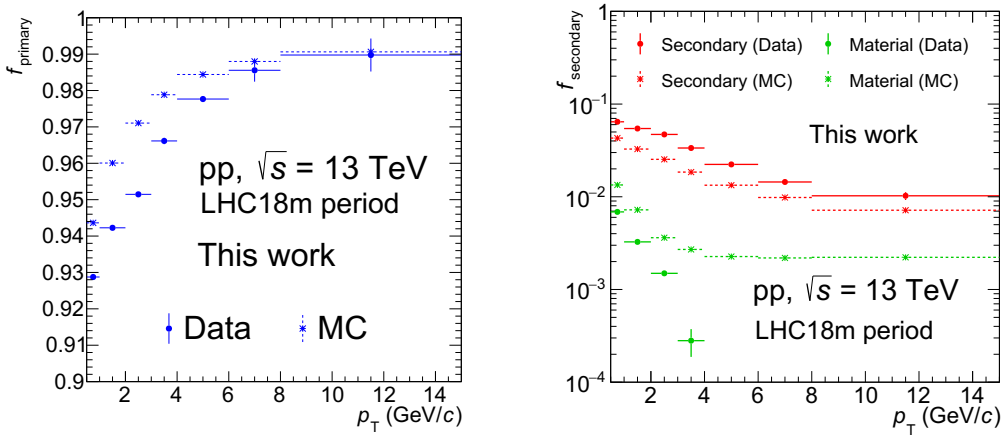

FIGURE 3.15: Primary (left) and secondary (right) relative abundances in a sample of pp collisions at $\sqrt{s} = 13$ TeV collected in 2018 compared with the values from MC simulations as a function of track p_T.

therefore the inclusive (primary + secondary tracks) ITS-TPC matching efficiency is measured and compared between data and MC. The MC simulations with PYTHIA + GEANT3 may not reproduce correctly the relative abundances of particles produced in data and this introduces a bias in the matching efficiency estimation. Therefore, the fractions of primary (f_{primary}) and secondary ($f_{\text{secondary}}$) particles measured in data are used to calculate the inclusive ITS-TPC matching efficiency in MC (ε^{MC}), namely:

$$\varepsilon^{\text{MC}} = f_{\text{primary}}(\text{TPC}) \cdot \varepsilon^{\text{MC}}_{\text{primary}} + (1 - f_{\text{primary}}(\text{TPC})) \cdot \varepsilon^{\text{MC}}_{\text{secondary}} \,, \tag{3.10}$$

where $\varepsilon^{\text{MC}}_{\text{primary}}$ and $\varepsilon^{\text{MC}}_{\text{secondary}}$ correspond to the primary and secondary particle matching efficiency estimated in MC simulations. The relative abundances of primary and secondary particles in the analysed data sample are estimated with a template fit of the single-track impact parameter d_0^{xy} distribution, as showed in Fig. 3.14 for a sample of pp collisions at $\sqrt{s} = 13$ TeV collected in 2018. The distribution in data (black) is well described by the global template (yellow), defined as the sum of the templates of primary (blue) and secondary (red) particles, as well as those produced by the particle interaction with the material (green), which are constrained by the requirement $f_{\text{primary}} + f_{\text{secondary}} + f_{\text{material}} = 1$.

The template of primary particles is peaked at $d_0^{\text{xy}} = 0$ cm, while the contribution of the tails in the templates of secondary particles and those produced in the interaction with material increases significantly, reflecting the larger distances with respect to the primary vertex where the conversions take place. The templates adopted in these fits are defined by the d_0^{xy} distribution shape for each category of tracks as described in the MC simulations. The fit procedure is performed separately in different p_T intervals, where the relative abundances are expected to change. In particular, with increasing p_T the amount of secondary particles is expected to significantly decrease, with a consequent increase of the primary particle fraction and a reduction of the distribution tails. The primary and secondary particle fractions deriving from these fits are shown in Fig. 3.15 as a function of single-track p_T. The values from data are compared with those from the simulations. A lower fraction of primary particles is obtained from the template fit in data at all transverse momenta, with a maximum

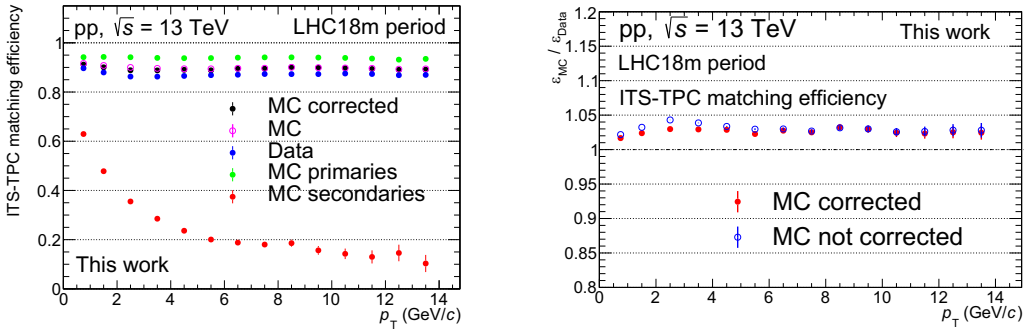

FIGURE 3.16: Left: single-track ITS-TPC matching efficiency estimated in pp collisions at $\sqrt{s} = 13$ TeV collected in 2018 and in simulated events. The values for the matching efficiency before and after the relative abundance correction are reported and the efficiency for primary and secondary particles separately in MC simulations is also shown. Right: ITS-TPC matching efficiency ratio between MC and data, with efficiency in MC measured before (blue) and after (red) the primary and secondary fraction correction from data.

difference of about 2% at low p_T. As a consequence, the secondary fraction from data is slightly larger than that in MC in all the p_T intervals. The fraction of particles produced in the interaction with material quickly decreases with p_T, being fully negligible for $p_T > 4$ GeV/c. The particle abundances obtained with this procedure represent the fractions of primary and secondary particles that satisfy the ITS-TPC matching, since the impact parameter distribution fitted with the template method is obtained considering particles that matched the ITS, so that a good pointing resolution is granted and the different contributions can be distinguished. However, the fractions of primary and secondary particles in the TPC are necessary to estimate the ε^{MC}. For this reason, the $f_{primary}$ obtained from the fits is further scaled before being used in Eq. 3.10, namely:

$$f_{primary}(\text{TPC}) = f_{primary}(\text{ITS} - \text{TPC}) \cdot \left[\frac{f_{primary}(\text{TPC})}{f_{primary}(\text{ITS} - \text{TPC})} \right]_{MC} , \tag{3.11}$$

where $f_{primary}(\text{ITS} - \text{TPC})$ is the fraction of primary particles obtained with the template fits mentioned above. This is then scaled by a correction factor from MC so that it refers to the fraction of primary particles in the TPC, without any requirement on the matching to the ITS. An alternative procedure is used to avoid the need of scaling the $f_{primary}$ obtained from the fit by a factor determined from MC simulations. The template fits on the impact-parameter distribution are referred to TPC tracks, without any constraint from the ITS detector, and this would directly provide the $f_{primary}(\text{TPC})$ quantity. However, in such a case the pointing resolution is much poorer due to missing points close to the primary vertex for several tracks, therefore the first method is preferred. The ITS-TPC matching efficiency measured in collected pp collisions at $\sqrt{s} = 13$ TeV and in simulated events is shown in the left panel of Fig. 3.16, where the efficiency for all particles in MC simulations before and after the relative abundance correction is reported. As a direct consequence of the different primary and secondary particle fractions in data and MC, the matching efficiency after the relative abundance correction is slightly different from that before such correction, especially for $p_T < 6$ GeV/c. In the same plot, the ITS-TPC matching efficiency for primary and secondary particles isolated in MC events are shown.

The efficiency for primary particles is higher by construction and it is observed to be flat with p_{T} at about 95%, while the efficiency for secondary particles decreases from about 60% at low p_{T} to about 10% at $p_{\mathrm{T}} = 14$ GeV/c. These different trends and magnitudes support the need of correcting the relative abundances in MC with those from data, otherwise wrong values of primary and secondary particle fractions would correspond to biased total efficiencies measured in MC events. In the right panel of Fig. 3.16 the ITS-TPC matching efficiency ratio between MC and data is shown before (blue) and after (red) the correction of primary and secondary particle fractions. The latter case is used to estimate the systematic uncertainty related to the ITS-TPC matching efficiency, given that the efficiency measured in MC simulations is systematically higher than that from data. This work is repeated separately for each data taking period and the associated MC productions. From the analysis of the 33 periods of pp collisions at $\sqrt{s} = 13$ TeV collected in 2016, 2017 and 2018 the overall mismatch in the ITS-TPC matching efficiency observed with the simulations amounts to 2-4% depending on the single-track p_{T} and the specific data taking period.

3.6.5 Track impact parameter smearing in MC simulations

The efficiency times acceptance correction estimated with MC simulations is valuable only if the simulation well reproduces the detector performance and the data taking conditions. Dedicated studies are done to quantify possible differences in the track impact parameter reconstruction between data and MC simulations. For all the analyses requiring a single-track impact parameter precision at the order of microns, the efficiency calculation is forerun by a smearing of the impact parameter of each reconstructed track, applied to reduce the systematic bias on the efficiency that a possible discrepancy may cause. Such difference between data and simulations may be related to residual misalignments of the ITS detector not well reproduced in MC simulations. This smearing is particularly important in the analyses that identify the decay vertices of charm particles, since the topological selections applied for this purpose are particularly sensitive on the resolution of the track position in the vicinity of the primary vertex. In panel (A) of Fig. 3.17 the impact parameter normalised distribution of reconstructed tracks in a sample of pp collisions at $\sqrt{s} = 13$ TeV collected by the ALICE experiment at the beginning of 2018 (period LHC18b) is shown. The distribution is described with an analytical function that aims to parametrise the contribution of primary particles peaking around 0 and that from secondary particles that populate the distribution tails:

$$f(d_0^{\mathrm{xy}}) = \frac{p_4}{\sqrt{2\pi}p_0} e^{-\frac{\left(d_0^{\mathrm{xy}} - p_1\right)^2}{2p_0^2}} + \frac{1-p_4}{2p_3} e^{-\frac{|x-p_1|}{p_3}} \,. \tag{3.12}$$

The primary track contribution is parametrised with a Gaussian function, while the tails of the distribution mainly populated by secondary tracks are described with an exponential. The distribution shown in Fig. 3.17 is related to tracks reconstructed on the whole azimuth at midrapidity and with transverse momentum within $0.47 < p_{\mathrm{T}} < 0.59$ GeV/c. This procedure is repeated in narrow p_{T} intervals and the p_{T}-dependence of the Gaussian mean and resolution is evaluated for reconstructed tracks in both collected and simulated pp collisions. Moreover, the whole procedure is repeated separately for each data taking period and associated MC samples. The impact parameter of each reconstructed track in MC simulations is corrected with the following relation:

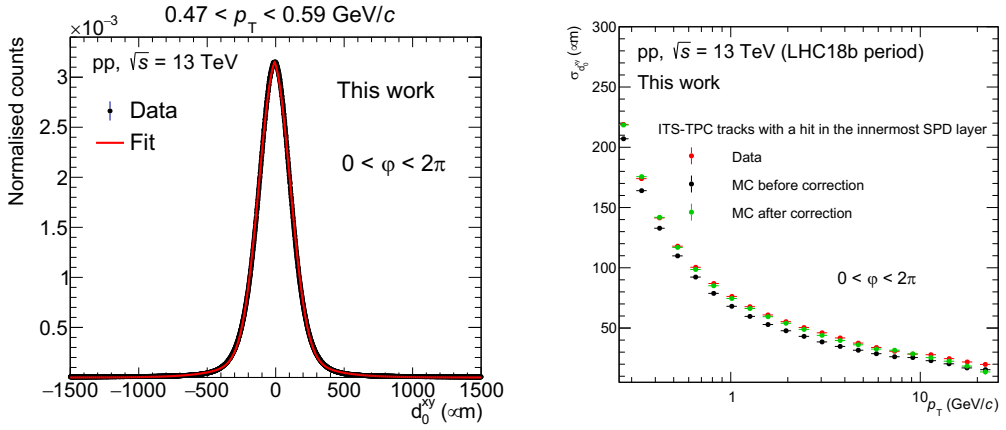

(A) (B)

FIGURE 3.17: (A): impact parameter distribution of reconstructed tracks, fitted with an analytical function. (B): impact parameter resolution of reconstructed tracks in data, compared with the same quantity for reconstructed tracks in MC simulations before and after the single track smearing.

$$
\begin{aligned}
d^{xy}_{0,\text{ reco. MC, corr.}}(p_T) = {} & d^{xy}_{0,\text{ gen. MC}}(p_T) \\
& + \left(d^{xy}_{0,\text{ reco. MC}}(p_T) - d^{xy}_{0,\text{ gen. MC}}(p_T) \right) \cdot \frac{\sigma^{\text{Data}}(p_T)}{\sigma^{\text{reco. MC}}(p_T)} \\
& + \left(\langle d^{xy}_{0,\text{ reco. MC}} \rangle (p_T) - \langle d^{xy}_{0,\text{ Data}} \rangle (p_T) \right) .
\end{aligned}
\tag{3.13}
$$

The value assigned to a reconstructed track in simulated events is calculated starting from the generated impact parameter ($d^{xy}_{0,\text{ gen. MC}}(p_T)$). The term in the second line of Eq. 3.13 scales the impact parameter residual between the reconstructed and generated values ($d^{xy}_{0,\text{ reco. MC}}(p_T) - d^{xy}_{0,\text{ gen. MC}}(p_T)$) in the simulation by the ratio between $\sigma^{\text{Data}}(p_T)$ and $\sigma^{\text{reco. MC}}(p_T)$. This correction term is introduced to adapt the impact parameter resolution in the simulation $\sigma^{\text{reco. MC}}(p_T)$ to that present in data $\sigma^{\text{Data}}(p_T)$. The values of $\sigma^{\text{reco. MC}}(p_T)$ and $\sigma^{\text{Data}}(p_T)$ come from the impact parameter distribution fit performed with the function reported in Eq. 3.12, as shown in the example plot in the panel (A) of Fig. 3.17. In the panel (B) the impact parameter resolution as a function of p_T of reconstructed tracks in data (red) and in simulations is shown. The resolution in simulated events derives from the fit to the impact parameter distribution of reconstructed tracks before (black) and after (green) the application of the smearing of Eq. 3.13 on each single track. The resolution in MC simulations is systematically lower than that in data, but the application of the smearing procedure ensures a better matching between the two cases. The same resolution correction is applied to all tracks, namely no distinction among different azimuthal angle ranges is considered, since no significant dependences on φ are observed. The impact parameter resolution in the considered pp collision sample decreases from about ~ 240 μm at $p_T = 0.3$ GeV/c to about ~ 20 μm at $p_T = 20$ GeV/c. The third row of Eq. 3.13 refers to the correction of the impact parameter mean, consisting in a shift by $\langle d^{xy}_{0,\text{ reco. MC}} \rangle (p_T) - \langle d^{xy}_{0,\text{ Data}} \rangle (p_T)$ thought to centre the $d^{xy}_{0,\text{ reco. MC, corr.}}(p_T)$ distribution

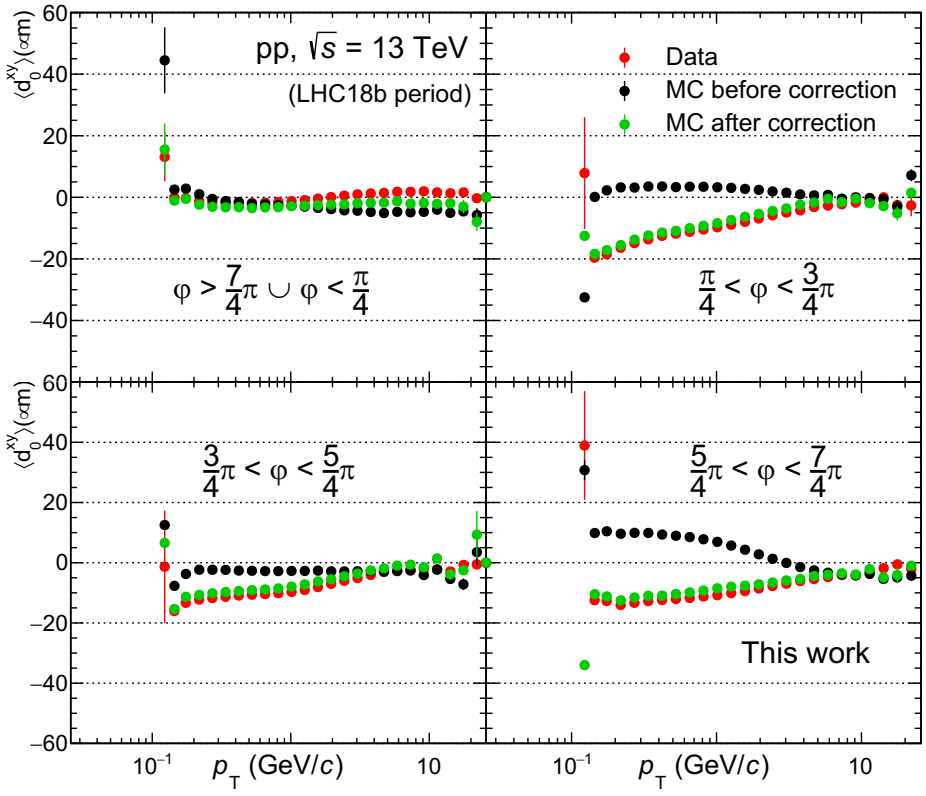

FIGURE 3.18: Impact parameter mean as a function of p_T for reconstructed tracks in collected pp collisions at $\sqrt{s} = 13$ TeV and for reconstructed tracks in simulated events before and after the single track smearing. The four quadrants refer to the four azimuthal angle intervals where the smearing procedure is separately performed.

around $\langle d^{xy}_{0,\,\mathrm{Data}} \rangle (p_T)$. The impact parameter mean of reconstructed tracks as a function of p_T in data (red) and simulated events before (black) and after (green) the single-track smearing is shown in Fig. 3.18. For the mean a more granular approach with respect to what done for the resolution correction is required, given that the p_T-trend of the impact parameter mean in data and MC is observed to be different in several azimuthal angle intervals. The four panels are related to four different azimuthal angle regions where the impact parameter distributions in narrow p_T intervals are evaluated separately: $\varphi > \frac{7\pi}{4} \bigcup \varphi < \frac{\pi}{4}$, $\frac{\pi}{4} < \varphi < \frac{3\pi}{4}$, $\frac{3\pi}{4} < \varphi < \frac{5\pi}{4}$ and $\frac{5\pi}{4} < \varphi < \frac{7\pi}{4}$. Also in this case, after the application of the single-track smearing on reconstructed tracks in simulated events the impact parameter mean well matches that measured in data and the procedure successfully cures differences up to 20 μm.

Also the uncertainty on the impact parameter in simulations is corrected to match that in data, via the scaling by $\sigma^{\mathrm{Data}}(p_T)/\sigma^{\mathrm{reco.\,MC}}(p_T)$ described above. On top of this, the data/MC ratio of the impact parameter pulls $d^{xy}_{0,\,\mathrm{reco}}(p_T)/\sigma^{\mathrm{reco.}}(p_T)$ is used to smear the covariance matrix entries, given that the resolution correction does not correct them. The correction of the mean is even more granular in Pb–Pb events, where the comparisons between data and simulations evidence discrepancies in the impact parameter values up to 60 μm. In this case, the $\langle d_0^{xy} \rangle$ correction is performed in 24 azimuthal sectors.

3.7 Particle identification

The ALICE apparatus can praise unique *particle identification* (PID) capabilities in a wide momentum range, due to the several techniques exploited by the different subsystems. The charged particle identification can be performed via the measurement of specific energy loss in ITS and TPC detectors, as well as through the measurement of their time of flight, measured by the TOF detectors. The usage of the HMPID pushes the particle identification capabilities in the central barrel to higher momentum values, thanks to the measurement of the Cherenkov angle emitted by charged particles traversing the apparatus. Specific electron identification is also provided by the TRD detector, which exploits the light emitted by high-energy particles crossing the boundary between two different dielectric materials, and the PHOS and EMCal calorimeters, where the energy deposit is compared to the particle momentum (E/p). In the following sections, a brief description of the particle identification in ITS, TPC and TOF, used in the analyses concerning this thesis, is reported. The electron identification capabilities of the ALICE apparatus in the central barrel are exploited to isolate a pure sample of electrons, necessary to extract the signal from charm and beauty hadron decays. Moreover, the proton, kaon and pion identification provided by the TPC and TOF detectors are exploited to enhance the signal-to-background ratio in the $\Lambda_c^+ \rightarrow \mathrm{pK}^-\pi^+$ reconstruction. The practical usage of such PID techniques in the analyses will be explained in Chapters 4 and 5.

3.7.1 Particle identification in the ITS

The charged particle identification in the ITS detector is performed by measuring the atomic electrons extracted via ionization from the material of the four outermost layers (SDD, SSD), where the analogical readout systems are able to collect the ionization charge. The $\mathrm{d}E/\mathrm{d}x$ of each track is calculated as a truncated mean of the measured values in each layer, if at least three of them returns a non-null response. If four points are available, the average of the lowest two is considered, otherwise in case of only three points the $\mathrm{d}E/\mathrm{d}x$ estimate consists in the weighted sum of the lowest and the second-lowest, with a weight of 1 and 1/2 respectively. This measurement is useful to identify low momentum particles. In the left panel of Fig. 3.19 charged particle $\mathrm{d}E/\mathrm{d}x$ measurement as function of momentum is shown, made by the only ITS in Pb–Pb collisions at $\sqrt{s_{\mathrm{NN}}} = 5.02$ TeV. In a short momentum range, this detector is useful to distinguish, for example, electrons from kaons ($p \lesssim 500$ MeV/c) or from protons ($p \lesssim 1.5$ GeV/c).

3.7.2 Particle identification in the TPC

The TPC detector is crucial for the identification of charged particles traversing the central barrel over a wide momentum range. The PID is performed by collecting the ionization charge produced by a charged particle on the 159 pad rows of the TPC end plates, as mentioned in Sec. 3.2.2. The final estimate of the released energy by the single track consists in a truncated mean among the 65% of lowest-amplitude signals, in order to reject the contribution of secondary ionizations. Measuring this quantity for each track and reconstructing its momentum p, the particle identification takes place through the comparison between the measured $\mathrm{d}E/\mathrm{d}x$ value and the expected one for each particle species with a momentum p. The expected $\mathrm{d}E/\mathrm{d}x$ for each particle species, rigorously described by the Bethe-Block equation, is obtained

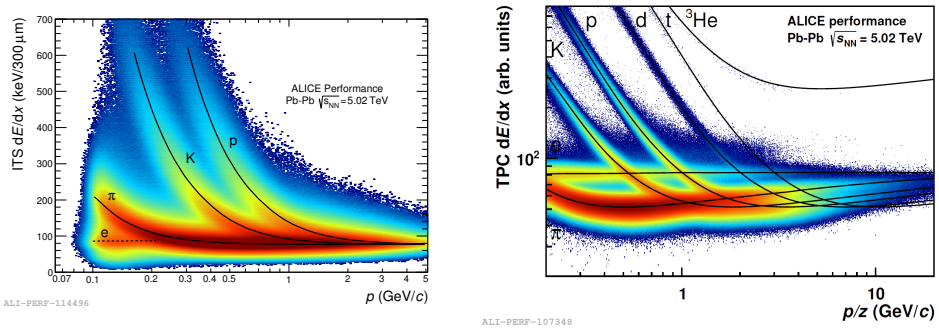

FIGURE 3.19: Charged particles $\mathrm{d}E/\mathrm{d}x$ as a function of momentum measured by the only ITS (left) and the TPC detector in (right) in Pb–Pb collisions at $\sqrt{s_{\mathrm{NN}}} = 5.02$ TeV. Figures taken from the ALICE Figure Repository ©.

with a data-driven approach, using the following parametrisation:

$$f(\beta\gamma) = \frac{P_1}{\beta^{P_4}} \left[P_2 - \beta^{P_4} - \ln\left(P_3 + \frac{1}{(\beta\gamma)^{P_5}} \right) \right] \tag{3.14}$$

In the formula, P_1–P_5 are free parameters, β is the particle velocity and $\gamma = 1/\sqrt{1-\beta^2}$ is the Lorentz boost factor obtained from the particle momentum $p = m\gamma\beta$. The measured $\mathrm{d}E/\mathrm{d}x$ in the TPC as a function of momentum in Pb–Pb collisions at $\sqrt{s_{\mathrm{NN}}} = 5.02$ TeV is shown in the right panel of Fig. 3.19. The solid lines represent the expected trends for different particle species, parametrized according to the Eq. 3.14. The largest separation power is achieved at low momenta ($p < 0.7$ GeV/c), where the particle can be identified on a track-by-track basis. At higher momenta, where the expected relativistic rise is observed and a nearly constant separation among the several species is visible on a wide momentum range, the identification can be still obtained with a statistical approach, based on multi-Gaussian fit of the $\mathrm{d}E/\mathrm{d}x$ distribution in a given momentum range. This possibility is guaranteed by an overall good $\mathrm{d}E/\mathrm{d}x$ resolution, which amounts to 5.2% and 6.5% in pp and most central Pb–Pb collisions respectively [242].

3.7.3 Particle identification in the TOF

As suggested by the name itself, the TOF detector identifies charged particles measuring the time of flight on a fixed length L. Given a particle with mass m and knowing its momentum p, the time of flight is:

$$t = \frac{L}{v} = L \cdot \frac{E}{pc^2} = L \cdot \frac{\sqrt{m^2c^4 + p^2c^2}}{pc^2} \,. \tag{3.15}$$

In the equation, the dependence on the particle momentum p, given by the tracking procedure described in Sec. 3.6.2, and the assumed particle mass m is highlighted. The measurement of the time of flight for charged particles takes place with respect to a given start time, which is provided either by the T0 detector or with a combinatorial analysis of arrival times at TOF. The latter method is particularly useful in case the T0 signal is absent. More details on the start time determination can be found in [252]. The overall TOF resolution, which includes the contribution from

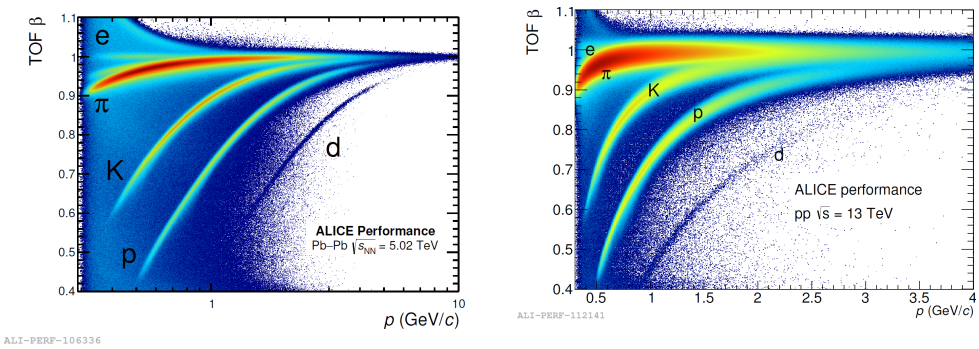

FIGURE 3.20: Charged particles β as a function of momentum, measured by the TOF detector in Pb–Pb collisions at $\sqrt{s_{\mathrm{NN}}} = 5.02$ TeV (left) and pp collisions at $\sqrt{s} = 13$ TeV (right). Note that primary charged particles revealed by the TOF have to own $p \gtrsim 300\mathrm{MeV}/c$. Images taken from the ALICE Figure Repository ©.

calibration and electronics, the resolution on the start time, the intrinsic detector resolution and the momentum precision from the tracking, is estimated to be around 80 ps for charged pions of momentum $p = 1$ GeV$/c$ produced in Pb–Pb collisions in the centrality range 0–70% [242].

The velocity of charged particles measured by the TOF detector in pp collisions at $\sqrt{s} = 13$ TeV and Pb–Pb collisions at $\sqrt{s_{\mathrm{NN}}} = 5.02$ TeV is shown in Fig. 3.20. The higher amount of background in the Pb–Pb case comes from tracks that are not correctly matched to TOF detector, due to the typically larger multiplicity in Pb–Pb collisions. The TOF detector is useful for the PID in the intermediate momentum range, ensuring a kaon versus pion separation better than 3σ up to $p \simeq 2.5$ GeV$/c$, and a kaon versus proton separation until $p \simeq 4.5$ GeV$/c$.

Chapter 4

Measurement of electrons from charm and beauty hadrons in Pb–Pb collisions at $\sqrt{s_{\rm NN}} = 5.02$ TeV

As discussed in Sec. 2.2.2, charm and beauty quarks produced in heavy-ion collisions lose energy either via multiple elastic scatterings with the QGP constituents or via the radiation of soft gluons induced by the deconfined medium. The nuclear modification factor $R_{\rm AA}$, introduced in Eq. 1.39, is an observable sensitive to the in-medium energy loss. It corresponds to the ratio of particle production yield in Pb–Pb to that in pp collisions scaled by the number of binary nucleon-nucleon collisions of the considered Pb–Pb centrality class. Any deviation from unity is driven by cold and/or hot nuclear-matter effects. $R_{\rm AA} < 1$ at intermediate $p_{\rm T}$ is a signature of the medium-induced energy loss of high-$p_{\rm T}$ partons. Experimental measurements of the nuclear modification factor of charm and beauty hadrons are necessary to study the heavy quark dynamics in the QGP. The most direct method to measure the heavy hadron production is to reconstruct them via their decay products, for example $\rm D^0 \rightarrow K^- \pi^+$ or $\rm B^+ \rightarrow J/\psi K^+$. This kind of measurements requires an excellent tracking system, able to reach spatial resolutions of a few tens of microns, corresponding to the typical $c\tau$ of heavy-flavour hadrons. Such a precision is mandatory to reconstruct the secondary decay vertices and resolve them from the beam interaction point, so that the decay signal can be separated from the huge combinatorial background. Indeed, the exclusive measurements of heavy-flavour hadrons are usually affected by low signal-to-background ratios, motivating the measurement of heavy-flavour hadron production via the reconstruction of single leptons coming from semileptonic decays of charm and beauty hadrons, exploiting the relatively large branching ratios ($\sim$ 10%) and the fact that this inclusive measurement does not require track resolutions of order of tens-hundred microns. High-$p_{\rm T}$ electrons in hadronic collisions were first observed in the 1970s in pp collisions at $\sqrt{s} = 52.7$ GeV at the CERN ISR [255], then the UA1 experiment measured the beauty hadron production via single muons in $\rm p\bar{p}$ collisions at $\sqrt{s} = 630$ GeV [256] and with the same data sample the UA2 experiment reported the charm cross section from single electron reconstruction [257]. Similar measurements were performed in $\rm p\bar{p}$ collisions at $\sqrt{s} = 1.8$ TeV at the Tevatron collider by the CDF [258] and D0 [259] experiments. The first measurements in pp, Au–Au and Cu–Cu collisions were performed by the STAR [260] and PHENIX [253,261,262] experiments at RHIC, where the $R_{\rm AA}$ of electrons from semileptonic decays of heavy-flavour hadrons (HFe) has been measured

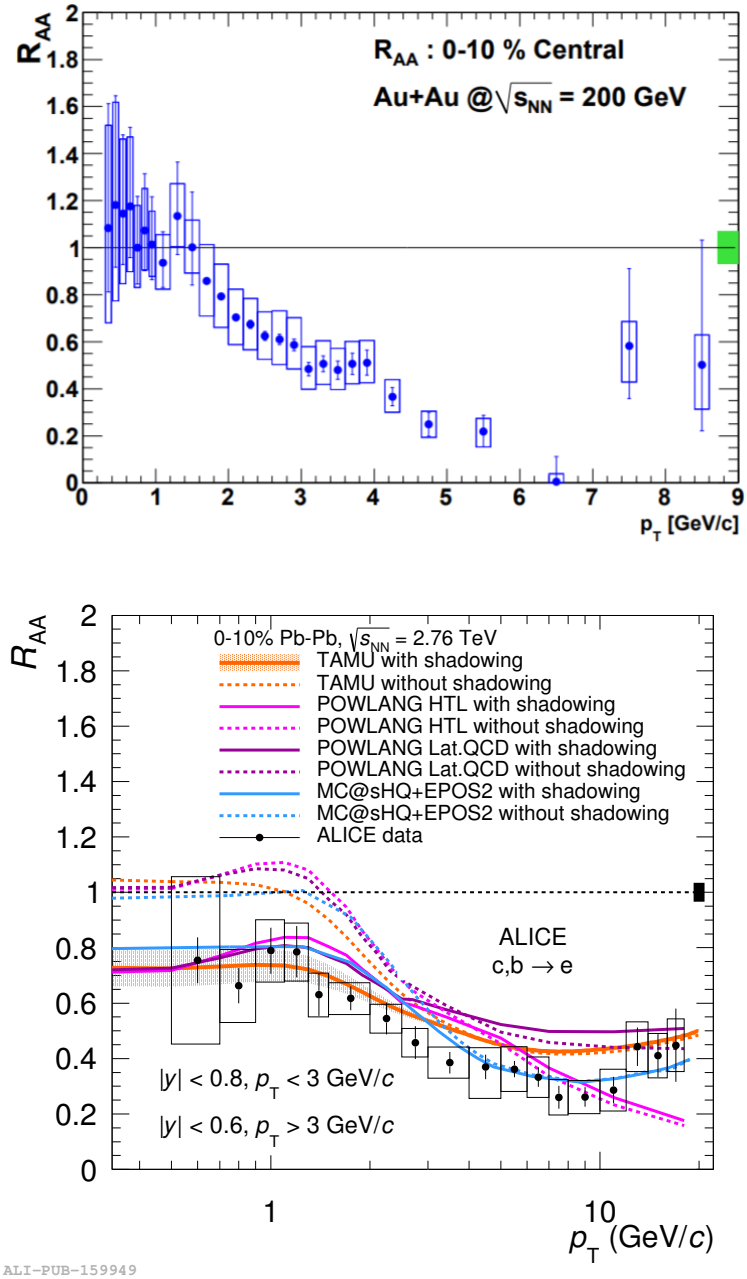

FIGURE 4.1: Nuclear modification factor $R_{\rm AA}$ of electrons from semileptonic decays of heavy-flavour hadrons in central (0–10%) Au–Au collisions at $\sqrt{s_{\rm NN}} = 200$ GeV measured by the PHENIX experiment at RHIC (top) and Pb–Pb collisions at $\sqrt{s_{\rm NN}} = 2.76$ TeV measured by the ALICE experiment at the LHC (bottom). Figures from [253] and [254].

in different centrality classes. The nuclear modification factor in central (0–10%) Au–Au collisions at $\sqrt{s_{\rm NN}} = 200$ GeV measured by the PHENIX experiment is shown in the upper panel of Fig. 4.1 and a significant suppression with respect to unity is observed, with a value of $R_{\rm AA} \approx 0.2$ at $p_{\rm T} \approx 5$ GeV/c. In absence of further effects that modify the charm and beauty production or their hadronisation, the $R_{\rm AA}$ is expected to increase towards lower $p_{\rm T}$ to compensate the depletion at high $p_{\rm T}$ and this is observed in the PHENIX result. A similar suppression of the $R_{\rm AA}$ is observed also

in Pb–Pb collisions at $\sqrt{s_{\rm NN}} = 2.76$ TeV, as measured by the ALICE experiment at the LHC (bottom panel of Fig. 4.1). In this case the expected rise at low $p_{\rm T}$ does not overcome unity, reaching a maximum value of about ~ 0.8. In this case, the low Bjorken-x values probed with the heavy quarks at such collision energies (see Tab. 2.1) make the $R_{\rm AA}$ sensitive to the shadowing effect, as explained in Sec. 2.2.1. The ALICE measurement is compared with theoretical predictions from TAMU [263], POWLANG [264] and MC@sHQ+EPOS2 [265] models and the experimental data at low $p_{\rm T}$ are well described only when the PDFs modification in the lead nucleus are taken into account. In all the other cases, the nuclear modification factor reaches unity and overestimates the measured $R_{\rm AA}$.

In this work, the $R_{\rm AA}$ of electrons from semileptonic decays of charm and beauty open hadrons in central (0–10%), semicentral (30–50%) and peripheral (60-80%) Pb–Pb collisions at $\sqrt{s_{\rm NN}} = 5.02$ TeV with the ALICE experiment at the LHC was measured. In particular, the work described in this Chapter, using the Pb–Pb data sample collected by the ALICE experiment in 2015, was published in Ref. [266] and concerns the range $p_{\rm T} < 3$ GeV/c (low-$p_{\rm T}$), where the analysis is sensitive to the shadowing effects on charm and beauty hadron production. The measurement is performed at midrapidity ($|y| < 0.8$) and the electrons are identified using the ITS, TPC and TOF detectors. For $p_{\rm T} > 3$ GeV/c (high-$p_{\rm T}$) the electron identification is performed using the signal in the TPC and EMCal detectors. The main aspects that differ from the work discussed in this thesis are briefly addressed in Sec. 4.6.

The analysis starts from the isolation of a pure sample of electrons, obtained with the track selections reported in Sec. 4.2. The electron identification is then performed with the ITS, TPC and TOF detectors, then the residual amount of hadrons is quantified from the distributions of the TPC signal in different momentum ranges, as explained in Sec. 4.2.2. The amount of electrons from charm and beauty hadron decays is obtained by subtracting the contribution of the background sources from the inclusive electron sample, as described in Sec. 4.3. The raw signal is then corrected for the selection efficiencies and properly normalised to provide the corrected invariant yield, as explained in Sec. 4.4. The $p_{\rm T}$-differential invariant yield is measured up to $p_{\rm T} = 6$ GeV/c, overlapping with the TPC+EMCal measurement for $p_{\rm T} > 3$ GeV/c. The nuclear modification factor $R_{\rm AA}$ is finally measured as the ratio to the production cross section in pp collisions at $\sqrt{s} = 5.02$ TeV and it is compared with model predictions, as discussed in 4.7.

4.1 Event selection

The Pb–Pb collision events used for the low-$p_{\rm T}$ analysis are selected with $\rm MB_{AND}$ trigger (see Sec. 3.4.1) and are required to have at least two reconstructed global tracks and a primary vertex within ± 10 cm with respect to the nominal beam interaction point. Moreover, the events affected by pile-up given by different bunch crossing, corresponding to less than 1% of the recorded sample, are rejected. As indicated above, the work described in this thesis is completed by another analysis performed at higher transverse momenta, namely $p_{\rm T} > 3$ GeV/c, which takes advantage from a sample of Pb–Pb collisions triggered with the EMCal detector, used to measure the electrons with $p_{\rm T} > 12$ GeV/c (see Sec. 4.6). Moreover, a similar analysis is performed on a sample of pp collisions recorded with a MB trigger at the same collision energy, in order to provide the reference necessary for the nuclear

	Centrality	MB trigger	EMCal trigger$^{(\dagger)}$	$\langle T_{\rm AA} \rangle$ (mb^{-1})
pp$^{(\dagger)}$	-	881×10^6	-	-
Pb–Pb	0–10%	6×10^6	1.2×10^6	23.26 ± 0.17
	30–50%	12×10^6	0.3×10^6	3.92 ± 0.07
	60–80%	12×10^6	-	0.42 ± 0.01

TABLE 4.1: Number of events and average nuclear overlap function used in the current work at $p_{\rm T} < 3$ GeV/c as well as for the complementary analysis with the EMCal trigger at higher $p_{\rm T}$ and in pp collisions at $\sqrt{s_{\rm NN}} = 5.02$ TeV. The entries labelled with "†" are not directly related to the work presented in this thesis. Numbers from [29, 267].

Variable	Selection
$\lvert y \rvert$	< 0.8
Number of clusters in TPC	≥ 120
Number of TPC clusters in dE/dx calculation	≥ 80
Number of clusters in ITS	4
Number of clusters in SPD	2
$\lvert \mathrm{DCA} \rvert_{xy}$	< 1 cm
$\lvert \mathrm{DCA} \rvert_{z}$	< 2 cm
Found / findable clusters in TPC	> 0.6
χ^2/clusters in TPC	< 4

TABLE 4.2: Track selections used to select candidate electrons. "DCA" stands for "distance to closest approach" of a track to the primary vertex.

modification factor measurement. The number of events analysed in the two collision systems with the two trigger configurations and the average nuclear overlap functions $\langle T_{\rm AA} \rangle$ used for the $R_{\rm AA}$ measurements are reported in Tab. 4.1.

4.2 Track selection and electron identification

The first necessary step for the measurement of electrons from semileptonic decays of heavy-flavour hadrons is the isolation of an inclusive electron sample, from which the signal is extracted via the subtraction of all background sources. In Tab. 4.2 the track selections adopted to select candidate primary particles are reported. The tracks are required to be reconstructed with at least 120 clusters in the TPC. The energy loss of each charged particle in the TPC is estimated as the truncated mean of the distribution of dE/dx from each ionisation process, where the tail at high values is dominated by the emission of δ-electrons. The minimum number of clusters in the TPC employed for the electron identification is 80. These selections suppress the contribution of short tracks, which are unlikely to originate from the primary vertex [268]. The analysis is performed with "global" tracks and at least 4 clusters in the ITS tracker are required. Furthermore, 2 out of the ITS clusters are asked to be in the SPD detector, namely in the two tracking layers closest to the primary vertex. This request helps to increase the fraction of primary electrons and, in particular, to

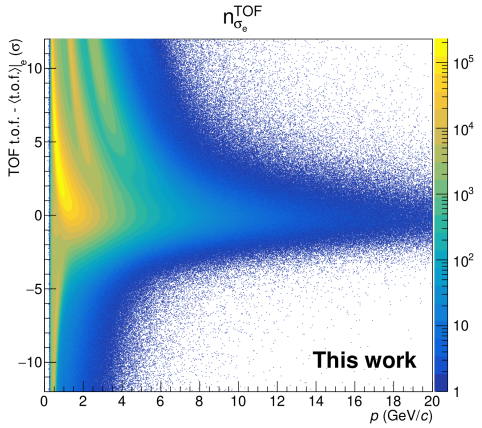

(A) $n_{\sigma_e}^{TOF}$ as a function of momentum.

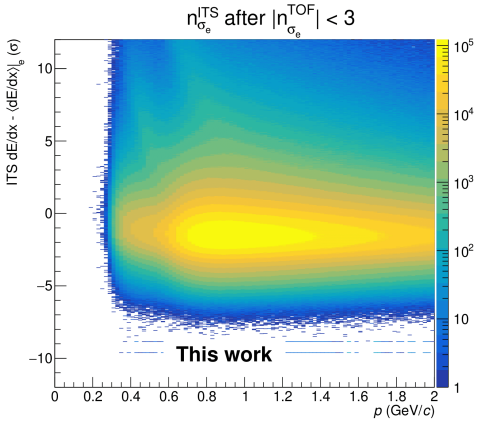

(B) $n_{\sigma_e}^{ITS}$ as a function of momemntum after the application of the $|n_{\sigma_e}^{TOF}| < 3$ selection.

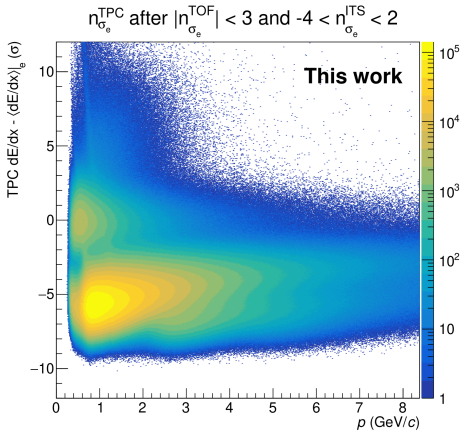

(C) $n_{\sigma_e}^{TPC}$ as a function of momentum after the application of the $|n_{\sigma_e}^{TOF}| < 3$ and $-4 < n_{\sigma_e}^{ITS} < 2$ selections.

FIGURE 4.2: n_σ distributions as a function of momentum around the electron signals in TOF, ITS and TPC in central (0–10%) Pb–Pb events.

reject electrons from late photon conversions taking place in the detector material. The electrons coming from long lived decay particles are further rejected requiring a maximum value for the distance to closest approach (DCA) with respect to the primary vertex, which is set to 1 cm on the transverse plane and to 2 cm along the z direction, where the two different values reflect the better spatial resolution of the ITS in the transverse plane than in the longitudinal direction (see Sec. 3.1). Moreover, a high track-quality is required by asking at least 60% of the clusters that can belong to it according to the track geometry, called "findable clusters" [269], and the χ^2/clusters in the TPC detector is required to be lower than 4.

From the sample of primary particles obtained with the selections described above, only candidate electrons are isolated by exploiting the particle identification

Pb–Pb centrality	TOF	ITS	TPC
0–10%	$-3 < n_{\sigma_e}^{TOF} < 3$	$-4 < n_{\sigma_e}^{ITS} < 2$	$-0.16 < n_{\sigma_e}^{TPC} < 3$
30–50%			$0 < n_{\sigma_e}^{TPC} < 3$
60–80%			$0.2 < n_{\sigma_e}^{TPC} < 3$

TABLE 4.3: PID selections applied for the electron identification in central (0–10%), semicentral (30–50%) and peripheral (60–80%) Pb–Pb collisions.

(PID) capabilities of the ALICE apparatus. According to the expected signal released in the detectors, the different particle species can be distinguished. Considering the species X and being $S_X(p)$ the expected signal at a given momentum p, the identification is performed through the variable:

$$n_{\sigma_X}^i(p) = \frac{s^i(p) - S_X(p)^i}{\sigma_X^i(p)} , \tag{4.1}$$

where $s^i(p)$ corresponds to the measured signal for a given particle with momentum p and $\sigma_X^i(p)$ is the experimental resolution on the signal in the given detector i. This variable is defined for ITS and TPC, where the signal corresponds to the dE/dx released by a charged particle traversing the detectors, as well as for the TOF, where in this case the signal corresponds to the time-of-flight of the particle from the instant of the collision measured with TOF (see Sec. 3.7.3). The variable defined in Eq. 4.1 quantifies the "number of sigmas" of compatibility for the measured signal $s^i(p)$ with the expected one $S_X^i(p)$ for a particle of species X at that momentum. The n_{σ_e} distributions as a function of momentum are shown in Fig. 4.2 for TOF, ITS and TPC detectors in central (0–10%) Pb–Pb events. Considering that the n_σ variables are defined around the electron expected signal, a real electron places around $n_{\sigma_e} = 0$ in all the cases. As visible in panel (A), in the TOF several bands related to different particle species are clearly distinguishable and intersect the region around $n_{\sigma_e} = 0$ at different momenta. This situation happens also in the ITS and the TPC, therefore a combination of selections on the n_{σ_e} variables for these detectors is applied to increase the purity of the electron sample. In panel (C) the n_{σ_e} distribution in the TPC is reported after the further selections $|n_{\sigma_e}^{TOF}| < 3$ and $-4 < n_{\sigma_e}^{ITS} < 2$. Despite these additional requirements, the electron sample at $p \lesssim 1.5$ GeV/c is contaminated mainly by kaons and protons, while for higher momenta the pion band approaches the region around $n_{\sigma_e} = 0$. For this reason, when an additional selection is applied on the $n_{\sigma_e}^{TPC}$ variable the residual amount of contaminating hadrons needs to be estimated. The PID selections adopted in this analysis are reported in Tab. 4.3. The $n_{\sigma_e}^{TPC}$ selection is determined to provide a 50% efficiency in data, on the basis of the low edge value that is fixed accordingly. This edge changes with the event centrality due to a shift of the electron distribution observed in data, not well reproduced by the MC simulations. Similarly, the mean of the ITS distribution in data and MC shows an evident shift with respect to $n_{\sigma_e} = 0$. A deep investigation was done to define a selection on $n_{\sigma_e}^{ITS}$ in order to be safe from biases that such a shift could introduce (see Sec. 4.2.1). In both cases, the shifts in the n_{σ_e} distributions are caused by an imperfect parametrization of the expected electron signal $S_X^i(p)$ in the Pb–Pb data, mainly due to the high-track multiplicity. No mismatch is observed between data and MC simulations for what concerns the TOF signal.

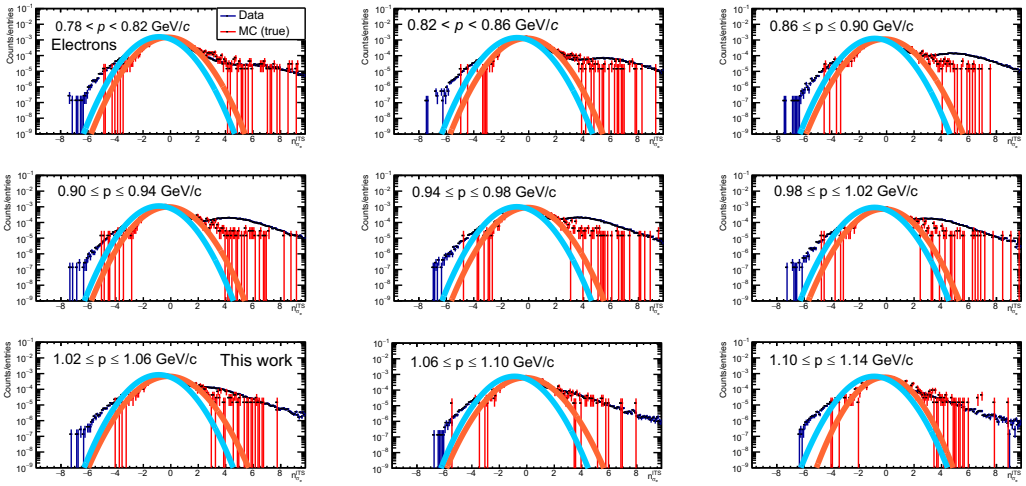

FIGURE 4.3: Examples of $n_{\sigma_e}^{ITS}$ distributions in different momentum intervals from collected and simulated central (0–10%) Pb–Pb collisions.

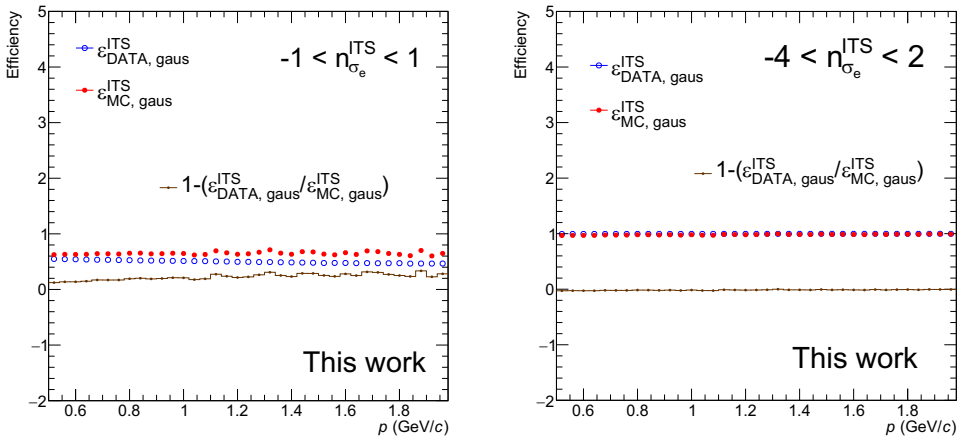

FIGURE 4.4: Electron identification efficiency in data and MC for different $n_{\sigma_e}^{ITS}$ selection criteria.

4.2.1 Studies on the ITS electron signal

As reported in Tab. 4.3, the ITS detector is used to identify electrons thanks to the analogue readout of SDD and SSD sub-detectors (see Sec. 3.7.1). The efficiency related to the applied $n_{\sigma_e}^{ITS}$ selection is estimated from the MC simulations. This requires a good description of data in order to avoid introducing biases with the MC correction. The $n_{\sigma_e}^{ITS}$ signal has been studied in data and MC in different momentum intervals. Some examples in central (0–10%) Pb–Pb collisions are reported in Fig. 4.3. The blue points describe the distribution of electrons in data, identified applying the PID selections on $n_{\sigma_e}^{TOF}$ and $n_{\sigma_e}^{TPC}$ reported in Tab. 4.3, while the red ones represent the electron distribution from MC, populated only with true electrons. The distribution in data is contaminated by kaons and protons, whose distributions are centred around different $n_{\sigma_e}^{ITS}$ values depending on the considered momentum. This comparison between data and MC is performed in different momentum intervals of width $\Delta p = 0.40$ MeV/c. The agreement between the two samples is studied by

comparing the Gaussian fits of the electron distributions. The fits in data are performed in the interval $-4 < n_{\sigma_e}^{ITS} < 1$, so that they are not biased by the shoulder at large $n_{\sigma_e}^{ITS}$ values given by the contaminating hadrons. For a pure electron sample, ideally the $n_{\sigma_e}^{ITS}$ distribution would be centred around 0 with $\sigma = 1$ in both data and MC. A resolution close to unity, compatible between the two samples, is observed at all momenta. The distributions in data are centred between $n_{\sigma_e} \sim -0.7$ and $n_{\sigma_e}^{ITS} \sim 1$, depending on the momentum. This behaviour in data, not reproduced in MC simulations, could bias the calculation of the PID selection efficiency. As clearly visible in the left panel of Fig. 4.4, the electron identification efficiency in data and MC show a difference of 10% at $p_T = 0.5$ GeV/c that increases to 30% at $p_T = 2$ GeV/c if the selection $-1 < n_{\sigma_e}^{ITS} < 1$ is applied. This discrepancy is gradually cured as soon as the selection criterion is loosened, since the mean discrepancies between data and MC have a smaller effect when integrating over a large range, for example when more than 90-95% of the Gaussian integral is considered. The discrepancy between data and MC becomes negligible for looser selections such as $-3 < n_{\sigma_e}^{ITS} < 3$ and $4 < n_{\sigma_e}^{ITS} < 2$. For these reasons, such looser selections are preferred in this analysis, since they do not require any further correction to account for the discrepancy between data and MC. Moreover, they ensure an electron identification efficiency close to 100%, still helping to remove a relevant amount of contaminating hadrons. In particular, the asymmetric selection $-4 < n_{\sigma_e}^{ITS} < 2$ is applied in the analysis, since it helps more to remove part of the kaon and proton contamination, which preferably centre around positive values of $n_{\sigma_e}^{ITS}$.

4.2.2 Estimation of the residual hadron contamination

The sample of candidate electrons isolated with the track selections reported in Tab. 4.2 and with the PID criteria listed in Tab. 4.3 still contains a residual amount of hadrons. This contamination is subtracted statistically in each p_T interval in which the analysis is performed. The following sources of contamination need to be taken into account:

1. pions ($\pi^{\pm}$), which consists in the most abundant hadron species, mostly placed in the region $-10 < n_{\sigma_e}^{TPC} < 1$;

2. kaons ($K^{\pm}$), which populate the region $n_{\sigma_e}^{TPC} > 0$ for momenta $p \lesssim 500$ MeV/c, then they cross the electron distribution around $500 \lesssim p \lesssim 600$ MeV/c and finally they get placed in the region $n_{\sigma_e}^{TPC} < 0$ at higher momenta, as shown in Fig. 4.7;

3. protons (p, $\bar{p}$), which behave analogously to the kaons, crossing the electron distribution in the interval $0.9 \lesssim p \lesssim 1$ GeV/c;

4. "others": this contribution, placed in the region $n_{\sigma_e}^{TPC} > 0$, represents particles that are not correctly reconstructed. This behaviour is observed for $p \lesssim 4$ GeV/c, where clusters of low-p particles with a large dE/dx in the TPC are wrongly associated. In particular, this background component is related to the wrong reconstruction of two particles as a unique one, with a consequent overestimation of the dE/dx in the TPC.

The hadron contamination is estimated in each momentum interval via a fit of the $n_{\sigma_e}^{TPC}$ distribution, where the contribution of each particle species is described with a dedicated analytical function. Some examples of $n_{\sigma_e}^{TPC}$ distribution fits in the intervals $0.46 < p < 0.48$ GeV/c, $0.66 < p < 0.68$ GeV/c, $0.70 < p < 0.72$ GeV/c and

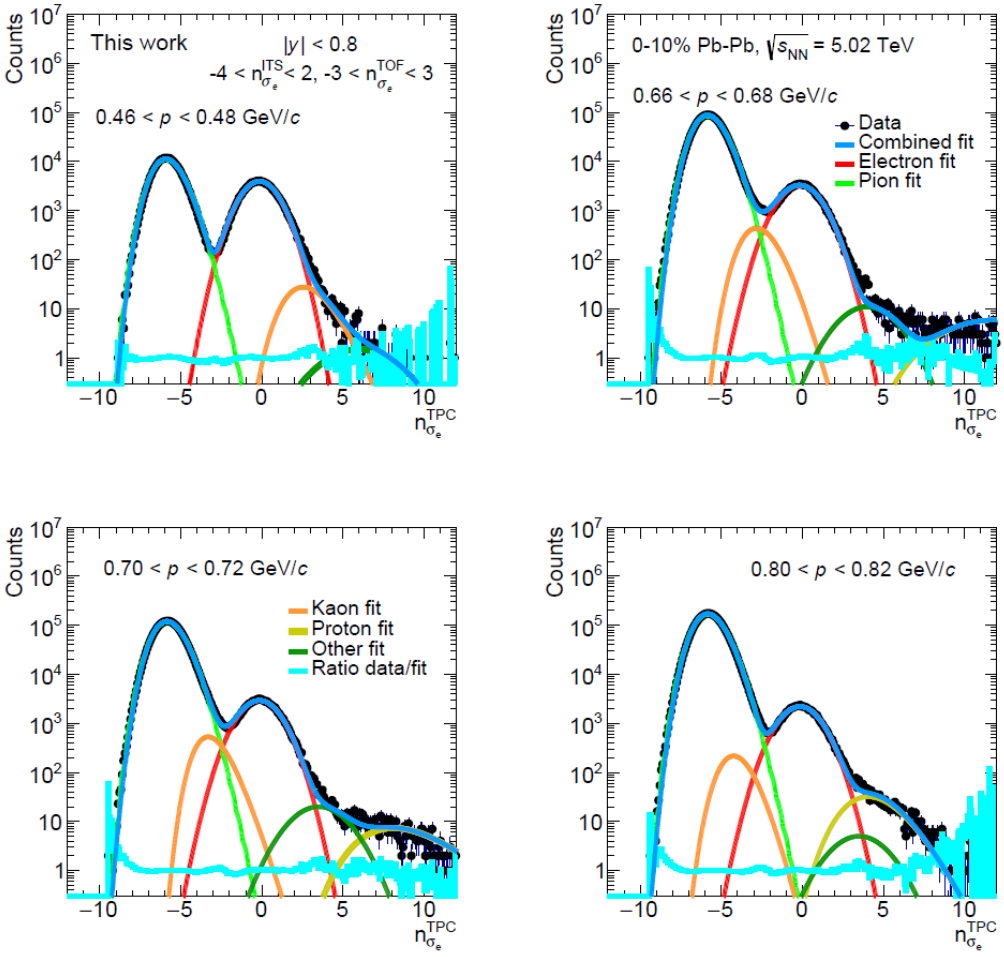

FIGURE 4.5: Examples of $n^{TPC}_{\sigma_e}$ distributions for the momentum intervals $0.46 < p < 0.48$ GeV/c, $0.66 < p < 0.68$ GeV/c, $0.70 < p < 0.72$ GeV/c and $0.80 < p < 0.82$ GeV/c obtained with the application of the selection criteria reported in Tab. 4.2 and 4.3 in central (0–10%) Pb–Pb collisions at $\sqrt{s_{NN}} = 5.02$ TeV.

$0.80 < p < 0.82$ GeV/c in central (0–10%) Pb–Pb collisions are shown in Fig. 4.5. In the region $p < 1$ GeV/c the behaviour of Bethe-Bloch curves for kaons and protons is strongly dependent on p and they cross the electron distribution, so it is necessary to evaluate the $n^{TPC}_{\sigma_e}$ distribution in momentum intervals narrower than in the higher momentum region. In the region (A) ($p < 1$ GeV/c) the projections are performed in momentum intervals $\Delta p = 20$ MeV/c wide, then the width is incremented to $\Delta p = 100$ MeV/c in the region (B) ($1 < p < 1.5$ GeV/c) and finally to $\Delta p = 300$ MeV/c in the region (C) ($p > 1.5$ GeV/c). The fit function and procedure differ in these intervals. In the regions (A) and (B) the pion sample is described with a Landau function multiplied by an exponential. This shape is also used to describe the kaon and proton distributions, while the electrons and "others" ones are parametrized with a Gaussian. The pion contribution (light green) stays in the region $n^{TPC}_{\sigma_e} < 0$, while the electron Gaussian is centred around $n^{TPC}_{\sigma_e} \approx 0$. The kaon (orange) and proton (yellow) samples at low momenta are placed in the region $n^{TPC}_{\sigma_e} > 0$, then they move towards lower $n^{TPC}_{\sigma_e}$ values as soon as the particle momentum increases. After crossing the electron sample, the kaon and proton peaks are hidden by the electron

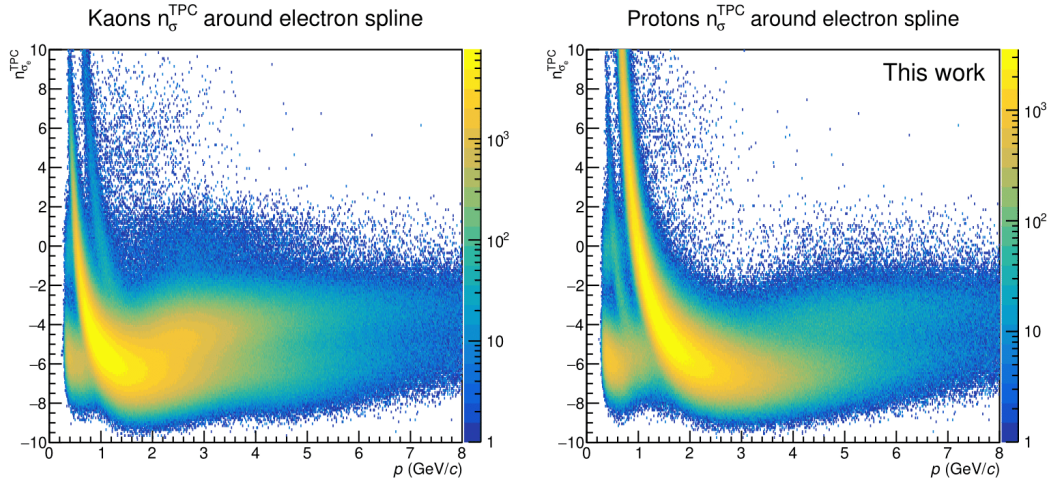

(A) $n_{\sigma_e}^{TPC}$ as a function of momentum for candidate kaons (left) and protons (right), selected with a PID requirement on the TOF detector (see details in the text).

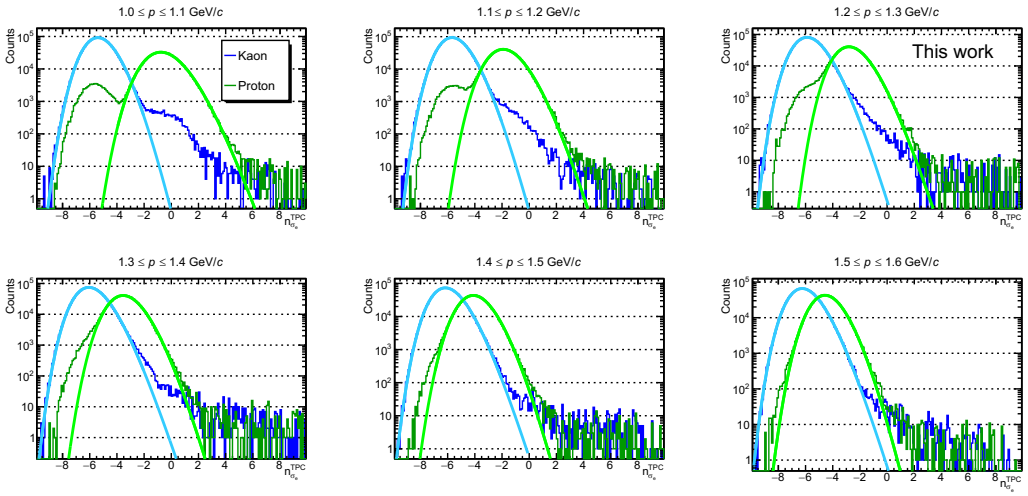

(B) Examples of $n_{\sigma_e}^{TPC}$ distributions of candidate kaons and protons selected in different momentum intervals, in the region $1 < p < 1.6$ GeV/c.

FIGURE 4.6

and pion distributions. However their abundances need to be estimated to be later removed from the candidate electron sample. A dedicated study about the shape and position of kaon and proton distributions is performed. The $n_{\sigma_e}^{TPC}$ distributions of a sample of candidate kaons and protons are obtained by requiring the tracks to be compatible within 3σ in the TOF either with the kaon or the proton hypothesis, as shown in Fig. 4.6. The shape of the kaon and proton samples is parametrised and used in the fits of Fig. 4.5. This approach is fundamental to fix position and shape of kaon and proton distributions, even in those momentum intervals where their profile cannot be appreciated from the full $n_{\sigma_e}^{TPC}$ distribution. Also in this case, the kaon and proton samples are not pure, due to the contamination of other particle species. For example, in the kaon sample a residual amount of electrons emerges around $n_{\sigma_e}^{TPC} \sim 0$, while in the proton one the contamination due to a residual pion peak at $n_{\sigma_e}^{TPC} \lesssim 4$ GeV/c is present. For this reason, the kaon and proton distributions are described through a fit with a Landau times exponential function, rather than

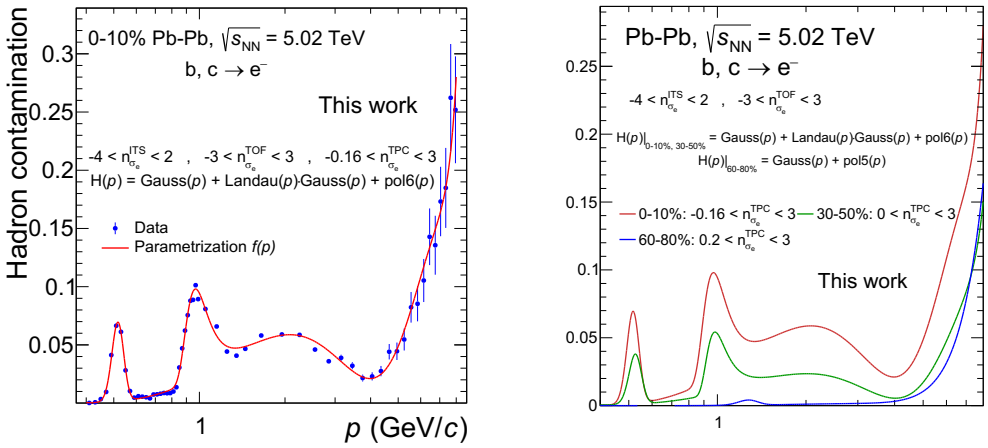

FIGURE 4.7: Left: hadron contamination percentage as a function of momentum in the electron sample selected in central (0–10%) Pb–Pb collisions using TOF, ITS and TPC detectors for PID. Right: comparison among the residual hadron contamination percentages in central (0–10%), semicentral (30–50%) and peripheral (60–80%) Pb–Pb collisions.

using a template-based technique. The fit function is then used in the fits of Fig. 4.5, leaving only the normalization as a free parameter. The "others" distribution, which is always placed at $n^{TPC}_{\sigma_e} \gtrsim 5$, is described with a Gaussian function (dark green). In the regions (A) and (B) the hadron contamination is mainly due to kaons and protons and in smaller amount to the "others" contribution. In the region (C) the kaons and protons become almost indistinguishable because of the full overlap of the dE/dx bands both placed at $n^{TPC}_{\sigma_e} < 0$. With increasing momentum, the amount of reconstructed electrons decreases and the hadron contamination is dominated by the pion sample, whose tail at higher $n^{TPC}_{\sigma_e}$ becomes more and more relevant in relative terms. The contribution from "others" quickly decreases with increasing p_T and finally disappears around $p = 4$ GeV/c.

The result of this procedure is shown in Fig. 4.7. In the left panel the estimated hadron contamination in each considered momentum interval in central (0–10%) Pb–Pb collisions is reported. The evolution as a function of p is parametrised as:

$$H(p) = \text{Gauss}(p) + \text{Landau} \cdot \text{Exp}(p) + \text{pol6}(p) \ . \tag{4.2}$$

The first Gaussian describes the crossing of the kaon sample with the electron one, which takes place around $p = 0.5$ GeV/c, the Landau·Exp term describes the proton crossing occurring around $p = 1$ GeV/c and the 6-order polynomial (pol6) is used to parametrise the hadron contamination trend for $p > 1$ GeV/c, where the contributions of "others" and pion sources are more relevant. The shown hadron contamination is measured after the application of the track and PID criteria mentioned before, with a centrality dependent selection on $n^{TPC}_{\sigma_e}$ that corresponds to $-0.16 < n^{TPC}_{\sigma_e} < 3$ in central (0–10%) Pb–Pb collisions. The lower edge is chosen in order to ensure a 50% efficiency for this specific selection, as described in Sec. 4.2. The parametrised $H(p)$ is necessary to properly evaluate the hadron contamination in the p_T intervals used to measure the yield of electrons from heavy-flavour decays. For each track a probability $H(p)$ to be a hadron is assigned and the transverse momentum distribution for the residual hadron contamination is built statistically. The inclusive

electron sample $N^{\rm incl.}_{\rm raw}(p_{\rm T})$ is quantified as the difference between all the tracks selected with the track and PID criteria listed in Tab. 4.2 and 4.3 ($N^{\rm tot.}_{\rm raw}(p_{\rm T})$) and the amount of contaminating hadrons ($N^{\rm had.}(p_{\rm T})$):

$$N^{\rm incl.}_{\rm raw}(p_{\rm T}) = N^{\rm tot.}_{\rm raw}(p_{\rm T}) - N^{\rm had.}(p_{\rm T}) \, . \tag{4.3}$$

The whole procedure is repeated independently in the three centrality classes. In the right panel of Fig. 4.7 the hadron contamination in central (0–10%), semicentral (30–50%) and peripheral (60–80%) Pb–Pb events are compared. The parametrisation in the semicentral class is performed using the same function as for central events (Eq. 4.2), while the function:

$$\mathrm{H}(p) = \mathrm{Gauss}(p) + \mathrm{pol5}(p) \tag{4.4}$$

is adopted in peripheral (60–80%) Pb–Pb events, considering that after the application of the PID criteria a negligible amount of residual background is observed for $p \lesssim 4$ GeV/c.

4.3 Background subtraction

The procedure described in the previous Section is used to measure the yield of inclusive electrons. The goal of the analysis is to isolate those from semileptonic decays of charm and beauty hadrons. Therefore, electrons from other sources need to be rejected. For this reason, the $p_{\rm T}$ distribution of background electrons is subtracted from the inclusive one. The considered background sources are:

- electrons from Dalitz decays of light neutral mesons, mainly π^0 and η, as well as photons, also coming from hard scattering processes and electromagnetic radiation of quarks in the medium (see Sec. 1.4.2) that later convert in the detector material. Such electrons called *photonic* in the following;
- dielectron decays of quarkonia: $\mathrm{J}/\psi, \Upsilon \rightarrow \mathrm{e}^+\mathrm{e}^-$;
- electrons from weak decays of kaons $\mathrm{K}^{0\pm} \rightarrow \mathrm{e}^{\pm}\pi^{\mp/0}\overset{(-)}{\nu}_{\mathrm{e}}$ (K_{e3}) and di-electron decays of light vector mesons ($\omega, \phi, \rho_0 \rightarrow \mathrm{e}^+\mathrm{e}^-$);
- electrons from W and Z/γ^*.

The last background component becomes sizeable only for $p_{\rm T} \gtrsim 10$ GeV/c, thus being completely negligible in the transverse momentum range treated in this analysis. The J/ψ contribution was found to reach a maximum of 5% in $2 < p_{\rm T} < 3$ GeV/c in central (0–10%) Pb–Pb collisions at $\sqrt{s_{\rm NN}} = 2.76$ TeV [254], quickly decreasing in semicentral (30–50%) and peripheral (60–80%) collisions and becoming negligible for lower and higher transverse momenta. For these reasons, the subtraction of this contribution is not performed, even if an effect related to the quarkonia contribution is considered in the estimate of the total systematic uncertainty (see Sec. 4.5). Moreover, the K_{e3} background source mentioned above is suppressed by the requirement of hits on both SPD layers and it is found to be negligible. Finally, the only relevant source of background to be removed from the detector sample is the photonic one.

4.3.1 Photonic background

The yield of photonic electrons is estimated using the photonic tagging method [254,270–272]. Photonic electrons are identified by pairing an inclusive electron track

Associated electron variable	Selection
p_{T} (GeV/c)	< 0.1
$\lvert y \rvert$	< 0.8
Number of clusters in TPC	≥ 60
Number of TPC clusters in dE/dx calculations	≥ 60
Number of clusters in ITS	≥ 2
$\lvert \mathrm{DCA}_{xy} \rvert$	< 1 cm
$\lvert \mathrm{DCA}_{z} \rvert$	< 2 cm
Found / findable clusters in TPC	> 0.6
χ^2/d.o.f. TPC	< 4
$\mathrm{n}_{\sigma_{\mathrm{e}}}^{\mathrm{TPC}}$	[-3,3]
$m_{\mathrm{e^+e^-}}$	< 140 MeV/c^2

TABLE 4.4: Selection criteria for associated electrons used to tag photonic background.

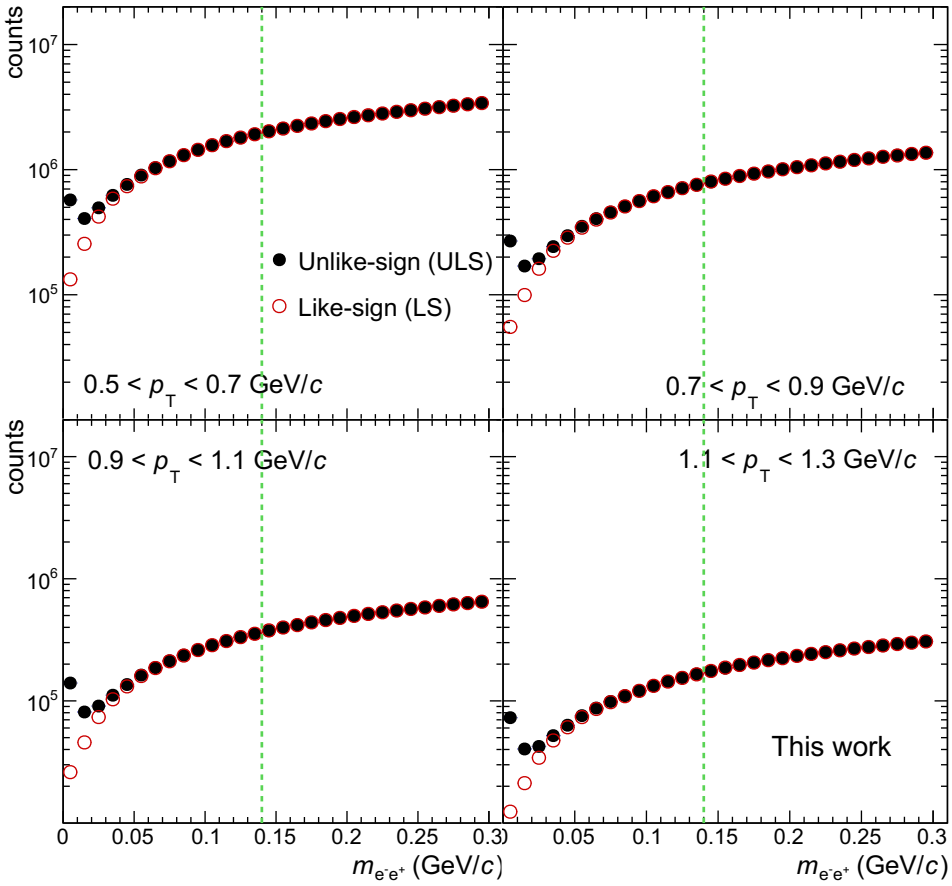

FIGURE 4.8: Invariant mass distribution for ULS and LS pairs in different p_{T} intervals measured in central (0–10%) Pb–Pb collisions.

with another one, called *associated* in the following. The associated tracks are selected with the criteria reported in Tab. 4.4, which are imposed to be looser than the inclusive track selections in Tab. 4.2 in order to maximise the efficiency of the photonic pair reconstruction. This operation produces two separate samples of pairs:

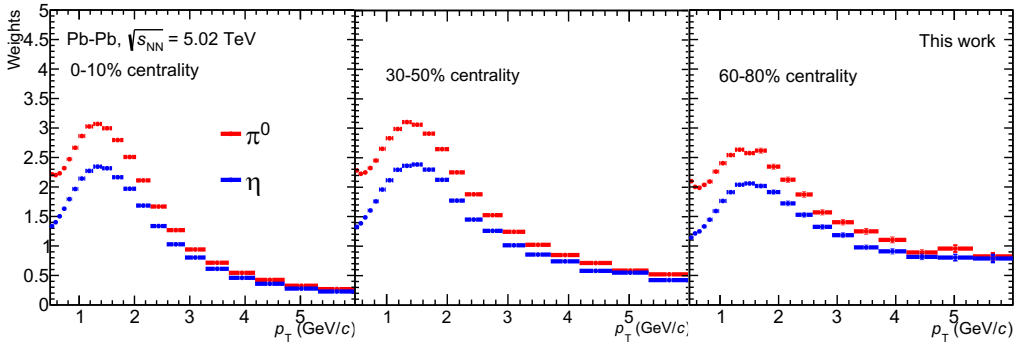

FIGURE 4.9: Weights for generated π^0 and η mesons defined by the ratio with the $p_{\rm T}$ distribution from data in central (0–10%), semicentral (30–50%) and peripheral (60–80%) Pb–Pb collision at $\sqrt{s_{\rm NN}} = 5.02$ TeV.

- e^+e^- pairs, formed by an electron and a positron, called *unlike sign* (ULS). This subsample contains the true photonic pairs plus combinatorial background pairs, produced by the pairing of opposite-sign charged particles randomly picked from the set of reconstructed tracks;
- e^+e^+ and e^-e^- pairs, formed either by two equally-charged particles, called *like sign* (LS). This subsample is used to describe the combinatorial background present in the ULS sample.

The invariant mass $m_{e^+e^-}$ distribution of the two samples is analysed and the photonic electron yield is estimated as the difference between the ULS and the LS ones. As visible in Fig. 4.8, the nice agreement between the ULS and LS distributions for high $m_{e^+e^-}$ indicates that the latter sample well describes the amount of combinatorial pairs present in the former one. At low $m_{e^+e^-}$ the ULS distribution shows a peak close to zero, typical of the photonic source. The subtraction of the LS from the ULS one is used to retrieve the amount of photonic electrons in the considered $p_{\rm T}$ interval. This is done in the range $m_{e^+e^-} < 140$ MeV/c^2, since for higher values the reconstructed pairs are dominated by the combinatorial component. The photonic electron yield estimation is strongly affected by statistical fluctuations for $p_{\rm T} \gtrsim 3$ GeV/c, where the number of electrons identified with the ITS, TPC and TOF is low.

The reconstruction of photonic pairs is subject to several inefficiencies, given by the selections of associated tracks (Tab. 4.4) as well as the limited acceptance of the detector. For this reason, the raw spectrum of photonic electrons tagged with the procedure described above needs to be corrected for the efficiency of the associated track detection. This is the so-called *tagging efficiency* ($\varepsilon_{\rm tag.}$), calculated using MC simulations were the underlying Pb–Pb event is simulated with the HIJING [273] generator and the particle transport is managed by the GEANT3 program, which relies on an accurate implementation of the detector response. Using the MC information, the tagging efficiency is computed as the ratio between the number of reconstructed inclusive photonic electrons (selected with criteria in Tab. 4.2 and 4.3) tagged as belonging to an ULS pair thanks to the correct reconstruction of the associated track coming from the same mother ($N^{\rm phot.}_{\rm ULS}$) and the number of reconstructed inclusive electrons coming from a photonic source ($N^{\rm phot.}$) within $|y| < 0.8$, namely:

$$\varepsilon_{\rm tag.}(p_{\rm T}) = \frac{N^{\rm phot.}_{\rm ULS}(p_{\rm T})}{N^{\rm phot.}(p_{\rm T})} \,. \tag{4.5}$$

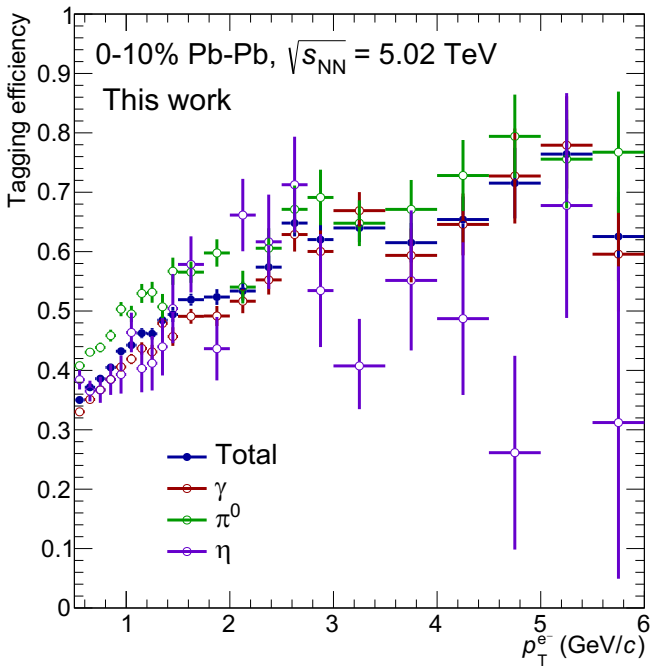

FIGURE 4.10: Tagging efficiency measured in central (0–10%) Pb–Pb collisions at $\sqrt{s_{NN}} = 5.02$ TeV. The efficiency for e^+e^- coming from γ conversions as well as π^0 and η Dalitz decays are also reported separately.

In the tagging efficiency the generated light mesons are considered to count how many photonic electrons are correctly reconstructed, but the efficiency risks to be influenced by the usage of an incorrect p_T distribution of the electron-mother particles. For this reason, the generated p_T spectra of π^0 and η mesons are rescaled to match the shape in data. In lack of precise and differential π^0 and η spectra measured at midrapidity in Pb–Pb collisions at $\sqrt{s_{NN}} = 5.02$ TeV, these correction weights are derived by the measured charged pion spectrum in the same data sample [40]. In particular, the π^0 p_T-spectrum from data is assumed to be equal to that of $\pi^\pm$, while the η one is obtained using a m_T-scaling approach [274, 275], according to which the m_T distributions of π^0 and η coincide modulo a constant factor. In particular, the $dN/dm_T|_{\pi^0}$ is obtained considering $dp_T = \frac{m_T}{p_T} dm_T$, then the transverse mass ratio is used to move to $dN/dm_T|_\eta$ and finally this relation is reused to retrieve the p_T spectrum of η mesons. The weights used to correct the shape of the generated p_T distribution of π^0 and η mesons in central (0–10%), semicentral (30–50%) and peripheral (60–80%) Pb–Pb collisions at $\sqrt{s_{NN}} = 5.02$ TeV are shown in Fig. 4.9. The tagging efficiency measured in central (0–10%) Pb–Pb collisions after the scaling of the generated p_T distribution of π^0 and η mesons is shown in Fig. 4.10. The efficiency for e^+e^- coming from γ conversions as well as π^0 and η Dalitz decays are also reported separately. The tagging efficiency related to electrons from γ is lower than that of Dalitz decays of π^0 mesons because the reconstruction of associated electrons may suffer from fake cluster association in the SPD or cluster sharing that, in the ITS, may prevent a complete tracking. This is not the case for the e^+e^- from Dalitz decays, since they are typically produced within the first SPD layer. Moreover, the efficiency for electrons from Dalitz decays of η mesons is lower than the π^0

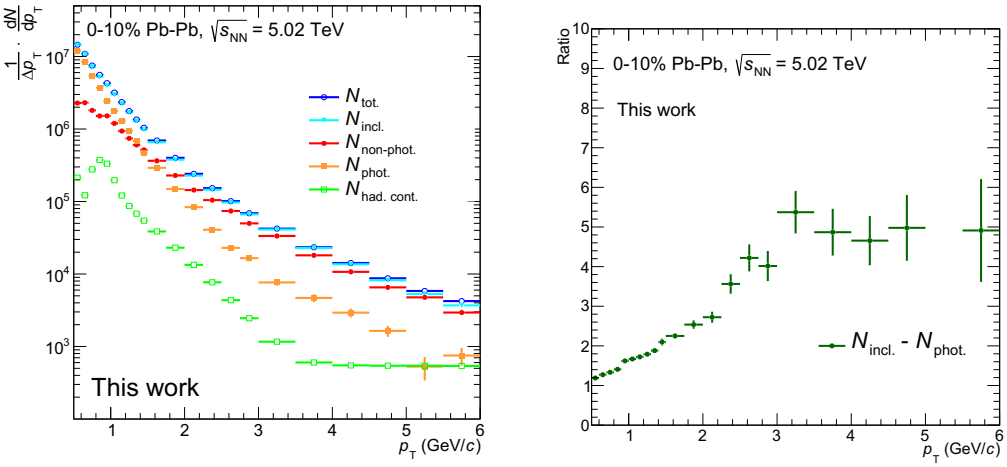

FIGURE 4.11: Left: raw non-photonic $p_{\rm T}$ spectrum (red) obtained removing the photonic contribution (orange) from the inclusive electron sample (light blue) after subtracting the residual hadron contamination (green) from the candidate electron sample (blue) selected with the track criteria in Tab. 4.2 and the PID ones listed in Tab. 4.3 in central (0–10%) Pb–Pb collisions at $\sqrt{s_{\rm NN}} = 5.02$ TeV. Right: ratio between inclusive and photonic samples as a function of electron $p_{\rm T}$ in the same sample.

one due to the typical wider pair invariant mass distribution that implies a larger rejection given the requirement $m_{\rm e^+e^-} < 140$ MeV/c^2. The total tagging efficiency increases from about 34% at $p_{\rm T} = 0.5$ GeV/c to about 70% at $p_{\rm T} = 6$ GeV/c.

The photonic spectrum corrected for the efficiency of tagging an associated electron is calculated as:

$$N^{\rm phot.}(p_{\rm T}) = N^{\rm phot.}_{\rm raw}(p_{\rm T})/\varepsilon_{\rm tag.}(p_{\rm T}) \,, \tag{4.6}$$

then the raw $p_{\rm T}$ distribution of the non-photonic electrons is obtained as follows:

$$N^{\rm non-phot.}_{\rm raw}(p_{\rm T}) = N^{\rm incl.}_{\rm raw}(p_{\rm T}) - N^{\rm phot.}(p_{\rm T}) \,. \tag{4.7}$$

The spectra obtained from the analysis of central (0–10%) Pb–Pb collisions are reported in the left panel of Fig. 4.11. The non-photonic raw spectrum (red) is obtained using Eq. 4.7: the inclusive spectrum (light blue) derives from the subtraction of the hadron contamination contribution (green) from the total sample of candidate electrons (blue), then the photonic spectrum (orange) obtained with Eq. 4.6 is subtracted from the inclusive one. From this comparison, it is easy to see that the photonic contribution dominates at low transverse momenta. This can be quantitatively appreciated from the ratio:

$$\begin{aligned} R_{\rm NP-P}(p_{\rm T}) &= \frac{N^{\rm non-phot.}_{\rm raw}(p_{\rm T})}{N^{\rm phot.}(p_{\rm T})} = \frac{N^{\rm incl.}(p_{\rm T}) - N^{\rm phot.}(p_{\rm T})}{N^{\rm phot.}(p_{\rm T})} \\ \Rightarrow 1 + R_{\rm NP-P}(p_{\rm T}) &= \frac{N^{\rm incl.}(p_{\rm T})}{N^{\rm phot.}(p_{\rm T})} \,, \end{aligned} \tag{4.8}$$

where Eq. 4.7 is used. The quantity $1 + R_{\rm NP-P}$ measured in central (0–10%) Pb–Pb

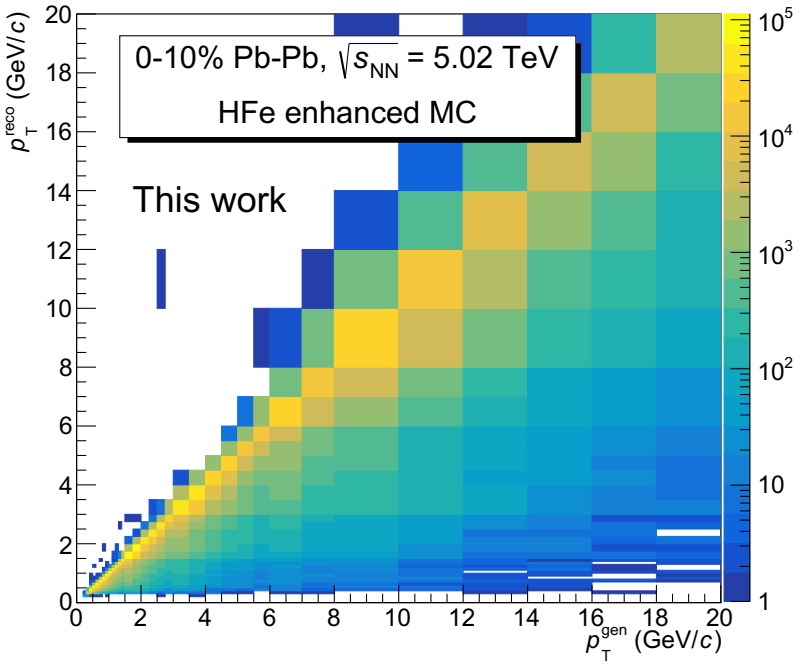

FIGURE 4.12: Correlation matrix between reconstructed and generated electron p_T in central (0–10%) Pb–Pb collisions from the enhanced MC simulations.

collisions is shown in the right panel of Fig. 4.11. This ratio shows that the photonic component represents about 80% of the inclusive electron sample at $p_T = 0.5$ GeV/c and reduces with increasing p_T, being about 25% at $p_T = 3$ GeV/c. At higher p_T the contribution of photonic electrons is lower than 20%, though its estimate becomes less precise because the ULS and LS pair distributions are subject to significant statistical fluctuations. In order to improve the quality of the electron sample at high p_T the usage of the EMCal calorimeter is beneficial (see Sec. 4.6) and it has been indeed adopted to release the final results reported in [266], where the work presented in this thesis contributes up to $p_T = 3$ GeV/c.

4.4 Efficiency correction and normalization

After the subtraction of the hadronic contamination and the background from photonic electrons, the invariant corrected spectrum of electrons from semileptonic decays of charm and beauty hadrons is measured as follows:

$$\frac{1}{2\pi p_T}\cdot\frac{d^2N^{HFe}}{dp_T dy} = \frac{1}{2}\frac{1}{2\pi p_T^{centre}}\frac{1}{N_{ev}^{MB}}\frac{1}{\Delta y \Delta p_T}\frac{N_{raw}^{HFe}(p_T)}{(\varepsilon^{geom.}\times\varepsilon^{reco.}\times\varepsilon^{eID})}\,. \tag{4.9}$$

The raw yield $N_{raw}^{HFe}(p_T)$, which corresponds to $N_{raw}^{non-phot}$ of Eq. 4.7, divided by the width $\Delta y = 1.6$ of the rapidity interval covered in the analysis, the transverse momentum interval width Δp_T and its central value p_T^{centre}. The factor 1/2 accounts for the fact that in this analysis both electrons and positrons are considered, therefore the final spectrum is defined as the average between particle and antiparticle ones. The factor $1/2\pi p_T$ in the left side of Eq. 4.9 is included to write the corrected yield in

a boost-invariant way. Furthermore, the measurement is normalised by the number of triggered events $N_{\rm ev}$ in the considered centrality class with an interaction between beams within $|z| < 10$ cm. Finally, the reconstructed spectrum needs to be corrected for the detector geometrical acceptance $\varepsilon^{\rm geom.}$, the efficiency due to the track reconstruction $\varepsilon^{\rm reco.}$ and that related to the electron identification $\varepsilon^{\rm eID}$. These efficiencies are determined using MC simulations with enhanced heavy-flavour signals. Every event contains several $\rm c\bar{c}$ or a $\rm b\bar{b}$ pairs, which produce heavy hadrons that are forced to decay semileptonically to electrons. The underlying Pb–Pb event is generated using the HIJING package and the heavy-flavour signals are added using PYTHIA 6 [276] event generator. On top of the efficiency correction, the $p_{\rm T}$ spectrum of the reconstructed electrons needs to be further corrected to take into account the effect of bremsstrahlung, that causes a softening of the $p_{\rm T}$ spectrum. For this reason, a Bayesian unfolding technique is adopted [277–279]. In this approach, the measured spectrum from data is defined as a vector "M" containing the reconstructed counts in each $p_{\rm T}$ interval and the true spectrum is defined as a vector "T", satisfying the relation:

$$\mathrm{M} = \mathrm{RT} \qquad \Rightarrow \qquad \mathrm{T} = \mathrm{R}^{-1}\mathrm{M}\,, \tag{4.10}$$

where R is the *response matrix* that parametrises the correlation of $p_{\rm T}^{\rm reco}$ and $p_{\rm T}^{\rm gen.}$. The R matrix for central (0–10%) Pb–Pb collisions from the enhanced MC simulations is shown in Fig. 4.12 and it shows that $\langle p_{\rm T}^{\rm reco.} \rangle \leq \langle p_{\rm T}^{\rm gen.} \rangle$. Given the limited detector resolution, some $p_{\rm T}^{\rm reco.}$ values migrate to adjacent intervals. To retrieve the corrected spectrum from the measured one, the inverse relation is needed, namely R^{-1}. However, the generated $p_{\rm T}$ distribution providing the measured one cannot be uniquely determined with a simple matrix inversion, which can be also not ideal in case of low counts, as explained in Ref. [278]. The unfolding procedure is based on the usage of a response matrix, built from a prior distribution U representing a reasonable hypothesis for the true distribution. Using an iterative procedure, the measured distribution M is smeared to approximate at best the true one. At each iteration, the Bayes theorem of probability is used:

$$P(\mathrm{A}|\mathrm{B}) = \frac{P(\mathrm{B}|\mathrm{A}) \cdot P(\mathrm{A})}{P(\mathrm{B})}\,. \tag{4.11}$$

The elements involved in Eq. 4.11 are:

- $P(\mathrm{B}|\mathrm{A})$ is associated to the conditioned probability to reproduce the detector measurement B knowing the true distribution A and it corresponds to the ij element of the response matrix R, given i and j the considered reconstructed and generated $p_{\rm T}$ intervals respectively;
- $P(\mathrm{A}|\mathrm{B})$ is associated to the conditioned probability to get the physical distribution A given the measured one B. It corresponds to the ji-th entry of the "smeared matrix" $\bar{\mathrm{R}}$, which estimates the "inverse" response matrix;
- $P(\mathrm{A})$ corresponds to the U_j entry of the prior $p_{\rm T}$ distribution;
- $P(\mathrm{B})$ is associated to the measured distribution, namely corresponding to $\mathrm{M}_i = \sum_k \mathrm{R}_{ik}\mathrm{U}_k$.

In other words, the ji-th element of the "smeared matrix" $\bar{\mathrm{R}}$ derives from Eq. 4.11 and corresponds to:

$$\bar{\mathrm{R}}_{ji}[\mathrm{U}] = \frac{\mathrm{R}_{ij}\mathrm{U}_j}{\sum_k \mathrm{R}_{ik}\mathrm{U}_k}\,, \tag{4.12}$$

then the unfolded spectrum $U^{'}$ from the measured one M corresponds to:

$$U^{'} = \bar{R}[U]M\,, \tag{4.13}$$

where $\bar{R}[U]$ is the "smeared matrix" given the prior distribution U from MC. If the unfolded spectrum $U^{'}$ corresponds to the true distribution, then $U^{'}$ is equal to T, otherwise it is in between U and T. The procedure is repeated by substituting $U^{'}$ in place of U in Eq. 4.12 to obtain the unfolded spectrum $U^{''}$ and update the "smeared matrix" in $\bar{R}[U^{'}]$, then this process is iterated as soon as a stable solution is obtained. In this analysis 100 iterations are used and no variations in the final results are observed when modifying the number of iterations around the default one. The total correction amounts to about 5% at $p_{\mathrm{T}} = 0.5$ GeV/c and then it increases up to about 13% at $p_{\mathrm{T}} = 3$ GeV/c.

4.5 Systematic uncertainty estimation

Several systematic uncertainties related to the assumptions specific to the analysis techniques adopted to perform the measurement as well as to possible imperfections in the description of detector effects in the MC simulations are studied. The related uncertainties are evaluated by repeating the analysis with different values for the selections of the signal candidates, or with dedicated studies to test the robustness of the analysis procedure.

The systematic uncertainties related to the reconstruction efficiency corrections are estimated with the variation of the inclusive-track selections, in particular the PID requirements on $n_{\sigma_e}^{\mathrm{ITS}}$, $n_{\sigma_e}^{\mathrm{TOF}}$ and $n_{\sigma_e}^{\mathrm{TPC}}$ and the number of clusters in the TPC and ITS. The variations from the default values are reported in Tab. 4.5. The cases in the top part of the Table refer to variations of a single parameter, while the cases in the bottom part refer to simultaneous variations of more than one parameter. All those cases are tested in order to study the effect of each parameter involved in the reconstruction, as well as the possible interference when two or more of them are modified. The corrected spectrum for electrons from semileptonic decays of heavy hadrons is measured for each configuration reported in Tab. 4.5 and the variations with respect to the default result are considered. The measurements obtained when multiple variations are performed are reported in Fig. 4.13 for central (0–10%) Pb–Pb collisions. Given the high number of cases analysed, the systematic uncertainty is estimated as the mean + RMS of the residuals distributions in each p_{T} interval. With this choice, the 1σ systematic uncertainty is quantified by the spread of the residual distribution and the estimate does not risk to be too much driven by the presence of outliers. Though, a possible average shift with respect to the default case is considered. According to these studies, this uncertainty reaches a maximum value of 4% in the most central (0–10%) Pb–Pb events for $p_{\mathrm{T}} \lesssim 1.5$ GeV/c. It is important to remark that in all the cases in which the PID criteria are modified, the hadron contamination is estimated again repeating the procedure explained in Sec. 4.2.2. When the $n_{\sigma_e}^{\mathrm{TOF}}$ is kept constant and the $\varepsilon_{\mathrm{PID}}^{\mathrm{TPC}}$ is varied from 40% to 60%, the relative amount of hadron contamination at low momentum decreases because the increase of electrons is higher in relative terms than that of hadrons. Vice-versa, an increase of hadron contamination is observed when enlarging the selection interval for $n_{\sigma_e}^{\mathrm{TPC}}$ at high p, due to the fact that the pion distribution is centred closer to $n_{\sigma_e}^{\mathrm{TPC}} = 0$. If the selection on $n_{\sigma_e}^{\mathrm{TOF}}$ is enlarged, the hadron contamination at low p_{T} increases, because in this case the amount of hadrons increases more in relative terms with

Parameter	Default value	Varied selections
$n_{\sigma_e}^{TPC}$ selection	$\varepsilon_{PID}^{TPC} = 50\%$	$\varepsilon_{PID}^{TPC} = 40\%, 60\%$
$n_{\sigma_e}^{TOF}$ selection	[-3,3]	[-2,2], [-2.5,2.5], [-3.5,3.5]
$n_{\sigma_e}^{ITS}$ selection	[-4,2]	[-3,3]
Number of clusters in TPC	≥ 120	$\geq 110, 115, 125, 130$
Number of TPC clusters for dE/dx calculation	≥ 80	$\geq 70, 75, 85, 90$
Number of clusters in ITS	≥ 4	$\geq 2, 3, 5$
Mixed variations (Num. TPC clusters, Num. TPC clusters for dE/dx, Num. ITS clusters, $n_{\sigma_e}^{TOF}$)	$(\geq 120, \geq 80, \geq 4, [-3, 3])$	$(110, 70, 1, [-3, 3])$ $(115, 75, 3, [-3, 3])$ $(125, 85, 2, [-3, 3])$ $(110, 70, 4, [-2.5, 2.5])$ $(115, 75, 4, [-2.5, 2.5])$ $(125, 85, 4, [-2.5, 2.5])$ $(130, 90, 4, [-2.5, 2.5])$ $(110, 70, 4, [-3.5, 3.5])$ $(115, 75, 4, [-3.5, 3.5])$ $(125, 85, 4, [-3.5, 3.5])$ $(130, 90, 4, [-3.5, 3.5])$

TABLE 4.5: Selection criteria variations on the inclusive track parameters studied for the systematic uncertainty estimation. The cases above the midline refer to variations of single parameters, while the cases below refer to simultaneous variations of more than one parameter.

respect to that of the electrons. At high momenta, the variation of the $n_{\sigma_e}^{TOF}$ does not cause a significant change in the amount of hadron contamination, given that in the TOF detector the particle species are no more well distinguishable. By imposing the selection $-3 < n_{\sigma_e}^{ITS} < 3$, the residual contamination changes at low momenta. In particular, the amount of selected kaons and protons increases, as discussed in Sec. 4.2.1. For momenta $p \gtrsim 2$ GeV/c, the usage of ITS for the electron identification is no more effective. The PID limits of ITS and TOF detectors at $p \gtrsim 2 \div 3$ GeV/c is the main reason that justifies the usage of the EMCal at $p_T > 3$ GeV/c, where the electron isolation with respect to hadrons is performed better (see Sec. 4.6).

In a similar way, the systematic uncertainty related to the photonic electron tagging efficiency correction is estimated by varying the selection criteria on the parameters related to the associated track and photonic pair reconstruction. The selection configurations adopted to quantify this effect, also in this case estimated as the mean + RMS of the residual distribution with respect to the default case in each p_T interval, are reported in Tab. 4.6. Given that the amount of photonic electrons reaches the $\sim$ 80% of the inclusive sample at low p_T in central (0–10%) collisions, the final measurement is very sensitive to the photonic background subtraction and this is reflected in a systematic uncertainty of 13% at $p_T < 0.7$ GeV/c, which amounts to 7% in semicentral (30–50%) and peripheral (60–80%) Pb–Pb events. This effect decreases at higher p_T and in more peripheral Pb–Pb collisions.

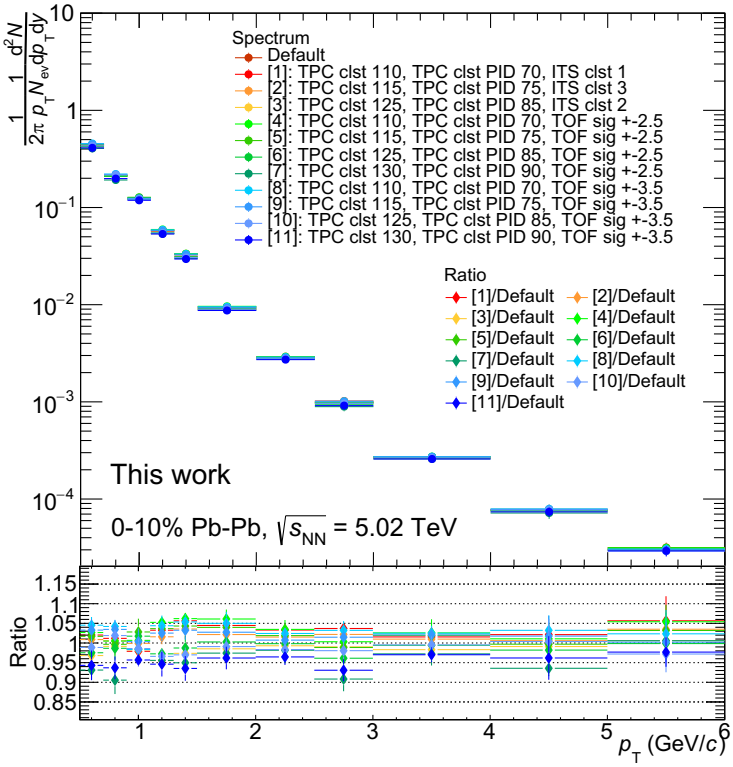

FIGURE 4.13: Corrected p_{T} spectrum of electrons from semileptonic decays of charm and beauty hadrons in central (0–10%) Pb–Pb collisions at $\sqrt{s_{\mathrm{NN}}} = 5.02$ TeV measured with different configurations of the inclusive track selection criteria.

As explained in Sec. 4.3.1, the efficiency of photonic electron tagging is evaluated with MC simulations requiring that the spectrum of light mesons decaying into electrons corresponds to that in data. In particular, the π^0 transverse momentum distribution shape is assumed to be equal to that of the charged pions measured in the same sample used for this analysis. The systematic uncertainty related to the weighting of the generated π^0 and η spectra is estimated by modifying the input spectrum. Given the uncertainties on the measurement, all the points are tilted on the upper or lower edge. Moreover, the p_{T} shape is modified by applying a p_{T}-dependent tilting, that causes either a hardening or a softening of the measured spectrum. Given the small uncertainties on the measured $\pi^{\pm}$ spectrum, the tagging efficiency changes by less than 1%. Therefore, no systematic uncertainty is assigned.

In order to test further the robustness of the photonic electron tagging method, the condition on the number of hits in the SPD is modified. In particular, the analysis is repeated by requiring at least only one hit in the two innermost layers of the ITS. This condition increases the probability to reconstruct electrons coming from photon conversions in the detector material close to the interaction point, changing the amount of the photonic component. It influences also the yield of inclusive electrons. The relative hadron contamination is expected to change. Repeating the measurement with this different selection, a deviation of 10% in $0.5 < p_{\mathrm{T}} < 0.7$ GeV/c and 5% up to $p_{\mathrm{T}} = 4$ GeV/c is observed in central (0–10%) Pb–Pb events. In more peripheral collisions, the effect looks less relevant and reaches a maximum value of 3%.

Parameter	Default Value	Varied selections
Photonic pair $m_{e^+e^-}$	≤ 140 MeV/c^2	$\leq$ 110, 120, 130, 150, 160, 170, 180 MeV/c^2
Number of clusters in TPC	≥ 60	$\geq 40, 50, 70, 80$
Number of TPC clusters for dE/dx calculation	≥ 60	$\geq 40, 50, 70, 80$
Number of clusters in ITS	≥ 2	$\geq 1, 3, 4, 5$
$p_{\rm T}^{\rm assoc.}$	> 0.10 GeV/c	$> 0.05, 0.15, 0.20, 0.25, 0.30$ GeV/c
Mixed variations ($p_{\rm T}^{\rm assoc.}$ and $m_{e^+e^-}$)	(≥ 0.10 GeV/c, ≤ 140 MeV/c^2)	All possible permutations among values reported above
Mixed variations (Num. TPC clusters, Num. TPC clusters for dE/dx, Num. ITS clusters, $p_{\rm T}^{\rm assoc.}$)	($\geq 60, \geq 60, \geq 2, \geq$ 0.10 GeV/c)	(40, 40, 1, 0.10 GeV/c) (50, 50, 3, 0.10 GeV/c) (70, 70, 4, 0.10 GeV/c) (40, 40, 2, 0.15 GeV/c) (50, 50, 2, 0.15 GeV/c) (70, 70, 2, 0.15 GeV/c) (80, 80, 2, 0.15 GeV/c) (40, 40, 2, 0.20 GeV/c) (50, 50, 2, 0.20 GeV/c) (70, 70, 2, 0.20 GeV/c) (80, 80, 2, 0.20 GeV/c)

TABLE 4.6: Selection criteria variations on the associated track parameters studied for the systematic uncertainty estimation. The cases above the midline refer to variations of single parameters, while the cases below refer to simultaneous variations of more than one parameter.

The larger effect in central collisions is caused by the subtraction of a higher hadron contamination accompanied by a huge photonic electron background, whose fraction is significantly enhanced by asking only at least one hit in the SPD layer.

Further possible biases introduced by the MC corrections are evaluated by studying the matching efficiency between TPC and ITS detectors in both data and MC simulations. A detailed study taking into account primary and secondary particles is performed, as explained in Sec. 3.6.4. The systematic uncertainty deriving from the data and MC simulation mismatch in the description of this matching efficiency ranges between 2% and 5%, depending on the $p_{\rm T}$ interval and the Pb–Pb collision centrality. Similarly, also the matching efficiency between TPC and TOF detectors is studied separately in data and MC simulations. In this case, a maximum effect of 3% is observed.

The analysis is repeated in pseudorapidity (η) and azimuthal angle (φ) narrower windows to further evaluate possible effects due to the presence of non-uniformity in the correction for the space-charge distortions in the TPC drift volume or irregularities in the detector coverage. The considered intervals are $|\eta| < 0.5, 0.6, 0.7,$

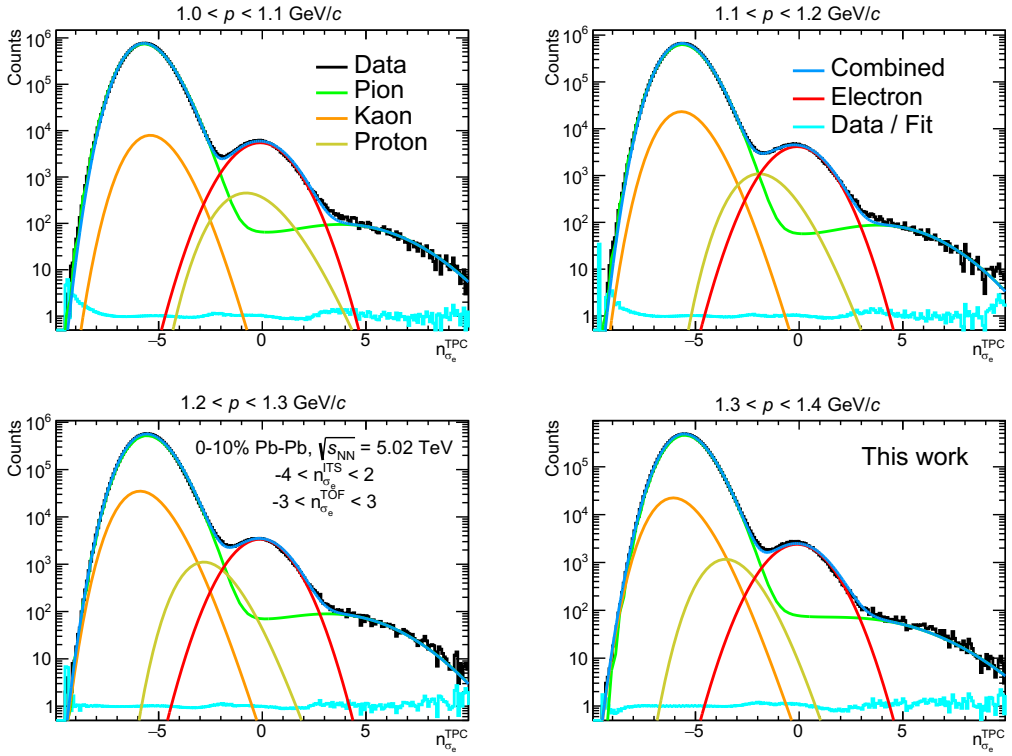

FIGURE 4.14: Examples of $n_{\sigma_e}^{TPC}$ distributions for different momentum intervals between $p = 1.0$ GeV/c and $p = 1.4$ GeV/c in central (0–10%) Pb–Pb collisions at $\sqrt{s_{NN}} = 5.02$ TeV. The track selection is performed applying the criteria reported in Tab. 4.2 and 4.3 and the fit is performed by describing the pion sample with the function reported in Eq. 4.14.

$0 < \eta < 0.8$, $-0.8 < \eta < 0$, $0 < \varphi < 1.4$, $1.4 < \varphi < 3.26$ (corresponding to the EMCal azimuthal acceptance) and $3.26 < \varphi < 2\pi$. A deviation of 10% is observed in $0.5 < p_T < 0.7$ GeV/c in central (0–10%) Pb–Pb events when the pseudorapidity interval is restricted to $|\eta| < 0.5, 0.6$, while no significant trends are observed at higher p_T. With the same variations, in semicentral (30–50%) and peripheral (60–80%) Pb–Pb collisions an effect of 5% is observed on the full p_T range. Analogously, a deviation of 10% for $p_T < 1.1$ GeV/c in central (0–10%) Pb–Pb events, that decreases to 5% at higher p_T, is quantified when restricting the φ interval used to select the electrons. In more peripheral events no significant variation is observed.

Further effects that may arise when the detector occupancy is higher are evaluated by repeating the analysis in two subsamples containing collected Pb–Pb collisions at low (< 5.5 kHz) and high (> 5.5 kHz) interaction rates. In the latter case, the occupancy in the TPC detector is higher due to the ~ 90 µs drift time of ionisation electrons during which tracks from past and future events with respect to the triggered one may be detected [213]. This may increase the influence of distortions as well as the contamination. The effect on the final result is of order of 5% in central (0–10%) Pb–Pb collisions and of 4% at $p_T > 1.5$ GeV/c in semicentral (30–50%) Pb–Pb events, while in more peripheral (60–80%) Pb–Pb collisions no significant effects are observed.

The robustness of the fitting routine described in Sec. 4.2.2 for the estimation of the hadron contamination in the $n_{\sigma_e}^{TPC}$ of the selected electron sample is tested by modifying the function adopted to describe the distributions of different particle

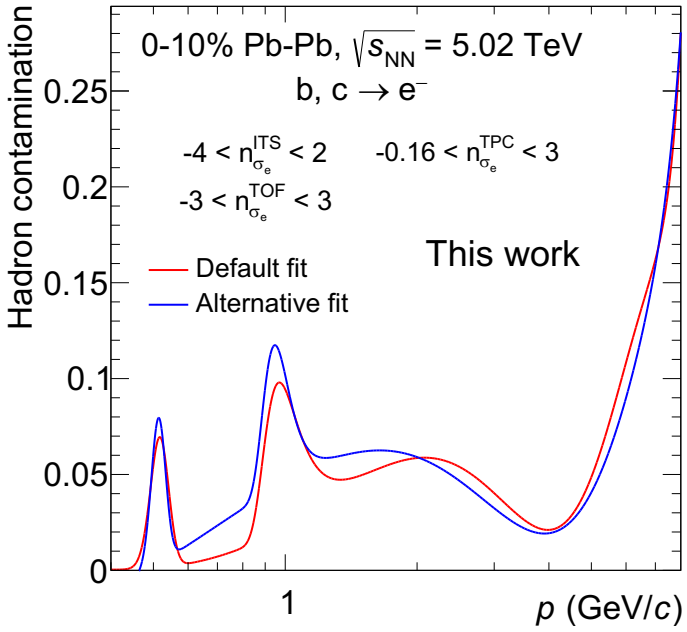

FIGURE 4.15: Comparison between the estimated hadron contamination in central (0–10%) Pb–Pb events describing the pion distribution with a Landau·Exp function (default) or using the parametrisation reported in Eq. 4.14 (alternative).

species. In particular, the main investigation concerns the pion and "others" distribution, which in the default procedure are kept separate in the fit. For the estimation of the systematic uncertainty, the "others" sample is considered as a prolongation of the pion one, re-parametrised using the following formula:

$$f(p) = \text{Landau}(p) \cdot \text{Exp}(p) \cdot \text{Landau}(p) \cdot \text{Exp}(p) \cdot \text{Gaus}(p) \,, \tag{4.14}$$

where the additional pion tail is described by the Landau·Exp·Gaus. Some example of the $n_{\sigma_e}^{TPC}$ distribution fit with the parametrisation of pions performed using the formula in Eq. 4.14 are shown in Fig. 4.14 for $1.0 < p < 1.4$ GeV/c. In this range the contribution of "others" is higher than in the other intervals and the contamination below the electron peak is not negligible. The fact that the "others" sample may belong to the pion one was checked also by looking at identified pion samples centred around the electron signal isolated with further selections in the TRD detector. However, the pion $n_{\sigma_e}^{TPC}$ templates that could be determined from this identified pion sample cannot be used directly in the fit, due to a significant contamination of electrons which evidently would bias the hadron contamination estimation below the electron peak. Therefore, the mimic of the pion tail is provided by the usage of the function reported in Eq. 4.14. The final spectrum of electrons from semileptonic decays of charm and beauty hadrons is then measured by subtracting the hadron contamination determined with this alternative procedure. The effect of subtracting $\times 1.5 - 2$ times this hadron contamination is also evaluated in the range $1.3 < p < 3$ GeV/c, where the pions and "others" provide the highest contamination contribution. The new fitting function provides a higher hadron contamination than the default one. The case for the central (0–10%) events is shown in Fig. 4.15. These studies are performed separately in the three centrality classes and the largest variations are

observed in the most central (0–10%) Pb–Pb events, where the final corrected yield undergoes a maximum variation of 8%. Given the lower amount of contaminating hadrons, a maximum systematic uncertainty of 2% and 1% is quantified in semicentral (30–50%) and peripheral (60–80%) Pb–Pb collisions.

As anticipated, the contributions of J/ψ and K_{e3} electrons are not removed from the electron sample, since the size of these backgrounds is small. Possible systematic uncertainties deriving from these sources are inherited from the same analysis performed in Pb–Pb collisions at $\sqrt{s_{NN}} = 2.76$ TeV and they amount to 2% up to $p_T = 2.5$ GeV/c and 4% at higher transverse momenta.

The systematic uncertainties on the corrected p_T spectrum of electrons from semileptonic charm and beauty hadron decays in central (0–10%), semicentral (30–50%) and peripheral (60–80%) Pb–Pb collisions at $\sqrt{s_{NN}} = 5.02$ TeV are reported in Fig. 4.16 and in Tab. 4.7. The systematic uncertainties deriving from all the sources mentioned above are considered as uncorrelated, therefore the total systematic uncertainty corresponds to their sum in quadrature. A systematic uncertainty related to the determination of the centrality intervals, mainly reflecting the fraction of hadronic cross section (anchor point) used in the Glauber fit on the V0M amplitude distribution to determine the event centrality, also affects the spectra, as shown in Fig. 3.9 [147,280]. This uncertainty amounts to 3% in peripheral (60–80%) Pb–Pb collisions, 2% in semicentral (30–50%) events and it is found to be negligible in central (0–10%) collisions.

TABLE 4.7: Systematic uncertainties estimated on the corrected $p_{\rm T}$ distribution of electrons from semileptonic decays of charm and beauty hadrons measured in central (0–10%), semicentral (30–50%) and peripheral (60–80%) Pb–Pb collisions at $\sqrt{s_{\rm NN}} = 5.02$ TeV.

	$p_{\rm T}$ (GeV/c)	Incl. tr.	Had. cont.	Assoc. tr.	TPC-TOF m.	SPD hits	η var.	φ var.	ITS-TPC m.	J/ψ, $\rm K_{e3}$ sub.	Int. rate
0–10%	0.5, 0.7	4%	6%	13%	3%	10%	10%	10%	2%	2%	5%
	0.7, 0.9	4%	8%	5%	3%	5%	-	10%	2%	2%	5%
	0.9, 1.1	3%	2%	4%	3%	5%	-	10%	3%	2%	5%
	1.1, 1.3	3%	2%	6%	3%	5%	-	5%	3%	2%	5%
	1.3, 1.5	4%	8%	2%	3%	5%	-	5%	3%	2%	5%
	1.5, 2.0	2%	6%	2%	3%	5%	-	5%	5%	2%	5%
	2.0, 2.5	2%	6%	2%	3%	5%	-	5%	5%	2%	5%
	2.5, 3.0	3%	6%	3%	3%	5%	-	5%	5%	4%	5%
	3.0, 4.0	2%	-	1%	3%	5%	-	5%	4%	4%	5%
	4.0, 5.0	3%	-	4%	3%	-	-	5%	4%	4%	5%
	5.0, 6.0	3%	-	3%	3%	-	-	5%	2%	4%	5%
30–50%	0.5, 0.7	1%	2%	7%	1%	-	5%	-	2%	2%	-
	0.7, 0.9	1%	2%	4%	2%	-	5%	-	2%	2%	-
	0.9, 1.1	2%	1%	2%	2%	-	5%	-	3%	2%	-
	1.1, 1.3	2%	1%	2%	3%	-	5%	-	3%	2%	-
	1.3, 1.5	2%	1%	2%	3%	-	5%	-	3%	2%	-
	1.5, 2.0	2%	1%	1%	3%	3%	5%	-	3%	2%	4%
	2.0, 2.5	2%	-	1%	4%	3%	5%	-	5%	2%	4%
	2.5, 3.0	1%	-	1%	4%	3%	5%	-	5%	4%	4%
	3.0, 4.0	1%	-	1%	3%	3%	5%	-	4%	4%	4%
	4.0, 5.0	1%	-	2%	2%	3%	5%	-	4%	4%	4%
	5.0, 6.0	1%	-	2%	2%	3%	5%	-	2%	4%	4%
60–80%	0.5, 0.7	2%	-	7%	1%	-	5%	-	2%	2%	-
	0.7, 0.9	2%	-	3%	2%	-	5%	-	2%	2%	-
	0.9, 1.1	2%	-	2%	2%	-	5%	-	3%	2%	-
	1.1, 1.3	3%	-	2%	2%	-	5%	-	3%	2%	-
	1.3, 1.5	3%	-	3%	3%	-	5%	-	3%	2%	-
	1.5, 2.0	2%	-	2%	3%	-	5%	-	3%	2%	-
	2.0, 2.5	2%	-	1%	3%	-	5%	-	5%	2%	-
	2.5, 3.0	2%	-	3%	3%	-	5%	-	5%	4%	-
	3.0, 4.0	2%	-	2%	3%	-	5%	-	4%	4%	-
	4.0, 5.0	2%	-	1%	3%	-	5%	-	4%	4%	-
	5.0, 6.0	2%	-	3%	3%	-	5%	-	2%	4%	-

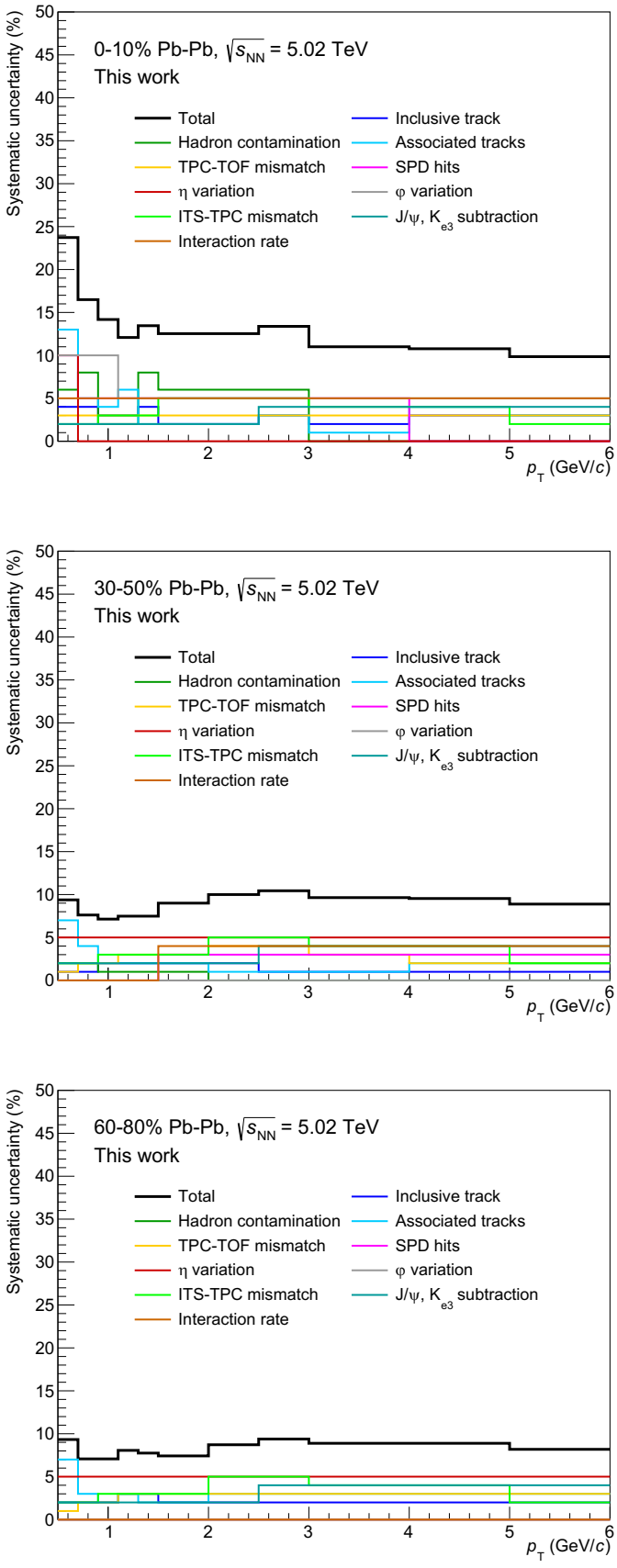

FIGURE 4.16: Systematic uncertainties on the corrected p_T spectrum of electrons from semileptonic charm and beauty hadron decays measured in central (0–10%), semicentral (30–50%) and peripheral (60–80%) Pb–Pb collisions at $\sqrt{s_{NN}} = 5.02$ TeV.

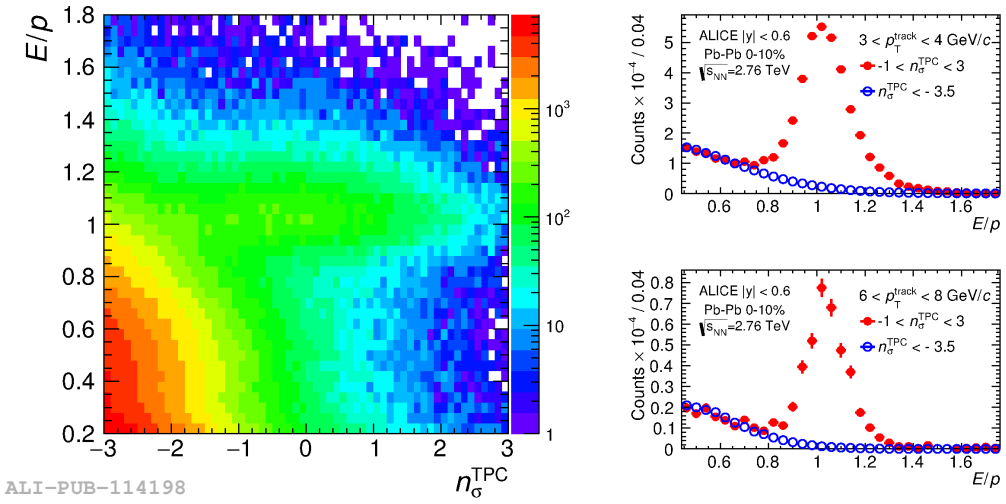

FIGURE 4.17: Left: correlation between E/p and $n_{\sigma_e}^{\rm TPC}$ for tracks with $p_{\rm T} > 3$ GeV/c reconstructed in central (0–10%) Pb–Pb collisions at $\sqrt{s_{\rm NN}} = 2.76$ TeV. Right: E/p distribution for electron (red) and hadron (blue) candidates reconstructed in two transverse momentum intervals in central (0–10%) Pb–Pb collisions at $\sqrt{s_{\rm NN}} = 2.76$ TeV. Figure from [281].

4.6 Electron reconstruction with the EMCal detector

The analysis described in this thesis contributes to the results published in [266] up to $p_{\rm T} = 3$ GeV/c, as remarked in the next Section. For $p_{\rm T} > 3$ GeV/c, the electron reconstruction and identification is performed by exploiting also the signal released in the EMCal detector. Track selections similar to those listed in Tab. 4.2 are applied. The electron identification is performed in the TPC with the selection $-1 < n_{\sigma_e}^{\rm TPC} < 3$ accompanied by specific criteria on the EMCal signal. The tracks reconstructed in the TPC are extrapolated outwards to be matched with clusters in the active volume of the EMCal detector. This matching is performed in case the cluster-track residual in azimuth and pseudorapidity is within $\sqrt{(\Delta\varphi)^2 + (\Delta\eta)^2} < 0.02$. The electromagnetic shower shape in the EMCal calorimeter is exploited to significantly reduce the hadron contamination [281]. The shape can be characterised by the two eigenvalues λ_0 and λ_1 of the covariance matrix built from the tower coordinates weighted by the algorithms of the tower energies. These eigenvalues can be used to separate different particle species. The selection $0.01 < \lambda_1^2 < 0.35$, where λ_1 corresponds to the short-axis of the shower shape projected along the EMCal surface, is applied. This selection is rather loose and does not reduce the electron reconstruction efficiency significantly, but it helps to remove a significant amount of hadron contamination, being the characteristic shower of an electron peaked at $\lambda_1^2 \approx 0.25$ independently on the cluster energy. The residual hadron contamination in the electron sample is estimated using the E/p distributions, where E is the matched EMCal cluster energy and p is the track momentum. In Fig. 4.17 the correlation between E/p and $n_{\sigma_e}^{\rm TPC}$ for tracks with $p_{\rm T} > 3$ GeV/c reconstructed in central (0–10%) Pb–Pb collisions at $\sqrt{s_{\rm NN}} = 2.76$ TeV is shown in the left panel. The E/p distributions in the intervals $3 < p_{\rm T} < 4$ GeV/c and $6 < p_{\rm T} < 8$ GeV/c for candidate electrons satisfying $-1 < n_{\sigma_e}^{\rm TPC} < 3$ (red) are shown in the right panel [281]. The electron distribution is peaked around $E/p = 1$, then the selection $0.9 < E/p < 1.3$ is applied. The residual hadron contamination is estimated using the E/p distributions of tracks selected

with $n_{\sigma_e}^{TPC} < -3.5$ and normalised to match the electron candidate distributions in $0.4 < E/p < 0.7$. The maximum amount of hadron contamination statistically subtracted from the selected electron sample is about $\sim$ 10% for $p_T > 22$ GeV/c in central (0–10%) Pb–Pb collisions at $\sqrt{s_{NN}} = 5.02$ TeV and it decreases at lower p_T and in more peripheral Pb–Pb collisions.

As anticipated in Sec. 4.3.1, the electrons from W and Z/γ^* decays constitute a significant source of background to be subtracted. These contributions are obtained from calculations using the POWHEG event generator for pp collisions and scaling the production yield by the $\langle N_{coll} \rangle$ of the considered Pb–Pb collision centrality class, assuming $R_{AA} = 1$. The fraction of electrons from W decays increases from 1% at $p_T = 10$ GeV/c to about 20% for $p_T > 22$ GeV/c in central (0–10%) Pb–Pb collisions, while the Z contribution reaches about 10% in the same p_T interval.

The measurement of electrons from semileptonic decays of charm and beauty hadrons is pushed up to $p_T = 26$ GeV/c in central (0–10%) and semicentral (30–50%) Pb–Pb collisions at $\sqrt{s_{NN}} = 5.02$ TeV thanks to the samples recorded with the EMCal trigger, that requires an EMCal cluster energy summed over a group of 4×4 calorimeter cells larger than a threshold of 10 GeV/c. This trigger is adopted for the measurement above $p_T = 12$ GeV/c. The measured per-event electron yield is scaled to the minimum bias one by normalisation factors determined with a data-driven approach based on the ratio of the energy distributions of the EMCal clusters in the two triggers [281].

4.7 Results

The measurement of the p_T-invariant yield of electrons from semileptonic decays of charm and beauty hadrons in central (0–10%), semicentral (30–50%) and peripheral (60–80%) Pb–Pb collisions at $\sqrt{s_{NN}} = 5.02$ TeV is performed in the following p_T intervals: $[0.5, 0.7)$ GeV/c, $[0.7, 0.9)$ GeV/c, $[0.9, 1.1)$ GeV/c, $[1.1, 1.3)$ GeV/c, $[1.3, 1.5)$ GeV/c, $[1.5, 2.0)$ GeV/c, $[2.0, 2.5)$ GeV/c, $[2.5, 3.0)$ GeV/c, $[3.0, 4.0)$ GeV/c, $[4.0, 5.0)$ GeV/c and $[5.0, 6.0)$ GeV/c. As already mentioned at the beginning of this Chapter, the analysis described in the previous Sections contributes to the results published in Ref. [266] up to $p_T = 3$ GeV/c. At higher p_T, a different analysis is performed with the exploitation of the EMCal calorimeter, used both as trigger and PID detector, granting a higher purity at high p_T, as well as smaller statistical and systematic uncertainties. As visible in Fig. 4.7, above $p = 3$ GeV/c the pion contamination in the $n_{\sigma_e}^{TPC}$ distribution quickly increases, reaching 15% or 25% at $p = 8$ GeV/c, depending on the event centrality. The systematic uncertainty deriving from this contamination increases accordingly. Moreover, at such transverse momenta the amount of electrons surviving the track and PID selections reported in Tabs. 4.2 and 4.3 quickly decreases. For these reasons, the measurement performed in the $3.0 < p_T < 4.0$ GeV/c, $4.0 < p_T < 5.0$ GeV/c and $5.0 < p_T < 6.0$ GeV/c are not included in the final results.

4.7.1 Invariant p_T- differential yield in Pb–Pb collisions

The invariant p_T spectra of electrons from semileptonic decays of charm and beauty hadrons in central (0–10%), semicentral (30–50%) and peripheral (60–80%) Pb–Pb collisions at $\sqrt{s_{NN}} = 5.02$ TeV are shown in Fig. 4.18. The statistical uncertainties are reported as vertical lines, while the boxes around the central values represent the systematic uncertainties. The results from the work described in this Chapter,

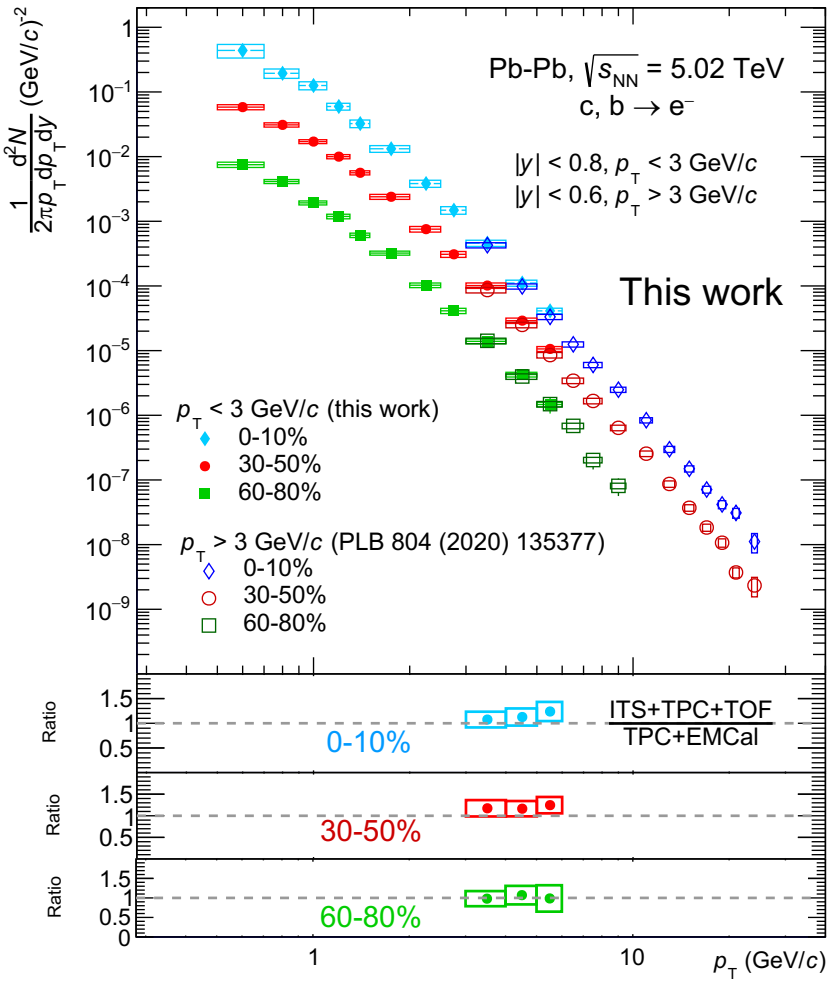

FIGURE 4.18: Invariant $p_{\rm T}$ spectra of electrons from semileptonic decays of charm and beauty hadrons identified with ITS, TPC and TOF at $p_{\rm T} < 3$ GeV/c (this work) and with EMCal at $p_{\rm T} > 3$ GeV/c in central (0–10%), semicentral (30–50%) and peripheral (60–80%) Pb–Pb collisions at $\sqrt{s_{\rm NN}} = 5.02$ TeV. Results for $p_{\rm T} > 3$ GeV/c from [266]. In the smaller bottom panels the ratio between the two analyses in the interval $3 < p_{\rm T} < 6$ GeV/c are reported. The statistical and systematic uncertainties are treated as uncorrelated in the propagation.

where the electron identification is performed using the ITS, TPC and TOF detectors, are reported with filled markers and they are compared with the mentioned measurement performed using the EMCal calorimeter for the electron identification at $p_{\rm T} > 3$ GeV/c. The results from the two analyses are compatible in the common range $3 < p_{\rm T} < 6$ GeV/c given the statistical and systematic uncertainties (see the smaller bottom panels). The spectra in central (0–10%) and semicentral (30–50%) Pb–Pb collisions are measured in the range $0.5 < p_{\rm T} < 26$ GeV/c, while the measurement in peripheral (60–80%) Pb–Pb events is limited in the range $0.5 < p_{\rm T} < 10$ GeV/c due to the more limited available statistics. The measured spectra show a

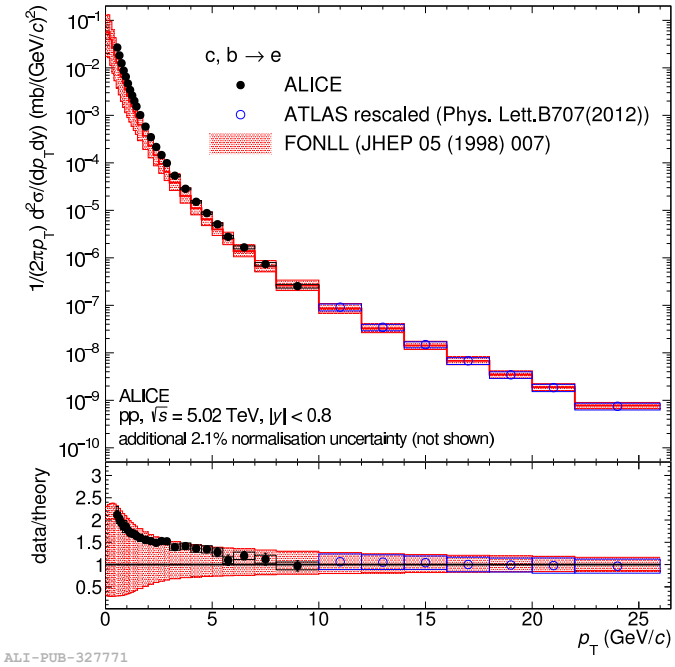

FIGURE 4.19: p_{T}-differential invariant production cross section of electrons from semileptonic heavy-flavour hadron decays in pp collisions at $\sqrt{s} = 5.02$ TeV. The measurement is compared with the FONLL calculation [100]. In the bottom panel, the ratio with respect to the central values of the FONLL calculation is shown. Figure from [266].

clear hierarchy with the Pb–Pb event centrality, given that the production yields decrease from central to peripheral collisions.

4.7.2 Invariant production cross section in pp collisions

The production cross section of electrons from semileptonic decays of charm and beauty hadrons measured in pp collisions at $\sqrt{s} = 5.02$ TeV is shown in Fig. 4.19 [266]. The measurement was performed with the ALICE experiment in the transverse momentum range $0.5 < p_{\mathrm{T}} < 10$ GeV/c and the results are reproduced by the FONLL calculations, lying on the upper edge of the uncertainty band. For $p_{\mathrm{T}} > 10$ GeV/c, the reference is obtained by a p_{T}-dependent $\sqrt{s}$-scaling of the measurement at $\sqrt{s} = 7$ TeV by the ATLAS collaboration [282]. Given the agreement of the measurements with the FONLL calculations, the scaling factor is calculated as the ratio of the cross section at the two collision energies computed with the FONLL calculation [283]. This ratio is calculated taking into account the different rapidity coverage of the ATLAS measurement ($|y| < 2$ excluding $1.37 < y < 1.52$). The systematic uncertainties on the extrapolated cross section at $\sqrt{s} = 5.02$ TeV range from 13% to 18% depending on the p_{T} interval. They are computed as the propagation of the uncertainties on the $\sqrt{s}$-scaling factor, estimated by consistently varying the FONLL parameters at the two energies, as explained in Ref. [283], and the systematic uncertainties of the ATLAS measurement. The statistical uncertainties come from the ATLAS measurement. This result is used as reference for the measurement of the nuclear modification factor R_{AA}.

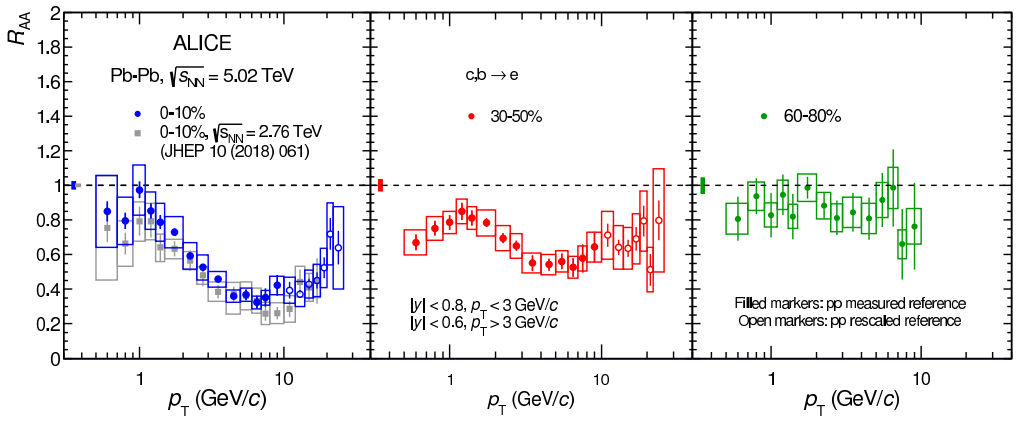

FIGURE 4.20: Nuclear modification factor of electrons from semileptonic decays of charm and beauty hadrons in central (0–10%), semicentral (30–50%) and peripheral (60–80%) Pb–Pb collisions at $\sqrt{s_{\rm NN}} = 5.02$ TeV. The work described in this thesis contributes in these results up to $p_{\rm T} = 3$ GeV/c. Figure from [266].

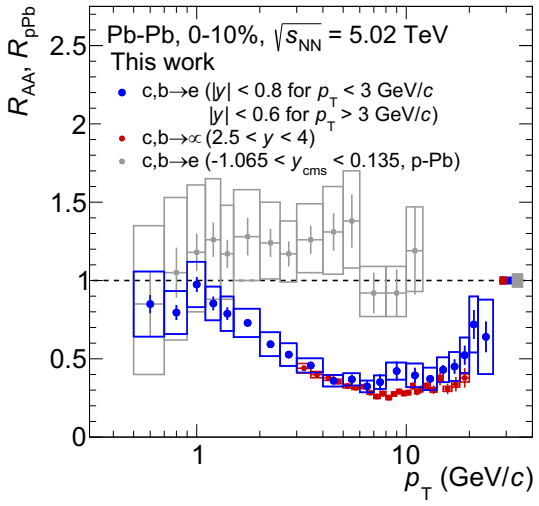

FIGURE 4.21: Nuclear modification factor $R_{\rm AA}$ of electrons (blue) [266] and muons (red) [284] from semileptonic decays of charm and beauty hadrons measured in central (0–10%) Pb–Pb collisions at $\sqrt{s_{\rm NN}} = 5.02$ TeV compared with the $R_{\rm pPb}$ of electrons (grey) measured in p–Pb collisions at the same centre-of-mass energy per nucleon pair [285].

4.7.3 Nuclear modification factor

In Fig. 4.20 the nuclear modification factor $R_{\rm AA}$ of electrons from semileptonic decays of charm and beauty hadrons in central (0–10%), semicentral (30–50%) and peripheral (60–80%) Pb–Pb collisions at $\sqrt{s_{\rm NN}} = 5.02$ TeV is shown. The statistical and systematic uncertainties on the $R_{\rm AA}$ are calculated by propagating the statistical and systematic uncertainties on the invariant cross section and yields in pp and Pb–Pb collisions, respectively, as fully uncorrelated. The boxes at unity correspond to the

normalization uncertainties, given by the $\langle T_{AA} \rangle$ uncertainty (see Tab. 4.1), the pp luminosity uncertainty equal to 2.1% and the centrality determination uncertainty, reported in Sec. 4.5. The measured R_{AA} shows a dependence on the collision centrality, considering that in most central events it reaches a minimum of about 0.3 around $p_T = 7$ GeV/c, while in more peripheral Pb–Pb collisions it gets closer to unity. Such a suppression is not observed in p–Pb collisions at the same energy [285] where the QGP is not expected to be produced. In this case, the nuclear modification factor is observed to be consistent with unity [285–287], as shown in Fig. 4.21. The suppression of electron production for $p_T \gtrsim 3$ GeV/c in Pb–Pb collisions can be then ascribed to final-state effects, such as partonic energy loss in the medium. Since electrons from semileptonic beauty decays are expected to dominate the spectrum at $p_T \gtrsim 3$ GeV/c while charm production dominates at $p_T \lesssim 3$ GeV/c [286], the measurements show that both charm and beauty quarks lose energy in the medium. The centrality dependence of the R_{AA} is compatible with the hypothesis of a partonic energy loss dependence on medium size and density, being larger in hotter and denser QGP, like that created in the most central (0–10%) Pb–Pb collisions. Indeed, it reflects a path-length dependence of energy loss. Moreover, it has been shown in Refs. [288,289] that a centrality selection bias is present in most peripheral Pb–Pb collisions, reducing the R_{AA} below unity even in the absence of any nuclear modification effects. This effect is considered to be responsible for a significant part of the apparent suppression seen in the measurement in peripheral (60–80%) Pb–Pb collisions, where the R_{AA} of electrons from semileptonic heavy-flavour hadron decays is around 0.9. For $p_T < 7$ GeV/c, the R_{AA} of electrons from semileptonic heavy-flavour hadron decays increases with decreasing transverse momentum as a consequence of the scaling of the total heavy-flavour yield with the number of binary collisions among nucleons in Pb–Pb collisions. However, the nuclear modification factor at low p_T does not rise above unity. This kinematic region is sensitive to the effects of nuclear shadowing, which causes a depletion of parton densities in nuclei at low Bjorken-x values compared to those in protons that can reduce the heavy-quark production cross section per binary collision in Pb–Pb collisions with respect to the pp ones [254]. Furthermore, the amount of electrons from semileptonic heavy-flavour hadron decays might be reduced due to the presence of hadrochemistry effects. For example, Λ_c^+ baryons decay into electrons with a branching ratio of about 5%, while for D mesons this is about 10%. Since in Pb–Pb collisions more charm quarks might hadronize into baryons [290], this effect may reduce the total amount of electrons from semileptonic charm hadron decays. Additional effects, such as collective motion induced by the medium, also have an influence on the measured nuclear modification factor. The radial flow can cause an additional yield enhancement at intermediate p_T [291–294]. According to models, in the case of electrons from heavy-flavour hadron decays the radial flow pushes up slow particles to higher momenta, causing a small increase in the nuclear modification factor around $p_T = 1$ GeV/c. It should be noted that the R_{AA} measurements in the most central (0–10%) collisions at $\sqrt{s_{NN}} = 2.76$ TeV [254] and 5.02 TeV are compatible within uncertainties, as shown in the left panel of Fig. 4.20. This similarity was predicted by the Djordjevic model [295], and it results from the compensation of the effect of a higher medium temperature at 5.02 TeV, which would increase the energy loss, decreasing the R_{AA} by about 10%, with a harder p_T distribution of heavy quarks at 5.02 TeV, which would increase the R_{AA} by about 5% in case the medium temperature

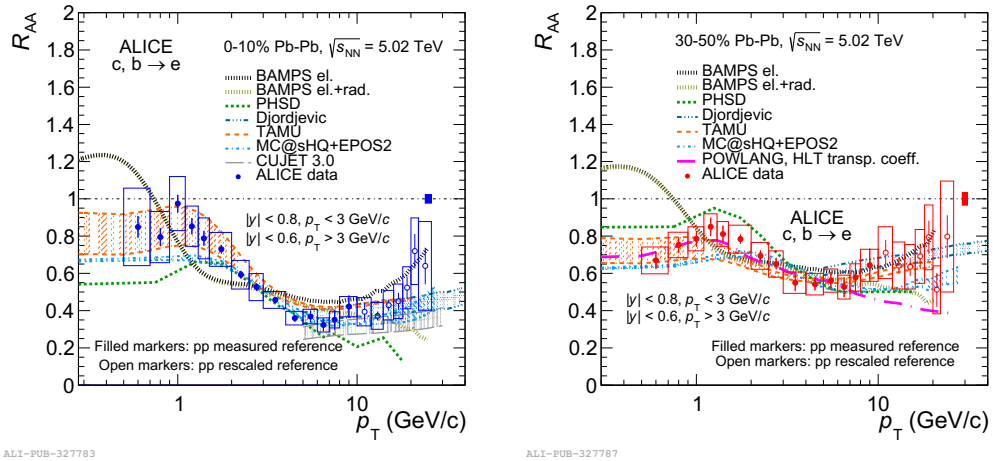

FIGURE 4.22: Nuclear modification factor of electrons from semileptonic decays of charm and beauty hadrons in central (0–10%) and semicentral (30–50%) Pb–Pb collisions at $\sqrt{s_{NN}} = 5.02$ TeV compared with model predictions. The work described in this thesis contributes in these results up to $p_T = 3$ GeV/c. Figure from [266].

were the same as at 2.76 TeV[1]. An analogous behaviour between the measured R_{AA} at the two energies is also observed for the D mesons [147]. The R_{AA} of electrons from semileptonic decays of heavy-flavour hadrons measured in Pb–Pb collisions at $\sqrt{s_{NN}} = 5.02$ at midrapidity is compared in Fig. 4.21 with that of muons from semileptonic decays of heavy-flavour hadrons in the same collision system at forward rapidity [284]. In the common p_T range the two results are compatible within uncertainties. Such agreement indicates that the nuclear modification factor of leptons from charm and beauty hadron decays does not depend on y within a range covering four units of rapidity.

The nuclear modification factor R_{AA} of electrons from semileptonic decays of charm and beauty hadrons measured in central (0–10%) and semicentral (30–50%) Pb–Pb collisions at $\sqrt{s_{NN}} = 5.02$ TeV are compared with the predictions from several model calculations, which take into account different hypotheses about the mass dependence of energy loss processes involving heavy quarks and their interactions with the QGP constituents, as well as different prescriptions for the heavy quark hadronisation in the QGP and their production in nucleus-nucleus collisions. The theoretical models can be essentially classified into two separate groups: pQCD-based models, which base their predictions on the high-p_T heavy quark energy loss in the QGP on pQCD-inspired calculations, and the transport models, which describe the QGP as a hydrodynamic expanding medium where heavy quarks can be dragged according to their spatial diffusion coefficient (Eq. 2.17). The pQCD-based models that are compared to the measured R_{AA} are described below.

1. **Djordjevic** [295, 296]. In this model the heavy quark energy loss in the QGP takes place through both elastic collisions and gluon radiation. In particular, calculations related to the radiative energy loss are an extension of the DGLV model predictions [297], taking into account the finite QGP dimensions and the running value of α_S. In this model, charm and beauty quarks fragment

[1]The final quark p_T-differential spectrum, prior to hadronisation, derives from the convolution of the original quark p_T spectrum and the energy loss in the medium. Thus, in case of equal energy loss, a harder initial p_T spectrum results in a higher R_{AA} than that obtained with a softer p_T spectrum.

into heavy-flavour hadrons according to the BCFY [298] and KLP [299] fragmentation functions respectively.

2. **CUJET3.0** [300]. In this model both collisional and radiative energy loss processes for jets are described, but no treatments of QGP hydrodynamic expansion as well as heavy quark recombination with medium constituents are considered. The 3.0 version is an update of the CUJET2.0 pQCD-based calculations [301], where the major news consist in the treatment of non-perturbative features to describe the cross-over of the QCD phase transition, such as the possible birth of chromo-magnetic monopoles and the parton degrees of freedom suppression.

The measured nuclear modification factors are compared also to the predictions from several transport models, which are described below.

3. **Boltzmann Approach to MultiParton Scatterings (BAMPS)** [302]. It consists in a parton transport model based on the Boltzmann equation (Eq. 2.13), where both collisional and radiative processes are considered to describe the 3+1D space-time evolution of gluons, light quarks, and heavy quarks in ultra-relativistic heavy-ion collisions. The quark hadronisation is implemented through the usage of Peterson [198] fragmentation functions.

4. **Parton-Hadron-String Dynamics (PHSD)** [303]. It is a microscopic transport model which describes the entire evolution of the heavy-ion collision. The charm quarks are produced through initial binary nucleon-nucleon collisions by using the PYTHIA event generator taking into account the (anti-)shadowing incorporated in the EPS09 package. The produced charm quarks are then subject to interactions with off-shell massive partons, assumed to be the degrees of freedom of the QGP medium, undergoing both collisional energy loss. The masses of the dynamical quarks and gluons in the QGP are distributed according to spectral functions whose pole positions and widths, respectively, are defined by the real and imaginary parts of their self-energies. The latter are defined in the dynamical quasiparticle model (DQPM [304]), in which the strong coupling and the self-energies are fitted to lattice QCD results. Heavy quarks are hadronized via both fragmentation and coalescence. The final-state charm hadrons are then supposed to interact with the hadrons in the final hadronic stage, where the interaction cross section is calculated in an effective Lagrangian approach implementing heavy-quark spin symmetry.

5. **MC@sHQ+EPOS2** [265]. In this model the Boltzmann equation rules the evolution of the heavy quarks in QGP, described as a 3+1D hydrodynamic expanding medium from the initial conditions provided by the EPOS framework. Both collisional and radiative energy loss processes are included and the heavy quark hadronisation is ruled either via fragmentation or coalescence. In this model the possible existence of hadronic bound states above the deconfinement transition temperature T_c and the influence on the heavy quark dynamics given a non-negligible amount of hadronic degrees of freedom in the QGP are studied.

6. **POWLANG** [305]. This models includes a viscous hydrodynamic expansion of the QGP and describes the heavy quark energy loss via the Langevin equation. The transport coefficients are evaluated with a pQCD approach for hard scatterings and using hard-thermal-loop calculations for soft processes. The

heavy quark energy loss is implemented only through collisional processes. The hadronisation is assumed to occur via the fragmentation of strings with a heavy (anti-)quark and a thermal (anti-)quark in the medium as endpoints.

7. **TAMU** [263]. In this transport model, the interaction between the heavy quarks and the QGP takes place through resonance formation, with momentum transfer performed only via collisional processes. The hydrodynamical description of the QGP evolution implemented with a Langevin approach is bound by the knowledge of light hadron spectra and elliptic flow measurements. Moreover, the heavy quark hadronisation is expected to take place also via coalescence.

Most of the models provide a fair description of the data in the interval $p_{\rm T} < 5$ GeV/c in both centrality classes, except for BAMPS calculations. The predictions from the MC@sHQ+EPOS2, PHSD, TAMU and POWLANG models include nuclear modification of the parton distribution functions, which is necessary to predict the observed suppression of the $R_{\rm AA}$ at low $p_{\rm T}$, while the BAMPS model does not consider it and consequently overestimates the measured $R_{\rm AA}$. The nuclear modification factor for central (0–10%) Pb–Pb collisions is well described by the TAMU predictions at $p_{\rm T} < 3$ GeV/c within the uncertainty band, related to the shadowing effect on charm quarks. However, this model tends to overestimate the $R_{\rm AA}$for $p_{\rm T} >$ 3 GeV/c, probably due to the missing implementation of the radiative energy loss, which may become the dominant mechanism at high $p_{\rm T}$. On the other hand, the agreement with TAMU predictions at low $p_{\rm T}$ confirms the dominance of elastic collisions at low transverse momenta, together with the need of including shadowing effects, which reduce the total heavy-flavour production in Pb–Pb collisions with respect to the expectations from binary scaling, in the model calculations. This is confirmed also by the nice agreement between the measured $R_{\rm AA}$ in semicentral (30–50%) Pb–Pb collisions and the predictions from POWLANG model, which however significantly underestimates the measurement for $p_{\rm T} > 7$ GeV/c due to the limited description of the heavy quark energy loss mechanisms, not including the radiative component. The CUJET3.0 and Djordjevic models provide a reasonable description of the radiative energy loss dependence on the path length, given that their predictions describe the $R_{\rm AA}$ within the uncertainties in both centrality intervals for $p_{\rm T} > 5$ GeV/c.

4.8 Conclusions and outlook

The invariant yield of electrons from semileptonic decays of heavy-flavour hadrons was measured in central (0–10%), semicentral (30–50%), and peripheral (60–80%) Pb–Pb collisions at $\sqrt{s_{\rm NN}} = 5.02$ TeV with the ALICE experiment. The work described in this thesis significantly contributes to these results, providing the measurement for $p_{\rm T} < 3$ GeV/c where the nuclear shadowing and the collisional energy loss are expected to significantly influence the heavy quark production and dynamics in QGP. In addition to what already obtained with the same work done on the sample at $\sqrt{s_{\rm NN}} = 2.76$ TeV, this analysis at $\sqrt{s_{\rm NN}} = 5.02$ TeV extends the $p_{\rm T}$ reach and provides an additional centrality class. The measurements in central (0–10%), semicentral (30–50%) and peripheral (60–80%) Pb–Pb collisions exhibit the dependence of heavy quark energy loss on the path length and energy density in the hot and dense medium. The results are compatible within uncertainties with several model predictions describing the centrality dependence of the in-medium radiative energy loss. These models provide similar predictions for the $R_{\rm AA}$, therefore more

information may derive from the comparison between measurements and model calculations on different observables, such as v_2. Further investigations and measurements of electrons from semileptonic decays of beauty hadrons will give more information about the mass dependence of the energy loss in the heavy-flavour sector. With the precision of the results presented here, the Pb–Pb data exhibit their sensitivity to the modification of the nuclear PDFs, whose implementation in theoretical calculations is a mandatory ingredient for the model predictions to correctly describe the measured R_{AA}.

For a complete understanding of the heavy quark production and dynamics in QGP further measurements and efforts are anyway necessary. The measurement shown here does not permit to appreciate the behaviour of the different charm and beauty hadrons, given the inclusive nature of the measurement itself. Moreover, the results are provided as a function of the electron transverse momentum, being not a variable directly related to the heavy hadron kinematics. For these reasons, exclusive measurements of charm and beauty mesons and baryons are required. With the Pb–Pb sample at $\sqrt{s_{\mathrm{NN}}} = 5.02$ TeV recorded by the ALICE experiment in 2015 the nuclear modification factor of prompt D mesons [147] was measured in the same three centrality classes considered in this work and similar conclusions were driven from the comparison with model calculations. The 2018 Pb–Pb sample, characterized by a factor $\times 8$ more statistics in central (0–10%) and $\times 4$ more statistic in semicentral (30–50%) events, can further help making this measurement more differential and in an extended p_{T} interval. Furthermore, it offers the opportunity to measure more precisely and differentially the production of charm baryon states in heavy ion collisions, such as Λ_{c}^{+} that for the moment was measured only for $6 < p_{\mathrm{T}} < 12$ GeV/c in Pb–Pb collisions by the ALICE experiment [290]. Such a result can give further insights in the heavy-flavour hadronisation in the QGP, thanks to the possibility to compare the baryon and meson productions, which in principle are sensitive in different ways to fragmentation and coalescence hadronisation.

Chapter 5

Λ_c^+ and $\Sigma_c^{0,++}$ production in pp collisions at $\sqrt{s} = 13$ TeV

The investigation of the QGP properties via the analysis of Pb–Pb collisions at the LHC requires a detailed understanding of the physics in pp collisions, used as a reference to correctly interpret what observed in heavy-ion collisions. A clear example has been shown in the previous Chapter, where the charm and beauty energy loss in the QGP was studied from the comparison of the R_{AA} with several model predictions. The physics of pp collisions carries a big intrinsic interest in per se, especially in the heavy-flavour sector. As anticipated in Sec. 2.1 and 2.3.2, the most recent results at the LHC indicate an enhancement in the charm and beauty baryon abundances relative to those of charm and beauty mesons with respect to what observed in e^+e^- and e^-p collisions. In particular, this concerns the production of Λ_c^+, $\Xi_c^{0,+}$ and Λ_b^0 baryons in pp collisions at $\sqrt{s} = 5.02$, 7 and 13 TeV [108, 109, 178, 306–312]. Another baryon whose production has not been measured yet in hadronic collisions at the LHC is the $\Sigma_c(2455)$. The $\Sigma_c^0(ddc)$, $\Sigma_c^+(udc)$ and $\Sigma_c^{++}(uuc)$ baryons belong to an isospin triplet $I = 1$ that can be recognised as partner of the Λ_c^+, corresponding to an isospin singlet $I = 0$. The measurement of light and heavy baryon abundances produced in e^+e^- is a fundamental brick in the comprehension of quark fragmentation and the same measurements at the LHC are fundamental to understand if new hadronisation mechanisms play a role in hadronic collisions. In e^+e^- collisions at KEKB collider the Belle experiment measured the production cross sections of hyperons and charm baryons using a $\mathcal{L} = 800$ fb^{-1} data sample taken at $\sqrt{s} = 10.52$ GeV, namely close to the $\Upsilon(4S)$ threshold [114]. In Fig. 5.1 the production cross sections of hyperons (left) and charm baryons (right) as a function of the hadron mass measured by the Belle experiment are shown. These results regard the direct production, obtained from the total by subtracting all the contributes deriving from the decay of heavier particles. The cross sections are scaled by the number of total angular momentum states $2J + 1$ and a clear ordering in the hyperon sectors is visible. All the baryons with strangeness number $S = -1$ are observed to follow an exponential trend as a function of the hadron mass within 3σ and for all baryons with a larger strange content a lower cross section is observed. This behaviour is ascribed to the higher mass of $s\bar{s}$ pairs, which are produced with a smaller probability than $u\bar{u}$ and $d\bar{d}$ pairs in a conventional string breaking process. Despite this difference, which causes a lower cross section with increasing strangeness content, a similar production mechanism is expected in the $S = -1$ and $S = -2$ cases and the dashed line in the left panel corresponds to the same exponential for the $S = -1$ case normalised to the Ξ^- abundance. From the plot it is evident that the production of the $\Xi^0(1530)$ excited state is significantly lower than the exponential expectation. This may be related to a decuplet suppression, as indicated also by the $\Sigma^+(1385)$ that however is in line with the $S = -1$ exponential within 2.8σ. On the right panel the data for

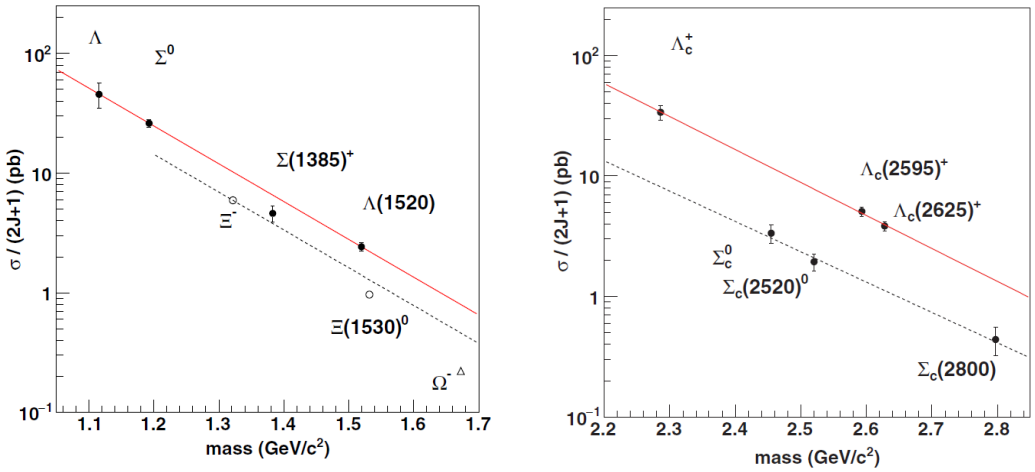

FIGURE 5.1: Direct production cross section of hyperons (left) and charm baryons (right) as a function of hadron mass scaled by the number of total angular momentum states $(2J+1)$ measured in e^+e^- collisions at $\sqrt{s} = 10.52$ GeV by the Belle Collaboration. Figures from [114].

charmed baryons are shown. Their production looks significantly higher than that expected from the hyperon exponential function. This behaviour can be explained by the fact that the centre of mass energy at the $\Upsilon(4S)$ threshold is high enough for the e^+e^- annihilation to produce a similar amount of $c\bar{c}$ pairs and $u\bar{u}$ ones[1]. Moreover, the production of charmed baryons differs from that of hyperons: considering that the $c\bar{c}$ production from fragmentation is significantly suppressed (see Eq. 2.29), basically it happens only in the direct annihilation of e^+e^-. This implies that in the conventional fragmentation picture the formation of a charm baryon requires that a charm quark picks up two light quarks. However, in the early stage of the fragmentation process, when the $c\bar{c}$ pair has just been produced, the number of light quarks is small and then the charm baryon production from a charm quark from two independent light quarks is suppressed compared to that from diquark and anti-diquark production. Moreover, as discussed in Ref. [114], the color-magnetic interactions between charm and light quarks are suppressed due to the high charm quark mass, therefore diquark degrees of freedom may be enhanced in relative terms in the production mechanisms. For these reasons, the production cross section of charmed baryons in e^+e^- collisions reflects the diquark production. In the case of charm baryons, the Λ_c^+ and Σ_c states lie on two exponentials with compatible slopes, differently for what observed for the hyperons Λ and Σ. In the conventional string fragmentation framework the suppression of $\Sigma_c^{0,+,++}(2455)$ with respect to Λ_c^+ is ascribed to the need for a charm quark to pick up a spin-1 diquark, whose production with respect to spin-0 diquarks is strongly suppressed due to their larger mass. These predictions from the fragmentation are confirmed by the experimental data, where the Σ_c-state production results $\times 3 - 4$ times smaller than the excited Λ_c^+ states [114].

[1]Note that the $e^+e^- \to q\bar{q}$ is an electroweak process where the couplings in the matrix element only depend on the quark electric charges, but larger masses of the final state quarks require a higher energy for the colliding particles.

	Σ_c^0	Σ_c^+	Σ_c^{++}
m (MeV/c^2)	2453.75 ± 0.14	2452.9 ± 0.4	2453.97 ± 0.14
Γ (MeV/c^2)	$1.83^{+0.11}_{-0.19}$	< 4.6 (90% CL)	$1.89^{+0.09}_{-0.18}$
Δm with Λ_c^+ (MeV/c^2)	167.290 ± 0.017	166.4 ± 0.4	167.510 ± 0.017
Δm with Σ_c^0 (MeV/c^2)	-	-0.9 ± 0.4	0.220 ± 0.013

TABLE 5.1: Kinematic variables of Σ_c^0, Σ_c^+ and Σ_c^{++}. Values from PDG 2020 [3].

In this thesis, the measurement of Λ_c^+ and $\Sigma_c^{0,++}(2455)$ production in pp collisions at $\sqrt{s} = 13$ TeV at midrapidity ($|y| < 0.5$) is performed. The goal of the analysis is to quantify the production of "prompt" baryons, namely those directly produced by the charm hadronisation or coming from the strong decays of higher-mass states. The component of charm baryons coming from the decay of beauty hadrons, called "non-prompt", is removed. For the Λ_c^+ baryon a dedicated measurement of the relative fraction deriving from $\Sigma_c^{0,++}(2455)$ decays is also done. This is the first measurement in hadronic collisions at the LHC at midrapidity of the Λ_c^+ prompt feed-down from $\Sigma_c^{0,++}(2455)$ decays and it covers a fundamental role to understand the composition of the prompt Λ_c^+ spectrum. The $\Sigma_c^{0,++}(2455)$ production is measured as well for the first time in hadronic collisions at the LHC at midrapidity. The results obtained from the work described in this thesis contribute to the results published in Ref. [313]. In the following, the $\Sigma_c(2455)$ baryons are indicated simply with Σ_c.

5.1 Data sample and event selection

The p_T-differential production cross section of prompt Λ_c^+, $\Lambda_c^+ (\leftarrow \Sigma_c^{0,++})$ and $\Sigma_c^{0,++}$ in pp collisions at $\sqrt{s} = 13$ TeV at the LHC was measured by analysing the data sample collected by the ALICE experiment during the 2016, 2017 and 2018 data-taking campaigns. The data were collected using a MB trigger requiring coincident signals in the V0 scintillators. The background events coming from the interaction of beam particles with gas or material in the beam pipe were rejected and only events with a primary interaction vertex within $|z_{vtx}| < 10$ cm were analysed. The available statistics for the analysis amounts to about 1.85×10^9 MB triggered events, corresponding to an integrated luminosity of $\mathcal{L}_{int.} \approx 32$ nb^{-1} given a minimum bias inelastic cross section of $\sigma_{MB} \approx 57.95$ mb [314]. In events where the primary vertex could be reconstructed with both tracks and SPD tracklets, the z_{vtx} positions were required to be compatible. Moreover, the pile-up contribution was suppressed by removing triggered events with more than one reconstructed primary vertex. After all these selections, the contribution of pile-up events is negligible.

5.2 Λ_c^+ and $\Sigma_c^{0,++}$ reconstruction in the $pK^-\pi^+$ decay channel

The Λ_c^+(udc) baryon has a mass of $m = 2286.46 \pm 0.14$ MeV/c^2 and a proper decay length of $c\tau = 60.7$ μm [3]. The Λ_c^+ reconstruction in this analysis is performed via the three-body decay $\Lambda_c^+ \rightarrow pK^-\pi^+$, which occurs with a total branching ratio (BR) of BR = (6.28 ± 0.32)% via resonant and non-resonant decay channels. Given a proper decay length of $\approx$ 60 μm, the Λ_c^+ secondary vertex is reconstructed and

Single track variable	Selection
$\lvert\eta\rvert$	< 0.8
p_T	> 0.3 GeV/c
ITS refit	yes
Track-to-vertex distance in xy plane	< 0.15 cm
Track-to-vertex distance in z direction	< 0.25 cm
Number of TPC crossed rows	> 70
Found / findable clusters in TPC	> 0.8
χ^2 / clusters in TPC	< 4
χ^2 / clusters in ITS	< 36
$\lvert n_\sigma^{TPC}\rvert$	< 3
$\lvert n_\sigma^{TOF}\rvert$ (if present)	< 3

TABLE 5.2: Single track selection criteria used to select candidate p, K^- and π^+ particles.

Candidate soft $\pi^\pm$ track variable	Selection
$\lvert\eta\rvert$	< 0.9
ITS refit	yes
Track-to-vertex distance in xy plane	< 0.065 cm
Track-to-vertex distance in z direction	< 0.15 cm

TABLE 5.3: Selection criteria used to select candidate soft $\pi^\pm$ particles.

resolved from the interaction point and variables related to the displaced topology are exploited in the analysis to increase the signal-to-background ratio, as described later. The Σ_c^0 and Σ_c^{++} baryons reconstruction is performed through the two-body strong decays $\Sigma_c^{0,++} \rightarrow \Lambda_c^+ \pi^{-,+}$, which occur with BR $\sim$ 100%. In this case the strong nature of the decay implies that the position of the decay vertex cannot be experimentally resolved from the primary vertex. The mass and widths of Σ_c^0, Σ_c^+ and Σ_c^{++} baryons are reported in Tab. 5.1.

5.2.1 Single track selections

The candidate Λ_c^+ baryons are reconstructed as triplets of p, K^- and π^+ tracks. The selection criteria used to select candidate p, K^- and π^+ particles are reported in Tab. 5.2. The single tracks are selected within the pseudorapidity range $|\eta| < 0.8$ and a minimum transverse momentum of 0.3 GeV/c is required to significantly reduce the combinatorial background when reconstructing triplets at low p_T. To improve the quality and pointing resolution, the TPC reconstructed tracks are required to be matched to the ITS detector and have a maximum value of the χ^2 / clusters in the TPC and ITS of 4 and 36, respectively. With the same purpose, at least 70 crossed pad rows in the TPC and at least 80% of the findable clusters are required for the track reconstruction. The amount of secondary particles coming from long-lived particle decays is suppressed by requiring a maximum track distance of closest approach (DCA) to the primary vertex of 0.15 cm and 0.25 cm along the xy plane and the longitudinal direction respectively. Finally, the combinatorics is reduced by applying some preliminary PID criteria. The negative charged tracks are required to

	Mass (MeV/c^2)	$c\tau$ (μm)	Decay (BR)
D^0	1684.83 ± 0.05	122.9	$K^-\pi^+$ ($(3.950 \pm 0.031)\%$)
D^+	1869.65 ± 0.05	311.8	$K^-\pi^+\pi^+$ ($(9.38 \pm 0.16)\%$)
D_s^+	1968.34 ± 0.07	151.2	$\phi\pi^+, \phi \to K^+K^-$ ($(2.24 \pm 0.08)\%$)
Λ_c^+	2286.46 ± 0.14	60.7	$pK^-\pi^+$ ($(6.28 \pm 0.32)\%$)
Ξ_c^+	$2467.94^{+0.17}_{-0.20}$	136.6	$\Xi^-\pi^+\pi^+$ ($(2.86 \pm 1.21 \pm 0.38)\%$ †)

TABLE 5.4: Kinematic properties of charmed mesons and baryons for which the ALICE experiment is able to resolve the secondary decay vertex. Numbers from [3]. †: number from [315].

be compatible within 3σ with a kaon, while the positive charged ones are asked to be compatible with the proton or pion species. The identification is performed by exploiting the TPC signal for all particles and that in TOF for the tracks that are matched to it. In the latter case, the particle is accepted as a proton, kaon or pion only if identified by both detectors. The Λ_c^+ candidates are finally reconstructed as triplets among two positive charged particles and a negative charged one selected with the criteria mentioned in this paragraph. With the same logic, the antiparticles Λ_c^- are reconstructed as triplets of two negative charged particles and a positive charged one. The primary vertex associated to each reconstructed candidate is recomputed excluding the candidate prongs, so that the primary vertex determination is not driven by the candidate itself. This is important given the typically low event multiplicity in MB triggered pp collisions.

The track selections mentioned above influence the rapidity window in which Λ_c^+ baryons are reconstructed, which in particular decreases at low p_T. In order to avoid border effects and at the same time to exploit as much as possible the rapidity coverage of the central barrel, the Λ_c^+ candidates are reconstructed within $|y| < |y_{fid.}|$, where $|y_{fid.}|$ is the so called *fiducial acceptance* region, defined by the following formula:

$$y_{fid.}(p_T) = \begin{cases} 0.5 + \frac{1.9}{15} p_T - \frac{0.2}{15} p_T^2, & \text{for } p_T < 5 \text{ GeV}/c \\ 0.8 & \text{for } p_T > 5 \text{ GeV}/c \end{cases} . \quad (5.1)$$

The fiducial acceptance region steeply widens from $|y| < 0.5$ at $p_T = 0$ to $|y| < 0.8$ at $p_T = 5$ GeV/c.

The $\Sigma_c^{0,++}$ candidates are reconstructed by pairing a $\Lambda_c^+ \to pK^-\pi^+$ candidate with an invariant mass within $2.28 \lesssim m(\Lambda_c^+) \lesssim 2.30$ GeV/c^2 with a *soft pion* candidate track, which is selected with the criteria reported in Tab. 5.3. In Fig. 5.2 the soft pion p_T distribution from PYTHIA 8 is shown in different $p_T(\Sigma_c^{0,++})$ intervals, generated with a flat shape between $p_T(\Sigma_c^{0,++}) = 0$ GeV/c and $p_T(\Sigma_c^{0,++}) = 12$ GeV/c. The pion daughter carries at most $\sim 10\%$ of the $\Sigma_c^{0,++}$ transverse momentum, therefore most of the $\Sigma_c^{0,++}$ momentum is carried by the produced Λ_c^+. For this reason, the pion track is labelled as "soft". In this case, the allowed pseudorapidity range is enlarged to $|\eta| < 0.9$ and a maximum value for the track-to-vertex distance of 0.065 cm and 0.15 cm in the xy plane and along the longitudinal direction, respectively, are required to remove the pions from long-lived particle decays. Also the soft $\pi^\pm$ tracks are required to be refitted in the ITS detector. This requirement implicitly imposes a threshold to the soft $\pi^\pm$ transverse momentum, as shown in Fig. 5.3. This threshold, compatible between data and MC, is of order of 110 MeV/c.

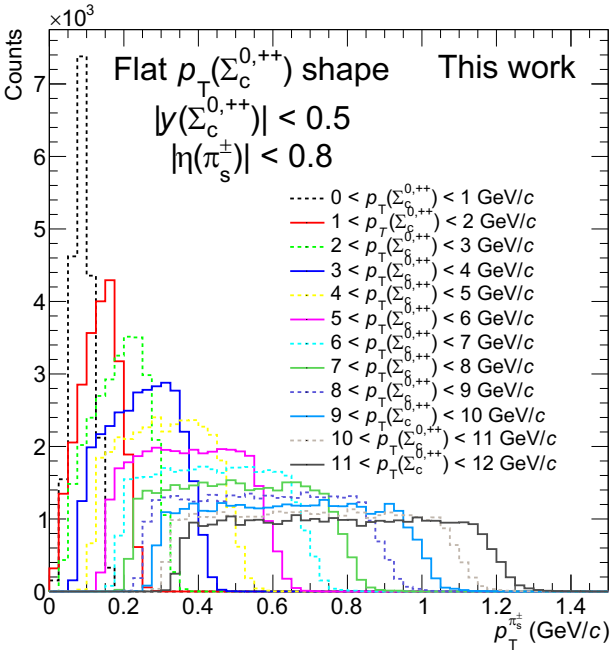

FIGURE 5.2: p_T distribution of $\pi^{\pm}$ produced in $\Sigma_c^{0,++} \rightarrow \Lambda_c^+ \pi^{-,+}$ decays simulated with PYTHIA 8. This distribution is shown in different $p_T(\Sigma_c^{0,++})$ ranges, where the $\Sigma_c^{0,++}$ are generated with a flat p_T distribution between $p_T = 0$ GeV/c and $p_T = 12$ GeV/c.

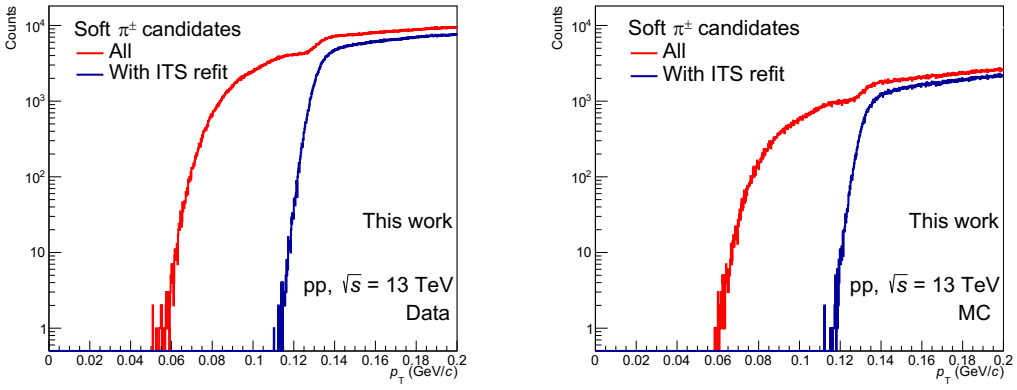

FIGURE 5.3: p_T distribution of candidate soft $\pi^{\pm}$ tracks in reconstructed (left) and simulated (right) pp events at $\sqrt{s} = 13$ TeV by requiring or not the refitting in the ITS detector.

5.2.2 Λ_c^+ secondary vertex reconstruction and topological variables

The Λ_c^+ reconstruction in the $pK^-\pi^+$ decay channel exploits the decay topology that is displaced from the primary interaction vertex. The decay point of the Λ_c^+ baryon, called *secondary vertex*, is found as the 3D space point that minimises the distance among the tracks identified as the decay products. The secondary vertex (x_0, y_0, z_0)

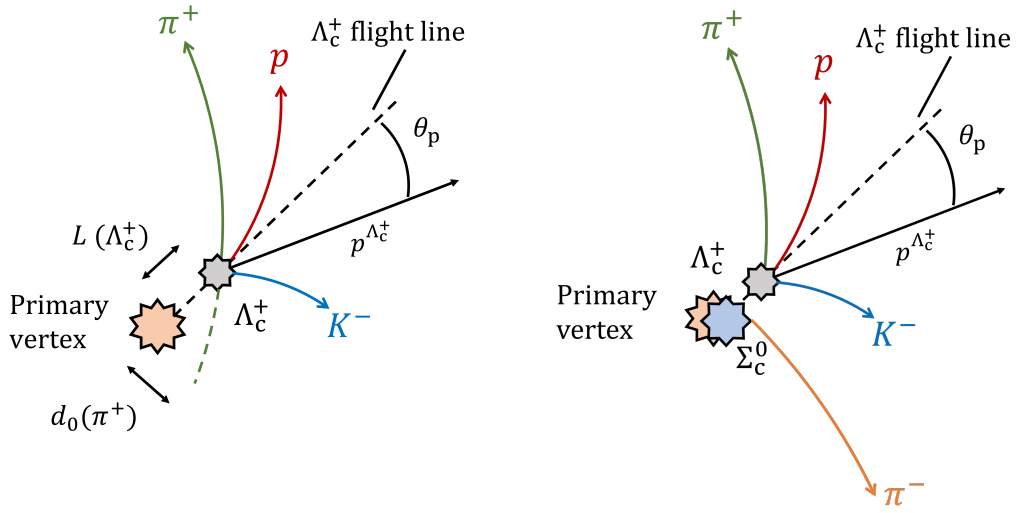

FIGURE 5.4: Cartoons representing the $\Lambda_c^+ \to pK^-\pi^+$ (left) and the $\Sigma_c^{0,++} \to \Lambda_c^+\pi^\mp$ one (right).

is found by minimising the quantity:

$$D = \sqrt{\sum_{i=1}^{3}\left[\left(\frac{x_i - x_0}{\sigma_{x_i}}\right)^2 + \left(\frac{y_i - y_0}{\sigma_{y_i}}\right)^2 + \left(\frac{z_i - z_0}{\sigma_{z_i}}\right)^2\right]}, \tag{5.2}$$

where (x_i, y_i, z_i) are the coordinates of the i-th track propagated to the point of closest approach among the daughter tracks (x_0, y_0, z_0) and $(\sigma_{x_i}, \sigma_{y_i}, \sigma_{z_i})$ are the related uncertainties. In Tab. 5.4 the decay lengths of a few charm baryons are reported. The position resolution close to the primary vertex delivered by the SPD (see Tab. 3.1) allows us to exploit several variables correlated to the displaced topology of the charm-hadron decays, in order to enhance the signal-to-background ratio. This is possible because the combinatorial background is mainly constituted by triplets of tracks coming directly from the primary vertex, therefore not characterised by a real displacement. Most of the displacement exhibited by the combinatorial triplets has to be ascribed to the resolution of the apparatus. A short description of the variables exploited in the analysis is provided below for Λ_c^+. Simple cartoons showing the $\Lambda_c^+ \to pK^-\pi^+$ and $\Sigma_c^{0,++} \to \Lambda_c^+\pi^\mp$ decays ares shown in Fig. 5.4.

- **Decay length (L).** The decay length is defined as the distance between the primary vertex and the Λ_c^+ decay point. This quantity is only an approximation of the real distance covered by the Λ_c^+ before decaying, because due to the non-null electric charge this hadron undergoes an helicoidal trajectory. However, given the short proper decay length of ≈ 60 μm, the effect of the curvature is totally negligible. In Fig. 5.5(A) the decay length component along the transverse plane L_{xy} is shown for prompt and non-prompt Λ_c^+ baryons, as well as for background candidates, in the interval $2 < p_T < 4$ GeV/c. The prompt and non-prompt signals are selected from MC simulations, while the background candidates correspond to combinatorial $pK^-\pi^+$ triplets reconstructed in data with an invariant mass in the sidebands of the Λ_c^+ peak. As anticipated above, the prompt signal is characterised by an intrinsic displacement that is absent in the background mainly formed by primary particles, and this is reflected in an average L_{xy} for prompt signal larger than that of background.

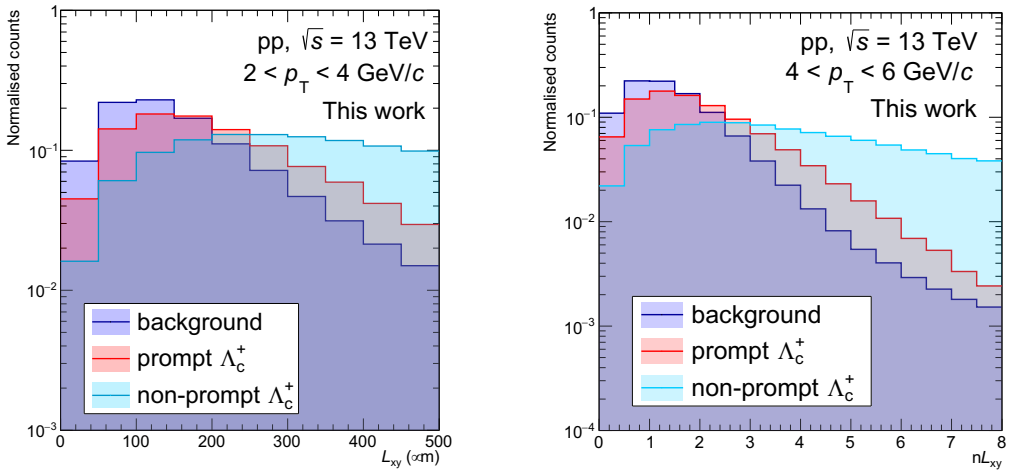

(A) L_{xy}. (B) nL_{xy}.

FIGURE 5.5: Projections along the transverse plane of (A) decay length (L_{xy}) and (B) normalised decay length (nL_{xy}) for prompt and non-prompt Λ_c^+ particles and background candidates with $2 < p_T < 4$ GeV/c and $4 < p_T < 6$ GeV/c, respectively. The integral of each distribution is normalised to unity.

Even larger values are observed for the non-prompt signal: the decay length of non-prompt Λ_c^+ baryons is influenced also by the space covered by the mother beauty hadron ($c\tau(\Lambda_b^0) = 441$ μm [3]), causing a further displacement with respect to the prompt component. The projection along the transverse plane is performed to better exploit the spatial resolution provided by the ITS, which is better on the xy plane with respect to that along the longitudinal direction.

- **Normalised decay length (nL)**. This quantity corresponds to the decay length L normalised by the uncertainty estimated from the covariance matrix of the decay product tracks. An example of the distributions for background and signal is reported in Fig. 5.5(B) for candidates with $4 < p_T < 6$ GeV/c. As for the decay length, the signal shows a larger average value and a longer tail compared to the background, with higher values for the non-prompt Λ_c^+ given the additional displacement from the mother beauty hadron. Also in this case, only the xy component is considered, exploiting the better spatial resolution provided by the ITS in the transverse plane.

- **Dispersion of tracks at the decay vertex (σ_{vtx})**. This quantity is defined as:

$$\sigma_{vtx} = \sqrt{\sum_{i=1}^{3} d_i^2}\,, \tag{5.3}$$

where d_i corresponds to the distance between the i-th track and the reconstructed secondary vertex at the point of closest approach. For a true Λ_c^+ this quantity is ideally 0 and deviations from this are due to the tracking and vertexing resolutions. A selection on this variable helps to discriminate the signal from the background, in combination with selections on the decay length.

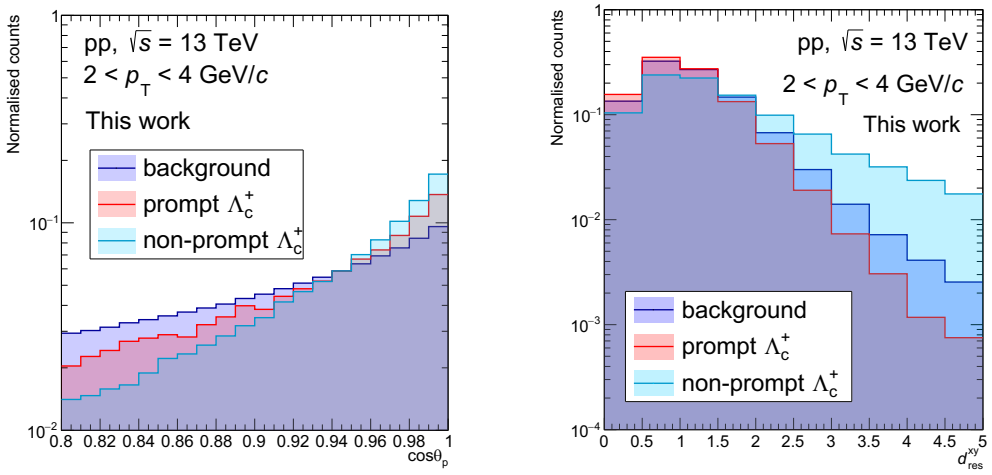

(A) $\cos(\theta_p)$. (B) $d_{res.}^{xy}$.

FIGURE 5.6: (A) Cosine of pointing angle ($\cos(\theta_p)$) and (B) maximum "topomatic" ($d_{res.}^{xy}$) for prompt and non-prompt Λ_c^+ particles and background candidates with $2 < p_T < 4$ GeV/c. The integral of each distribution is normalised to unity.

- **Cosine of pointing angle (θ_p).** The pointing angle is defined as the angle between the direction of the reconstructed Λ_c^+ momentum and the "flight line" connecting the primary vertex with the Λ_c^+ decay point. This angle is expected to have a null value in case of perfect reconstruction of a prompt Λ_c^+ baryon, since the flight line and the direction of the momentum of the decaying Λ_c^+ are expected to be aligned, but the finite resolution of the apparatus smears the measured angles. As visible in Fig. 5.6(A), the reconstructed signal is anyway much more peaked around $\cos(\theta_p) = 1$ than the background. Moreover, the non-prompt signal is more peaked at unity with respect to the prompt one. Despite the non-prompt Λ_c^+ flight line may not coincide in principle with the direction of the reconstructed momentum, the boost given by the parent b-hadron keeps them almost aligned. Moreover, given the short Λ_c^+ proper decay length ($c\tau \approx 60$ μm) the resolution on the prompt Λ_c^+ flight line is poorer than that of the non-prompt Λ_c^+ baryons, causing a broadening of the $\cos(\theta_p)$ distribution in the former case.

- **Maximum "topomatic" in the transverse plane ($d_{res.}^{xy}$).** This quantity derives from the transverse decay length (L_{xy}) and the single-track *impact parameter* d_0^{xy}, defined as the distance of closest approach in the transverse plane between the primary vertex and the reconstructed track propagated at the point of closest approach in xy with respect to it. The maximum "topomatic" $d_{res.}^{xy}$ is defined as:

$$d_{res.}^{xy} = \max_{i=1}^{3} \left(\frac{d_{0,i}^{xy} - d_{0,i}^{xy}(\text{exp})}{\sqrt{\sigma^2(d_{0,i}^{xy}) + \sigma^2(d_{0,i}^{xy}(\text{exp}))}} \right) , \tag{5.4}$$

where the index i denotes one of the three Λ_c^+ decay products. This quantity corresponds to the maximum normalised difference between the measured

and the expected daughter impact parameter, where the normalization corresponds to the quadrature sum of the uncertainties. The expected impact parameter is calculated with the transverse decay length L_{xy} and the angle θ_i^{xy} between the reconstructed Λ_c^+ transverse momentum and that of the i-th track as:

$$d_{0,i}^{xy}(\text{exp}) = L_{xy} \cdot \sin(\theta_i^{xy}) \ , \tag{5.5}$$

where the uncertainty on this quantity is computed neglecting that on θ_i^{xy}, namely:

$$\sigma(d_{0,i}^{xy}(\text{exp})) = \sigma(L_{xy}) \cdot \sin(\theta_i^{xy}) \ . \tag{5.6}$$

In Fig. 5.6(B) the $d_{\text{res.}}^{xy}$ distributions for prompt and non-prompt Λ_c^+, as well as for the combinatorial background, in the interval $2 < p_T < 4$ GeV/c are shown. The prompt signal is more peaked to small values with respect to the background and the non-prompt signal, characterised by an average larger value. Imposing a maximum value on this variable can help rejecting a significant amount of non-prompt signal, as well as background.

In the reconstruction of the candidate Λ_c^+ from data, other two variables are exploited.

- **Distance between the primary vertex and the decay point estimated with only two tracks (dist$_{12}$)**. This quantity is a proxy of the decay length L calculated before the secondary vertex computation and it is exploited to reject combinatorics. This variable is mainly exploited to perform a first filtering among all the reconstructable candidates, which are then subject to further selections on the variables described above.

- **Distance of closest approach of tracks from primary vertex (DCA)**. The candidate Λ_c^+ daughters are required to have a distance of closest approach to the primary vertex lower than a given threshold, since the daughters of prompt Λ_c^+ baryons are expected to be close to the interaction point, while the non-prompt component is expected to be characterised by larger values.

In Tab. 5.5 the criteria used to isolate a first sample of candidates among all the possible reconstructable ones are reported. These selections, called in the following *filtering* selections, include also minimum values for the daughter p_T, which further help to reject many combinatorial triplets that can be formed with low-p_T primary tracks. These selections are applied to reconstruct Λ_c^+ candidates in data in all the p_T intervals. On top of them, further selections are applied to reject more background, depending on the transverse momentum interval considered and to the specific reconstructed baryon, namely either prompt Λ_c^+ or $\Sigma_c^{0,++}$, as discussed later. Moreover, apart from selections on single-track, kinematic and topological variables, specific PID selections are applied to increase the purity of the $\Lambda_c^+ \to \text{pK}^-\pi^+$ candidate sample, as discussed in the next Section.

5.2.3 PID selection - a Bayesian approach

Another ingredient exploited in the identification of $\Lambda_c^+ \to \text{pK}^-\pi^+$ signal is the excellent PID capability of the ALICE detector. As already mentioned in Sec. 5.2.1, the tracks used for the combinatorics are filtered according to "nσ" selections on the TPC and TOF signals, namely for each positive charged track the $\text{n}_{\sigma_\text{p}}^{\text{TPC}}$, $\text{n}_{\sigma_\text{p}}^{\text{TOF}}$, $\text{n}_{\sigma_\pi}^{\text{TPC}}$ and $\text{n}_{\sigma_\pi}^{\text{TOF}}$ variables are calculated, while for negative charged tracks the $\text{n}_{\sigma_\text{K}}^{\text{TPC}}$ and $\text{n}_{\sigma_\text{K}}^{\text{TOF}}$

Λ_c^+ variable	Selection
$p_T(p)$ (GeV/c)	> 0.5
$p_T(K^-)$ (GeV/c)	> 0.4
$p_T(\pi^+)$ (GeV/c)	> 0.4
DCA (μm)	< 500
$dist_{12}$ (μm)	> 100
σ_{vtx} (μm)	< 600
L (μm)	> 50
$\cos(\theta_p)$	> 0

TABLE 5.5: Selections adopted to filter the prompt Λ_c^+ candidates in data. These selections are called "filtering" selections in the following.

quantities are considered (see. Eq. 4.1). The requirements $|n_{\sigma_p}^{TPC}| < 3$, $|n_{\sigma_\pi}^{TOF}| < 3$, ..., may not identify uniquely a track, because of the overlaps among the "nσ" distributions of different particle species. For this reason, a single track may be used to build more than one triplet, contributing to the combinatorial background, making the "nσ" selections not optimal. For the reconstruction of the $\Lambda_c^+ \rightarrow pK^-\pi^+$ candidates a Bayesian PID method is employed [316], based on the detector response combination in terms of probabilities. For a given detector α with an expected produced signal $\hat{S}_\alpha(H_i)$ when a particle of species H_i traverses it, a likelihood can be defined as:

$$P_\alpha(S_\alpha|H_i) = \frac{1}{\sqrt{2\pi}\sigma} e^{-\frac{(S_\alpha - \hat{S}_\alpha(H_i))^2}{2\sigma^2}} . \tag{5.7}$$

This quantity corresponds to the probability for a particle of species H_i to produce a signal S_α in the detector α (= TPC, TOF, ...). The formulation in Eq. 5.7 is valid for detectors with a Gaussian response, but it can be easily extended to all other cases by using the proper probability distribution function. The advantage of this approach is that the responses from different detectors can be combined as the product:

$$P(\vec{S}|H_i) = \prod_{\alpha=\text{TPC, TOF, ...}} P_\alpha(S_\alpha|H_i) , \tag{5.8}$$

corresponding to the combined probability that a particle of species H_i produces a signal $\vec{S} = (S_{TPC}, S_{TOF}, ...)$ in the different detectors. Using the Bayes' theorem [317]:

$$P(H_i|\vec{S}) = \frac{P(\vec{S}|H_i)C(H_i)}{\sum_{k=e,\mu,\pi,...} P(\vec{S}|H_k)C(H_k)} , \tag{5.9}$$

the combined probability in Eq. 5.8 is used to calculate the probability that the particle which released a set of signals $\vec{S}$ on the different detectors belongs to the species H_i. This "posterior" probability $P(H_i|\vec{S})$ depends on the detector response enclosed in the likelihood $P(\vec{S}|H_i)$ and on the prior probability to measure a particle of a given species H_i, represented by the quantity $C(H_i)$. The prior probability represents the real yield per each particle species and it is chosen to be normalised to that of pions. In other words, the quantity $C(H_i)$ is used to represent the relative abundance of a particle species H_i with respect to the $\pi^\pm$ one in the analysed data sample. The priors are determined as a function of particle p_T with an iterative procedure, assuming

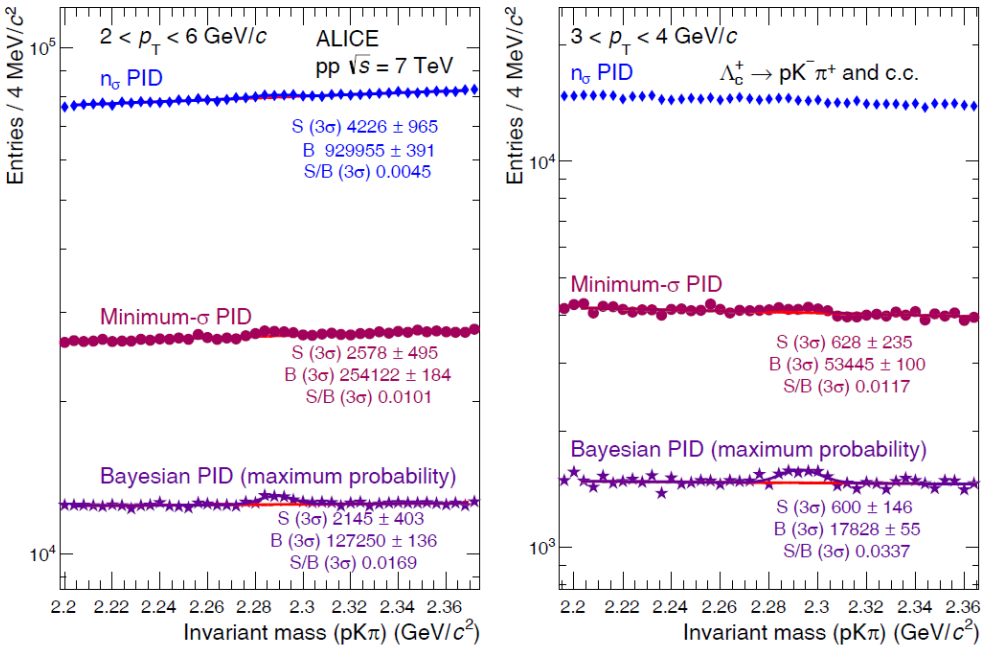

FIGURE 5.7: Invariant mass distribution of $\Lambda_c^+ \to pK^-\pi^+$ candidates using "nσ" PID, minimum-σ PID and Bayesian PID with maximum probability criterion in a sample of about 3×10^8 pp collisions at $\sqrt{s} =$ 7 TeV in the transverse momentum intervals $2 < p_T < 6$ GeV/c (left) and $3 < p_T < 4$ GeV/c (right). Figure from [316].

a flat distribution at unity for all particles as a starting point. The posterior probability $P(H_i|\vec{S})$ is calculated with Eq. 5.9 by using these flat priors and this is used to determine the p_T distribution of identified hadrons $Y(H_i, p_T)$ to be used for the next iteration. The posterior probability calculated at the n iteration is used to define the prior probability for the $n+1$ step:

$$C_{n+1}(H_i, p_T) = \frac{Y_{n+1}(H_i, p_T)}{Y_{n+1}(H_\pi, p_T)}, \qquad \text{where} \qquad Y_{n+1}(H_i, p_T) = \sum_S P_n(H_i|S)\,, \quad (5.10)$$

where the sum is performed over all the signals S induced by particles in a given p_T. The procedure is iterated until it converges. Less than 10 steps were found to represent in a realistic way the particle abundances in data [316][2]. The posterior probability for p, K^- and π^+ is calculated for each track.

The final identification can take place in different ways. The criteria adopted in this work are the following:

- **maximum probability** criterion, according to which a track is identified as the particle species with the maximum posterior probability;
- **threshold probability** criterion, according to which a track is identified with a given particle species if the corresponding posterior probability is higher than a fixed threshold.

[2]It is fundamental that the distributions employed as prior in data are used also in the reconstruction in MC simulations, so that the efficiency correction does not introduce any bias. In case the priors do not quantify the relative abundances among the different particle species, the PID selection will not benefit of the best performances, but it would not be biased.

Baryon p_T (GeV/c)	Prompt Λ_c^+	Prompt $\Lambda_c^+ (\leftarrow \Sigma_c^{0,++})$ and $\Sigma_c^{0,++}$
$[1,2)$	F + Bayes PID	-
$[2,4)$	F + Bayes PID	F + Bayes PID + $\cos\theta_p > 0.8$
$[4,6)$	F + Bayes PID	F + Bayes PID + $\cos\theta_p > 0.8$ + $d^{xy}_{res.} < 2.5$
$[6,8)$	F + Bayes PID	F + Bayes PID
$[8,10)$	F + Bayes PID	F + Bayes PID
$[10,12)$	F + $L_{xy} > 0.01$ cm + n$L_{xy} > 1$ + Bayes PID only p	F + Bayes PID
$[12,24)$	F + $L_{xy} > 0.01$ cm + n$L_{xy} > 1$ + Bayes PID only p	-
(all)	-	$2.277 < m(\Lambda_c^+) < 2.299$ GeV/c^2

TABLE 5.6: Selections on topological variables and PID adopted to reconstruct the prompt Λ_c^+ as well as the prompt $\Lambda_c^+ (\leftarrow \Sigma_c^{0,++})$ and $\Sigma_c^{0,++}$ signals. The letter "F" refers to the "filtering" selections reported in Tab. 5.5.

With the maximum probability criterion a single identity is assigned to each track, while with the threshold criterion multiple identifications are possible for a given track. Even if it implies a lower efficiency, the maximum probability criterion has been proven to be the most effective for the reconstruction of $\Lambda_c^+ \rightarrow pK^-\pi^+$ candidates. In Fig. 5.7 the performances of different PID methods adopted for the signal extraction of candidate $\Lambda_c^+ \rightarrow pK^-\pi^+$ decays in a sample of about 3×10^8 pp collisions at $\sqrt{s} = 7$ TeV are shown [316]. The "nσ" approach uses the TPC and TOF detectors with a 2σ or 3σ selection, depending on the p_T and particle species. With the minimum-σ approach a track is identified as belonging to the species that provides the minimum "nσ", calculated as the quadrature sum between TPC and TOF "nσ". The usage of the Bayesian PID with maximum probability criterion is found to improve the $\Lambda_c^+ \rightarrow pK^-\pi^+$ signal extraction, increasing the background rejection by about a factor 7 and resulting in a signal-to-background larger by about a factor 3. Moreover, the maximum probability criterion simplifies the fitting routine used for the signal estimation, since the amount of reflected candidates, deriving from the wrong identification of protons as pions and viceversa, is found to be negligible. For these reasons, the Bayes PID with the maximum probability criterion is adopted to extract the $\Lambda_c^+ \rightarrow pK^-\pi^+$ signal in the work described in this thesis.

5.2.4 Λ_c^+ signal extraction

After a first pre-selection performed with the filtering criteria reported in Tab. 5.5, the $\Lambda_c^+ \rightarrow pK^-\pi^+$ candidates are finally selected according to what reported in Tab. 5.6. The measurement of prompt Λ_c^+ baryons is performed in the following ten p_T intervals: $[1,2)$ GeV/c, $[2,3)$ GeV/c, $[3,4)$ GeV/c, $[4,5)$ GeV/c, $[5,6)$ GeV/c, $[6,7)$ GeV/c, $[7,8)$ GeV/c, $[8,10)$ GeV/c, $[10,12)$ GeV/c, $[12,24)$ GeV/c. In all the intervals the $\Lambda_c^+ \rightarrow pK^-\pi^+$ reconstruction is based on the preliminary track selections listed in Tab. 5.2 and on the filtering criteria reported in Tab. 5.5. For the reconstruction of candidates with $p_T(\Lambda_c^+) > 10$ GeV/c tighter selections on the topological variables are applied in order to improve the signal-to-background (S/B) ratio. In

particular, the Λ_c^+ candidates are required to satisfy $L_{xy} > 0.01$ cm and $nL_{xy} > 1$, since the large boost at such high momenta induces a significant displacement of the Λ_c^+ baryon decay vertices, while the background candidates are intrinsically less displaced. Furthermore, at such high p_T also the PID selections are modified with respect to the other intervals. Considering that at such high momenta the TPC and TOF signal distributions of different particle species overlap, the application of the Bayes PID with the maximum probability criterion results only in a loss of efficiency without an improvement in the signal extraction. It was decided to preserve this PID selection for $p_T(\Lambda_c^+) > 10$ GeV/c only to identify the proton track. The summary of all the criteria applied to reconstruct the prompt Λ_c^+ baryons are listed in the second column of Tab. 5.6. The amount of signal surviving the analysis selections is quantified looking at the invariant mass distribution of the triplets:

$$\begin{aligned} M^2(\mathrm{pK}\pi) &= p^\mu p_\mu \\ &= \left(\sqrt{m_\mathrm{p}^2 + \vec{p}_\mathrm{p}^2} + \sqrt{m_{\mathrm{K}^-}^2 + \vec{p}_{\mathrm{K}^-}^2} + \sqrt{m_{\pi^+}^2 + \vec{p}_{\pi^+}^2}\right)^2 - (\vec{p}_\mathrm{p} + \vec{p}_{\mathrm{K}^-} + \vec{p}_{\pi^+})^2 \,. \end{aligned} \tag{5.11}$$

In the calculation of Eq. 5.11, the particle momentum derives from the tracking while the true proton, kaon and pion masses (from [3]) are assigned to the identified tracks to compute the invariant mass of the triplet. The $M(\mathrm{pK}\pi)$ distribution of the prompt $\Lambda_c^+ \rightarrow \mathrm{pK}^-\pi^+$ (and charge conjugate) reconstructed candidates in the ten p_T intervals mentioned above are shown in Fig. 5.9. The signal is characterised by an excess of counts around the $m(\Lambda_c^+) \simeq 2.286$ GeV/c^2 that emerges on top of a smooth background deriving from the combinatorics of $\mathrm{pK}^-\pi^+$ triplets. The signal is quantified via a binned likelihood fit to the invariant-mass distribution, using the following fit function:

$$f(M) = \frac{C}{\sqrt{2\pi}\sigma} e^{-\frac{(M-\mu)^2}{2\sigma^2}} + aM^2 + bM + c \,, \tag{5.12}$$

where the Gaussian function is used to describe the $\Lambda_c^+ \rightarrow \mathrm{pK}^-\pi^+$ signal peak and the parabola is chosen to parametrise the combinatorial background. Given the normalised notation, the integral of the signal Gaussian corresponds to C. The total amount of signal is computed as C divided by the width of the $M(\mathrm{pK}\pi)$ intervals used for the binned likelihood fit. The measured amount of signal, the S/B ratios and the statistical significance $S/\sqrt{S+B}$ within 3σ from the Gaussian mean μ in all the p_T intervals are reported in Tab 5.7. The significance of the signal peak is calculated in an invariant-mass window covering $\pm 3\sigma$ around the Gaussian mean μ, namely:

$$\mathcal{S}(3\sigma) = \frac{S(3\sigma)}{\sqrt{S(3\sigma) + B(3\sigma)}} = \frac{S(3\sigma)}{\sqrt{B(3\sigma)}} \cdot \frac{1}{\sqrt{1 + S(3\sigma)/B(3\sigma)}} \,, \tag{5.13}$$

and it can be considered as a proxy of the inverse relative uncertainty on the measured signal. It varies between about 4 and 14, depending on the $p_T(\Lambda_c^+)$ interval. The lowest significance is obtained in the $1 < p_T(\Lambda_c^+) < 2$ GeV/c interval, where also the lowest S/B is observed. With increasing p_T the S/B increases and an enhancement of the statistical significance is observed. The significance value is however strongly influenced by the absolute amount of signal S as well as background B that survived the selections, as shown in Eq. 5.13. In particular, the amount of reconstructed signal significantly decreases at high p_T and this is reflected in a lower

p_T (GeV/c)	$S(3\sigma)$	$S/B(3\sigma)$	Significance (3σ)
[1, 2)	4686 ± 1256	0.0038	4.2 ± 1.1
[2, 3)	10532 ± 934	0.0083	9.3 ± 0.8
[3, 4)	9404 ± 700	0.0142	11.5 ± 0.8
[4, 5)	5669 ± 423	0.0218	11.0 ± 0.8
[5, 6)	4424 ± 270	0.0448	13.8 ± 0.8
[6, 7)	2236 ± 180	0.0579	11.1 ± 0.9
[7, 8)	1345 ± 121	0.0800	10.0 ± 0.9
[8, 10)	1382 ± 109	0.1124	11.8 ± 0.9
[10, 12)	611 ± 90	0.0730	6.4 ± 0.9
[12, 24)	379 ± 71	0.0671	4.9 ± 0.9

TABLE 5.7: Raw signal, signal-to-background ratio (S/B) and significance within 3σ of Λ_c^+ from $M(pK^-\pi^+)$ distributions in different p_T intervals in pp collisions at $\sqrt{s} = 13$ TeV.

significance. In Fig. 5.10 the residuals with respect to the background function are shown. They are used to monitor the quality of the fit: in case of a correct background description, the residual distribution is expected to fluctuate around 0, with the exception of the signal region, where a Gaussian excess of counts is observed. The experimental points in the sideband regions fluctuate around 0, without showing any significant modulation that would suggest a wrong parametrization of the background. The signal mean and σ as a function of p_T are shown in Fig. 5.8. The measured mean of the $\Lambda_c^+ \to pK^-\pi^+$ peak results to be systematically higher than the value from PDG [3], as observed for other charm hadron analysis in the same data sample. The difference is fully covered by the reconstruction resolution (right panel Fig. 5.8) and this shift does not influence the efficiency correction, since no invariant mass fit is performed in simulations. The resolution σ increases with p_T, as a consequence of the increasing absolute uncertainty on the transverse momentum of reconstructed tracks (see Eq. 3.7). The resolution estimated from the MC simulations is always compatible within 2σ with the one measured in data, however in the latter case the effects of the statistical fluctuations are relevant. This behaviour was observed also for the D^0 signal extraction, where the signal-to-background ratio and the statistical significance are larger and more robust conclusions can be driven. For this reason, the fits shown in Fig. 5.9 are performed by constraining the σ around the values obtained from MC, with the possibility to vary only within $\pm 1\%$.

5.2.5 $\Sigma_c^{0,++}$ signal extraction

The measurement of $\Lambda_c^+ (\leftarrow \Sigma_c^{0,++})$ and $\Sigma_c^{0,++}$ baryons is performed in four wider p_T intervals, namely $2 < p_T < 4$ GeV/c, $4 < p_T < 6$ GeV/c, $6 < p_T < 8$ GeV/c and $8 < p_T < 12$ GeV/c, where the transverse momentum is consistently that of $\Lambda_c^+ (\leftarrow \Sigma_c^{0,++})$ or $\Sigma_c^{0,++}$, depending on the hadron for which the signal is measured. In both cases, the strategy consists in reconstructing a Σ_c^0 or a Σ_c^{++} by pairing a candidate Λ_c^+ with a charged pion. Only candidate Λ_c^+ with a mass in the range $2.277 < m(\Lambda_c^+) < 2.299$ GeV/c^2 are coupled to a soft $\pi^\pm$ track to form a Σ_c^0 or Σ_c^{++} candidate. In this case, the topological selections on the candidate Λ_c^+ are different with respect to those used for the prompt Λ_c^+ analysis in finer bins. In particular, the criteria $\cos\theta_p > 0.8$ for $p_T(\Lambda_c^+ (\leftarrow \Sigma_c^{0,++}), \Sigma_c^{0,++}) < 6$ GeV/c and $d_{res.}^{xy} < 2.5$

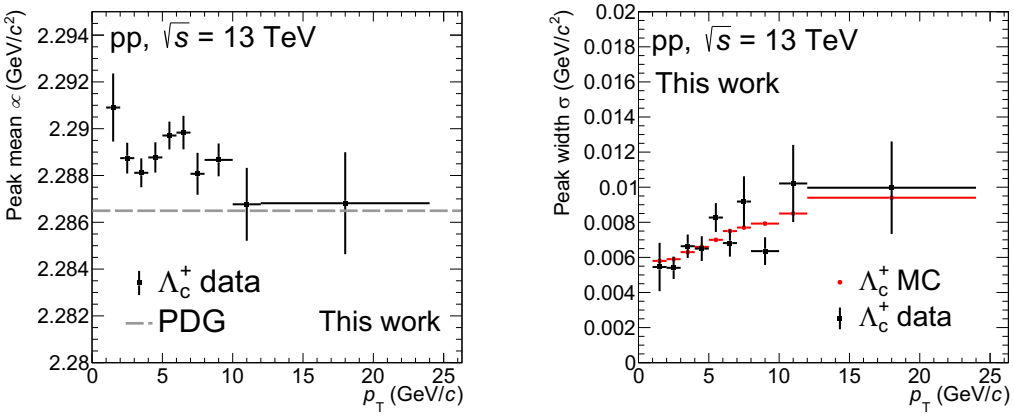

FIGURE 5.8: Mean (left) and width (right) of the Λ_c^+ signal peak measured from the binned likelihood fits of the $M(\mathrm{pK}\pi)$ distributions in different $p_T(\Lambda_c^+)$ intervals in pp collisions at $\sqrt{s} = 13$ TeV.

	Signal S ($S/\sigma(S)$)
$2 < p_T(\Lambda_c^+(\leftarrow \Sigma_c^{0,++})) < 4$ GeV/c	1403 ± 296 (4.7)
$4 < p_T(\Lambda_c^+(\leftarrow \Sigma_c^{0,++})) < 6$ GeV/c	1153 ± 157 (7.4)
$6 < p_T(\Lambda_c^+(\leftarrow \Sigma_c^{0,++})) < 8$ GeV/c	393 ± 72 (5.5)
$8 < p_T(\Lambda_c^+(\leftarrow \Sigma_c^{0,++})) < 12$ GeV/c	164 ± 37 (4.4)
$2 < p_T(\Sigma_c^{0,++}) < 4$ GeV/c	1102 ± 285 (3.9)
$4 < p_T(\Sigma_c^{0,++}) < 6$ GeV/c	1213 ± 175 (6.9)
$6 < p_T(\Sigma_c^{0,++}) < 8$ GeV/c	555 ± 86 (6.4)
$8 < p_T(\Sigma_c^{0,++}) < 12$ GeV/c	222 ± 44 (5.1)

TABLE 5.8: Signal and inverse relative uncertainty of reconstructed $\Lambda_c^+(\leftarrow \Sigma_c^{0,++})$ and $\Sigma_c^{0,++}$ in pp collisions at $\sqrt{s} = 13$ TeV.

for $p_T(\Lambda_c^+(\leftarrow \Sigma_c^{0,++}), \Sigma_c^{0,++}) < 4$ GeV/c^2 are applied on the candidate Λ_c^+, since they improve the S/B ratio without a reduction of the statistical significance. The measurement of $\Lambda_c^+(\leftarrow \Sigma_c^{0,++})$ and $\Sigma_c^{0,++}$ signal is performed from the distribution of $\Delta M = M(\mathrm{pK}\pi\pi) - M(\mathrm{pK}\pi)$ as a function of $p_T(\Lambda_c^+(\leftarrow \Sigma_c^{0,++}))$ and $p_T(\Sigma_c^{0,++})$ respectively. In this way, the signal is expected to appear as a narrow peak on top of the background, mainly influenced by the resolution on the pion track reconstruction. The ΔM distributions in the four p_T intervals fitted to measure the raw yield of $\Lambda_c^+(\leftarrow \Sigma_c^{0,++})$ and $\Sigma_c^{0,++}$ are shown in Fig. 5.11 and Fig. 5.12. The signal is expected to be centred around ≈ 0.167 GeV/c, which corresponds to the mass difference between $\Sigma_c^{0,++}$ and Λ_c^+, as reported in Tab. 5.1. Considering that the mass difference $\delta m = m(\Sigma_c^{++}) - m(\Sigma_c^0) = 0.22$ MeV/c^2, both Σ_c^0 and Σ_c^{++} contribute to the signal around $\Delta M \approx 0.167$ GeV/c^2, which is described with the following analytical function:

$$f(\Delta M) = \frac{C}{2}\left[\mathcal{V}(\Delta M - \mu_{\Sigma_c^{++}}; \sigma, \Gamma_{\Sigma_c^{++}}) + \mathcal{V}(\Delta M - \mu_{\Sigma_c^{++}} + \delta M; \sigma, \Gamma_{\Sigma_c^0})\right], \quad (5.14)$$

where $\mathcal{V}$ indicates a Voigt function, which is defined as a convolution between a Gaussian and a Breit-Wigner function. Given the sizeable decay width of $\sim$ 1.9

MeV/c^2, which is of the same order of the experimental resolution, as explained later, the Breit-Wigner profile of the signal cannot be ignored. This is not the case for the Λ_c^+, and more in general for the charmed hadrons listed in Tab. 5.4 with an average proper decay length $c\tau$ of order of hundreds of microns, because the experimental resolution on the invariant mass reconstruction is not good enough to resolve the Breit-Wigner shape. By definition, the Voigt distribution is normalised to unity, therefore the integral of the function in Eq. 5.14 corresponds to C. As for the prompt Λ_c^+ measurement, also in this case the total reconstructed signal corresponds to C divided by the width of the ΔM intervals used to perform the binned likelihood fit. The parameter C as well as the Σ_c^{++} peak average $\mu_{\Sigma_c^{++}}$ are the only parameters left free in the fitting procedure. The Breit-Wigner widths $\Gamma_{\Sigma_c^0}$ and $\Gamma_{\Sigma_c^{++}}$ and the mass difference δm between Σ_c^{++} and Σ_c^0 are fixed to the values reported in Tab. 5.1, while the Gaussian resolution is constrained according to the following study done on MC simulations. The effect of the detector resolution on the reconstructed ΔM is studied from the following quantity:

$$\Delta M_{\text{Gauss}} = (m_{\Sigma_c}^{\text{reco}} - m_{\Sigma_c}^{\text{MC calc.}}) + m_{\Sigma_c}^{\text{PDG}} - m_{\Lambda_c^+}^{\text{reco}} \,. \tag{5.15}$$

The quantity $m_{\Sigma_c}^{\text{reco}}$ corresponds to the reconstructed mass, which follows a Voigt profile. The Breit-Wigner component is removed by subtracting the Σ_c mass calculated with the generated momentum ($m_{\Sigma_c}^{\text{MC calc.}}$), then the result is shifted by the true mass ($m_{\Sigma_c}^{\text{PDG}}$). Finally, the reconstructed Λ_c^+ mass is subtracted ($m_{\Lambda_c^+}^{\text{reco}}$). The distribution of ΔM_{Gauss} is observed to follow a Gaussian profile. This is evaluated in each p_{T} interval considered for the signal extraction in data. From this analysis, a very mild dependence of the Gaussian σ with the baryon p_{T} is observed. The Gaussian σ is quantified to be order of ~ 1 MeV/c^2 and used to constrain this parameter in the fit in data. The background component of the ΔM distribution produced by the reconstruction of combinatorial pairs is parametrised with a polynomial of third order for $p_{\text{T}}(\Lambda_c^+(\leftarrow \Sigma_c^{0,++}), \Sigma_c^{0,++}) > 4$ GeV/c. For lower transverse momenta, the low S/B requires a more sophisticated procedure. In this case, a template of combinatorial Λ_c^+-$\pi^\pm$ pairs is created by recalculating nine times the value of ΔM for each $\Sigma_c^{0,++}$ candidate, after rotating the pion momentum vector around the longitudinal direction. In this way, any possible correlation between a soft pion and a Λ_c^+ is broken and a sample of pure combinatorial background is built. The resulting template is modulated with a parabola in the fit. With this procedure, the $\Lambda_c^+(\leftarrow \Sigma_c^{0,++})$ and $\Sigma_c^{0,++}$ signals are measured with a statistical precision between 15% and 30%, depending on the transverse momentum and the considered baryon. Considering that the variance for the signal function in Eq. 5.14 can not be trivially defined, since the Breit-Wigner does not have a finite σ, it is not possible to define a signal-to-background ratio as well as a statistical significance within 3σ. A reasonable proxy for the latter quantity is given by the inverse relative uncertainty on the extracted signal ($S/\sigma(S)$), which is always around 4 (see Tab. 5.8).

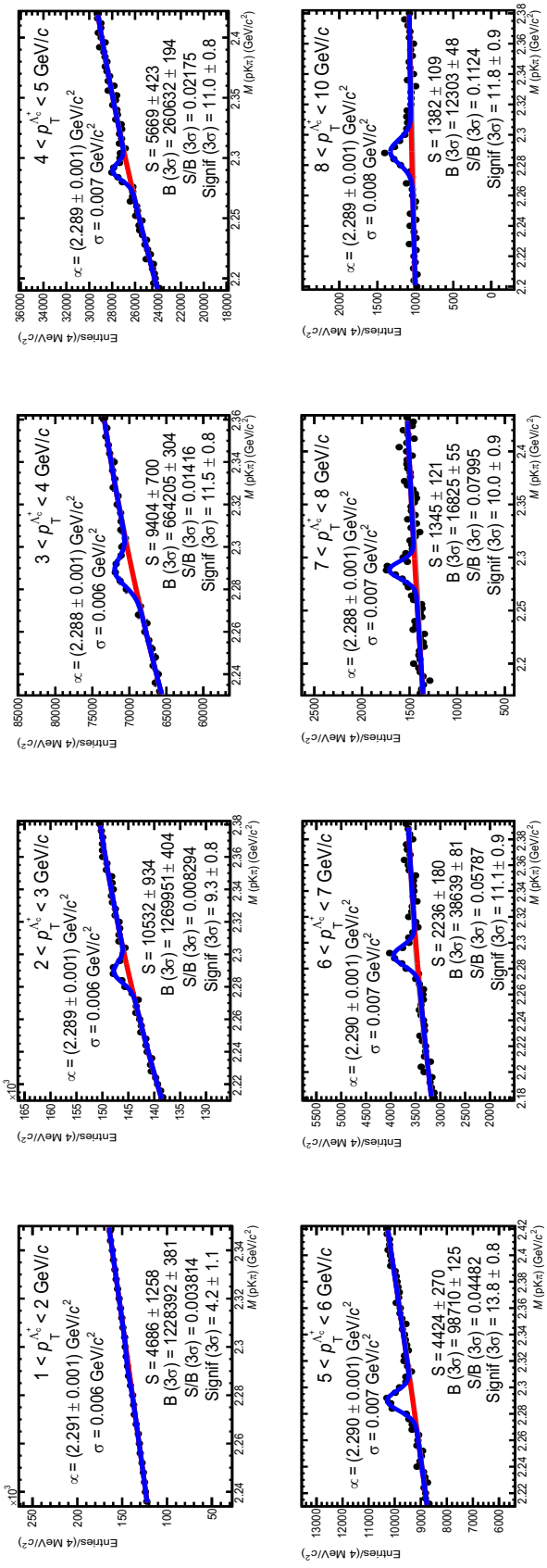

FIGURE 5.9: Invariant mass distributions of $pK^-\pi^+$ triplets reconstructed in different candidate p_T intervals in pp collisions at $\sqrt{s} = 13$ TeV.

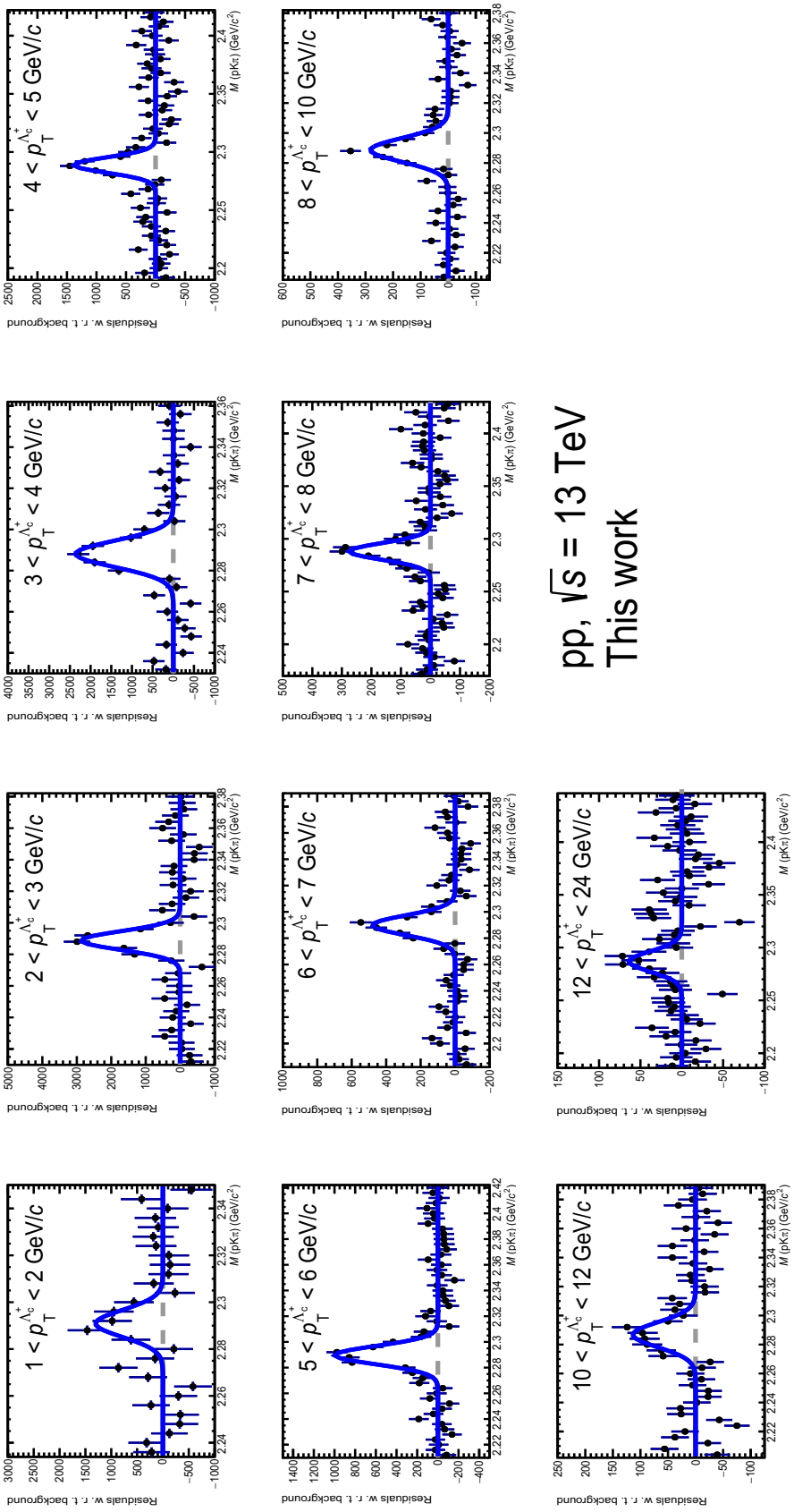

FIGURE 5.10: Residuals with respect to background of invariant mass distribution fits of $pK^-\pi^+$ triplets reconstructed in different candidate p_T intervals in pp collisions at $\sqrt{s} = 13$ TeV.

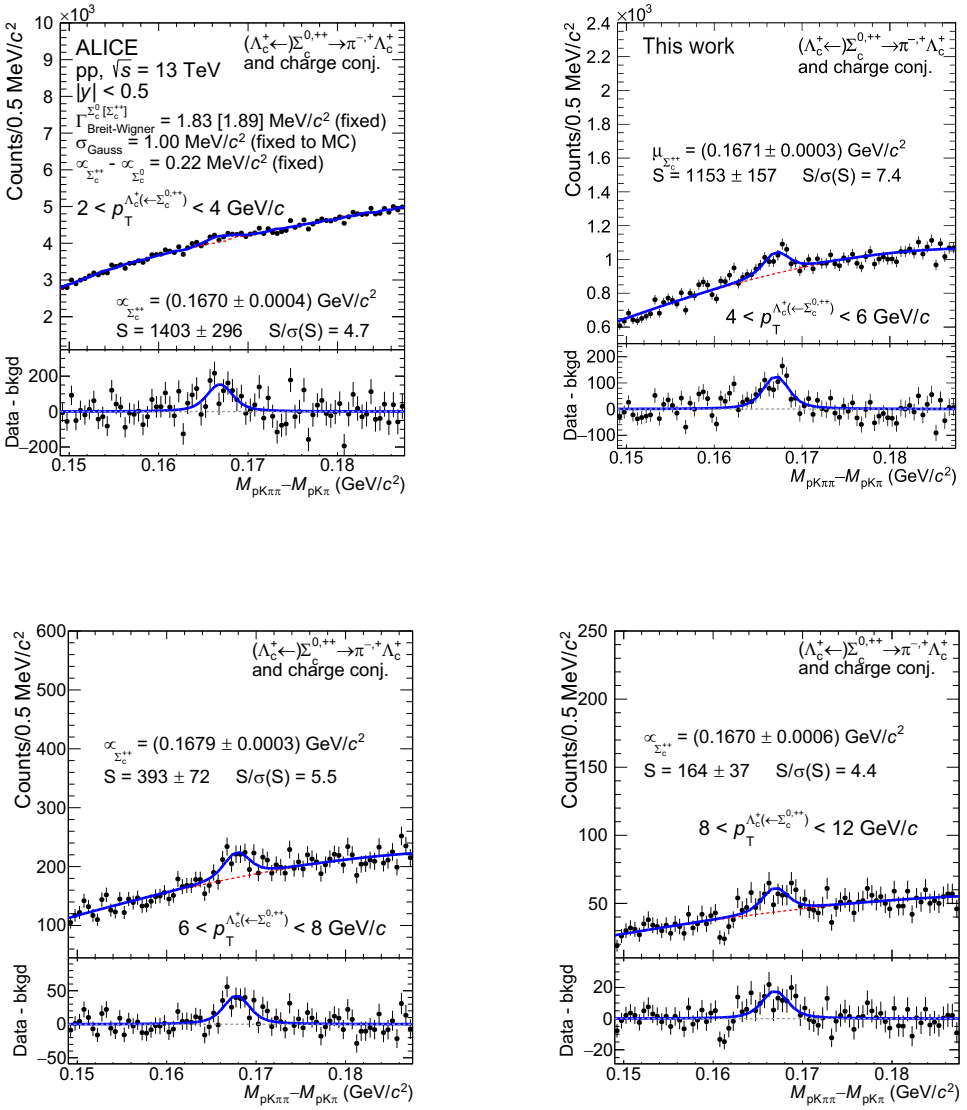

FIGURE 5.11: Distribution of $\Delta M = M(\mathrm{pK}\pi\pi) - M(\mathrm{pK}\pi)$ difference as a function of $p_{\mathrm{T}}(\Lambda_c^+(\leftarrow \Sigma_c^{0,++}))$ in pp collisions at $\sqrt{s} = 13$ TeV.

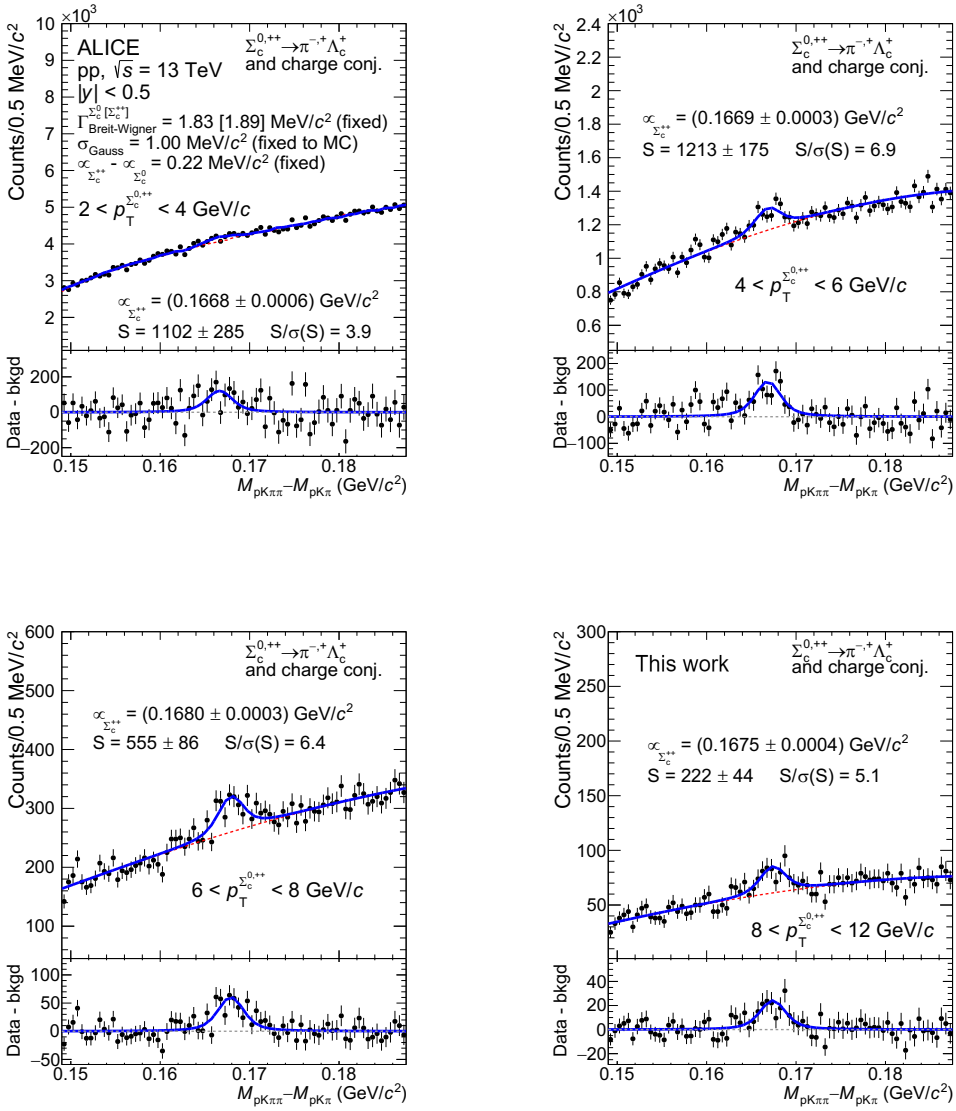

FIGURE 5.12: Distribution of $\Delta M = M(pK\pi\pi) - M(pK\pi)$ difference as a function of $p_T(\Sigma_c^{0,++})$ in pp collisions at $\sqrt{s} = 13$ TeV.

5.3 Efficiency correction and normalization

The raw signals measured with the fits shown in Figs. 5.9, 5.11 and 5.12 are used to obtain the p_T-differential cross section of prompt Λ_c^+, $\Lambda_c^+ (\leftarrow \Sigma_c^{0,++})$ and $\Sigma_c^{0,++}$ baryon production, according to the following relation:

$$\left.\frac{d\sigma^H}{dp_T}\right|_{|y|<0.5} = \frac{1}{2}\frac{1}{\Delta p_T} \cdot \frac{f_{\text{prompt}} N^H_{|y|<y_{\text{fid.}}}}{\alpha_y (\text{acc} \times \varepsilon)_{\text{prompt}}} \cdot \frac{1}{\text{BR}} \cdot \frac{1}{\mathcal{L}_{\text{int.}}} \,. \tag{5.16}$$

The 1/2 factor is used considering that baryons and antibaryons are not separated in the analysis and $N^H_{|y|<y_{\text{fid.}}}$ represents their signal measured with the fits mentioned above in the fiducial rapidity acceptance defined in Eq. 5.1 in different transverse momentum intervals, whose width is indicated with Δp_T. The total branching ratio of the $\Lambda_c^+ \rightarrow pK^-\pi^+$ channel is represented by BR and it is equal to $(6.28 \pm 0.32)\%$ [3], while $\mathcal{L}_{\text{int.}}$ is the integrated luminosity associated to the analysed sample. The other two ingredients correspond to the prompt fraction (f_{prompt}) and the efficiency times acceptance ($\alpha_y(\text{acc} \times \varepsilon)$) correction term. They are described in detail in the next Sections.

The number of events N_{ev} that defines the integrated luminosity $\mathcal{L}_{\text{int.}}$ needs to take into account all those events that do not have an associated reconstructed primary vertex, but that triggered the data acquisition because of the presence of particles in the forward rapidity region that satisfy the V0 trigger conditions. For these reason, the number of normalization events is calculated as follows[3]:

$$\begin{aligned} N_{\text{ev}} &= N_{\text{ev}}^{\text{vtx}}(|z_{\text{vtx}}| < 10 \text{ cm}) + N_{\text{ev}}^{\text{no vtx}}(|z_{\text{vtx}}| < 10 \text{ cm}) \\ &= N_{\text{ev}}^{\text{vtx}}(|z_{\text{vtx}}| < 10 \text{ cm}) + N_{\text{ev}}^{\text{no vtx}} \cdot \frac{N_{\text{ev}}^{\text{vtx}}(|z_{\text{vtx}}| < 10 \text{ cm})}{N_{\text{ev}}^{\text{vtx}}} \\ &= N_{\text{ev}}^{\text{vtx}}(|z_{\text{vtx}}| < 10 \text{ cm}) + N_{\text{ev}}^{\text{no vtx}} \cdot f_{\text{ev}}^{\text{vtx}}(|z_{\text{vtx}}| < 10 \text{ cm}) \,. \end{aligned} \tag{5.17}$$

The quantity $N_{\text{ev}}^{\text{vtx}}(|z_{\text{vtx}}| < 10 \text{ cm})$ corresponds to the number of events with a reconstructed vertex within the range $|z_{\text{vtx}}| < 10$ cm, while the second term corresponds to a correction that considers the number of trigger events without a reconstructed vertex. This correction term provides a negligible contribution in Pb–Pb collisions,

[3] The second term derives from the assumption that the primary vertex reconstruction efficiency is independent from the z_{vtx} position. If we define:

$$f_0 \equiv \frac{N_{\text{ev}}^{\text{vtx}}(|z_{\text{vtx}}| < 10 \text{ cm})}{N_{\text{ev}}(|z_{\text{vtx}}| < 10 \text{ cm})} \quad , \quad f_1 \equiv \frac{N_{\text{ev}}^{\text{vtx}}(|z_{\text{vtx}}| > 10 \text{ cm})}{N_{\text{ev}}(|z_{\text{vtx}}| > 10 \text{ cm})} \,,$$

then we can say that:

$$\begin{aligned} N_{\text{ev}}^{\text{no vtx}}(|z_{\text{vtx}}| < 10 \text{ cm}) &= (1 - f_0) N_{\text{ev}}(|z_{\text{vtx}}| < 10 \text{ cm}) \,, \\ N_{\text{ev}}^{\text{no vtx}}(|z_{\text{vtx}}| > 10 \text{ cm}) &= (1 - f_1) N_{\text{ev}}(|z_{\text{vtx}}| > 10 \text{ cm}) \,. \end{aligned}$$

Given these relations, the fractions of events with(out) reconstructed vertex within $|z_{\text{vtx}}| < 10$ cm can be written as follows:

$$\frac{N_{\text{ev}}^{\text{vtx}}(|z_{\text{vtx}}| < 10 \text{ cm})}{N_{\text{ev}}^{\text{vtx}}} = \frac{f_0 \cdot N_{\text{ev}}(|z_{\text{vtx}}| < 10 \text{ cm})}{f_0 \cdot N_{\text{ev}}(|z_{\text{vtx}}| < 10 \text{ cm}) + f_1 \cdot N_{\text{ev}}(|z_{\text{vtx}}| > 10\text{cm})} \,,$$

$$\frac{N_{\text{ev}}^{\text{no vtx}}(|z_{\text{vtx}}| < 10 \text{ cm})}{N_{\text{ev}}^{\text{no vtx}}} = \frac{(1 - f_0) \cdot N_{\text{ev}}(|z_{\text{vtx}}| < 10 \text{ cm})}{(1 - f_0) \cdot N_{\text{ev}}(|z_{\text{vtx}}| < 10 \text{ cm}) + (1 - f_1) \cdot N_{\text{ev}}(|z_{\text{vtx}}| > 10\text{cm})} \,.$$

If now the requirement of independent primary vertex reconstruction efficiency is assumed, namely $f_0 = f_1$, then the two terms reported in the last two equations are equal and this justifies the notation in Eq. 5.17.

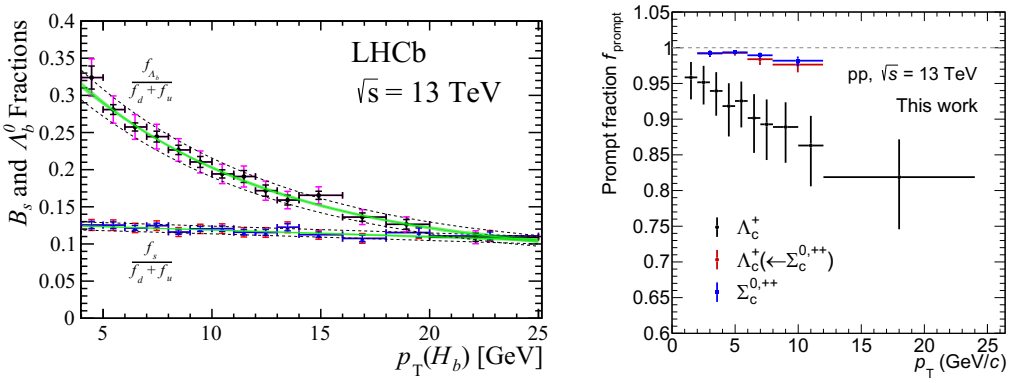

(A) (B)

FIGURE 5.13: (A) Ratios of B_s^0 and Λ_b^0 with respect to the sum of $\bar{B}^0$ and B^- measured by the LHCb experiment in pp collisions at $\sqrt{s}$ = 13 TeV. Image from [310]. (B) Prompt fraction f_{prompt} of Λ_c^+, $\Lambda_c^+(\leftarrow \Sigma_c^{0,++})$ and $\Sigma_c^{0,++}$ in the same collision system.

while in smaller collision systems like pp where the charged particle multiplicity is lower, this correction can reach $\sim 10\%$ [318].

5.3.1 Prompt fraction f_{prompt} determination

The measurement of the prompt baryon cross section requires to isolate only the prompt component of the signal, since the quantity $N^{\text{H}}_{|y|<y_{\text{fid.}}}$ also contains the raw non-prompt signal deriving from the $M(\text{pK}\pi)$ and ΔM fits. The prompt baryon cross section in this analysis is obtained by multiplying the total raw signal $N^{\text{H}}_{|y|<y_{\text{fid.}}}$ by the *prompt fraction* f_{prompt}, defined as:

$$\begin{aligned} f_{\text{prompt}} &= \frac{N^{\text{H}}_{\text{prompt}}}{N^{\text{H}}} = 1 - \frac{N^{\text{H}}_{\text{non-prompt}}}{N^{\text{H}}} \\ &= 1 - \frac{\alpha_y(\text{acc}\times\varepsilon)_{\text{non-prompt}}\cdot\Delta p_{\text{T}}\cdot\text{BR}\cdot\mathcal{L}_{\text{int.}}}{N^{\text{H}}_{|y|<y_{\text{fid.}}}/2}\cdot\left(\frac{\mathrm{d}^2\sigma^{\text{H}}}{\mathrm{d}p_{\text{T}}\mathrm{d}y}\right)^{\text{theory}}_{\text{non-prompt}}. \end{aligned} \tag{5.18}$$

Also in this case, the 1/2 factor is introduced because the measured signal regards both baryons and antibaryons, and $\alpha_y(\text{acc}\times\varepsilon)_{\text{non-prompt}}$ corresponds to the efficiency times acceptance correction term for non-prompt baryons. The last term in Eq. 5.18, $\left(\frac{\mathrm{d}^2\sigma^{\text{H}}}{\mathrm{d}p_{\text{T}}\mathrm{d}y}\right)^{\text{theory}}_{\text{non-prompt}}$, corresponds to the production cross section of feed-down charm baryons from the decays of beauty hadrons. For the Λ_c^+, this term is computed using the b-quark p_{T}-differential cross section from FONLL calculations [100, 101], the fraction of beauty quarks fragmenting into a Λ_b^0 baryon $b \to \Lambda_b^0$ and the $\Lambda_b^0 \to \Lambda_c^+ + X$ decay kinematics, which is evaluated with PYTHIA 8 simulations [236], finally it is normalised by the branching ratio $\text{BR}(\Lambda_b^0 \to \Lambda_c^+ + X) \approx 82\%$ as implemented in PYTHIA 8. The fraction of beauty quarks $b \to \Lambda_b^0$ derives from the b-hadron fragmentation fractions measured by LHCb experiment in pp collisions at $\sqrt{13}$ TeV [310]. In the panel (A) of Fig. 5.13 the production cross

sections of B_s^0 and Λ_b^0 normalised to the sum of $\bar{B}^0$ and B^- are shown as a function of hadron p_T. These quantities correspond to the beauty fragmentation fraction ratios $f_s/(f_d + f_u) \equiv X$ and $f_{\Lambda_b^0}/(f_d + f_u) \equiv Y$ respectively, where $f_{\Lambda_b^0}$ indicates the fraction of beauty quarks producing a Λ_b^0, namely $b \to \Lambda_b^0$. Neglecting the fragmentation of beauty quarks into heavier hadrons, it can be assumed that $f_{\Lambda_b^0} + f_s + f_d + f_u = f_{\Lambda_b^0}\left(1 + \frac{X}{Y} + \frac{1}{Y}\right) = 1$. Therefore, it is possible to write $f_{\Lambda_b^0} = Y/(X + Y + 1)$. The p_T dependence of the fragmentation fraction ratios is described with a polynomial of first order for the meson-to-meson ratio and with an exponential for the baryon-to-meson ratio in the transverse momentum interval $4 < p_T < 25\,\mathrm{GeV}/c$ where the measurement is performed. The value assigned to $f_{\Lambda_b^0}$ at lower p_T is around 0.2, chosen assuming a flat fragmentation function for $p_T < 5$ GeV/c given that the $\Lambda_b^0/\bar{B}^0$ ratio measured in pp collisions at $\sqrt{s} = 7,8$ TeV is observed to be constant in this range within the experimental uncertainties [309]. The fragmentation function $f_{\Lambda_b^0}$ is assumed to be the same at midrapidity, considering that the beauty production ratios measured by the LHCb collaboration do not show a significant dependence as a function of rapidity [309,310]. In panel (B) of Fig. 5.13 the prompt fraction for Λ_c^+, $\Lambda_c^+(\leftarrow \Sigma_c^{0,++})$ and $\Sigma_c^{0,++}$ baryons calculated with Eq. 5.18 and the elements described above are shown as a function of baryon p_T. The prompt fraction of Λ_c^+ decreases with p_T from $\sim 95\%$ to $\sim 80\%$. For f_{prompt} calculation of $\Lambda_c^+(\leftarrow \Sigma_c^{0,++})$ and $\Sigma_c^{0,++}$ it has been observed from dedicated PYTHIA 8.243 simulations [319] that the only relevant source of feed-down for $\Sigma_c^{0,++}$ baryons derives from the decays of Λ_b^0. As a matter of fact, according to the simulations the Λ_b^0 baryon is the most relevant source of Λ_c^+ feed-down, given that the branching ratios for other b-hadrons is lower by at least one order of magnitude. In particular, the $\Sigma_c^{0,++}$ baryons do not receive any direct feed-down from $\Sigma_b^{\pm}$, since they strongly decay into Λ_b^0 baryons [3]. Given that $\mathrm{BR}(\Lambda_b^0 \to \Sigma_c^{0,++} + X)/\mathrm{BR}(\Lambda_b^0 \to \Lambda_c^+ + X) \simeq 3\%$, then the $\left(\frac{\mathrm{d}^2\sigma^{\mathrm{H}}}{\mathrm{d}p_T\mathrm{d}y}\right)^{\mathrm{theory}}_{\mathrm{non-prompt}}$ term is scaled by 3% in the measurement of the production cross section of $\Lambda_c^+(\leftarrow \Sigma_c^{0,++})$ and $\Sigma_c^{0,++}$ baryons. In this case, f_{prompt} is observed to be always higher than 97%.

5.3.2 Efficiency and acceptance determination

The prompt signal $N^{\mathrm{H}}_{|y|<y_{\mathrm{fid.}}}$ quantifies the amount of baryons that satisfy the selection criteria on track and candidate variables as well as daughter identification criteria (Tabs. 5.2 and 5.6). All these selections, which are applied to separate the signal from the combinatorial background, also reject a significant amount of signal. This fraction is estimated with the aid of MC simulations. The generation of pp events is performed with PYTHIA 8.243 event generator [319], where $c\bar{c}$ and $b\bar{b}$ pairs are included. They produce heavy hadrons that are then forced to decay in hadronic channels and the particles are propagated through the ALICE apparatus using the GEANT 3 package [237]. The detector layouts as well as the data taking conditions are reproduced in the simulations.

The baryon yield measured in data needs to be corrected by two terms. The first one, called *efficiency*, corresponds to the reconstruction efficiency of the "reconstructable" baryons, namely those generated in the considered rapidity range with reconstructable daughters in the detector acceptance. The second term, called *acceptance*, quantifies the fraction of reconstructable baryons among those generated within the same rapidity interval. The efficiency for Λ_c^+ baryons is calculated as

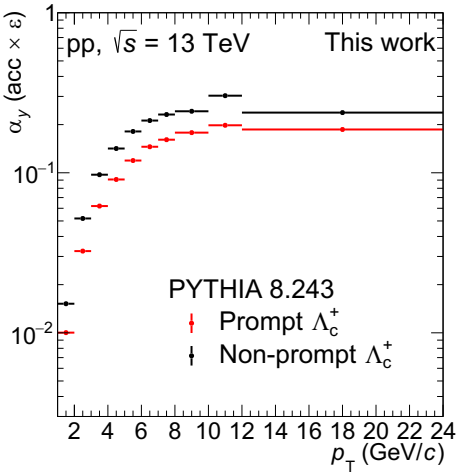

(A) Prompt and non-prompt Λ_c^+.

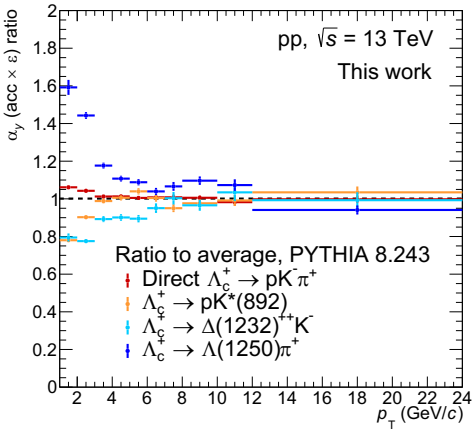

(B) Prompt Λ_c^+.

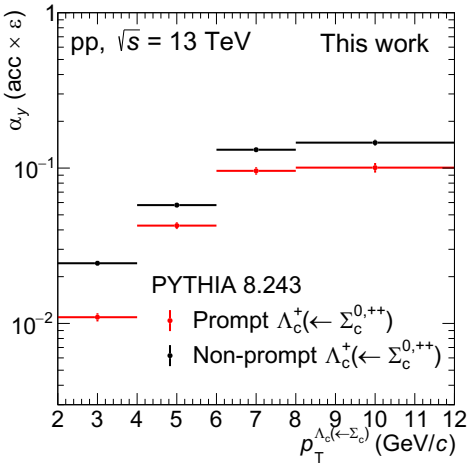

(C) Prompt and non-prompt $\Lambda_c^+ \leftarrow \Sigma_c$.

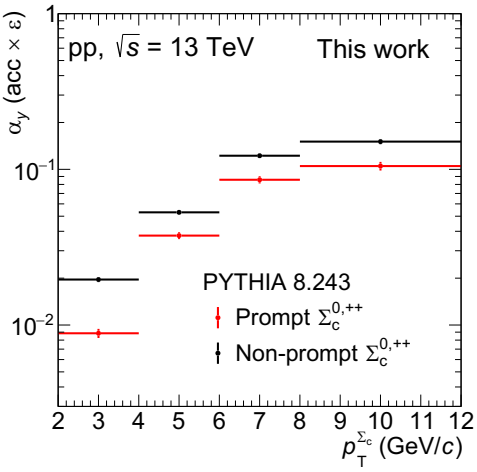

(D) Prompt and non-prompt $\Sigma_c^{0,++}$.

FIGURE 5.14: (A), (C), (D): correction term $\alpha_y(\text{acc} \times \varepsilon)$ for prompt and non-prompt Λ_c^+, $\Lambda_c^+(\leftarrow \Sigma_c^{0,++})$ and $\Sigma_c^{0,++}$ obtained from simulated pp collisions at $\sqrt{s} = 13$ TeV generated with PYTHIA 8.243 event generator. (B): $\alpha_y(\text{acc} \times \varepsilon)$ correction terms of prompt Λ_c^+ evaluated for different resonant and non-resonant $\Lambda_c^+ \to pK^-\pi^+$ decay channels and normalised to the averaged one in simulated pp events. See the text for details.

follows:

$$\varepsilon = \frac{N_{\text{reco.}}|_{|y|<y_{\text{fid.}}}(p_{\text{T}}^{\text{reco.}})}{N_{\text{gen.}}^{\text{daug. in acc.}}|_{|y|<y_{\text{fid.}}}(p_{\text{T}}^{\text{gen.}})} \,. \tag{5.19}$$

The efficiency is defined as the ratio between the amount of reconstructed baryons within the fiducial acceptance and the amount of generated baryons within the same rapidity interval and with the decay products in acceptance. The latter condition is satisfied by daughter tracks with pseudorapidity $|\eta| < 0.9$. Only events with a generated primary vertex within $|z_{\text{vtx}}| < 10$ cm are considered. A similar definition holds for the $\Sigma_c^{0,++}$ particles, where the denominator is defined by $\Sigma_c^{0,++}$ generated

Decay channel	BR($\Lambda_c^+ \to X$)	Resonance BR
Total $\Lambda_c^+ \to pK^-\pi^+$	$(6.28 \pm 0.32)\%$	-
Direct $\Lambda_c^+ \to pK^-\pi^+$	$(3.50 \pm 0.40)\%$	-
$\Lambda_c^+ \to pK^+(892)^0$	$(1.96 \pm 0.27)\%$	0.667
$\Lambda_c^+ \to \Delta(1232)^{++}K^-$	$(1.08 \pm 0.25)\%$	0.994
$\Lambda_c^+ \to \Lambda(1520)\pi^+$	$(2.20 \pm 0.50)\%$	$(22.5 \pm 0.5)\%$

TABLE 5.9: $\Lambda_c^+ \to pK^-\pi^+$ resonant and non-resonant channels. Numbers from [3, 320].

baryons with daughter Λ_c^+ in the fiducial acceptance and with the soft pion daughter within $|\eta| < 0.9$. The acceptance term is calculated as:

$$\alpha_y \cdot \text{acc} = \frac{N_{\text{gen.}}^{\text{daug. in acc.}}|_{|y|<y_{\text{fid.}}}(p_{\text{T}}^{\text{gen.}})}{N_{\text{gen.}}|_{|y|<0.5}(p_{\text{T}}^{\text{gen.}})} \,. \tag{5.20}$$

This is defined as the number of generated candidates within the fiducial rapidity acceptance and with decay products in acceptance divided by the number of generated particles decaying in the desired channel and within $|y| < 0.5$, namely the rapidity range in which the measurement is finally provided. This acceptance term implicitly accounts for the fraction of generated candidates within the fiducial acceptance that have the daughters outside the acceptance, then it includes the correction factor α_y to go from $|y| < y_{\text{fid.}}$ to $|y| < 0.5$. Finally, the efficiency times acceptance correction factor is written as:

$$\begin{aligned} \alpha_y(\text{acc} \times \varepsilon) &= \frac{N_{\text{reco.}}|_{|y|<y_{\text{fid.}}}(p_{\text{T}}^{\text{reco.}})}{N_{\text{gen.}}^{\text{daug. in acc.}}|_{|y|<y_{\text{fid.}}}(p_{\text{T}}^{\text{gen.}})} \cdot \frac{N_{\text{gen.}}^{\text{daug. in acc.}}|_{|y|<y_{\text{fid.}}}(p_{\text{T}}^{\text{gen.}})}{N_{\text{gen.}}|_{|y|<0.5}(p_{\text{T}}^{\text{gen.}})} \\ &= \frac{N_{\text{reco.}}|_{|y|<y_{\text{fid.}}}(p_{\text{T}}^{\text{reco.}})}{N_{\text{gen.}}|_{|y|<0.5}(p_{\text{T}}^{\text{gen.}})} \,. \end{aligned} \tag{5.21}$$

The $\alpha_y(\text{acc} \times \varepsilon)$ correction factors for prompt and non-prompt Λ_c^+, $\Lambda_c^+(\leftarrow \Sigma_c^{0,++})$ and $\Sigma_c^{0,++}$ baryons are shown in (A), (C) and (D) panels of Fig. 5.14. They are strongly dependent on the particle p_{T} due to the selections applied on the tracks and candidates for background rejection. Moreover, the acceptance term is sensitive to the decay kinematics, which changes significantly with increasing p_{T}. In Tab. 5.9 the resonant and non-resonant channels contributing to the decay of a Λ_c^+ baryon in the $pK^-\pi^+$ final state are listed. A correct calculation of the $\alpha_y(\text{acc} \times \varepsilon)$ correction factor requires to take into account all the resonant and non-resonant channels that contribute to the final state, given the different decay kinematics. For this reason, the total correction term is calculated as a weighted average of the correction factors from each resonant and non-resonant decay, where the total branching ratio of each channel is used as weight. This procedure is adopted to avoid the efficiency times acceptance term to be influenced by wrong relative abundances of resonant and non-resonant decays in the simulated events. The correction factors of the resonant and non-resonant $\Lambda_c^+ \to pK^-\pi^+$ decays normalised to the averaged one are shown in panel (B) of Fig. 5.14. The direct channel provides a $\alpha_y(\text{acc} \times \varepsilon)$ term closer to the averaged one with respect to the resonant channels, which are characterised

by a lower branching ratio. This procedure is adopted for the efficiency times acceptance determination of prompt and non-prompt Λ_c^+, $\Lambda_c^+(\leftarrow \Sigma_c^{0,++})$ and $\Sigma_c^{0,++}$ baryons, since in all cases a $\Lambda_c^+ \rightarrow pK^-\pi^+$ decay is reconstructed. The $\alpha_y(\text{acc} \times \varepsilon)$ grows from about 1% at low p_T to about 10% for prompt $\Lambda_c^+(\leftarrow \Sigma_c^{0,++})$ and $\Sigma_c^{0,++}$ for $8 < p_T < 12$ GeV/c and to about 20% for prompt Λ_c^+ at $12 < p_T < 24$ GeV/c.

The $\Lambda_c^+(\leftarrow \Sigma_c^{0,++})$ and $\Sigma_c^{0,++}$ baryon measurement is performed through the reconstruction of $\Sigma_c^{0,++}$ candidates, defined as a candidate Λ_c^+ that is paired with a candidate soft $\pi^\pm$. As specified in Tab. 5.6, this is done only with Λ_c^+ baryons with a mass within $2.277 < m(\Lambda_c^+) < 2.299$ GeV/c^2, in order to reduce the combinatorial background in data. This selection rejects parts of the reconstructed Λ_c^+ candidates and this effect is observed to be slightly different in data and MC simulation. The efficiency related to this mass selection is calculated separately in data and simulations as the fraction of reconstructed Λ_c^+ baryons within the considered mass window. In particular, the number of Λ_c^+ baryons in data derives from the fit with the function in Eq. 5.12 of the $pK\pi$ invariant mass distributions. It was observed that the fraction of reconstructed Λ_c^+ within this mass interval in simulation is about 1% higher than in data in all the p_T intervals, therefore the $\alpha_y(\text{acc} \times \varepsilon)$ term is scaled down accordingly to cure this bias. Finally, the efficiency times acceptance terms are calculated after applying a smearing of the track impact parameter in the MC, as explained in detail in Section 3.6.5. Such a smearing is applied separately in the MC productions anchored to the analysed pp collision samples and the effect on the efficiency estimation is observed to reach a maximum value of about 2%.

5.4 Systematic uncertainty estimation

Systematic uncertainties on the measurement of Λ_c^+, $\Lambda_c^+(\leftarrow \Sigma_c^{0,++})$ and $\Sigma_c^{0,++}$ baryons can derive from the possible imperfections of MC simulations in describing the layout and performance of the apparatus during the data taking and from the analysis procedure itself. In the following Sections, the different sources of systematic uncertainty evaluated in this analysis are described in detail. The summary of all the systematic uncertainties assigned to the final results is reported in Tabs. 5.13, 5.14 and 5.15 and shown in Fig. 5.22.

5.4.1 Track reconstruction efficiency

The systematic uncertainty deriving from possible difference in data and MC on the track-reconstruction efficiency includes effects from the track finding in the TPC and their quality, as well as from the matching from TPC to ITS.

The TPC track finding and quality dependence is evaluated at the level of the baryon cross section, which has been measured with modified selections with respect to what listed in Tab. 5.2, in particular on:

- number of TPC crossed pad rows, which is required to be $> 120 - 5/p_T$;
- number of found-over-findable cluster in TPC, asked to be > 0.9.

From this test, the maximum observed variation at the cross section level is of order of 2-3%, that corresponds to a per-track systematic uncertainty of about 1% at $p_T < 2$ GeV/c and quickly decreases for higher candidate p_T. The same values are obtained by repeating this study with the D^0 meson, whose reconstruction in data is affected by lower statistical fluctuations. The systematic uncertainty related to the ITS-TPC

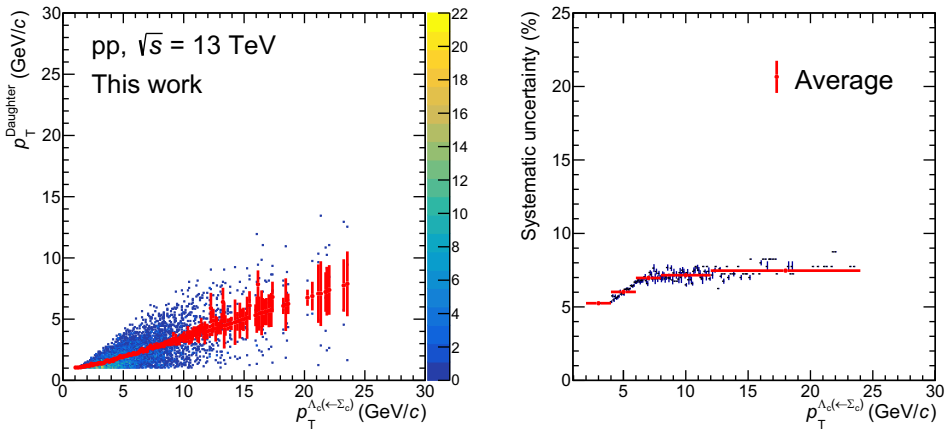

FIGURE 5.15: Left: correlation between transverse momentum of generated $\Lambda_c^+(\leftarrow \Sigma_c^{0,++})$ particles and the one of the Λ_c^+ decay daughters from MC simulations. Right: tracking efficiency systematic uncertainty at the $\Lambda_c^+(\leftarrow \Sigma_c^{0,++})$ baryon level as the sum of the p, K^- and π^+ daughter particles uncertainties.

matching efficiency is estimated with a dedicated single-track study, as explained in Sec. 3.6.4.

The uncertainty on the track-reconstruction efficiency is defined by the results from the studies mentioned above: the variation of the TPC track quality criteria and the ITS-TPC matching efficiency. The total systematic uncertainty associated to each track is calculated as the quadrature sum of these two contributions. The single-track systematic uncertainty is then propagated to the Λ_c^+ by considering the correlation between the baryon p_T and the daughter ones. In the left panel of Fig. 5.15 the case for $\Lambda_c^+(\leftarrow \Sigma_c^{0,++})$ baryons taken from MC simulations is shown. For each simulated Λ_c^+, the systematic uncertainty of the p, K^- and π^+ daughters is calculated according to the particle p_T, then the systematic uncertainty associated to the baryon corresponds to the linear sum of the daughter uncertainties, given that this uncertainty is considered as fully correlated for the three daughters. The result of this propagation for all the generated $\Lambda_c^+(\leftarrow \Sigma_c^{0,++})$ is reported in the right panel of Fig. 5.15, where the red graph indicates the average value assigned as systematic uncertainty in each p_T interval considered in the analysis. For the case of Λ_c^+ baryons, the total tracking efficiency uncertainty increases from about 5% for $p_T < 2$ GeV/c to about 7% for $p_T > 7$ GeV/c. In the case of $\Lambda_c^+(\leftarrow \Sigma_c^{0,++})$ and $\Sigma_c^{0,++}$ baryons the contribution of the soft pion is considered as well and it is added linearly to the sum of Λ_c^+ daughter systematic uncertainties. Also in this case, the uncertainty associated to the soft-pion track is estimated according to the track p_T and it is summed to those of the Λ_c^+ daughters to calculate the uncertainty for the $\Lambda_c^+(\leftarrow \Sigma_c^{0,++})$ and $\Sigma_c^{0,++}$. Considering that the soft pion average p_T is between 200 and 600 MeV/c for $\Sigma_c^{0,++}$ baryons simulated with PYTHIA in the interval $2 < p_T(\Sigma_c^{0,++}) < 12$ GeV/c, a systematic uncertainty of 2% is assigned to the soft pion track, according to the estimates reported in [321]. The total systematic uncertainty related to track reconstruction for prompt Λ_c^+, $\Lambda_c^+(\leftarrow \Sigma_c^{0,++})$ and $\Sigma_c^{0,++}$ is shown in Tabs. 5.13, 5.14 and 5.15 for each p_T interval considered in the analysis.

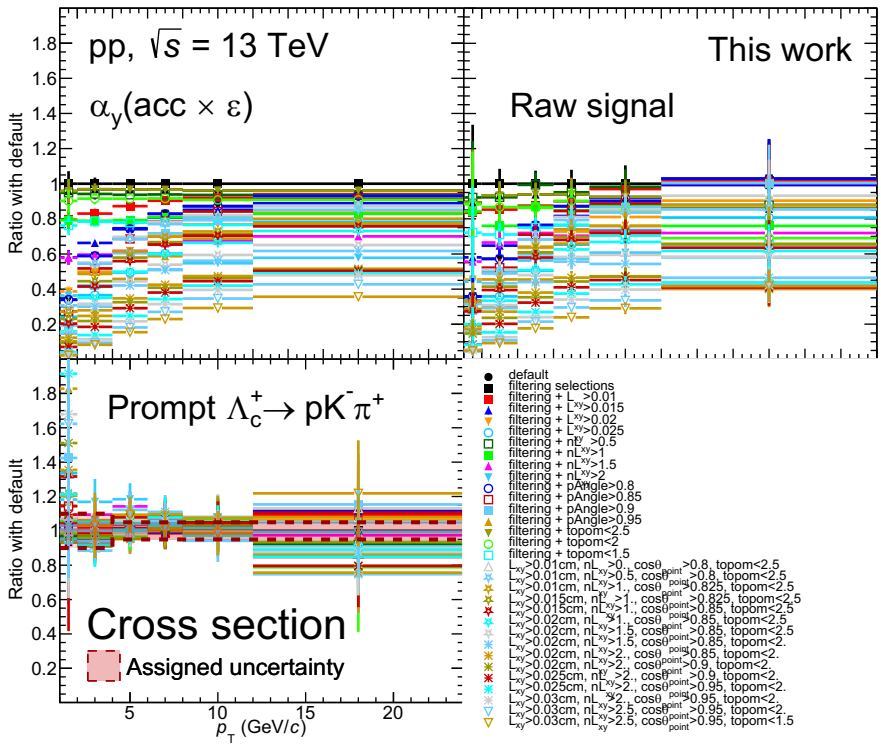

FIGURE 5.16: Efficiency times acceptance correction term (top left), raw signal (top right) and corrected cross section (bottom left) ratios of prompt $\Lambda_c^+ \rightarrow pK^-\pi^+$ baryon measured in pp collisions at $\sqrt{s} = 13$ TeV with different selection configurations on Λ_c^+ topological variables.

5.4.2 Topological-selection efficiency correction

Monte Carlo simulations do not perfectly reproduce the layout, status and performance of the detector during the data taking. The discrepancies between data and simulations are the origin of the systematic uncertainty related to the $\alpha_y(\text{acc} \times \varepsilon)$ correction. The contribution of this source of systematic uncertainty is evaluated by repeating the cross section measurement with different selections on the topological variables and evaluating the spread of the results with respect to the default one. The selections on the transverse projection of decay length (L_{xy}) and its value normalised by the uncertainty (nL_{xy}), the cosine of pointing angle ($\cos(\theta_p)$) and the maximum "topomatic" in the transverse plane ($d^{xy}_{\text{res.}}$) are varied. All the configurations considered to estimate the systematic uncertainty are listed in Tab. 5.10. As in the previous Chapter, the topological variables are firstly varied singularly, then many configurations where more than one topological variable is modified are considered. In this way, the effect of each of them is tested and also the influence on the final cross section of their correlation is evaluated. As soon as the selections are tightened, the measurement of the raw signal from data may become challenging due to the drop of the reconstruction efficiency and the signal extraction becomes more influenced by the statistical fluctuations. This occurs in particular for the measurement of $\Lambda_c^+ (\leftarrow \Sigma_c^{0,++})$ and $\Sigma_c^{0,++}$ signal, given the low signal-to-background ratio observed

Configuration index	Selections
1	Filtering
2	$L_{xy} > 0.01$ cm
3	$L_{xy} > 0.015$ cm
4	$L_{xy} > 0.02$ cm
5	$L_{xy} > 0.025$ cm
6	$\mathrm{n}L_{xy} > 0.5$
7	$\mathrm{n}L_{xy} > 1$
8	$\mathrm{n}L_{xy} > 1.5$
9	$\mathrm{n}L_{xy} > 2$
10	$\cos(\theta_p) > 0.8$
11	$\cos(\theta_p) > 0.85$
12	$\cos(\theta_p) > 0.9$
13	$\cos(\theta_p) > 0.95$
14	$d_{\mathrm{res.}}^{\mathrm{xy}} < 2.5$
15	$d_{\mathrm{res.}}^{\mathrm{xy}} < 2$
16	$d_{\mathrm{res.}}^{\mathrm{xy}} < 1.5$
17	$L_{xy} > 0.01$ cm, $\mathrm{n}L_{xy} > 0$, $\cos(\theta_{\mathrm{p}}) > 0.8$, $d_{\mathrm{res.}}^{\mathrm{xy}} < 2.5$
18	$L_{xy} > 0.01$ cm, $\mathrm{n}L_{xy} > 0.5$, $\cos(\theta_{\mathrm{p}}) > 0.8$, $d_{\mathrm{res.}}^{\mathrm{xy}} < 2.5$
19	$L_{xy} > 0.01$ cm, $\mathrm{n}L_{xy} > 1$, $\cos(\theta_{\mathrm{p}}) > 0.825$, $d_{\mathrm{res.}}^{\mathrm{xy}} < 2.5$
20	$L_{xy} > 0.015$ cm, $\mathrm{n}L_{xy} > 1$, $\cos(\theta_{\mathrm{p}}) > 0.825$, $d_{\mathrm{res.}}^{\mathrm{xy}} < 2.5$
21	$L_{xy} > 0.015$ cm, $\mathrm{n}L_{xy} > 1$, $\cos(\theta_{\mathrm{p}}) > 0.85$, $d_{\mathrm{res.}}^{\mathrm{xy}} < 2.5$
22	$L_{xy} > 0.02$ cm, $\mathrm{n}L_{xy} > 1$, $\cos(\theta_{\mathrm{p}}) > 0.85$, $d_{\mathrm{res.}}^{\mathrm{xy}} < 2.5$
23	$L_{xy} > 0.02$ cm, $\mathrm{n}L_{xy} > 1.5$, $\cos(\theta_{\mathrm{p}}) > 0.85$, $d_{\mathrm{res.}}^{\mathrm{xy}} < 2$
24	$L_{xy} > 0.02$ cm, $\mathrm{n}L_{xy} > 1.5$, $\cos(\theta_{\mathrm{p}}) > 0.85$, $d_{\mathrm{res.}}^{\mathrm{xy}} < 2$
25	$L_{xy} > 0.02$ cm, $\mathrm{n}L_{xy} > 2$, $\cos(\theta_{\mathrm{p}}) > 0.85$, $d_{\mathrm{res.}}^{\mathrm{xy}} < 2$
26	$L_{xy} > 0.02$ cm, $\mathrm{n}L_{xy} > 2$, $\cos(\theta_{\mathrm{p}}) > 0.9$, $d_{\mathrm{res.}}^{\mathrm{xy}} < 2$
27	$L_{xy} > 0.025$ cm, $\mathrm{n}L_{xy} > 2$, $\cos(\theta_{\mathrm{p}}) > 0.9$, $d_{\mathrm{res.}}^{\mathrm{xy}} < 2$
28	$L_{xy} > 0.025$ cm, $\mathrm{n}L_{xy} > 2$, $\cos(\theta_{\mathrm{p}}) > 0.95$, $d_{\mathrm{res.}}^{\mathrm{xy}} < 2$
29	$L_{xy} > 0.03$ cm, $\mathrm{n}L_{xy} > 2$, $\cos(\theta_{\mathrm{p}}) > 0.95$, $d_{\mathrm{res.}}^{\mathrm{xy}} < 2$
30	$L_{xy} > 0.03$ cm, $\mathrm{n}L_{xy} > 2.5$, $\cos(\theta_{\mathrm{p}}) > 0.95$, $D_0^{xy} < 2$
31	$L_{xy} > 0.03$ cm, $\mathrm{n}L_{xy} > 2.5$, $\cos(\theta_{\mathrm{p}}) > 0.95$, $D_0^{xy} < 1.5$

TABLE 5.10: Different selection configurations on the topological variables related to the $\Lambda_c^+ \to \mathrm{pK}^-\pi^+$ decay adopted for the estimation of the efficiency correction systematic uncertainty. The keyword "filtering" refers to the selections listed in Tab. 5.5, which are the criteria on top of which the listed selections are applied.

in data, but also for the measurement of $\Lambda_c^+ \to \mathrm{pK}^-\pi^+$ signal in transverse momentum intervals $\Delta p_{\mathrm{T}} = 1$ GeV/c. For this reason, the systematic uncertainty on the correction for the topological selection efficiency is calculated considering the variations of the prompt Λ_c^+ cross sections measured in coarser p_{T} intervals with respect to those addressed for the analysis, namely $1 < p_{\mathrm{T}} < 2$ GeV/c, $2 < p_{\mathrm{T}} < 4$ GeV/c, $4 < p_{\mathrm{T}} < 6$ GeV/c, $6 < p_{\mathrm{T}} < 8$ GeV/c, $8 < p_{\mathrm{T}} < 12$ GeV/c, where the Λ_c^+ candidates are reconstructed by adopting the "filtering" selections listed in Tab. 5.5. In Fig. 5.16 the ratios with respect to the results obtained with the "filtering" selections of efficiency times acceptance correction term (top left), the raw signal measured from the $M(\mathrm{pK}^-\pi^+)$ distributions in data (top right) and the resulting

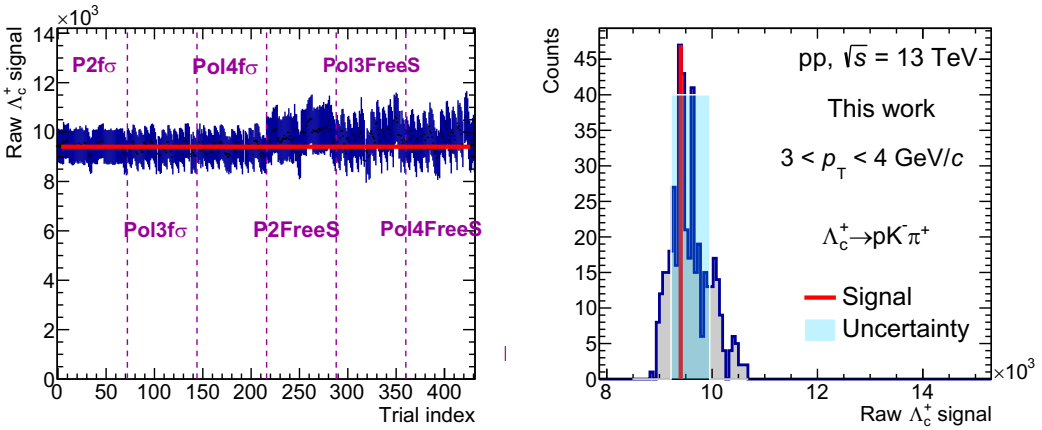

FIGURE 5.17: Left: raw Λ_c^+ signal measured for each trial, characterised by histogram binning, low and up edge values, background function and condition on the Gaussian σ for the signal description different from the default settings adopted for the signal measurement from $M(\mathrm{pK}^-\pi^+)$ distribution in the $3 < p_\mathrm{T} < 4$ GeV/c interval. P2: polynomial of 2$^{\mathrm{nd}}$ order; Pol3: polynomial of 3$^{\mathrm{rd}}$ order; Pol4: polynomial of 4$^{\mathrm{th}}$ order; FreeS: Gaussian σ left free in the fit. Right: raw Λ_c^+ signal distribution given by the repetition of the $M(\mathrm{pK}^-\pi^+)$ distribution fit in $3 < p_\mathrm{T} < 4$ GeV/c given the modified fit conditions mentioned above.

corrected cross section (bottom left) measured by applying the different selection configurations listed in Tab. 5.10 are shown. The cross section measurement in the $1 < p_\mathrm{T} < 2$ GeV/c interval is observed to change dramatically with some selection configurations with respect to the filtering one. The reason for these outliers has to be ascribed to the low signal-to-background ratio, which decreases below 1‰ for tighter selections, accompanied by a statistical significance that falls down below 2. Therefore, the raw signal extraction becomes challenging and strongly affected by huge statistical fluctuations. Without considering these cases, the overall variations on the final cross section are contained within 10%. Also the variations related to the measurement in the interval $12 < p_\mathrm{T} < 24$ GeV/c show some fluctuations caused by the low amount of signal surviving the selection criteria. Given the comparable efficiency, the systematic uncertainty in $12 < p_\mathrm{T} < 24$ GeV/c is then considered equal to that of the previous adjacent interval. The final systematic uncertainty assigned to the cross section measurements of prompt Λ_c^+, $\Lambda_c^+ (\leftarrow \Sigma_c^{0,++})$ and $\Sigma_c^{0,++}$ corresponds to 10% for $p_\mathrm{T} < 4$ GeV/c and 5% for higher transverse momenta. As a cross-check, this study is repeated for the $\Lambda_c^+ (\leftarrow \Sigma_c^{0,++})$ and $\Sigma_c^{0,++}$ baryons separately, as well as for the Λ_c^+ in the finer p_T intervals considered in the analysis. By comparing the variations with respect to the default selection configuration listed in Tab. 5.6, the cross sections do not show critical instabilities when the selection criteria are changed. However, given the large statistical fluctuations affecting the invariant mass distribution in data and the consequent impact on the observed variations, the study shown in Fig. 5.16 is taken into account to assign the systematic uncertainty related to the correction for the topological variable selection efficiency.

	Conditions	Number of cases
$M(\mathrm{pK}^-\pi^+)$ bin width	$4^{(\dagger)}$, 8 MeV/c^2	2
Low $M(\mathrm{pK}^-\pi^+)$ edge	-30, -20, -10, $+0^{(\dagger)}$, +10, +20 MeV/c^2	6
Up $M(\mathrm{pK}^-\pi^+)$ edge	-20, -10, $+0^{(\dagger)}$, +10, +20, +30 MeV/c^2	6
Background function	$2^{\mathrm{nd},(\dagger)}$, 3^{rd}, 4^{th} order polynomial	3
Signal σ	Free, Fixed to MC$^{(\dagger)}$	2
Total number of cases		432

TABLE 5.11: Variation of $M(\mathrm{pK}^-\pi^+)$ distribution fit conditions considered to quantify the systematic uncertainty associated to the Λ_c^+ raw signal measurement. The variations of low and up edge listed here have to be considered with respect to the default edges used in the fits shown in Fig. 5.9. The $^{(\dagger)}$ symbol indicates the default configuration.

Parameter	Value
$\Gamma_{\Sigma_c^{++}}$	$1.89^{+0.09}_{-0.18}$ MeV/c^2
$\Gamma_{\Sigma_c^0}$	$1.83^{+0.11}_{-0.19}$ MeV/c^2
δM	0.220 ± 0.013 MeV/c^2
Gaussian σ	0.8, 1.0, 1.2 MeV/c^2
Background function	D^{*+}, polynomial of 3^{rd} order, rotation templates $\times$ polynomial of 2^{nd} order, rotation templates + polynomial of 2^{nd} order
Low ΔM edge	0.14, 0.144, 0.148, 0.152, 0.156 GeV/c^2
High ΔM edge	0.184, 0.186, 0.190, 0.195, 0.200, 0.205, 0.210 GeV/c^2

TABLE 5.12: Variation of ΔM distribution fit conditions considered to quantify the systematic uncertainty on the $\Lambda_c^+ (\leftarrow \Sigma_c^{0,++})$ and $\Sigma_c^{0,++}$ raw signal measurement.

5.4.3 Raw signal measurement

As described in Sec. 5.2.4, the raw signal of Λ_c^+ baryons is measured from the $M(\mathrm{pK}^-\pi^+)$ distribution from data through a binned likelihood fit with the analytical function reported in Eq. 5.12. However, the description of the signal peak and the background profile may not be ideal with the chosen functions. The systematic uncertainty related to the raw signal measurement is then evaluated by repeating the $M(\mathrm{pK}^-\pi^+)$ fits under different conditions in all the p_T intervals separately. In Tab. 5.11 all the considered variations are listed. The histogram bins, which by default are 4 MeV/c^2 wide, are merged to 8 MeV/c^2 wide ones before repeating the fit. Moreover, the considered range for the overall fit is modified, with the lowest edge that is varied between -30 MeV/c^2 and +20 MeV/c^2 and the highest edge between -20 MeV/c^2 and +30 MeV/c^2 with respect to the default values, in order to test the sensitivity to the background concavity. Furthermore, higher order polynomials are tested for the background description, and, finally, the fits are repeated also by leaving free the Gaussian σ of the signal. Considering all these variations,

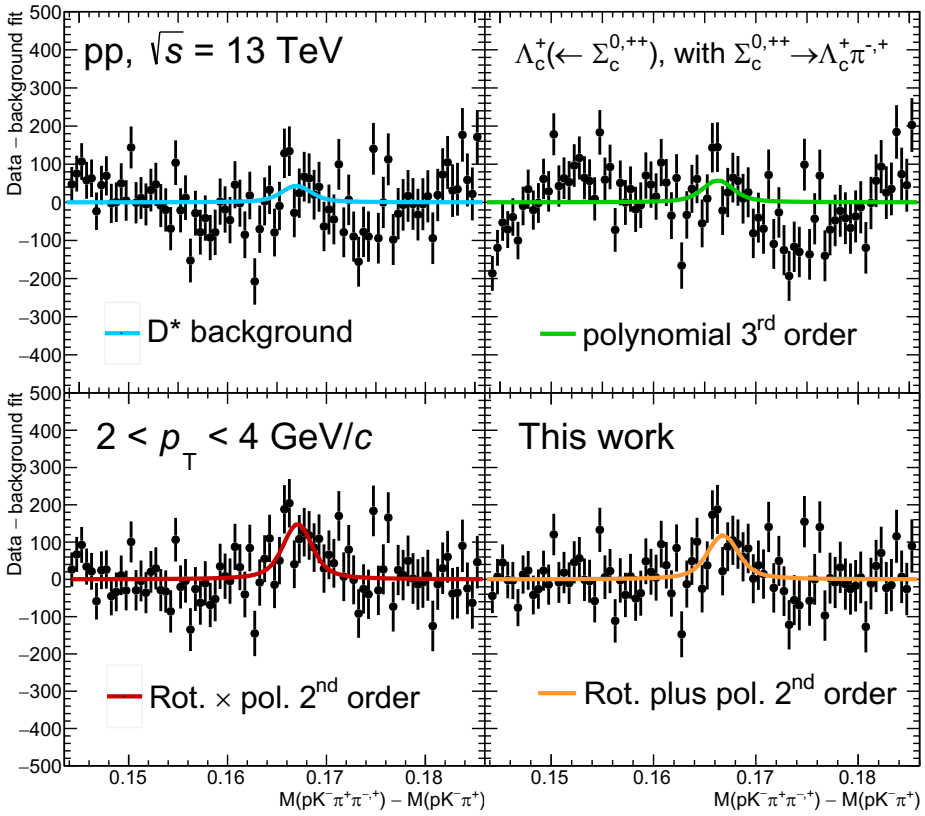

FIGURE 5.18: Residual distribution of ΔM distribution with respect to background parametrization performed with four different functions in the $2 < p_T(\Lambda_c^+(\leftarrow \Sigma_c^{0,++})) < 4$ GeV/c interval in pp collisions at $\sqrt{s} = 13$ TeV.

the $M(\mathrm{pK}^-\pi^+)$ binned likelihood fit in each p_T interval is repeated more than 400 times. The full outcome of the trials performed on the $M(\mathrm{pK}^-\pi^+)$ distribution in the $3 < p_T < 4$ GeV/c interval is shown in Fig. 5.17. The left panel shows the $\Lambda_c^+ \rightarrow \mathrm{pK}^-\pi^+$ signal measured in each trial. The trials are grouped according to the background fit function and the Gaussian σ condition adopted in the fit. In particular, in the first $\sim$ 200 cases the Gaussian σ is fixed to MC value, while in the last $\sim$ 200 trials it is left free in the fit. The raw signal measured with the default fit configuration is reported with a solid red line. It is possible to notice that the trials are distributed around this value. The projection on the y-axis is reported in the right panel. The root-mean-square error of the distribution is considered to quantify the systematic uncertainty on the raw signal measurement. In the $3 < p_T < 4$ GeV/c interval shown in Fig. 5.17 the root-mean-square is observed to be about 4% of the distribution mean value, thus a symmetric 4% uncertainty is assigned to the final measurement. The value of this uncertainty runs between 4% to 11%, depending on the p_T interval, as reported in detail in Tab. 5.13.

With a similar logic, the systematic uncertainty related to the $\Lambda_c^+(\leftarrow \Sigma_c^{0,++})$ and $\Sigma_c^{0,++}$ raw signal measurement coming from the $\Delta M = M(\mathrm{pK}\pi\pi) - M(\mathrm{pK}\pi)$ distribution fit is quantified by modifying the signal and background function properties. As described in Sec. 5.2.4, several parameters related to the signal function are fixed

to the values reported in the PDG [3] or coming from dedicated MC studies. This is the case for the Breit-Wigner widths $\Gamma_{\Sigma_c^{++}}$ and $\Gamma_{\Sigma_c^0}$, the mass difference between the two charge states δM and the Gaussian resolution σ. The Breit-Wigner widths and the δM parameters are varied within their uncertainties, while the Gaussian σ is changed within $\pm 20\%$, as reported in the top part of Tab. 5.12. Configurations where the parameters are changed individually, as well as containing multiple variations are considered and the measured raw signal for $\Lambda_c^+(\leftarrow \Sigma_c^{0,++})$ and $\Sigma_c^{0,++}$ is observed to change within 5%. The effects deriving from these variations are anyway subdominant with respect to what observed in another bunch of trials, related to the description of the background distribution. The default parametrization in the $2 < p_T(\Lambda_c^+(\leftarrow \Sigma_c^{0,++}), \Sigma_c^{0,++}) < 4$ GeV/c is provided with a template of pure combinatorial $\Sigma_c^{0,++}$ candidates, built with candidate Λ_c^+ located in the sidebands of the $M(\mathrm{pK}^-\pi^+)$ distribution around the expected $\Lambda_c^+ \rightarrow \mathrm{pK}^-\pi^+$ signal that are paired with rotated pions, while for higher p_T intervals the background is described with a polynomial of third order. The choice of using the template in the lowest p_T interval is dictated by the low signal-to-background ratio observed in the ΔM distribution and the need of correctly parametrise the background trend to avoid under- or over- estimations of the raw signal measurement. This problem may emerge if the parametrisation of the background concavity is strongly driven by the statistical fluctuations as well as by intrinsic background modulations, but also if the tails of the signal peak are confused with the background distribution and not counted in the measurement. The template-based approach better describes possible higher-order modulations of the background distribution that cannot be easily parametrised with an analytical function. This can be appreciated in Fig. 5.18, where the residuals with respect to the background for four different parametrisation in the ΔM range between 0.144 and 0.186 GeV/c^2 are shown. In the top-left panel, the $f(\Delta M) = p_1\sqrt{\Delta M - \bar{m}}e^{p_2(\Delta M - \bar{m})}$ function, with $\bar{m} = 139$ MeV/c^2, used for the D^{*+} meson signal measurement [107] is chosen to parametrise the background, while in the top-right panel a polynomial of third order is adopted. The distributions shown in the bottom row correspond to the residuals with respect to the background parametrised with the combinatorial candidate template. The bottom-left panel refers to the case in which the background template is modulated by a polynomial of 2$^{\mathrm{nd}}$ order, where the latter function is used to smoothen the template and better catch the reconstructed background shape. In this case, the template normalization factor is a free parameter of the fit. The bottom-right panel shows the residual distribution obtained performing the fit with the double Voigt function to describe the $\Lambda_c^+(\leftarrow \Sigma_c^{0,++})$ signal and a polynomial of 2$^{\mathrm{nd}}$ order to parametrise the remaining background after the subtraction of the combinatorial template from the measured ΔM distribution. The combinatorial background template is normalised to match the ΔM distribution integral in the range $0.170 < \Delta M < 0.190$ GeV/c^2 before the subtraction. The D^{*+} and 3$^{\mathrm{rd}}$ order polynomial functions evidently do not appropriately describe the background: in the former case, the residuals show a parabola-like baseline, which increases for low and high ΔM values, while in the latter case the residuals show a sinusoidal-like profile. The usage of these functions is particularly critical if the fit range is enlarged below 0.150 GeV/c^2, where the ΔM distribution quickly drops due to phase-space constraints to the decay kinematics. The template fit approach provides better performance, as shown in the bottom row, where the residuals look flat at zero in the sideband region. The description of the background through the template modulated with a polynomial of 2$^{\mathrm{nd}}$ order is preferred with respect to the other approach. The reason has to be ascribed to the non-trivial normalization of the combinatorial template before subtracting it from the reconstructed

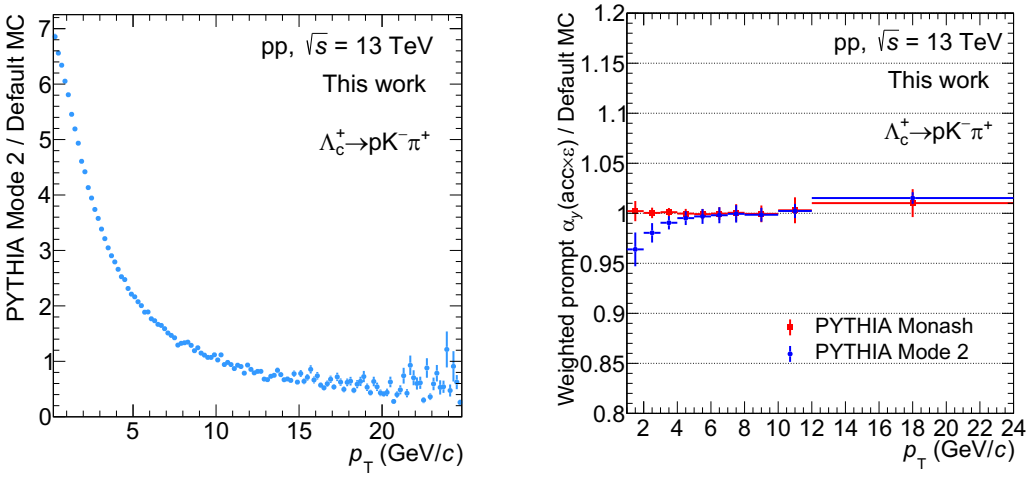

FIGURE 5.19: Left: ratio between generated p_T distribution of Λ_c^+ baryons in dedicated PYTHIA simulations with Mode 2 tune and the same quantity taken from the MC simulations used for the efficiency times acceptance correction. Right: ratios of prompt efficiency times acceptance after re-weighting the generated p_T distribution of Λ_c^+ baryons with respect to the same quantity obtained with no re-weighting.

ΔM distribution. Commonly, the normalization is determined from the sideband region integral, however this approach may be dangerous in case of significant signal tails around the expected peak. The ΔM fits are repeated with the mentioned background functions and in the ranges specified in the second part of Tab. 5.12. Only the cases showing a flat residual shape in the sidebands and making a normalised χ^2 not higher than 1.3 are considered to estimate the final value of the systematic uncertainty of the $\Lambda_c^+ (\leftarrow \Sigma_c^{0,++})$ and $\Sigma_c^{0,++}$ raw signal measurement. According to these studies, this consists in the main source of systematic uncertainty, decreasing from 25% and 30% for $\Lambda_c^+ (\leftarrow \Sigma_c^{0,++})$ and $\Sigma_c^{0,++}$ respectively in the $2 < p_T < 4$ GeV/c interval to 10% in the last p_T interval. The description of the background distribution is observed to provide the dominant contribution for this source of uncertainty.

5.4.4 Generated baryon p_T distribution

The $\alpha_y(\text{acc} \times \varepsilon)$ term depends significantly on p_T, because of the evolution of the decay kinematics and the impact parameter resolution (see Fig. 3.17(B)). Given the finite width of the p_T intervals considered in the analysis, the efficiency times acceptance term changes within. For this reason, the p_T distribution of generated baryons influences the efficiency times acceptance calculation. A systematic uncertainty related to the p_T shape is estimated by changing this distribution according to what predicted by different models. In particular, the generated p_T distribution obtained from the MC simulations used for the $\alpha_y(\text{acc} \times \varepsilon)$ correction (called "default" from now on) is re-weighted in order to reproduce the shape given by PYTHIA Monash and Mode 2 tunes. In the left panel of Fig. 5.19 the ratio between the PYTHIA Mode 2 p_T distribution of prompt Λ_c^+ and the same quantity taken from the default MC simulations is shown. This ratio is used to re-weight the default p_T shape in p_T intervals that are $\Delta p_T = 200$ MeV/c wide, which are much narrower than the ones used to perform the measurement. A similar procedure is performed also with the

usage of PYTHIA Monash tune. The variations of the $\alpha_y(\text{acc} \times \varepsilon)$ correction factor of prompt Λ_c^+ baryons with respect to that obtained from the default p_T distribution are shown in the right panel of Fig. 5.19. When the PYTHIA Monash shape is adopted, no significant changes are observed on the efficiency times acceptance correction term, as expected, considering that this tune is one of the default ingredients used in PYTHIA 8, which is the generator chosen for the MC simulations. Using the PYTHIA Mode 2 p_T shape, a maximum variation of 4% is observed in the $1 < p_T < 2$ GeV/c interval, then the difference quickly decreases with increasing p_T, given that the p_T shapes considered in the two cases show a steeper difference at low transverse momenta. The final systematic uncertainty is estimated as the maximum variation observed in the $\alpha_y(\text{acc} \times \varepsilon)$ correction term. The values are reported in Tabs. 5.13, 5.14 and 5.15 for Λ_c^+ baryons, as well as for $\Lambda_c^+ (\leftarrow \Sigma_c^{0,++})$ and $\Sigma_c^{0,++}$. In the two latter cases, the variations show an analogous behaviour with respect to the one shown in the right panel of Fig. 5.19. In these cases, a maximum variation of 10% is observed in the $2 < p_T < 4$ GeV/c interval, then it quickly decreases with increasing p_T.

5.4.5 Bayes PID criterion

As discussed in Sec. 5.2.3, the $\Lambda_c^+ \rightarrow pK^-\pi^+$ candidate reconstruction exploits the excellent PID capabilities of the TPC and TOF detectors, which responses are mixed with a Bayesian approach. The systematic uncertainty related to the Λ_c^+ daughter track identification is estimated by repeating the measurement using the Bayesian approach based on the threshold probability criterion and comparing the results with what obtained using the maximum probability one. The ratios with respect to the results obtained with the latter strategy, which is chosen as default in the analysis, are shown in Fig. 5.20 for prompt Λ_c^+, where the variations of prompt efficiency times acceptance correction factor (top left), raw signal (top right) and final cross section (bottom left) are shown. The results obtained with the maximum probability criterion are compared with the outcome from the usage of the threshold probability method, where the values 30%, 40%, 50% and 60% for the threshold itself are tested. As expected, the reconstruction efficiency is higher in case of lower threshold and this is accompanied by a higher reconstructed yield. Looking at the variations at the cross section level, a 5% uncertainty is estimated in all the p_T intervals. This study has been repeated also in larger p_T intervals, as done for the estimation of the efficiency times acceptance correction systematic uncertainty (see Sec. 5.4.2), to make sure that the final uncertainty estimate is not influenced by the statistical fluctuations affecting the raw signal measurement. By repeating this study in coarser p_T intervals an overall 5% variation is observed at the level of the final cross section. For this reason, a 5% systematic uncertainty is assigned to the measurement in all the p_T intervals for Λ_c^+, $\Lambda_c^+ (\leftarrow \Sigma_c^{0,++})$ and $\Sigma_c^{0,++}$.

5.4.6 Feed-down subtraction

The systematic uncertainty on the Λ_c^+ prompt fraction derives from the beauty production cross-section uncertainty coming from FONLL calculations, as well as the uncertainty band related to the Λ_b^0 fragmentation function. For the latter ingredient, the fit parameters of the fragmentation fraction ratios reported in [310] and mentioned in Sec. 5.3.1 are varied within their uncertainties. For $p_T(\Lambda_b^0) < 5$ GeV/c the lower uncertainty bound of $f_{\Lambda_b^0}$ was fixed to the value obtained at $p_T(\Lambda_b^0) = 5$ GeV/c, while the upper edge description is parametrised with the p_T dependent

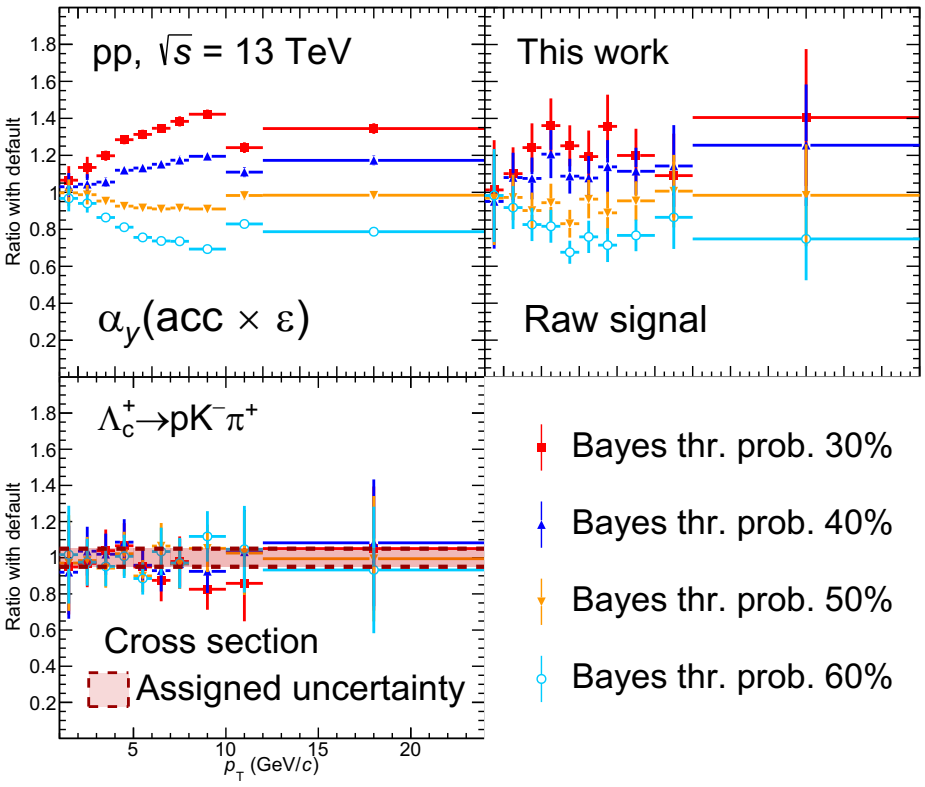

FIGURE 5.20: Efficiency times acceptance correction term (top left), raw signal (top right) and corrected cross section (bottom left) ratios of prompt $\Lambda_c^+ \rightarrow pK^-\pi^+$ baryon measurement in pp collisions at $\sqrt{s} = 13$ TeV measured with different threshold values of Bayes PID compared with what obtained with the maximum probability criterion.

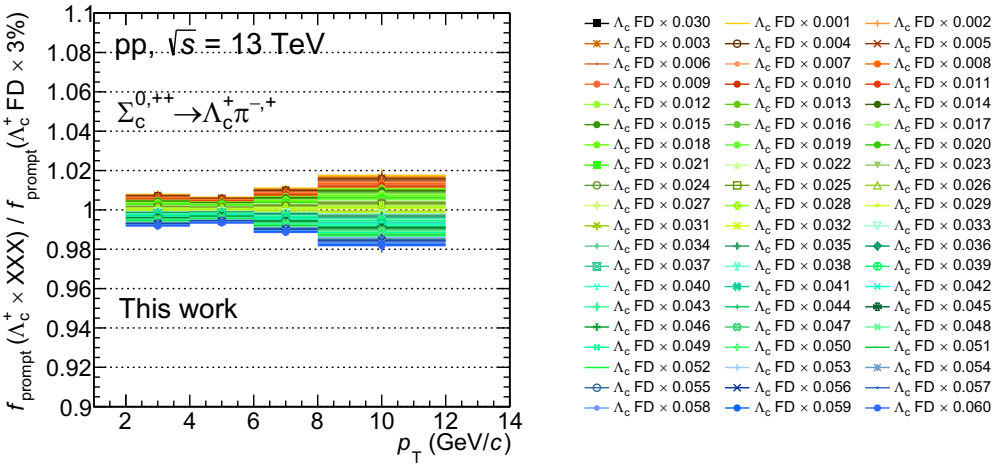

FIGURE 5.21: Variation of the $\Sigma_c^{0,++}$ prompt fraction f_{prompt} obtained changing the fraction of Λ_c^+ feed-down contributing to $\Sigma_c^{0,++}$ one.

p_T (GeV/c)	Raw signal	α_y(acc $\times$ ε)	PID	Track-ing	MC p_T-shape	α_y(acc $\times$ ε) unc.	Feed-down
[1,2)	11%	10%	5%	5%	4%	2%	$^{+2\%}_{-3\%}$
[2,3)	4%	10%	5%	6%	2%	2%	$^{+2\%}_{-3\%}$
[3,4)	4%	10%	5%	6%	1%	1%	$^{+3\%}_{-4\%}$
[4,5)	4%	5%	5%	6%	-	1%	$^{+4\%}_{-5\%}$
[5,6)	4%	5%	5%	6%	-	1%	$^{+3\%}_{-4\%}$
[6,7)	4%	5%	5%	7%	-	1%	$^{+4\%}_{-6\%}$
[7,8)	8%	5%	5%	7%	-	1%	$^{+4\%}_{-7\%}$
[8,10)	8%	5%	5%	7%	-	1%	$^{+4\%}_{-6\%}$
[10,12)	8%	5%	5%	7%	-	2%	$^{+5\%}_{-7\%}$
[12,24)	9%	5%	5%	7%	-	2%	$^{+7\%}_{-9\%}$
BR				5.1%			
$\mathcal{L}$				1.6%			

TABLE 5.13: Systematic uncertainties assigned to the prompt Λ_c^+ cross section measured in pp collisions at $\sqrt{s} = 13$ TeV.

trend given by the fit. The spread of all these variations determines the uncertainties in the different p_T intervals shown in Fig. 5.13 for the Λ_c^+ prompt fraction, that increase from about 2-3% at low p_T to about 8-9% in the $12 < p_T < 24$ GeV/c interval, where the prompt fraction is lower. The same source of uncertainty affects the $\Lambda_c^+ (\leftarrow \Sigma_c^{0,++})$ and $\Sigma_c^{0,++}$ measurements, but given the high prompt fraction the uncertainty is observed to be negligible. In these cases, a further source of systematic uncertainty is studied, namely the hypothesis that the $\Sigma_c^{0,++}$ baryon feed-down from beauty hadrons corresponds to 3% of Λ_c^+ feed-down. As discussed in Sec. 5.3.1, this percentage was obtained with dedicated PYTHIA 8 simulations and the hypothesis assumed to compute the uncertainty is that the simulation may fail by a factor ≤ 2 in determining the correct feed-down fraction. For this reason, the f_{prompt} quantity for $\Lambda_c^+ (\leftarrow \Sigma_c^{0,++})$ and $\Sigma_c^{0,++}$ is recomputed assuming different percentages from 0% up to 6%. The ratios of $\Sigma_c^{0,++}$ prompt fractions under different hypothesis with respect to the f_{prompt} obtained considering 3% of the Λ_c^+ feed-down are shown in Fig. 5.21. As expected, the prompt fraction increases for lower values of percentage and it gradually decreases with increasing Λ_c^+ feed-down considered. The systematic uncertainty assigned to the final measurement is estimated as the maximum observed variation and it is assigned asymmetrically, assuming an underestimation from the PYTHIA simulations. The maximum observed effect amounts to 2%, as reported in Tabs. 5.14 and 5.15.

5.4.7 Summary of systematic uncertainties

The systematic uncertainties assigned to the Λ_c^+, $\Lambda_c^+ (\leftarrow \Sigma_c^{0,++})$ and $\Sigma_c^{0,++}$ cross sections measured in pp collisions at $\sqrt{s} = 13$ TeV are listed in Tabs. 5.13, 5.14 and

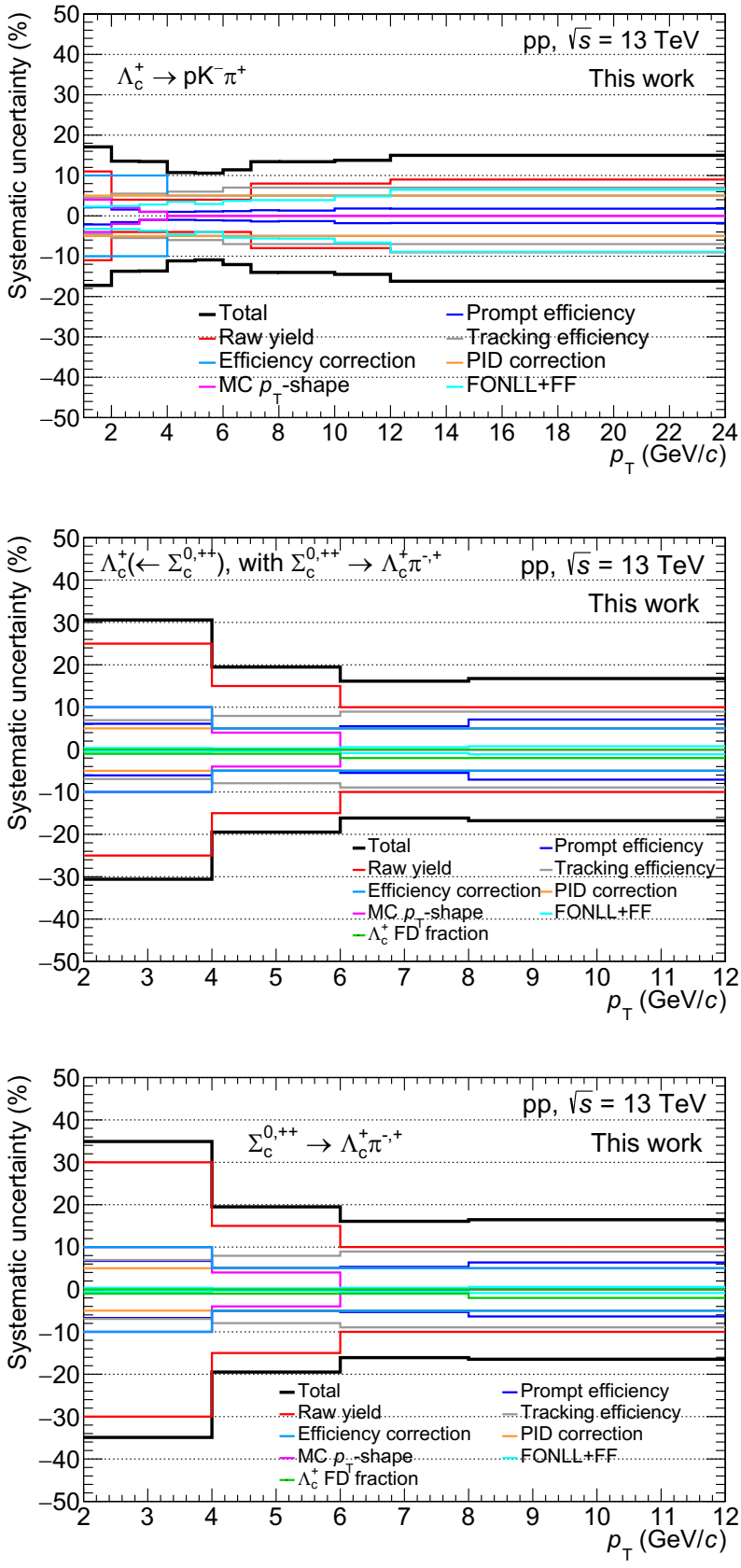

FIGURE 5.22: Systematic uncertainties assigned to the prompt Λ_c^+, $\Lambda_c^+(\leftarrow \Sigma_c^{0,++})$ and $\Sigma_c^{0,++}$ cross sections measured in pp collisions at $\sqrt{s} = 13$ TeV.

p_T (GeV/c)	Raw signal	α_y(acc $\times$ ε)	PID	Track-ing	MC p_T-shape	α_y(acc $\times$ ε) unc.	Feed-down
[2, 4)	25%	10%	5%	7%	10%	6%	$^{+0\%}_{-1\%}$
[4, 6)	15%	5%	5%	8%	4%	5%	$^{+0\%}_{-1\%}$
[6, 8)	10%	5%	5%	9%	-	6%	$^{+0\%}_{-2\%}$
[8, 12)	10%	5%	5%	9%	-	7%	$^{+0\%}_{-2\%}$
BR				5.1%			
$\mathcal{L}$				1.6%			

TABLE 5.14: Systematic uncertainties assigned to the prompt $\Lambda_c^+(\leftarrow \Sigma_c^{0,++})$ cross section measured in pp collisions at $\sqrt{s} = 13$ TeV.

p_T (GeV/c)	Raw signal	α_y(acc $\times$ ε)	PID	Track-ing	MC p_T-shape	α_y(acc $\times$ ε) unc.	Feed-down
[2, 4)	30%	10%	5%	7%	10%	7%	$^{+0\%}_{-1\%}$
[4, 6)	15%	5%	5%	8%	4%	5%	$^{+0\%}_{-1\%}$
[6, 8)	10%	5%	5%	9%	-	5%	$^{+0\%}_{-1\%}$
[8, 12)	10%	5%	5%	9%	-	6%	$^{+0\%}_{-2\%}$
BR				5.1%			
$\mathcal{L}$				1.6%			

TABLE 5.15: Systematic uncertainties assigned to the prompt $\Sigma_c^{0,++}$ cross section measured in pp collisions at $\sqrt{s} = 13$ TeV.

5.15 and they are also shown graphically in Fig. 5.22. The total uncertainty on the prompt Λ_c^+ cross section is dominated by the raw signal extraction and efficiency times acceptance correction at low p_T, then at higher transverse momenta the tracking uncertainty becomes one of the dominant sources. Similar arguments are valid for the $\Lambda_c^+(\leftarrow \Sigma_c^{0,++})$ and $\Sigma_c^{0,++}$ cases, where the relative contribution of the raw signal measurement source is much more relevant, as discussed in Sec. 5.4.3. In addition to the sources described in detail in the previous Sections, another source of systematic uncertainty assigned to the final measurement is the statistical uncertainty on the prompt efficiency times acceptance ("α_y(acc $\times$ ε) unc." in Tabs. 5.13, 5.14 and 5.15), which is strictly related to the statistics used in the MC simulations. This uncertainty stays within 2% in the case of prompt Λ_c^+ and runs between 5% and 7% for $\Lambda_c^+(\leftarrow \Sigma_c^{0,++})$ and $\Sigma_c^{0,++}$ baryons, depending on the p_T interval. Moreover, uncertainties related to the BR($\Lambda_c^+ \rightarrow pK^-\pi^+$) and the luminosity $\mathcal{L}$ are assigned in all the p_T intervals and they amount to 5.1% and 1.6% respectively. The total systematic uncertainty assigned to the measured cross sections corresponds to the quadrature sum of the values related to the different sources, which are considered as non-correlated.

5.5 Cross section of prompt baryons in pp collisions at $\sqrt{s} = 13$ TeV

The $p_{\rm T}$-differential production cross sections of prompt $\Lambda_{\rm c}^{+}$, $\Lambda_{\rm c}^{+}(\leftarrow \Sigma_{\rm c}^{0,++})$ and $\Sigma_{\rm c}^{0,++}$ are measured with the procedure indicated in Eq. 5.16. The production cross sections measured in this analysis (blue) are shown in panel (A), (B) and (C) of Fig. 5.23, respectively, and they are compared to the results obtained from the analysis of the $\rm pK_S^0$ decay channel (light blue). The vertical lines correspond to the statistical uncertainty, while the empty boxes quantify the total systematic uncertainties. The production cross sections measured in the two $\Lambda_{\rm c}^{+}$ decay channels are compatible within the statistical and systematic uncertainties (see smaller bottom panels in Fig. 5.23 (A), (B) and (C)) and they both contribute to the results published in [313]. The cross sections of $\Lambda_{\rm c}^{+}(\leftarrow \Sigma_{\rm c}^{0,++})$ and $\Sigma_{\rm c}^{0,++}$ are multiplied by 3/2 to quantify the production of $\Lambda_{\rm c}^{+}(\leftarrow \Sigma_{\rm c}^{0,+,++})$ and $\Sigma_{\rm c}^{0,+,++}$, assuming an isospin symmetry among the three charge states of $\Sigma_{\rm c}$. To obtain a more precise result, the cross sections measured in the two $\Lambda_{\rm c}^{+}$ decay channels are averaged following the procedure already adopted for previous measurements [108, 178]. This method makes use of the uncorrelated uncertainties between the two results to define the weights to average them. The sources of uncertainty considered as uncorrelated between the two $\Lambda_{\rm c}^{+}$ channels are the statistical and all those related to the raw signal measurement, the selection efficiency correction, the PID efficiency correction and the uncertainties on the efficiency times acceptance term. The uncertainties related to the branching ratios of $\Lambda_{\rm c}^{+}$ channels are considered as partially correlated, given a linear correlation between the $\Lambda_{\rm c}^{+} \rightarrow \rm pK^{-}\pi^{+}$ and the $\Lambda_{\rm c}^{+} \rightarrow \rm pK_S^0$ channels of 54% [3]. The weights associated to each of the two measurements are quantified considering the relative uncertainty of all the sources assumed as uncorrelated. The choice of using the relative values instead of the absolute ones has to be ascribed to the fact that the values of the systematic uncertainty of each single source are assigned as relative. Nevertheless, similar results are obtained by computing the average with weights defined by the absolute uncertainties. The average cross section of the baryon H is calculated as

$$\langle \sigma_{\rm H}(p_{\rm T}) \rangle = \sum_i w_i(p_{\rm T}) \sigma_{{\rm H},i}(p_{\rm T}) \,, \tag{5.22}$$

where the index i indicates the result obtained employing either the $\Lambda_{\rm c}^{+} \rightarrow \rm pK^{-}\pi^{+}$ or the $\Lambda_{\rm c}^{+} \rightarrow \rm pK_S^0$ decay channel. The term w_i indicates the weight associated to the i-th cross section, which is computed as:

$$w_i(p_{\rm T}) = \frac{\sum_k \left(V_x^{-1}\right)_{ik}}{\sum_{jk} \left(V_x^{-1}\right)_{jk}} \,. \tag{5.23}$$

The term V_x indicates the covariance matrix between the two measurements, which corresponds to the 2×2 symmetric matrix defined by:

$$V_x(p_{\rm T}) = \begin{pmatrix} \mathrm{syst}^2_{\rm pK^-\pi^+}(p_{\rm T}) + \mathrm{stat}^2_{\rm pK^-\pi^+}(p_{\rm T}) & r \cdot \sigma_{\rm pK^-\pi^+}(p_{\rm T}) \sigma_{\rm pK_S^0}(p_{\rm T}) \\ r \cdot \sigma_{\rm pK^-\pi^+}(p_{\rm T}) \sigma_{\rm pK_S^0}(p_{\rm T}) & \mathrm{syst}^2_{\rm pK_S^0}(p_{\rm T}) + \mathrm{stat}^2_{\rm pK_S^0}(p_{\rm T}) \end{pmatrix} \,, \tag{5.24}$$

where "stat" indicates the statistical uncertainty, "syst" the uncorrelated systematic uncertainties, $\sigma_{\rm pK^-\pi^+,pK_S^0}$ the uncertainty related to the BR($\rm pK^-\pi^+$) and BR($\rm pK_S^0$) respectively and r is the linear correlation between them. The out-of-diagonal terms

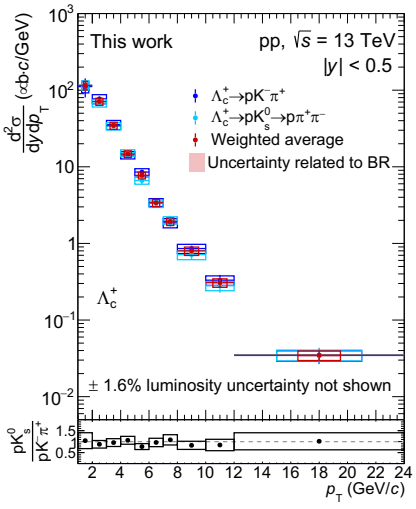

(A) Production cross section of prompt Λ_c^+.

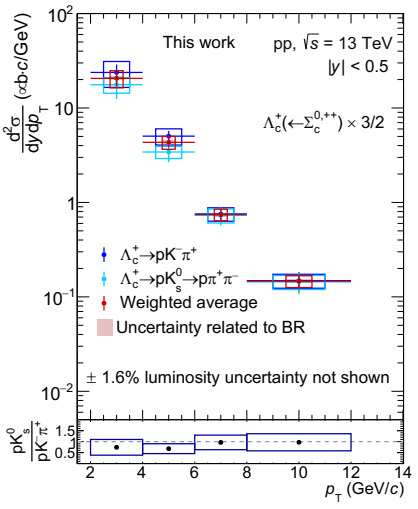

(B) Production cross section of prompt $\Lambda_c^+(\leftarrow\Sigma_c^{0,++}) \times 3/2$.

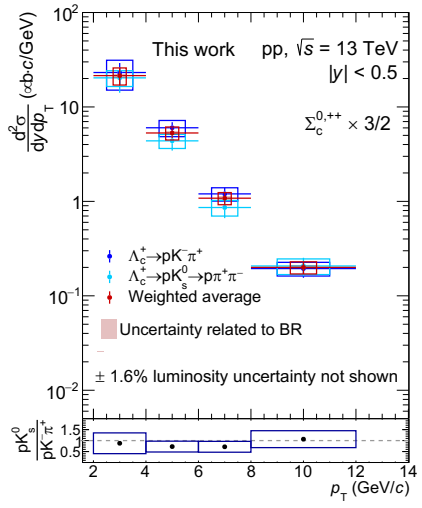

(C) Production cross section of prompt $\Sigma_c^{0,++} \times 3/2$.

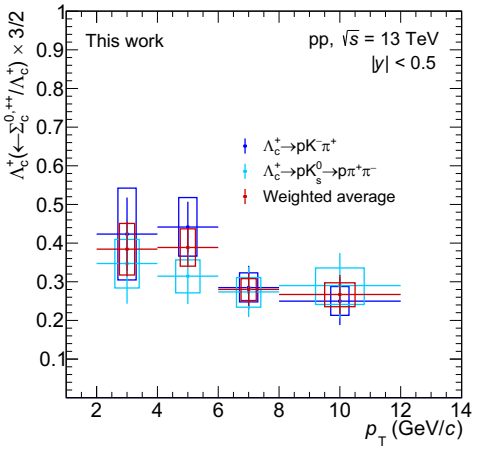

(D) Cross section of prompt $\Lambda_c^+(\leftarrow\Sigma_c^{0,++})$ divided by the one of prompt Λ_c^+ ratio scaled by 3/2.

FIGURE 5.23: Production cross section of (A) prompt Λ_c^+, (B) prompt $\Lambda_c^+(\leftarrow \Sigma_c^{0,+,++})$ and (C) prompt $\Sigma_c^{0,+,++}$ in pp collisions at $\sqrt{s} = 13$ TeV. The latter two results are obtained scaling by a factor 3/2 the $\Lambda_c^+(\leftarrow \Sigma_c^{0,++})$ and $\Sigma_c^{0,++}$ production cross sections measured in this work. The ratio between the prompt $\Lambda_c^+(\leftarrow \Sigma_c^{0,+,++})$ and prompt Λ_c^+ is shown in panel (D). The work described in this thesis produced the results in the $\Lambda_c^+ \to pK^-\pi^+$ channel, which are published with the ones obtained in the $\Lambda_c^+ \to pK_S^0$ channel in [313]. In panels (A), (B) and (C) the ratio between the results obtained in the two Λ_c^+ decay channels is shown. Only the uncertainties related to the sources assumed as uncorrelated between the two Λ_c^+ decay channels (see text) are considered in the ratio.

quantify the covariance between the two cross sections, which is given by the linear correlation between the branching ratios of the two Λ_c^+ decay channels. The same procedure is used to measure the weighted average of the $\Lambda_c^+(\leftarrow \Sigma_c^{0,++})/\Lambda_c^+$ ratio, which is shown in the panel (D) of Fig. 5.23. In this case, in order to better exploit the cancellations of the uncertainties related to the sources assumed as correlated between numerator and denominator, this ratio is computed separately in the $\Lambda_c^+ \to pK^-\pi^+$ and $\Lambda_c^+ \to pK_S^0$ decay channels before computing the average. In this way, the systematic uncertainties related to the topological variables and PID selection efficiency corrections can be partially cancelled between numerator and denominator, given the strict correlation among the selections used to reconstruct the baryons within the same Λ_c^+ decay channel. Also the tracking systematic uncertainties and those related to the prompt fraction are assumed to be fully correlated. In this case, the out-of-diagonal term of the covariance matrix V_x is null, since the branching ratio cancels out in the ratio between $\Lambda_c^+(\leftarrow \Sigma_c^{0,++})$ and Λ_c^+ performed in the same decay channel. Therefore the weight w_i corresponds to the inverse of the quadrature sum of relative values of statistical and uncorrelated systematic uncertainties. The weighted averaged of the production cross section of prompt Λ_c^+, $\Lambda_c^+(\leftarrow \Sigma_c^{0,+,++})$ and $\Sigma_c^{0,+,++}$ as well as the weighted average of the $\Lambda_c^+(\leftarrow \Sigma_c^{0,+,++})/\Lambda_c^+$ ratio are shown with the red colour in Fig. 5.23. The systematic uncertainty related to each source is calculated according to the correlation of the given source between the two decay channels. In particular:

- the statistical uncertainty and the systematic uncertainties associated to sources assumed as uncorrelated between the $\Lambda_c^+ \to pK^-\pi^+$ and the $\Lambda_c^+ \to pK_S^0$ decay channels are propagated with the following formula:

$$\text{err.}^{\text{uncorr.}}_{\langle\sigma_H\rangle}(p_T) = \frac{\sqrt{\left(w_{pK^-\pi^+} \cdot \text{err.}^{\text{uncorr.}}_{pK^-\pi^+}\right)^2(p_T) + \left(w_{pK_S^0} \cdot \text{err.}^{\text{uncorr.}}_{pK_S^0}\right)^2(p_T)}}{w_{pK^-\pi^+}(p_T) + w_{pK_S^0}(p_T)}\,; \tag{5.25}$$

- the systematic uncertainties associated to sources assumed as fully correlated between the $\Lambda_c^+ \to pK^-\pi^+$ and the $\Lambda_c^+ \to pK_S^0$ decay channels are propagated with the following formula:

$$\text{err.}^{\text{corr.}}_{\langle\sigma_H\rangle}(p_T) = \frac{\left(w_{pK^-\pi^+} \cdot \text{err.}^{\text{corr.}}_{pK^-\pi^+}\right)(p_T) + \left(w_{pK_S^0} \cdot \text{err.}^{\text{corr.}}_{pK_S^0}\right)(p_T)}{w_{pK^-\pi^+}(p_T) + w_{pK_S^0}(p_T)}\,; \tag{5.26}$$

- the uncertainty of the branching ratios related to the $\Lambda_c^+ \to pK^-\pi^+$ and $\Lambda_c^+ \to pK_S^0$ channels are considered as partially correlated and are propagated with the following formula:

$$\begin{aligned}\text{err.}^{\text{uncorr.}}_{\langle\sigma_H\rangle}(p_T) = \Bigg[&\left(\frac{w_{pK^-\pi^+} \cdot \text{err.}^{\text{uncorr.}}_{BR(pK^-\pi^+)}}{w_{pK^-\pi^+} + w_{pK_S^0}}\right)^2(p_T) \\ &+ \left(\frac{w_{pK_S^0} \cdot \text{err.}^{\text{uncorr.}}_{BR(pK_S^0)}}{w_{pK^-\pi^+} + w_{pK_S^0}}\right)^2(p_T) \\ &+ \frac{2r \cdot w_{pK^-\pi^+} w_{pK_S^0} \text{err.}_{BR(pK^-\pi^+)} \text{err.}_{BR(pK_S^0)}}{\left(w_{pK^-\pi^+} + w_{pK_S^0}\right)^2}(p_T)\Bigg]^{1/2}\end{aligned}\,. \tag{5.27}$$

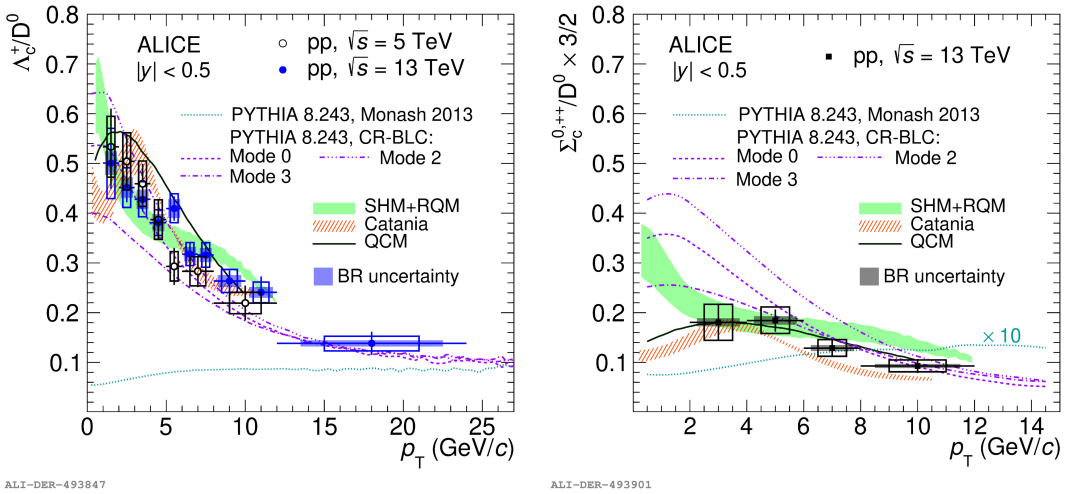

FIGURE 5.24: Left: Λ_c^+/D^0 cross section ratio measured in pp collisions at $\sqrt{s} = 13$ TeV compared to model predictions [179, 187, 190, 200] and to the results measured in pp collisions at $\sqrt{s} = 5$ TeV [108, 109]. Right: $\Sigma_c^{0,+,++}/D^0$ cross section ratio measured in pp collisions at $\sqrt{s} = 13$ TeV compared with model predictions [179, 187, 190, 200]. Figures from [313].

The total systematic uncertainty on the average result corresponds to the quadrature sum of the values related to the different sources, which are considered uncorrelated by definition. The systematic uncertainty related to the BR are represented separately with a shaded-filled box for each p_T interval.

5.5.1 Charm hadron cross section ratios

The prompt Λ_c^+ and $\Sigma_c^{0,+,++}$ cross sections deriving from the average procedure described in the previous Section are divided by the production cross section of prompt D^0 meson in pp collisions at $\sqrt{s} = 13$ TeV [313]. In the ratios, shown in Fig. 5.24, the systematic uncertainties of the tracking and luminosity are considered as correlated and they cancel partly and completely, respectively. The feed-down uncertainty is propagated as partially correlated, depending on each source contributing to it. The FONLL-related uncertainty is correlated among charm hadrons and it is partly cancelled out in the ratio, while the contribution deriving from the assumption on the Λ_c^+ feed-down fraction for the calculation of f_{prompt} of $\Sigma_c^{0,+,++}$ is propagated as uncorrelated in the ratio. The values from all the other sources of uncertainty are propagated as fully uncorrelated between numerator and denominator. The Λ_c^+/D^0 ratio decreases with increasing p_T and it is significantly larger than the results in e^+e^- and e^-p collisions at different collision energies [322–328], where the ratio is about 0.12. A similar trend is observed for the results in pp collisions at the two energies, which are compatible within uncertainties. A similar ordering among collision systems is observed also looking at the $\Sigma_c^{0,+,++}/D^0$ ratio. In pp collisions, it is close to about 0.2 for $2 < p_T < 6$ GeV/c, then it decreases at about 0.1 at higher transverse momenta, but with the current uncertainties no definitive conclusions can be driven about the p_T dependence. However, an enhancement of a factor of about $\times 10$ is observed with respect to e^+e^- collisions at $\sqrt{s} = 10.52$ GeV: from Table IV in Ref. [114] a value of about 0.17 can be evaluated for the $\Sigma_c^{0,+,++}/\Lambda_c^+$ and, consequently, the $\Sigma_c^{0,+,++}/D^0$ ratio amounts to about 0.02. These values show a remarkable difference

between e^+e^- collisions and pp events at the LHC. This is corroborated by the comparison of the experimental results to the PYTHIA 6 and PYTHIA 8 predictions. The e^+e^- results [114] are reasonably described by the default tune, while the Monash tune is not able to describe the measurements in pp collisions. For both Λ_c^+/D^0 and $\Sigma_c^{0,+,++}/D^0$ ratios in pp collisions the PYTHIA 8 Monash tune significantly underestimates the experimental results, furthermore the predictions do not describe the p_T dependence of the measurements. Moreover, a larger discrepancy between Monash and data is observed for the $\Sigma_c^{0,+,++}/D^0$ ratio, note the factor $\times 10$ applied on the model prediction to make it more visible in Fig. 5.24. In the left panel of Fig. 5.25 the $\Lambda_c^+(\leftarrow \Sigma_c^{0,+,++})/\Lambda_c^+$ cross section ratio measured in pp collisions at $\sqrt{s} = 13$ TeV is shown, compared to the predictions from several model calculations. This ratio quantifies the fraction of Λ_c^+ baryons deriving from $\Sigma_c^{0,+,++}$, measured for the first time ever in hadronic collisions. Similarly to what already observed for the $\Sigma_c^{0,+,++}/D^0$ ratio, the experimental result decreases from about 0.4 for $2 < p_T < 6$ GeV/c to about 0.3 at higher transverse momenta. An integrated value for this ratio is calculated in the transverse momentum range considered for the measurement of $\Lambda_c^+(\leftarrow \Sigma_c^{0,+,++})$ as:

$$\left.\frac{\Lambda_c^+(\leftarrow \Sigma_c^{0,+,++})}{\Lambda_c^+}\right|_{2<p_T<12\,\mathrm{GeV}/c} = \frac{\sum_i \Delta p_T^i \cdot \Lambda_c^+(\leftarrow \Sigma_c^{0,+,++})(p_T^i)}{\sum_i \Delta p_T^i \cdot \Lambda_c^+(p_T^i)}\,, \tag{5.28}$$

where the index i refers to the i-th transverse momentum interval. For the measurement of the integrated cross section, the statistical uncertainty as well as the systematic uncertainty related to the raw signal measurement are assumed as fully uncorrelated among the p_T intervals, while the other sources are treated as fully correlated. From this calculation, the integrated $\Lambda_c^+(\leftarrow \Sigma_c^{0,+,++})/\Lambda_c^+$ ratio in the $2 < p_T < 12$ GeV/c range corresponds to $0.38 \pm 0.06(\mathrm{stat.}) \pm 0.06(\mathrm{syst.})$, which is significantly higher than the $\Sigma_c^{0,+,++}/\Lambda_c^+$ ratio from Belle that amounts to 0.17. The experimental result is also significantly larger than the PYTHIA 8 Monash curve, which predicts a value of about 0.13 independently of the baryon p_T. These comparisons are in line with the enhancement observed for the $\Sigma_c^{0,+,++}/D^0$ ratio, showing a larger relative difference among collision systems with respect to the Λ_c^+/D^0 ratio. The larger Λ_c^+ prompt feed-down from $\Sigma_c^{0,+,++}$ decays observed in pp collisions at the LHC partially explains the Λ_c^+/D^0 difference with e^+e^- and e^-p results.

The charm hadron cross section ratios are compared to the predictions from the model calculations [179,187,190,200] described in Sec. 2.3.2. Given the uncertainties assigned to the measured ratios, the predictions from PYTHIA 8 modes implementing the colour reconnection beyond leading colour approximation, from the Catania model and the SHM+RQM describe the measured Λ_c^+/D^0 and $\Sigma_c^{0,+,++}/D^0$ ratios. The data are also compared to the Quark Coalescence Model (QCM [200]), according to which the charm quarks produced in the hard scattering can coalesce with light quarks at equal velocity. This model uses the Λ_c^+/D^0 ratio measured in pp collisions at $\sqrt{s} = 7$ TeV to set the total charm baryon-to-meson ratio. The prediction well describes the p_T trend and the magnitude of Λ_c^+/D^0, $\Sigma_c^{0,+,++}/D^0$ and $\Lambda_c^+(\leftarrow \Sigma_c^{0,+,++})/\Lambda_c^+$ ratios within the uncertainties. The latter result is significantly overestimated by the PYTHIA 8 modes, which in addition foresees a p_T dependence that is significantly steeper with respect to the measured one. This discrepancy between the model and the data suggests that the model still misses some ingredients in the full description of the Λ_c^+ baryon production and that a further tuning of the

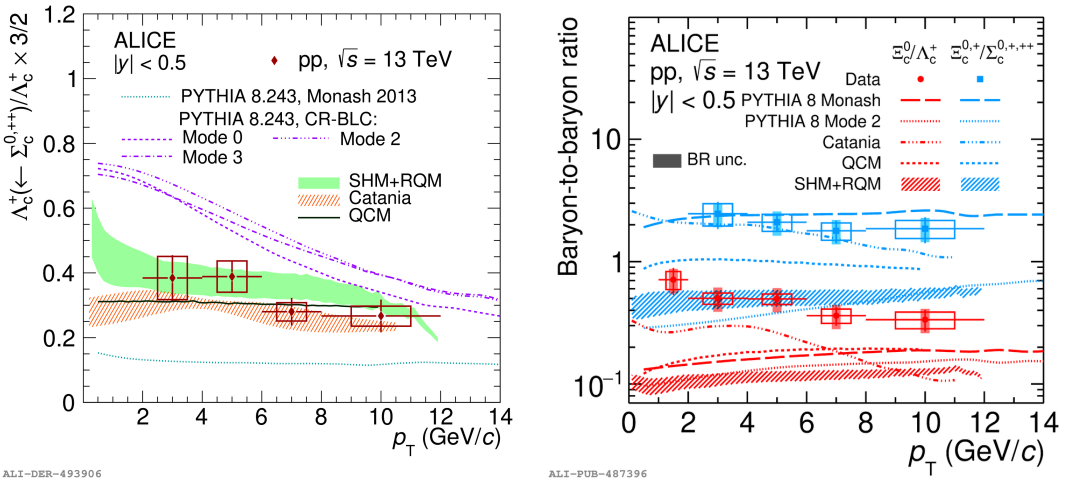

FIGURE 5.25: Left: $\Lambda_c^+(\leftarrow \Sigma_c^{0,+,++})/\Lambda_c^+$ cross section ratio measured in pp collisions at $\sqrt{s} = 13$ TeV compared to model predictions [179,187,190,200]. Figure from [313]. Right: Ξ_c^0/Λ_c^+ and $\Xi_c^{0,+}/\Sigma_c^{0,+,++}$ cross section ratio measured in pp collisions at $\sqrt{s} = 13$ TeV compared to model predictions [179,187,190]. Figure from [312].

PYTHIA parameters involving the charm quark reconnection via junction topologies, as discussed in Sec. 2.3.2, is necessary to possibly validate this as the core process that removes the assumed suppression in the $\Sigma_c^{0,+,++}$ baryon formation in e^+e^- and e^-p collisions [114, 179]. The production of $\Sigma_c^{0,+,++}$ states is not penalised by any process in the calculations of QCM, Catania and SHM+RQM. In particular, the fact that the three measured ratios well agree with the predictions of the SHM+RQM model may suggest that higher-mass excited state charm baryons not yet observed exist and are produced more abundantly in pp collisions at the LHC energies than in e^+e^- and e^-p collisions.

The production of Λ_c^+ and $\Sigma_c^{0,+,++}$ baryons in hadronic collisions at the LHC is compared with that of $\Xi_c^{0,+}$ in the same collision system and energy. Differently from Λ_c^+ and $\Sigma_c^{0,+,++}$, the $\Xi_c^{0,+}$ baryons include a strange quark, whose presence may influence the charm baryon production. In the right panel of Fig. 5.25 the Ξ_c^+/Λ_c^+ and $\Xi_c^{0,+}/\Sigma_c^{0,+,++}$ baryon ratios measured in pp collisions at $\sqrt{s} = 13$ TeV are shown, together with the predictions from the theory groups mentioned above [312]. The Ξ_c^+/Λ_c^+ ratio is approximately at 0.5 and it does not show a significant p_T dependence within the current uncertainties. Differently to what observed before, the Ξ_c^+/Λ_c^+ charm baryon ratio is significantly underestimated by most of the models. Only the Catania model, which assumes that the charm quark hadronizes via both fragmentation and coalescence with lighter quarks, gets closer to the measurement, even if it misses the data by about a factor 2. On the other hand, the Catania model describes the measured $\Xi_c^{0,+}/\Sigma_c^{0,+,++}$ ratio within uncertainties and the same holds for the PYTHIA 8 Monash tune. In the latter case, the agreement between the measured ratio and the model prediction is consistent with the fact that the Monash tune underestimates both the $\Xi_c^{0,+}/D^0$ and $\Sigma_c^{0,+,++}/D^0$ ratios by the same amount in all the p_T intervals [312]. For both ratios, the PYTHIA 8 modes implementing colour reconnection beyond leading colour approximation, the SHM+RQM model and the QCM model significantly underestimate the measured ratios, differently from what observed for the $\Lambda_c^+(\leftarrow \Sigma_c^{0,+,++})/\Lambda_c^+$ charm baryon ratio. Similarly, the $\Xi_c^{0,+}/D^0$ ratio in the same collision system and energy (not shown here) looks significantly larger to what predicted by model calculations. Also in this case, only the Catania

model is able to get closer to the data and to reproduce the measured p_{T} dependence of the $\Xi_{\mathrm{c}}^{0,+}/\mathrm{D}^0$ ratio within the uncertainties [312].

5.6 Conclusions and outlook

The production cross section of prompt Λ_{c}^+, $\Lambda_{\mathrm{c}}^+(\leftarrow \Sigma_{\mathrm{c}}^{0,+,++})$ and $\Sigma_{\mathrm{c}}^{0,+,++}$ charm baryons has been measured in pp collisions at $\sqrt{s} = 13$ TeV. In the work presented in this thesis, the charm baryon production is measured via the reconstruction of $\Lambda_{\mathrm{c}}^+ \rightarrow \mathrm{pK}^-\pi^+$ decays and it contributes to the final measurement, corresponding to the average performed with the results coming from the $\Lambda_{\mathrm{c}}^+ \rightarrow \mathrm{pK}_{\mathrm{S}}^0$ decay channel reconstruction [313]. The $\Lambda_{\mathrm{c}}^+/\mathrm{D}^0$, $\Sigma_{\mathrm{c}}^{0,+,++}/\mathrm{D}^0$ charm baryon-to-meson ratios and the Λ_{c}^+ feed-down from $\Sigma_{\mathrm{c}}^{0,+,++}$ are significantly larger than what observed in $\mathrm{e}^+\mathrm{e}^-$ and $\mathrm{e}^-\mathrm{p}$ collisions. These results are compared to several model predictions, assuming that the charm quark can hadronise via different mechanisms compared to the conventional string fragmentation in $\mathrm{e}^+\mathrm{e}^-$ collisions. Within the current uncertainties, several theoretical models describe the data and suggest that different scenarios for the charm quark hadronisation are possible. According to this comparison, the charm baryon production may take advantage from the introduction of junction topologies, which remove any penalty in the formation possibly arising from diquarks quantum numbers and symmetries, as implemented in PYTHIA 8 modes including colour reconnection beyond leading colour approximation. Furthermore, the agreement with Catania and QCM models supports the hypothesis that the charm quark can coalesce with lighter quarks produced in the collision, enhancing the charm baryon production expected in a scenario only with hadronisation via fragmentation. Finally, a possible enhancement of the charm baryon production may come from the decay of yet-unobserved excited charm baryon states, whose presence is foreseen by the RQM model and with relative abundances dictated by statistical weights.

Despite the insight provided by the results discussed in this thesis, further efforts from both the experimental and theoretical sides are mandatory to address the yet unresolved aspects. In particular, the comparison between data and models for the ratios of charm hadrons does not provide a clear picture, given the significant lack for models in describing the particle relative abundance of $\Xi_{\mathrm{c}}^{0,+}$ with respect to other charm hadrons. Moreover, differential measurements as a function of event multiplicity in pp collisions showed that for transverse momenta in the interval $2 < p_{\mathrm{T}} < 8$ GeV/c the prompt $\Lambda_{\mathrm{c}}^+/\mathrm{D}^0$ ratio measured in pp collisions smoothly increases to the values observed in p–Pb and Pb–Pb collisions [329]. In this context, pushing this kind of measurement down to low event multiplicities may help to further investigate the transition from $\mathrm{e}^+\mathrm{e}^-$ to pp collisions. The ALICE experiment upgrade will ensure better performances of the full apparatus, to be fully exploited during the next data-taking campaigns. Given the improved detector granularity and resolution, as well as the larger expected statistics, the Run 3 and Run 4 of LHC will be crucial to improve the precision of the charm hadron production measurements and will open new frontiers in the measurement of heavy hadrons. Precise measurements of Λ_{c}^+, $\Sigma_{\mathrm{c}}^{0,+,++}$ and $\Xi_{\mathrm{c}}^{0,+}$ charm baryon production will be granted by the larger statistics and the possibility to precisely measure the production of heavier (multi-)charm baryons as Ω_{c}^0, Ξ_{cc}^+, Ξ_{cc}^{++} and Ω_{cc}^0 may become accessible also thanks to future experiments, like ALICE 3 [330]. Recently, the LHCb and CMS experiments measured the production of Ξ_{cc}^{++} [331], $\mathrm{B}_{\mathrm{c}}^+$ and $\mathrm{B}_{\mathrm{c}}^{(*)}(2\mathrm{S})$ [332] hadrons in pp collisions at $\sqrt{s} = 13$ TeV, but more differential and precise measurements are required

to further understand the charm quark hadronisation in hadronic collisions at the LHC.

Chapter 6

Future prospects for charm baryon production measurements with the ALICE experiment

As discussed in the previous Chapter, a complete understanding of the charm quark hadronisation mechanisms in hadronic collisions at TeV scales requires an experimental effort aimed at measuring the production of several charm-baryon species in pp and Pb–Pb collisions. With the recorded statistics and the apparatus available so far, the Λ_c^+ production could be measured in transverse momentum intervals $\Delta p_T = 1$ GeV/c wide down to $p_T = 1$ GeV/c in pp collisions at $\sqrt{s} = 5.02, 13$ TeV and p–Pb collisions at $\sqrt{s_{NN}} = 5.02$ TeV [108, 109, 313]. Furthermore, the Ξ_c^0 baryon production has been recently measured in pp collisions at $\sqrt{s} = 5.02, 13$ TeV [311, 312] down to $p_T = 1$ GeV/c also thanks to the exploitation of Machine Learning techniques. On the other hand, the Ξ_c^+ baryon production in pp collisions at $\sqrt{s} = 13$ TeV was measured only above $p_T = 4$ GeV/c with a very limited statistical precision. Another possible Ξ_c^+ decay channel not yet explored with the ALICE detector is the $\Xi_c^+ \rightarrow pK^-\pi^+$ one, that corresponds to the same final state of the Λ_c^+ measurement in pp collisions at $\sqrt{s} = 13$ TeV described in the previous Chapter. The $\Xi_c^+ \rightarrow pK^-\pi^+$ is Cabibbo suppressed, but it has been already adopted by the LHCb experiment to measure the Ξ_c^+ [333]. In addition, the branching ratio of this decay channel is not well determined, as discussed later in this Chapter. The measurement of charm baryon production in hadronic collision would significantly benefit from the improvement of the spatial resolution of the apparatus and from a larger collected statistics during the Run 3 and 4 at the LHC.

The Chapter is organised as follows. In Section 6.1 a few pilot studies about the $\Xi_c^+ \rightarrow pK^-\pi^+$ decay channel reconstruction in the Run 2 pp collision sample at $\sqrt{s} = 13$ TeV collected in 2016, 2017 and 2018 based on the exploitation of machine learning techniques are described. In Section 6.3 more details about the ITS detector upgrade in Run 3 and Run 4 are delivered. Finally, the Chapter is concluded by Sections 6.5 and 6.6, where some performance studies about the expected significance for the $\Xi_c^+ \rightarrow pK^-\pi^+$ signal measurement in Pb–Pb collisions at $\sqrt{s_{NN}} = 5.5$ TeV with the upgraded ITS and the reconstruction of $\Omega_c^0 \rightarrow \Omega^-\pi^+$ decays in Run 4 respectively are presented.

6.1 Search for $\Xi_c^+ \rightarrow pK^-\pi^+$ signal in pp collisions at $\sqrt{s} = 13$ TeV with machine learning techniques

As also shown in Chapter 5 for the $\Lambda_c^+ \rightarrow pK^-\pi^+$ and $\Sigma_c^{0,++} \rightarrow \Lambda_c^+\pi^{-,+}$ cases, the reconstruction and isolation of rare signals is typically challenged by the presence

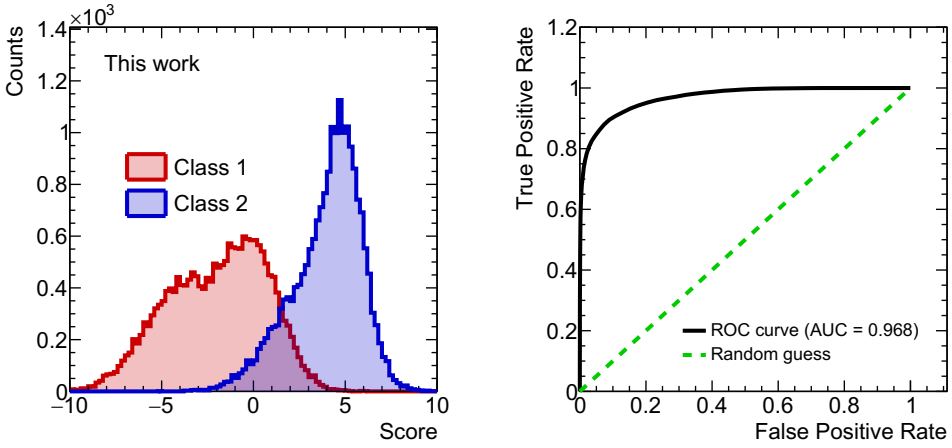

FIGURE 6.1: Example of training performances for a supervised learning algorithm. Left: output score discribution for two classes of events. Right: Receiver Operating Characteristics curve.

of a huge combinatorial background. The real decays are characterised by a specific event topology and selection criteria on the decay variables can be exploited to reject the background and increase the signal purity. The application of tight selections is often accompanied by a huge loss of signal, which may negatively counterbalance the gain from the background rejection and prevent the observation of a significant signal. Therefore, the optimisation of the selection criteria is a delicate task, which is usually treated with multivariate techniques in high-energy physics analyses.

In this thesis, a multivariate approach with the Toolkit for Multi-Variate Analysis (TMVA) [334] package in ROOT was employed as an attempt to isolate the $\Xi_c^+ \to pK^-\pi^+$ signal in the pp collision sample at $\sqrt{s} = 13$ TeV used in Chapter 5. Given a proper decay length of about $c\tau \simeq 136.6$ μm [3], which is more than twice the Λ_c^+ one (see Tab. 5.4), the Ξ_c^+ reconstruction may hugely benefit from the selections on topological variables. Moreover, the Ξ_c^+ reconstruction in the $pK^-\pi^+$ channel may significantly profit from the better pointing resolution and secondary vertex determination provided by the upgraded ITS (see Sec. 6.3), then the studies described in this Section may be preparatory for future analyses. In the next Section an introduction to the machine learning tools adopted in this work is provided, then the application to the $\Xi_c^+ \to pK^-\pi^+$ physics case is described.

6.1.1 Machine learning

The *machine learning (ML)* is a branch of the artificial intelligence (AI) dealing with algorithms (also called *models*) that "learn" to perform a task. The two most common tasks addressed with this tool are *classification* problems, where the discrimination among two or more classes of events is asked, and *regression* problems, where the algorithm provides predictions according to the input data. The separation of real-decay events from combinatorial background ones is a typical binary-classification problem in high-energy physics. Such classification is possible thanks to the *supervised learning* of an algorithm, which is educated to distinguish the different classes of events present in a labelled dataset.

The algorithm education is called *training* and it represents the stage in which the model learns how to classify the data according to a set of examples, called *training*

sample, for which the belonging class is known a priori. This step is fundamental to establish the model parameter configuration, determined as that providing the best event classification in the training sample according to its properties, called *features*. In case of the reconstruction of $\Xi_c^+ \to pK^-\pi^+$ decays, the features of each event include the topological variables and the PID signals of daughter tracks, as discussed later. Ideally, the algorithm learns general patterns specific of the different classes, so that it can be employed to classify unlabelled datasets. The output of the model is a *score*, a numerical value that is calculated for each event according to the features. This value is used to decide which class each event of an unknown dataset belongs to, comparing it with a fixed *threshold*. In the left panel of Fig. 6.1 an example of output score distributions for two separate classes of events after the training of a supervised learning algorithm is shown. All the events with a score lower (higher) than the threshold value are classified as belonging to the "class 1" ("class 2"). The accuracy of such discrimination is related to the shape of the score distributions and the threshold value itself. Considering the example in the left panel of Fig. 6.1, setting the threshold at -10 the class discrimination is not performed, since all events are classified as belonging to the "class 2", while fixing the threshold at 7 all the "class 1" are correctly classified, but a huge fraction of "class 2" events is misclassified. This behaviour is driven by the intersection between the output score distributions of the two classes, which would be completely separated in case of a perfectly discriminating algorithm. In general, the application of a threshold determines the fraction of well classified and misclassified events for each class, which can be used to evaluate the discrimination power of the trained model. Labelling as "negative" the "class 1" and as "positive" the "class 2", each negative event classified as a negative or positive is defined *true negative (TN)* and *false positive (FP)*, respectively, while each positive event in the two cases is defined *false negative (FN)* and *true positive (TP)*, respectively. According to this, it is possible to define these two quantities:

$$\mathrm{TPR} = \frac{\sum \mathrm{TP}}{\sum \mathrm{TP} + \sum \mathrm{FN}}, \quad \mathrm{FPR} = \frac{\sum \mathrm{FP}}{\sum \mathrm{FP} + \sum \mathrm{TN}} . \tag{6.1}$$

The *true positive rate (TPR)* defines the fraction of correctly classified positive events, while the *false positive rate (FPR)* corresponds to the fraction of negative events classified as positive. An idea of the discrimination capability of a binary-classification algorithm is provided by the area under the *Receiver Operating Characteristics (ROC)* curve, shown in the right panel of Fig. 6.1. This curve is defined as the TPR as a function of the FPR and it is built by scanning all the possible threshold values within the output score range of the two classes. It would correspond to a constant at unity in case of a perfectly discriminating algorithm, namely if the output score distributions were perfectly separated, and the area under curve (AUD) would be equal to unity. In case of equal output score distributions for the two classes, the ROC curve would correspond to the bisector of the Cartesian plane (grey dashed line) and the area under it would be 0.5. In the latter case, the model would be completely useless, since each event would be randomly classified as positive or negative. Normally, a trained algorithm is characterised by a ROC AUC between 0.5 and 1 and algorithms with ROC AUC close to unity are normally preferable. This number just gives an indication of the overall separation power of the model independently from the threshold employed for the classification, moreover it is not sensitive to the relative abundances of the two classes. The performances of the trained model are usually evaluated during the *testing* procedure by applying the model on a *test sample*. Also in this case the belonging class of each event is known a priori, but the dataset is

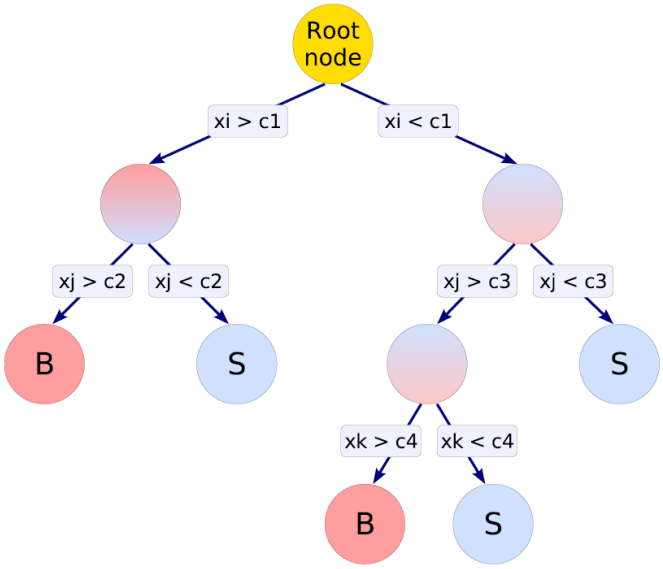

FIGURE 6.2: Structure of a decision tree built to distinguished signal events (S) from background ones (B). Figure from [334].

independent from the training one. The goal of this stage is to assess the model discrimination capabilities on a dataset independent from the training one, validating the algorithm before the usage on a completely unknown dataset. The testing on the training sample would not be significant, since the algorithm easily classifies events that has already seen. Furthermore, the testing stage is very important to evaluate the quality of the training. In case of a well-trained model, the output score distributions of the test sample events should be close to those from the training sample and the ROC curve after the two stages should coincide. A problematic case is instead when the ROC AUC from the training is higher than the testing one. In this case, the model is declared as *overtrained*, meaning that the model learnt how to classify the events in the training samples without extrapolating the general patterns from the classes. As a consequence, the application of the model to an independent dataset does not provide the same separation power, since the learning was too much based on the training sample fluctuations. In this situation, the training procedure needs to be repeated with a different parameter configuration or with a revised training sample. Once the algorithm is trained and tested, it is ready for the *application* on a completely unknown sample. The employment of this model would provide a discrimination among the classes with the performances evaluated during the previous stages.

In the context of this analysis, the separation between the $\Xi_c^+ \to pK^-\pi^+$ signal and the background can be identified as a binary classification model. The training and testing samples are formed by $\Xi_c^+ \to pK^-\pi^+$ signal generated with Monte Carlo simulations and combinatorial background formed by fake $pK^-\pi^+$ triplets from a small subset of data, then the model is applied on data to search for the $\Xi_c^+ \to pK^-\pi^+$ signal.

6.1.2 Boosted Decision Trees (BDT)

A commonly used algorithm in binary classification problems is the *Boosted Decision Trees (BDT)* one, whose building block is the *Decision Tree (DT)* [335]. A DT corresponds to a sequential model combining a series of simple tests to distinguish two classes of events according to their features. The typical structure of a DT is shown in Fig. 6.2, where the signal (S) and background (B) correspond to the two classes of events to be distinguished. The tree develops from a root node where a first test is performed. Such a test corresponds to the comparison of a numeric feature with a threshold value established to separate the two classes. A single event is then sent to either of the two directions before being subject to another "left/right" test based on a different feature. The sequence of these binary classifications stops when the stopping criterion, established a priori by the user, is fulfilled. The logic behind this classifier is quite simple, since the decision taken at each node is understandable. The construction of a DT takes place automatically during the training step and a commonly used variable at this stage is the so-called *Gini index*, defined as:

$$G_{ini} = \left(\sum_{i=1}^{N} w_i\right) P(1-P) \,, \tag{6.2}$$

where w_i is the weight of the i-th event and P is the signal purity in the considered node. The criterion for the best splitting consists in minimizing the G_{ini} index difference between the parent and children nodes, namely:

$$C = G_{ini} - \left(G_{ini}^{\text{left child}} + G_{ini}^{\text{right child}}\right) \,. \tag{6.3}$$

Such minimisation is performed sequentially, looking for the features and selection criteria providing the best splitting at each node. In this way, big DTs may be built to well classify the training dataset, but the risk that the algorithm does not catch the general patterns characterising the two classes is high. For this reason, the DT depth is usually constrained to avoid the overtraining. However, the discrimination power of a small DT is limited and the algorithm stability may be severely changed by a small fluctuation in the training dataset. In order to build a robust model with a good discrimination power, more DTs may be used and the final classification is performed by combining the outcome of all the DTs. A *Random Forest* [336] exploits the usage of several DTs and provides a classification according to the (weighted) average of the outcomes from all the DTs in the forest. A ranking among all the possible features describing the training dataset can be done basing on the frequency of use of each feature in the DTs creation. This ranking is particularly interesting in high-energy physics analyses, where the features correspond to variables with a precise physical meaning and the more important ones should be those that better differentiate the signal and background events.

The creation of hundreds of independent trees may be demanding in terms of computational resources. Moreover, one may naturally expect that adding a new DT helps to improve the discrimination power of the whole algorithm, without being a copy of the previous classifier that does not improve the classification. For this reason *boosting* techniques are usually adopted. In such procedures the DTs are built sequentially, trying to add a new DT that compensates the lacks of the previous classifier. This is based on the event re-weighting, with the goal of increasing the importance of the events misclassified by the previous classifier so that the new one will take more care of them. The BDT model corresponds to the ensemble of these

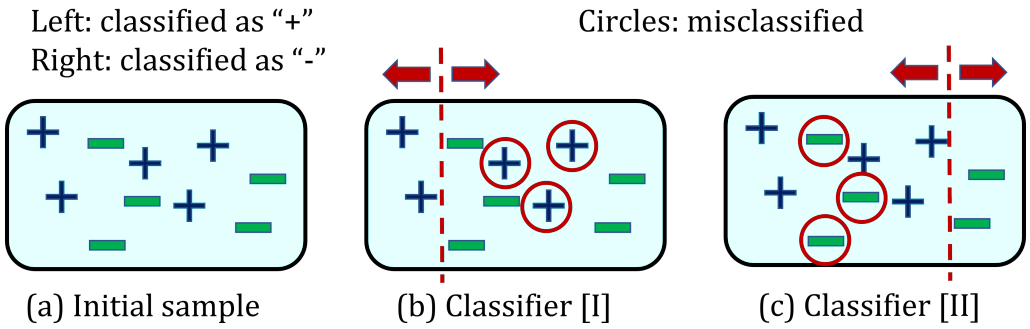

FIGURE 6.3: Schematic sketch representing the AdaBoost boosting algorithm logic. Left: original dataset of "+" and "-" signs. Middle: first classifier that misses three "+" signs, classifying them as "-" ones. Right: second classifier. Notice that it correctly classifies the three "+" signs missed by the previous classifier, even if now new elements are wrongly classified. They will be treated in priority by the following classifier.

trees and its response is more stable than a single DT with respect to the training-set fluctuations. The BDT provides an output score that is related to the outcome of each DTs, called *weak learners* in this context, according to the boosting algorithm. The most popular one is called *Adaptive Boost (AdaBoost)* [337] and this is the algorithm adopted in this work. In the following, a typical explanation of the algorithm is presented. Calling x the set of features characterising an event and y the known class label of the training data (e.g.: +1: signal; -1: background), then each event can be indicated with the pair (x_i, y_i). Considering the t-th classifier (i.e.: decision tree) it is possible to define a misclassification rate ϵ_t on m events as:

$$\epsilon_t = \frac{\sum_{i=1}^{m} w_t(i) \cdot m_t(x_i)}{\sum_{i=1}^{m} w_t(i)} , \tag{6.4}$$

where $w_t(i)$ is the weight assigned to the i-th event and $m_t(x)$ is equal to 1 if $h_t(x_i) \neq y_i$, where $h_t(x_i)$ is the classifier response (i.e.: +1 if the event is classified as signal, -1 if it is classified as background) and equal to 0 in case the event is well classified. Therefore, only misclassified events contribute to the sum at the numerator. The misclassification rate ϵ_t is used to re-weight all the m events and the definition of the $t+1$-th classifier is influenced by the value of ϵ_t. The new weights, modulo a normalization factor, are expressed as:

$$w_{t+1}(i) \propto w_t(i) \times \begin{cases} e^{+\alpha_t}, \text{ if misclassified} \\ e^{-\alpha_t}, \text{ if well classified} \end{cases} , \tag{6.5}$$

where the *boost weight* α_t is defined as:

$$\alpha_t = \frac{1}{2} \ln \left(\frac{1-\epsilon_t}{\epsilon_t} \right) . \tag{6.6}$$

The α_t coefficient increases the weight for the misclassified events, according to Eq. 6.5, so that the $t+1$-th classifier will consider such cases with higher priority. A discrete example is reported in Fig. 6.3, where in panel (a) the sample with the two classes to be separated is reported. A first classifier is applied in panel (b) and it classifies all the elements on the right as "-" and those on the left as "+" and the

red circles identify the misclassified elements. Now, using Eq. 6.4 and giving equal importance to all the elements (i.e.: $w_I(i) \propto 1/m = 1/10$ fo all i), then the misclassification rate of the classifier I is $\epsilon_I = 3/10$ and the boost weight corresponds to $\alpha_I = 0.5 \cdot \ln(7/3) = 0.42$. If a second classifier is added, as shown in panel (c), it will concentrate more on the three events wrongly classified by I, having a weight $w_{II}(i) \propto w_I \times \exp(+\alpha_1) = 0.3 \times \exp(0.42)$ that is higher than that of the correctly classified events $w_{II}(i) \propto w_I \times \exp(-\alpha_1) = 0.3 \times \exp(-0.42)$. The classifier II produces other three misclassified events and the misclassification rate ϵ_2 is influenced by the new weights w_{II}. Adding more classifiers, they will always concentrate on the elements previously misclassified, according to the weight $w_t(i)$ deriving from the application of the first t classifiers. The BDT output score is calculated considering all the T classifiers as[1]:

$$y_{\text{Boost}}(x_i) \propto \sum_{t=I}^{T} \alpha_t \cdot h_t(x_i) \ , \tag{6.7}$$

where h_t is the response of the t-th classifier, namely +1 for the classification in signal and -1 for that in background. According to this procedure, the larger (lower) the $y_{\text{Boost}}(x_i)$ value the more the event is signal-(background-)like. This boosting algorithm better performs with weak classifiers, namely DTs with a three depth of 2 or 3 that own a low discrimination power by themselves. By construction, such small trees are much less prone to overtraining with respect to deep binary trees. Moreover, the AdaBoost algorithm may further enhance its performance by enabling a slow learning and using a larger number of boosting steps instead. This is controlled by the so-called *learning rate* parameter β, which is used to change the boost weight $\alpha_t \mapsto \beta\alpha_t$, with $0 < \beta < 1$. Given the boosting procedure, the feature importance ranking may change with respect to a case without boosting, especially due to the weight unbalance introduced by the misclassification rate of each classifier.

6.1.3 Search for $\Xi_c^+ \to pK^-\pi^+$ signal with AdaBoost

The signal related to the $\Xi_c^+ \to pK^-\pi^+$ decays has been searched in the pp collision sample at $\sqrt{s} = 13$ TeV analysed in Chapter 5 in the transverse momentum interval $3 < p_T < 5$ GeV/c. The $pK^-\pi^+$ candidates are reconstructed with the same single-track and filtering selections reported in Tab. 5.2[2] and 5.5 within the fiducial rapidity acceptance interval defined in Eq. 5.1. In addition, good secondary vertices are selected with the requirement of a vertex $\chi^2 < 1.5$ and the tracks with $p_T < 1$ GeV/c are used only if they have a point in the first SPD layer, so that the combinatorial background given by secondary tracks and particles from conversions in the material is reduced.

The optimisation of single-track and topological selections is performed with a BDT model based on the AdaBoost boosting method. As explained in Sec. 6.1.1 and 6.1.2, the model needs to be trained to recognise true $\Xi_c^+ \to pK^-\pi^+$ signal events and distinguish them from the combinatorial background formed by fake $pK^-\pi^+$ triplets. The signal events are taken from PYTHIA 6 simulations anchored to 2017 and 2018 data taking periods with injected $\Xi_c^+ \to pK^-\pi^+$ decays that are all employed for the BDT training and testing. The background candidates, taken from

[1] In a discrete problem, like the one shown in Fig. 6.3, the BDT score usually corresponds to the quantity in Eq. 6.7.

[2] The $pK^-\pi^+$ candidates in this case are reconstructed using tracks with at least 70 clusters in the TPC, without any specific requirement on the number of crossed rows and on the found/findable clusters.

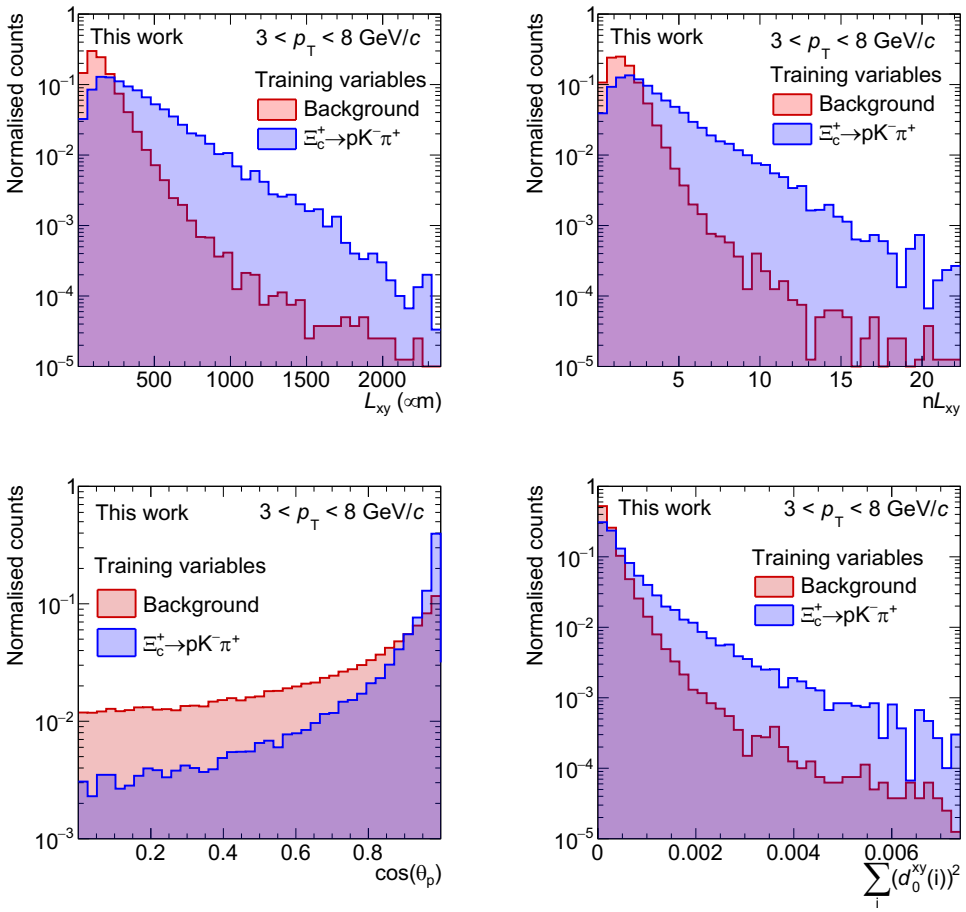

FIGURE 6.4: Examples of variable distributions for signal and background candidates used to train the BDT in the interval $3 < p_T < 8$ GeV/c.

data, are required to be located in the sideband regions of the invariant mass distribution, around the expected position of the Ξ_c^+ signal. In particular, the background candidates for the training dataset are asked to satisfy the condition $m_{\text{inv.}} \lesssim 2.43$ GeV/c^2 or $m_{\text{inv.}} \gtrsim 2.51$ GeV/c^2, to be sure not to include any signal candidate in the background sample. The invariant mass of each background candidate is calculated by assigning the kaon mass to the opposite-charged track and either the proton or the pion one to the two equal-charged tracks. If the candidate satisfies with the $pK^-\pi^+$ (π^+K^-p) hypothesis according to the criteria in Tab. 5.2 and 5.5, then the $m_{pK^-\pi^+}$ ($m_{\pi^+K^-p}$) invariant mass value is calculated. In case both hypothesis are possible, two copies of the same candidate with swapped identities for the equal-charged tracks are considered. The background training dataset is built by randomly-selected $pK^-\pi^+$ candidates from data and keeping the relative size with respect to the full dataset negligible, to avoid overtraining with respect to the application data themselves.

The BDT algorithm adopted in this work is constituted by 1500 DTs with a maximum of 3 splits. The learning rate parameter β used in the boosting is fixed to 0.6. The training dataset is composed by 30000 and 80000 events for signal and background respectively, selected in the interval $3 < p_T < 8$ GeV/c. Even if the signal search in data will be performed in the range $3 < p_T < 5$ GeV/c, the former interval is considered to build the training and testing samples, in order to increase

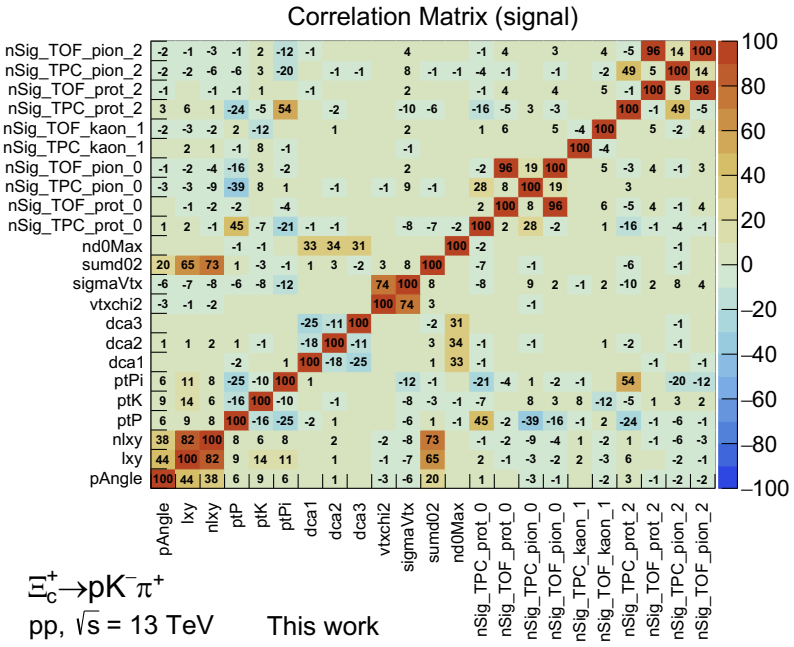

(A) Signal.

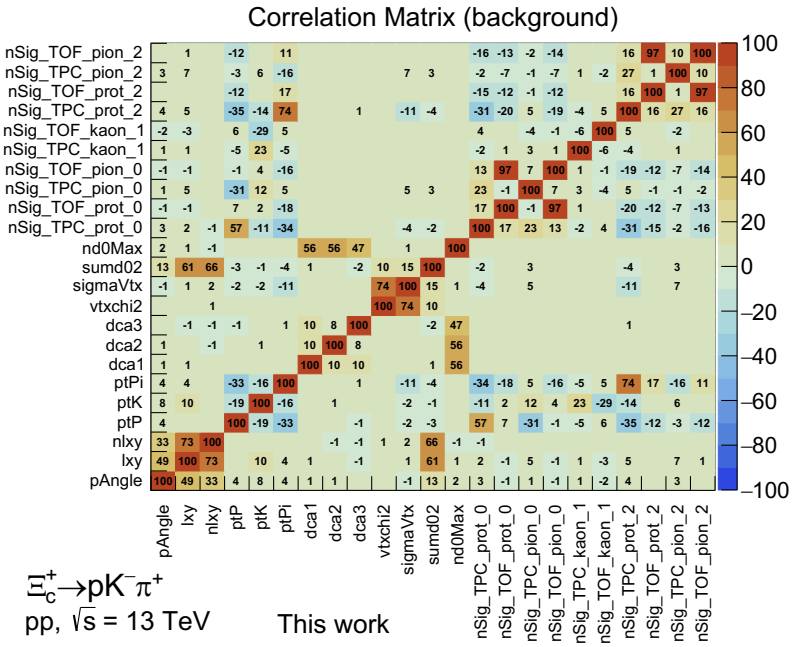

(B) Background.

FIGURE 6.5: Variable correlation matrices for signal and background candidates used for the BDT training in the interval $3 < p_T < 8$ GeV/c.

their statistics. The residual signal used for the training amounts to about 13000 events, while 160000 background candidates are used for testing. In Fig. 6.4 the distributions of L_{xy}, nL_{xy}, $\cos(\theta_p)$ and $\sum_i (d_0^{xy(i)})^2$ variables for signal and background candidates used for the BDT training are shown. Given the proper decay length $c\tau = 136.6$ µm, the $\Xi_c^+ \to pK^-\pi^+$ signal shows a larger displacement with respect

Rank	Variable	Frequency
1	L_{xy}	2.749×10^{-1}
2	nL_{xy}	2.112×10^{-1}
3	$\cos(\theta_p)$	1.736×10^{-1}
4	$n^{TOF}_{\sigma_K}(1)$	1.015×10^{-1}
5	$\sum_i (d_0^{xy}(i))^2$	8.927×10^{-2}
6	$n^{TPC}_{\sigma_K}(1)$	7.891×10^{-2}
7	$n^{TOF}_{\sigma_p}(2)$	7.578×10^{-2}
8	$n^{TOF}_{\sigma_p}(0)$	7.072×10^{-2}
9	$n^{TOF}_{\sigma_\pi}(0)$	6.644×10^{-2}
10	$n^{TOF}_{\sigma_\pi}(2)$	5.716×10^{-2}
11	$p_T(2)$	5.551×10^{-2}
12	$n^{TPC}_{\sigma_p}(2)$	4.900×10^{-2}
13	$d_0^{xy}(0)$	4.739×10^{-2}
14	$p_T(1)$	4.298×10^{-2}
15	$d_0^{xy}(2)$	4.221×10^{-2}
16	$n^{TPC}_{\sigma_\pi}(0)$	3.556×10^{-2}
17	$d_0^{xy}(1)$	3.498×10^{-2}
18	$p_T(0)$	3.376×10^{-2}
19	$n^{TPC}_{\sigma_\pi}(2)$	2.614×10^{-2}
20	$d^{xy}_{res.}$	2.169×10^{-2}
21	$n^{TPC}_{\sigma_p}(0)$	1.967×10^{-2}
22	σ_{vtx}	1.142×10^{-2}
23	χ^2_{vtx}	6.785×10^{-3}

Rank	Variable	Frequency
1	L_{xy}	5.948×10^{-2}
2	nL_{xy}	5.542×10^{-2}
3	$p_T(K)$	5.270×10^{-2}
4	$n^{TPC}_{\sigma_K}(1)$	5.231×10^{-2}
5	$d^{xy}_{res.}$	5.182×10^{-2}
6	$n^{TPC}_{\sigma_p}(2)$	4.886×10^{-2}
7	$n^{TPC}_{\sigma_p}(0)$	4.814×10^{-2}
8	$n^{TPC}_{\sigma_\pi}(0)$	4.496×10^{-2}
9	$p_T(0)$	4.472×10^{-2}
10	$p_T(2)$	4.326×10^{-2}
11	d_0^{xy}	4.245×10^{-2}
12	$n^{TOF}_{\sigma_K}(1)$	4.228×10^{-2}
13	$n^{TPC}_{\sigma_\pi}(2)$	4.220×10^{-2}
14	$d_0^{xy}(0)$	4.196×10^{-2}
15	$d_0^{xy}(2)$	4.173×10^{-2}
16	$\cos(\theta_p)$	4.014×10^{-2}
17	χ^2_{vtx}	3.858×10^{-2}
18	$n^{TOF}_{\sigma_p}(0)$	3.772×10^{-2}
19	σ_{vtx}	3.712×10^{-2}
20	$\sum_i (d_0^{xy}(i))^2$	3.631×10^{-2}
21	$n^{TOF}_{\sigma_p}(2)$	3.489×10^{-2}
22	$n^{TOF}_{\sigma_\pi}(2)$	3.277×10^{-2}
23	$n^{TOF}_{\sigma_\pi}(0)$	3.018×10^{-2}

TABLE 6.1: Feature importance ranking for the $\Xi_c^+ \to pK^-\pi^+$ candidates from the training of 1500 decision trees using 30000 and 80000 candidates for signal and background respectively within the range $3 < p_T < 8$ GeV/c. The left Table refers to the ranking of independent decision trees, the right one instead shows the updated raking in case of boosting with AdaBoost. The indices "0", "1" and "2" are used to refer to the daughter tracks of the $\Xi_c^+ \to pK^-\pi^+$ candidate decays.

to the background candidates. This behaviour covers a key role in the separation of signal candidates from the combinatorial background and this is reflected in the feature importance ranking after the training. In Tab. 6.1 the list of variables used to train the BDT algorithm is reported. In the left side of the Table, the variable ranking deriving from the creation of 1500 independent DTs is reported, while the updated list after the boosting is shown on the right side. The decay length along the transverse plane L_{xy} and its normalised value nL_{xy} cover the first two positions in the ranking, being the two most used features in the DT creation. Also the PID variables are included in this procedure and the $n\sigma$ for TPC and TOF detectors are largely used in the training. Apart from the variables associated to the single-track and candidate displacement, also the transverse momentum of the daughter tracks is inserted in the training, in order to exploit the correlations with the PID variables, as shown in Fig. 6.5.

In panel (A) of Fig. 6.6 the BDT score distributions for signal and background events after the training and testing of the BDT model are shown. The background

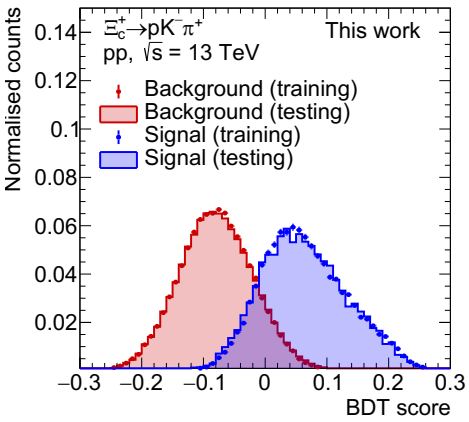

(A) BDT output score distributions for signal and background events used in the training and testing of the algorithm.

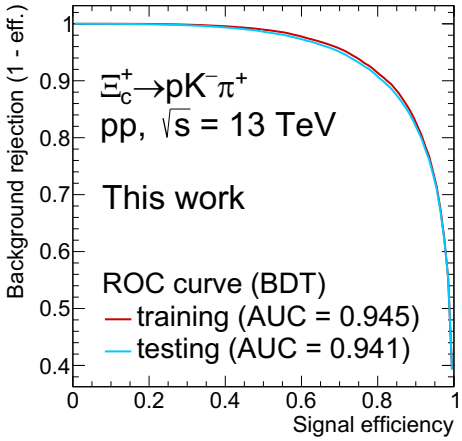

(B) ROC curves from the training and testing of the BDT models. The ROC AUC in the two cases is reported.

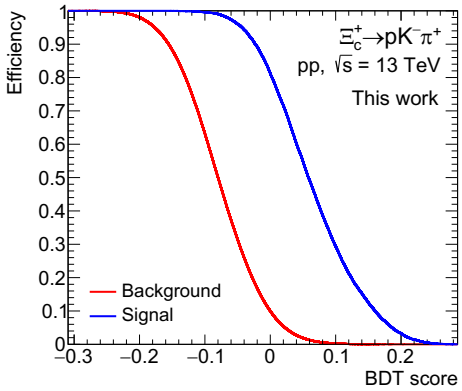

(C) Signal and background efficiency provided by the trained BDT model.

FIGURE 6.6

distribution peaks around -0.1, while the signal one around 0.05. The BDT score distributions from the training are compatible with those obtained after the testing for both classes, indicating that the model is not overtrained. This is confirmed by the ROC curves obtained after the training and testing of the model, which are shown in panel (B) of Fig. 6.6[3]. The two curves are very similar and the ROC AUC for the training (0.945) is close to that for the testing (0.941). Such values larger than 94%

[3]The ROC curves shown in Fig. 6.6 do not have the same structure of that introduced in the right panel of Fig. 6.1. This is a consequence of the TMVA package implementation, which defines the ROC curve as the correlation between the "true negative rate" ("background rejection (1-eff.)") and the "true positive rate" (signal efficiency). This convention is driven by the physics meaning carried by these two categories of events, since the two classes always refer to signal and background in high-energy physics analyses. Despite the different implementations, the information provided by the ROC curve does not change.

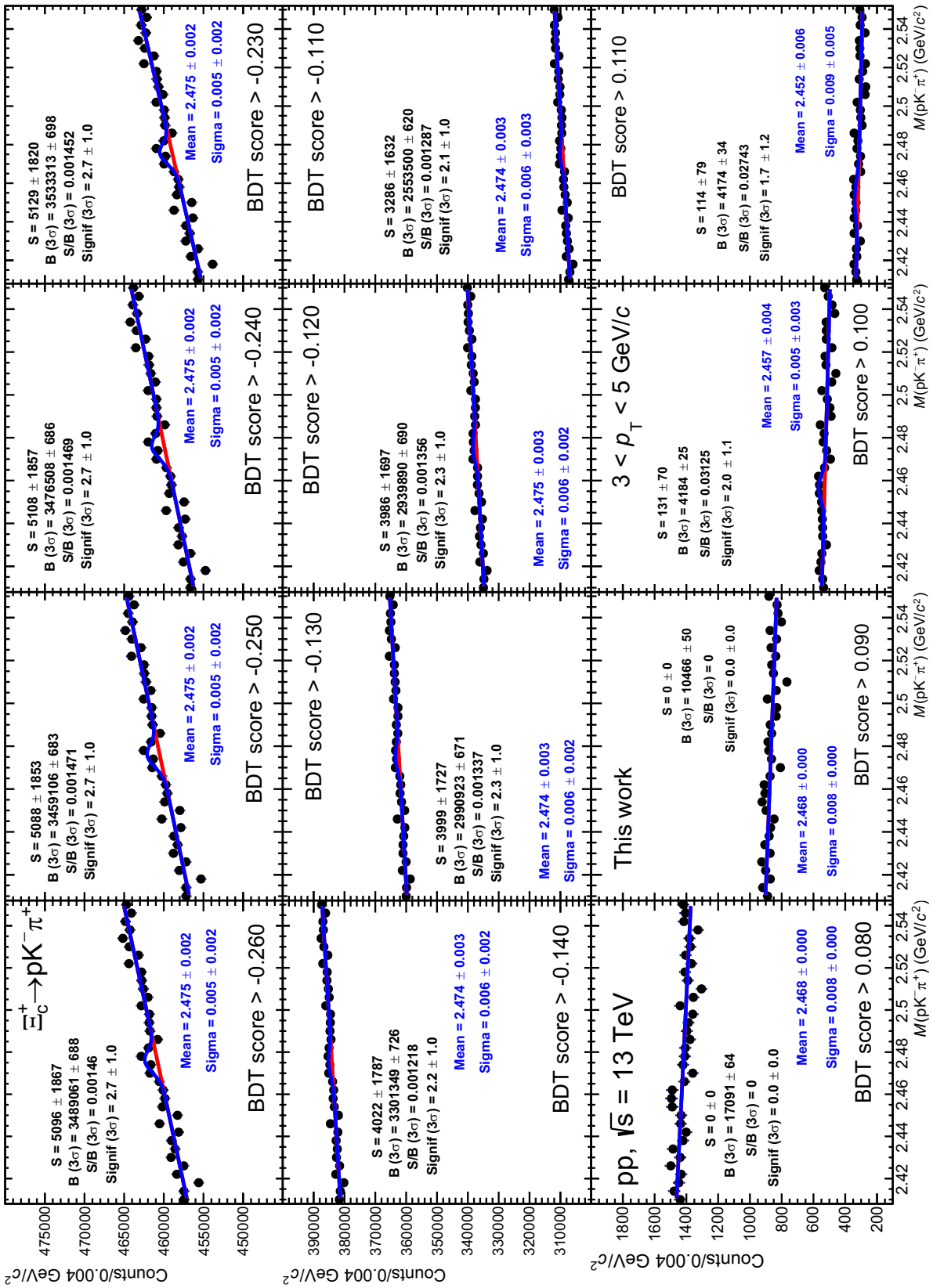

FIGURE 6.7: Invariant mass distribution of $pK^-\pi^+$ selected with different thresholds on the output score provided by the trained BDT model and applied on pp collision dataset at $\sqrt{s} = 13$ TeV with integrated luminosity of about $\mathcal{L} \approx 32$ nb^{-1}.

indicate that the overall separation power of the trained model is good.

The trained BDT model is finally applied on real data in order to look for the $\Xi_c^+ \to pK^-\pi^+$ signal. The invariant mass distribution of $pK^-\pi^+$ candidates in the $3 < p_T < 5$ GeV/c interval selected with different thresholds on the BDT output score is shown in Fig. 6.7. The invariant mass distribution is evaluated in three different regions of the BDT score distributions, according to the signal and background efficiencies reported in panel (C) of Fig. 6.6. The first row shows the invariant mass distributions of $pK^-\pi^+$ candidates selected with loose threshold values around -0.25, where the signal and background efficiencies are both close to unity. The region around the expected $\Xi_c^+ \to pK^-\pi^+$ signal is fitted with a Gaussian plus an exponential and an excess of the order of 2.7σ is observed around $m_{pK^-\pi^+} = 2.475$ GeV/c^2. In the second row the invariant mass distribution for the $pK^-\pi^+$ candidates selected with thresholds of -0.14, -0.13, -0.12, -0.11 are reported. These thresholds still guarantee a signal efficiency of almost 100%, but they provide a background rejection that grows from about 20% to 35%, with an expected improvement in the signal extraction with respect to the first row. However, the excess around the expected mass decreases to about 2.1σ, indicating that the larger excess observed in the first row is probably driven by the statistical fluctuations of background. The last row of Fig. 6.7 shows the invariant mass distribution obtained with $pK^-\pi^+$ triplets selected applying threshold values around 0.1, where the highest signal purity is expected given a background rejection larger than 98%. However, the $\Xi_c^+ \to pK^-\pi^+$ signal is not visible in these cases. The fit with a Gaussian for the signal and an exponential for the background does not even converge for threshold values equal to 0.08 and 0.09, while in the other two cases the fit picks up an excess of counts below 2σ in correspondence of mass values that are significantly lower than $m(\Xi_c^+)$ (see Tab. 5.4). These results suggest that despite the huge rejection the residual background is still overwhelming the signal, which is apparently too low to be visible.

6.1.4 Outlook for future analyses

Despite the current analysis does not provide any satisfactory extraction of the $\Xi_c^+ \to pK^-\pi^+$ signal in pp collisions at $\sqrt{s} = 13$ TeV, the work described in this Section provides some useful suggestions to address this analysis in the next future. The collection of a larger dataset, expected during Run 3 and 4 at the LHC, as well as the expected improvements in terms of pointing resolution granted by the upgraded ITS (see next Section) can further enhance the performance of this analysis. However, a precise measurement of the Ξ_c^+ production cross section through the reconstruction of the $pK^-\pi^+$ decay channel is actually precluded by the huge ambiguity on the branching ratio value, as explained in Sec. 6.5. All the points listed below may be helpful to improve the quality of the analysis.

- The first fundamental point regards the lack of statistics for the signal in the training and testing samples. The total amount of signal available in the range $3 < p_T < 8$ GeV/c is about 43000, which needs to be split for the BDT training and testing. Looking at the blue distributions in the left panel of Fig. 6.6 some fluctuations of the testing distribution in correspondence of the left tail as well as of the peak region are noticeable. This can be ascribed to the limited size of the testing sample, counting only $\sim$ 13000 signal events. A larger amount of signal is necessary to properly train and test the algorithm in such a large p_T interval, where the decay kinematics significantly changes at lower and higher p_T due to the different boost. Moreover, the Monte Carlo simulations available for the BDT training and testing are not fully representative of the whole

dataset. The signal is obtained from generated events anchored to only one data taking period from 2017 and another one in 2018. Such events may be not enough for the algorithm to learn the properties of the whole data sample of pp collisions at $\sqrt{s} = 13$ TeV collected by the ALICE experiment, considering that they do not cover the sample collected in 2016 and even do not represent completely those collected in 2017 and 2018. At the moment of this work there were no alternative Monte Carlo productions available. Larger statistics would be beneficial also to perform the training in the same transverse momentum interval considered for the data, in order to train the algorithm with candidates whose kinematics is fully in line with those in data. Finally, such a larger statistics would be useful to study the effect of preselections on single-track and topological variables, which now is prevented by the too large fluctuations and instability with the current sample.

- A second aspect to be taken with care is the management of the TOF signal in the BDT training. Being a feature of the events processed by the algorithm, a value for the n_σ^{TOF} of each daughter track is necessary, which however is not defined in case of low-momentum tracks that do not match the TOF. An unphysical value of +999 is assigned to all these cases. Such a hack would not introduce any bias in case of a standard analysis with rectangular selections, but this is not granted to be safe for the training of an algorithm that bases its behaviour on the variable distributions, which are evidently altered by this choice. In case of larger available statistics, the ideal choice would be to use the TOF signal to preselect the candidates and get rid of a significant amount of background before the BDT training and application. A derived PID variable defined by the quadrature sum of n_σ^{TPC} and n_σ^{TOF} signals, or by the former one only in case the latter one is not available, was also explored in the BDT training and application, but no significant changes in the $\Xi_c^+ \to pK^-\pi^+$ signal extraction were noticed.

- The determination of the BDT score threshold value may be driven by some quantitative arguments. As it will be described in Sec. 6.5, the expected significance for the signal extraction can be determined by quantifying the amount of expected background from data and that of raw signal using an assumption of the cross section and deconvolving it by the efficiency related to the chosen threshold. The model working point can be then identified with that ensuring the maximum expected significance, which is calculated using an independent dataset with respect to the application one, avoiding picking-up background fluctuations from the peak region. Such an approach was not adopted in this work, given that no significant signal was observed for any BDT score threshold value.

- The transverse momentum of the candidate daughters is inserted in the list of training features. These variables are strongly correlated with the invariant mass and particular selections applied by the BDT may alter their distribution and consequently influence the invariant-mass one and $p_T(\Xi_c^+)$. This may be not ideal for the signal extraction, since the presence of high-concavity background may be delicate to be treated with a polynomial function, so that no background fluctuations are confused with the signal. This does not seem to be relevant for this analysis. Other attempts without inserting the single-track transverse momenta were explored as well, without any particular gain in the $\Xi_c^+ \to pK^-\pi^+$ signal extraction.

6.2 The ALICE upgrade during the LS2

During the ongoing long shutdown number 2 (LS2) of the LHC several subsystems of the ALICE apparatus are undergoing a major upgrade process. This was conceived in the last decade to provide the ALICE experiment with the possibility of extending its physics case and performances, with the main objective of high-precision measurements of rare QCD probes down to low transverse momenta, with a special focus on heavy-ion collisions. To achieve such goals, the ongoing upgrades are finalised to provide a significant enhancement in the low-p_{T} vertexing and tracking capabilities, as well as substantially higher data acquisition rates, preserving the excellent PID capabilities that are already granted by the current apparatus. The ALICE upgrade has been designed with the goal of exploiting an increased luminosity of the LHC accelerator, with peak values reaching $\mathcal{L} = 6 \times 10^{27}$ cm^{-2}s^{-1} and an expected interaction rate of about 50 kHz in Pb–Pb collisions. In this scenario, the upgraded ALICE apparatus is expected to collect about $\mathcal{L} = 13$ nb^{-1} of Pb–Pb collisions at $\sqrt{s_{\mathrm{NN}}} = 5.5$ TeV during Run 3 and 4 at the LHC, accompanied by a pp data sample at the same collision energy corresponding to an integrated luminosity of about 6 pb^{-1}, which may be collected within few months at an event readout rate of about 200 kHz. The ongoing upgrades on the ALICE apparatus include [338]:

- a new beam pipe, characterised by a smaller diameter and a lower material budget;
- a new, high-resolution, low-material-budget Inner Tracking System (ITS), conceived to improve by a factor of about $\times 3$ (5) the resolution on the distance of closest approach of the tracks to the primary vertex in the xy (z) directions, as well as a significant improvement of the performance of ITS standalone tracking [339]. A more detailed description of the upgraded ITS layout and performances will be provided in Section 6.3;
- the substitution of the multi-wire proportional chambers with GEM (Gas Electron Multipliers) detectors for the Time Projection Chamber (TPC) readout, together with the pipelined electronics, which will enable an ungated usage of this gas detector with a consequent cancellation of readout dead-time [340];
- the upgrade of the TRD, TOF, PHOS and Muon Spectrometer readout electronics, allowing for a higher data acquisition rate in these devices;
- the addition of a Muon Forward Telescope (MFT), to allow vertex capabilities to the existing Muon Spectrometer aimed at separating prompt charmonia from beauty feed-down ones [341];
- the upgrade of the trigger detectors at forward rapidity and of the full trigger system, as well as of the data acquisition (DAQ) system and the High Level Trigger (HLT), to allow for high-rate acquisition [342];
- the upgrade of the offline data processing software to manage the reconstruction of the expected statistics during Run 3 and Run 4 at LHC, constituting the O^2 framework [240]. With the O^2 tool the detector data are all transferred to the computing system and their reduction is performed by an on-the-fly processing running in parallel with the data collection. The system will perform an online partial calibration and reconstruction, so that the original raw data can be replaced with compressed ones. This step is fundamental to keep the data storage contained and able to fit within the available resources.

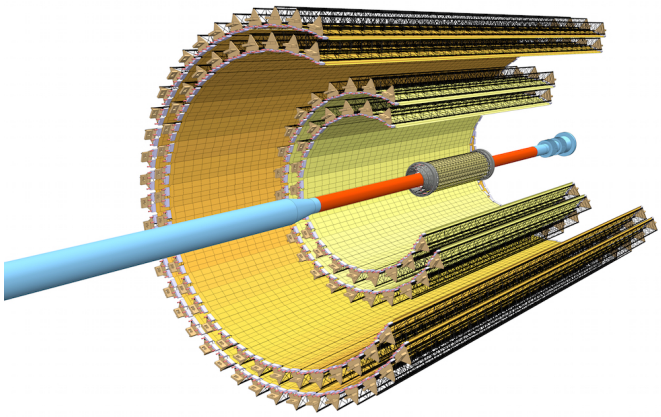

FIGURE 6.8: Layout of the upgraded Inner Tracking system detector for Run 3 at the LHC (ITS 2). Figure from [339].

	Inner Barrel			Outer Barrel			
	Inner Layers			Middle Layers		Outer Layers	
	0	1	2	3	4	5	6
Minimum radius (mm)	22.4	30.1	37.8	194.4	243.9	342.3	391.8
Maximum radius (mm)	26.7	34.6	42.1	197.7	243.9	342.3	394.9
Length (sensitive area) (mm)	271	271	271	843	843	1475	1475
η coverage	± 2.5	± 2.3	± 2.0	± 1.5	± 1.4	± 1.4	± 1.3
Active area (cm^2)	421	562	702	10483	13104	32105	36691
Pixel Chip size (mm^2)	15×30						
Nr. Pixel Chips	108	144	180	2688	3360	8232	9408
Nr. Staves	12	16	20	24	30	42	48
Staves overlap in $r\varphi$ (mm)	2.23	2.22	2.30	4.3	4.3	4.3	4.3
Gap between Chips in z (μm)	100						
Chip dead area in $r\varphi$ (mm)	2						
Pixel size (μm^2)	29×27			29×27			

TABLE 6.2: Geometrical parameters of the upgraded Inner Tracking system detector during Run 3 at the LHC (ITS 2). Numbers from [339] and [343].

6.3 The upgrade of the ITS for Run 3

The Inner Tracking System layout that would be available during the Run 3 at the LHC, called in the following "ITS 2" [339], is shown in Fig. 6.8. It is formed by seven detection layers, which are grouped in two separate barrels: the Inner Barrel, represented by the three Inner Layers, and the Outer Barrel, which is in turn divided in Middle and Outer Layers, as reported in Tab. 6.2. The ITS detector is azimuthally segmented in mechanically independent units called *staves*, used to refer to the whole detector element. Differently from the old ITS, the upgraded one is characterised by a unique technology for all the layers, based on silicon Monolithic Active Pixel Sensors (MAPS) implemented using the 0.18 μm CMOS technology of TowerJazz. The basic component is the Pixel Chip, consisting in a single silicon die of

dimensions 15 mm $\times$ 30 mm incorporating a high-resistivity silicon epitaxial layer (sensor active volume), a matrix of charge collection diodes (pixels) with a pitch of about $\sim$ 30 µm and finally the electronics performing the signal amplification, digitisation and zero-suppression. The Pixel Chip that integrates the sensor matrix and the readout composing the ITS 2 is called ALPIDE (ALice PIxel DEtector). The output provided by this module is a digital signal, giving only the information on whether a charged particle crossed the pixel. The main geometrical parameters of the ITS 2 layout are reported in Tab. 6.2.

The ITS 2 represents a major upgrade with respect to the previous detector, given the several improvements listed below.

- **Detector closer to the beam line**. The $\sim$ 29 mm diameter beam pipe will be squashed by a factor of about 34%, giving the possibility to the ITS 2 to be closer to the interaction point. The innermost layer of the SPD detector was located at a radial distance of about 3.9 cm, while the innermost layer of the ITS 2 has a radius of about 2.5 cm.

- **Reduced material budget**. The usage of MAPS technology allows for a reduction of the silicon material budget per layer by a factor of about $\times$7 with respect to the first ITS, that is reduced from about 350 µm to about 50 µm. Moreover, a further reduction of about a factor $\times$5 is granted by the lower power consumption and a more optimised scheme for the electrical power and signal distribution. The thickness of the ITS 2 Inner Barrel layers is of the order of 0.3% X_0. The reduction of the material budget is fundamental for the improvement of the pointing resolution at low p_{T}, which is significantly affected by multiple Coulomb scatterings (innermost layer), and for the improvement of the overall tracking performances and momentum resolution.

- **Highly-segmented detector**. The ITS 2 detector is constituted by seven layers equipped with maps of pixels with dimensions of about 30 µm $\times$ 30 µm, granting high performances in the pointing resolution. Such a new ITS is equipped with about 10^5 pixels/cm^2, while the granularity of the older ITS was about 5×10^3 pixels/cm^2.

- **Low read-out time**. The ITS 2 detector is designed to cope with a read-out rate of 100 kHz for Pb–Pb collisions and 400 kHz for pp collisions. This corresponds to a read-out rate of about a factor $\times$2 higher with respect to the requirements from the ALICE upgrade and it provides a gain in statistics of more than a factor $\times$100 with respect to the older ITS, which was able to operate at a maximum read-out rate of 1 kHz.

Combining all these elements together, the ITS 2 detector will provide better tracking and pointing performances with respect to the older ITS. In the left panel of Fig. 6.9 the tracking efficiency of the standalone ITS in the two layouts is compared. The old ITS detector ("Current ITS") provided a tracking efficiency of about $\sim$ 10% at $p_{\mathrm{T}} = 100$ MeV/c, dropping at 0 at about $p_{\mathrm{T}} = 80$ MeV/c. With the ITS 2 ("Upgraded ITS") a gain of a factor of about $\times$7 is estimated at $p_{\mathrm{T}} = 100$ MeV/c and the track reconstruction can be pushed down to even lower transverse momenta. In the right panel of Fig. 6.9 the pointing resolution along the z direction and in the transverse $r\varphi$ plane with the ITS 2 and the older ITS detector is reported. At $p_{\mathrm{T}} = 200$ MeV/c the pointing resolution is improved by a factor of about 3 in the transverse plane and by a factor of about 4 along the longitudinal direction, given the significant

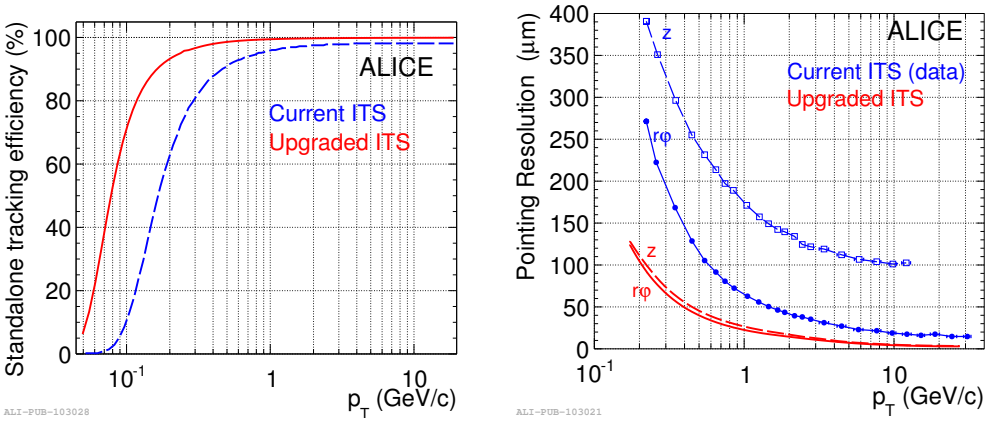

(A) Tracking efficiency with ITS standalone. (B) Pointing resolution.

FIGURE 6.9: Tracking performances of the ITS 2 compared with the ones of the older detector. "Upgraded ITS" indicates the ITS 2 layout, while "Current ITS" refers to the older detector. Figures from [339].

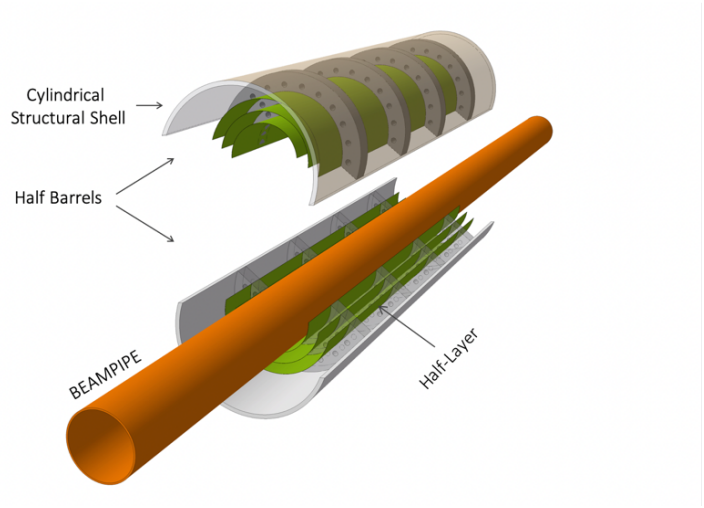

FIGURE 6.10: Layout of the ITS 3 Inner Barrel, where the two half-barrels mounted around the beam pipe are shown. Figure from [344].

reduction of the material budget and the increased granularity. This improvement is even larger at higher p_T: at $p_T = 10$ GeV/c the pointing resolution decreases of about a factor 4 in the transverse plane and 20 along the longitudinal direction. The ITS 2 detector will not measure the ionisation energy loss in the silicon material, given the logic signal provided by the read-out modules and this would prevent to exploit the PID techniques for tracks not reaching the TPC. According to the studies performed on the benchmark measurements of $\Lambda_c^+ \to pK^-\pi^+$ decays and low-mass di-electron reconstruction [339], the benefits coming from the preservation of the PID capabilities of the older ITS would have been marginal and it was finally decided to equip the upgraded detector with a binary read-out.

IB layer parameters	Layer 0	Layer 1	Layer 2
Radius (mm)	18.0	24.0	30.0
Length (sensitive area) (mm)	270	270	270
η coverage	$\pm$2.5	$\pm$2.3	$\pm$2.0
Active area (cm^2)	305	408	508
Pixel sensors size (mm^2)	280×56.5	280×75.5	280×94
# pixel sensors / layer		2	
Pixel size (μm^2)		$\mathcal{O}(15 \times 15)$	
Beam pipe inner/outer radius (mm)		16.0/16.5	

TABLE 6.3: Geometrical parameters of the ITS 3 Inner Barrel layout. Table from [345].

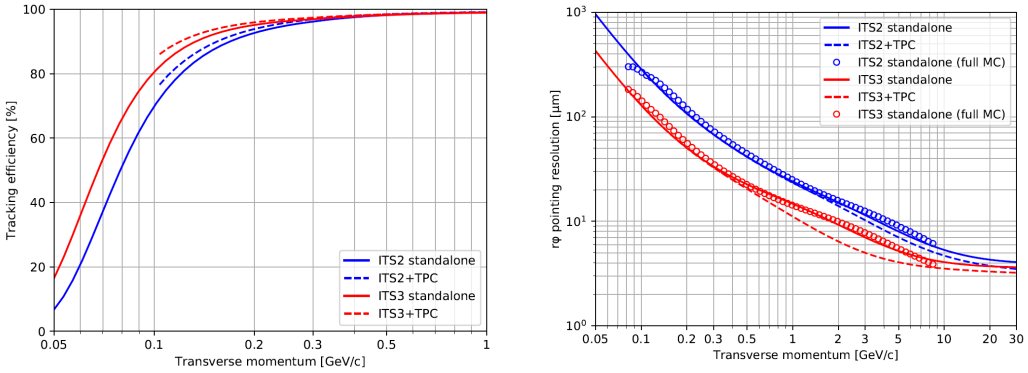

(A) Tracking efficiency.

(B) Pointing resolution on the transverse plane.

FIGURE 6.11: Tracking performances of the ITS 3 detector compared with the ones of the ITS 2. Figure from [345].

6.4 The upgrade concept of the ITS detector for Run 4

Despite the outstanding improvement provided by the usage of the ALPIDE for the single-particle detection in terms of signal/noise ratio, spatial resolution, readout speed and material budget, there is still much room for further MAPS improvements, given the rapid progress of this technology. The CMOS sensor technology recently offered the so called *stitching*, a feature that will allow realising large size MAPS with an area of the order of 14×14 cm^2 and with a reduced sensor thickness of about 20-40 μm. This would allow exploiting the flexible nature of silicon for the construction of large-area curved sensors, to be used to assembly truly cylindrical layers of silicon-only sensors that will further reduce the material budget in a significant way [344]. This technology is conceived to realise a further version of the ITS detector, the "ITS 3", to be commissioned during the long shutdown number 3 (LS3) of the LHC [345]. It will consist of an Inner and Outer Barrel, where the latter corresponds to that of the ITS 2 detector. A completely new Inner Barrel will instead fully replace the ITS 2 one. The new Inner Barrel will consist of two half-barrels, each consisting in three half-layers with a truly cylindrical shape, mounted around the beam pipe as shown in Fig. 6.10. The geometrical parameters of the ITS 3 Inner Barrel

layers are reported in Tab. 6.3. The ITS 3 commissioning will be accompanied by the installation of a new beam pipe, with a lower inner radius of 16 mm and a thickness of 500 μm with respect to that installed during the LS2, with an inner radius of 18.2 mm and a thickness of 800 μm. All the Inner Barrel layers of the ITS 3 detector will be installed closer to the interaction point with respect to the correspondent layers of the ITS 2, with the radius of the innermost one that will decrease from $\sim$ 2.2 cm to $\sim$ 1.8 cm. Furthermore, the usage of stitched sensors, where the distribution of power and electrical signals can be entirely done inside the silicon chip [344], will reduce the material budget for each layer down to 0.05% X_0. This improvement, together with the closer position to the interaction point of the innermost layer will significantly improve the tracking efficiency and impact parameter resolution at low p_T. This can be appreciated in Fig. 6.11, where the tracking efficiency (left) and the pointing resolution along the transverse plane (right) provided by the ITS 2 and ITS 3 detectors are shown. The tracking efficiency of charged particles with transverse momentum below $p_T = 100$ MeV/c is increased by about $\times 1.2 - 2$ with the ITS 3 and a gain of a factor of about $\times 2$ is observed for the impact parameter resolution at all transverse momenta.

The mentioned improvement on the ITS detector for the Run 3 and 4 at the LHC will have a huge impact on the measurement of charmed baryons, especially at low p_T. In the next Sections, the ITS 2 and ITS 3 detector performances for the reconstruction of $\Xi_c^+ \to pK^-\pi^+$ decays in Pb–Pb collisions at $\sqrt{s_{NN}} = 13$ TeV as well as some pilot exploration for the reconstruction of $\Omega_c^0 \to \Omega^-\pi^+$ signal with ITS 3 are described.

6.5 Prospects for $\Xi_c^+ \to pK^-\pi^+$ signal measurement in Pb–Pb collisions at $\sqrt{s} = 5.5$ TeV with the upgraded ITS

The understanding of the charm hadronisation in hadronic collisions at the LHC energies can significantly profit from the measurement of the Ξ_c^+ baryon production in Pb–Pb collisions. According to the most recent measurements of Λ_c^+/D^0, $\Xi_c^{0,+}/D^0$, $\Sigma_c^{0,+,++}/D^0$ and $\Lambda_c^+(\leftarrow \Sigma_c^{0,+,++})/\Lambda_c^+$ in pp collisions at $\sqrt{s} = 13$ TeV, discussed exhaustively in the previous Chapter, the charm quark hadronisation into baryons is not well understood yet, given the not conclusive comparison to the predictions from several theoretical calculations assuming different hadronisation mechanisms for heavy quarks in a hadronic environment. Analogously, the measurement of charm baryons in Pb–Pb collisions would be crucial to understand the influence of the deconfined medium in the heavy baryon formation. The production of Ξ_c^+ baryon is particularly interesting given its strange content, that may boost the Ξ_c^+ production with respect to that of non-strange baryons for $p_T \lesssim 8$ GeV/c in a scenario of hadronisation via coalescence, given the significant increase of strangeness production observed in heavy-ion collisions at the LHC (see Sec. 1.4.5). A hint of larger nuclear modification factor for prompt D_s^+ meson with respect to non-strange D mesons in $4 < p_T < 8$ GeV/c has been already measured with the ALICE experiment in Pb–Pb collisions at $\sqrt{s_{NN}} = 5.02$ TeV [147] and for the B_s^0 meson with respect to B^+ for $7 < p_T < 15$ GeV/c with the CMS experiment [346]. Similarly, a hint of enhancement in Pb–Pb collisions has been observed with the ALICE experiment for the D_s^+/D^+ ratio in the $4 < p_T < 8$ GeV/c interval [147] and for the B_s^0/B^+ ratio in the $10 < p_T < 50$ GeV/c interval in central (0–30%) Pb–Pb collisions by the CMS

collaboration [347]. The comparison of Ξ_c^+ production with that of D mesons in Pb–Pb collision may give further insights in the heavy baryon-to-meson fragmentation fraction ratios in the QGP.

In this work, a performance study for the $\Xi_c^+ \to pK^-\pi^+$ decay channel reconstruction in Pb–Pb collisions at $\sqrt{s_{NN}} = 5.5$ TeV with the upgraded ITS detector layouts were done. In the next Sections, the reconstruction of the Ξ_c^+ candidates is briefly recalled, and the data samples and MC simulations used in the current studies are described. In addition, the performances of ITS 2 and ITS 3 layouts in the $\Xi_c^+ \to pK^-\pi^+$ secondary vertex and decay length reconstruction, and in the significance of the signal reconstruction are discussed.

6.5.1 Data and MC samples and $\Xi_c^+ \to pK^-\pi^+$ reconstruction

The $\Xi_c^+ \to pK^-\pi^+$ performance studies are performed on a sample of about $\sim 3 \times 10^6$ central (0–10%) Pb–Pb events simulated with the HIJING event generator [248, 273], in which charm hadron signals are injected with PYTHIA 8 [319]. In this MC simulations, the ITS 2 geometry is implemented and the performance provided by the ITS 3 layout is mimicked by applying a track-by-track rescaling of the DCA and track parameters with a procedure analogous to that described in 5.3.2, applied to simulate the pointing resolution performances expected with the ITS 3 layout. About 0.6×10^6 Pb–Pb collision events from the 2015 recorded sample are used, as well as about $\sim 0.9 \times 10^6$ simulated events anchored to these collected data. Their usage is described in detail later.

The $\Xi_c^+ \to pK^-\pi^+$ candidates are reconstructed following the same procedure used to tag the $\Lambda_c^+ \to pK^-\pi^+$ decays in the analysis of pp collisions at $\sqrt{s} = 13$ TeV collected in 2016, 2017 and 2018, as discussed in the previous Chapter. The $pK^-\pi^+$ triplets are built with tracks satisfying the criteria reported in Tab. 5.2 and compatible with the searched particle species within 3σ in the TPC and TOF, if its signal is available. On top of these selections, the normalised χ^2 associated to the vertex fitting [348] is asked to be lower than 2 to increase the signal purity. The effect of the selections on the PID variables and on the secondary vertex topology is investigated in detail in the context of the performance studies for the significance of the $\Xi_c^+ \to pK^-\pi^+$ signal measurement.

6.5.2 $\Xi_c^+ \to pK^-\pi^+$ vertex reconstruction

The spatial resolution granted by the upgraded ITS layouts for the reconstruction of the $\Xi_c^+ \to pK^-\pi^+$ decay is quantified by looking at the distribution of residual between generated and reconstructed secondary vertex position coordinates and decay length components. In panels (A) of Fig. 6.12 and 6.13 the residuals of the reconstructed $\Xi_c^+ \to pK^-\pi^+$ decay vertex and decay length, respectively, with respect to the generated quantities and their dependence on the Ξ_c^+ baryon p_T are shown. In the top row, the residuals for $\Xi_c^+ \to pK^-\pi^+$ decays reconstructed with the ITS 2 layout are shown, while in the bottom row the performance granted by the ITS 3 layout is reported. The left columns in Fig. 6.12 shows the residuals for the global x coordinate of the reconstructed secondary vertex, while in the left column of Fig. 6.13 the residuals of the decay length projected along the transverse plane (L_{xy}) are shown. For both Figures, the right column shows the residuals of the global z component of the two quantities. For both variables, the spread of the residuals is observed to decrease with increasing p_T, as expected from the improvement of the pointing resolution (see panel (B) in Fig. 3.17). This behaviour is observed for both ITS 2 and ITS 3

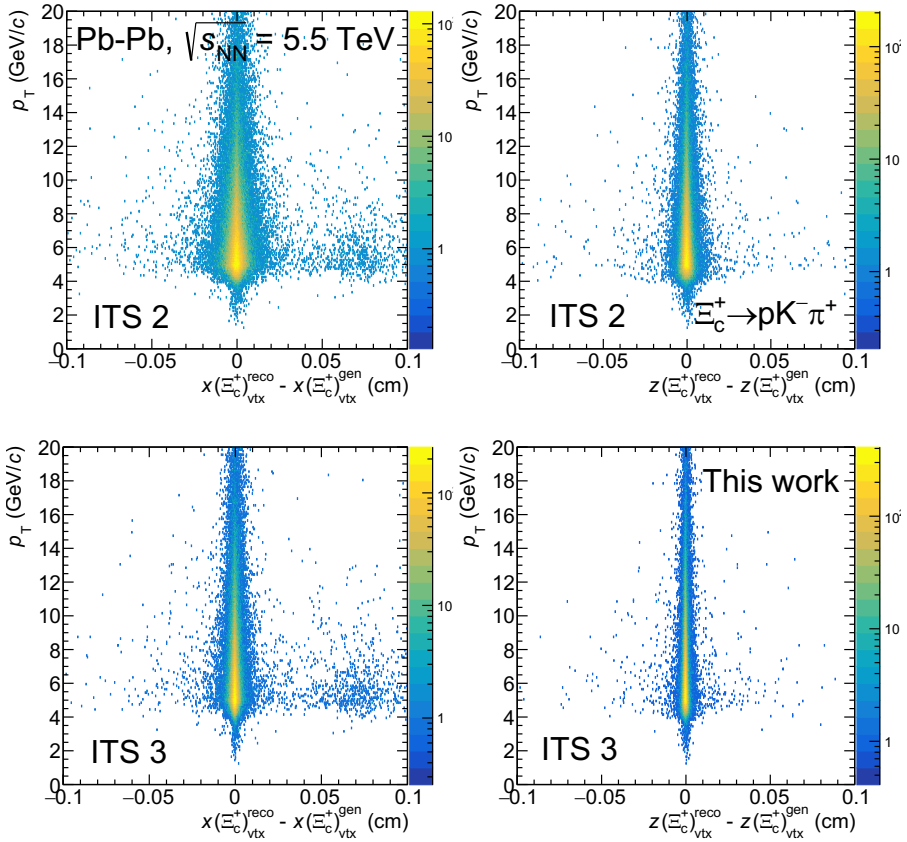

(A) Correlation between Ξ_c^+ baryon p_T and the residuals of the reconstructed $\Xi_c^+ \to pK^-\pi^+$ decay vertex with respect to the generated position for ITS 2 (top row) and ITS 3 (bottom row) layouts. In the left column, the residuals for the global x coordinate are shown, while on the right one the same quantity for the global z coordinate is reported.

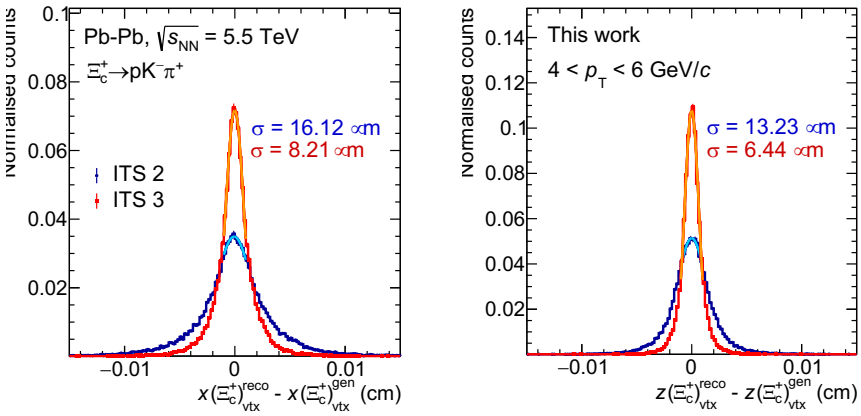

(B) $\Xi_c^+ \to pK^-\pi^+$ secondary vertex residuals along the global x (left) and z (right) global coordinates for Ξ_c^+ baryons with transverse momentum in the $4 < p_T < 6$ GeV/c interval reconstructed with ITS 2 and ITS 3 layouts.

FIGURE 6.12: $\Xi_c^+ \to pK^-\pi^+$ secondary vertex global coordinates.

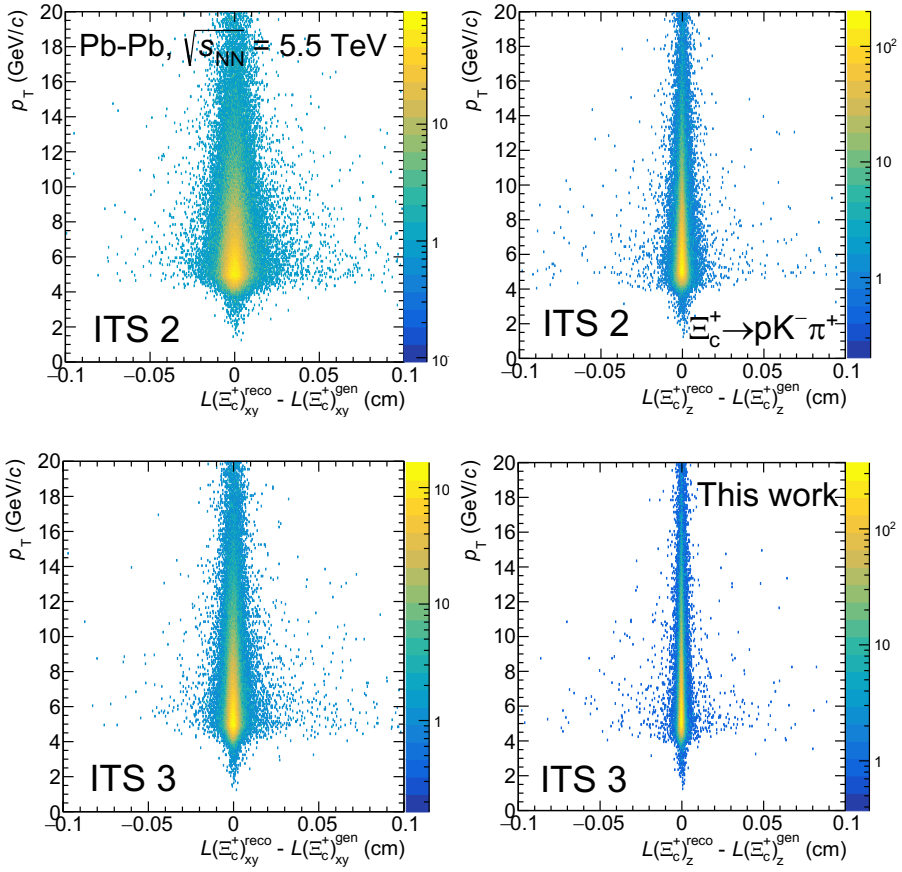

(A) Correlation between Ξ_c^+ baryon p_T and the residuals of the reconstructed $\Xi_c^+ \to pK^-\pi^+$ decay length with respect to the generation one for ITS 2 (top row) and ITS 3 (bottom row) layouts. In the left column, the residuals for the decay length projection along the transverse plane (L_{xy}) are shown, while on the right one the same quantity along the global z coordinate is reported.

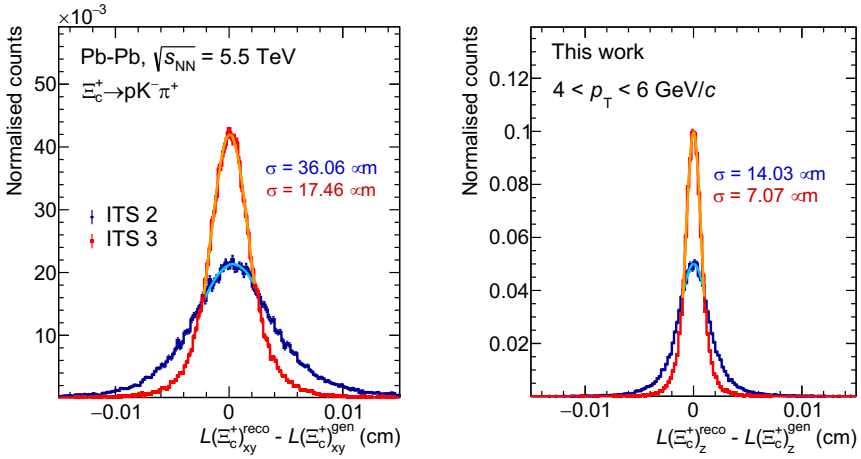

(B) $\Xi_c^+ \to pK^-\pi^+$ decay length residuals along the transverse plane (left) and along the global z coordinate (right) for Ξ_c^+ baryons with transverse momentum in the $4 < p_T < 6\,\mathrm{GeV}/c$ interval with ITS 2 and ITS 3 layouts.

FIGURE 6.13: $\Xi_c^+ \to pK^-\pi^+$ decay length along global coordinates.

detector layouts. The spread of the residuals reconstructed with the ITS 3 is smaller that that observed with the ITS 2. This difference is quantified for the $4 < p_T < 6$ GeV/c transverse momentum interval in the panels (B) of Fig. 6.12 and 6.13. The spatial resolution provided by the two ITS layouts in the reconstruction of the secondary vertex position and the decay length are estimated as the σ of Gaussian fit performed around the peak at null residual. The Gaussian fits are performed within ± 10 µm with the aim of avoiding the non-Gaussian tails of the distributions. However, this approach may introduce some bias in the resolution estimate, due to the arbitrary choice of the range around zero considered for the fit and the consequent influence of the non-Gaussian tails in the σ value. For this reason, the residual distributions are also fitted with the function reported in Eq. 3.12 along the full range, where the exponential trend is used to parametrise the distribution tails. Another approach adopted in this work is to estimate the resolution as the full-width at half-maximum divided by 2.355, in order to avoid possible biases given by an arbitrary treatment of the tails. The resolution estimates from all these tests agree within about 1.5 µm. As reported in Fig. 6.12 and 6.13, the ITS 3 detector (red) grants a spatial precision that is better than the ITS 2 layout (blue) by about a factor 2.

6.5.3 Significance of $\Xi_c^+ \to pK^-\pi^+$ reconstruction in Pb–Pb collisions

The significance optimisation requires to find the best compromise between rejecting background and preserving signal. This study is performed considering Ξ_c^+ baryons with transverse momentum in the intervals $4 < p_T < 6$ GeV/c, $6 < p_T < 8$ GeV/c and $8 < p_T < 12$ GeV/c, assuming an integrated luminosity of Pb–Pb collisions of $\mathcal{L}_{int}^{\text{Run 3, 4}} = 10\ \text{nb}^{-1}$, corresponding to a number of events equal to $N_{ev}^{\text{expected}} \approx 8 \times 10^9$ for the 0–10% centrality class.

The expected background obtained with a given set of single-track and topological variable selection is estimated as follows:

$$B(3\sigma, p_T) = \frac{B_{MC}^{\text{ITS2–3}}(3\sigma, p_T)}{N_{ev}^{\text{MC, ITS2–3}}} \cdot \frac{\frac{B_{\text{data}}^{\text{Run 2}}(\text{full range}, p_T)}{N_{ev}^{\text{Run 2 data}}}}{\frac{B_{MC}^{\text{Run2}}(\text{full range}, p_T)}{N_{ev}^{\text{Run 2 MC}}}} \cdot N_{ev}^{\text{expected}} \cdot \frac{1}{(15/100)^3} \,. \tag{6.8}$$

The amount of background per event within 3σ with respect to the signal mean[4] $B_{MC}^{\text{ITS2–3}}(3\sigma, p_T)$ is estimated from the simulated Pb–Pb collision events. The number of background candidates is counted from the invariant mass distribution, which is fitted with a 3$^{\text{rd}}$ order polynomial and it is normalised to the number of simulated Pb–Pb collisions analysed ($N_{ev}^{\text{MC, ITS2–3}}$). This sample does not include the products of the injected $\Xi_c^+ \to pK^-\pi^+$ decays, but only reconstructed particles generated with HIJING, then associated to the underlying event, are considered to build the triplets. This quantity is scaled assuming that the background per event ratio in data and in MC corresponds to that observed for Run 2 periods and associated MC productions. This scaling is thought to reproduce the expected background given the particle multiplicity measured in Pb–Pb collisions at a similar energy, cancelling any possible effect related to a wrong event multiplicity of the simulated Pb–Pb events. Moreover, this scaling is useful to provide more realistic p_T distributions of primary p, K^- and π^+ particles. Also in these cases the background shape is fitted with a polynomial function and loose selections are used to calculate this ratio. In particular, the background present in the mass range $2.15 < M(pK^-\pi^+) < 2.64$ GeV/c^2 ("full range") is taken into account for the calculation. Then, the absolute quantity

[4] This 3σ interval is used to estimate both signal and background, and consequently the significance.

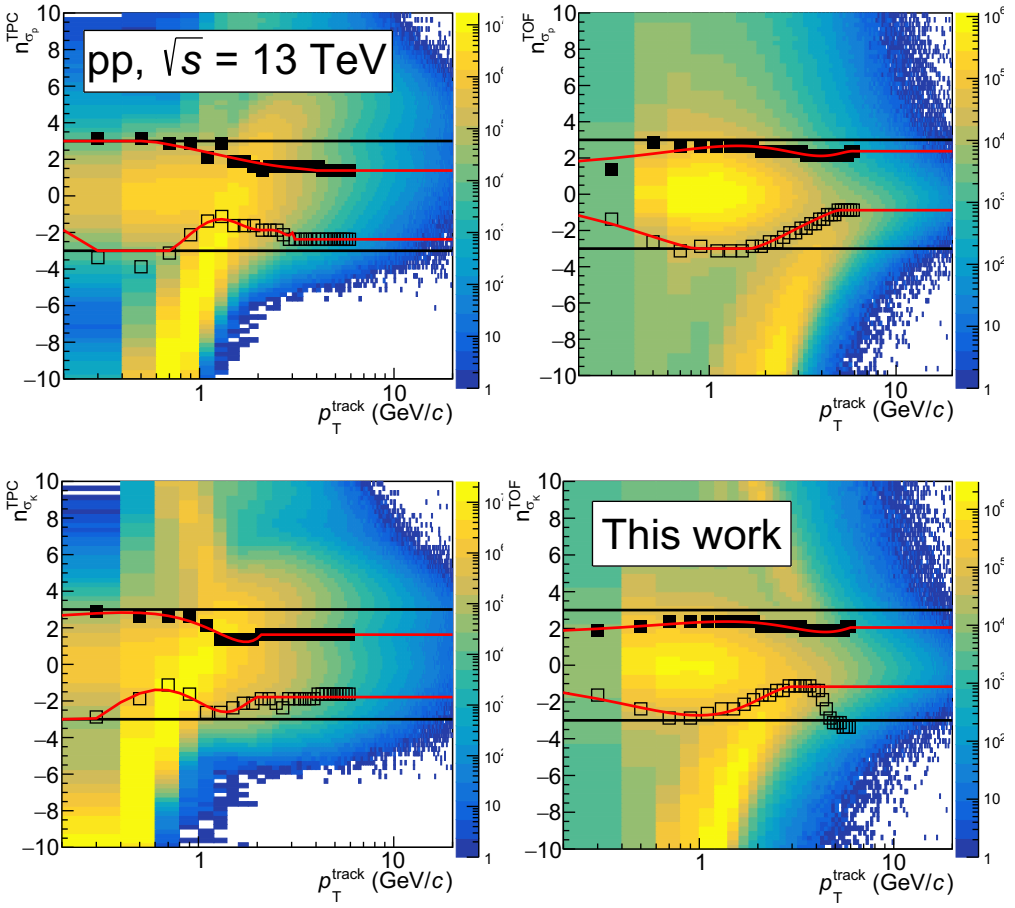

FIGURE 6.14: Distributions of $n^{TPC}_{\sigma_p}$, $n^{TOF}_{\sigma_p}$, $n^{TPC}_{\sigma_K}$ and $n^{TOF}_{\sigma_K}$ as a function of reconstructed transverse momentum of charge particles measured in pp collisions at $\sqrt{s} = 13$ TeV. The red lines circumscribe a region of higher purity for the inspected particle species.

of background is obtained by scaling by the number of expected events ($N_{ev}^{MC,\ ITS2-3}$). Finally, the correct amount of background is obtained with a further scaling by a factor $(1/(15/100)^3)$, which reflects the fact that only 15% of the tracks present in the simulated Pb–Pb events at $\sqrt{s_{NN}} = 5.5$ TeV are considered to build background $pK^-\pi^+$ triplets, to avoid unaffordable CPU times required to produce them from the filtered tracks.

The signal amount, given the value of integrated luminosity, is estimated as follows:

$$S^{Pb-Pb,\ 5.5\ TeV}_{\Xi_c^+,\ raw}(3\sigma, p_T) = \left(\frac{\Xi_c^+}{\Lambda_c^+}\right)_{pp}\Bigg|_{|y|<0.5}(p_T) \cdot \frac{d^2N^{Pb-Pb,\ 5.02\ TeV}_{\Lambda_c^+}}{dp_T dy}\Bigg|_{|y|<0.5}(p_T) \cdot \\ \cdot 2\Delta p_T \Delta y \cdot BR \cdot N_{ev}^{expected} \cdot \alpha_y(acc \times \varepsilon)\ . \tag{6.9}$$

The $\alpha_y(acc \times \varepsilon)$ term defined in Eq. 5.21 is calculated from the dedicated MC production mentioned above. In this study all prompt Ξ_c^+ baryons are considered, since they are directly injected in the simulated Pb–Pb event. This term is used to extract the expected raw yield starting from the expected production yield, given as input.

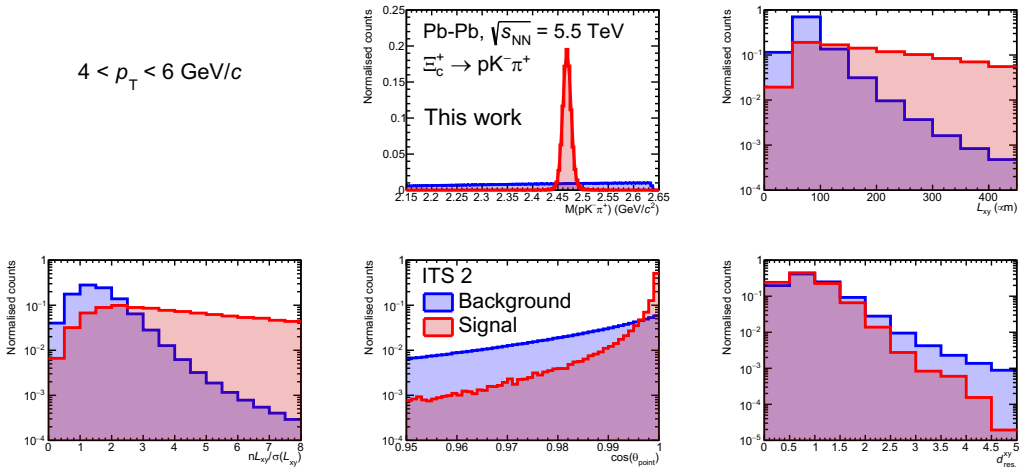

FIGURE 6.15: Variable distributions for signal and background $\Xi_c^+ \to pK^-\pi^+$ candidates in the $4 < p_T < 6$ GeV/c interval in Pb–Pb collisions at $\sqrt{s_{NN}} = 5.5$ TeV reconstructed with the ITS 2 detector.

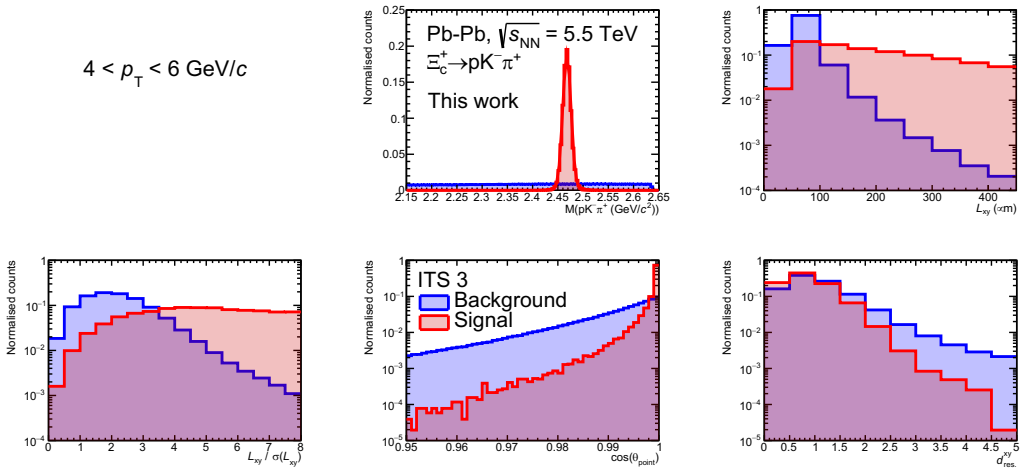

FIGURE 6.16: Variable distributions for signal and background $\Xi_c^+ \to pK^-\pi^+$ candidates in the $4 < p_T < 6$ GeV/c interval in Pb–Pb collisions at $\sqrt{s_{NN}} = 5.5$ TeV reconstructed with the ITS 3 detector.

In this case, the expected yield for the Ξ_c^+ in Pb-Pb collisions at $\sqrt{s_{NN}} = 5.5$ TeV is derived from two independent ALICE measurements:

- the Λ_c^+ corrected yield measured at midrapidity in central Pb–Pb collisions at $\sqrt{s_{NN}} = 5.02$ TeV. The preliminary result shown at SQM2019 conference [349] is used for this study ($d^2N^{\text{Pb–Pb, 5.02 TeV}}_{\Lambda_c^+}/dp_T dy|_{|y|<0.5}$), neglecting the difference on the corrected yield measured at 5.02 TeV and at 5.5 TeV;
- the Ξ_c^+/Λ_c^+ ratio measured at midrapidity ($|y| < 0.5$) in pp collisions at $\sqrt{s} = 13$ TeV [312].

In absence of a measurement in Pb–Pb collisions, the Ξ_c^+/Λ_c^+ ratio in pp is used, being aware that this may underestimate the final estimate of the significance. As a matter of fact, due to the strangeness enhancement expected in the QGP the Ξ_c^+ production may undergo a larger increase with respect to pp compared to what is

Variable	Conditions	Number of cases
L_{xy} (cm)	$> 0, > 0.01, > 0.02$	3
nL_{xy}	$> 1, > 2, > 3$	3
$\cos(\theta_{\text{point}})$	$> 0.990, > 0.995, > 0.999$	3
$d_{\text{res.}}^{xy}$	$< 99, < 3, < 2$	3
Total number of cases		81

TABLE 6.4: Values of topological variables associated to the $\Xi_c^+ \to pK^-\pi^+$ decay used in the context of the significance studies for the signal measurement in Pb–Pb collisions at $\sqrt{s_{NN}} = 5.5$ TeV with ITS 2 and ITS 3 detector layouts.

expected for the non-strange baryons, like the Λ_c^+. The additional factor introduced in Eq. 6.9 restores the dependence on the kinematic range in which the measurement is performed ($2\Delta p_T \Delta y$), as well as the number of considered events ($N_{ev}^{expected}$) and the branching ratio of the chosen decay channel (BR), directly influencing the absolute number of signal counts expected. As remarked later, the ambiguity on the branching ratio BR($\Xi_c^+ \to pK^-\pi^+$) is the cause of the main source of uncertainty on the significance estimate.

In Fig. 6.15 and 6.16 the distributions of the $pK^-\pi^+$ invariant mass $M(pK^-\pi^+)$ and of the topological variables, namely the transverse decay length L_{xy}, the normalised transverse decay length $L_{xy}/\sigma(L_{xy})$, the cosine of pointing angle $\cos(\theta_{\text{point}})$ and the maximum "topomatic" along the transverse plane $d_{\text{res.}}^{xy}$ for signal and background $\Xi_c^+ \to pK^-\pi^+$ candidates in the $4 < p_T < 6$ GeV/c interval with the ITS 2 and ITS 3 detectors, respectively, are shown. The invariant mass distribution of generated $\Xi_c^+ \to pK^-\pi^+$ decays is fitted with a Gaussian function to determine the 3σ interval for the significance estimate, while the combinatorial background shows a pretty flat distribution between 2.15 and 2.64 GeV/c^2. The topological variables are exploited to separate the $\Xi_c \to pK^-\pi^+$ signal from the combinatorial background, together with additional PID selections on the candidate decay products. Apart from the Bayesian PID with maximum probability criterion, a set of 10 different "nσ" selections are tested, according to the correlation of the reconstructed p_T of the candidate Ξ_c^+ and the one of the single tracks exploited in the vertex reconstruction. As a matter of fact, the PID selection criteria are established as a function of the single-track p_T, independently from that of the Ξ_c^+ candidate p_T. They are established according to a study performed originally for the prompt Λ_c^+ reconstruction in pp collisions at $\sqrt{s} = 13$ TeV (previous Chapter), before the final decision of using the Bayesian PID technique. In Fig. 6.14 the distributions of $n_{\sigma_p}^{TPC}$, $n_{\sigma_p}^{TOF}$, $n_{\sigma_K}^{TPC}$ and $n_{\sigma_K}^{TOF}$ as a function of reconstructed single-track p_T measured in pp collisions at $\sqrt{s} = 13$ TeV are shown. The empty and full squares represent respectively the lower and upper limits of a high-purity region determined around zero, where the distribution of the considered particle species is supposed to peak. This limits are determined by projecting the 2D-correlation plots along the y-axis in adjacent p_T intervals and fitting the signal peak around zero with a Gaussian function. Given the significant amount of different particle species contaminating the distribution of interest, the Gaussian function is able to describe only the region around zero and it strongly underestimates the distribution profiles at lower and higher nσ. The edges are then defined as the points where the Gaussian fit underestimates by a factor 2 the distribution profile and this is repeated for adjacent p_T intervals up to $p_T = 6$ GeV/c.

Case	PID selections
0	Bayes PID on n_σ^{TPC} and n_σ^{TOF} (when available) for all decay products
1	$(n_{\sigma_p}^{TPC}(0) \vee n_{\sigma_p}^{TPC}(2)) \wedge n_{\sigma_K}^{TPC}(1)$
2	$\left[(n_{\sigma_p}^{TPC}(0) \wedge n_{\sigma_p}^{TOF}(0)) \vee (n_{\sigma_p}^{TPC}(2) \wedge n_{\sigma_p}^{TOF}(2))\right] \wedge n_{\sigma_K}^{TPC}(1)$
3	$\left[(n_{\sigma_p}^{TPC}(0) \wedge n_{\sigma_p}^{TOF}(0)) \vee (n_{\sigma_p}^{TPC}(2) \wedge n_{\sigma_p}^{TOF}(2))\right] \wedge n_{\sigma_K}^{TOF}(1)$
4	$\left[(n_{\sigma_p}^{TPC}(0) \wedge n_{\sigma_p}^{TOF}(0)) \vee (n_{\sigma_p}^{TPC}(2) \wedge n_{\sigma_p}^{TOF}(2))\right] \wedge n_{\sigma_K}^{TPC}(1) \wedge n_{\sigma_K}^{TOF}(1)$
5	$(n_{\sigma_p}^{TOF}(0) \vee n_{\sigma_p}^{TOF}(2)) \wedge n_{\sigma_K}^{TOF}(1)$
6	$(n_{\sigma_p}^{TOF}(0) \vee n_{\sigma_p}^{TOF}(2)) \wedge n_{\sigma_K}^{TPC}(1)$
7	$(n_{\sigma_p}^{TOF}(0) \vee n_{\sigma_p}^{TOF}(2)) \wedge n_{\sigma_K}^{TPC}(1) \wedge n_{\sigma_K}^{TOF}(1)$
8	$\left[(\lvert n_{\sigma_p}^{TPC}(0)\rvert < 3 \wedge n_{\sigma_p}^{TOF}(0)) \vee (\lvert n_{\sigma_p}^{TPC}(2)\rvert < 3 \wedge n_{\sigma_p}^{TOF}(2))\right] \wedge n_{\sigma_K}^{TOF}(1)$
9	$\left[(\lvert n_{\sigma_p}^{TPC}(0)\rvert < 3 \wedge n_{\sigma_p}^{TOF}(0)) \vee (\lvert n_{\sigma_p}^{TPC}(2)\rvert < 3 \wedge n_{\sigma_p}^{TOF}(2))\right] \wedge n_{\sigma_K}^{TPC}(1)$
10	$\left[(\lvert n_{\sigma_p}^{TPC}(0)\rvert < 3 \wedge n_{\sigma_p}^{TOF}(0)) \vee (\lvert n_{\sigma_p}^{TPC}(2)\rvert < 3 \wedge n_{\sigma_p}^{TOF}(2))\right] \wedge n_{\sigma_K}^{TPC}(1) \wedge n_{\sigma_K}^{TOF}(1)$

TABLE 6.5: Sets of PID selection conditions used in the context of the significance studies of the $\Xi_c^+ \to pK^-\pi^+$ decay signal measurement in Pb–Pb collisions at $\sqrt{s_{NN}} = 5.5$ TeV with ITS 2 and ITS 3 detector layouts. The candidate Ξ_c^+ decay products are labelled with 0, 1 and 2, where the daughter number 1 indicates the track with opposite electric charge with respect to the other two, namely the candidate kaon particle.

The red lines represent the parametrisation of the edge p_T trend, when the defined selection region is narrower than $-3 < n\sigma < 3$, otherwise this is constrained at ± 3 number of σ. This kind of study was originally tried for the prompt Λ_c^+ reconstruction in pp collisions at $\sqrt{s} = 13$ TeV (previous Chapter), before the final decision of using the Bayesian PID technique, and indeed the 2D-correlation plots shown in Fig. 6.14 regard this data sample. The same parametrizations are exploited here to explore their performance for the Ξ_c^+ signal extraction, given a larger flexibility with respect to the Bayesian PID technique and ensuring at the same time a higher purity than that obtained with rectangular $n\sigma$ selections. The different collision system with respect to that in which these significance studies are performed affects the relative amount of particle species, but this does not compromise the performance in terms of efficiency.

The full set of topological variable and PID selection criteria tested in this work is reported in Tabs. 6.4 and 6.5. In particular, three values for each topological variable are considered, as well as eleven different PID selections. In the latter Table, the candidate Ξ_c^+ decay products are labelled with 0, 1 and 2, where the daughter number 1 indicates the track with opposite electric charge with respect to the other two, namely the candidate kaon product. When not specifically indicated, the "$n_{\sigma_p}^{TPC}(0)$" notation indicates that the daughter 0 is required to satisfy the condition

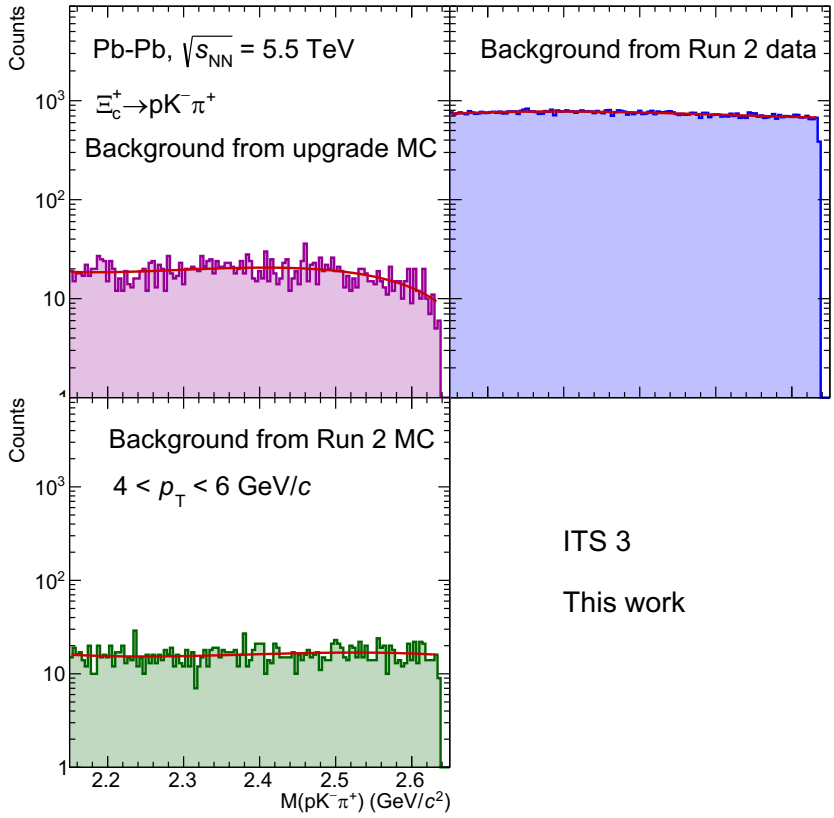

FIGURE 6.17: Invariant mass $M(pK^-\pi^+)$ distribution in the simulated Pb–Pb events at $\sqrt{s_{NN}} = 5.5$ TeV (top left), in the collected Pb–Pb collisions at $\sqrt{s_{NN}} = 5.02$ TeV (top right) and in the associated MC production (bottom left) of combinatorial $pK^-\pi^+$ triplets in the $4 < p_T < 6$ GeV/c interval reconstructed with the ITS 3 detector using the selections reported in Tab. 6.6.

$\text{low}(p_T) < n_{\sigma_p}^{TPC}(p_T) < \text{up}(p_T)$, where "low" and "up" refer to the red lines delimiting the selection region shown in Fig. 6.14. A similar notation is used also for the TOF signal and the other decay products. Combining all the variations on the topological variables and the PID selection, the expected significance for a total of 891 sets is calculated in the three p_T intervals considered in the analysis. The background within $\pm 3\sigma$ is estimated following the recipe given by Eq. 6.8, applying on the combinatorial $pK^-\pi^+$ triplets the different selection criteria listed in Tabs. 6.4 and 6.5. The invariant mass distribution from the simulated Pb–Pb collisions at $\sqrt{s_{NN}} = 5.5$ TeV, the one from collected Pb–Pb events at $\sqrt{s_{NN}} = 5.02$ TeV and from the associated MC simulations for combinatorial $pK^-\pi^+$ triplets with $4 < p_T < 6$ GeV/c reconstructed with the ITS 3 detector are shown in Fig. 6.17. In particular, these distributions are obtained with the set of selections chosen for the final estimate of the significance, reported in Tab. 6.6. At the same time, the expected $\Xi_c^+ \to pK^-\pi^+$ signal within $\pm 3\sigma$ is estimated using Eq. 6.9 for each of the considered set of selections, which influences the value of the $\alpha_y(\text{acc} \times \varepsilon)$ correction term. Another ingredient entering the signal estimate consists in the BR($\Xi_c^+ \to pK^-\pi^+$) value, which at the time of writing this thesis is not precisely known. In this work, three different values for the branching ratio are taken into account, according to what present in literature:

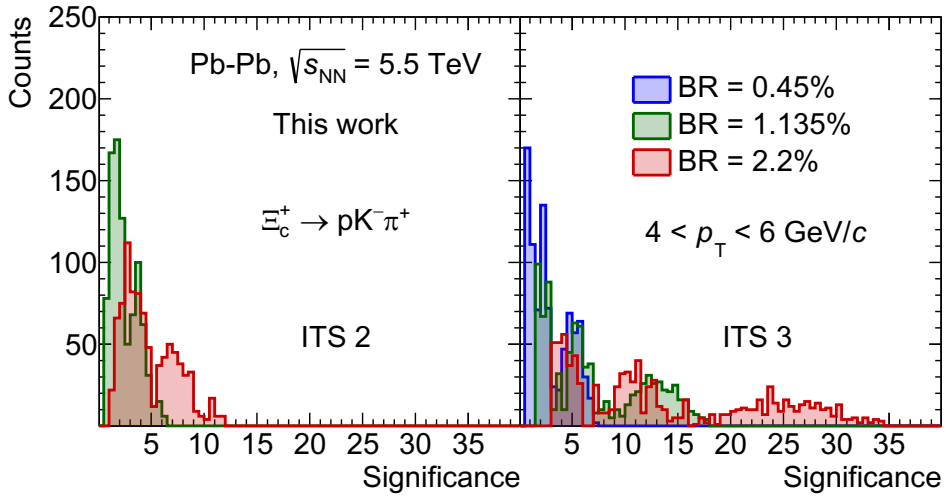

FIGURE 6.18: Expected significance for the $\Xi_c^+ \to pK^-\pi^+$ signal measurement in the $4 < p_T < 6$ GeV/c interval in Pb–Pb collisions at $\sqrt{s_{NN}} = 5.5$ TeV obtained with the combinations of topological variable and PID selections listed in Tabs. 6.4 and 6.5 and with the three BR($\Xi_c^+ \to pK^-\pi^+$) values available in the literature [315, 333, 350]. The left panel shows the results for $\Xi_c^+ \to pK^-\pi^+$ candidates reconstructed with the ITS 2 detector, while in the right one the results obtained with the ITS 3 detector are reported.

1. the experimental measurement performed by the Belle experiment [315], providing the value BR=$(0.45 \pm 0.21 \pm 0.07)$%;

2. the experimental measurement performed by the LHCb experiment [333], providing the value BR=$(1.135 \pm 0.002 \pm 0.387)$%;

3. the theoretical prediction provided in Ref. [350], providing the value BR = (2.2 ± 0.8)%.

In Fig. 6.18 the expected significance for the $\Xi_c^+ \to pK^-\pi^+$ signal measurement in the $4 < p_T < 6$ GeV/c interval in Pb–Pb collisions at $\sqrt{s_{NN}} = 5.5$ TeV obtained with the combinations of topological variable and PID selections listed in Tabs. 6.4 and 6.5 is shown. The results obtained by reconstructing the $\Xi_c^+ \to pK^-\pi^+$ decays with the ITS 2 and ITS 3 detectors are shown in the left and right panel, respectively, where the different distributions are obtained with the BR($\Xi_c^+ \to pK^-\pi^+$) values listed above. The significance reaches higher maximum values as soon as the branching ratio increases, as expected. Furthermore, the expected significance estimated with the ITS 3 layout is higher than that obtained with the ITS 2 for the same value of the branching ratio. In particular, the gain provided by the ITS 3 can be quantified with a factor of about 3 and, given that the maximum significance estimated with the highest branching ratio value, is of the order of about 30 with ITS 3. The feasibility of this analysis with ITS 2 is not granted. As clearly visible from the left panel, in case of BR($\Xi_c^+ \to pK^-\pi^+$) = 1.135% the estimated significance in the signal extraction is always contained below 5 with the ITS 2 detector, while with a branching ratio value smaller of about a factor 2.5 the signal extraction looks not doable. Even with the ITS 3 the maximum expected significance is of the order of ~ 5 in case of BR($\Xi_c^+ \to pK^-\pi^+$) = 0.45%, which would not grant an outstanding statistical precision in the signal extraction even if the analysis would be still doable.

	p_T (GeV/c)		
Variable	$[4, 6)$	$[6, 8)$	$[8, 12)$
L_{xy} (cm)	> 0.02	> 0.02	> 0.02
nL_{xy}	> 3	> 2 (ITS 2) > 1 (ITS 3)	> 3 (ITS 2) > 1 (ITS 3)
$\cos(\theta_{\text{point}})$	> 0.995 (ITS 2) > 0.99 (ITS 3)	> 0.99	> 0.999 (ITS 2) > 0.99 (ITS 3)
$d_{\text{res.}}^{xy}$	< 2	< 2	< 99 (ITS 2) < 2 (ITS 3)
PID set	1	1	1
$\alpha_y(\text{acc} \times \varepsilon)$	7% (ITS 2) 8% (ITS 3)	19%	26%

TABLE 6.6: Topological variable and PID selection criteria chosen for the significance estimated on the $\Xi_c^+ \to pK^-\pi^+$ signal measurement in Pb–Pb collisions at 5.5 TeV with the ITS 2 and ITS 3 detectors. The "PID set " field refers to the combinations of PID selections listed in Tab. 6.5.

To provide a final estimate of the expected significance for the $\Xi_c^+ \to pK^-\pi^+$ signal measurement, one set of topological variables and PID selection criteria is chosen in each p_T interval for the reconstruction done with ITS 2 and ITS 3 detectors. This choice is done looking at the significance, as well as the ingredients used for the background calculation. As a matter of fact, the application of tight selections may reject almost all the statistics of combinatorial $pK^-\pi^+$ triplets, especially in the simulated events where the generated statistics is not large. This may cause an increase of the significance, though not always corresponding to a real gain in the signal extraction. This statement is supported by the fact that using only 5% of the tracks to build the combinatorial triplets high relative statistical fluctuations are observed given the low statistics for tight selections, accompanied by a bad background description. This feature causes a fake increase up to about a factor 2 in the expected significance with respect to what obtained with the same selections but keeping 15% of tracks for the combinatorics. This effect is observed for the tightest selections and consequently the highest expected significance is observed to be associated always to one of such "pathologic" sets of selections. For this reason, a more conservative approach is finally employed and looser selections are chosen to provide the final results, given that they ensure a good background description, as shown in Fig. 6.17. The selection criteria chosen to provide the significance estimate for the $\Xi_c^+ \to pK^-\pi^+$ signal measurement in Pb–Pb collisions at $\sqrt{s_{NN}} = 5.5$ TeV with ITS 2 and ITS 3 detectors are reported in Tab. 6.6. The selection efficiency for the $\Xi_c^+ \to pK^-\pi^+$ signal granted by these selections increases from about 7% at $4 < p_T < 6$ GeV/c to about 26% at $8 < p_T < 12$ GeV/c and it does not show any significant difference between ITS 2 and ITS 3 detectors. However, the usage of either the two layouts affects the background rejection, and consequently the expected significance. This quantity is shown in Fig. 6.19, where the final results in the three p_T intervals obtained with the ITS 3 detector are reported. The result is accompanied by the uncertainties deriving from the statistical uncertainties of the different ingredients involved in the significance calculation, (empty box), such as

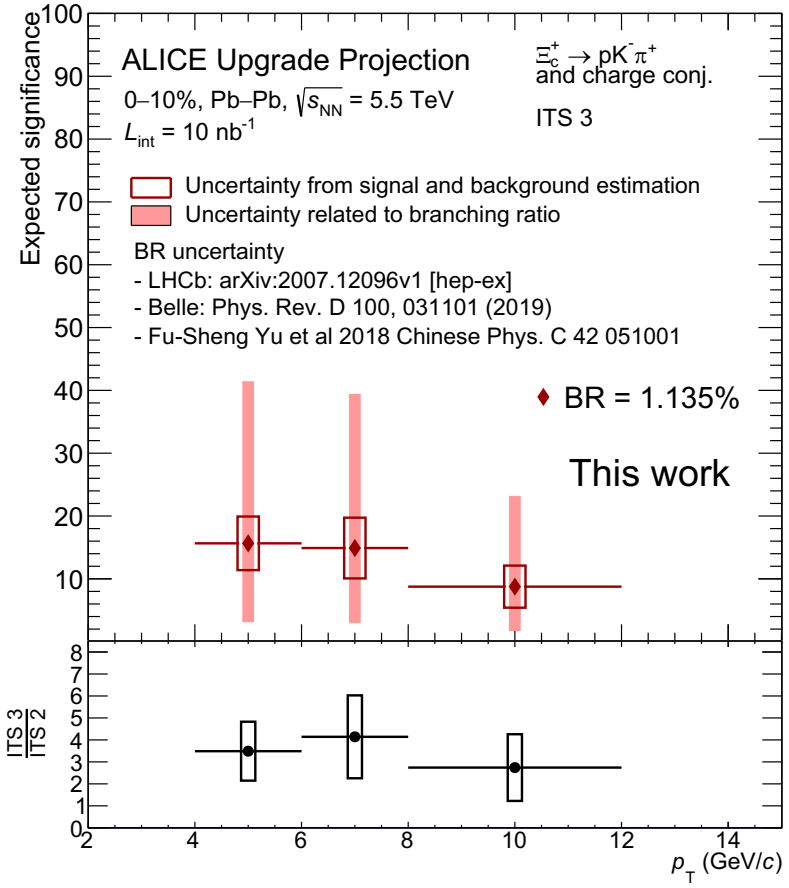

FIGURE 6.19: Expected significance for the $\Xi_c^+ \to pK^-\pi^+$ signal measurement in Pb–Pb collisions at $\sqrt{s_{NN}} = 5.5$ TeV with the ITS 3 detector. The significance is estimated considering the BR($\Xi_c^+ \to pK^-\pi^+$) provided by the LHCb measurement [333]. The bottom panel shows the gain with respect to the same estimate performed with the ITS 2 detector.

the signal and background counts. The significance is estimated considering the BR($\Xi_c^+ \to pK^-\pi^+$) provided by the LHCb measurement [333] and the other two values are used to provide a further systematic uncertainty, which is reported as a shaded box. This corresponds to the envelope between the upper and lower significance obtained with the three branching ratios varied within their uncertainties. In the bottom panel, the gain provided by the ITS 3 with respect to the ITS 2 is quantified as the ratio of the significance given by the reconstruction using the two detector layouts. In this case, the branching ratio related uncertainty cancels out since it is fully correlated between the two estimates, under the assumption of $S/B \ll 1$. The ITS 3 provides a gain of about a factor $\times 3$ with respect to the ITS 2, thanks to the higher capability in the rejection of combinatorial background. This can be considered the most important piece of information learnt from this study, and it strongly supports the proposal of the ITS 3 detector, being crucial for the measurement of charm baryons in hadronic collisions with the ALICE apparatus using the collected data during Run 4. However, this study does not provide a definitive value of the expected significance for the $\Xi_c^+ \to pK^-\pi^+$. A larger sample of simulated Pb–Pb

Species	Valence quarks	Mass (MeV/c^2)	$c\tau$ (cm)	Decay channel (BR)
Σ^+	uus	1189.37 ± 0.07	2.404	$p\pi^0$ ($\sim 52\%$), $n\pi^+$ ($\sim 48\%$)
Ξ^-	dss	1321.71 ± 0.07	4.91	$\pi^-\Lambda(\rightarrow p\pi^-)$ ($\sim 100\% \times 64\%$)
Ω^-	sss	1672.45 ± 0.29	2.461	$K^-\Lambda(\rightarrow p\pi^-)$ ($\sim 68\% \times 64\%$)
Ξ_c^+	usc	$2467.94^{+0.17}_{-0.20}$	136.6×10^{-4}	$\Xi^-\pi^+\pi^+$ (Defined as 1)
Ξ_c^0	dsc	$2470.90^{+0.22}_{-0.29}$	45.8×10^{-4}	$\Xi^-\pi^+$ ($\sim 1.43\%$)
Ω_c^0	ssc	2695.2 ± 1.7	80×10^{-4}	$\Omega^-\pi^+$ (Defined as 1)

TABLE 6.7: Multi-strange and strange-charm baryons. Numbers taken from [3].

events is needed to increase the combinatorial background statistics and see if even larger significance values can be achieved with tighter selections than those listed in Tab. 6.6. Moreover, this performance studies can benefit also from the application of ML techniques, as discussed in Sec. 6.1.1. Anyway, at the moment a precise estimate is still compromised by the huge ambiguity on the BR($\Xi_c^+ \rightarrow pK^-\pi^+$), given the different values available in the literature.

6.6 The upgraded ITS as a "strangeness tracker"

The layers of ITS inner barrel will be characterised by radii going from about 2.2 cm to 4.2 cm in the ITS 2 and from about 1.8 cm to 3.0 cm in the ITS 3. As reported in Tab. 6.7 the proper decay length of multi-strange charged baryons is of the order of some centimetres, thus the same magnitude of the inner barrel layers of the ITS. Given the improved spatial resolution granted by this detector, it will be possible to reconstruct and identify the signal released by these strange charged particles. In other words, with a read-out rate of 400 kHz in pp collisions, the new ITS might be thought as a "MHz bubble chamber", with the possibility to be used to reconstruct the short tracks associated to each strange charged particles similarly to what could be done with bubble chambers. The reconstruction of these mini tracks can improve the pointing at the primary vertex of the cascades associated to the multi-strange baryon decays, whose reconstruction only with the TPC tracks does not grant a comparable spatial resolution. This aspect is fundamental to improve the identification of secondary vertices of strange-charm baryons decaying to strange hadrons, given the intrinsic spatial displacement with respect to the primary vertex of the order of tens or hundreds of microns, as reported in Tab. 6.7. Promising physics cases are the reconstruction of the $\Xi_c^+ \rightarrow \Xi^-\pi^+\pi^+$ decay, exploiting the intrinsic displacement of about 137 μm of the Ξ_c^+ and the proper decay length of about 4.9 cm of the Ξ^-, and the $\Omega_c^0 \rightarrow \Omega^-\pi^+$ decay, which can profit from the tracking of the Ω^- baryon, whose proper decay length is about ~ 2.5 cm, as well as from the Ω_c^0 lifetime, giving an intrinsic displacement of about ~ 80 μm. The performance achieved with this innovative reconstruction technique is sensitive to the detector layout. Therefore, its

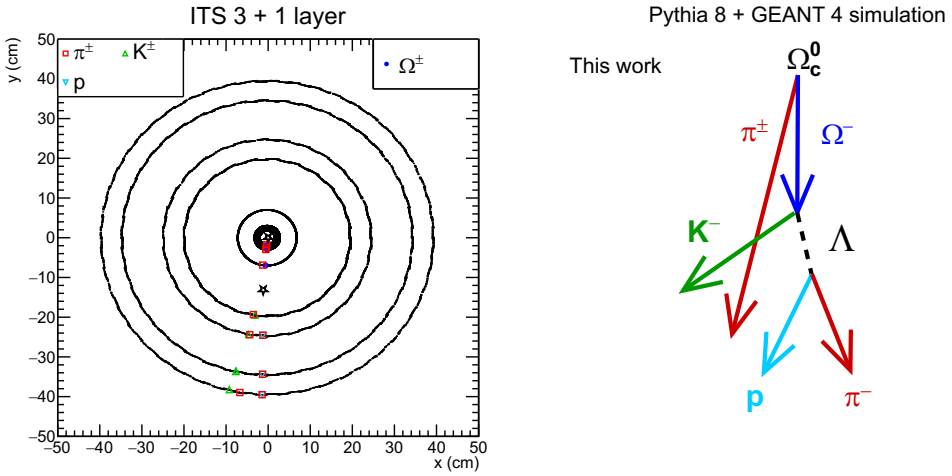

FIGURE 6.20: Example of $\Omega_c^0 \to \Omega^-\pi^+$ decay simulated with PYTHIA 8 event generator and GEANT 4 transport code then reconstructed with the ITS. The adopted layout for the detector consists in the ITS 3 one with the addition of a further layer with a radius of $R = 7$ cm. A schematic representation of the decay is reported in the right panel.

study is fundamental to define the ideal geometry and layout for the ITS 3 detector, whose final design may be revisited in case these studies provide positive outcomes.

In this thesis, an exploratory study for the $\Omega_c^0 \to \Omega^-\pi^+$ decay reconstruction exploiting the strangeness tracking technique is described. In particular, the main goal of this work is to study the feasibility of the primary Ω^- baryon separation from the $\Omega^-(\leftarrow \Omega_c^0)$ ones in an ideal environment, without considering possible inefficiencies or fake-cluster associations in the tracking. Moreover, some preliminary studies about alternative ITS 3 layouts are touched, starting from an "improved ITS" layout used as default, as discussed in the next Section. In these studies, only the ITS detector is exploited, namely no track reconstruction using the information from TPC is used.

6.6.1 The $\Omega_c^0 \to \Omega^-\pi^+$ decay: primary Ω^- vs. $\Omega^-(\leftarrow \Omega_c^0)$

The decay channel chosen to explore the performance of the strangeness tracking technique with the upgraded ITS 3 detector is the $\Omega_c^0 \to \Omega^-\pi^+$. In Fig. 6.20 a typical event display related to a $\Omega_c^0 \to \Omega^-\pi^+$ decay and the consequent $\Omega^- \to \Lambda K^- \to p\pi^- K^-$ cascade is shown. The kinematic of the Ω_c^0 decay is simulated with the PYTHIA 8 event generator, while the decay of strange hadrons as well as the transport of charged particles through the ITS layers is managed with the GEANT 4 transport code. The simulations are based on a realistic implementation of the beam pipe. Furthermore, in these simulations no magnetic field is applied (B = 0) and the intrinsic resolution of the detector is not implemented. The latter aspect is mimicked with a smearing of the generated hit coordinates, as explained later in this Section. The default ITS geometry adopted in these studies corresponds to the ITS 3 one, to which an additional layer with a radius of $R = 7$ cm is added. The coloured points highlighted in the event display correspond to the generated hits related to the charged particles crossing the ITS layers and the different colours indicate the species taken into account. With the upgraded ITS 3 layout is possible to observe the

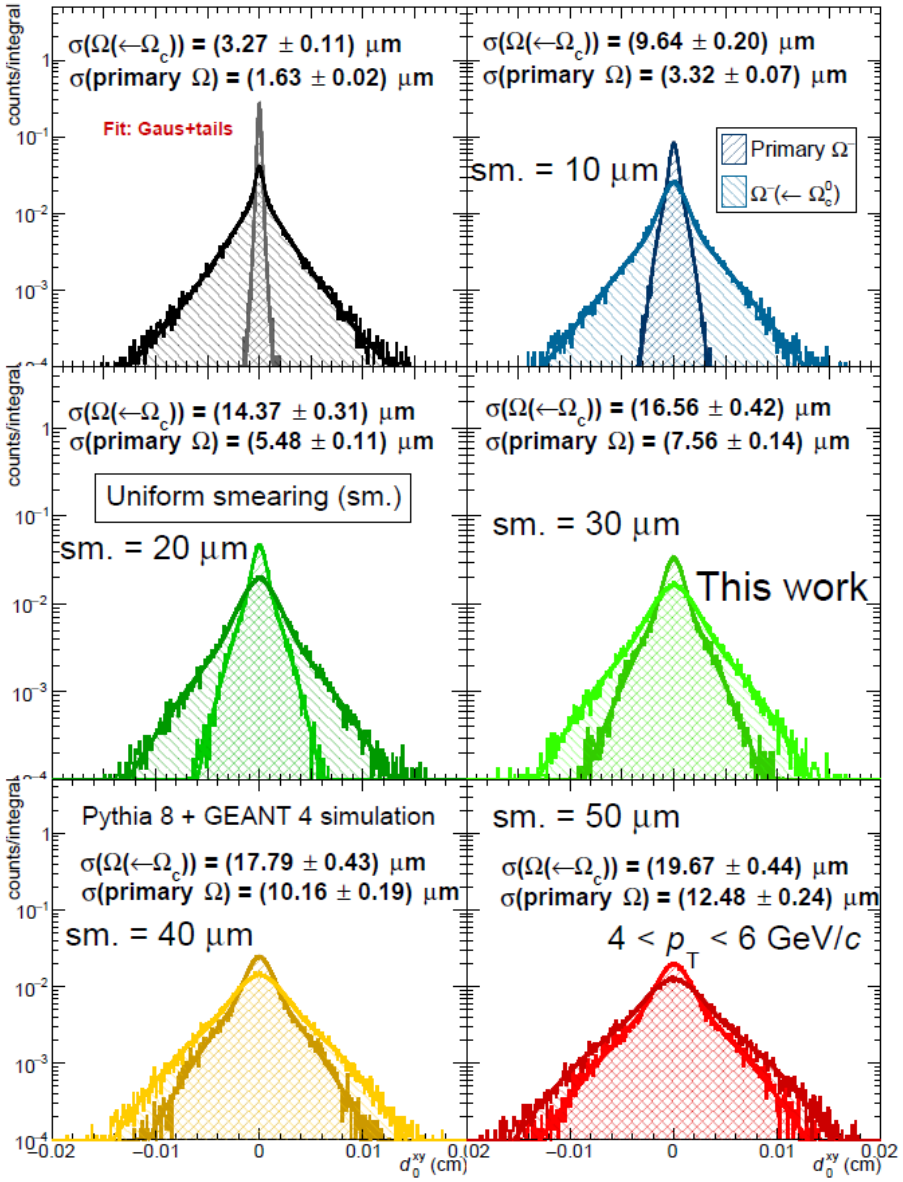

FIGURE 6.21: Impact parameter (d_0^{xy}) distribution for primary Ω^- and $\Omega^-(\leftarrow \Omega_c^0)$ baryons with $4p_T < 6$ GeV/c from PYTHIA 8 + GEANT 4 simulations with the ITS detector. The adopted layout for the detector consists in the ITS 3 one with the addition of a further layer with a radius of $R = 7$ cm. The comparison between primary Ω^- and $\Omega^-(\leftarrow \Omega_c^0)$ baryons is proposed under the hypothesis of different uniform smearing for the generated hits in the ITS, within a range of 0 μm (no smearing), 10 μm, 20 μm, 30 μm, 40 μm and 50 μm.

signal released in the 4 innermost layers by the charged Ω^- baryon (blue), which is produced together with a π^+ (red) from the Ω_c^0 decay, that takes place in correspondence of the nominal interaction point (star). A K^- meson (green) and a Λ baryon, which decays (star) into a proton (light blue) and a π^- (red), deriving from the Ω^- cascade are also fully reconstructed in the ITS detector.

The events with a $\Omega_c^0 \rightarrow \Omega^-\pi^+$ decay are compared with those containing a primary Ω^-, namely directly produced at the interaction point. Such a comparison is fruitful to understand whether the $\Omega_c^0 \rightarrow \Omega^-\pi^+$ secondary vertex can be resolved

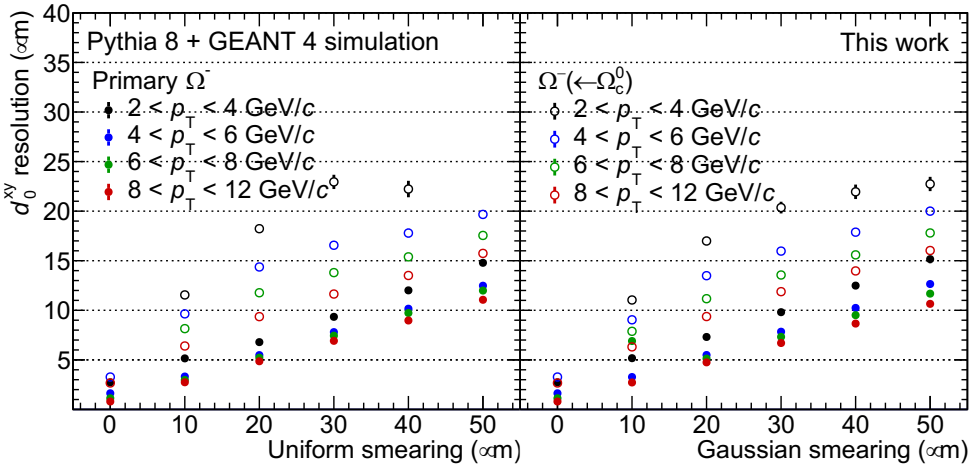

FIGURE 6.22: Impact parameter resolution for the reconstruction of primary Ω^- and $\Omega^-(\leftarrow \Omega_c^0)$ baryons in different transverse momentum intervals obtained with several uniform (left) and Gaussian (right) smearing ranges from the simulation with PYTHIA 8 + GEANT 4 of 300k primary Ω^- baryons and 300k $\Omega_c^0 \to \Omega^-\pi^+$ decays. The adopted layout for the detector is the ITS 3 one with the addition of a further layer with a radius of $R = 7$ cm.

from the primary one. This is possible only if the Ω^- deriving from the Ω_c^0 decay can be separated from the bulk of primary Ω^- baryons. The performance on this separation is investigated by means of the reconstructed impact parameter d_0^{xy} of the Ω^- baryon, corresponding to the distance of closest approach of the Ω^- reconstructed track to the primary vertex in the transverse plane. Given the decay kinematics, the impact parameter of $\Omega^-(\leftarrow \Omega_c^0)$ baryons is higher with respect to the primary Ω^- ones, because of the non-negligible proper decay length of the Ω_c^0 of $c\tau = 80$ μm that causes a displacement from the interaction point. For this reason, the impact parameter distribution for primary Ω^- is expected to be narrower than that of $\Omega^-(\leftarrow \Omega_c^0)$ baryons. However, the effective spread observed on the reconstructed Ω^- baryons is also influenced by other aspects which may prevent us from resolving the two cases. First of all, the multiple scattering in the beam pipe as well as in the innermost layers of the ITS detector is expected to broaden the impact parameter distribution especially at low p_T. Furthermore, the effective spread of the impact parameter distribution is influenced by the intrinsic spatial resolution of the detector, which is not implemented in the MC simulations. For this purpose, the global coordinates of the generated hits are randomly smeared with respect to the original position according to two different approaches:

- uniform smearing: given a value r for the range of the i-th spatial coordinate, then the original value $x_i^{\text{orig.}}$ is mapped into x_i' so that $x_i' = x_i^{\text{orig.}} + \text{Uniform}(-r/2, +r/2)$;
- Gaussian smearing: in this case, the original value $x_i^{\text{orig.}}$ is mapped into x_i' so that $x_i' = x_i^{\text{orig.}} + \text{Gaus}(0, r/\sqrt{12})$.

Given that the pixel dimensions in the ITS 2 and ITS 3 detectors are respectively about 30×30 μm and 15×15 μm, reasonable choices for the range r consist in

values of the order of some tens of microns. In this work, both the uniform and Gaussian smearing approaches are considered to study the separation between primary Ω^- and $\Omega^-(\leftarrow \Omega_c^0)$ baryons considering a smearing range increasing up to 50 μm. In Fig. 6.21 the impact parameter (d_0^{xy}) distributions for primary Ω^- and $\Omega^-(\leftarrow \Omega_c^0)$ baryons in the $4 < p_T < 6$ GeV/c interval obtained from the generation of 3×10^5 primary Ω^- baryons as well as 3×10^5 $\Omega_c^0 \rightarrow \Omega^-\pi^+$ decays with PYTHIA 8 + GEANT 4 simulations given an uniform smearing of the hit coordinates are shown. As expected, the d_0^{xy} distribution of primary Ω^- baryons looks narrower than what observed for $\Omega^-(\leftarrow \Omega_c^0)$ ones and the separation between the two samples worsen with increasing smearing range. In particular, the top left panel shows the case without applying any smearing, which would reflect the performances granted by a detector with a perfect resolution. In this case, only the spread given by the multiple scattering emerges, since it is implemented in the GEANT transport, but the hit coordinates are not affected by the intrinsic resolution of the detector. The impact parameter distributions are fitted with the function defined in Eq. 3.12 and the Gaussian resolution σ is considered to quantify the separation between the two samples. The distributions shown in Fig. 6.21 refer to Ω^- baryons with a transverse momentum in the interval $4 < p_T < 6$ GeV/c and they are obtained after applying a uniform smearing on the global coordinates of the generated hits. To study the dependence of the detector performance as a function of p_T, the analysis is repeated for Ω^- baryons with a transverse momentum in $2 < p_T < 4$ GeV/c, $6 < p_T < 8$ GeV/c and $8 < p_T < 12$ GeV/c, and also the Gaussian smearing on the global coordinates of the generated hits is tested. In Fig. 6.22 the measured impact parameter resolution for the reconstruction of primary Ω^- and $\Omega^-(\leftarrow \Omega_c^0)$ baryons in different transverse momentum intervals obtained with several uniform (left) and Gaussian (right) smearing values are shown. For all the p_T intervals considered in this work, the impact parameter resolution of the primary Ω^- baryons looks smaller by about a factor of about $\times 1.5 - 3$ with respect to the $\Omega^-(\leftarrow \Omega_c^0)$ ones. This is valid for both smearing strategies. The d_0^{xy} resolution for each value of the smearing range is observed to decrease with increasing p_T. This behaviour is the direct consequence of the decreasing influence of the multiple scattering with increasing p_T, which provokes an improvement of the pointing resolution.

As soon as the smearing range increases the tails become more relevant, especially for the primary Ω^-. This effect, that in principle may prevent a significant separation from the decay products of Ω_c^0 decays, derives from the lack of a minimum number of ITS hits required for the Ω-tracklet reconstruction. As a matter of fact, all the generated Ω^- baryons releasing a hit in at least 2 layers of the ITS are kept in this study[5], but the description of the trajectory is much less accurate for particles with only 2 or 3 associated points and this causes the broadening of the tails and, as a consequence, of the estimated resolution. In Fig. 6.23 the impact parameter distribution of primary Ω^- (left) and $\Omega^-(\leftarrow \Omega_c^0)$ baryons (right) reconstructed with a transverse momentum in the $4 < p_T < 6$ GeV/c interval after applying a uniform smearing on the generated hit coordinates within a range of 30 μm and requiring a different number of hits for the track reconstruction is shown. When

[5]The simulations are performed with a null magnetic field (B = 0), hence the charged particles are not bended and follow a straight-line trajectory. A polynomial of first order is used to interpolate the points on the transverse plane. Therefore, 2 points are enough. This would not be true in case of non-null magnetic field (B ≠ 0), given the induced trajectory bending. However, the assumption of linear trajectories should not bias the results, considering that for transverse momenta of the order of GeV/c the curvature radius is about 7 m.

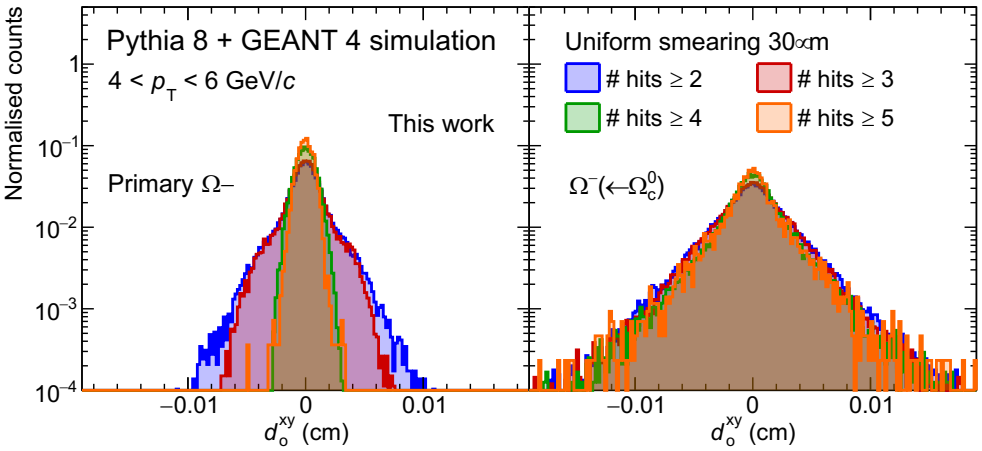

FIGURE 6.23: Impact parameter d_0^{xy} distribution of primary Ω^- and $\Omega^-(\leftarrow \Omega_c^0)$ baryons reconstructed with a transverse momentum in the $4 < p_T < 6$ GeV/c interval in PYTHIA 8 + GEANT 4 simulations with different requirements on the number of hits in the ITS detector, after applying a uniform smearing along a range of 30 μm of the generated hit coordinates. The layout adopted for these studies corresponds to the ITS 3 one with the addition of a further layer with a radius of $R = 7$ cm.

reconstructing a primary Ω^- with at least 4 hits in the ITS detector, the d_0^{xy} gets suddenly sharper, with a relative increase of statistics around the peak. This gets even more evident when requiring at least 5 hits in the ITS. On the other hand, the distribution of $\Omega^-(\leftarrow \Omega_c^0)$ baryons undergoes a milder modification when modifying the condition on the minimum number of hits, considering the intrinsic larger displacement provoked by the proper decay length of Ω_c^0 baryon. Finally, a higher number of points involved in the Ω^- baryon reconstruction implies a better separation between the two sample. In particular, the fourth layer added at a radius of $R = 7$ cm seems to significantly help to constrain the quality of the reconstructed Ω^-, given the observed improvement when requiring at least 3 or 4 hits in the ITS.

Another variable to be exploited for the separation of $\Omega_c^0 \to \Omega^-\pi^+$ signal from the combinatorial background is the product of the daughter impact parameters $d_0^{xy}(\Omega^-) \times d_0^{xy}(\pi^+)$. By definition, the impact parameter is a kinematic variable associated to each reconstructed track defined either with positive or negative sign determined by $\cos(\arctan(p_y/p_x))$, where p_x and p_y correspond to the track momentum components along the global x and y axes. Given the non-negligible proper decay length of the Ω_c^0 baryon and the consequent induced displacement from the primary vertex, the $\Omega_c^0 \to \Omega^-\pi^+$ decay products are expected to have a larger impact parameter with respect to primary particles and with an opposite sign, considering the decay kinematics that forces the Ω^- and the π^+ to fly on opposite directions. For this reason, the $d_0^{xy}(\Omega^-) \times d_0^{xy}(\pi^+)$ distribution measured considering the products of $\Omega_c^0 \to \Omega^-\pi^+$ decays is expected to be strongly asymmetric, with a significant amount of statistics populating the $d_0^{xy}(\Omega^-) \times d_0^{xy}(\pi^+) < 0$ region. On the other hand, the impact-parameter product distribution for combinatorial background is expected to show a more symmetric shape around 0, given the random orientation of uncorrelated Ω^- and π^+ hadrons. The impact parameter distributions of $\Omega_c^0 \to \Omega^-\pi^+$ decay products for reconstructed Ω_c^0 baryons are compared with the

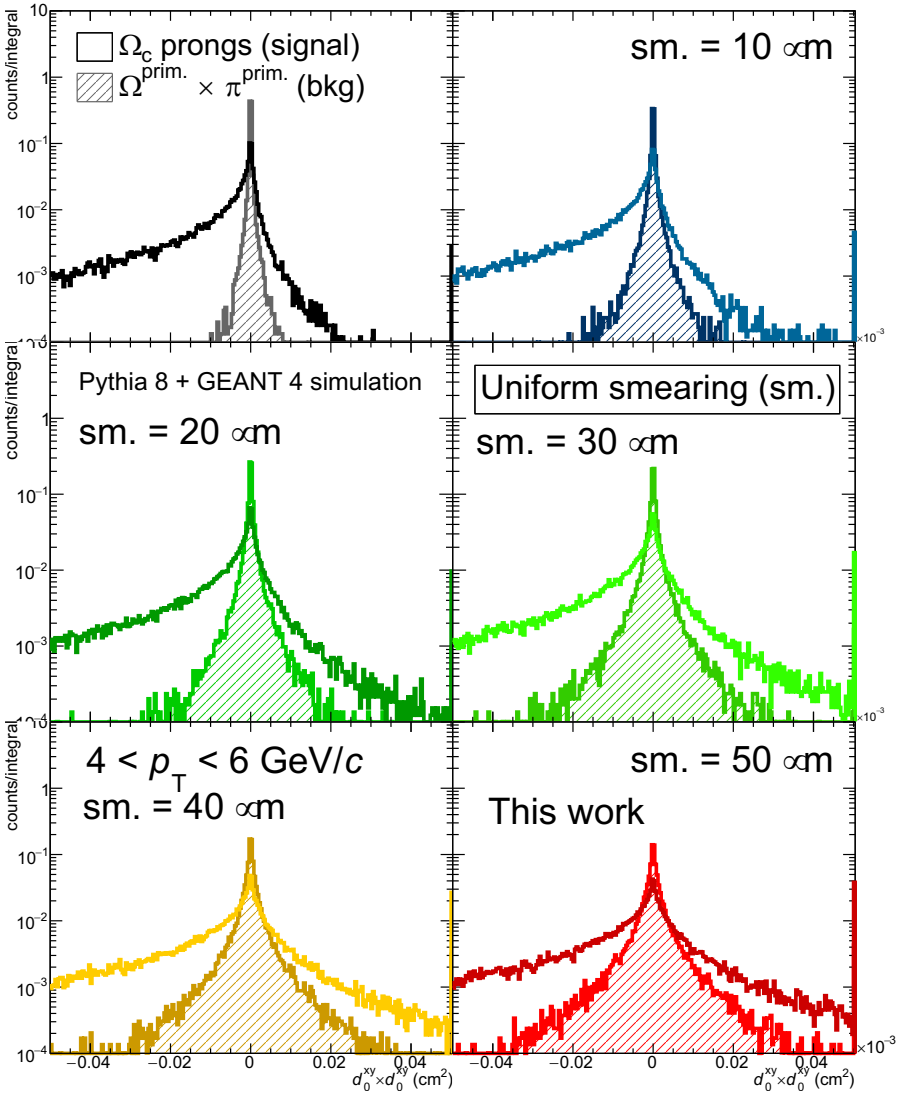

FIGURE 6.24: Impact parameter product $d_0^{xy}(\Omega^-) \times d_0^{xy}(\pi^+)$ distribution of $\Omega_c^0 \rightarrow \Omega^-\pi^+$ decay products compared with the one of primary Ω^- and primary π^+ in the $4 < p_T < 6$ GeV/c interval simulated with PYTHIA 8 + GEANT 4. The ITS layout adopted in this study corresponds to the ITS 3 one with the addition of a further layer with a radius of $R = 7$ cm. For these studies, 3×10^5 $\Omega_c^0 \rightarrow \Omega^-\pi^+$ decays and 3×10^5 events containing a primary Ω^- and a primary π^+ are simulated.

same quantity measured for combinatorial background of primary Ω^- and primary π^+ in Fig. 6.24. This comparison is performed simulating 3×10^5 $\Omega_c^0 \rightarrow \Omega^-\pi^+$ decays, as well as 3×10^5 events containing a primary Ω^- and a primary π^+ with PYTHIA 8 + GEANT 4 codes. The comparison is performed in the $4 < p_T < 6$ GeV/c interval, where the transverse momentum for the combinatorial $\Omega^-\pi^+$ pair derives from the four-momentum sum of the constituent primary particles. As done for the impact parameter d_0^{xy} in Fig. 6.21, the reconstructed $d_0^{xy}(\Omega^-) \times d_0^{xy}(\pi^+)$ distributions are evaluated with different smearing ranges for the generated hit coordinates, in order to appreciate the effect of the detector resolution. In the top left

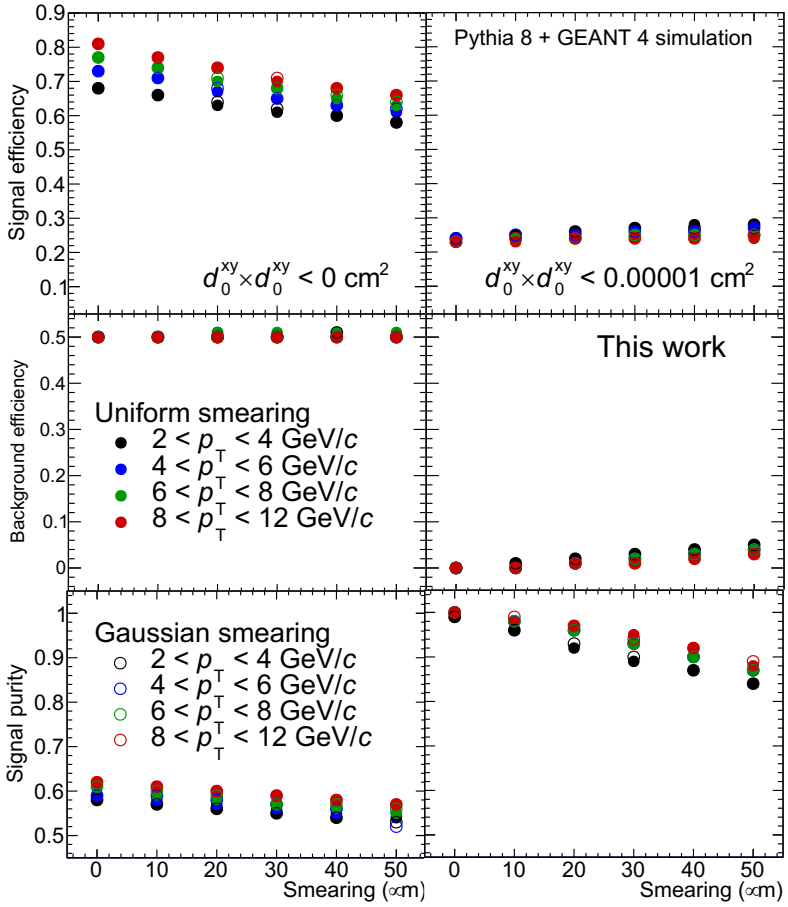

FIGURE 6.25: Efficiency of $\Omega_c^0 \to \Omega^-\pi^+$ signal (top row) as well as for combinatorial $\Omega^-\pi^+$ background reconstruction (middle row) and signal purity (bottom row) estimated with $d_0^{xy}(\Omega^-) \times d_0^{xy}(\pi^+) < 0$ cm^2 (left column) and $d_0^{xy}(\Omega^-) \times d_0^{xy}(\pi^+) < 0.00001$ cm^2 (right column) obtained with PYTHIA 8 + GEANT 4 simulation of 3×10^5 $\Omega_c^0 \to \Omega^-\pi^+$ decays and 3×10^5 events containing a primary Ω^- and a primary π^+. The results in different p_T intervals and with several either uniform or Gaussian smearing values for the generated hit coordinates are reported. The ITS layout used in these studies is the ITS 3 one with the addition of a further layer with a radius of $R = 7$ cm.

panel the $d_0^{xy}(\Omega^-) \times d_0^{xy}(\pi^+)$ distribution of the $\Omega_c^0 \to \Omega^-$ decays shows the expected asymmetric shape, with the $d_0^{xy}(\Omega^-) \times d_0^{xy}(\pi^+) < 0$ region containing about $\sim 73\%$ of the total generated signal. The distribution associated to the combinatorial background is symmetric around 0 and the spread is driven by the multiple scattering in the beam pipe and the innermost layers of ITS. This effect is the main responsible for the population of the $d_0^{xy}(\Omega^-) \times d_0^{xy}(\pi^+) > 0$ region in the signal distribution. With the increase of the, the shape of signal distribution is broadened. Moreover, the $d_0^{xy}(\Omega^-) \times d_0^{xy}(\pi^+)$ unbalance toward negative values becomes less relevant and the signal distribution gets closer to the combinatorial background one, which also broadens for higher smearing values. The results shown in Fig. 6.24 refer to $\Omega_c^0 \to \Omega^-\pi^+$ decays and combinatorial $\Omega^-\pi^+$ pairs reconstructed in the $4 < p_T < 6$ GeV/c interval after the application of a uniform smearing of the generated hit coordinates. The same analysis is repeated in different p_T intervals and

testing the Gaussian smearing. In Fig. 6.25 the efficiency for the $\Omega_c^0 \rightarrow \Omega^-\pi^+$ signal (top row) as well as for combinatorial $\Omega^-\pi^+$ reconstruction (middle row) and the signal purity (bottom row) estimated with the $d_0^{xy}(\Omega^-) \times d_0^{xy}(\pi^+) < 0$ cm^2 (left column) and $d_0^{xy}(\Omega^-) \times d_0^{xy}(\pi^+) < 0.00001$ cm^2 selections obtained from the same simulations used before are shown. The three quantities are computed in the transverse momentum intervals $2 < p_T < 4$ GeV/c, $4 < p_T < 6$ GeV/c, $6 < p_T < 8$ GeV/c and $8 < p_T < 12$ GeV/c. The signal efficiency shows a clear ordering as a function of p_T in case of $d_0^{xy}(\Omega^-) \times d_0^{xy}(\pi^+) < 0$ cm, showing decreasing values from high to low p_T. This behaviour reflects the larger displacement of the products of $\Omega_c^0 \rightarrow \Omega^-\pi^+$ decays given the larger p_T of decaying baryon, reflected into a higher population of the negative side of the distribution. Furthermore, the signal efficiency shows a decreasing trend with increasing smearing value, going from $\sim$ 80% ($\sim$ 68%) without smearing to $\sim$ 0.66% ($\sim$ 0.58%) with a smearing range of 50 μm in the $8 < p_T < 12$ GeV/c ($2 < p_T < 4$ GeV/c) interval. This is a direct consequence of the distribution broadening, since some statistics moves to the positive side due to the worsening of the pointing resolution. On the contrary, given the symmetric nature of its $d_0^{xy}(\Omega^-) \times d_0^{xy}(\pi^+)$ distribution, the reconstruction efficiency of the combinatorial background is independent on the reconstructed p_T and the smearing value and amounts to $\sim$ 50%. As a consequence, the signal purity shows the same dependencies of the signal efficiency. For the tighter selection $d_0^{xy}(\Omega^-) \times d_0^{xy}(\pi^+) < 0.00001$ cm^2 the signal efficiency drops to $\sim$ 25%, with slightly higher values registered at low p_T due to the larger influence of the multiple scattering that tends to populate the tails of the distribution. This behaviour affects also the background and what observed at the level of signal purity is again an increase with transverse momentum and a decreasing trend with increasing smearing. However, the tighter selection on the $d_0^{xy}(\Omega^-) \times d_0^{xy}(\pi^+)$ product ensures in this case a higher background rejection, with a maximum amount of $\sim$ 3% combinatorial pairs surviving this criterion, and a consequent higher signal purity with respect to the looser $d_0^{xy}(\Omega^-) \times d_0^{xy}(\pi^+) < 0$ cm^2 selection that was constraining the purity below $\sim$ 60%. As a matter of fact, applying the $d_0^{xy}(\Omega^-) \times d_0^{xy}(\pi^+) < 0.00001$ cm^2 criterion the signal purity is always higher than $\sim$ 84%, even in the worst scenario of a spatial smearing of 50 μm. Also in this case, the uniform and Gaussian smearing approaches provide similar conclusions.

6.6.2 Performances with different ITS 3 layouts

The studies presented in the previous Section are performed considering the ITS 3 layout with the addition of a further layer with a radius of $R = 7$ cm, whose presence was found to be important to improve the quality of the reconstructed primary Ω^- baryons (see Fig. 6.23). The design of the ITS 3 detector for Run 4 does not include this additional layer and the possibility to insert it in the final detector configuration must be justified by demonstrating an important gain in terms of physics performance. Exploiting again the reconstruction of primary Ω^- and $\Omega^-(\leftarrow \Omega_c^0)$ baryons with the ITS 3 detector and the measurement of the impact parameter d_0^{xy} distribution, a first investigation of the performances provided by different ITS 3 configurations is addressed. In this work, three versions of the ITS 3 layout are considered, which differ one from the other by the presence and position of a fourth layer in the inner barrel, thought to provide an additional space point to better constrain the reconstruction of a charged particle trajectory. The main aspect investigated in this study is the radius of the possible additional layer, which is correlated with the momentum needed for a charged particle to reach it. In a scenario without

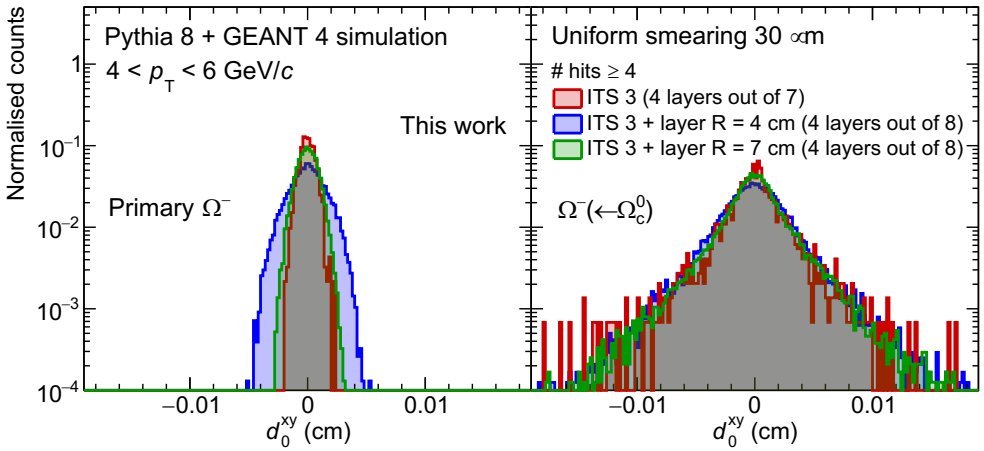

FIGURE 6.26: Impact parameter d_0^{xy} distribution of primary Ω^- and $\Omega^-(\leftarrow \Omega_c^0)$ baryons reconstructed in the $4 < p_T < 6$ GeV/c interval with PYTHIA 8 + GEANT 4 simulations requiring at least 4 hits in the ITS, comparing different layouts for the detector based on the ITS 3 one: without any addition layer and with an additional one, either at a radius of $R = 4$ cm or $R = 7$ cm.

magnetic field (B = 0), the average covered distance $\langle L \rangle$ by a charged particle of momentum p and mass m corresponds to $\langle L \rangle = c\tau\beta\gamma = c\tau\langle p \rangle/(mc)$, implying a linear dependence of the particle momentum $\langle p \rangle$ with the covered distance $\langle L \rangle$, namely $\langle p \rangle = mc\langle L \rangle/(c\tau)$. Taking into account a Ω^-, with a mass of 1.672 GeV/c^2 and a proper decay length $c\tau = 2.461$ cm, the average momentum $\langle p \rangle$ needed to cover a range $\langle L \rangle$ corresponding to $\langle p(\Omega^-) \rangle \approx 0.679 \cdot \langle L \rangle$ cm$^{-1}\cdot$ GeV/c. If the kinematics fully develops along the transverse plane, the average p_T that a Ω^- baryon needs to have to reach a given layer with a radius R is directly proportional to the radius itself. Considering the detector layout adopted so far, the average p_T of a Ω^- baryon that reaches the additional layer at $R = 7$ cm corresponds to $\langle p_T(\Omega^-) \rangle \simeq 4.75$ GeV/c. The average p_T reduces to about $\langle p_T(\Omega) \rangle \simeq 2.72$ GeV/c[6] in case the radius of the additional layer is put at $R = 4$ cm, ensuring a higher reconstruction efficiency for low p_T particles if one requires a point on this layer in the reconstruction. For this reason, an additional layer put at $R = 4$ cm instead of $R = 7$ cm is taken into account. In Fig. 6.26 the impact parameter distribution of primary Ω^- and $\Omega^-(\leftarrow \Omega_c^0)$ baryons reconstructed in the $4 < p_T < 6$ GeV/c interval using the three mentioned ITS 3 layouts is shown. The track reconstruction is performed using at least 4 space points in all the three cases. In the case of the ITS 3, the inner barrel is composed by 3 layers and the fourth one is located at a radius of $R = 19$ cm, which requires an average transverse momentum of $\langle p_T(\Omega^-) \rangle \simeq 12.90$ GeV/c to be reached by a Ω^- baryon. On the other hand, in the two improved scenarios the fourth space point used for the track reconstruction is closer to the inner barrel, with a consequent decrease of the average p_T for the Ω^- baryon. As shown in the left panel of Fig. 6.26 the ITS 3 original layout provides a spatial resolution that is comparable with that obtained by inserting the additional layer at $R = 7$ cm. However, the requirement of at least 4 hits causes a drop of about a factor 10 in the former scenario, given that the track is

[6] Note that in this case the curvature effect is negligible, since $\mathrm{R[m]} = \frac{p_T[\mathrm{GeV}/c]}{0}.3e\mathrm{B[T]} \simeq \frac{2.7\mathrm{GeV}/c}{0.3\cdot 0.5} \simeq$ 18 m.

forced to pass through a more distant layer with respect to the latter case. A broadening of about a factor 2.5 is observed when the additional layer is put at $R = 4$ cm instead of $R = 7$ cm, but the reconstruction efficiency increases by a factor of about 1.7 in the former case with respect to the latter. A milder dependence from the ITS 3 layout is observed for the $\Omega^-(\leftarrow \Omega_c^0)$ baryons, whose impact parameter distribution reflects the larger displacement given by the decay kinematics. According to these studies, the insertion of a eighth layer in the ITS 3 layout would be fruitful in case it has a radius about 2 times larger than the third inner barrel layer, in order to reach a good compromise between pointing resolution and tracking efficiency and at the same time a significant separation between primary Ω^- and $\Omega^-(\leftarrow \Omega_c^0)$ baryons.

6.6.3 Outlook for future developments

The concept of strangeness tracking in Run 3 and Run 4 may be the key for the ALICE experiment to extend the physics case and performances regarding the heavy-flavour hadron reconstruction. However, in order to provide a quantitative overview of the improvements by this technique, further commitment is necessary to bring the simulation framework to a more realistic description of the data taking and reconstruction. First of all, the implementation of realistic resolution effects in the detector simulations are required to provide more punctual conclusions about the spatial precision granted by the upgraded ITS and the test on bended particle trajectory by the application of a non-null magnetic field is also important. Another crucial aspect to be considered to correctly interpret the studies shown in Section 6.6 concerns the global track and cascade topology reconstruction. In this work, the Ω^- trajectories are reconstructed only using the ITS detector, constraining the tracks with at most 8 points in the scenario of the improved ITS 3 layout. A fundamental ingredient still completely missing in the simulation framework is the charged particle transport and tracking in the TPC detector, which covers a key role in the cascade topology reconstruction. The strange-particle momentum is precisely measured in the TPC with the cascade reconstruction, but a precise determination of the impact parameter to the primary vertex requires some points constraining the propagation. In this context, the idea is to exploit the clusters released by the strange charged particle on the ITS detector to further constrain the propagation of the equivalent track obtained from the cascade reconstruction towards the primary vertex. This may offer the opportunity to perform precise measurements of multi-charm baryon production that at the moment are not affordable due to the limited spatial resolution of the apparatus. The tracking in the TPC and ITS detectors in the context of the continuous readout foreseen in the coming data-taking campaigns and the matching between the two trackers are still under development. Finally, the overall performances (e.g. matching and tracking efficiency) need to be studied with realistic detector occupancies, differently for what done in this work where only the desired signal was considered in the simulations (see Fig. 6.20). A crucial aspects that requires dedicated studies is the fake-cluster association probability, which is not negligible in a high-multiplicity environment and may increase significantly close to the interaction point.

Chapter 7

Conclusions and outlook

The two data analyses presented in this thesis contribute to the investigation of the charm and beauty quark production and dynamics in hadronic collisions at the LHC. With the measurement of electrons from semileptonic decays of charm and beauty hadrons in Pb–Pb collisions the charm and beauty quark energy loss in the QGP is studied. Such measurement is sensitive to the shadowing effect, which suppresses the heavy quark production at low Bjorken-x. The measurement of $\Sigma_c^{0,++}$ and Λ_c^+ baryons in pp collisions contributes to the investigation of charm baryon production, whose ratio to the D^0 meson one is observed to be enhanced compared to what measured in e^+e^- collisions.

The measurement of the p_T-differential invariant yield and nuclear modification factor R_{AA} of electrons from semileptonic decays of charm and beauty hadrons in central (0–10%), semicentral (30–50%) and peripheral (60–80%) Pb–Pb collisions at $\sqrt{s_{NN}} = 5.02$ TeV collected by the ALICE experiment in 2015 is described in Chapter 4. The work presented in this thesis corresponds to the results published in [266] in the interval $p_T < 3$ GeV/c. The R_{AA} measured in the three centrality classes exhibits the dependence of the charm and beauty quark energy loss on the path length and energy density of the deconfined medium produced in Pb–Pb collisions at the LHC. The results in central (0–10%) and semicentral (30–50%) collisions are compatible within uncertainties with the predictions from several theoretical models describing the centrality dependence of the in-medium radiative energy loss. The measurement described in this thesis covers transverse momenta down to $p_T = 500$ MeV/c, where nuclear shadowing is expected to suppress the heavy quark production in Pb–Pb collisions at low Bjorken-x. Only model calculations that implement this cold nuclear matter effect are able to describe the measurement for $p_T \lesssim 3$ GeV/c.

The measurement of the production cross section of prompt Λ_c^+ and $\Sigma_c^{0,+,++}$ baryons in pp collisions at $\sqrt{s} = 13$ TeV collected by the ALICE experiment in 2016, 2017 and 2018 is described in Chapter 5. These charm baryons are reconstructed via the $\Lambda_c^+ \to pK^-\pi^+$ decays. Selections on specific variables related to the intrinsic displacement of the decay vertex with respect to the interaction point and on the PID of daughter tracks are applied to separate the signal from the combinatorial background. The results discussed in this thesis contribute to those published in [313], where a weighted average with the results obtained from the $\Lambda_c^+ \to pK_S^0$ decay reconstruction is performed, as explained in Sec. 5.5. The Λ_c^+/D^0 charm baryon-to-meson ratio is compared with several model predictions. The Monash tune of PYTHIA 8 generator, tuned to reproduce the results in e^+e^- and e^-p collisions, significantly underestimates the measurement and does not reproduce the measured trend in p_T. This is observed also for the $\Sigma_c^{0,+,++}/D^0$ ratio, with a discrepancy between the measurement and the model expectation even larger in relative terms than that of Λ_c^+/D^0. Only model calculations implementing different hadronization mechanisms for the charm quark compared to the conventional string

fragmentation are able to describe the measurements within uncertainties. The first measurement of the prompt Λ_c^+ feed-down from strong decays of $\Sigma_c^{0,+,++}$ baryons ($\Lambda_c^+ (\leftarrow \Sigma_c^{0,+,++})$) in pp collisions at the LHC is also presented and it amounts to about $\sim 38\%$ in the interval $2 < p_T < 12$ GeV/c.

Despite the interesting insights provided by the results discussed in this thesis, a complete understanding of the charm and beauty quark production and dynamics in hadronic collisions at the LHC requires further measurements. The measurement of electrons from semileptonic decays of heavy-flavour hadrons does not permit to disentangle the contribution of charm and beauty flavours and the measurement as a function of electron p_T does not give a direct access to the heavy-flavour hadron kinematics. These points can be addressed with direct measurements of charm and beauty hadron productions, which at the moment are precluded by the available recorded luminosity and the challenging separation of the signal from the overwhelming background. New production measurements need to be performed also in pp collisions, in order to further study the charm quark hadronization in such collision system and distinguish the new mechanisms introduced in Pb–Pb collisions by the formation of a deconfined medium. Also in this case, more precise and differential results are required. Some perspectives for such measurements in the Run 3 and 4 data-taking campaigns at the LHC are discussed in Chapter 6. Emphasis is given to the upgrade of the ITS detector, which will provide improved performances in the track and vertex reconstruction at low p_T and open the door to new measurements. Thanks to the improved spatial resolution of the upgraded ITS, the $\Xi_c^+ \rightarrow pK^-\pi^+$ signal can be reconstructed with a sample of $\mathcal{L} = 10$ nb^{-1} central (0–10%) Pb–Pb collisions at $\sqrt{s_{NN}} = 5.5$ TeV. If this measurement may still be at limit with the ITS 2, the upgrade to the ITS 3 can guarantee a gain of about a factor $3 \div 4$ in significance. These performances can be further boosted by the optimisation of the PID and topological selections via the usage of Machine Learning techniques. Finally, the improved spatial resolution of the ITS detector as well as its layout closer to the beam interaction point will enable the direct tracking of strange charge particles with a typical decay length of the same order of the innermost ITS layer radii. A first exploratory study employing this innovative approach is discussed in the last Section of Chapter 6. According to simulations performed with PYTHIA, the pointing resolution provided by the ITS 3 detector will permit to separate primary Ω^- baryons from those coming from Ω_c^0 by reconstructing their impact parameter to the primary vertex. These studies show that the separation improves where more points are included in the tracking. Therefore, this technique can be fruitful to precisely propagate to the primary vertex the strange baryon tracks coming from the cascade reconstruction in the TPC. Even if the real performances of this innovative technique are still to be assessed, this approach should pave the way to the reconstruction of multi-charm (strange) baryons, such as Ξ_{cc}^+, Ξ_{cc}^{++} and Ω_{cc}^0 baryons.

Bibliography

[1] T. P. Cheng and L. F. Li, *GAUGE THEORY OF ELEMENTARY PARTICLE PHYSICS*. 1984.

[2] F. Mandl and G. Shaw, *QUANTUM FIELD THEORY*. 1985.

[3] **Particle Data Group** Collaboration, P. A. Zyla *et al.*, "Review of Particle Physics", *PTEP* **2020** no. 8, (2020) 083C01.

[4] A. Mocsy and P. Petreczky, "Can quarkonia survive deconfinement?", *Phys. Rev. D* **77** (2008) 014501, arXiv:0705.2559 [hep-ph].

[5] O. Kaczmarek, F. Karsch, P. Petreczky, and F. Zantow, "Heavy quark anti-quark free energy and the renormalized Polyakov loop", *Phys. Lett. B* **543** (2002) 41–47, arXiv:hep-lat/0207002.

[6] O. Kaczmarek, F. Karsch, P. Petreczky, and F. Zantow, "Heavy quark free energies, potentials and the renormalized Polyakov loop", *Nucl. Phys. B Proc. Suppl.* **129** (2004) 560–562, arXiv:hep-lat/0309121.

[7] O. Kaczmarek, F. Karsch, F. Zantow, and P. Petreczky, "Static quark anti-quark free energy and the running coupling at finite temperature", *Phys. Rev. D* **70** (2004) 074505, arXiv:hep-lat/0406036. [Erratum: Phys.Rev.D 72, 059903 (2005)].

[8] H. D. Politzer, "Reliable Perturbative Results for Strong Interactions?", *Phys. Rev. Lett.* **30** (1973) 1346–1349.

[9] D. J. Gross and F. Wilczek, "Ultraviolet Behavior of Nonabelian Gauge Theories", *Phys. Rev. Lett.* **30** (1973) 1343–1346.

[10] A. Bettini, *Introduction to elementary particle physics*. 2008.

[11] T. Matsui and H. Satz, "J/ψ Suppression by Quark-Gluon Plasma Formation", *Phys. Lett. B* **178** (1986) 416–422.

[12] G. Martinez, "Advances in Quark Gluon Plasma", 4, 2013. arXiv:1304.1452 [nucl-ex].

[13] K. G. Wilson, "Confinement of Quarks", *Phys. Rev. D* **10** (1974) 2445–2459.

[14] K. Rajagopal and F. Wilczek, *The Condensed matter physics of QCD*, pp. 2061–2151. 11, 2000. arXiv:hep-ph/0011333.

[15] F. Karsch, "Lattice QCD at high temperature and density", *Lect. Notes Phys.* **583** (2002) 209–249, arXiv:hep-lat/0106019.

[16] F. Karsch, "Lattice results on QCD thermodynamics", *Nucl. Phys. A* **698** (2002) 199–208, arXiv:hep-ph/0103314.

[17] A. Polyakov, "Thermal properties of gauge fields and quark liberation", *Physics Letters B* **72** no. 4, (1978) 477–480. https://www.sciencedirect.com/science/article/pii/0370269378907372.

[18] K. Fukushima and V. Skokov, "Polyakov loop modeling for hot QCD", *Prog. Part. Nucl. Phys.* **96** (2017) 154–199, arXiv:1705.00718 [hep-ph].

[19] K. Hübner, *The Polyakov Loop and Its Correlators in Higher Representations of SU(3) at Finite Temperature*. Verlag nicht ermittelbar, 2006. https://books.google.it/books?id=wqLwvgEACAAJ.

[20] *Conceptual design of the Relativistic Heavy Ion Collider (RHIC)*. Brookhaven Nat. Lab., Upton, NY, 1986. https://cds.cern.ch/record/108613.

[21] **LHC Study Group** Collaboration, T. S. Pettersson and P. Lefèvre, "The Large Hadron Collider: conceptual design", Tech. Rep. CERN-AC-95-05-LHC, Oct, 1995. https://cds.cern.ch/record/291782.

[22] J. D. Bjorken, "Highly Relativistic Nucleus-Nucleus Collisions: The Central Rapidity Region", *Phys. Rev. D* **27** (1983) 140–151.

[23] N. Tahir, R. Schmidt, M. Brugger, R. Assmann, A. Shutov, I. Lomonosov, A. Piriz, D. Hoffmann, C. Deutsch, and V. Fortov, "The CERN Super Proton Synchrotron as a tool to study high energy density physics", *New J. Phys.* **10** (2008) 073028.

[24] R. A. Beth and C. Lasky, *The Brookhaven alternating gradient synchrotron*. [s.n.], [S.l.], 1958. https://cds.cern.ch/record/109983.

[25] **STAR** Collaboration, G. Odyniec, "Beam Energy Scan Program at RHIC (BES I and BES II) – Probing QCD Phase Diagram with Heavy-Ion Collisions", *PoS* **CORFU2018** (2019) 151.

[26] **NICA** Collaboration, A. N. Sissakian, V. D. Kekelidze, and A. S. Sorin, "The nuclotron-based ion collider fAcility at the Joint Institute for Nuclear Research", *Nucl. Phys. A* **827** (2009) 630C–637C.

[27] R. J. Glauber, "Lectures on Theoretical Physics", *Interscience, New York* **1** 315.

[28] M. L. Miller, K. Reygers, S. J. Sanders, and P. Steinberg, "Glauber modeling in high energy nuclear collisions", *Ann. Rev. Nucl. Part. Sci.* **57** (2007) 205–243, arXiv:nucl-ex/0701025.

[29] **ALICE Collaboration** Collaboration, "Centrality determination in heavy ion collisions",. https://cds.cern.ch/record/2636623.

[30] R. Stock, "Relativistic Nucleus-Nucleus Collisions and the QCD Matter Phase Diagram", arXiv:0807.1610 [nucl-ex].

[31] **ALICE** Collaboration, J. Adam *et al.*, "Measurement of transverse energy at midrapidity in Pb-Pb collisions at $\sqrt{s_{\mathrm{NN}}} = 2.76$ TeV", *Phys. Rev. C* **94** no. 3, (2016) 034903, arXiv:1603.04775 [nucl-ex].

[32] A. Andronic, P. Braun-Munzinger, K. Redlich, and J. Stachel, "Decoding the phase structure of QCD via particle production at high energy", *Nature* **561** no. 7723, (2018) 321–330, arXiv:1710.09425 [nucl-th].

[33] **ALICE** Collaboration, J. Adam *et al.*, "Centrality dependence of the charged-particle multiplicity density at midrapidity in Pb-Pb collisions at $\sqrt{s_{\rm NN}}$ = 5.02 TeV", *Phys. Rev. Lett.* **116** no. 22, (2016) 222302, arXiv:1512.06104 [nucl-ex].

[34] **ALICE Collaboration** Collaboration, J. Adam *et al.*, "Direct photon production in Pb-Pb collisions at $\sqrt{s_{NN}}$=2.76 TeV", *Phys. Lett. B* **754** no. CERN-PH-EP-2015-254. CERN-PH-EP-2015-254, (Sep, 2015) 235–248. 25 p. http://cds.cern.ch/record/2051887. 25 pages, 6 captioned figures, 2 tables, authors from page 20, published version, figures at http://aliceinfo.cern.ch/ArtSubmission/node/1887.

[35] U. W. Heinz, "Concepts of heavy ion physics", in *2nd CERN-CLAF School of High Energy Physics*. 7, 2004. arXiv:hep-ph/0407360.

[36] M. Petrán, J. Letessier, V. Petráček, and J. Rafelski, "Hadron production and quark-gluon plasma hadronization in Pb-Pb collisions at $\sqrt{s_{NN}} = 2.76$ TeV", *Phys. Rev. C* **88** no. 3, (2013) 034907, arXiv:1303.2098 [hep-ph].

[37] S. Wheaton and J. Cleymans, "THERMUS: A Thermal model package for ROOT", *Comput. Phys. Commun.* **180** (2009) 84–106, arXiv:hep-ph/0407174.

[38] P. Braun-Munzinger, K. Redlich, and J. Stachel, "Particle production in heavy ion collisions", arXiv:nucl-th/0304013.

[39] Y. Pan and S. Pratt, "Baryon Annihilation in Heavy Ion Collisions", arXiv:1210.1577 [nucl-th].

[40] **ALICE** Collaboration, S. Acharya *et al.*, "Production of charged pions, kaons, and (anti-)protons in Pb-Pb and inelastic pp collisions at $\sqrt{s_{NN}}$ = 5.02 TeV", *Phys. Rev. C* **101** no. 4, (2020) 044907, arXiv:1910.07678 [nucl-ex].

[41] G. Gatoff and C. Y. Wong, "Origin of the soft p(T) spectra", *Phys. Rev. D* **46** (1992) 997–1006.

[42] **Aachen-Berlin-Bonn-CERN-Cracow-Heidelberg-London-Vienna-Warsaw** Collaboration, M. Deutschmann *et al.*, "Transverse spectra in pi+- p and K- p interactions between 8-GeV/c and 16-GeV/c", *Nucl. Phys. B* **70** (1974) 189–204.

[43] J. Bartke, M. Deutschmann, H. Kirk, P. Sixel, H. Kaufmann, M. Klein, K. Böckmann, R. Hartmann, D. Kocher, P. Malhotra, D. Morrison, P. Porth, F. Triantis, J. Zaorska, W. Zieliński, and J. Królikowski, "Simplicity of "transverse energy" spectra of hadrons", *Nuclear Physics B* **120** no. 1, (1977) 14–22. https://www.sciencedirect.com/science/article/pii/055032137790092X.

[44] L. Altenkämper, F. Bock, C. Loizides, and N. Schmidt, "Applicability of transverse mass scaling in hadronic collisions at energies available at the CERN Large Hadron Collider", *Phys. Rev. C* **96** no. 6, (2017) 064907, arXiv:1710.01933 [hep-ph].

[45] **ALICE** Collaboration, B. Abelev *et al.*, "Pion, Kaon, and Proton Production in Central Pb–Pb Collisions at $\sqrt{s_{NN}} = 2.76$ TeV", *Phys. Rev. Lett.* **109** (2012) 252301, arXiv:1208.1974 [hep-ex].

[46] E. Schnedermann, J. Sollfrank, and U. W. Heinz, "Thermal phenomenology of hadrons from 200-A/GeV S+S collisions", *Phys. Rev. C* **48** (1993) 2462–2475, arXiv:nucl-th/9307020.

[47] J. Rafelski and B. Muller, "Strangeness Production in the Quark - Gluon Plasma", *Phys. Rev. Lett.* **48** (1982) 1066. [Erratum: Phys.Rev.Lett. 56, 2334 (1986)].

[48] A. Tounsi and K. Redlich, "Strangeness enhancement and canonical suppression", arXiv:hep-ph/0111159.

[49] **STAR** Collaboration, G. Agakishiev *et al.*, "Strangeness Enhancement in Cu+Cu and Au+Au Collisions at $\sqrt{s_{NN}} = 200$ GeV", *Phys. Rev. Lett.* **108** (2012) 072301, arXiv:1107.2955 [nucl-ex].

[50] **ALICE** Collaboration, B. B. Abelev *et al.*, "Multi-strange baryon production at mid-rapidity in Pb-Pb collisions at $\sqrt{s_{NN}} = 2.76$ TeV", *Phys. Lett. B* **728** (2014) 216–227, arXiv:1307.5543 [nucl-ex]. [Erratum: Phys.Lett.B 734, 409–410 (2014)].

[51] **ALICE** Collaboration, J. Adam *et al.*, "Enhanced production of multi-strange hadrons in high-multiplicity proton-proton collisions", *Nature Phys.* **13** (2017) 535–539, arXiv:1606.07424 [nucl-ex].

[52] **ALICE** Collaboration, S. Acharya *et al.*, "Anisotropic flow of identified particles in Pb-Pb collisions at $\sqrt{s}_{\rm NN} = 5.02$ TeV", *JHEP* **09** (2018) 006, arXiv:1805.04390 [nucl-ex].

[53] S. Voloshin and Y. Zhang, "Flow study in relativistic nuclear collisions by Fourier expansion of Azimuthal particle distributions", *Z. Phys. C* **70** (1996) 665–672, arXiv:hep-ph/9407282.

[54] R. S. Bhalerao and J.-Y. Ollitrault, "Eccentricity fluctuations and elliptic flow at RHIC", *Phys. Lett. B* **641** (2006) 260–264, arXiv:nucl-th/0607009.

[55] **PHOBOS** Collaboration, B. Alver *et al.*, "Importance of correlations and fluctuations on the initial source eccentricity in high-energy nucleus-nucleus collisions", *Phys. Rev. C* **77** (2008) 014906, arXiv:0711.3724 [nucl-ex].

[56] B. Alver and G. Roland, "Collision geometry fluctuations and triangular flow in heavy-ion collisions", *Phys. Rev. C* **81** (2010) 054905, arXiv:1003.0194 [nucl-th]. [Erratum: Phys.Rev.C 82, 039903 (2010)].

[57] B. H. Alver, C. Gombeaud, M. Luzum, and J.-Y. Ollitrault, "Triangular flow in hydrodynamics and transport theory", *Phys. Rev. C* **82** (2010) 034913, arXiv:1007.5469 [nucl-th].

[58] D. Teaney and L. Yan, "Non linearities in the harmonic spectrum of heavy ion collisions with ideal and viscous hydrodynamics", *Phys. Rev. C* **86** (2012) 044908, arXiv:1206.1905 [nucl-th].

[59] **ALICE** Collaboration, S. Acharya *et al.*, "Linear and non-linear flow modes in Pb-Pb collisions at $\sqrt{s_{\rm NN}} = 2.76$ TeV", *Phys. Lett. B* **773** (2017) 68–80, arXiv:1705.04377 [nucl-ex].

[60] **ATLAS** Collaboration, G. Aad *et al.*, "Measurement of the Azimuthal Angle Dependence of Inclusive Jet Yields in Pb+Pb Collisions at $\sqrt{s_{NN}} = 2.76$ TeV with the ATLAS detector", *Phys. Rev. Lett.* **111** no. 15, (2013) 152301, arXiv:1306.6469 [hep-ex].

[61] **ALICE** Collaboration, J. Adam *et al.*, "Azimuthal anisotropy of charged jet production in $\sqrt{s_{\rm NN}}$ = 2.76 TeV Pb-Pb collisions", *Phys. Lett. B* **753** (2016) 511–525, arXiv:1509.07334 [nucl-ex].

[62] **CMS** Collaboration, A. M. Sirunyan *et al.*, "Azimuthal anisotropy of charged particles with transverse momentum up to 100 GeV/ c in PbPb collisions at $\sqrt{s_{NN}}$=5.02 TeV", *Phys. Lett. B* **776** (2018) 195–216, arXiv:1702.00630 [hep-ex].

[63] **ALICE** Collaboration, S. Acharya *et al.*, "Energy dependence and fluctuations of anisotropic flow in Pb-Pb collisions at $\sqrt{s_{\rm NN}} = 5.02$ and 2.76 TeV", *JHEP* **07** (2018) 103, arXiv:1804.02944 [nucl-ex].

[64] S. McDonald, C. Shen, F. Fillion-Gourdeau, S. Jeon, and C. Gale, "Hydrodynamic predictions for Pb+Pb collisions at 5.02 TeV", *Phys. Rev. C* **95** no. 6, (2017) 064913, arXiv:1609.02958 [hep-ph].

[65] W. Zhao, H.-j. Xu, and H. Song, "Collective flow in 2.76 A TeV and 5.02 A TeV Pb+Pb collisions", *Eur. Phys. J. C* **77** no. 9, (2017) 645, arXiv:1703.10792 [nucl-th].

[66] P. Kovtun, D. T. Son, and A. O. Starinets, "Viscosity in strongly interacting quantum field theories from black hole physics", *Phys. Rev. Lett.* **94** (2005) 111601, arXiv:hep-th/0405231.

[67] S. Cremonini, "The Shear Viscosity to Entropy Ratio: A Status Report", *Mod. Phys. Lett. B* **25** (2011) 1867–1888, arXiv:1108.0677 [hep-th].

[68] D. d'Enterria and B. Betz, *High-pT Hadron Suppression and Jet Quenching*, vol. 785, pp. 285–339. 11, 2009.

[69] **STAR** Collaboration, J. Adams *et al.*, "Evidence from d + Au measurements for final state suppression of high p(T) hadrons in Au+Au collisions at RHIC", *Phys. Rev. Lett.* **91** (2003) 072304, arXiv:nucl-ex/0306024.

[70] **ALICE** Collaboration, S. Acharya *et al.*, "Transverse momentum spectra and nuclear modification factors of charged particles in Xe-Xe collisions at $\sqrt{s_{\rm NN}}$ = 5.44 TeV", *Phys. Lett. B* **788** (2019) 166–179, arXiv:1805.04399 [nucl-ex].

[71] **ALICE** Collaboration, J. Adam *et al.*, "Measurement of jet suppression in central Pb-Pb collisions at $\sqrt{s_{\rm NN}}$ = 2.76 TeV", *Phys. Lett. B* **746** (2015) 1–14, arXiv:1502.01689 [nucl-ex].

[72] **CMS** Collaboration, V. Khachatryan *et al.*, "Measurement of inclusive jet cross sections in pp and PbPb collisions at $\sqrt{s_{NN}} = 2.76$ TeV", *Phys. Rev. C* **96** no. 1, (2017) 015202, arXiv:1609.05383 [nucl-ex].

[73] **ATLAS** Collaboration, G. Aad *et al.*, "Measurements of the Nuclear Modification Factor for Jets in Pb+Pb Collisions at $\sqrt{s_{\rm NN}} = 2.76$ TeV with the ATLAS Detector", *Phys. Rev. Lett.* **114** no. 7, (2015) 072302, arXiv:1411.2357 [hep-ex].

[74] **PHENIX** Collaboration, K. Adcox *et al.*, "Suppression of hadrons with large transverse momentum in central Au+Au collisions at $\sqrt{s_{NN}}$ = 130-GeV", *Phys. Rev. Lett.* **88** (2002) 022301, arXiv:nucl-ex/0109003.

[75] **STAR** Collaboration, C. Adler *et al.*, "Centrality dependence of high p_T hadron suppression in Au+Au collisions at $\sqrt{s_{NN}}$ = 130-GeV", *Phys. Rev. Lett.* **89** (2002) 202301, arXiv:nucl-ex/0206011.

[76] **ATLAS** Collaboration, G. Aad *et al.*, "Centrality, rapidity and transverse momentum dependence of isolated prompt photon production in lead-lead collisions at $\sqrt{s_{\mathrm{NN}}} = 2.76$ TeV measured with the ATLAS detector", *Phys. Rev. C* **93** no. 3, (2016) 034914, arXiv:1506.08552 [hep-ex].

[77] **ATLAS** Collaboration, G. Aad *et al.*, "Measurement of Z boson Production in Pb+Pb Collisions at $\sqrt{s_{NN}} = 2.76$ TeV with the ATLAS Detector", *Phys. Rev. Lett.* **110** no. 2, (2013) 022301, arXiv:1210.6486 [hep-ex].

[78] **CMS** Collaboration, S. Chatrchyan *et al.*, "Study of W boson production in PbPb and pp collisions at $\sqrt{s_{NN}} = 2.76$ TeV", *Phys. Lett. B* **715** (2012) 66–87, arXiv:1205.6334 [nucl-ex].

[79] **CMS** Collaboration, S. Chatrchyan *et al.*, "Measurement of isolated photon production in pp and PbPb collisions at $\sqrt{s_{NN}} = 2.76$ TeV", *Phys. Lett. B* **710** (2012) 256–277, arXiv:1201.3093 [nucl-ex].

[80] **CMS** Collaboration, A. M. Sirunyan *et al.*, "Measurement of nuclear modification factors of Υ(1S), Υ(2S), and Υ(3S) mesons in PbPb collisions at $\sqrt{s_{\mathrm{NN}}} = 5.02$ TeV", *Phys. Lett. B* **790** (2019) 270–293, arXiv:1805.09215 [hep-ex].

[81] **ALICE** Collaboration, J. Adam *et al.*, "Differential studies of inclusive J/ψ and ψ(2S) production at forward rapidity in Pb-Pb collisions at $\sqrt{s_{\mathrm{NN}}} = 2.76$ TeV", *JHEP* **05** (2016) 179, arXiv:1506.08804 [nucl-ex].

[82] H. Satz, "Charm and beauty in a hot environment", in *Sense of Beauty in Physics: Miniconference in Honor of Adriano Di Giacomo on his 70th Birthday*. 2, 2006. arXiv:hep-ph/0602245.

[83] S. Digal, P. Petreczky, and H. Satz, "Quarkonium feed down and sequential suppression", *Phys. Rev. D* **64** (2001) 094015, arXiv:hep-ph/0106017.

[84] H. Satz, "Quarkonium Binding and Dissociation: The Spectral Analysis of the QGP", *Nucl. Phys. A* **783** (2007) 249–260, arXiv:hep-ph/0609197.

[85] M. Monteno *et al.*, "Results from the na50 experiment on j/ψ suppression in pb–pb collisions at the cern sps", *Nuclear Physics B - Proceedings Supplements* **92** no. 1, (2001) 43–54. https://www.sciencedirect.com/science/article/pii/S0920563200010185.

[86] **PHENIX** Collaboration, S. S. Adler *et al.*, "J / psi production in Au Au collisions at s(NN)**(1/2) = 200-GeV at the Relativistic Heavy Ion Collider", *Phys. Rev. C* **69** (2004) 014901, arXiv:nucl-ex/0305030.

[87] P. Braun-Munzinger and J. Stachel, "(Non)thermal aspects of charmonium production and a new look at J / psi suppression", *Phys. Lett. B* **490** (2000) 196–202, arXiv:nucl-th/0007059.

[88] R. L. Thews, M. Schroedter, and J. Rafelski, "Enhanced J/ψ production in deconfined quark matter", *Phys. Rev. C* **63** (2001) 054905, arXiv:hep-ph/0007323.

[89] X. Du and R. Rapp, "Sequential Regeneration of Charmonia in Heavy-Ion Collisions", *Nucl. Phys. A* **943** (2015) 147–158, arXiv:1504.00670 [hep-ph].

[90] M. L. Mangano, "Two lectures on heavy quark production in hadronic collisions", *Proc. Int. Sch. Phys. Fermi* **137** (1998) 95–137, arXiv:hep-ph/9711337.

[91] J. C. Collins, D. E. Soper, and G. F. Sterman, "Factorization of Hard Processes in QCD", *Adv. Ser. Direct. High Energy Phys.* **5** (1989) 1–91, arXiv:hep-ph/0409313.

[92] J. Pumplin, D. R. Stump, J. Huston, H. L. Lai, P. M. Nadolsky, and W. K. Tung, "New generation of parton distributions with uncertainties from global QCD analysis", *JHEP* **07** (2002) 012, arXiv:hep-ph/0201195.

[93] S. Dulat, T.-J. Hou, J. Gao, M. Guzzi, J. Huston, P. Nadolsky, J. Pumplin, C. Schmidt, D. Stump, and C. P. Yuan, "New parton distribution functions from a global analysis of quantum chromodynamics", *Phys. Rev. D* **93** no. 3, (2016) 033006, arXiv:1506.07443 [hep-ph].

[94] **NNPDF** Collaboration, R. D. Ball *et al.*, "Parton distributions from high-precision collider data", *Eur. Phys. J. C* **77** no. 10, (2017) 663, arXiv:1706.00428 [hep-ph].

[95] V. G. Kartvelishvili, A. K. Likhoded, and V. A. Petrov, "On the Fragmentation Functions of Heavy Quarks Into Hadrons", *Phys. Lett. B* **78** (1978) 615–617.

[96] M. Cacciari, P. Nason, and C. Oleari, "A Study of heavy flavored meson fragmentation functions in e+ e- annihilation", *JHEP* **04** (2006) 006, arXiv:hep-ph/0510032.

[97] G. Altarelli and G. Parisi, "Asymptotic Freedom in Parton Language", *Nucl. Phys. B* **126** (1977) 298–318.

[98] M. Benzke, M. V. Garzelli, B. Kniehl, G. Kramer, S. Moch, and G. Sigl, "Prompt neutrinos from atmospheric charm in the general-mass variable-flavor-number scheme", *JHEP* **12** (2017) 021, arXiv:1705.10386 [hep-ph].

[99] G. Kramer and H. Spiesberger, "Study of heavy meson production in p–Pb collisions at $\sqrt{S}$= 5.02 TeV in the general-mass variable-flavour-number scheme", *Nucl. Phys. B* **925** (2017) 415–430, arXiv:1703.04754 [hep-ph].

[100] M. Cacciari, M. Greco, and P. Nason, "The P(T) spectrum in heavy flavor hadroproduction", *JHEP* **05** (1998) 007, arXiv:hep-ph/9803400.

[101] M. Cacciari, S. Frixione, N. Houdeau, M. L. Mangano, P. Nason, and G. Ridolfi, "Theoretical predictions for charm and bottom production at the LHC", *JHEP* **10** (2012) 137, arXiv:1205.6344 [hep-ph].

[102] D. d'Enterria and A. M. Snigirev, "Triple parton scatterings in high-energy proton-proton collisions", *Phys. Rev. Lett.* **118** no. 12, (2017) 122001, arXiv:1612.05582 [hep-ph].

[103] D. d'Enterria and A. M. Snigirev, "Triple-parton scatterings in proton–nucleus collisions at high energies", *Eur. Phys. J. C* **78** no. 5, (2018) 359, arXiv:1612.08112 [hep-ph].

[104] S. Catani, S. Devoto, M. Grazzini, S. Kallweit, and J. Mazzitelli, "Bottom-quark production at hadron colliders: fully differential predictions in NNLO QCD", *JHEP* **03** (2021) 029, arXiv:2010.11906 [hep-ph].

[105] **ALICE** Collaboration, S. Acharya *et al.*, "Charm-quark fragmentation fractions and production cross section at midrapidity in pp collisions at the LHC", arXiv:2105.06335 [nucl-ex].

[106] **ALICE** Collaboration, S. Acharya *et al.*, "Measurement of beauty and charm production in pp collisions at $\sqrt{s}$ = 5.02 TeV via non-prompt and prompt D mesons", *JHEP* **05** (2021) 220, arXiv:2102.13601 [nucl-ex].

[107] **ALICE** Collaboration, S. Acharya *et al.*, "Measurement of D^0 , D^+ , D^{*+} and D_s^+ production in pp collisions at $\sqrt{s}$ = 5.02 TeV with ALICE", *Eur. Phys. J. C* **79** no. 5, (2019) 388, arXiv:1901.07979 [nucl-ex].

[108] **ALICE** Collaboration, S. Acharya *et al.*, "Λ_c^+ production in pp and in p-Pb collisions at $\sqrt{s_\mathrm{NN}}$ = 5.02 TeV", arXiv:2011.06079 [nucl-ex].

[109] **ALICE** Collaboration, S. Acharya *et al.*, "Λ_c^+ production and baryon-to-meson ratios in pp and p-Pb collisions at $\sqrt{s_\mathrm{NN}}$ = 5.02 TeV at the LHC", arXiv:2011.06078 [nucl-ex].

[110] **LHCb** Collaboration, R. Aaij *et al.*, "Measurements of prompt charm production cross-sections in pp collisions at $\sqrt{s}$ = 13 TeV", *JHEP* **03** (2016) 159, arXiv:1510.01707 [hep-ex]. [Erratum: JHEP 09, 013 (2016), Erratum: JHEP 05, 074 (2017)].

[111] **ATLAS** Collaboration, G. Aad *et al.*, "Measurement of the differential cross-section of B^+ meson production in pp collisions at $\sqrt{s}$ = 7 TeV at ATLAS", *JHEP* **10** (2013) 042, arXiv:1307.0126 [hep-ex].

[112] **CMS** Collaboration, A. M. Sirunyan *et al.*, "Measurement of B_s^0 meson production in pp and PbPb collisions at $\sqrt{s_\mathrm{NN}}$ = 5.02 TeV", *Phys. Lett. B* **796** (2019) 168–190, arXiv:1810.03022 [hep-ex].

[113] **OPAL** Collaboration, G. Alexander *et al.*, "A Study of charm hadron production in Z0 —> c anti-c and Z0 —> b anti-b decays at LEP", *Z. Phys. C* **72** (1996) 1–16.

[114] **Belle** Collaboration, M. Niiyama *et al.*, "Production cross sections of hyperons and charmed baryons from e^+e^- annihilation near $\sqrt{s}$ = 10.52~GeV", *Phys. Rev. D* **97** no. 7, (2018) 072005, arXiv:1706.06791 [hep-ex].

[115] S. Frixione, P. Nason, and G. Ridolfi, "A Positive-weight next-to-leading-order Monte Carlo for heavy flavour hadroproduction", *JHEP* **09** (2007) 126, arXiv:0707.3088 [hep-ph].

[116] **ALICE** Collaboration, S. Acharya *et al.*, "Transverse momentum spectra and nuclear modification factors of charged particles in pp, p-Pb and Pb-Pb collisions at the LHC", *JHEP* **11** (2018) 013, arXiv:1802.09145 [nucl-ex].

[117] H. Paukkunen, "Nuclear pdfs in the beginning of the lhc era", *Nuclear Physics A* **926** (2014) 24–33. https://www.sciencedirect.com/science/article/pii/S0375947414000839. IS2013.

[118] M. Arneodo, "Nuclear effects in structure functions", *Physics Reports* **240** no. 5, (1994) 301–393. https://www.sciencedirect.com/science/article/pii/0370157394900485.

[119] A. Bodek and J. L. Ritchie, "Fermi-motion effects in deep-inelastic lepton scattering from nuclear targets", *Phys. Rev. D* **23** (Mar, 1981) 1070–1091. https://link.aps.org/doi/10.1103/PhysRevD.23.1070.

[120] G. Berlad, A. Dar, and G. Eilam, "A Quark-parton Model of Nuclear Production", *Phys. Rev. D* **22** (1980) 1547.

[121] L. L. Frankfurt and M. I. Strikman, "Nuclear Structure Function at Large X and Λ (QCD)", *Phys. Lett. B* **114** (1982) 345–348.

[122] M. Braun and M. Tokarev, "Deuteron and neutron structure functions and the effect of relativistic fermi motion", *Physics Letters B* **320** no. 3, (1994) 381–387. https://www.sciencedirect.com/science/article/pii/0370269394906742.

[123] K. Saito and T. Uchiyama, "Effect of the Fermi Motion on Nuclear Structure Functions and the Emc Effect", *Z. Phys. A* **322** (1985) 299.

[124] N. Armesto, "Nuclear shadowing", *J. Phys. G* **32** (2006) R367–R394, arXiv:hep-ph/0604108.

[125] **H1** Collaboration, F. D. Aaron *et al.*, "A Precision Measurement of the Inclusive ep Scattering Cross Section at HERA", *Eur. Phys. J. C* **64** (2009) 561–587, arXiv:0904.3513 [hep-ex].

[126] F. Gelis, E. Iancu, J. Jalilian-Marian, and R. Venugopalan, "The Color Glass Condensate", *Ann. Rev. Nucl. Part. Sci.* **60** (2010) 463–489, arXiv:1002.0333 [hep-ph].

[127] K. J. Eskola, P. Paakkinen, H. Paukkunen, and C. A. Salgado, "EPPS16: Nuclear parton distributions with LHC data", *Eur. Phys. J. C* **77** no. 3, (2017) 163, arXiv:1612.05741 [hep-ph].

[128] J. R. Andersen and A. Sabio Vera, "Solving the BFKL equation in the next-to-leading approximation", *Phys. Lett. B* **567** (2003) 116–124, arXiv:hep-ph/0305236.

[129] **European Muon** Collaboration, J. J. Aubert *et al.*, "The ratio of the nucleon structure functions $F2_n$ for iron and deuterium", *Phys. Lett. B* **123** (1983) 275–278.

[130] K. Kovarik *et al.*, "nCTEQ15 - Global analysis of nuclear parton distributions with uncertainties in the CTEQ framework", *Phys. Rev. D* **93** no. 8, (2016) 085037, arXiv:1509.00792 [hep-ph].

[131] D. Antreasyan, J. W. Cronin, H. J. Frisch, M. J. Shochet, L. Kluberg, P. A. Piroué, and R. L. Sumner, "Production of hadrons at large transverse momentum in 200-, 300-, and 400-gev $p-p$ and p-nucleus collisions", *Phys. Rev. D* **19** (Feb, 1979) 764–778. https://link.aps.org/doi/10.1103/PhysRevD.19.764.

[132] R. Sharma, I. Vitev, and B.-W. Zhang, "Light-cone wave function approach to open heavy flavor dynamics in QCD matter", *Phys. Rev. C* **80** (2009) 054902, arXiv:0904.0032 [hep-ph].

[133] Z.-B. Kang, I. Vitev, E. Wang, H. Xing, and C. Zhang, "Multiple scattering effects on heavy meson production in p+A collisions at backward rapidity", *Phys. Lett. B* **740** (2015) 23–29, arXiv:1409.2494 [hep-ph].

[134] Y. Xu, S. Cao, G.-Y. Qin, W. Ke, M. Nahrgang, J. Auvinen, and S. A. Bass, "Heavy-flavor dynamics in relativistic p-Pb collisions at $\sqrt{S_{NN}} = 5.02$ TeV", *Nucl. Part. Phys. Proc.* **276-278** (2016) 225–228, arXiv:1510.07520 [nucl-th].

[135] A. Beraudo, A. De Pace, M. Monteno, M. Nardi, and F. Prino, "Heavy-flavour production in high-energy d-Au and p-Pb collisions", *JHEP* **03** (2016) 123, arXiv:1512.05186 [hep-ph].

[136] **ALICE** Collaboration, S. Acharya *et al.*, "Measurement of prompt D^0, D^+, D^{*+}, and D_S^+ production in p–Pb collisions at $\sqrt{s_{NN}}$ = 5.02 TeV", *JHEP* **12** (2019) 092, arXiv:1906.03425 [nucl-ex].

[137] M. L. Mangano, "Introduction to QCD", in *1998 European School of High-Energy Physics*. 1998.

[138] S. Cao, G.-Y. Qin, and S. A. Bass, "Heavy-quark dynamics and hadronization in ultrarelativistic heavy-ion collisions: Collisional versus radiative energy loss", *Phys. Rev. C* **88** (2013) 044907, arXiv:1308.0617 [nucl-th].

[139] S. Peigne and A. V. Smilga, "Energy losses in a hot plasma revisited", *Phys. Usp.* **52** (2009) 659–685, arXiv:0810.5702 [hep-ph].

[140] S. Peigne and A. Peshier, "Collisional energy loss of a fast heavy quark in a quark-gluon plasma", *Phys. Rev. D* **77** (2008) 114017, arXiv:0802.4364 [hep-ph].

[141] E. Braaten and M. H. Thoma, "Energy loss of a heavy quark in the quark - gluon plasma", *Phys. Rev. D* **44** no. 9, (1991) R2625.

[142] F. Prino and R. Rapp, "Open Heavy Flavor in QCD Matter and in Nuclear Collisions", *J. Phys. G* **43** no. 9, (2016) 093002, arXiv:1603.00529 [nucl-ex].

[143] C. A. Salgado and U. A. Wiedemann, "Calculating quenching weights", *Phys. Rev. D* **68** (2003) 014008, arXiv:hep-ph/0302184.

[144] Y. L. Dokshitzer and D. E. Kharzeev, "Heavy quark colorimetry of QCD matter", *Phys. Lett. B* **519** (2001) 199–206, arXiv:hep-ph/0106202.

[145] W.-C. Xiang, H.-T. Ding, and D.-C. Zhou, "Radiative energy loss of heavy quark and dead cone effect in ultra-relativistic heavy ion collisions", *Chin. Phys. Lett.* **22** (2005) 72–75.

[146] **ALICE** Collaboration, N. Zardoshti, "First Direct Observation of the Dead-Cone Effect", *Nucl. Phys. A* **1005** (Apr, 2020) 121905. 4 p, arXiv:2004.05968. https://cds.cern.ch/record/2715338.

[147] **ALICE** Collaboration, S. Acharya *et al.*, "Measurement of D^0, D^+, D^{*+} and D_s^+ production in Pb-Pb collisions at $\sqrt{s_{NN}} = 5.02$ TeV", *JHEP* **10** (2018) 174, arXiv:1804.09083 [nucl-ex].

[148] **ALICE** Collaboration, J. Adam *et al.*, "Centrality dependence of high-p_T D meson suppression in Pb-Pb collisions at $\sqrt{s_{NN}} = 2.76$ TeV", *JHEP* **11** (2015) 205, arXiv:1506.06604 [nucl-ex]. [Addendum: JHEP 06, 032 (2017)].

[149] **CMS** Collaboration, V. Khachatryan *et al.*, "Suppression and azimuthal anisotropy of prompt and nonprompt J/ψ production in PbPb collisions at $\sqrt{s_{NN}} = 2.76$ TeV", *Eur. Phys. J. C* **77** no. 4, (2017) 252, arXiv:1610.00613 [nucl-ex].

[150] M. Djordjevic and M. Gyulassy, "Where is the charm quark energy loss at RHIC?", *Phys. Lett. B* **560** (2003) 37–43, arXiv:nucl-th/0302069.

[151] **ALICE** Collaboration, S. Acharya *et al.*, "Transverse-momentum and event-shape dependence of D-meson flow harmonics in Pb–Pb collisions at $\sqrt{s_{NN}} = 5.02$ TeV", *Phys. Lett. B* **813** (2021) 136054, arXiv:2005.11131 [nucl-ex].

[152] **ALICE** Collaboration, S. Acharya *et al.*, "Higher harmonic non-linear flow modes of charged hadrons in Pb-Pb collisions at $\sqrt{s_{NN}} = 5.02$ TeV", *JHEP* **05** (2020) 085, arXiv:2002.00633 [nucl-ex].

[153] **ALICE** Collaboration, S. Acharya *et al.*, "J/ψ elliptic and triangular flow in Pb-Pb collisions at $\sqrt{s_{NN}} = 5.02$ TeV", *JHEP* **10** (2020) 141, arXiv:2005.14518 [nucl-ex].

[154] **ALICE** Collaboration, S. Acharya *et al.*, "Elliptic Flow of Electrons from Beauty-Hadron Decays in Pb-Pb Collisions at $\sqrt{s_{NN}} = 5.02$ TeV", *Phys. Rev. Lett.* **126** no. 16, (2021) 162001, arXiv:2005.11130 [nucl-ex].

[155] **ALICE** Collaboration, S. Acharya *et al.*, "Measurement of $\Upsilon(1S)$ elliptic flow at forward rapidity in Pb-Pb collisions at $\sqrt{s_{NN}} = 5.02$ TeV", *Phys. Rev. Lett.* **123** no. 19, (2019) 192301, arXiv:1907.03169 [nucl-ex].

[156] D. Molnar, "Charm elliptic flow from quark coalescence dynamics", *J. Phys. G* **31** (2005) S421–S428, arXiv:nucl-th/0410041.

[157] D. Molnar and S. A. Voloshin, "Elliptic flow at large transverse momenta from quark coalescence", *Phys. Rev. Lett.* **91** (2003) 092301, arXiv:nucl-th/0302014.

[158] **STAR** Collaboration, J. Adam *et al.*, "First measurement of Λ_c baryon production in Au+Au collisions at $\sqrt{s_{NN}} = 200$ GeV", *Phys. Rev. Lett.* **124** no. 17, (2020) 172301, arXiv:1910.14628 [nucl-ex].

[159] **STAR Collaboration** Collaboration, G. e. A. Agakishiev, "Strangeness enhancement in cu-cu and au-au collisions at $\sqrt{s_{NN}} = 200$ GeV", *Phys. Rev. Lett.* **108** (Feb, 2012) 072301. https://link.aps.org/doi/10.1103/PhysRevLett.108.072301.

[160] **ALICE** Collaboration, B. B. Abelev *et al.*, "K^0_S and Λ production in Pb-Pb collisions at $\sqrt{s_{NN}}$ = 2.76 TeV", *Phys. Rev. Lett.* **111** (2013) 222301, arXiv:1307.5530 [nucl-ex].

[161] Y. Oh, C. M. Ko, S. H. Lee, and S. Yasui, "Heavy baryon/meson ratios in relativistic heavy ion collisions", *Phys. Rev. C* **79** (2009) 044905, arXiv:0901.1382 [nucl-th].

[162] S. Cho, K.-J. Sun, C. M. Ko, S. H. Lee, and Y. Oh, "Charmed hadron production in an improved quark coalescence model", *Phys. Rev. C* **101** no. 2, (2020) 024909, arXiv:1905.09774 [nucl-th].

[163] M. He and R. Rapp, "Hadronization and Charm-Hadron Ratios in Heavy-Ion Collisions", *Phys. Rev. Lett.* **124** no. 4, (2020) 042301, arXiv:1905.09216 [nucl-th].

[164] J. Zhao, S. Shi, N. Xu, and P. Zhuang, "Sequential Coalescence with Charm Conservation in High Energy Nuclear Collisions", arXiv:1805.10858 [hep-ph].

[165] S. Plumari, V. Minissale, S. K. Das, G. Coci, and V. Greco, "Charmed Hadrons from Coalescence plus Fragmentation in relativistic nucleus-nucleus collisions at RHIC and LHC", *Eur. Phys. J. C* **78** no. 4, (2018) 348, arXiv:1712.00730 [hep-ph].

[166] P. Skands, S. Carrazza, and J. Rojo, "Tuning PYTHIA 8.1: the Monash 2013 Tune", *Eur. Phys. J. C* **74** no. 8, (2014) 3024, arXiv:1404.5630 [hep-ph].

[167] C. Bierlich and J. R. Christiansen, "Effects of color reconnection on hadron flavor observables", *Phys. Rev. D* **92** no. 9, (2015) 094010, arXiv:1507.02091 [hep-ph].

[168] A. Chodos, R. L. Jaffe, K. Johnson, and C. B. Thorn, "Baryon Structure in the Bag Theory", *Phys. Rev. D* **10** (1974) 2599.

[169] T. DeGrand, R. L. Jaffe, K. Johnson, and J. Kiskis, "Masses and other parameters of the light hadrons", *Phys. Rev. D* **12** (Oct, 1975) 2060–2076. https://link.aps.org/doi/10.1103/PhysRevD.12.2060.

[170] M. H. Seymour and M. Marx, "Monte Carlo Event Generators", in *69th Scottish Universities Summer School in Physics: LHC Physics*. 4, 2013. arXiv:1304.6677 [hep-ph].

[171] X. Artru and G. Mennessier, "String model and multiproduction", *Nucl. Phys. B* **70** (1974) 93–115.

[172] R. D. Field and R. P. Feynman, "A Parametrization of the Properties of Quark Jets", *Nucl. Phys. B* **136** (1978) 1.

[173] B. Andersson, G. Gustafson, G. Ingelman, and T. Sjostrand, "Parton Fragmentation and String Dynamics", *Phys. Rept.* **97** (1983) 31–145.

[174] B. Andersson, *The Lund model*, vol. 7. Cambridge University Press, 7, 2005.

[175] S. Ferreres-Solé and T. Sjöstrand, "The space–time structure of hadronization in the Lund model", *Eur. Phys. J. C* **78** no. 11, (2018) 983, arXiv:1808.04619 [hep-ph].

[176] P. Eden and G. Gustafson, "Baryon production in the string fragmentation picture", *Z. Phys. C* **75** (1997) 41–49, arXiv:hep-ph/9606454.

[177] J. Bellm *et al.*, "Herwig 7.0/Herwig++ 3.0 release note", *Eur. Phys. J. C* **76** no. 4, (2016) 196, arXiv:1512.01178 [hep-ph].

[178] **ALICE** Collaboration, S. Acharya *et al.*, "Λ_c^+ production in pp collisions at $\sqrt{s} = 7$ TeV and in p-Pb collisions at $\sqrt{s_{\rm NN}} = 5.02$ TeV", *JHEP* **04** (2018) 108, arXiv:1712.09581 [nucl-ex].

[179] J. R. Christiansen and P. Z. Skands, "String Formation Beyond Leading Colour", *JHEP* **08** (2015) 003, arXiv:1505.01681 [hep-ph].

[180] **CMS** Collaboration, V. Khachatryan *et al.*, "Strange Particle Production in pp Collisions at $\sqrt{s} = 0.9$ and 7 TeV", *JHEP* **05** (2011) 064, arXiv:1102.4282 [hep-ex].

[181] G. Gustafson, "Dual description of a confined colour field", *Physics Letters B* **175** no. 4, (1986) 453–456. https://www.sciencedirect.com/science/article/pii/0370269386906222.

[182] T. Sjöstrand and M. van Zijl, "A multiple-interaction model for the event structure in hadron collisions", *Phys. Rev. D* **36** (Oct, 1987) 2019–2041. https://link.aps.org/doi/10.1103/PhysRevD.36.2019.

[183] S. Gieseke, C. Rohr, and A. Siodmok, "Colour reconnections in Herwig++", *Eur. Phys. J. C* **72** (2012) 2225, arXiv:1206.0041 [hep-ph].

[184] **CMS** Collaboration, V. Khachatryan *et al.*, "Charged Particle Multiplicities in pp Interactions at $\sqrt{s} = 0.9$, 2.36, and 7 TeV", *JHEP* **01** (2011) 079, arXiv:1011.5531 [hep-ex].

[185] **ATLAS** Collaboration, G. Aad *et al.*, "Charged-particle multiplicities in pp interactions measured with the ATLAS detector at the LHC", *New J. Phys.* **13** (2011) 053033, arXiv:1012.5104 [hep-ex].

[186] **ALICE** Collaboration, B. B. Abelev *et al.*, "Multiplicity dependence of the average transverse momentum in pp, p-Pb, and Pb-Pb collisions at the LHC", *Phys. Lett. B* **727** (2013) 371–380, arXiv:1307.1094 [nucl-ex].

[187] M. He and R. Rapp, "Charm-baryon production in proton-proton collisions", *Physics Letters B* **795** (2019) 117–121. https://www.sciencedirect.com/science/article/pii/S037026931930382X.

[188] D. Ebert, R. N. Faustov, and V. O. Galkin, "Spectroscopy and Regge trajectories of heavy baryons in the relativistic quark-diquark picture", *Phys. Rev. D* **84** (2011) 014025, arXiv:1105.0583 [hep-ph].

[189] A. Bazavov *et al.*, "The melting and abundance of open charm hadrons", *Phys. Lett. B* **737** (2014) 210–215, arXiv:1404.4043 [hep-lat].

[190] V. Minissale, S. Plumari, and V. Greco, "Charm Hadrons in pp collisions at LHC energy within a Coalescence plus Fragmentation approach", arXiv:2012.12001 [hep-ph].

[191] **CMS Collaboration** Collaboration, V. t. Khachatryan, "Measurement of long-range near-side two-particle angular correlations in pp collisions at $\sqrt{s} = 13$ TeV", *Phys. Rev. Lett.* **116** (Apr, 2016) 172302. https://link.aps.org/doi/10.1103/PhysRevLett.116.172302.

[192] R. D. Weller and P. Romatschke, "One fluid to rule them all: viscous hydrodynamic description of event-by-event central p+p, p+Pb and Pb+Pb collisions at $\sqrt{s} = 5.02$ TeV", *Phys. Lett. B* **774** (2017) 351–356, arXiv:1701.07145 [nucl-th].

[193] C. Shen, J.-F. Paquet, G. S. Denicol, S. Jeon, and C. Gale, "Collectivity and electromagnetic radiation in small systems", *Phys. Rev. C* **95** no. 1, (2017) 014906, arXiv:1609.02590 [nucl-th].

[194] M. Greif, C. Greiner, B. Schenke, S. Schlichting, and Z. Xu, "Importance of initial and final state effects for azimuthal correlations in p+Pb collisions", *Phys. Rev. D* **96** no. 9, (2017) 091504, arXiv:1708.02076 [hep-ph].

[195] Y. Sun, S. Plumari, and V. Greco, "Study of collective anisotropies v_2 and v_3 and their fluctuations in pA collisions at LHC within a relativistic transport approach", *Eur. Phys. J. C* **80** no. 1, (2020) 16, arXiv:1907.11287 [nucl-th].

[196] C.-W. Hwang, "Charge radii of light and heavy mesons", *Eur. Phys. J. C* **23** (2002) 585–590, arXiv:hep-ph/0112237.

[197] C. Albertus, J. E. Amaro, E. Hernandez, and J. Nieves, "Charmed and bottom baryons: A Variational approach based on heavy quark symmetry", *Nucl. Phys. A* **740** (2004) 333–361, arXiv:nucl-th/0311100.

[198] C. Peterson, D. Schlatter, I. Schmitt, and P. M. Zerwas, "Scaling violations in inclusive e^+e^- annihilation spectra", *Phys. Rev. D* **27** (Jan, 1983) 105–111. https://link.aps.org/doi/10.1103/PhysRevD.27.105.

[199] M. Lisovyi, A. Verbytskyi, and O. Zenaiev, "Combined analysis of charm-quark fragmentation-fraction measurements", *Eur. Phys. J. C* **76** no. 7, (2016) 397, arXiv:1509.01061 [hep-ex].

[200] J. Song, H.-h. Li, and F.-l. Shao, "New feature of low p_T charm quark hadronization in pp collisions at $\sqrt{s} = 7$ TeV", *Eur. Phys. J. C* **78** no. 4, (2018) 344, arXiv:1801.09402 [hep-ph].

[201] H.-H. Li, F.-L. Shao, J. Song, and R.-Q. Wang, "Production of single-charm hadrons by quark combination mechanism in p-Pb collisions at $\sqrt{s_{NN}} = 5.02$ TeV", *Phys. Rev. C* **97** no. 6, (2018) 064915, arXiv:1712.08921 [hep-ph].

[202] J. Song, X.-r. Gou, F.-l. Shao, and Z.-T. Liang, "Quark number scaling of hadronic p_T spectra and constituent quark degree of freedom in p-Pb collisions at $\sqrt{s_{NN}} = 5.02$ TeV", *Phys. Lett. B* **774** (2017) 516–521, arXiv:1707.03949 [hep-ph].

[203] R. Rapp and E. V. Shuryak, "D meson production from recombination in hadronic collisions", *Phys. Rev. D* **67** (2003) 074036, arXiv:hep-ph/0301245.

[204] X.-r. Gou, F.-l. Shao, R.-q. Wang, H.-h. Li, and J. Song, "New insights into hadron production mechanism from p_T spectra in pp collisions at $\sqrt{s} = 7$ TeV", *Phys. Rev. D* **96** no. 9, (2017) 094010, arXiv:1707.06906 [hep-ph].

[205] **ALICE** Collaboration, J. Adam *et al.*, "D-meson production in p-Pb collisions at $\sqrt{s_{\rm NN}}$ =5.02 TeV and in pp collisions at $\sqrt{s}$ =7 TeV", *Phys. Rev. C* **94** no. 5, (2016) 054908, arXiv:1605.07569 [nucl-ex].

[206] **ALICE** Collaboration, B. B. Abelev *et al.*, "Measurement of prompt D-meson production in $p-Pb$ collisions at $\sqrt{s_{NN}}$ = 5.02 TeV", *Phys. Rev. Lett.* **113** no. 23, (2014) 232301, arXiv:1405.3452 [nucl-ex].

[207] *LEP design report*. CERN, Geneva, 1984. http://cds.cern.ch/record/102083. Copies shelved as reports in LEP, PS and SPS libraries.

[208] **ATLAS** Collaboration, G. Aad *et al.*, "The ATLAS Experiment at the CERN Large Hadron Collider", *JINST* **3** (2008) S08003. 437 p. https://cds.cern.ch/record/1129811. Also published by CERN Geneva in 2010.

[209] **CMS** Collaboration, S. Chatrchyan *et al.*, "The CMS Experiment at the CERN LHC", *JINST* **3** (2008) S08004.

[210] **ATLAS** Collaboration, G. Aad *et al.*, "Observation of a new particle in the search for the Standard Model Higgs boson with the ATLAS detector at the LHC", *Phys. Lett. B* **716** (2012) 1–29, arXiv:1207.7214 [hep-ex].

[211] **CMS** Collaboration, S. Chatrchyan *et al.*, "Observation of a New Boson at a Mass of 125 GeV with the CMS Experiment at the LHC", *Phys. Lett. B* **716** (2012) 30–61, arXiv:1207.7235 [hep-ex].

[212] **LHCb** Collaboration, J. Alves, A.Augusto *et al.*, "The LHCb Detector at the LHC", *JINST* **3** (2008) S08005.

[213] **ALICE** Collaboration, K. Aamodt *et al.*, "The ALICE experiment at the CERN LHC", *JINST* **3** (2008) S08002.

[214] K. Schindl, "The Injector Chain for the LHC; rev. version",. https://cds.cern.ch/record/384396.

[215] A. Beuret *et al.*, "The LHC Lead Ion Injector Chain", in *9th European Particle Accelerator Conference (EPAC 2004)*. 7, 2004.

[216] "Linear accelerator 2",. https://cds.cern.ch/record/1997427.

[217] "The Proton Synchrotron Booster",. https://cds.cern.ch/record/1997372.

[218] G. K. Green and E. D. Courant, *The Proton Synchrotron*, pp. 218–340. Springer Berlin Heidelberg, Berlin, Heidelberg, 1959. https://doi.org/10.1007/978-3-642-45926-9_6.

[219] "Linear accelerator 3",. http://cds.cern.ch/record/1997426.

[220] "The Low Energy Ion Ring",. https://cds.cern.ch/record/1997352.

[221] "Cern optics repository." https://acc-models.web.cern.ch/acc-models/structure/.

[222] **ALICE** Collaboration, K. Aamodt *et al.*, "Alignment of the ALICE Inner Tracking System with cosmic-ray tracks", *JINST* **5** (2010) P03003, arXiv:1001.0502 [physics.ins-det].

[223] **ALICE** Collaboration, G. Dellacasa *et al.*, *ALICE time projection chamber: Technical Design Report*. Technical Design Report ALICE. CERN, Geneva, 2000. https://cds.cern.ch/record/451098.

[224] A. Maire, "Production des baryons multi-étranges au LHC dans les collisions proton-proton avec l'expérience ALICE", 2011. https://cds.cern.ch/record/1490315. Presented 13 Oct 2011.

[225] **ALICE** Collaboration, P. Cortese *et al.*, "ALICE: Physics performance report, volume I", *J. Phys. G* **30** (2004) 1517–1763.

[226] **ALICE Collaboration** Collaboration, *ALICE Time-Of-Flight system (TOF): Technical Design Report*. Technical design report. ALICE. CERN, Geneva, 2000. https://cds.cern.ch/record/430132.

[227] **ALICE** Collaboration, F. Carnesecchi, "Performance of the ALICE Time-Of-Flight detector at the LHC", *JINST* **14** no. 06, (2019) C06023, arXiv:1806.03825 [physics.ins-det].

[228] **ALICE EMCal** Collaboration, U. Abeysekara *et al.*, "ALICE EMCal Physics Performance Report", arXiv:1008.0413 [physics.ins-det].

[229] **ALICE Collaboration** Collaboration, V. I. Man'ko, W. Klempt, L. Leistam, J. De Groot, and J. Schükraft, *ALICE Photon Spectrometer (PHOS): Technical Design Report*. Technical design report. ALICE. CERN, Geneva, 1999. https://cds.cern.ch/record/381432.

[230] **ALICE** Collaboration, E. Abbas *et al.*, "Performance of the ALICE VZERO system", *JINST* **8** (2013) P10016, arXiv:1306.3130 [nucl-ex].

[231] K. Bos *et al.*, *LHC computing Grid: Technical Design Report. Version 1.06 (20 Jun 2005)*. Technical design report. LCG. CERN, Geneva, 2005. https://cds.cern.ch/record/840543.

[232] "Worldwide lhc computing grid." https://wlcg-public.web.cern.ch/.

[233] "The monarc project." https://monarc.web.cern.ch/MONARC/.

[234] "Alice environment." https://alien.web.cern.ch/.

[235] R. Brun and F. Rademakers, "ROOT: An object oriented data analysis framework", *Nucl. Instrum. Meth. A* **389** (1997) 81–86.

[236] T. Sjostrand, S. Mrenna, and P. Z. Skands, "A Brief Introduction to PYTHIA 8.1", *Comput. Phys. Commun.* **178** (2008) 852–867, arXiv:0710.3820 [hep-ph].

[237] R. Brun, F. Bruyant, F. Carminati, S. Giani, M. Maire, A. McPherson, G. Patrick, and L. Urban, *GEANT: Detector Description and Simulation Tool; Oct 1994*. CERN Program Library. CERN, Geneva, 1993. https://cds.cern.ch/record/1082634. Long Writeup W5013.

[238] **GEANT4** Collaboration, S. Agostinelli *et al.*, "GEANT4–a simulation toolkit", *Nucl. Instrum. Meth. A* **506** (2003) 250–303.

[239] A. Ferrari, P. R. Sala, A. Fassò, and J. Ranft, *FLUKA: A multi-particle transport code (program version 2005)*. CERN Yellow Reports: Monographs. CERN, Geneva, 2005. https://cds.cern.ch/record/898301.

[240] P. Buncic, M. Krzewicki, and P. Vande Vyvre, "Technical Design Report for the Upgrade of the Online-Offline Computing System", tech. rep., Apr, 2015. https://cds.cern.ch/record/2011297.

[241] **ALICE** Collaboration, C. W. Fabjan, L. Jirdén, V. Lindestruth, L. Riccati, D. Rorich, P. Van de Vyvre, O. Villalobos Baillie, and H. de Groot, *ALICE trigger data-acquisition high-level trigger and control system: Technical Design Report*. Technical design report. ALICE. CERN, Geneva, 2004. https://cds.cern.ch/record/684651.

[242] **ALICE** Collaboration, B. B. Abelev *et al.*, "Performance of the ALICE Experiment at the CERN LHC", *Int. J. Mod. Phys. A* **29** (2014) 1430044, arXiv:1402.4476 [nucl-ex].

[243] **ALICE** Collaboration, F. Carena *et al.*, "The ALICE data acquisition system", *Nucl. Instrum. Meth. A* **741** (2014) 130–162.

[244] T. Alt, G. Grastveit, H. Helstrup, V. Lindenstruth, C. Loizides, D. Röhrich, B. Skaali, T. Steinbeck, R. Stock, H. Tilsner, K. Ullaland, A. Vestbø, T. Vik, A. Wiebalck, and (for the ALICE Collaboration), "The ALICE high level trigger", *Journal of Physics G: Nuclear and Particle Physics* **30** no. 8, (Jul, 2004) S1097–S1100. https://doi.org/10.1088/0954-3899/30/8/066.

[245] J. Conrad, J. G. Contreras, and C. E. Jorgensen, "Minimum bias triggers in proton-proton collisions with VZERO and pixel detectors", tech. rep., CERN, Geneva, 2005. http://cds.cern.ch/record/960438.

[246] **ALICE** Collaboration, B. Abelev *et al.*, "Centrality determination of Pb-Pb collisions at $\sqrt{s_{NN}}$ = 2.76 TeV with ALICE", *Phys. Rev. C* **88** no. 4, (2013) 044909, arXiv:1301.4361 [nucl-ex].

[247] D. Kharzeev, E. Levin, and M. Nardi, "Color glass condensate at the LHC: Hadron multiplicities in pp, pA and AA collisions", *Nucl. Phys. A* **747** (2005) 609–629, arXiv:hep-ph/0408050.

[248] W.-T. Deng, X.-N. Wang, and R. Xu, "Hadron production in p+p, p+Pb, and Pb+Pb collisions with the HIJING 2.0 model at energies available at the CERN Large Hadron Collider", *Phys. Rev. C* **83** (2011) 014915, arXiv:1008.1841 [hep-ph].

[249] R. Fruhwirth, "Application of Kalman filtering to track and vertex fitting", *Nucl. Instrum. Meth. A* **262** (1987) 444–450.

[250] V. Karimäki, "Effective Vertex Fitting", Tech. Rep. CMS-NOTE-1997-051, CERN, Geneva, Jun, 1997. http://cds.cern.ch/record/687531.

[251] "The fitting of power series, meaning polynomials, illustrated on band-spectroscopic data", *Technometrics* **16** no. 2, (1974) 147–185. http://www.jstor.org/stable/1267936.

[252] A. Akindinov *et al.*, "Performance of the ALICE Time-Of-Flight detector at the LHC", *Eur. Phys. J. Plus* **128** (2013) 44.

[253] **PHENIX** Collaboration, A. Adare *et al.*, "Heavy Quark Production in $p + p$ and Energy Loss and Flow of Heavy Quarks in Au+Au Collisions at $\sqrt{s_{NN}} = 200$ GeV", *Phys. Rev. C* **84** (2011) 044905, arXiv:1005.1627 [nucl-ex].

[254] **ALICE** Collaboration, S. Acharya *et al.*, "Measurements of low-p_T electrons from semileptonic heavy-flavour hadron decays at mid-rapidity in pp and Pb-Pb collisions at $\sqrt{s_{\rm NN}} = 2.76$ TeV", *JHEP* **10** (2018) 061, arXiv:1805.04379 [nucl-ex].

[255] F. B. et *al.*, "Observation of high transverse momentum electrons at the cern isr", *Physics Letters B* **53** no. 2, (1974) 212–216. https://www.sciencedirect.com/science/article/pii/0370269374905358.

[256] C. A. et *al.*, "Beauty production at the cern $p\overline{p}$ collider", *Physics Letters B* **256** no. 1, (1991) 121–128. https://www.sciencedirect.com/science/article/pii/037026939190228I.

[257] O. Botner, L. Eek, T. Ekelöf, K. Fransson, A. Hallgren, P. Kostarakis, G. Lenzen, and B. Lund-Jensen, "Production of prompt electrons in the charm pt region at $\sqrt{s}$ = 630 gev", *Physics Letters B* **236** no. 4, (1990) 488–494. https://www.sciencedirect.com/science/article/pii/037026939090389N.

[258] D. e. a. Acosta, "Study of the heavy flavor content of jets produced in association with w bosons in $p\overline{p}$ collisions at $\sqrt{s} = 1.8$ tev", *Phys. Rev. D* **65** (Feb, 2002) 052007. https://link.aps.org/doi/10.1103/PhysRevD.65.052007.

[259] **D0 Collaboration** Collaboration, S. e. a. Abachi, "Inclusive μ and b-quark production cross sections in $p\overline{p}$ collisions at $\sqrt{s} = 1.8$ tev", *Phys. Rev. Lett.* **74** (May, 1995) 3548–3552. https://link.aps.org/doi/10.1103/PhysRevLett.74.3548.

[260] **STAR** Collaboration, B. I. Abelev *et al.*, "Transverse momentum and centrality dependence of high-p_T non-photonic electron suppression in Au+Au collisions at $\sqrt{s_{NN}} = 200$\,GeV", *Phys. Rev. Lett.* **98** (2007) 192301, arXiv:nucl-ex/0607012. [Erratum: Phys.Rev.Lett. 106, 159902 (2011)].

[261] **PHENIX** Collaboration, S. S. Adler *et al.*, "Nuclear modification of electron spectra and implications for heavy quark energy loss in Au+Au collisions at s(NN)**(1/2) - 200-GeV", *Phys. Rev. Lett.* **96** (2006) 032301, arXiv:nucl-ex/0510047.

[262] **PHENIX** Collaboration, A. Adare *et al.*, "System-size dependence of open-heavy-flavor production in nucleus-nucleus collisions at $\sqrt{s_{NN}}$=200 GeV", *Phys. Rev. C* **90** no. 3, (2014) 034903, arXiv:1310.8286 [nucl-ex].

[263] M. He, R. J. Fries, and R. Rapp, "Heavy Flavor at the Large Hadron Collider in a Strong Coupling Approach", *Phys. Lett. B* **735** (2014) 445–450, arXiv:1401.3817 [nucl-th].

[264] W. M. Alberico, A. Beraudo, A. De Pace, A. Molinari, M. Monteno, M. Nardi, F. Prino, and M. Sitta, "Heavy flavors in AA collisions: production, transport and final spectra", *Eur. Phys. J. C* **73** (2013) 2481, arXiv:1305.7421 [hep-ph].

[265] M. Nahrgang, J. Aichelin, P. B. Gossiaux, and K. Werner, "Influence of hadronic bound states above T_c on heavy-quark observables in Pb + Pb collisions at at the CERN Large Hadron Collider", *Phys. Rev. C* **89** no. 1, (2014) 014905, arXiv:1305.6544 [hep-ph].

[266] S. A. et *al.*, "Measurement of electrons from semileptonic heavy-flavour hadron decays at midrapidity in pp and pb–pb collisions at snn=5.02 tev", *Physics Letters B* **804** (2020) 135377. https://www.sciencedirect.com/science/article/pii/S0370269320301817.

[267] C. Loizides, J. Kamin, and D. d'Enterria, "Improved Monte Carlo Glauber predictions at present and future nuclear colliders", *Phys. Rev. C* **97** no. 5, (2018) 054910, arXiv:1710.07098 [nucl-ex]. [Erratum: Phys.Rev.C 99, 019901 (2019)].

[268] **ALICE** Collaboration, J. Adam *et al.*, "Elliptic flow of electrons from heavy-flavour hadron decays at mid-rapidity in Pb-Pb collisions at $\sqrt{s_{\rm NN}} = 2.76$ TeV", *JHEP* **09** (2016) 028, arXiv:1606.00321 [nucl-ex].

[269] D. Leermakers, "Systematic study of track quality cuts at ALICE",. https://cds.cern.ch/record/2045797.

[270] **ATLAS Collaboration** Collaboration, M. e. a. Aaboud, "Measurement of the suppression and azimuthal anisotropy of muons from heavy-flavor decays in pb+pb collisions at $\sqrt{s_{NN}} = 2.76$ tev with the atlas detector", *Phys. Rev. C* **98** (Oct, 2018) 044905. https://link.aps.org/doi/10.1103/PhysRevC.98.044905.

[271] **ALICE** Collaboration, J. Adam *et al.*, "Measurement of the production of high-$p_{\rm T}$ electrons from heavy-flavour hadron decays in Pb-Pb collisions at $\sqrt{\mathbf{s}_{\rm NN}}$ = 2.76 TeV", *Phys. Lett. B* **771** (2017) 467–481, arXiv:1609.07104 [nucl-ex].

[272] **ALICE Collaboration** Collaboration, Abelev, B. et *al.*, "Measurement of electrons from semileptonic heavy-flavor hadron decays in pp collisions at $\sqrt{s} = 2.76$ TeV", *Phys. Rev. D* **91** (Jan, 2015) 012001. https://link.aps.org/doi/10.1103/PhysRevD.91.012001.

[273] M. Gyulassy and X.-N. Wang, "HIJING 1.0: A Monte Carlo program for parton and particle production in high-energy hadronic and nuclear collisions", *Comput. Phys. Commun.* **83** (1994) 307, arXiv:nucl-th/9502021.

[274] P. K. Khandai, P. Shukla, and V. Singh, "Meson spectra and m_T scaling in p + p, d + au, and au + au collisions at $\sqrt{s_{NN}} = 200$ gev", *Phys. Rev. C* **84** (Nov, 2011) 054904. https://link.aps.org/doi/10.1103/PhysRevC.84.054904.

[275] L. Altenkämper, F. Bock, C. Loizides, and N. Schmidt, "Applicability of transverse mass scaling in hadronic collisions at energies available at the cern large hadron collider", *Phys. Rev. C* **96** (Dec, 2017) 064907. https://link.aps.org/doi/10.1103/PhysRevC.96.064907.

[276] T. Sjostrand, S. Mrenna, and P. Z. Skands, "PYTHIA 6.4 Physics and Manual", *JHEP* **05** (2006) 026, arXiv:hep-ph/0603175.

[277] G. D'Agostini, *Bayesian reasoning in high-energy physics: principles and applications*. CERN Yellow Reports: Monographs. CERN, Geneva, 1999. https://cds.cern.ch/record/395902.

[278] G. D'Agostini, "A Multidimensional unfolding method based on Bayes' theorem", *Nucl. Instrum. Meth. A* **362** (1995) 487–498.

[279] G. D'Agostini, "Improved iterative Bayesian unfolding", in *Alliance Workshop on Unfolding and Data Correction*. 10, 2010. arXiv:1010.0632 [physics.data-an].

[280] **ALICE** Collaboration, J. Adam *et al.*, "Transverse momentum dependence of D-meson production in Pb-Pb collisions at $\sqrt{s_{\rm NN}} = 2.76$ TeV", *JHEP* **03** (2016) 081, arXiv:1509.06888 [nucl-ex].

[281] **ALICE** Collaboration, J. Adam *et al.*, "Measurement of the production of high-$p_{\rm T}$ electrons from heavy-flavour hadron decays in Pb-Pb collisions at $\sqrt{s_{\rm NN}}$ = 2.76 TeV", *Phys. Lett. B* **771** (2017) 467–481, arXiv:1609.07104 [nucl-ex].

[282] **ATLAS** Collaboration, G. Aad *et al.*, "Measurements of the electron and muon inclusive cross-sections in proton-proton collisions at $\sqrt{s} = 7$ TeV with the ATLAS detector", *Phys. Lett. B* **707** (2012) 438–458, arXiv:1109.0525 [hep-ex].

[283] R. Averbeck, N. Bastid, Z. C. del Valle, P. Crochet, A. Dainese, and X. Zhang, "Reference Heavy Flavour Cross Sections in pp Collisions at \surd s = 2.76 TeV, using a pQCD-Driven \surd s-Scaling of ALICE Measurements at \surd s = 7 TeV", arXiv:1107.3243 [hep-ph].

[284] **ALICE** Collaboration, S. Acharya *et al.*, "Production of muons from heavy-flavour hadron decays at high transverse momentum in Pb-Pb collisions at $\sqrt{s_{\rm NN}} = 5.02$ and 2.76 TeV", arXiv:2011.05718 [nucl-ex].

[285] **ALICE** Collaboration, J. Adam *et al.*, "Measurement of electrons from heavy-flavour hadron decays in p-Pb collisions at $\sqrt{s_{\rm NN}} = 5.02$ TeV", *Phys. Lett. B* **754** (2016) 81–93, arXiv:1509.07491 [nucl-ex].

[286] **ALICE** Collaboration, J. Adam *et al.*, "Measurement of electrons from beauty-hadron decays in p-Pb collisions at $\sqrt{s_{\rm NN}} = 5.02$ TeV and Pb-Pb collisions at $\sqrt{s_{\rm NN}} = 2.76$ TeV", *JHEP* **07** (2017) 052, arXiv:1609.03898 [nucl-ex].

[287] **ALICE** Collaboration, B. B. Abelev *et al.*, "Measurement of prompt D-meson production in $p - Pb$ collisions at $\sqrt{s_{NN}}$ = 5.02 TeV", *Phys. Rev. Lett.* **113** no. 23, (2014) 232301, arXiv:1405.3452 [nucl-ex].

[288] **ALICE** Collaboration, S. Acharya *et al.*, "Analysis of the apparent nuclear modification in peripheral Pb–Pb collisions at 5.02 TeV", *Phys. Lett. B* **793** (2019) 420–432, arXiv:1805.05212 [nucl-ex].

[289] C. Loizides and A. Morsch, "Absence of jet quenching in peripheral nucleus–nucleus collisions", *Phys. Lett. B* **773** (2017) 408–411, arXiv:1705.08856 [nucl-ex].

[290] **ALICE** Collaboration, S. Acharya *et al.*, "$\Lambda_{\rm c}^{+}$ production in Pb-Pb collisions at $\sqrt{s_{\rm NN}} = 5.02$ TeV", *Phys. Lett. B* **793** (2019) 212–223, arXiv:1809.10922 [nucl-ex].

[291] M. He, R. J. Fries, and R. Rapp, "Heavy-Quark Diffusion and Hadronization in Quark-Gluon Plasma", *Phys. Rev. C* **86** (2012) 014903, arXiv:1106.6006 [nucl-th].

[292] M. He, R. J. Fries, and R. Rapp, "$\mathbf{D_s}$-Meson as Quantitative Probe of Diffusion and Hadronization in Nuclear Collisions", *Phys. Rev. Lett.* **110** no. 11, (2013) 112301, arXiv:1204.4442 [nucl-th].

[293] P. B. Gossiaux, J. Aichelin, T. Gousset, and V. Guiho, "Competition of Heavy Quark Radiative and Collisional Energy Loss in Deconfined Matter", *J. Phys. G* **37** (2010) 094019, arXiv:1001.4166 [hep-ph].

[294] P. B. Gossiaux, M. Nahrgang, M. Bluhm, T. Gousset, and J. Aichelin, "Heavy quark quenching from RHIC to LHC and the consequences of gluon damping", *Nucl. Phys. A* **904-905** (2013) 992c–995c, arXiv:1211.2281 [hep-ph].

[295] M. Djordjevic and M. Djordjevic, "Predictions of heavy-flavor suppression at 5.1 TeV Pb + Pb collisions at the CERN Large Hadron Collider", *Phys. Rev. C* **92** no. 2, (2015) 024918, arXiv:1505.04316 [nucl-th].

[296] M. Djordjevic and M. Djordjevic, "LHC jet suppression of light and heavy flavor observables", *Phys. Lett. B* **734** (2014) 286–289, arXiv:1307.4098 [hep-ph].

[297] M. Gyulassy, P. Levai, and I. Vitev, "Reaction operator approach to nonAbelian energy loss", *Nucl. Phys. B* **594** (2001) 371–419, arXiv:nucl-th/0006010.

[298] M. Cacciari and P. Nason, "Charm cross-sections for the Tevatron Run II", *JHEP* **09** (2003) 006, arXiv:hep-ph/0306212.

[299] V.G. Kartvelishvili and A.K. Likhoded and V.A. Petrov, "On the fragmentation functions of heavy quarks into hadrons", *Physics Letters B* **78** no. 5, (1978) 615–617. https://www.sciencedirect.com/science/article/pii/0370269378906536.

[300] J. Xu, J. Liao, and M. Gyulassy, "Bridging Soft-Hard Transport Properties of Quark-Gluon Plasmas with CUJET3.0", *JHEP* **02** (2016) 169, arXiv:1508.00552 [hep-ph].

[301] J. Xu, A. Buzzatti, and M. Gyulassy, "The tricky azimuthal dependence of jet quenching at RHIC and LHC via CUJET2.0", *Nucl. Phys. A* **932** (2014) 128–133, arXiv:1404.0384 [hep-ph].

[302] J. Uphoff, O. Fochler, Z. Xu, and C. Greiner, "Elastic and radiative heavy quark interactions in ultra-relativistic heavy-ion collisions", *J. Phys. G* **42** no. 11, (2015) 115106, arXiv:1408.2964 [hep-ph].

[303] T. Song, H. Berrehrah, D. Cabrera, W. Cassing, and E. Bratkovskaya, "Charm production in Pb + Pb collisions at energies available at the CERN Large Hadron Collider", *Phys. Rev. C* **93** no. 3, (2016) 034906, arXiv:1512.00891 [nucl-th].

[304] W. Cassing, "Dynamical quasiparticles properties and effective interactions in the sQGP", *Nucl. Phys. A* **795** (2007) 70–97, arXiv:0707.3033 [nucl-th].

[305] A. Beraudo, A. De Pace, M. Monteno, M. Nardi, and F. Prino, "Heavy flavors in heavy-ion collisions: quenching, flow and correlations", *Eur. Phys. J. C* **75** no. 3, (2015) 121, arXiv:1410.6082 [hep-ph].

[306] **ALICE** Collaboration, S. Acharya *et al.*, "First measurement of Ξ_c^0 production in pp collisions at $\sqrt{\mathbf{s}}$ = 7 TeV", *Phys. Lett. B* **781** (2018) 8–19, arXiv:1712.04242 [hep-ex].

[307] **CMS** Collaboration, A. M. Sirunyan *et al.*, "Production of Λ_c^+ baryons in proton-proton and lead-lead collisions at $\sqrt{s_{\mathrm{NN}}} = 5.02$ TeV", *Phys. Lett. B* **803** (2020) 135328, arXiv:1906.03322 [hep-ex].

[308] **LHCb** Collaboration, R. Aaij *et al.*, "Prompt charm production in pp collisions at $\sqrt{(s)}$=7 TeV", *Nucl. Phys. B* **871** (2013) 1–20, arXiv:1302.2864 [hep-ex].

[309] **LHCb** Collaboration, R. Aaij *et al.*, "Study of the production of Λ_b^0 and $\overline{B}^0$ hadrons in pp collisions and first measurement of the $\Lambda_b^0 \to J/\psi p K^-$ branching fraction", *Chin. Phys. C* **40** no. 1, (2016) 011001, arXiv:1509.00292 [hep-ex].

[310] **LHCb** Collaboration, R. Aaij *et al.*, "Measurement of b hadron fractions in 13 TeV pp collisions", *Phys. Rev. D* **100** no. 3, (2019) 031102, arXiv:1902.06794 [hep-ex].

[311] **ALICE** Collaboration, S. Acharya *et al.*, "Measurement of the production cross section of prompt Ξ_c^0 baryons at midrapidity in pp collisions at $\sqrt{s}$ = 5.02 TeV", arXiv:2105.05616 [nucl-ex].

[312] **ALICE** Collaboration, S. Acharya *et al.*, "Measurement of the cross sections of Ξ_c^0 and Ξ_c^+ baryons and branching-fraction ratio $\mathrm{BR}(\Xi_c^0 \to \Xi^- e^+ \nu_e)/\mathrm{BR}(\Xi_c^0 \to \Xi^- \pi^+)$ in pp collisions at 13 TeV", arXiv:2105.05187 [nucl-ex].

[313] **ALICE** Collaboration, S. Acharya *et al.*, "Measurement of prompt D^0, Λ_c^+, and $\Sigma_c^{0,++}(2455)$ production in pp collisions at $\sqrt{s}$ = 13 TeV", arXiv:2106.08278 [hep-ex].

[314] **ALICE** Collaboration, S. Acharya *et al.*, "ALICE 2016-2017-2018 luminosity determination for pp collisions at $\sqrt{s} = 13$ TeV", Tech. Rep. ALICE-PUBLIC-2021-005, CERN, 2021. https://cds.cern.ch/record/2776672/.

[315] **Belle** Collaboration, Y. B. Li *et al.*, "First measurements of absolute branching fractions of the Ξ_c^+ baryon at Belle", *Phys. Rev. D* **100** (Aug, 2019) 031101. https://link.aps.org/doi/10.1103/PhysRevD.100.031101.

[316] **ALICE** Collaboration, J. Adam *et al.*, "Particle identification in ALICE: a Bayesian approach", *Eur. Phys. J. Plus* **131** no. 5, (2016) 168, arXiv:1602.01392 [physics.data-an].

[317] P. Gregory, *Bayesian Logical Data Analysis for the Physical Sciences: A Comparative Approach with Mathematica Support*. Cambridge University Press, 2005.

[318] F. Grosa, "Strange and non-strange D-meson production in pp, p-Pb, and Pb-Pb collisions with ALICE at the LHC", 2020. https://cds.cern.ch/record/2713513. Presented 11 Feb 2020.

[319] Sjöstrand, Torbjörn and Ask, Stefan and Christiansen, Jesper R. and Corke, Richard and Desai, Nishita and Ilten, Philip and Mrenna, Stephen and Prestel, Stefan and Rasmussen, Christine O. and Skands, Peter Z., "An introduction to PYTHIA 8.2", *Comput. Phys. Commun.* **191** (2015) 159–177, arXiv:1410.3012 [hep-ph].

[320] **NA61/SHINE** Collaboration, A. Aduszkiewicz *et al.*, "$K^*(892)^0$ meson production in inelastic p+p interactions at 158 GeV/c beam momentum measured by NA61/SHINE at the CERN SPS", *Eur. Phys. J. C* **80** no. 5, (2020) 460, arXiv:2001.05370 [nucl-ex].

[321] **ALICE** Collaboration, S. Acharya *et al.*, "Multiplicity dependence of π, K, and p production in pp collisions at $\sqrt{s} = 13$ TeV", *Eur. Phys. J. C* **80** no. 8, (2020) 693, arXiv:2003.02394 [nucl-ex].

[322] L. Gladilin, "Fragmentation fractions of c and b quarks into charmed hadrons at LEP", *Eur. Phys. J. C* **75** no. 1, (2015) 19, arXiv:1404.3888 [hep-ex].

[323] **ZEUS** Collaboration, S. Chekanov *et al.*, "Measurement of charm fragmentation ratios and fractions in photoproduction at HERA", *Eur. Phys. J. C* **44** (2005) 351–366, arXiv:hep-ex/0508019.

[324] **ZEUS** Collaboration, H. Abramowicz *et al.*, "Measurement of D^+ and Λ_c^+ production in deep inelastic scattering at HERA", *JHEP* **11** (2010) 009, arXiv:1007.1945 [hep-ex].

[325] **ZEUS** Collaboration, H. Abramowicz *et al.*, "Measurement of charm fragmentation fractions in photoproduction at HERA", *JHEP* **09** (2013) 058, arXiv:1306.4862 [hep-ex].

[326] **ARGUS** Collaboration, H. Albrecht *et al.*, "Observation of the Charmed Baryon $\Lambda(c)$ in e^+e^- Annihilation at 10-GeV", *Phys. Lett. B* **207** (1988) 109–114.

[327] **CLEO** Collaboration, P. Avery *et al.*, "Inclusive production of the charmed baryon Lambda(c) from e+ e- annihilations at s**(1/2) = 10.55-GeV", *Phys. Rev. D* **43** (1991) 3599–3610.

[328] **ARGUS** Collaboration, H. Albrecht *et al.*, "Inclusive production of D0, D+ and D*+ (2010) mesons in B decays and nonresonant e+ e- annihilation at 10.6-GeV", *Z. Phys. C* **52** (1991) 353–360.

[329] M. Faggin, "Heavy-flavour hadron production", 9, 2021. arXiv:2109.09348 [hep-ex].

[330] D. Adamová *et al.*, "A next-generation LHC heavy-ion experiment", arXiv:1902.01211 [physics.ins-det].

[331] **LHCb** Collaboration, R. Aaij *et al.*, "Measurement of $\blacksquare_{cc}^{++}$ production in pp collisions at $\sqrt{s} = 13$ TeV", *Chin. Phys. C* **44** no. 2, (2020) 022001, arXiv:1910.11316 [hep-ex].

[332] **CMS Collaboration** Collaboration, Sirunyan, A. M. and others, "Measurement of $B_c(2S)^+$ and $B_c^*(2S)^+$ cross section ratios in proton-proton collisions at $\sqrt{s} = 13$ TeV", *Phys. Rev. D* **102** (Nov, 2020) 092007. https://link.aps.org/doi/10.1103/PhysRevD.102.092007.

[333] **LHCb** Collaboration, R. Aaij *et al.*, "First branching fraction measurement of the suppressed decay $\Xi_c^0 \to \pi^- \Lambda_c^+$", *Phys. Rev. D* **102** no. 7, (2020) 071101, arXiv:2007.12096 [hep-ex].

[334] A. Hocker *et al.*, "TMVA - Toolkit for Multivariate Data Analysis", arXiv:physics/0703039.

[335] L. Breiman, J. Friedman, R. A. Olshen, and C. J. Stone, *Classification and regression trees*. Chapman and Hall/CRC, 1984.

[336] T. K. Ho, "Random decision forests", in *Proceedings of 3rd International Conference on Document Analysis and Recognition*, vol. 1, pp. 278–282 vol.1. 1995.

[337] Y. Freund and R. E. Schapire, "A decision-theoretic generalization of on-line learning and an application to boosting", *Journal of Computer and System Sciences* **55** no. 1, (1997) 119–139. https://www.sciencedirect.com/science/article/pii/S002200009791504X.

[338] **ALICE** Collaboration, B. Abelev *et al.*, "Upgrade of the ALICE Experiment: Letter of Intent", tech. rep., CERN, Geneva, Aug, 2012. https://cds.cern.ch/record/1475243.

[339] **ALICE** Collaboration, B. Abelev *et al.*, "Technical Design Report for the Upgrade of the ALICE Inner Tracking System", *J. Phys. G* **41** (2014) 087002.

[340] **ALICE** Collaboration, C. Lippmann, "Upgrade of the ALICE Time Projection Chamber",.

[341] "Technical Design Report for the Muon Forward Tracker", tech. rep., Jan, 2015. https://cds.cern.ch/record/1981898.

[342] **ALICE** Collaboration, P. Antonioli, A. Kluge, and W. Riegler, "Upgrade of the ALICE Readout and Trigger System", tech. rep., Sep, 2013. https://cds.cern.ch/record/1603472. Presently we require a LHCC-TDR reference number.At a later stage we will fill the required information.

[343] **ALICE** Collaboration, D. Colella, "ALICE ITS upgrade for LHC Run 3: commissioning in the laboratory", in *International Conference on Technology and Instrumentation in Particle Physics*. 6, 2021. arXiv:2106.16168 [physics.ins-det].

[344] **ALICE** Collaboration, "Expression of Interest for an ALICE ITS Upgrade in LS3",. https://cds.cern.ch/record/2644611.

[345] L. Musa, "Letter of Intent for an ALICE ITS Upgrade in LS3", tech. rep., CERN, Geneva, Dec, 2019. https://cds.cern.ch/record/2703140.

[346] **CMS** Collaboration, A.M. Sirunyan and others, "Measurement of B_s^0 meson production in pp and PbPb collisions at $\sqrt{s_{NN}} = 5.02$ TeV", *Physics Letters B* **796** (2019) 168–190. https://www.sciencedirect.com/science/article/pii/S0370269319304708.

[347] **CMS** Collaboration, "Measurement of B_s^0 and B^+ meson yields in Pb-Pb collisions at $\sqrt{s_{NN}} = 5.02$ TeV", tech. rep., CERN, Geneva, 2020. https://cds.cern.ch/record/2719500.

[348] E. Bruna, A. Dainese, M. Masera, and F. Prino, "Vertex reconstruction for proton-proton collisions in ALICE",. https://cds.cern.ch/record/1225497.

[349] Springer, *The XVIII International Conference on Strangeness in Quark Matter (SQM 2019)*. Springer, Cham, 2019. https://cds.cern.ch/record/2310290. Organisers: Elia, D (INFN Bari, chairman); Bruno, GE (Politecnico Bari); Colangelo, P (INFN Bari); Cosmai, L (INFN Bari); Di Bari, D (University Bari); Fini, RA (INFN Bari); Manzari, V (INFN Bari);.

[350] F.-S. Yu, H.-Y. Jiang, R.-H. Li, C.-D. Lü, W. Wang, and Z.-X. Zhao, "Discovery Potentials of Doubly Charmed Baryons", *Chin. Phys. C* **42** no. 5, (2018) 051001, arXiv:1703.09086 [hep-ph].

Acknowledgements

If I am writing these words at the end of my thesis, it means that my Ph. D. is going to end. I have not realised yet that this long journey made of effort, hard work and downfalls, as well as redemptions and satisfactions is going to be concluded and another chapter of my life is going to be written. At this point, I want to spend few words to acknowledge all the people that played a role during this important period of my life. I must apologise in advance with all those I am going to forget.

My deepest gratitude goes to my supervisors in Padova. I am grateful to Andrea Dainese and Andrea Rossi for the huge work and dedication spent during the last three years to follow and supervise me. Apart from being two outstanding physicists that I will always keep as model, they are both exquisite people from the human point of view. They are always available for discussions, support, suggestions and they taught me a lot. I will never stop thanking them. In the same way, I would really thank Prof. Marcello Lunardon, who met me for the first time when I was a bachelor student and now treats me as a colleague. I will be always grateful to him for the constant presence during all these years and the nice opportunity he gave me recently to interact with young students.

Due to the Covid-19 pandemic my year at CERN was quite unlucky, however I want to thank the CERN group for accepting me and being interested in my activity in 2020. I want to thank Alexander Kalweit for the (unfortunately short) discussions about the strangeness tracking when I was at CERN, and thanks also to David Chinellato for the help in this project. It is really a pity that during this time at CERN I had no chance to work closer also to other people.

Many thanks to the PWGHF and DPG people that I worked with during all these years. Just to mention somebody (it is a very long list, sorry for the others ...): Andrea, Cristina, Francesco, Chiara, Xiaoming, Alessandro, Fabrizio, Xinye (hope to see you soon either at CERN or in Padova!) ...: it was a pleasure to work with you, I hope you appreciated my contribution. Big thanks also to the "Torino crew" (Fabrizio, Fabio, Francesco, Alessandro, Matteo, Max, Ivan, Luca, Luca, Pietro) for the hard work together, as well as the nice moments at CERN (crepes... delicious!). A special thank to Luca Micheletti, for the pleasant living together in Saint-Genis-Pouilly and the funny moments we lived, despite Covid-19.

All the other people in Padova also deserve my gratitude. It was a pleasure to share many meetings with Francesca Soramel, Federico Antinori and Piero Giubilato, with the possibility to look at the ALICE world from different point of views. Many thanks also to Filippo Baruffaldi for being a good mate during the courses and the ITS commissioning activities. A special thank goes then to Rosario Turrisi, who significantly contributes to the welfare of the Padova group with his cheerfulness. Thanks a lot for all the time spent in chatting, eating, drinking, laughing and profitably discussing about everything we had in mind, included physics. Another person that I must thank for the good time spent together in Padova is Stefano Trogolo. He is a friend apart from a colleague, a nice person with whom to nicely work and share doubts, worries and hopes. Don't worry Stefano, I will always remember that life is a matter of "black and white". Thanks a lot also to Cristina Terrevoli, effectively the first person that I encountered in my ALICE life when I was a disoriented student and that I proudly work with closely now. I want to thank then all the other people sharing the corridor of the fourth floor of the Paolotti building, such as Laura, Giorgia, Isacco, Nicolò, Luca, Sandra, Cristiano (the rafting was amazing!): thanks to all for the good moments. Finally, good luck to my old mates Leonardo, Fabio,

Luigi, Emanuele, Davide, Alexandru, Paolo and Federica for their future projects, we had many nice moments when we were students together.

I cannot forget all the people that made my spare time funny and restorative after work. Many thanks to the "Cúculi", in the last years we shared everything and I am really grateful to all of you (sorry if I am always dumb, I hope you can still patiently accept me). Long live to the "LAN" group and the infinite battles fought together (TIL BARDAGÁ!) and to the "Lega Sega PD" for the exciting fanta-football seasons (after > 10 years I finally won!). Many thanks also to the "[...] 3G" team for accepting me despite my questionable football skills (Luigino, sempre in forma!). Thanks to my old friends Barbu, Marci, Tommy, Sara, Gabri, Sorga, that unfortunately I have met too rarely recently, but all the times we stay together is just like when we were children or teenagers. Finally, I want to thank other two people that covered a crucial role during my teenage: thanks to Prof. Alberto Trevisanello, who supported me in a crucial moment in my life in which I was risking to fall down due to my fears, and to Don Francesco Tondello, for giving me healthy values and his friendship.

I cannot conclude this work without being enormously grateful to those people that have been supporting and tolerating me the most during these years. Many thanks to my mother Lina and my father Loris for their patience and presence. They have been believing in me more than I did and were always proud of me despite the several moments in which I was disappointed in my results. I am not sure that I would have reached such a goal alone. Finally, my sweetest thoughts go to Chiara, with the hope that this step will act as a springboard for our life together.

Padova,
September 2021